# Caractérisation des effets de PD-1 sur la synapse immunologique

Noémie Paillon

Université Paris Cité

École doctorale Frontières de l'Innovation en Recherche et Éducation ED 474

*Laboratoire Immunité et Cancer INSERM U932*

# Caractérisation des effets de PD-1 sur la synapse immunologique

Par Noémie Paillon

Thèse de doctorat d'Immunologie

Dirigée par Claire Hivroz
Et par Julien Husson

Présentée et soutenue publiquement le 15 septembre 2023

Devant un jury composé de :

| | |
|---|---|
| **Dr. Claire Hivroz**<br>DR INSERM, Université de Paris | Directrice de thèse |
| **Dr. Julien Husson**<br>Professeur associé HDR, École Polytechnique | Co-Directeur de thèse |
| **Dr. Margot Thomé**<br>Full Professor, Université de Lausanne | Rapportrice |
| **Dr. Loïc Dupré**<br>CR INSERM, Université Toulouse III Paul Sabatier | Rapporteur |
| **Dr. Emmanuel Donnadieu**<br>DR INSERM, Université de Paris | Examinateur |
| **Dr. Kheya Sengupta**<br>DR CNRS, Université Aix Marseille | Examinatrice |

# ABSTRACT

The protein PD-1 is essential for the maintenance of central and peripheral tolerance by inducing inhibitory signals upon interaction with its ligand PD-L1. Expression of PD-1 receptor is induced during T cell activation, and its ligand is present on many tissue-forming cells, such as epithelial, endothelial, but also professional antigen presenting cells. The interaction between PD-1 and PD-L1 inhibits effector functions of T cells, thus preventing the development of autoimmune diseases. In some disease contexts, such as cancer or chronic infections, the persistent presence of an antigen can result in prolonged expression of PD-1 and lead to an exhausted phenotype of T cells that prevents them from eliminating the pathogen. The PD-1/PD-L1 interaction is then deleterious and leads to tumor progression or prevents resolution of a chronic viral infection. Numerous studies have proposed the PD-1/PD-L1 interaction as a therapeutic target for cancer treatment, and monoclonal antibodies preventing this binding have shown significant clinical efficacy. However, these treatments are not effective in some patients, and it is therefore essential to better understand the mechanisms of PD-1-mediated T cell inactivation.

An essential mechanism for efficient T cell activation is the formation of an immunological synapse with an antigen presenting cell. Thus, the objective of my thesis was to characterize the impact of the PD-1/PD-L1 interaction on the formation of an immunological synapse. Specifically, I addressed the following questions:

1. *What are the effects of PD-1 on actin cytoskeleton remodeling at the immunological synapse?* My work has shown that PD-1 inhibits actin remodeling at the immunological synapse. Indeed, it prevents the formation of a dense ring-shaped actin meshwork at the periphery of the contact, and a hypodense zone in the center. The PD-1/PD-L1 interaction also prevents the morphological changes of T cells at the immunological synapse. The results suggest that PD-1/PD-L1 interaction alters the activity of the Arp2/3 complex initiating branched actin polymerization.

2. *What are the implications of these alterations on the effector functions of T cells, in particular on the cytotoxicity of $CD8^+$ T cells?* The absence of the hypodense area in the center of the contact causes a physical barrier preventing the secretion of cytolytic granules. It can be restored by the pharmacological opening of the actin meshwork at the synapse. Thus, the effects of PD-1 on actin may bring a new explanation for the inability of T cells to lyse target cells in the presence of PD-1/PD-L1.

3. *Are these alterations dependent on PD-1 signaling motifs?* The inhibitory effects of PD-1 are generally attributed to its ability to recruit the phosphatase SHP-2 which dephosphorylates key proteins in the TCR and CD28 signaling pathways. By studying the effects of PD-1 mutated on the motifs that recruit SHP-2, I was able to demonstrate that the defects in actin remodeling induced by PD-1 are independent of the signaling motifs. This result is the first report of an SHP-2-independent inhibitory effect of PD-1.

Thus, we report a novel inhibitory effect of PD-1 on T cell actin remodeling at the immunological synapse. This PD-1 inhibitory effect results in an absence of actin clearance at the center of the contact zone, which prevents the secretion of cytolytic granules, and thus the cytotoxic capacity of T cells. This inhibition appears to be independent of PD-1 signaling motifs that allow the recruitment of the SHP-2 phosphatase.

**Keywords:** PD-1, immune synapse, actin remodeling, T lymphocyte

# RESUME

La protéine PD-1 est essentielle au maintien de la tolérance en induisant des signaux inhibiteurs lors de l'interaction avec son ligand PD-L1. Le récepteur PD-1 est exprimé lors de l'activation des lymphocytes T, et son ligand est présent sur de nombreuses cellules formant les tissus, comme les cellules épithéliales, endothéliales, mais également des cellules présentatrices d'antigène professionnelles. L'interaction entre PD-1 et PD-L1 inhibe les fonctions effectrices des lymphocytes T, empêchant ainsi le développement de maladies auto-immunes. Dans certains contextes pathologiques, comme le cancer ou les infections chroniques, la persistante de l'antigène peut entraîner l'expression prolongée de PD-1 et conduire les lymphocytes T à adopter un phénotype d'épuisement qui les empêche d'éliminer des pathogènes. L'interaction PD-1/PD-L1 est alors délétère et entraîne une progression tumorale ou empêche la résolution d'une infection virale chronique. De nombreuses études ont ainsi proposé de cibler l'interaction PD-1/PD-L1 dans le traitement des cancers, et des anticorps monoclonaux empêchant cette liaison ont montré une efficacité clinique notable. Cependant, ces traitements sont inefficaces chez certains patients, et il est donc essentiel de mieux comprendre l'inactivation des lymphocytes T par PD-1.

Un mécanisme essentiel à une activation des lymphocytes T efficace est la formation d'une synapse immunologique avec une cellule présentatrice d'antigène. Ainsi, l'objectif de ma thèse a été de caractériser l'impact de l'interaction PD-1/PD-L1 sur la formation d'une synapse immunologique. Plus précisément, j'ai abordé les questions suivantes :

1. *Quels sont les effets de PD-1 sur le remodelage du cytosquelette d'actine à la synapse immunologique ?* Mon travail a mis en évidence que PD-1 inhibe le remodelage des réseaux d'actine à la synapse immunologique. En effet, il empêche la formation d'un dense réseau d'actine en forme d'anneau en périphérie du contact, et d'une zone hypodense au centre. L'interaction PD-1/PD-L1 empêche également le changement de morphologie des lymphocytes T à la synapse immunologique. Ce mécanisme semble être provoqué par une altération de l'activité du complexe Arp2/3 qui permet la polymérisation de l'actine branchée.

2. *Quelles sont les implications de ces altérations sur les fonctions effectrices des lymphocytes T, en particulier sur la cytotoxicité des lymphocytes T CD8$^+$ ?* L'absence de la zone hypodense au centre du contact provoque une barrière physique empêchant la sécrétion des granules cytolytiques. Cette dernière est restaurée par l'ouverture pharmacologique du réseau d'actine à la synapse. Ainsi, les effets de PD-1 sur l'actine pourraient être une nouvelle cause expliquant l'incapacité des lymphocytes T à lyser les cellules cibles en présence de PD-1/PD-L1.

3. *Est-ce que ces altérations sont dépendantes des motifs de signalisation de PD-1 ?* Les effets inhibiteurs de PD-1 sont généralement attribués à sa capacité à recruter la phosphatase SHP-2 qui déphosphoryle les protéines clé des voies de signalisation du TCR et de CD28. En étudiant les effets de la protéine PD-1 mutée sur les motifs permettant le recrutement de SHP-2, j'ai mis en évidence que les défauts du remodelage d'actine induits par PD-1 sont indépendants de ces motifs. Ce résultat est le premier effet inhibiteur de PD-1 indépendant du recrutement de SHP-2 à être rapporté.

Ainsi, nous mettons en évidence un nouvel effet inhibiteur de PD-1 sur le remodelage de l'actine des lymphocytes T à la synapse immunologique. Cela entraîne une absence de la clairance d'actine au centre de la zone de contact, qui empêche la sécrétion de granules cytolytiques, et donc la capacité cytotoxique des lymphocytes T. Cette inhibition ne dépend pas des motifs de signalisation de PD-1 permettant le recrutement de la phosphatase SHP-2.

**Mots-clés :** PD-1, synapse immunologique, remodelage de l'actine, lymphocyte T

# Table des matières

## Liste des figures

# ABREVIATIONS

| | |
|---|---|
| ADAP | Adhesion and degranulation promoting adaptor protein |
| ADN | Acide désoxyribonucléique |
| ADP | Adénosine diphosphate |
| AMP | Adénosine monophosphate |
| AMPK | AMP-activated protein kinase |
| Arp2/3 | Actin-related protein 2/3 |
| ArpC | Actin-related protein 2/3 complex |
| ATP | Adénosine triphosphate |
| BCR | Récepteur des lymphocytes B |
| CAMKK | Calcium/calmodulin-activated kinase kinase |
| CCR7 | C-C chemokine receptor type |
| CD | Cluster of differentiation |
| Cdc42 | Cell division control protein 42 |
| CMH | Complexe majeur d'histocompatibilité |
| CMHp | Complexe CMH-peptide |
| CPA | Cellule présentatrice d'antigène |
| cSMAC | Central SMAC |
| CTL | Cytotoxic T lymphocyte |
| CTLA-4 | Cytotoxic T-lymphocyte-associated protein 4) |
| DAG | Diacylglycérol |
| DC | Cellule dendritique |
| Dia1 | Diaphanous-1 |
| dSMAC | Distal SMAC |
| F-actine | Actine filamentaire |
| FAD | Flavin adenin dinucleotide |
| FBXO38 | F-box protein 38 |
| FH | Formin homology |
| FLNa | Filamine A |
| FMNL-1 | Formin-like-1 |
| Fut8 | Fucosyltransferase 8 |
| GADS | Grb2-related adaptor downstream of Shc |
| G-actine | Actine globulaire |
| GAPDH | Glycéraldéhyde-3-phosphate déshydrogénase |

| | |
|---|---|
| GDP | Guanosine diphosphate |
| GEF | Guanine nucleotide exchange factor |
| Grb2 | Growth factor receptor-bound protein 2 |
| GTP | Guanosine triphosphate |
| ɣTuRC | ɣ tubulin ring complex |
| HS1 | Hematopoietic lineage cell-specific protein 1 |
| ICAM-1 | Intracellular adhesion molecule-1 |
| ICOS | Inducible T cell costimulator |
| IFN | Interféron |
| Ig | Immunoglobuline |
| IgV | Immunoglobuline variable |
| IL | Interleukine |
| IP3 | Inositol 1,4,5-triphosphate |
| ITAM | Immunoreceptor tyrosine-based activation motif |
| ITIM | Immunoreceptor tyrosine-based inhibitory motif |
| ITK | Interleukin-2-inducible T cell kinase |
| iTreg | Lymphocytes T régulateurs induits |
| ITSM | Immunoreceptor tyrosine-based switch motif |
| Lag-3 | Lymphocyte-activation gene 3 |
| LAT | Linker for activation of T cells |
| LB | Lymphocyte B |
| Lck | Lymphocyte-specific protein tyrosine kinase |
| LFA-1 | Lymphocyte function associated antigen-1 |
| LICOS | Ligand of ICOS |
| LKB1 | Liver kinase B1 |
| LT | Lymphocyte T |
| FH | Formin homology |
| MC | Microcluster |
| MICI | Maladies inflammatoires chroniques de l'intestin |
| MTOC | Microtubule organizing center |
| mTOR | Mammalian target of rapamycin |
| mTORC | Mammalian target of rapamycin complex |
| NADH | Nicotinamide adénine dinucléotide |
| NK | Natural killer |

| | |
|---|---|
| NKT | Natural killer T cell |
| NOD | Non-obese diabetic |
| NPF | Nucleation promoting factor |
| OXPHOS | Oxidative phosphorylation |
| p70S6K | Ribosomal protein S6 kinase beta-1 |
| PD-1 | Programmed cell death protein-1 |
| PDK1 | Phosphoinositide-dependent kinase-1 |
| PD-L1 | Programmed death-ligand 1 |
| PFK-1 | Phosphofructokinase 1 |
| PI3K | Phosphatidylinositol-3 kinase |
| PIP2 | Phosphatidylinositol 4,5-biphosphate |
| PIP3 | Phosphatidylinositol-3-phosphate |
| PKC | Protéine kinase C |
| PLCγ | Phospholipase-C-γ |
| PTP | Protein tyrosine phosphatase |
| pSMAC | Peripheral SMAC |
| Rho | Ras homology family member |
| SEE | *Staphylococcys* enterotoxin E |
| SH2 | Src homology region 2 |
| SHP-1 | Src homology region 2 domain-containing phosphatase-2 |
| SHP-2 | Src homology region 2 domain-containing phosphatase-2 |
| SMAC | Complexe supramoléculaire d'adhésion, supramolecular activation cluster |
| SI | Synapse immunologique |
| TCR | T cell receptor |
| Th | T helper |
| TIGIT | T cell immunoreceptor with Ig and ITIM domains |
| TIL | Lymphocyte T infiltrant une tumeur |
| Tim-3 | T cell immunoglobulin domain and mucin domain 3 |
| Treg | Lymphocyte T régulateur |
| WASP | Wiskott Aldrich syndrom protein |
| WAVE | WASp-family verprolin-homologous protein |
| WCA | WH2 central acidic |
| WH2 | WASP homology domain 2 |
| ZAP-70 | Zeta-chain associated protein-70 |

# PREAMBULE

« *L'Homme est un être sociable* » écrivait Aristote au IV$^{ème}$ siècle avant J-C, sûrement sans avoir la connaissance de l'infime organisation qui nous constitue : le monde cellulaire. Au fil des années et des découvertes scientifiques, cette citation s'est avérée exacte à toutes les échelles. En effet, notre survie dépend d'une coopération hautement organisée entre les cellules constituant notre corps. Le monde cellulaire est composé de multiples acteurs, possédant chacun leur rôle et leur caractère, qui communiquent et interagissent dans notre corps. Le monde cellulaire n'existe qu'à travers les échanges finement codifiés entre différentes familles de cellules, possédant chacune leur propre langage et fonction.

Si nous sommes capables de réfléchir et d'organiser nos pensées, c'est grâce à la collaboration qui prend place au sein de notre système nerveux, qui discute par neurones interposés à l'aide de signaux chimiques ou électriques envoyés par des contacts organisés entre les cellules appelés les synapses. Notre peau nous confère une protection contre les dangers extérieurs grâce à la cohésion de cellules capables d'établir des jonctions puissantes qui constituent une véritable barrière isolante. Enfin, notre système immunitaire patrouille en permanence dans l'intégralité de notre corps pour le défendre contre tous types de pathogènes. Cette garde rapprochée nécessite un lien étroit, établi par des signaux chimiques et des contacts physiques, entre tous ses membres afin de défendre son hôte. Son rôle est de nous maintenir en bonne santé, mais elle peut, en cas de dysfonctionnement, se retourner contre son hôte et déclencher des maladies auto-immunes en attaquant les tissus. Ainsi, une communication extrêmement précise est de mise entre les cellules immunitaires, afin de réguler les réponses.

Les interactions physiques entre les cellules sont régies par leur cytosquelette qui confère une morphologie et un support adaptés à tous types de fonctions. Il permet notamment aux cellules immunitaires de patrouiller dans notre corps par une migration dépendante d'un intense remodelage des différents réseaux de filaments du cytosquelette. Ces réseaux, et plus particulièrement les filaments d'actine, permettent également aux cellules immunitaires d'établir des contacts physiques pour échanger des signaux, communiquer et déclencher une réponse lors de la détection d'un pathogène.

Dans le premier chapitre de l'introduction je présenterai donc les différents réseaux de cytosquelette structurant nos cellules, afin de mieux comprendre leur fonctionnement. Nous verrons ainsi comment ils sont assemblés, et quelles protéines régulent leur polymérisation. Je prendrai un soin particulier à décrire avec plus de détails les éléments essentiels aux fonctions des lymphocytes T qui seront utiles au fil de ce manuscrit.

Au cours de la deuxième partie de l'introduction je présenterai en détail la formation et la structure d'une synapse immunologique, ainsi que la signalisation qui y est associée. Je mettrai ensuite en évidence l'importance du cytosquelette dans la formation de la synapse, et enfin, présenterai l'exemple de la synapse lytique.

Le troisième chapitre de l'introduction aura pour objectif de présenter comment les lymphocytes T puisent de l'énergie selon différents programmes métaboliques distincts afin de soutenir leurs fonctions effectrices. Après avoir présenté quels programmes les lymphocytes T utilisent en fonction de leur stade d'activation, je présenterai les voies de signalisation qui les régulent. Pour finir, je mettrai en évidence le lien entre le cytosquelette et le métabolisme.

Enfin, la quatrième partie de l'introduction présentera la cible d'immunothérapie PD-1. Après avoir mis en évidence l'importance de cette protéine dans l'homéostasie, je présenterai les aspects néfastes qu'elle représente dans un contexte inflammatoire et cancéreux, ainsi que le potentiel thérapeutique qui en résulte. Pour comprendre le fonctionnement de cette voie inhibitrice, je décrirai ensuite sa structure, sa régulation et la voie de signalisation qui en résulte. Enfin, je présenterai les fonctions effectrices des LT inhibées par PD-1, et les premières études mettant en évidence une altération de la synapse immunologique par la protéine.

La partie résultats consiste en deux articles actuellement en révision, résultant de mon travail de thèse. Le premier, qui a fait l'objet de la majeure partie de mon temps et répond aux questions principales de mon projet, porte sur les effets de PD-1 sur la formation de la synapse immunologique. Le second, fruit d'une collaboration, porte sur le changement métabolique qui s'opère dans les lymphocytes T lors de l'activation, et le lien avec le cytosquelette d'actine.

Dans l'ensemble, l'objectif de ce travail de thèse est de caractériser les effets de PD-1 sur la synapse immunologique, et plus particulièrement sur le remodelage du cytosquelette d'actine. Les résultats générés au cours de ce projet permettront en premier lieu de définir plus précisément d'un point de vue fondamental le mécanisme d'inhibition des lymphocytes T par PD-1. Plus largement, ils consolideront les connaissances actuelles et permettront, ensemble, d'améliorer les stratégies thérapeutiques fondées sur la voie PD-1.

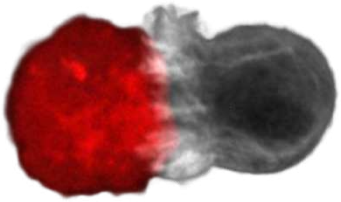

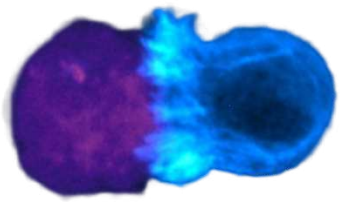

# INTRODUCTION

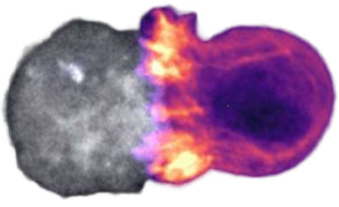

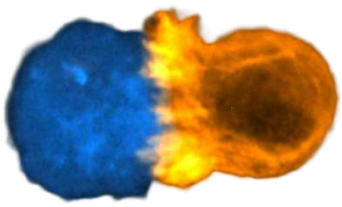

# CHAPITRE 1

## Le cytosquelette des lymphocytes T

Cette première partie de l'introduction a pour objectif de présenter les différents réseaux de cytosquelette structurant nos cellules, et de comprendre leur fonctionnement. Nous verrons ainsi comment ils sont assemblés, et quelles protéines régulent leur polymérisation. Je prendrai un soin particulier à décrire avec plus de détails les éléments essentiels aux fonctions des lymphocytes T qui seront utiles au fil de ce manuscrit.

## 1.1 Les filaments du cytosquelette

Les cellules eucaryotes sont capables d'adapter leur morphologie selon leur environnement ou selon les fonctions qu'elles doivent accomplir. Au repos, les lymphocytes T sont des cellules rondes et symétriques. Dès lors qu'ils entament une migration, ils adoptent une forme élongée polarisée avec un large lamellipode à l'avant et un uropode à l'arrière. Lors de la transmigration endothéliale, le processus par lequel les lymphocytes T migrent à travers les parois des vaisseaux sanguins pour pénétrer dans divers tissus et organes, ils adoptent des formes exiguës qui leur permettent d'accéder aux organes lymphoïdes secondaires. Enfin, ils sont capables d'adopter une forme convexe lorsqu'ils rencontrent une cellule présentatrice d'antigène. Cette importante plasticité est partagée par toutes les cellules eucaryotes et leur est conférée grâce au même réseau de filaments : le cytosquelette.

Le cytosquelette est constitué de trois types de filaments complémentaires, possédant chacun un rôle distinct : **les filaments d'actine** structurent la morphologie et permettent les déformations cellulaires, **les microtubules** régulent la division cellulaire et permettent le transport intracellulaire et la polarisation des organelles et **les filaments intermédiaires** assurent la résistance mécanique des cellules.

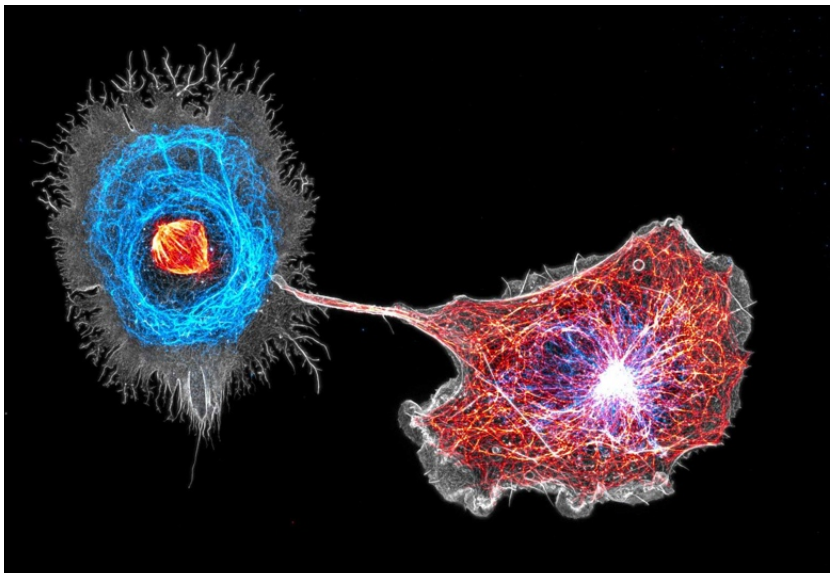

Figure 1 : Réseaux du cytosquelette des cellules COS-7
Gris : actine, rouge : microtubules, bleu : vimentine (filaments intermédiaires)
Crédits : Christophe Leterrier, NeuroCyto, INP, Marseille

**LES FILAMENTS D'ACTINE** ou microfilaments, sont localisés sous la membrane plasmique et confèrent la morphologie et la force de la membrane. La dynamique de croissance des microfilaments permet aux cellules de former des projections telles que des filopodes, minces faisceaux d'actine qui servent d'antennes pour sonder l'environnement, et des lamellipodes, larges extensions membranaires d'actine qui leur permettent d'explorer et de se déplacer. La plasticité conférée aux cellules par les filaments d'actine permet aux lymphocytes T de migrer de la périphérie vers les tissus ou organes lymphoïdes, ainsi que de former des contacts avec les cellules présentatrices d'antigène.

**LES MICROTUBULES** déterminent la position des organelles, dirigent le transport intracellulaire et contrôlent le positionnement des chromosomes pendant la mitose. Assemblés à partir du centrosome, ils forment un réseau en étoile dans le cytoplasme de la cellule. Pendant de la migration des lymphocytes T (LT), le centrosome est positionné dans l'uropode de la cellule. Lors du contact avec une cellule présentatrice d'antigène, le centrosome est polarisé vers la zone de contact et permet la relocalisation des organites essentiels à la sécrétion de cytokines ou de granules cytolytiques.

**LES FILAMENTS INTERMEDIAIRES** confèrent un support mécanique aux cellules. Ce réseau s'étend de l'enveloppe nucléaire, formant une cage qui protège l'ADN de la cellule, jusqu'à la membrane plasmique. Les filaments intermédiaires contrôlent la rigidité des cellules et se positionnent dans l'uropode des cellules en migration.

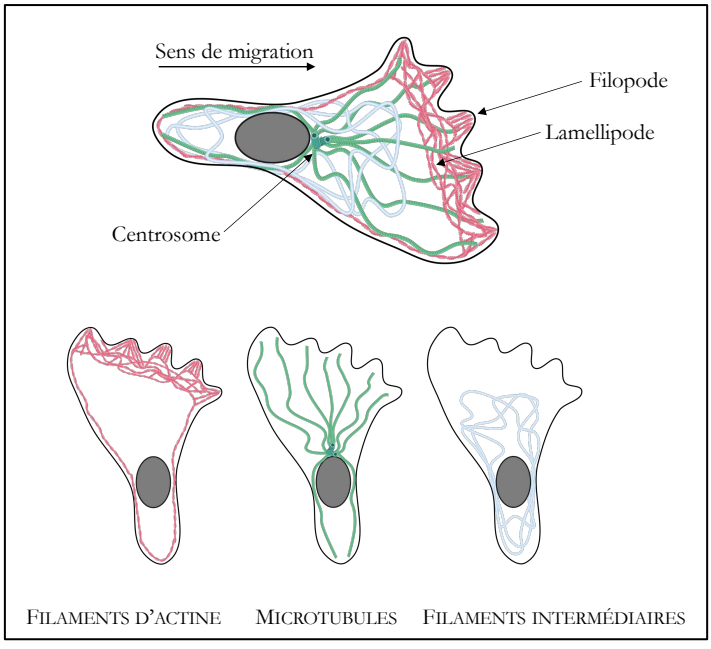


Figure 2: Localisation des différents réseaux du cytosquelette

## 1.2 L'assemblage des filaments de cytosquelette

Les différentes structures du cytosquelette forment des réseaux dans l'intégralité de l'espace disponible d'une cellule, pouvant atteindre jusqu'à plusieurs centaines de micromètres. Pourtant, chaque réseau est constitué de protéines ne mesurant chacune pas plus de quelques nanomètres. Afin de construire ces longs réseaux de cytosquelette, différentes sous-unités sont assemblées pour constituer chaque type de filament.

**LES FILAMENTS D'ACTINE** (F-actine) sont constitués de monomères d'actine globulaire (G-actine). Les molécules de G-actine sont polarisées et s'assemblent en formant deux protofilaments parallèles qui s'enroulent l'un autour de l'autre en une hélice mesurant 7nm. Chaque filament est lui-même polarisé et possède une extrémité dite positive, aussi appelée *barbed end*, et une extrémité négative, ou *pointed end*. Les nouveaux monomères de G-actine liés à l'adénosine triphosphate (ATP) se lient à l'extrémité positive pour allonger le filament, alors que du côté de l'extrémité négative, une dépolymérisation des monomères de G-actine dont l'ATP a été hydrolysée en adénosine diphosphate (ADP) se produit. Il en résulte une polymérisation à l'extrémité positive et une dépolymérisation à l'extrémité négative de manière continue, qui provoque un déplacement du filament d'actine permettant aux cellules de changer de forme et de produire des protrusions pour migrer ou établir des contacts avec d'autres cellules.

**LES MICROTUBULES** sont composés de sous-unités de tubuline α et β formant un hétérodimère α-β. Les sous-unités de tubuline interagissent pour former un protofilament constitué d'interactions α-β longitudinalement, et α-α ou β-β latéralement. Ainsi, en moyenne 13 protofilaments s'assemblent en un tube creux polarisé de 25nm de diamètre formant le microtubule (Gall, 1966). L'assemblage unidirectionnel des hétérodimères de tubuline confère une polarité aux microtubules. La croissance est rapide à l'extrémité positive, alors qu'elle est lente à l'extrémité négative qui est ancrée dans le centrosome. L'énergie de polymérisation et de dépolymérisation des microtubules est fournie par le guanosine triphosphate (GTP) lié aux sous-unités de tubuline. Les sous-unités α et β de la tubuline possédant une activité GTPase, elles hydrolysent le GTP en GDP lors de l'incorporation de nouvelles sous-unités au polymère. Lorsque la majorité des sous-unités de tubuline est liée à du GDP, le microtubule devient instable et se dépolymérise. A l'inverse, l'incorporation de nouvelles tubulines liées au GTP stabilise le microtubule et favorise sa croissance. Les microtubules sont donc des polymères dynamiques oscillant entre des cycles de polymérisation et de dépolymérisation. Lors d'une transition de la polymérisation vers la

dépolymérisation on parle de « catastrophe », alors que la transition inverse est appelée un « sauvetage ».

**LES FILAMENTS INTERMEDIAIRES** peuvent être constitués de différents types de protéines mais partagent une structure commune. Pour l'assemblage, deux dimères enroulés en hélice s'associent de manière antiparallèle et forment une sous-unité tétramérique appelée un protofilament. Un filament intermédiaire est constitué de 8 protofilaments et mesure 10nm de diamètre. L'assemblage et la dissociation des filaments intermédiaires sont des processus plus lents que ceux de l'actine et des microtubules (quelques minutes contre quelques secondes). De ce fait, ce sont des structures plus stables mais moins dynamiques. Les lamines sont des filaments intermédiaires qui renforcent la structure du noyau et permettent d'établir les liaisons entre la chromatine et la membrane nucléaire. Le rôle des filaments intermédiaires est très peu étudié dans les LT. Dans les cellules T circulantes, la vimentine est responsable de la rigidité cellulaire (Brown et al., 2001), l'adhésion et la migration trans-endothéliale (Nieminen et al., 2006).

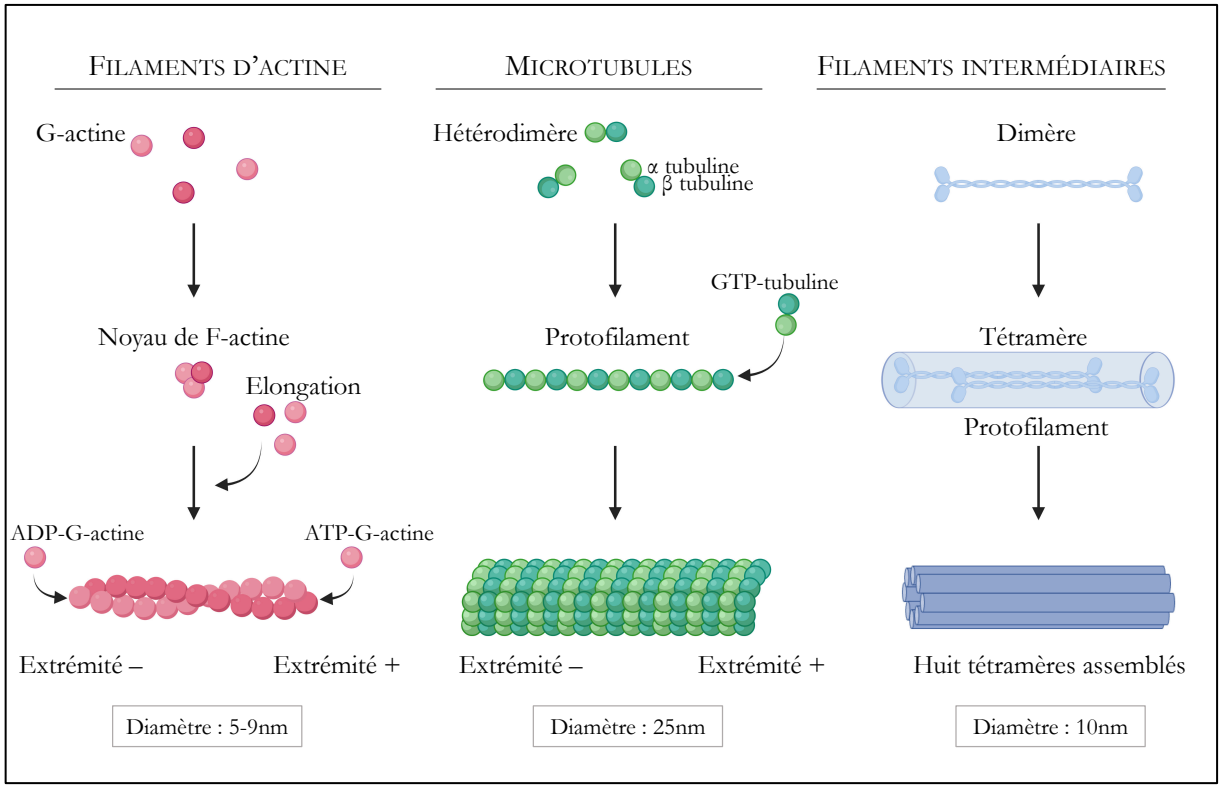


Figure 3 : Assemblage des filaments du cytosquelette

## 1.3 Les protéines de nucléation

Les filaments de cytosquelette peuvent donc se polymériser simplement en assemblant des sous-unités de polymères. Sans régulation de ce processus, l'intégralité des monomères serait consommée et les cellules seraient remplies de filaments non organisés. Pourtant, les cellules sont constituées de structures de cytosquelette hautement organisées, et sont capables d'établir une polarité et des cycles de polymérisation de filaments selon leurs besoins, puisque 50% de l'actine est conservée sous forme de monomère dans une cellule au repos (Dominguez and Holmes, 2011). Ce contrôle rigoureux de la localisation, de l'organisation et de la croissance des filaments de cytosquelette est effectué par des protéines qui interagissent avec les sous-unités et les filaments de cytosquelette.

Les filaments d'actine et les microtubules s'allongent à partir d'un noyau constitué de plusieurs monomères. Pourtant, l'association de monomères de G-actine ou de tubuline forme des noyaux très instables qui ne peuvent pas être suffisamment maintenus pour générer un filament. C'est pourquoi des protéines de nucléation interviennent, afin de stabiliser les noyaux formés ou de servir de modèle pour l'assemblage d'un nouveau filament.

**LES FILAMENTS D'ACTINE** sont nuclées à partir d'un noyau constitué de trois monomères de G-actine grâce à deux familles de protéines de nucléation : le complexe Arp2/3 et les formines.

- **Le complexe Arp2/3** est à l'origine de la nucléation de réseaux d'actine branchée qui exercent des forces permettant la motilité, le trafic vésiculaire et la scission membranaire. Arp2/3 se fixe sur un filament d'actine préexistant, appelé le filament mère, et favorise la nucléation d'un nouveau brin, le filament fille, avec un angle de 70° par rapport au premier (Mullins et al., 1998). Ce complexe est constitué de sept sous-unités comprenant les protéines liées à l'actine Arp2 et Arp3, ainsi que cinq autres sous-unités ArpC1 à ArpC5. Les protéines Arp2 et Arp3 servent de pseudo-actine durant la nucléation, alors que les cinq autres sous-unités tiennent les protéines Arp ensemble et permettent les interactions avec le filament mère (Fäßler et al., 2020). Lorsque le complexe est seul, il est dans une conformation qui le maintient inactif, où les protéines Arp sont dissociées. Pour son activation, des protéines favorisant la nucléation appelées *nucleating protein factors* (NPF) se lient au complexe Arp2/3 et modifient sa conformation pour que les protéines Arp soient disposées comme un filament, en conformation dite *short-pitch* (Espinoza-Sanchez et al.,

2018). Les NPF établissent également un lien entre les monomères de G-actine et le complexe Arp2/3 pour permettre la nucléation de nouveaux filaments d'actine. Une fois les réseaux d'actine branchée polymérisés, ils sont stabilisés par la cortactine, une autre protéine NPF.

Dans les LT, le complexe Arp2/3 est associé à la formation d'un dense lamellipode d'actine branchée à l'avant des cellules qui migrent et en périphérie de la zone de contact avec les cellules présentatrices d'antigène (CPA). Les réseaux d'actine branchée sont stabilisés par l'homologue hématopoïétique de la cortactine, la protéine HS1, qui se lie à WASP, induit l'activité du complexe Arp2/3 et stabilise les filaments d'actine branchée (Gomez et al., 2006). En régulant la formation du lamellipode, Arp2/3 est essentiel à la migration des LT (Obeidy et al., 2020). Ce complexe est également clé pour leur activation, car il permet le maintien des récepteurs de lymphocytes T (TCR) à la surface (Zhang et al., 2017), et régule la formation d'une protrusion qui leur permet d'exercer des forces sur les CPA (Basu et al., 2016 ; Zucchetti et al., 2021). Ces forces sont essentielles à la cytotoxicité des LT (Randzavola et al., 2019). Au-delà des forces qu'il exerce, le réseau d'actine dépendant d'Arp2/3 contrôle également la sécrétion de granules cytolytiques puisque son inhibition locale au centre de la zone de contact offre une zone permissive aux échanges entre le LT et la cellule cible (Ritter et al., 2015).

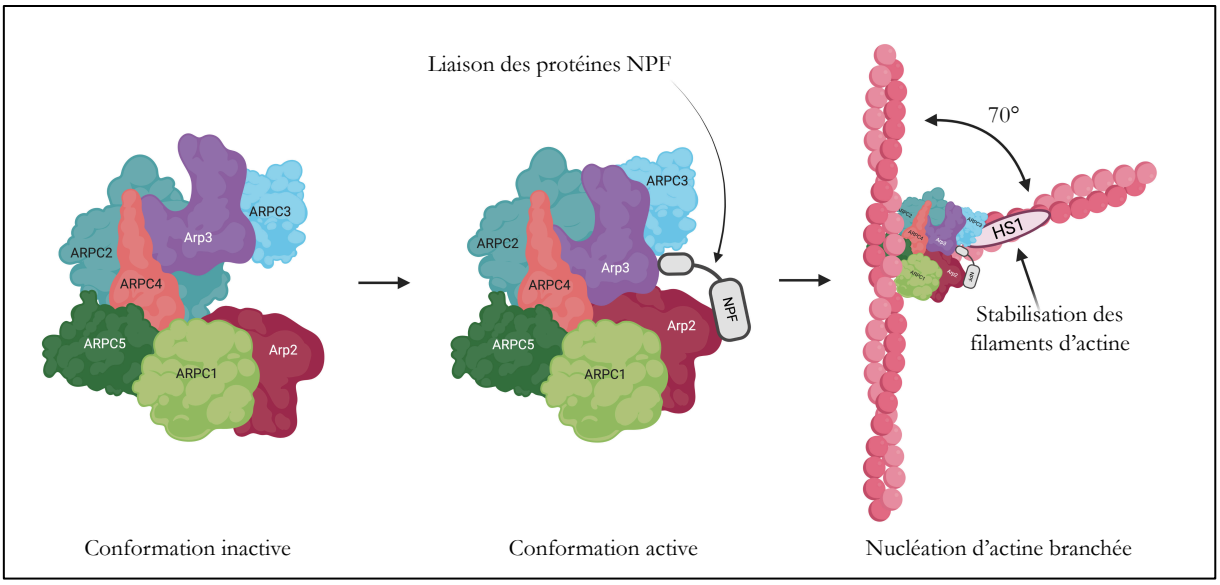


Figure 4 : Le complexe Arp2/3

- **Les protéines de la famille WASP** sont des protéines NPF possédant un domaine riche en proline en C-terminal et un domaine WH2 central acide (WCA). Les régions riches en proline permettent le recrutement d'actine pour alimenter la croissance d'un nouveau filament, alors que la région WCA est essentielle pour activer le complexe Arp2/3 (Padrick et al., 2011). Les protéines de la famille WASP (*Wiskott-Aldrich syndrome protein*) sont impliquées dans différentes fonctions : N-WASP régule l'endocytose, WAVE (*WASP-family verprolin-homologous protein*) est impliquée dans la formation de protrusions et la migration, WASP est essentielle à la formation de la synapse immunologique. Les protéines de la famille WASP activent toutes le complexe Arp2/3, mais sont elles-mêmes activées par différents facteurs. En effet, la protéine WASP est activée par la RhoGTPase Cdc42 (Symons et al., 1996), alors que l'activation de WAVE dépend de Rac (Lebensohn and Kirschner, 2009).

Dans les LT, WASP a d'abord été identifiée comme étant impliquée dans l'assemblage de la synapse immunologique (Dupré et al., 2002). Plus tard, il a été mis en évidence que WASP est surtout impliquée dans la stabilisation de la synapse (Sims et al., 2007), et que les LT de patients WAS rencontrant des CPA forment des kinapses instables plutôt que des synapses (Calvez et al., 2011). Cette incapacité à former des synapses immunologiques matures empêche une activation efficace des LT, et notamment la capacité cytotoxique des LT $CD8^+$. En effet, les cellules des patients WAS présentent une activité cytotoxique réduite malgré la conservation de leur capacité à sécréter des granules lytiques (De Meester et al., 2010). WASP et Arp2/3 jouent également un rôle dans l'activation des LT en favorisant la formation de denses foci d'actine associés aux microclusters de TCR, qui servent de plateforme pour l'organisation du signalosome de TCR (Kumari et al., 2015). Ces foci d'actine représentent également une structure qui permet aux LT d'interagir avec des CPA et d'exercer des forces sur ces dernières. En l'absence de WASP, l'assemblage des foci d'actine et la phosphorylation de la protéine mécano sensible CasL sont nettement diminués, suggérant une implication de WASP dans l'exertion de tensions membranaires (Kumari et al., 2020). Il a également été mis en évidence que WASP permet la liaison de nombreuses protéines clé de l'activation par le TCR au cytosquelette d'actine (Ditlev et al., 2019).

- **Les formines** sont des protéines homodimériques localisées à la membrane plasmique, qui initient la nucléation de filaments d'actine. A l'inverse du complexe Arp2/3, les formines interagissent avec l'extrémité positive des filaments d'actine. Elles possèdent un domaine FH2 qui sert de site d'ancrage et de modèle, et d'un long domaine FH1 qui capture les monomères de G-actine et les transfère au domaine FH2 (Pollard, 2016). Les formines favorisent l'allongement de filaments d'actine préexistants en éliminant les protéines de coiffe de l'extrémité positive et en formant un anneau autour des sous-unités d'actine. Elles permettent l'extension de filaments d'actine non branchés dont l'intégrité structurelle est conservée grâce à leur maintien par les fascines (Yang and Svitkina, 2011). Les filaments d'actine linéaires résultant d'une polymérisation dépendante des formines permet de former des fibres de stress, des filopodes et l'anneau de cytokinèse.

Dans les LT, les formines Diaphanous-1 (Dia1) et Formin-like-1 (FMNL1) contrôlent la polarisation du centrosome (Gomez et al., 2007) et de la kinase essentielle à l'activation par le TCR, ZAP-70 (Thumkeo et al., 2020)à la synapse immunologique. FMNL1 permet la migration des LT effecteurs aux sites inflammatoires par une polymérisation d'actine à l'arrière de la cellule qui permet le passage du noyau à travers les barrières physiques des organes secondaires lymphoïdes (Thompson et al., 2020).

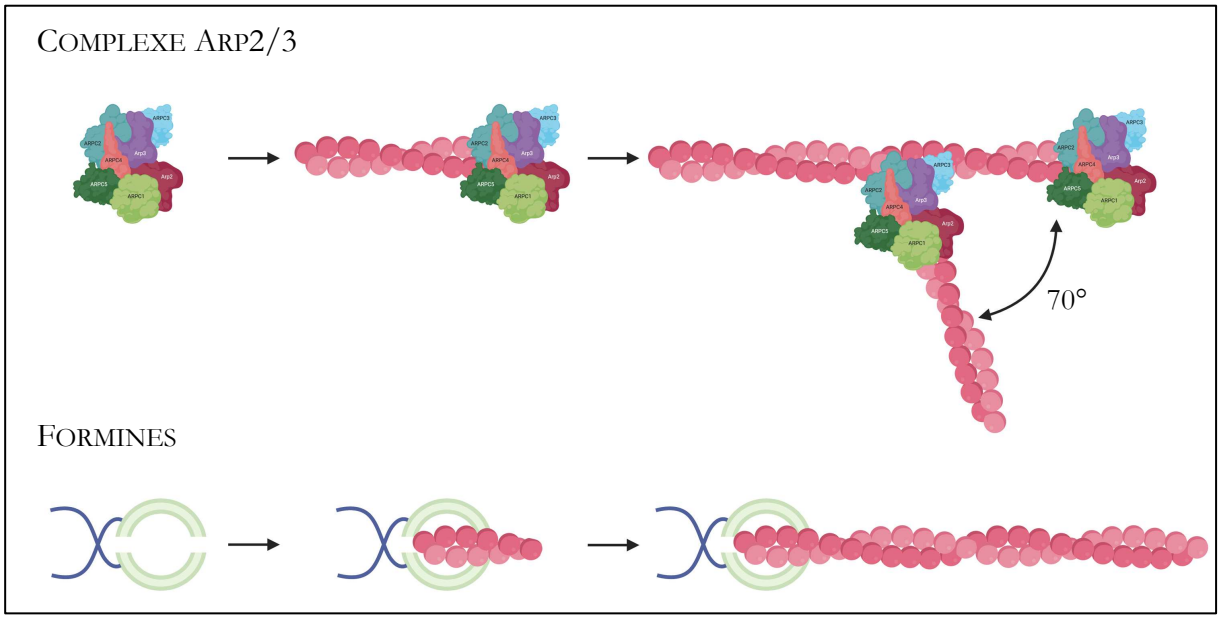


Figure 5 : Nucléation de filaments d'actine par le complexe Arp2/3 et les formines

La quantité de monomères de G-actine disponibles pour la création de nouveaux filaments dans une cellule T au repos est limitante, ce qui génère une compétition entre le complexe Arp2/3 et les formines pour l'accès aux monomères. Ainsi, il a été démontré que l'inhibition d'Arp2/3 entraîne une très forte augmentation de la quantité de structures d'actine dépendantes des formines, et vice versa en cas d'inhibition des formines (Lomakin et al., 2015). Pour que l'assemblage de l'actine puisse continuer, des monomères de G-actine doivent donc être continuellement libérés par le désassemblage des filaments d'actine. L'acteur principal du désassemblage des filaments d'actine est la protéine **cofiline** (Kanellos and Frame, 2016). C'est pour cette raison que les signaux qui entraînent l'assemblage d'actine dépendant d'Arp2/3 en aval de WAVE (le principal consommateur de monomères) entraînent également l'activation de la cofiline (Roybal et al., 2016). Sans le renouvellement des filaments par la cofiline, l'assemblage des microfilaments ralentirait rapidement, car Arp2/3 serait privé de monomères.

**LES MICROTUBULES** sont nuclées à partir d'un unique centre organisateur des microtubules (MTOC) : le centrosome. Une polymérisation spontanée sans intervention de protéines de nucléation est possible, mais elle requiert beaucoup d'énergie aux cellules (Kuchnir Fygenson et al., 1995). Dans des cellules non polarisées, le centrosome est localisé au centre et est constitué de deux centrioles qui sont eux-mêmes composés de courts microtubules, entourés d'une matrice appelée le matériel péricentriolaire. Les complexes de nucléation sont constitués de tubuline ɣ, une troisième forme de tubuline, associée à des *ɣ complex proteins*. Ensemble, ce complexe forme un anneau appelé le *ɣ tubulin ring complex* (ɣTuRC). Sa forme caractéristique impose la structure cylindrique des microtubules (Moritz et al., 2000). Les microtubules s'allongent à partir du centrosome, avec leur extrémité négative attachée au ɣTuRC en une structure en forme d'étoile appelée aster.

Dans les LT, le positionnement du centrosome lors du contact avec une CPA permet le transport de vésicules contenant des molécules effectrices vers la CPA et leur sécrétion polarisée (Stinchcombe et al., 2006).

## 1.4 Les moteurs moléculaires

Après la polymérisation des filaments et la régulation de leur croissance et de leur structure, un autre type de protéines se liant aux filaments de cytosquelette entre en jeu pour leur permettre des déplacements : les moteurs moléculaires. Les moteurs moléculaires interagissent avec les filaments polarisés et se déplacent le long des filaments grâce à des réactions d'hydrolyse de l'ATP qui leur permettent de s'accrocher et de se décrocher des filaments. Il existe différentes sortes de moteurs moléculaires, qui diffèrent dans leur habilité à transporter des cargos, leur vitesse et leur directionalité. Il existe deux types de moteurs moléculaires : les moteurs processifs et non processifs (Howard, 1997). Les moteurs processifs ont la capacité d'effectuer plusieurs pas avant de se détacher du filament, et un seul moteur est suffisant pour transporter un cargo sur une distance importante. Des exemples notables sont les kinésines, les myosines V et VI, et les dynéines. Les moteurs non-processifs se dissocient des filaments après chaque pas, mais peuvent toutefois déplacer des charges sur de longues distances lorsqu'ils coopèrent en grand nombre. Les moteurs non processifs les plus étudiés sont les myosines musculaires et les dynéines des axonèmes.

- **Les myosines** confèrent aux cellules leur contractilité et leur permettent de générer des forces mécaniques. Elles ont d'abord été identifiées comme étant à l'origine de la contractilité musculaire. Ces moteurs moléculaires se déplacent sur les filaments d'actine en direction de l'extrémité positive. Les myosines sont capables de convertir l'énergie chimique stockée dans l'ATP, en énergie mécanique, générant un mouvement et de la force. Les myosines ne sont pas seulement utiles à la contraction musculaire, mais également au mouvement de cellules non musculaires, comme pour la division cellulaire ou la motilité.

  La myosine la plus étudiée dans les LT est la myosine IIA. Cette longue protéine formée de deux hélices α entremêlées en *coiled-coil* possédant chacune une tête globulaire en N-terminal contient la machinerie responsable à la production de forces. Lors de l'activation des LT, la myosine IIA MyH9 est essentielle à la formation de la synapse immunologique où elle permet la génération de forces (Kumari et al., 2012). Les LT expriment également la myosine I Myo1g, qui maintient la tension de membrane essentielle à la migration et à l'interaction entre les cellules (Gérard et al., 2014).

- **Les kinésines** sont des protéines motrices qui se déplacent le long des microtubules. Leur structure est similaire à la myosine II puisqu'elles possèdent deux domaines moteurs à tête

globulaire et une longue queue *coiled-coil*. Les kinésines se déplacent vers les extrémités positives des microtubules et possèdent un site de liaison pour un organelle membranaire dans la queue.

Dans les LT, la kinésine 4 contrôle la croissance des microtubules et la polarisation du centrosome vers la synapse immunologique (Hooikaas et al., 2020). La motilité des granules lytiques des lymphocytes T cytotoxiques vers la synapse immunologique est dépendante de la kinésine 1 (Burkhardt et al., 1993 ; Kurowska et al., 2012). La kinésine 7 est un moteur ciliaire nécessaire au développement des LT (Lau et al., 2017). Malgré l'absence de cil primaire dans les LT, ils expriment des composants de la machinerie de transport ciliaire, impliqués dans la synapse immunologique (Finetti et al., 2014).

- **Les dynéines** se déplacent vers l'extrémité négative des microtubules et sont composées de deux chaînes lourdes capables de lier l'ATP et les microtubules, et de 4 chaînes légères qui lient des vésicules ou des organites cellulaires.

Dans les LT, la dynéine est recrutée à la synapse immunologique (Combs et al., 2006) et contribue à la polarisation du centrosome (Martín-Cófreces et al., 2008) en tirant sur les microtubules pour repositionner le centrosome à la synapse. Le recrutement de la dynéine dépend de l'accumulation polarisée du second messager lipidique diacylglycérol (DAG) et de la protéine kinase C (PKC) (Liu et al., 2013). Ces deux facteurs coordonnent à la fois la polarisation des dynéines et la clairance d'actine au centre de la synapse immunologique (Sanchez et al., 2019), qui permet aux dynéines de former des groupes (Gros et al., 2021).

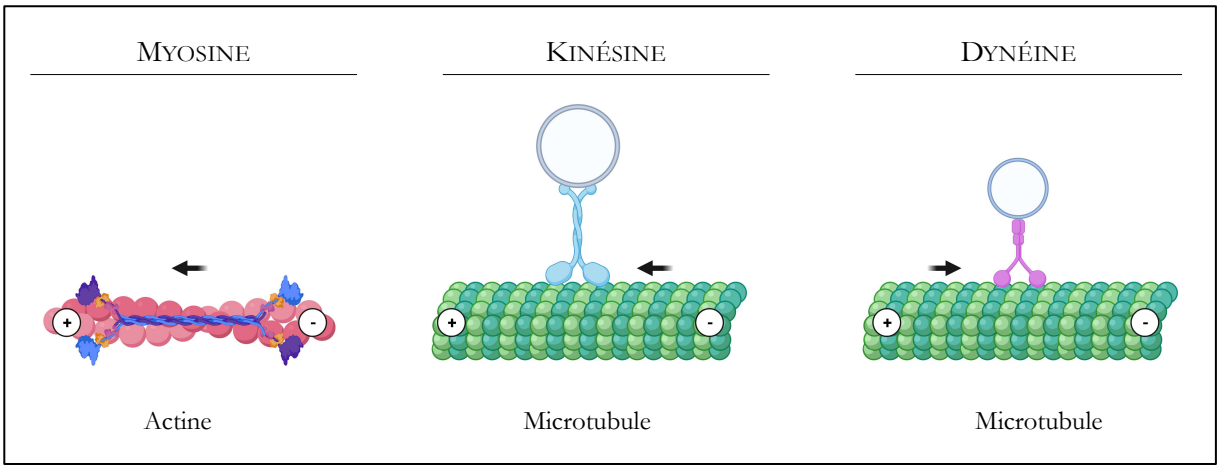


Figure 6 : Les moteurs moléculaires

# CHAPITRE 2

## La synapse immunologique

Dans cette deuxième partie de l'introduction je présenterai en détail la formation et la structure d'une synapse immunologique, ainsi que la signalisation qui y est associée. Je mettrai ensuite en évidence l'importance du cytosquelette dans la formation de la synapse, et enfin, présenterai l'exemple de la synapse lytique.

## 2.1 Formation de la synapse immunologique

L'activation des LT joue un rôle essentiel dans les réponses immunes adaptatives. Elle est induite par l'interaction entre les récepteurs des LT (TCR) et leurs ligands, les complexes d'histocompatibilité majeure liés à un peptide (CMHp), présents sur les cellules présentatrices d'antigène (CPA). L'interaction entre un LT et une CPA établit une zone de contact hautement organisée dans le temps et l'espace, que l'on appelle la synapse immunologique (SI). Cette structure a été décrite pour la première fois en 1984 comme une zone d'accumulation des TCR et d'autres molécules accessoires entre les deux cellules, permettant la reconnaissance de l'antigène présenté et l'activation du LT (Norcross, 1984). Quelques années plus tard, la SI a été définie selon une architecture moléculaire permettant la reconnaissance d'antigène et la signalisation. Les récepteurs et les molécules d'adhésion sont hautement organisés pour permettre une activation efficace des LT (Grakoui et al., 1999 ; Monks et al., 1998).

Le développement des LT prend place dans le thymus, puis les cellules matures rejoignent la circulation sanguine. En absence de pathogènes, les LT naïfs migrent entre le sang et les organes lymphoïdes secondaires à la recherche d'antigènes. Dans les zones T des ganglions, les LT interagissent avec des cellules dendritiques (DC) (Memel et al., 2004). Les LT peuvent également interagir avec des lymphocytes B (LB) dans les ganglions. Ces interactions sont essentielles aux fonctions des LB puisqu'elles permettent leur prolifération et leur maturation en cellules plasmocytes ou en LB mémoires. Ces premières rencontres d'antigènes du soi présentés par des CPA pré-activent les LT et les rendent fonctionnels pour reconnaître et éliminer des pathogènes.

Lors du développement des LT dans le thymus, les clones possédant un TCR capable de reconnaître un antigène associé à une infection ou à d'autres facteurs perturbant l'homéostasie comme le cancer, sont sélectionnés. Les LT expriment un TCR hautement polymorphique, capable de reconnaître des peptides liés à des protéines membranaires du CMH. Les protéines présentes dans le cytoplasme des cellules sont présentées sur le CMH de classe I par toutes les populations cellulaires, alors que les protéines qui restent dans des endosomes ou des lysosomes sont présentées par des molécules de CMH de classe II par des CPA professionnelles. Le TCR et ses ligands ne mesurant que 7,5nm, les membranes du LT et de la CPA doivent se rapprocher à 13nm l'une de l'autre pour la reconnaissance de l'antigène (Garboczi et al., 1996). Ainsi, la formation d'une SI hautement organisée dans le temps et l'espace est essentielle à l'activation des LT.

Dans la circulation, les LT sont ronds et non polarisés. Ils présentent alors de petites projections flexibles appelées *microvillis* ou microvillosités, constituées de nombreux faisceaux parallèles de filaments d'actine qui prolongent la membrane cellulaire et forment des sortes de doigts. Les microvillosités ont d'abord été montrés comme étant essentiels à la phase initiale de l'extravasation des LT, car ils sont recouverts de molécules d'adhésion, ce qui permet aux LT de s'attacher et de rouler sous un flux physiologique (von Andrian et al., 1995). Plus récemment, une approche de microscopie à super résolution a permis de mettre en évidence que les TCR sont regroupés au bout des microvillosités (Jung et al., 2016), mettant en évidence que ces projections de surface sont des senseurs efficaces qui permettent aux LT de scanner rapidement la surface des CPA ou des cellules cibles pour y trouver des motifs antigéniques (Cai et al., 2017). Enfin, les LT peuvent déposer des particules dérivées des microvillosités contenant des TCR à la surface des CPA activatrices qui présentent des antigènes. Ces particules sont enrichies en molécules d'adhésion et en cytokines qui permettent l'activation des DC, et il a donc été proposés que les microvillosités constituent également des « synaptosomes immunologiques », capables de transmettre des messages d'activation aux CPA (Kim et al., 2018).

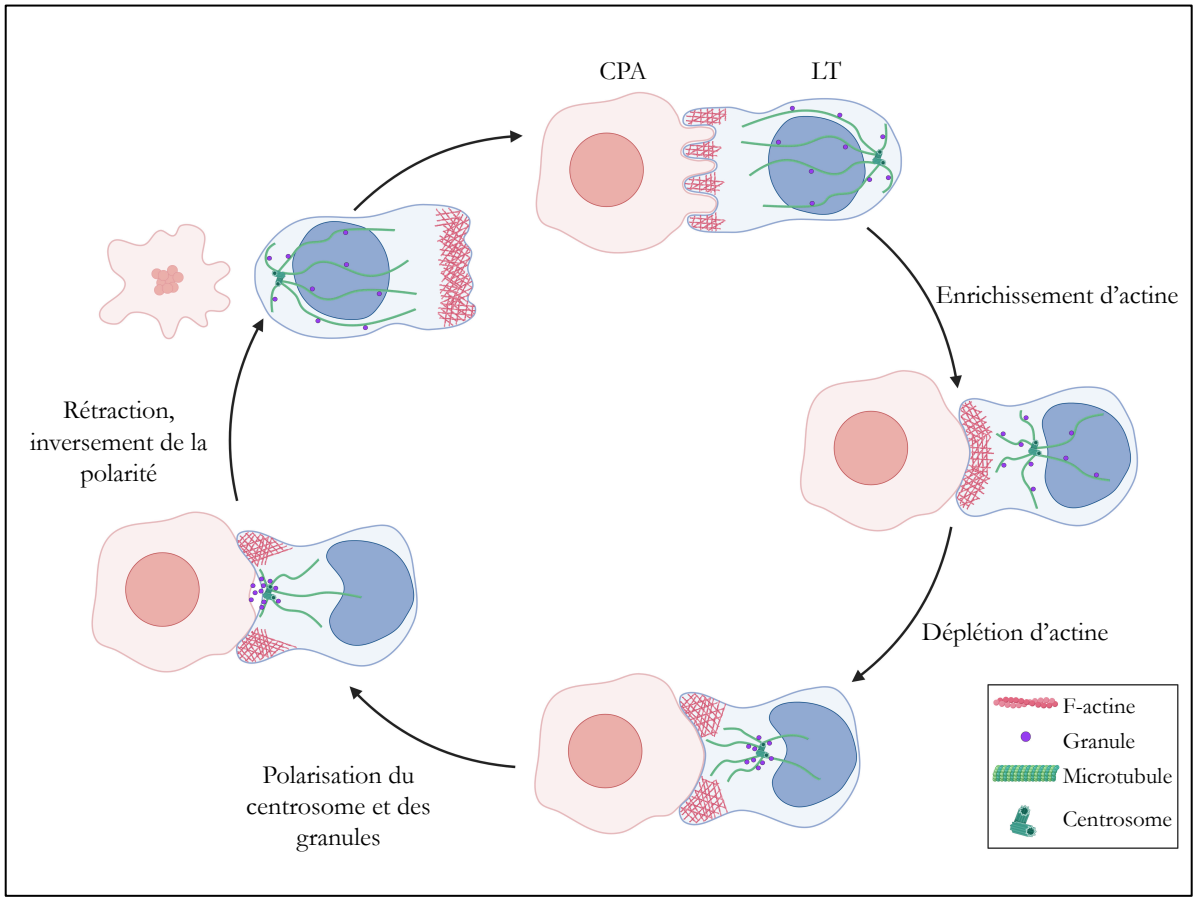


Figure 7 : Les événements de la formation d'une synapse immunologique
Schéma inspiré de la revue (Douanne and Griffiths, 2021)

Lors d'une infection, la présence de chimiokines induit une polarisation qui permet la migration et l'extravasation des LT vers les organes lymphoïdes secondaires. L'exposition aux chimiokines active également des molécules d'adhésion comme LFA-1 (*leukocyte function-associated antigen-1)*. Les cellules T polarisées présentent un lamellipode riche en F-actine à l'avant avec les microvillosités au bout, et un uropode riche en myosine II à l'arrière. Lors de la migration, le centrosome est positionné dans l'uropode des LT (Dustin et al., 1997). L'engagement du TCR inverse la polarité des LT et augmente leur adhésion, ce qui provoque une décélération puis finalement l'arrêt des LT sur les CPA.

Le premier contact avec la CPA se fait par de longues projections à l'avant des LT, formant un contact initial interdigité (Jenkins et al., 2014 ; Sanderson and Glauert, 1979). Ces projections riches en actine s'aplatissent rapidement pour obtenir un contact étendu entre le LT et la CPA. Lors de la formation d'une synapse entre un LT et une CPA, le centrosome est transloqué au centre de la zone de contact (Geiger et al., 1982). Cette réorientation permet dans la plupart des cas une sécrétion dirigée des granules cytolytiques par les LT $CD8^+$ cytotoxiques (Stinchcombe et al., 2006), et de certaines cytokines par les LT $CD4^+$ auxiliaires (Huse et al., 2006).

Enfin, une zone hypodense en actine se forme au centre du contact pour permettre l'échange de cytokines et de granules (Ritter et al., 2015). A la fin du contact, l'actine est relocalisée au centre et arrête ainsi la sécrétion (Ritter et al., 2017), puis le centrosome est à nouveau transloqué vers l'uropode.

## 2.2 Architecture de la synapse immunologique

La formation d'une interaction stable entre un LT et une CPA est contrôlée par une organisation spatiotemporelle précise permettant l'activation des LT. De nombreuses molécules sont réorganisées à la zone de contact pour permettre une activation optimale. Les LT sont capables de former différents types de synapses immunologiques en fonction de leur stade de développement et des CPA qu'ils rencontrent. L'architecture particulière de chaque synapse immunologique sera décrite dans cette section pour constituer la fondation de la partie suivante qui décrira plus en détail la signalisation qui y est associée.

**LA SYNAPSE CONCENTRIQUE** est la première organisation de molécules à avoir été décrite dans un contact entre des LT et des LB (Monks et al., 1998) ou une bicouche lipidique (Grakoui et al., 1999). Ce type de synapse s'établit entre des LT et des LB ou des DC matures. La synapse concentrique s'organise en différents groupements structurés de molécules, notamment des récepteurs antigéniques et des molécules d'adhésion, formant des zones appelées des *supramolecular activation clusters* (SMAC). Ces synapses sont également appelées synapses de Kupfer ou synapses en œil de bœuf en raison de leur structure. En effet, elles s'organisent en trois régions dans lesquelles les molécules membranaires sont ségrégées (Monks et al., 1998) :

- **Le *central* SMAC (cSMAC)** est une zone centrale où le réseau d'actine est hypodense (Carisey et al., 2018), dans laquelle sont regroupés les complexes de TCR-CD3 et les protéines qui s'y associent avant d'être internalisés, ainsi que les molécules de costimulation positives comme CD28 ou négatives comme PD-1 (Yokosuka et al., 2012). Le cSMAC détermine aussi la polarisation du centrosome par l'intermédiaire de la position du diacylglycérol (DAG) qui forme un gradient centré au cSMAC (Quann et al., 2009 ; Spitaler et al., 2006).

- **Le *peripheral* SMAC (pSMAC)** est une zone périphérique qui entoure le cSMAC, enrichie en molécules d'adhésion comme l'intégrine LFA-1. Elle contient également des protéines associées au cytosquelette qui forment le réseau d'actomyosine. Ensemble, les molécules d'adhésion et l'actomyosine permettent la stabilisation de la synapse.

- **Le *distal* SMAC (dSMAC)** est une zone distale autour du pSMAC où un lamellipode d'actine filamenteuse branchée se forme, et où se localisent des molécules exclues de la SI en raison de leur encombrement stérique, comme les phosphatases CD43 et CD45 (Dustin, 2014). C'est également une zone dans laquelle se forme une corolle de CD2, une protéine qui amplifie l'adhésion et la signalisation (Demetriou et al., 2020). La signalisation du TCR commence dans le dSMAC puisque les *microclusters* de TCR/CD28 s'y forment avant de ségréger dans le cSMAC où les TCR sont ensuite internalisés (Cassioli and Baldari, 2022).

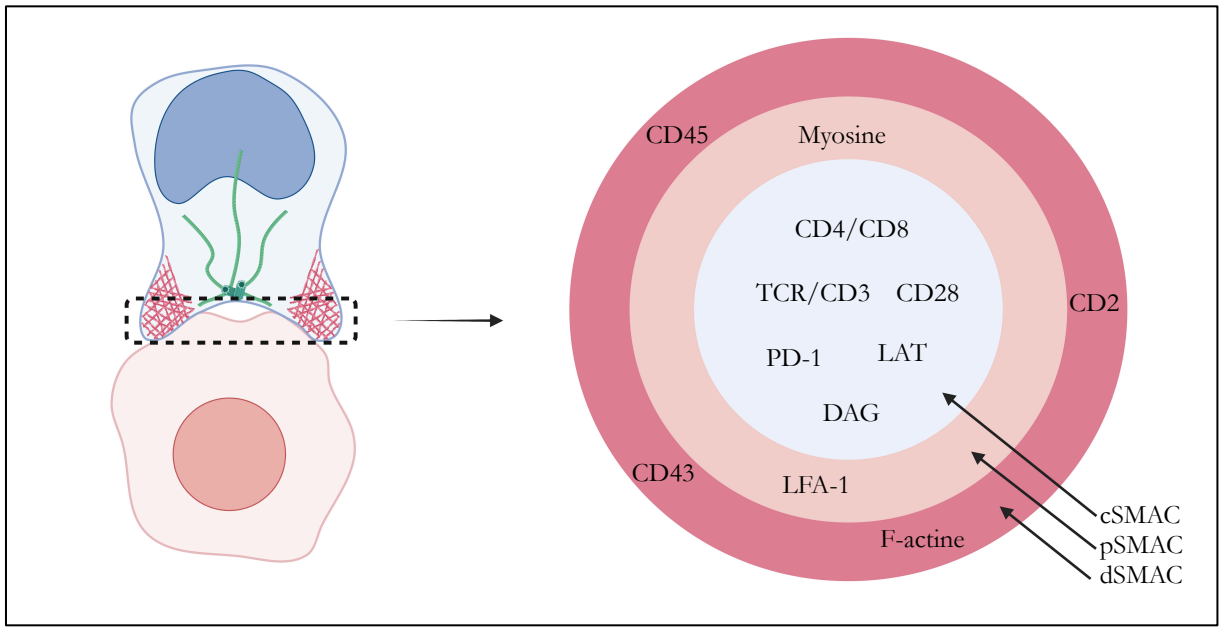


Figure 8 : Structure de la synapse concentrique

**LA SYNAPSE MULTIFOCALE** est une structure formée lors du contact entre un LT naïf et une DC immature (Benvenuti et al., 2004 ; Brossard et al., 2005). Contrairement aux synapses concentriques qui permettent aux cellules d'établir des contacts stables et durables, les synapses multifocales n'induisent pas la formation d'un cSMAC, mais plutôt de multiples zones de contact éparses, sans recrutement du TCR et de ceinture de LFA-1. Ces contacts désorganisés sont moins stables et ne permettent pas une activation complète des LT.

**LES KINAPSES** sont des jonctions adhérentes motiles qui permettent aux LT d'intégrer des signaux lors de mouvements sur la surface des CPA (Dustin and Kimmel, 2007). Contrairement aux synapses concentriques qui sont des contacts stables et symétriques, les kinapses sont asymétriques et en mouvement. Les kinapses sont constituées d'un lamellipode au front de migration, dans lequel des *microclusters* de TCR sont formés, entouré d'une zone où les TCR et les intégrines sont entremêlés, et d'un uropode où l'adhésion et les TCR se désengagent lorsque le LT se déplace. Dans ces structures, les organelles des LT sont positionnés dans l'uropode des LT, de manière similaire aux LT en migration. Malgré l'instabilité du contact, les TCR engagés dans les kinapses sont capables d'induire une signalisation (Mempel et al., 2004) et d'être internalisés (Friedman et al., 2010). Les signaux accumulés par les kinapses permettent aux LT de diminuer l'expression de CCR7, un récepteur de chimiokines, et ainsi de réduire les signaux chimio-cinétiques pour leur permettre finalement de s'arrêter sur la CPA et d'établir une synapse concentrique stable (Dustin, 2008). Les LT peuvent passer d'une synapse à une kinapse par le contrôle de la protéine DAG-dépendante PKCθ, alors que la protéine WASP aide à la conversion des kinapses en synapses (Sims et al., 2007). Les kinapses permettent donc aux LT de scanner les CPA, accumulant ainsi des signaux qui les pré-activent, pour finalement ralentir leur vitesse de migration et s'arrêter afin de former une synapse stable et efficace pour induire une activation complète des LT.

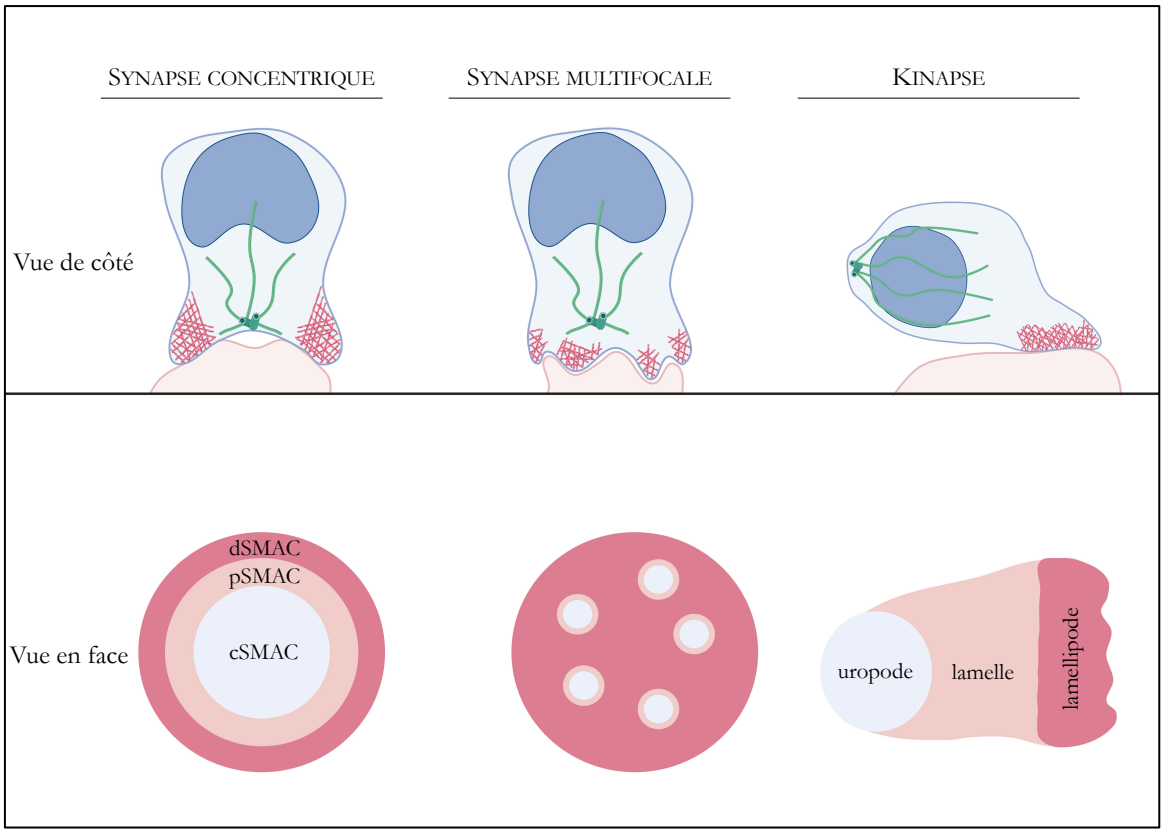


Figure 9 : Les différentes structures de synapses immunologiques

## 2.3 Signalisation à la synapse immunologique

L'interaction entre un LT et une CPA présentant un antigène induit la formation d'une synapse immunologique qui résulte en une activation efficace des LT. Afin de recevoir les signaux activateurs, les LT mettent en place plusieurs voies de signalisation à partir de la reconnaissance de l'antigène par le TCR.

**LA SIGNALISATION PAR LE TCR** prend place lors de la reconnaissance d'un complexe CMH-peptide. Le TCR est présent à la surface des LT et composé de deux sous-unités capables de reconnaître l'antigène qui sont uniques à chaque cellule T, complexées de manière non-covalente aux dimères CD3ε-CD3δ, CD3ε-CD3ɣ et CD3ζ-CD3ζ (Call et al., 2002). Ce complexe est capable de reconnaître des antigènes mais ne possède pas d'activité catalytique. Les protéines CD3 liées au TCR possèdent dans leur région cytoplasmique des motifs de signalisation contenant des tyrosines, appelés les motifs ITAM (*immunoreceptor tyrosine-based activation motifs)* (Barber et al., 1989 ; Reth, 1989). Il existe plusieurs hypothèses pour expliquer comment la signalisation du TCR est initiée :

- **L'hypothèse de la ségrégation cinétique (*kinetic segregation)***, (Davis and van der Merwe, 2006 ; Van Der Merwe et al., 2000)

  Ce modèle postule que la signalisation du TCR à la SI se déclenche par la ségrégation des protéines membranaires selon leur taille. D'après cette hypothèse, dans les LT au repos, les complexes TCR diffusent librement dans la membrane avec les kinases et les phosphatases qui maintiennent la signalisation basale nécessaire à la survie des LT, appelée signalisation tonique, sans déclencher une réponse complète. Lorsque le LT interagit avec une CPA, les paires récepteur-ligand les plus courtes, comme la paire TCR-CMHp, ségrégent dans des zones de contact étroit, excluant les molécules plus volumineuses, comme les phosphatases CD45 et CD148. Cela fait pencher la balance vers la phosphorylation des motifs ITAM du complexe TCR et favorise la formation de nouvelles liaisons TCR-CMHp spécifiques de l'antigène dans les zones de contact étroit.

- **L'hypothèse de relecture cinétique (*kinetic proofreading)***, (Mckeithan, 1995)

  Ce modèle a été proposé pour expliquer comment les LT peuvent échantillonner de nombreux CMH porteurs de peptides du soi inoffensifs et répondre sélectivement aux rares CMHp agonistes. Il postule que l'engagement

initial du TCR n'est pas suffisant pour déclencher une activation efficace des LT. Au contraire, plusieurs étapes consécutives impliquant des phosphorylations de tyrosines et l'assemblage de complexes moléculaires sont nécessaires. Au cours de la période de latence qui en résulte, la dissociation du lien entre le TCR et le CMH permet d'inverser ces modifications, généralement par l'activité des phosphatases. Ainsi, les liaisons TCR-CMHp non spécifiques de courte durée se dissocient avant l'activation des LT, alors que les liaisons TCR-CMHp spécifiques de longue durée favorisent la formation de complexes de signalisation stables qui soutiennent l'activation complète des LT.

- **L'hypothèse de l'activation en série** (*serial triggering)*, (Valitutti, 2012 ; Valitutti et al., 1995)

  Ce modèle répond au problème des CMHp agonistes très rares et des liaisons entre TCR et CMHp qui présentent de faibles affinités, ce qui rend l'activation des LT improbable. Ce modèle intègre la découverte qu'un seul CMHp peut engager et déclencher en série environ 200 TCR. L'hypothèse est que la faible affinité du couple TCR-CMHp contribue à l'activation des LT en permettant à un seul CMHp d'interagir avec de nombreuses molécules de TCR en série. Si la durée de chaque liaison individuelle est suffisante pour permettre une relecture cinétique, même un CMHp rare peut fournir un stimulus suffisamment robuste pour activer le LT. Ainsi, une prédiction de ce modèle est que les antigènes puissants ont des temps de liaison suffisamment longs pour permettre une relecture cinétique, mais pas trop longs pour empêcher un déclenchement en série.

Les premières structures formées lors de la reconnaissance d'un antigène sont des groupes de TCR qui se forment de manière dépendante de la F-actine, et que l'on appelle des *microclusters* (MC) de TCR (Bunnell et al., 2002 ; Varma et al., 2006). Les MC servent de signalosome, c'est-à-dire de plateforme de signalisation, pour l'activation des LT. Ils recrutent les protéines de signalisation les plus proches du TCR pour induire l'activation. Chaque MC contient des TCR, des protéines kinases et des adaptateurs. Il a été proposé que la liaison du CMHp par le complexe TCR induise une déformation des ITAM, exposant les chaînes CD3 à la phosphorylation par Lck, une protéine kinase membranaire de la famille Src (Lee et al., 2015 ; Swamy et al., 2016). Cela induit le recrutement de ZAP-70 au complexe TCR/CD3 et son activation (Iwashima et al., 1994). ZAP-70 phosphoryle ensuite la protéine membranaire adaptatrice LAT (*linker of activated T cells*) qui recrute

alors la phospholipase Cγ (PLCγ) et facilite l'activation par la kinase inductible des LT ITK (Samelson et al., 1986). La protéine PLCγ catalyse la formation d'inositol 1,4,5-triphosphate (IP3) et de diacylglycérol (DAG) à partir de phosphatidylinositol 4,5-biphosphate (PIP2). Cela mène à l'activation de Ras, PKC et aux voies dépendantes des ions calcium qui entraînent l'activation transcriptionnelle de la croissance des LT et de cytokines comme l'interleukine-2 (IL-2) (Shah et al., 2021). La signalisation par le TCR peut également activer le facteur d'échange de nucléotide Vav qui active Notch et contrôle la transcription de Myc et la prolifération indépendante de l'IL-2 (Guy et al., 2013).

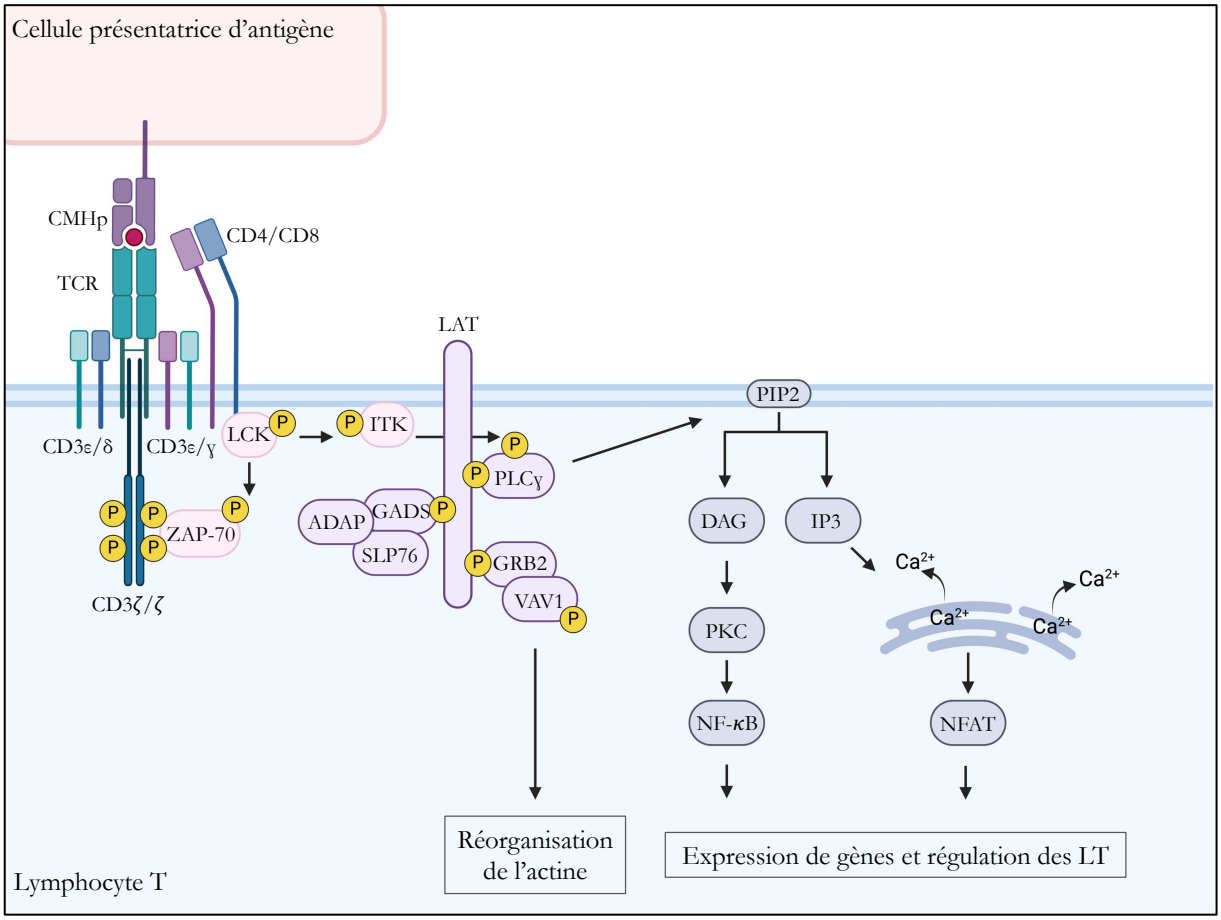


Figure 10 : Signalisation du TCR

**LES RECEPTEURS DE COSTIMULATION** permettent de renforcer la signalisation et l'adhésion lorsqu'ils sont combinés à d'autres stimuli comme l'activation du TCR (Bromley et al., 2001 ; Martin et al., 1986). L'activation de LT matures en absence de costimulation entraîne une délétion clonale qui protège l'hôte contre les réponses immunes aux antigènes inoffensifs environnementaux (Linsley and Ledbetter, 2003). La reconnaissance d'un antigène avec une costimulation suboptimale peut induire une insensibilité que l'on nomme anergie (Jenkins and Schwartz, 1987).

- **CD28** est le récepteur de costimulation essentiel à une stimulation efficace par le TCR. Cette protéine fait partie de la famille des immunoglobulines et possède une structure homodimérique et un domaine cytoplasmique dépourvu d'activité enzymatique. Les signaux CD28 permettent de réduire le seuil d'activation des LT en améliorant l'activation par un nombre réduit de complexes CHMp (Andres et al., 2004). L'activité de CD28 dépend de la présence de ses ligands B7-1 (CD80) et B7-2 (CD86), présents sur les DC matures et les LB activés, lors de la formation d'une SI (Tseng et al., 2008). CD28 contient des motifs qui recrutent et activent Lck et la protéine adaptatrice RLTPR qui contribue à l'activation des facteurs de transcription NF-$\kappa$B (Roncagalli et al., 2016) et à la production d'IL-2 (Kong et al., 2011). Les motifs de CD28 permettent également le recrutement de PI3K et Grb2 qui régulent positivement l'activation des LT et leur survie (Burr et al., 2001 ; Schneider and Rudd, 2008). Ainsi, CD28 régule le métabolisme par l'activation de la voie PI3K/AKT qui induit la signalisation mTOR, augmentant la quantité et l'efficacité de la glycolyse (Frauwirth et al., 2002 ; Jacobs et al., 2008). Cette voie sera reprise plus en détail dans le chapitre 3 de l'introduction abordant le métabolisme des LT.

  Une des fonctions principales de la voie CD28 est son habilité à réguler des réarrangements de cytosquelette. L'activation à la SI du TCR et de CD28 induit une polymérisation d'actine régulée par l'activité du facteur d'échange de nucléotide Vav1 (Dennehy et al., 2007 ; Raab et al., 2001), la Rho GTPase Cdc42 (Salazar-Fontana et al., 2003), WASP et Arp2/3 (Dupré et al., 2002). L'interaction physique entre CD28 et l'actine est nécessaire à sa localisation à la SI autour du cSMAC (Siokis et al., 2018). Elle est médiée par la protéine filamine A (FLNa) qui lie l'actine et CD28, permettant ainsi le recrutement et l'activation de Cdc42 et de Vav1 par la voie CD28, et donc le remodelage de l'actine à la SI (Tavano et al., 2006).

- **ICOS** est une autre molécule de costimulation inductible des LT, faisant également partie de la famille des immunoglobulines. Contrairement à CD28, ICOS n'est pas exprimé par les LT naïfs mais seulement suivant l'activation des LT. Elle interagit avec son ligand LICOS (CD275) qui est présent principalement sur les DC et les LB, mais peut également être induit sur les cellules stromales par des cytokines inflammatoires. ICOS est essentiel pour les réactions du centre germinatif en raison de sa capacité à activer la phosphatidylinositol-3 kinase (PI3K) (Xu et al., 2013). Les LT costimulés par ICOS peuvent atteindre des niveaux d'activation comparables à ceux de la costimulation par CD28.

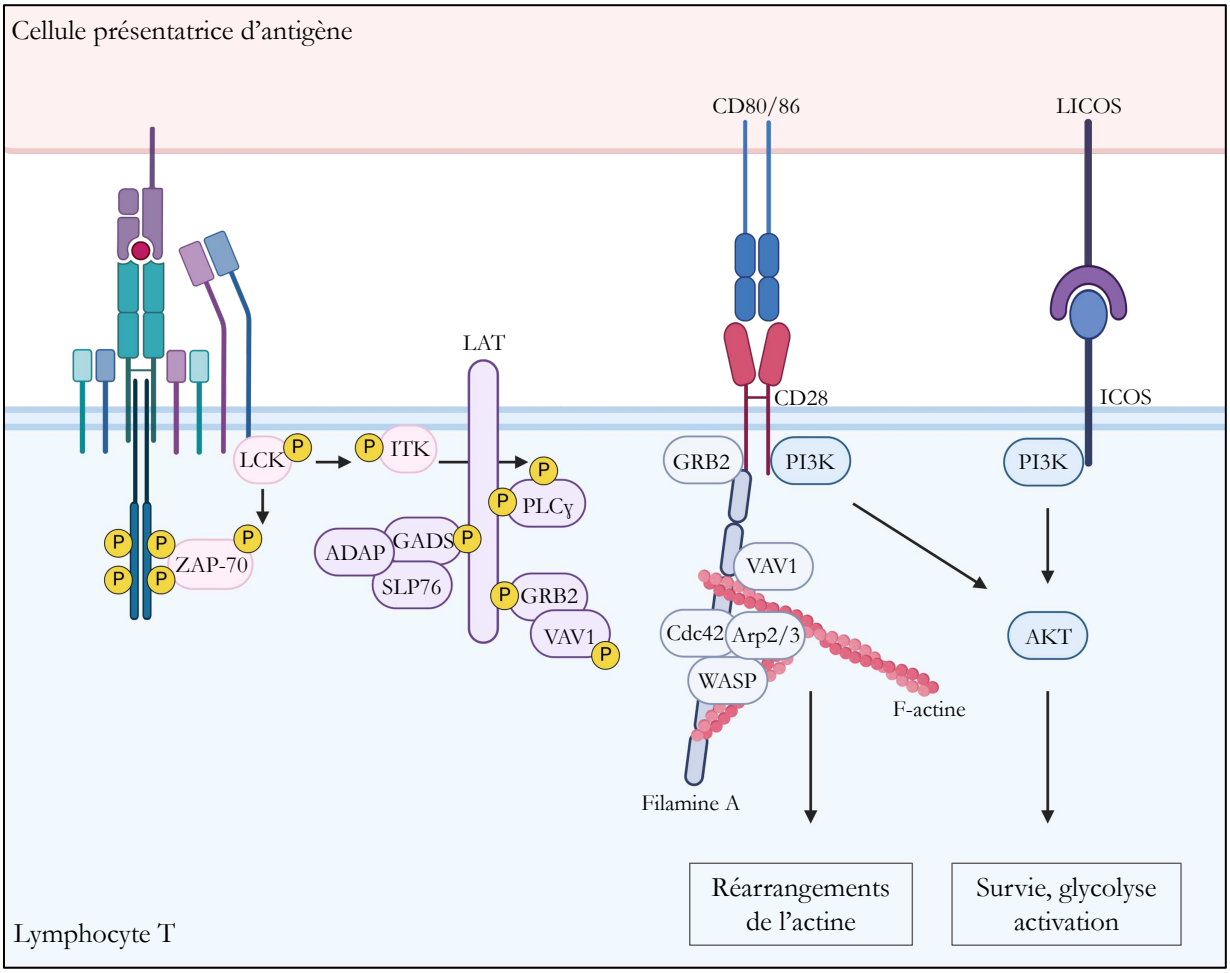


Figure 11 : Les voies de costimulation du TCR

A l'inverse de CD28, la costimulation par ICOS est inefficace pour la production d'IL-2, mais permet la sécrétion d'autres cytokines comme l'IL-4, l'IL-10 et l'IL-21 (Gigoux et al., 2009). Cela permet à ICOS de réguler la différenciation des LT $CD4^+$ auxiliaires lors de l'activation. Ce récepteur costimulateur est également exprimé par les LT régulateurs et leur confère une meilleure activité immunosuppressive. L'axe ICOS/LICOS représente un intérêt thérapeutique dans les traitements du cancer, puisqu'il permet d'augmenter les réponses antitumorales des LT (lorsqu'il agit dans des LT auxiliaires ou d'autres LT effecteurs), mais également de provoquer des réponses protumorales (en augmentant la capacité suppressive des LT régulateurs). Ainsi, des anticorps monoclonaux agonistes et antagonistes ciblant cette voie sont en cours de développement (Amatore et al., 2018).

## 2.4 Le cytosquelette dans la formation de la synapse

Comme décrit précédemment, les LT ont besoin de former des SI pour établir un contact physique rapproché avec les membranes des CPA pour détecter l'antigène. Ce mécanisme implique de profonds réarrangements du cytosquelette d'actine et des microtubules pour établir une polarité asymétrique des LT vers la SI. Le remodelage du cytosquelette est un des événements les plus précoces lors du contact avec une CPA (Locard-Paulet et al., 2020) et aboutit à la formation d'un anneau de F-actine synaptique et à la polarisation du centrosome, ensemble avec l'appareil de Golgi, les mitochondries et les vésicules sécrétoires contenant des cytokines ou les granules cytolytiques.

**LE CENTROSOME** détermine la polarité des LT. Lorsque les cellules migrent, il se situe dans l'uropode puis, lors d'un contact avec une CPA, il est relocalisé à la SI dans la région où l'actine est hypodense (Kuhn and Poenie, 2002). La réorientation du MTOC vers la SI dépend de la stimulation du TCR (Sedwick et al., 1999) et le couplage entre la signalisation et le remodelage du cytosquelette de microtubules est effectué par la protéine PKCθ activée par DAG (Huse, 2011). À la suite de l'accumulation de DAG et de PKCθ à la SI, des moteurs dynéines transloquent le centrosome vers la SI (Gros et al., 2021). La polarisation du centrosome à la SI est essentielle pour diriger le transport des granules et des cytokines vers le site précis de sécrétion. Ce mouvement du centrosome permet également d'orienter l'appareil de Golgi pour que les nouvelles cytokines soient synthétisées vers la synapse et directement sécrétées vers la CPA (Kupfer and Dennert, 1984). Ce contrôle de la sécrétion est essentiel pour maintenir la spécificité des réponses et, dans le cas des LT cytotoxiques, pour éviter d'endommager le tissu environnant. Le MTOC est également important pour la division asymétrique des LT en réponse à une stimulation antigénique par des DC (Chang et al., 2007). Dans ce contexte la polarisation du MTOC est importante pour que la division intervienne sur un plan parallèle à la SI. Toutefois, les cellules T sont également capables de sécréter des cytokines (Huse et al., 2006) et de lyser des cellules cibles (Tamzalit et al., 2020) de manière indépendante de la polarisation du MTOC.

**LE CYTOSQUELETTE D'ACTINE** permet aux LT de maximiser la zone de contact avec la CPA lors de la formation d'une SI, grâce à l'assemblage de différents réseaux d'actine et d'actomyosine. Les dynamiques de ces réseaux permettent le transport et le positionnement des protéines dans la membrane des LT pour former les zones SMAC de la SI. Les structures d'actine et d'actomyosine à la SI permettent l'assemblage des *microclusters* de TCR afin d'initier la signalisation, le transport des MC de TCR pour favoriser la maturation des SI, l'activation des

intégrines et leur positionnement pour l'adhésion des LT aux CPA, et enfin le contrôle des fonctions effectrices des LT comme la sécrétion polarisée. La plupart des études sur la formation, l'organisation et les dynamiques des réseaux d'actine et d'actomyosine à la SI a été effectuée par imagerie des LT en contact avec des surfaces activatrices (verre recouvert d'anticorps ou bicouches lipidiques planes), permettant un positionnement de cette structure corticale dans le plan d'imagerie idéal. Dès les premières minutes du contact, quatre différents types de réseaux d'actine se forment et ont chacun une organisation, des dynamiques et une contribution aux fonctions des LT propre :

1. **Le réseau d'actine branchée dans le dSMAC** est un anneau d'actine qui se forme à la périphérie de la SI peu après le contact avec une CPA ou une surface activatrice (Bunnell et al., 2001). Cet anneau très dense d'actine est observé dans la lignée de LT Jurkat ainsi que dans les cellules primaires. Il est composé d'un réseau d'actine branchée nuclée par le complexe Arp2/3 localisé en périphérie de la SI. L'assemblage de ce réseau sert initialement à l'étalement du LT sur la surface activatrice. Une fois la cellule entièrement étalée, l'assemblage continu de ce réseau provoque un flux de F-actine vers l'intérieur communément appelé flux rétrograde (Babich et al., 2012 ; Yi et al., 2012). Ce réseau est localisé dans le dSMAC et désassemblé à la frontière entre le dSMAC et le pSMAC. L'assemblage de ce réseau peut être bloqué en utilisant l'inhibiteur du complexe Arp2/3 CK666 (Hetrick et al., 2013). Le réseau d'actine branchée du dSMAC est le lieu d'assemblage des *microclusters* de TCR et donc de la signalisation dépendante du TCR et de l'activation des LT (Le Floc'h and Huse, 2015). Les MC de TCR signalisent efficacement lorsqu'ils transitent entre le dSMAC et le pSMAC, mais n'induisent plus de signalisation lorsqu'ils atteignent le cSMAC (Varma et al., 2006). Ainsi, avec une force d'adhésion augmentée qui retarde le flux d'actine, la signalisation du TCR augmente car le temps que les MC de TCR passent dans le dSMAC et le pSMAC est allongé (Nguyen et al., 2008). A l'inverse, en bloquant le flux rétrograde généré par la polymérisation d'actine branchée, la signalisation du TCR est alterée. Cela induit des défauts de phosphorylation et d'activation de ZAP-70 et LAT, mais également plus en aval, des défauts d'activation de PLCγ et la signalisation de calcium qui en résulte (Babich et al., 2012).

2. **Le réseau d'arcs d'actomyosine dans le pSMAC** est le second réseau majeur d'actine à la SI. L'actine constituant ce réseau est polymérisée à l'aide de la formine Dia1 qui est active à la membrane plasmique à l'extérieur de la SI (Murugesan et al., 2016). Dia1 forme des filaments d'actine linéaires qui traversent le réseau d'actine branchée du dSMAC, puis se courbent à la sortie du dSMAC pour donner naissance à des arcs d'actine concentriques dans le pSMAC.

L'assemblage des arcs est rapide et peut être inhibé par l'inhibiteur pan-formine SMIFH2 (Rizvi et al., 2009). Les arcs sont décorés par des myosines IIA qui provoquent leur contraction lorsque qu'ils se déplacent vers l'intérieur. La myosine IIA est nécessaire pour organiser les arcs en structures concentriques, et son inhibition par la blebbistatine désorganise les arcs (Murugesan et al., 2016). Ce réseau d'arcs d'actomyosine occupe le pSMAC de la SI et est désassemblé à la frontière entre le pSMAC et le cSMAC. Le réseau d'actomyosine a d'abord été identifié dans des LT Jurkat (Yi et al., 2012), puis il a été mis en évidence également dans les SI formées par des LT primaires (Hong et al., 2017). Les arcs d'actomyosine sont également un lieu de résidence des MC de TCR, et leur disruption par l'inhibition des formines diminue la signalisation du TCR (Murugesan et al., 2016). Le réseau d'actine dépendant des formines mDia1/3 contrôle également la localisation et la phosphorylation de LAT par ZAP-70 à la SI (Thumkeo et al., 2020). Ainsi, ces structures sont essentielles à l'activation des LT par la signalisation du TCR.

3. **Le réseau hypodense dans le cSMAC** résulte d'un désassemblage des arcs d'actomyosine. En effet, le cSMAC est pauvre en actine comparé aux réseaux d'actine dans le dSMAC et le pSMAC, mais les images de microscopie à haute résolution ont néanmoins révélé de petites quantités de F-actine distribuées au centre de la SI (Babich et al., 2012). Le cSMAC de SI matures est constitué d'un fin maillage de filaments d'actine qui comprend des petits foci d'actine intégrés dans les filaments d'actine branchée (Brown et al., 2011). Ce réseau est statique d'un point de vue du flux directionnel, en revanche il est dynamique à l'échelle nanométrique : le déplacement individuel de chaque filament conduit à la clairance de la zone centrale (Carisey et al., 2018). Il a été indiqué à l'aide de CK-666 que ce fin maillage d'actine est dépendant de l'activité du complexe Arp2/3.

4. **LES FOCI D'ACTINE DANS LE DSMAC ET LE PSMAC** ont été identifiés seulement dans des SI formées par des LT primaires (Kumari et al., 2015). Ces structures représentent une fraction minoritaire de la F-actine synaptique, et sont créées par le complexe Arp2/3 à l'aide de la protéine NPF WASP (Kumari et al., 2020). Environ 35% des *microclusters* de TCR colocalisent avec les foci d'actine (Kumari et al., 2015). Les foci présents en périphérie de la SI se déplacent avec le flux d'actine rétrograde formé dans le dSMAC et disparaissent lorsqu'ils atteignent la frontière entre le pSMAC et le cSMAC. Une grande partie des foci d'actine n'est pas associée aux MC de TCR. Ce fait, ainsi que leur apparence générale (c'est-à-dire des points d'actine), leur dépendance de WASP et d'Arp2/3, et le fait que leur formation nécessite également HS1

(la version hématopoïétique de la cortactine, qui sert à stabiliser l'actine branchée) fait de ces structures un intermédiaire entre des podosomes (Eddy et al., 2017) et des adhésions focales. Ce qui les en différencie est que les foci d'actine sont créés en réponse à la stimulation du TCR (Kumari et al., 2015)et qu'ils ont une durée de vie plus courte que les podosomes (Kumari et al., 2020). Les foci d'actine stabilisent les SI en générant un système d'actomyosine qui organise la tension mécanique à l'interface du contact cellule-substrat, ce qui les rapproche des adhésions focales des fibroblastes (Kanchanawong et al., 2010). Les foci d'actine dépendants de WASP qui s'associent aux MC de TCR contribuent également au recrutement de PLCγ, à son activation et au flux calcique qui en résulte (Kumari et al., 2015).

Ensemble, les différents réseaux de cytosquelette sont donc essentiels à la formation et à la maturation des SI, et donc à l'activation des LT.

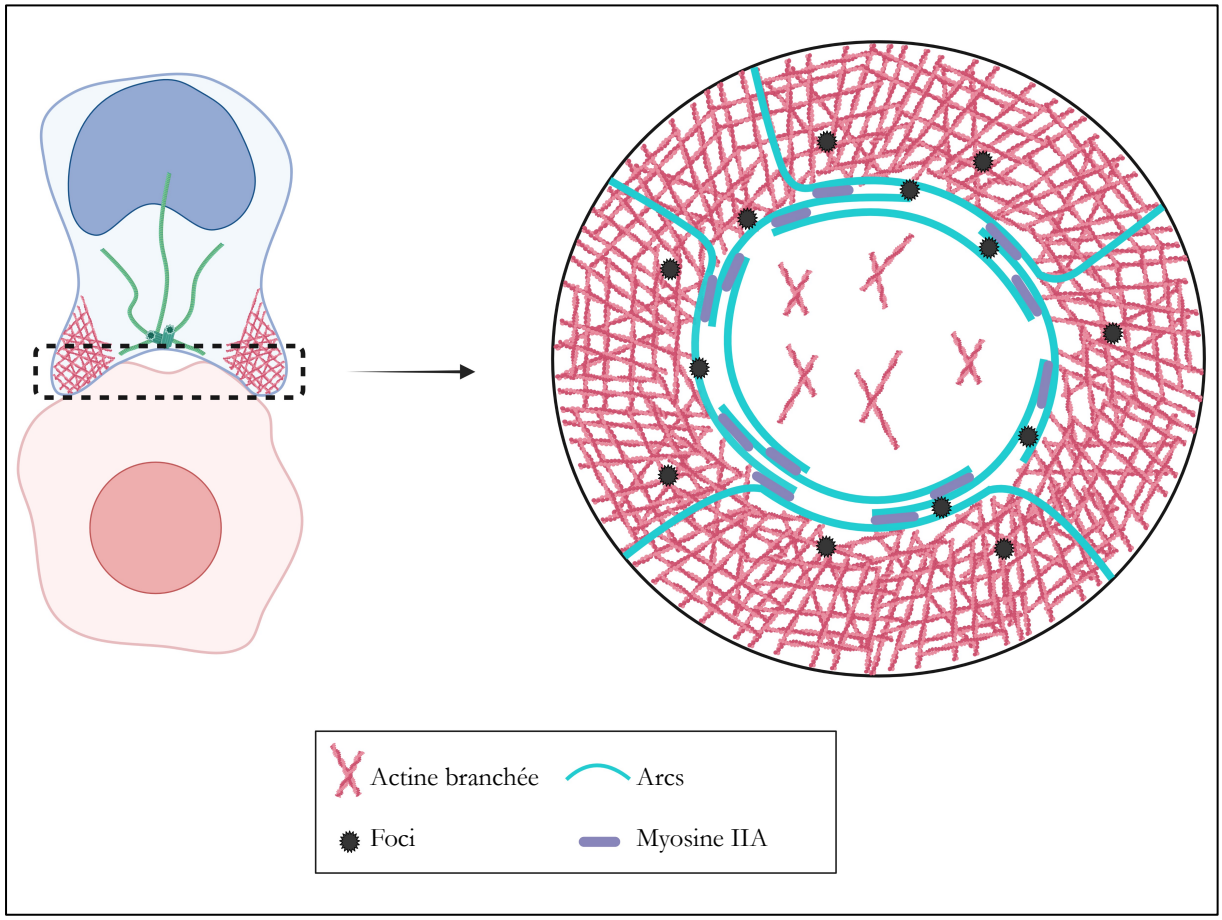


Figure 12: Les réseaux d'actine à la synapse immunologique

Schéma inspiré de la revue (Blumenthal and Burkhardt, 2020)

## 2.5 Stabilisation du contact : l'adhésion

Lors de la reconnaissance d'un complexe CMHp par un TCR le LT établit une SI avec la CPA, rapprochant les deux membranes à une échelle nanométrique. Comme peu de ligands CMHp sont disponibles à la surface des CPA, la reconnaissance de ces complexes dépend des molécules d'adhésion des LT, qui leur permettent de stabiliser le contact. L'adhésion peut se faire grâce à différents types de protéines, notamment les intégrines et les protéines de la famille des immunoglobulines (Springer, 1990). Les molécules de costimulation sont souvent considérées comme des molécules d'adhésion, ce qui rend la distinction entre les deux types de protéines assez floue. Par définition, l'adhésion augmente l'interaction physique entre le LT et la CPA et la liaison entre le TCR et le CMHp, alors que la costimulation augmente la signalisation du TCR ou génère des signaux indépendants qui s'intègrent avec ceux du TCR pour augmenter l'activation des LT. Cependant, la majorité des molécules d'adhésion possède une activité costimulatrice.

**LFA-1** est l'intégrine principale des LT qui permet leur adhésion en se liant à ICAM-1 à la surface des CPA (Springer and Dustin, 2012). Ces interactions multiplient par 100 la sensibilité au CMHp (Bachmann et al., 1997). Dans les SI matures, LFA-1 se trouve principalement dans le pSMAC enrichi en actomyosine, avec la densité la plus importante située à la frontière entre le pSMAC et le cSMAC (Yi et al., 2012). Cette organisation crée un joint adhésif circulaire autour du cSMAC dans les conjugués entre LT et CPA. Cette adhésion, couplée au repositionnement du centrosome au cSMAC, permet à la machinerie sécrétoire des LT de se positionner en direction de la cellule cible, et sert à concentrer et limiter les fonctions effectrices des LT à la CPA liée (Stinchcombe et al., 2006). Les couples LFA-1/ICAM-1 sont exclus du cSMAC en raison de la taille de leur domaine extracellulaire qui est plus grand que celui des TCR/CMHp agrégés au cSMAC. L'association entre LFA-1 et ICAM-1 nécessite que l'intégrine soit dans sa conformation active ouverte (Comrie and Burkhardt, 2016). La conversion de LFA-1 de sa conformation fermée à faible affinité, à sa conformation à haute affinité est induite selon plusieurs étapes. Tout d'abord, l'activation du TCR permet le recrutement du complexe Rap1-RIAM à la queue cytoplasmique de LFA-1 par un mécanisme appelé *inside-out signaling* (Lagarrigue et al., 2016). Ce complexe recrute et change la conformation pour activer la protéine taline associée à l'actine et liant LFA-1. Cela permet à l'intégrine de passer de sa forme inactive repliée à une conformation de faible affinité. Enfin, une force perpendiculaire à la membrane plasmique est appliquée à la queue cytoplasmique de LFA-1 pour convertir la protéine de faible affinité en une intégrine à haute affinité, avec une conformation ouverte (Comrie et al., 2015). Cette force est appliquée par le flux d'actine corticale qui se trouve

sous la membrane plasmique, et est connecté à la queue de LFA-1 par la taline. Les intégrines LFA-1 peuvent également être activées par des signaux *outside-in* comme les taux de magnésium dans le milieu. Le magnésium extracellulaire active LFA-1 et contribue ainsi aux fonctions effectrices des LT, et il a par ailleurs été montré que de faibles taux de magnésium sérique sont associés à de moins bons résultats dans l'immunothérapie du cancer (Lötscher et al., 2022).

**LA VOIE CD2/CD58** ou LFA-2/LFA-3 est le premier système d'adhésion impliquant des interactions récepteur/ligand directs à avoir été décrit en 1987 (Dustin et al., 1987 ; Selvaraj et al., 1987). CD2 est une glycoprotéine transmembranaire de la famille des immunoglobulines exprimée par tous les LT matures humains, qui augmente la sensibilité des LT au complexe CMHp, en particulier dans des conditions où CD28 est absent (Green et al., 2000). Lorsque les LT cherchent des antigènes à l'aide de leurs microvillosités, la molécule CD2 se trouve au bout de ces structures, et l'interaction avec son ligand CD58 permet aux LT de traverser le glycocalyx des CPA formant de nombreux petits contacts dont chacun est stabilisé par la protéine d'adhésion CD2 (Jenkins et al., 2023). Ces contacts rapprochés entre les membranes du LT et de la CPA excluent les grandes protéines, y compris la phosphatase CD45, ce qui permet l'augmentation de la sensibilité du TCR aux antigènes. Ainsi, les LT utilisent les microvillosités pour scanner la surface des CPA, puis, l'interaction de la protéine d'adhésion CD2 avec son ligand permet aux LT d'engager spécifiquement la signalisation de son TCR. Une fois que la synapse entre le LT et la CPA est mature, CD2 contribue à la signalisation des LT en activant des kinases comme Fyn, et participe également à la formation de MC de TCR (Douglass and Vale, 2005). L'interaction entre CD2 et CD58 forme des microdomaines enrichis en molécules de signalisation comme Lck, LAT et exclut CD45 (Kaizuka et al., 2009). CD2 est localisée dans le dSMAC, à l'extérieur de LFA-1 et forme une corolle qui engage les molécules de costimulation CD28, ICOS, CD226 et SLAM-F1 (Demetriou et al., 2020). Les interactions CD2/CD58 amplifient les signaux du TCR et semblent essentielles à l'activité antitumorale dans LT, puisqu'il a été mis en évidence que de nombreux patients atteints de cancer de l'endomètre et de cancer ovarien présentent une expression diminuée de CD2 sur les LT $CD8^+$ infiltrant les tumeurs (Demetriou et al., 2020).

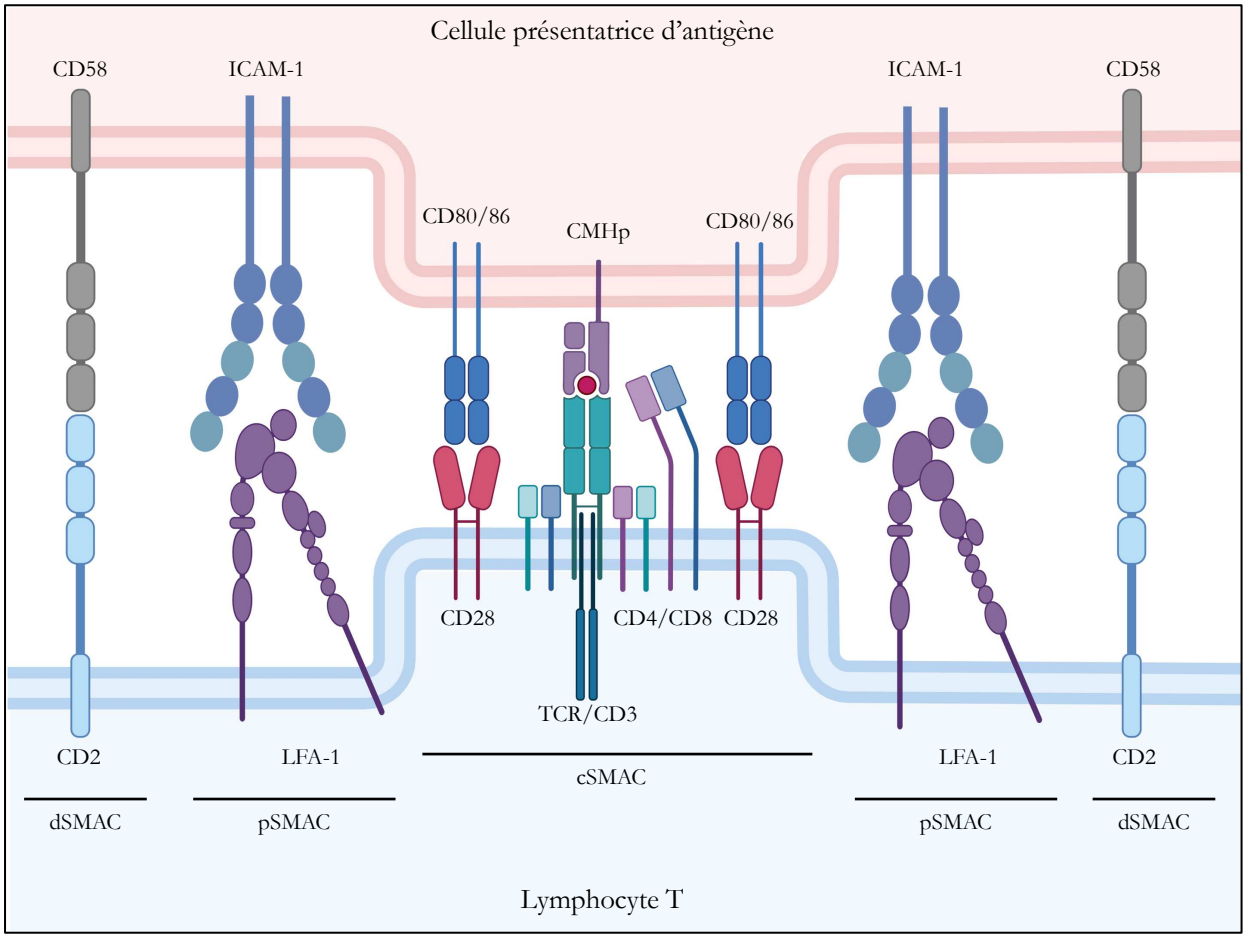


Figure 13 : Les molécules d'adhésion à la synapse immunologique

## 2.6 La synapse lytique

Les LT cytotoxiques (CTL) sont un élément clé du système immunitaire adaptatif car ils sont capables d'éliminer les cellules infectées par des pathogènes intracellulaires et les cellules tumorales. Lors de la rencontre d'une cellule cible, l'interaction est initiée par des protrusions qui forment un contact interdigité entre les deux cellules (Sanderson and Glauert, 1979). Après maturation de la SI, on observe une zone étendue de contact étroit entre les membranes. La sécrétion de granules lytiques au cSMAC de la SI par les CTL a lieu après la formation d'une jonction adhésive au pSMAC et le repositionnement du centrosome. Ce dernier sert à diriger la machinerie sécrétoire liée aux microtubules dans la direction de la cellule cible (Stinchcombe et al., 2006). Néanmoins, dans certaines conditions, la polarisation du MTOC vers la SI n'est pas nécessaire à la sécrétion polarisée des granules cytolytiques. En effet, la polarisation des granules et leur sécrétion vers la cellule cible (Bertrand et al., 2013) ou même vers plusieurs cellules cibles reconnues simultanément par le lymphocyte T $CD8^+$ cytotoxique (Wiedemann et al., 2006) peuvent précéder la polarisation du MTOC.

Comme décrit précédemment, le cSMAC est constitué d'un fin maillage d'actine qui contient des pores d'une taille moyenne de la moitié du diamètre d'un granule lytique, servant de barrière à la sécrétion (Carisey et al., 2018). L'activation des LT conduit à l'apparition de pores plus larges permettant le passage des granules lytiques à travers le maillage. Ce mécanisme est essentiel à la sécrétion des granules, car l'actine corticale qui s'accumule au point de contact initial entre le LT et la CPA bloque la sécrétion à la SI immature (Ritter et al., 2015). La barrière d'actine disparaît lorsque la SI mature, pour laisser place au fin maillage d'actine branchée. Les réarrangements nanométriques de F-actine dans cette région, provoqués par les dynamiques de l'actine et la contractilité de la myosine permettent de réguler la sécrétion des granules lytiques (Carisey et al., 2018).

**LA MECANO TRANSDUCTION** permet aux cellules de transduire des signaux mécaniques en signaux biochimiques (Na et al., 2008). Dans les LT, le cytosquelette d'actine sert d'intermédiaire mécanique pour intégrer les signaux dépendants des forces (Blumenthal and Burkhardt, 2020). Lors de la formation d'une SI, les forces sont établies selon deux étapes : lors de la reconnaissance d'un antigène les LT poussent d'abord la CPA, puis dans un deuxième temps, la tirent et la ramènent vers leur membrane pour établir un contact physique (Husson et al., 2011 ; Sawicka et al., 2017). Les forces de traction et de poussée exercées sont dépendantes des réseaux d'actine et l'inhibition

de l'actine bloque les deux types de forces exercées (Hu and Butte, 2016 ; Zucchetti et al., 2021). Les signaux mécaniques sont essentiels à l'activation des LT à plusieurs niveaux. D'abord, les forces sont exercées au niveau moléculaire des récepteurs. Il a été montré que les forces appliquées par les LT exercent une tension sur la liaison entre le TCR et le complexe CMHp, qui renforce leur interaction, et donc la signalisation par le TCR (Li et al., 2010 ; Liu et al., 2014). Il a également été proposé que les forces exercées seraient responsables du changement de conformation des ITAM des chaînes CD3 associées au TCR, permettant leur phosphorylation et la signalisation qui en résulte (Das et al., 2015).

Au niveau cellulaire, les forces mécaniques jouent un rôle important dans les premiers événements de la formation d'une SI. Les surfaces des LT et des CPA sont recouvertes de glycocalyx, constitué de longues protéines glycosylées, formant une barrière physique à l'interaction entre les petites molécules de TCR et de CMHp (Shaw and Dustin, 1997). Deux protéines constituant ce glycocalyx sont les phosphatases CD45 et CD148, qui maintiennent les phosphorylations dépendantes du TCR en-dessous du seuil d'activation (Imbert et al., 1994). Au repos, la surface des LT est recouverte de microvillosités mesurant d'environ 100 nm à quelques micromètres. La longueur de ces structures leur permet de pénétrer le glycocalyx et de créer des zones de contact rapproché avec la membrane de la CPA. Au bout des microvillosités se trouvent des TCR qui permettent aux LT de scanner la membrane des CPA à la recherche d'antigènes. Une fois que la liaison entre un TCR et le CMHp a eu lieu, elle est stabilisée par des forces. Les intégrines LFA-1 sont également associées au développement de forces et permettent aux CTL d'exercer des forces de traction dans les domaines sécrétoires qui régulent la cytotoxicité. Ces forces sont dépendantes de la taline qui établit le lien entre la F-actine et LFA-1 (Wang et al., 2022). Les protrusions d'actine des CTL sont nécessaires pour l'exertion de forces à la SI, et pour éliminer les cellules cibles efficacement. En effet, elles déforment la membrane des CPA et les perforines sont relarguées à la base des protrusions (Tamzalit et al., 2019).

Les forces dépendantes de l'actomyosine exercées par les CTL sur les cellules cibles augmentent l'efficacité de destruction de la CPA en améliorant la capacité des perforines à former des pores dans la membrane de la cellule cible (Basu et al., 2016). Ainsi, les forces générées par le cytosquelette d'actomyosine des LT contribuent à la cytotoxicité en augmentant la tension dans la membrane de la cellule cible pour favoriser la formation de pores par la perforine. Ces forces induisent un changement de la topologie des CTL, qui adoptent une forme incurvée négativement par rapport à la SI, formant des poches de membranes dans lesquelles sont transportés les granules

cytolytiques. Ces poches de dégranulation concaves sont précisément positionnées en face de zones convexes de la membrane de la cellule cible, permettant aux perforines de percer les membranes. Ainsi, la cytotoxicité des CTL est un système dépendant de forces mécaniques qui polarisent les granules lytiques et courbent localement la membrane à la SI pour favoriser la perforation unidirectionnelle de la cellule cible (Govendir et al., 2022).

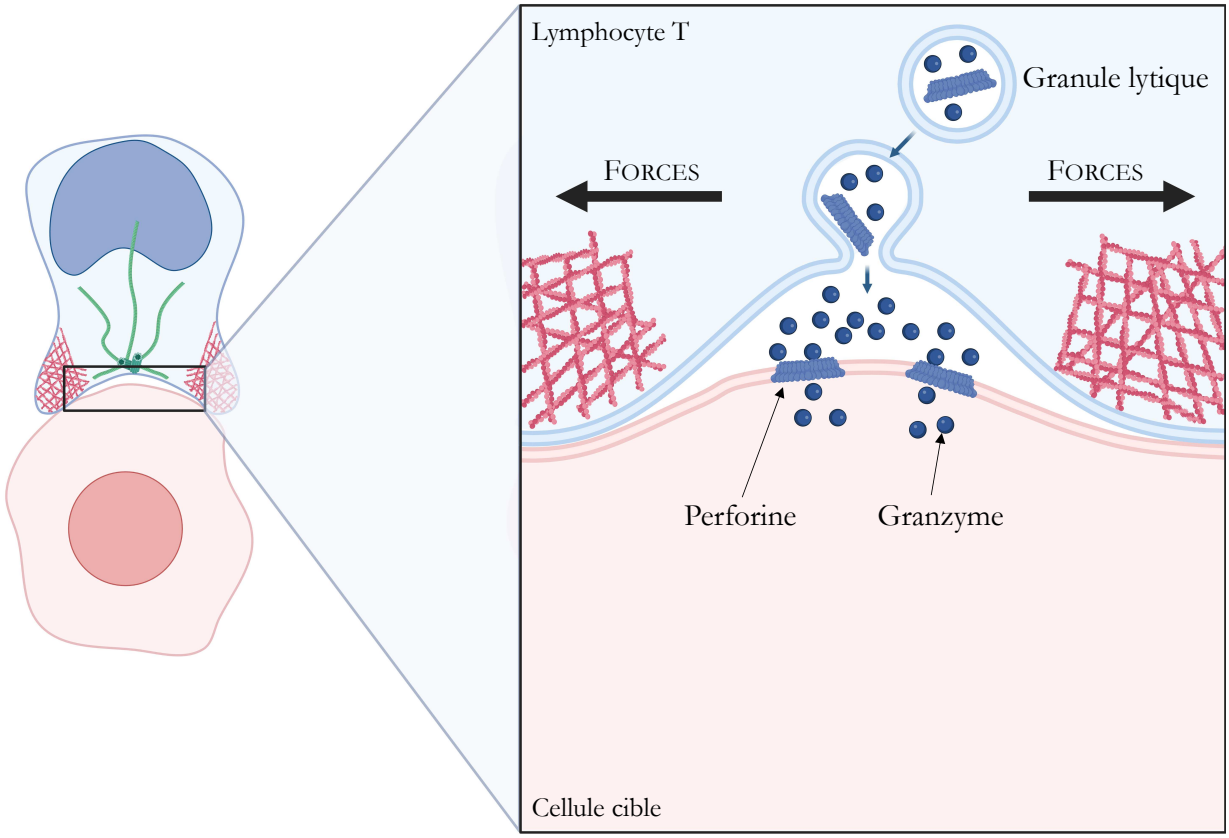


Figure 14 : La synapse lytique
Dégranulation des LT cytotoxiques dans une zone concave, positionnée en face d'une région convexe de la membrane de la cellule cible. Les réseaux d'actine à la SI génèrent des forces qui exercent une tension sur la membrane de la cellule cible, facilitant ainsi la formation de pores.

# CHAPITRE 3

## Le métabolisme des lymphocytes T

Ce troisième chapitre de l'introduction a pour objectif de présenter comment les lymphocytes T puisent de l'énergie selon différents programmes métaboliques distincts afin de soutenir leurs fonctions effectrices. Après avoir présenté quels programmes les lymphocytes T utilisent en fonction de leur stade d'activation, je présenterai les voies de signalisation qui les régulent. Pour finir, je mettrai en évidence le lien entre le cytosquelette et le métabolisme.

## 3.1 La respiration cellulaire

L'une des exigences cellulaires les plus fondamentales est la capacité d'accéder à des nutriments suffisants et appropriés pour soutenir les fonctions cellulaires essentielles. Lors de l'activation les LT grandissent, prolifèrent et meurent ou se transforment en cellules mémoires une fois leurs fonctions accomplies. Au cours de ces événements les besoins métaboliques évoluent, et l'adaptation du métabolisme cellulaire est essentielle. La régulation de l'absorption de nutriments et de leur utilisation est essentielle pour contrôler le nombre et la fonction des cellules.

Les voies métaboliques ont pour objectif de fabriquer ou de décomposer les molécules de glucose à l'aide de séries de réactions chimiques. La réaction prend en charge une ou plusieurs molécules de départ et, par le biais d'une série d'intermédiaires, les convertit en produits. Les voies métaboliques peuvent être divisées en deux catégories principales : les voies anaboliques, qui fabriquent du glucose, et les voies cataboliques, qui le décomposent. La photosynthèse par exemple, est une voie anabolique qui permet de fabriquer du glucose à partir de lumière. Les cellules utilisent des voies cataboliques pour décomposer des molécules complexes en petites molécules, et ainsi libérer de l'énergie. L'énergie stockée dans les liaisons de molécules complexes, telles que le glucose et les graisses, est libérée dans les voies cataboliques. Elle est ensuite récoltée sous des formes qui peuvent alimenter les fonctions de la cellule, comme l'ATP. Cette décomposition des combustibles organiques comme le glucose est appelée la respiration cellulaire. Afin de produire l'énergie nécessaire aux fonctions effectrices, la respiration cellulaire prend place selon plusieurs étapes, toutes capables de produire de l'énergie.

1. **LA GLYCOLYSE** est constituée d'une série de réactions chimiques prenant place dans le cytosol, qui extraient de l'énergie à partir du glucose en le décomposant en pyruvate. À l'issue de ces réactions, deux molécules d'ATP sont générées et le transporteur d'électrons nicotinamide adénine dinucléotide ($NAD^+$) est réduit en NADH.

2. **L'OXYDATION DU PYRUVATE** permet de convertir les pyruvates générés par la glycolyse, qui sont transportés du cytosol à la matrice mitochondriale, en acétyle coenzyme A (acétyl-CoA). Cette étape libère du dioxyde de carbone et génère du NADH mais ne produit pas directement d'ATP.

3. **LE CYCLE DE L'ACIDE CITRIQUE** aussi appelé le cycle de Krebs, oxyde l'acétyl-CoA produit lors de la dernière étape dans la matrice mitochondriale, produisant deux molécules d'ATP, du NADH et du $FADH_2$ (la flavine adénine dinucléotide, un autre transporteur d'électrons), libérant du dioxyde de carbone et de l'eau.

4. **LA PHOSPHORYLATION OXYDATIVE** (*oxidative phosphorylation*, OXPHOS) permet au NADH et au $FADH_2$ fabriqués lors des étapes précédentes de déposer leurs électrons dans la chaîne de transport des électrons, retournant alors à leurs formes « vides » $NAD^+$ et FAD. À mesure que les électrons parcourent la chaîne, de l'énergie est libérée et utilisée pour pomper les protons hors de la matrice, formant ainsi un gradient. Les protons retournent dans la matrice par l'intermédiaire d'une enzyme appelée ATP synthase, produisant ainsi de l'ATP. À la fin de la chaîne de transport des électrons, l'oxygène accepte les électrons et absorbe les protons pour former de l'eau. La phosphorylation oxydative permet donc de régénérer les transporteurs d'électrons NADH et $FADH_2$ et de mettre à disposition les formes oxydées $NAD^+$ et FAD qui sont utilisées pour la glycolyse et le cycle de l'acide citrique. En général, environ 30 à 32 ATP sont générés à partir d'une molécule de glucose (Rich, 2003).

Ainsi, la glycolyse et la phosphorylation oxydative sont régulées par de nombreux effecteurs moléculaires communs. Par conséquent, elles ne fonctionnent généralement pas de manière indépendante. Au contraire, les deux événements sont couplés dans les cellules et sont régulés par la quantité de mitochondries, ainsi que par leur microenvironnement et la disponibilité de l'oxygène.

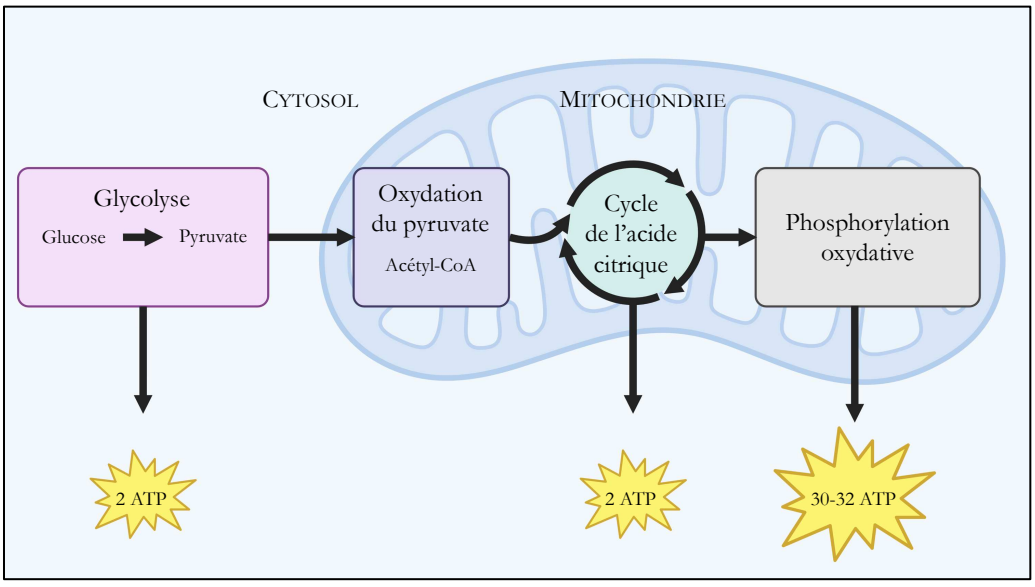


Figure 15 : La respiration cellulaire

**Décomposition des lipides**

En plus du glucose, les graisses, aussi appelées **triglycérides** peuvent également être décomposées en composants pouvant intégrer la respiration cellulaire à différentes étapes. Les triglycérides sont constitués de glycérol auquel sont attachées trois queues d'acides gras. Le glycérol peut être converti en glyceraldehyde-3-phosphate, un intermédiaire de la glycolyse, et continuer à suivre le reste de la voie de décomposition de la respiration cellulaire.

À l'inverse, les **acides gras** doivent être décomposés par un processus appelé la β-oxydation, qui a lieu dans la matrice des mitochondries. Lors de la β-oxydation, les queues des acides gras sont décomposées en molécules qui se combinent au coenzyme A, formant de l'acétyl-CoA. Cet acétyl-CoA alimente ensuite le cycle de l'acide citrique.

## 3.2 Programmation du métabolisme des lymphocytes T

L'activation des lymphocytes T requiert de l'énergie pour accomplir différents types de fonctions effectrices. Cette énergie leur est fournie par des programmes métaboliques distincts, adaptés à chaque besoin. Lors de la reconnaissance d'un antigène présenté par un CMH du soi et de signaux de costimulation, les LT se développent, prolifèrent et se différencient en sous-ensembles distincts qui jouent des rôles uniques dans le maintien des réponses fonctionnelles et la régulation de l'homéostasie immunitaire. Lors d'une primo-infection, les LT $CD4^+$ et $CD8^+$ naïfs sont activés, prolifèrent massivement, et deviennent des LT effecteurs capables de recruter d'autres cellules immunitaires et d'éliminer le pathogène. Une fois que l'infection est résolue, les LT effecteurs ne sont plus nécessaires et subissent alors une contraction pour éviter la destruction de tissus. Cependant, tous les LT spécifiques d'un antigène ne meurent pas, et une petite population devient des cellules mémoires à longue durée de vie qui offrent une protection contre les infections secondaires (Williams and Bevan, 2007). L'activation des LT ne conduit pas à une reprogrammation métabolique uniforme dans toutes les conditions. En plus de leurs fonctions distinctes, les LT possèdent également des profils métaboliques uniques qui sont essentiels à leur fonction et à leur maintien.

- **Les LT naïfs** sont des cellules matures qui n'ont pas encore rencontré leur antigène spécifique. Leur survie est assurée par des cytokines homéostatiques comme l'IL-7 (Rathmell et al., 2000). L'IL-7 active des voies de signalisation qui leur permettent d'absorber du glucose. Ils sont métaboliquement quiescents, c'est-à-dire qu'ils reposent principalement sur la phosphorylation oxydative pour subvenir à leurs besoins énergétiques et leur survie.

- **Les LT effecteurs** sont des cellules métaboliquement très actives, avec de hauts taux de glycolyse et de phosphorylation oxydative, couplés à leur état hautement prolifératif. Il existe différents sous-ensembles de LT $CD4^+$ effecteurs, aussi appelés *T helper* (Th), ainsi que des LT $CD4^+$ régulateurs (Treg), distincts métaboliquement. Même si tous les LT effecteurs dépendent de la glycolyse, les Treg sont moins glycolytiques que les Th (Michalek et al., 2011). Les LT $CD8^+$ activés puisent également leur énergie par la glycolyse aérobie (He et al., 2011). Les Treg ne sont pas métaboliquement inactifs, mais puisent plutôt leur énergie par l'oxydation des acides gras. Cette énergie est

essentielle pour assurer la prolifération, ainsi que la production de cytokines inflammatoires et de granules cytolytiques.

- **Les LT mémoires** se développent à la suite d'une primo-infection, en persistant à partir d'un pool de LT qui possède des adaptations métaboliques leur permettant une survie à très long terme, qui peut atteindre une durée de vie au-delà même de celle de l'individu (Nasi et al., 2006 ; Soerens et al., 2023). Ils reprogramment leur métabolisme vers un état plus quiescent, mais métaboliquement actif, en s'appuyant principalement sur des processus cataboliques tels que la β-oxydation des acides gras et la phosphorylation oxydative. Ce profil métabolique permet aux LT mémoires de répondre plus rapidement et plus efficacement à un antigène déjà rencontré, permettant le blocage complet, ou du moins un rapide contrôle de l'infection (Wherry and Ahmed, 2004).

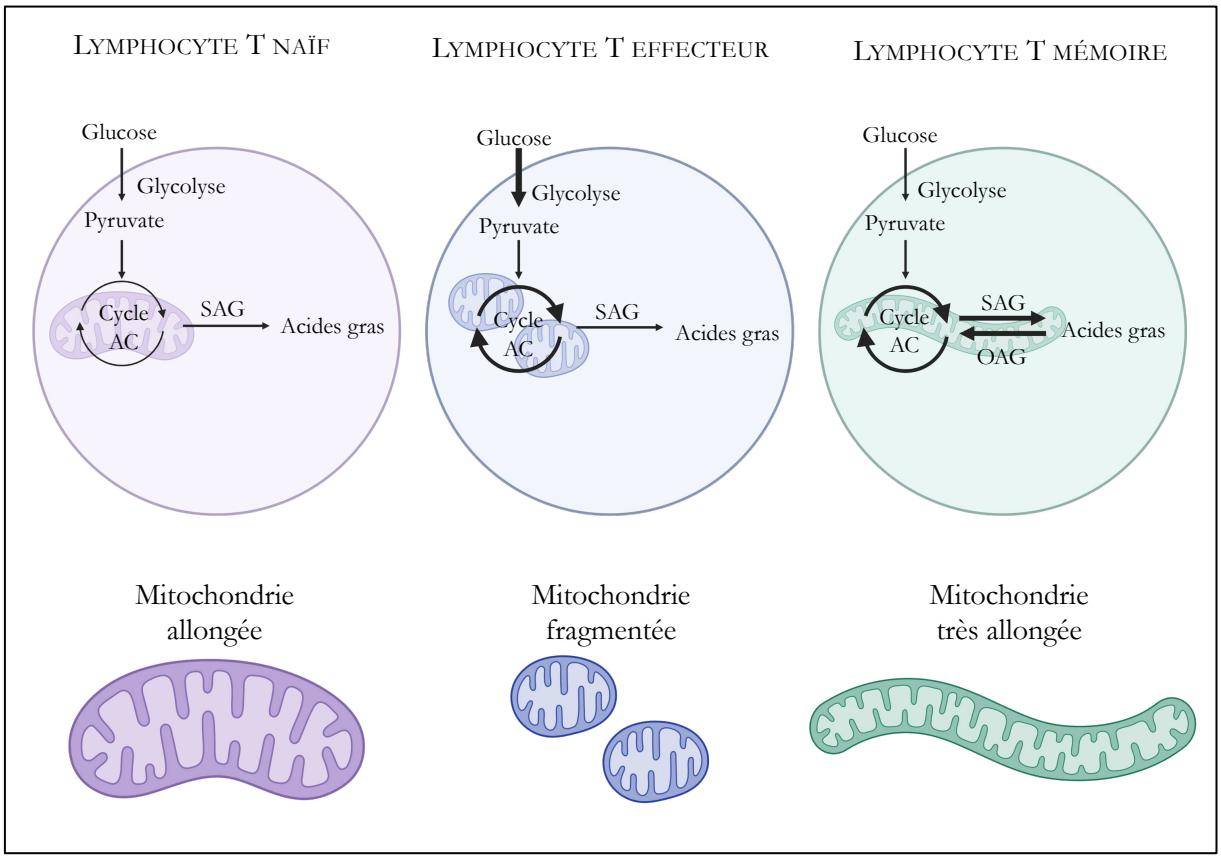


Figure 16 : Les différents programmes métaboliques des lymphocytes T

**LES MITOCHONDRIES** sont les organelles principales de la respiration cellulaire, et régulent donc les différents programmes métaboliques. Elles ajustent leur fonction selon les besoins métaboliques dynamiques de la cellule (Spinelli and Haigis, 2018). Elles sont capables de changer de morphologie et de localisation intracellulaire pour produire de l'énergie plus efficacement (Pernas and Scorrano, 2016). Par exemple, les mitochondries sont recrutées à la SI par le clivage des sites de contact entre les mitochondries et le réticulum endoplasmique, afin de permettre l'afflux de calcium et l'activation des LT effecteurs à la zone de contact (Quintana et al., 2007). Les mitochondries fusionnent et se divisent, formant ainsi des réseaux interconnectés d'organelles ou des unités fragmentées isolées (Chan, 2020). L'ultrastructure des mitochondries varie également considérablement pour permettre aux cellules d'effectuer de l'OXPHOS de manière très efficace, en adoptant des invaginations serrées de la membrane mitochondriale, appelées *cristae*. Ces invaginations sont associées à une organisation moléculaire plus élevée des complexes de la chaîne respiratoire en super complexes (Cogliati et al., 2013).

## 3.3 Switch métabolique lors de l'activation des lymphocytes T

Otto Warburg a observé pour la première fois qu'au lieu d'utiliser les voies d'oxydation mitochondriales pour une production maximale d'énergie, les cellules cancéreuses utilisent le processus moins efficace de la glycolyse, produisant ainsi de l'acide lactique même en présence d'une quantité suffisante d'oxygène (Warburg, 1956). Plus tard, il a mis en évidence que ce phénomène de glycolyse aérobie alors appelé « l'effet Warburg » était présent également chez les leucocytes activés : les leucocytes au repos utilisent principalement un métabolisme aérobique oxydatif, alors que la stimulation conduit à une transition vers la glycolyse comme programme métabolique majeur (Warburg et al., 1958). Cette observation a ensuite été étendue à d'autres types de cellules immunitaires des lignées myéloïde et lymphoïde, au sein des systèmes immunitaires inné et adaptatif (Geltink et al., 2018 ; Kelly and O'Neill, 2015). Ainsi, la glycolyse aérobie est un marqueur des types cellulaires inflammatoires et cancéreux, et représente une cible thérapeutique d'intérêt pour traiter des maladies auto-immunes et des cancers.

**LES LYMPHOCYTES T** utilisent ce switch métabolique de l'OXPHOS à la glycolyse lors de leur activation. En 2002, il a été mis en évidence que l'augmentation de la glycolyse dans les LT est une réponse couplée à l'activation immunitaire par la costimulation par CD28, entraînant une augmentation de l'expression du transporteur de glucose, de l'absorption de glucose, et de la glycolyse via la PI3K (Frauwirth et al., 2002). Dans ce contexte, le glucose est préférentiellement métabolisé en lactate plutôt qu'oxydé dans les mitochondries, ce qui est la caractéristique principale de l'effet Warburg. Peu après, il a été montré que ce switch métabolique coordonné est nécessaire aux fonctions des LT $CD8^+$ effecteurs telles que la transcription de cytokines et l'activité cytolytique, puisqu'elles sont inhibées en absence de glucose et lors de l'inhibition de la glycolyse (Cham et al., 2008 ; Cham and Gajewski, 2005). Plusieurs groupes ont par la suite élargi ces observations fondamentales, montrant que l'augmentation de la glycolyse est également nécessaire à la survie et la prolifération, à la différenciation et aux fonctions effectrices des LT $CD4^+$ (Gerriets et al., 2015 ; Macintyre et al., 2014 ; Shi et al., 2011).

La balance entre la glycolyse et l'OXPHOS est essentielle lors de l'activation des LT. Bien que la glycolyse soit très augmentée après une stimulation pro-inflammatoire des LT naïfs, l'OXPHOS augmente également, dans une moindre mesure, et remplit des fonctions critiques. Par exemple, les espèces réactives de l'oxygène dérivées de la chaîne de transport d'électrons sont essentielles à l'activation des LT (Sena et al., 2013), et l'inhibition de l'OXPHOS bloque l'activation

et la prolifération des LT (Chang et al., 2013). La reconnaissance d'un antigène par le TCR induit la glycolyse aérobie en seulement quelques minutes. Ce switch précoce diffère de la glycolyse plus tardive, par son indépendance des voies CD28 et AKT, et il est essentiel à la synthèse de cytokines lors de cette première phase d'activation (Menk et al., 2018). Ainsi, un contrôle de l'équilibre entre la glycolyse et l'OXPHOS permet de réguler les fonctions effectrices des LT.

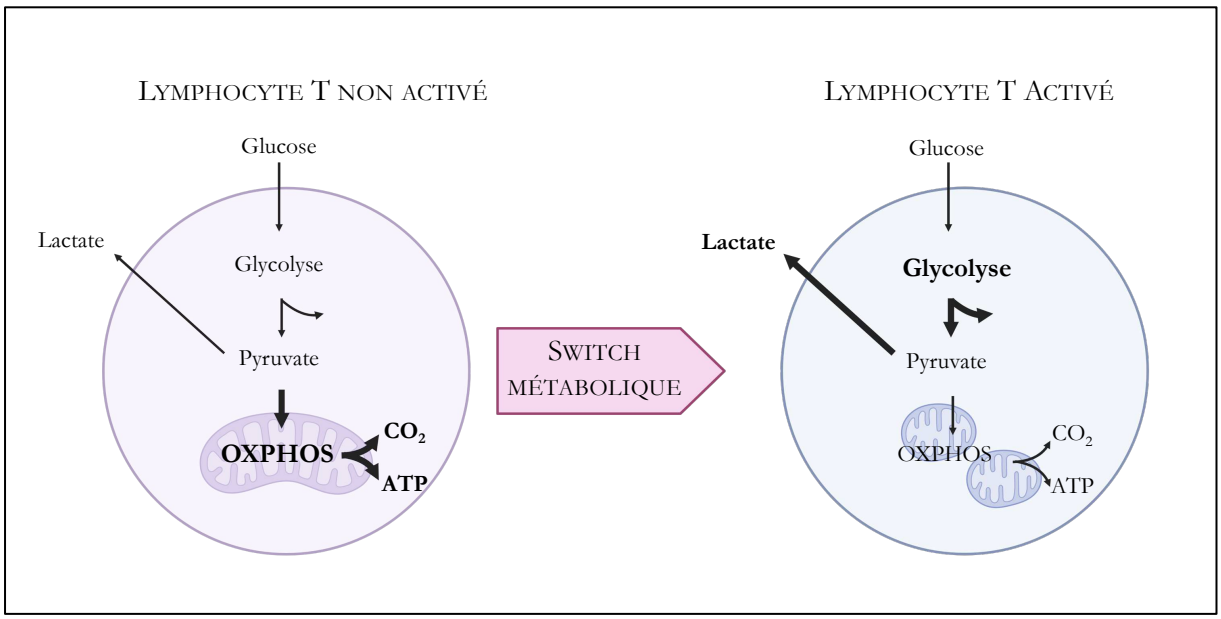


Figure 17 : Le switch métabolique lors de l'activation des lymphocytes T

## 3.4 Les voies de régulation du métabolisme des lymphocytes T

Les différents stades d'activation des LT requièrent des programmes métaboliques compatibles à leurs demandes fonctionnelles. La transition entre les états est accompagnée par une reprogrammation active du métabolisme cellulaire. Chaque transition est orchestrée par une série de voies de signalisation.

**LA VOIE PI3K/AKT/MTOR** permet l'augmentation de la glycolyse et la reprogrammation métabolique lors de l'activation des LT, de manière dépendante de la costimulation (Frauwirth et al., 2002). En particulier, la signalisation par CD28 permet l'activation de la voie PI3K/Akt/mTOR. Cette voie joue un rôle essentiel pour induire le métabolisme du glucose et la glycolyse aérobie, et est essentielle pour la croissance cellulaire et la prolifération. L'activation de PI3K en réponse à l'engagement de CD28 génère du phosphatidylinositol-3-phosphate (PIP3) qui recrute Akt et la kinase dépendante de PIP3, PDK1 à la membrane cellulaire. PDK1 phosphoryle ensuite Akt, qui est lui-même phosphorylé par le complexe 2 de mTOR (mTORC2), permettant son activation. A son tour, Akt initie ensuite une cascade de signalisation qui mène à l'activation de mTORC1. Akt et mTORC1 peuvent ensuite induire la glycolyse aérobie pour soutenir la croissance et les fonctions des LT effecteurs. Akt joue également un rôle essentiel dans la régulation des transporteurs de glucose. En effet, il induit le trafic du transporteur de glucose Glut1 à la surface cellulaire et empêche son internalisation lors de l'activation (Gerriets and Rathmell, 2012). En aval d'Akt, l'activation de mTORC1 induit des événements post-traductionnels qui stimulent la glycolyse aérobie et coordonnent les voies qui régulent la croissance cellulaire (Chi, 2012). Une des fonctions principales du complexe mTORC1 est de phosphoryler 4EBP et la kinase p70S6 (p70S6K) pour favoriser l'augmentation de la traduction de protéines. L'activation de p70S6K induit les effets glycolytiques de mTORC1.

**LA PROTEINE KINASE AMP-ACTIVEE (AMPK**) fonctionne en opposition au complexe mTORC1. Alors que mTORC1 favorise les processus anaboliques qui puisent de l'énergie pour synthétiser des protéines, l'AMPK régule l'énergie en induisant des voies cataboliques (Hardie, 2007). Le complexe AMPK détecte l'augmentation du ratio AMP/ATP à l'aide de la kinase LKB1 (*liver kinase B1*), et freine alors le métabolisme pour assurer le maintien de quantités suffisantes d'ATP dans la cellule pour procéder à son activation complète (MacIver et al., 2011). Le deuxième signal qui stimule l'AMPK est l'activation de la calcineurine par l'importation de calcium et l'activation en aval de la kinase kinase activée par le calcium/calmoduline (CAMKK) (Tamás et al.,

2006). L'AMPK est activée transitoirement lors de l'activation des LT pour permettre aux cellules de stimuler rapidement les processus de production d'énergie afin de préparer les cellules à une croissance rapide. Une fois activée, l'AMPK induit la génération d'énergie et inhibe l'activation de mTORC1. L'AMPK n'inhibe pas seulement la glycolyse, mais également le métabolisme des acides gras (Houten et al., 2016). En régulant la consommation d'énergie de la voie mTOR, l'AMPK est donc essentielle à l'activation et la survie des LT. En effet, en absence de l'AMPK les LT ne sont plus capables de répondre au stress métabolique et d'effectuer la transition de la glycolyse et du métabolisme anabolique, à l'oxydation des acides gras et le métabolisme catabolique (MacIver et al., 2011).

Ainsi, les voies PI3K/Akt/mTOR et la kinase AMPK sont des régulateurs clé des programmes métaboliques et servent de balance pour maintenir l'homéostasie de l'énergie cellulaire.

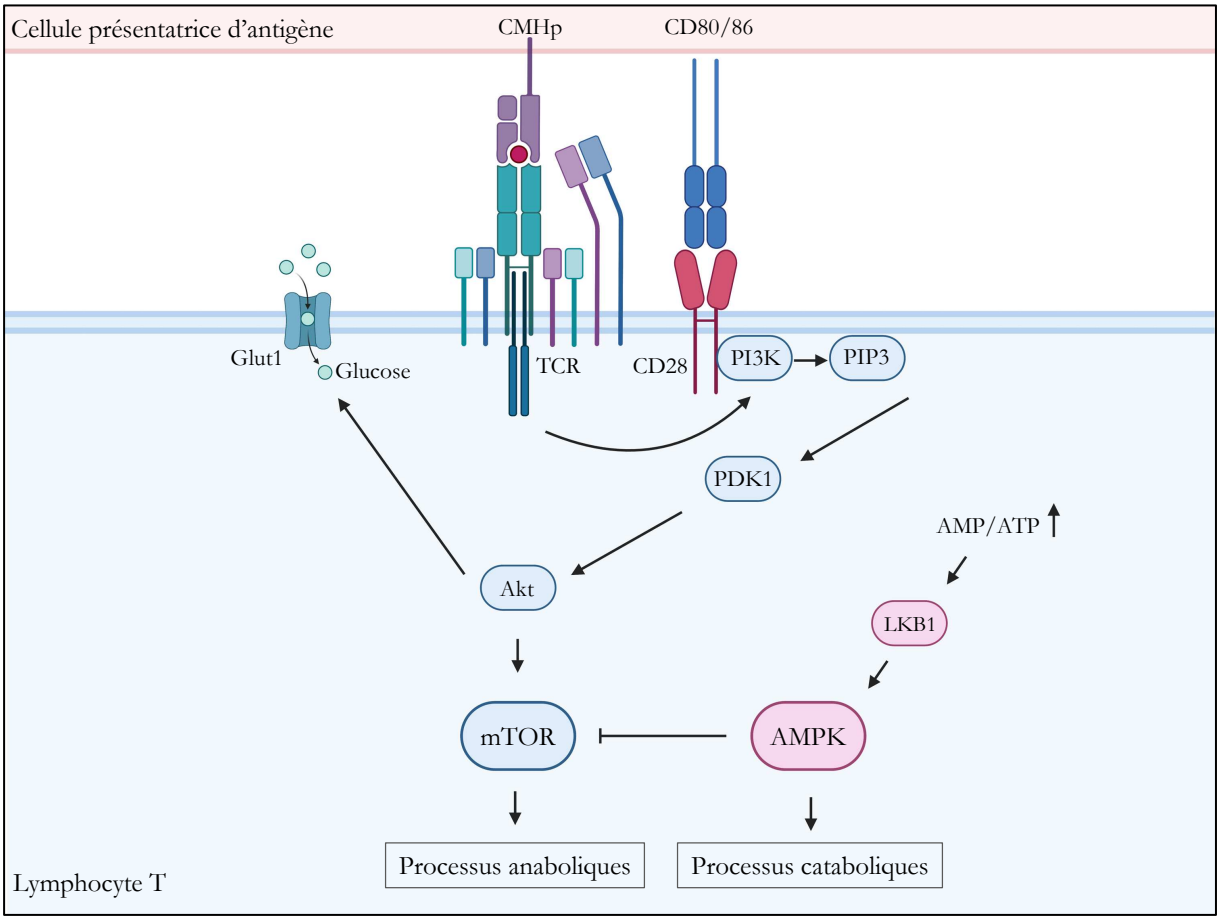


Figure 18 : Régulation des voies métaboliques par mTOR et l'AMPK

## 3.5 Relation entre métabolisme et cytosquelette

Les différents programmes métaboliques sont finement régulés par des voies de signalisation et permettent aux LT de se fournir l'énergie suffisante pour leurs fonctions effectrices. Il y a plus de 40 ans, il a été observé que le cytosquelette d'actine se lie directement aux enzymes métaboliques (Luther and Lee, 1986). Comme nous l'avons vu dans le premier chapitre de cette introduction, la polymérisation des filaments d'actine repose sur l'énergie contenue dans l'ATP, ce qui rend ce processus très consommateur en énergie. La quantité d'ATP nécessaire au remodelage du cytosquelette d'actine représente environ 50% de l'ATP présent dans une cellule (Bernstein and Bamburg, 2003 ; Daniel et al., 1986). Ainsi, le métabolisme cellulaire fournit le carburant, l'ATP, nécessaire au remodelage du cytosquelette d'actine.

**LES ENZYMES GLYCOLYTIQUES SE LIANT A L'ACTINE** permettent d'établir un lien direct, physique, entre le cytosquelette et les voies du métabolisme, pour une régulation spatiale et fonctionnelle de l'actine.

- **PFK-1** est une enzyme qui se lie à l'actine par des interactions électrostatiques (Roberts and Somero, 1987). Cette liaison est inhibée par de faibles concentrations d'ATP, mais ne l'est pas par la concentration de son substrat, suggérant que le site de liaison pour l'actine chevauche celui de l'ATP (Roberts and Somero, 1989). Seule la conformation enzymatique active de la PFK-1 est capable de s'associer à l'actine. Cette spécificité permet d'initier de nouvelles réactions de glycolyse localement, afin de produire de l'ATP directement sur le site qui en nécessite.

- **L'aldolase** est une enzyme qui catalyse la quatrième étape de la glycolyse, et qui se lie préférentiellement à la F-actine plutôt qu'à la G-actine (Ouporov et al., 1999). La liaison est médiée par des interactions électrostatiques à l'aide d'une région basique présente sur l'aldolase qui s'associe à une région acide sur l'actine. L'aldolase lie l'actine dans un état inactif. La liaison du substrat force l'aldolase à adopter une conformation active qui est défavorable à sa fixation à l'actine et provoque sa dissociation (Schindler et al., 2011). La voie PI3K mobilise l'aldolase de la F-actine, et sa dissociation augmente le flux glycolytique (Hu et al., 2016).

- **Le glyceraldehyde-3-phosphate (GAPDH)** est l'enzyme qui catalyse la sixième étape de la glycolyse, qui se lie également à la F-actine. Cette enzyme est, elle aussi, dans sa conformation inactive lorsqu'elle est liée à la F-actine (Forlemu et al., 2011). Lorsque le métabolisme est faible, comme dans des cellules non-proliférantes, confluentes ou des cellules privées de sérum, le GAPDH se trouve principalement dans la fraction insoluble, liée à l'actine (Schmitz and Bereiter-Hahn, 2002). À l'inverse, dans des cellules en prolifération, lorsque le métabolisme est élevé, le GAPDH se situe dans la fraction soluble cytoplasmique. Ainsi, le GAPDH est inhibé lorsqu'il est lié à la F-actine, et actif lorsqu'il est libéré du cytosquelette d'actine.

Ainsi, le cytosquelette d'actine consomme de l'énergie via la glycolyse, mais contrôle également la localisation, l'activité et la stabilisation de ces enzymes glycolytiques clés. La raison pour laquelle la liaison à la F-actine sert à activer certaines enzymes glycolytiques alors que d'autres sont inhibées n'est pas encore établie. Une possibilité serait qu'en se liant à la F-actine dans sa forme active, la PFK-1 permettrait d'engager une première vague de glycolyse localement, qui serait ensuite relayée par l'aldolase et le GAPDH une fois relâchés de l'actine en raison du remodelage.

Jusqu'ici le lien entre le métabolisme et l'actine dans les LT a été très peu étudié. Une équipe a mis en évidence que lors de la migration des LT régulateurs, l'enzyme glycolytique glucokinase se lie directement au cytosquelette d'actine et induit une augmentation des flux de glycolyse, suggérant qu'elle permette de localiser la production d'ATP aux sites où le cytosquelette est activement remodelé (Kishore et al., 2017).

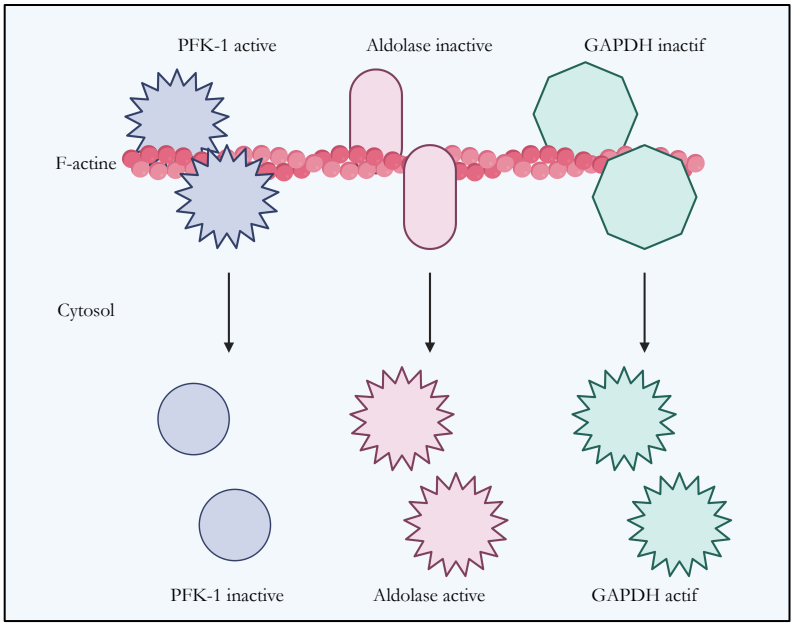


Figure 19 : Les enzymes glycolytiques liant la F-actine

# CHAPITRE 4

## PD-1 : une cible de l'immunothérapie

Dans cette quatrième partie de l'introduction je présenterai la cible d'immunothérapie PD-1. Après avoir mis en évidence l'importance de cette protéine dans l'homéostasie, je présenterai les aspects néfastes qu'elle représente dans un contexte inflammatoire et cancéreux, ainsi que le potentiel thérapeutique qui en résulte. Pour comprendre le fonctionnement de la voie inhibitrice par PD-1, je décrirai ensuite sa structure et la régulation de son expression, puis la voie de signalisation qui en résulte. Enfin, je présenterai les fonctions effectrices des LT inhibées par PD-1, et les premières études mettant en évidence une altération de la synapse immunologique par la protéine.

## 4.1 PD-1 dans la tolérance et l'auto-immunité

*Programmed death 1* (PD-1, CD279) est un récepteur de la famille CD28 qui a été découvert en 1992 par l'équipe du Dr. Honjo (Ischida et al., 1992). Initialement, cette protéine a été identifiée comme étant surexprimée par des cellules apoptotiques et a donc été associée à la mort cellulaire. Il a ensuite été montré que la fonction principale de PD-1 est en fait d'atténuer les réponses immunitaires. En effet, en 1999 il a été mis en évidence qu'en absence de la protéine, les souris *Pdcd1*$^{-/-}$ développaient de sévères maladies auto-immunes (Nishimura et al., 1999). Les ligands PD-L1 (aussi appelé B7-H1 ou CD274) et PD-L2 (aussi appelé B7-DC ou CD273) du récepteur ont été découverts en 2000 et 2001 respectivement (Freeman et al., 2000 ; Watchman et al., 2001).

**REGULATION DE LA TOLERANCE CENTRALE.** La liaison de PD-1 à ses ligands déclenche des signaux inhibiteurs qui régulent la tolérance centrale et périphérique du système immunitaire. PD-1 est exprimé par les thymocytes doubles négatifs ($CD4^-CD8^-$) lors de leur maturation pendant l'induction de la tolérance centrale. À ce stade, PD-L1/L2 sont présents dans le thymus et la liaison de PD-1 à ses ligands inhibe la sélection positive des thymocytes passant du stade double négatifs à double positifs ($CD4^+CD8^+$) (Nishimura et al., 2000). Les lymphocytes T auto-réactifs qui ont échappé à la sélection négative sont contrôlés en périphérie par des mécanismes de tolérance périphérique. Les premières interactions entre des LT et des CPA comme les cellules dendritiques atténuent les réponses auto-réactives grâce à la présentation d'auto-antigènes. PD-1 joue un rôle essentiel dans l'inhibition des réponses auto-réactives des LT, et l'absence de PD-1 augmente la réponse des cellules T $CD8^+$ aux DC non activées (Probst et al., 2005).

**REGULATION DE LA TOLERANCE PERIPHERIQUE.** L'interaction PD-1/PD-L n'a pas une importance uniquement au stade de la maturation des thymocytes et de l'expansion des lymphocytes T auto-réactifs, mais également lors de nouvelles rencontres de l'antigène. Par exemple, dans le modèle d'encéphalomyélite auto-immune expérimentale (EAE), un modèle murin de la sclérose en plaques, PD-1 et ses ligands contrôlent les cellules T auto-réactives et empêchent le développement de la maladie (Liang et al., 2003). De la même manière, l'interaction PD-1/PD-L1 régule l'initiation et la progression du diabète auto-immun dans le modèle murin NOD (Fife et al., 2006). La voie PD-1 a également été associée au contrôle des maladies inflammatoires chroniques de l'intestin (MICI). En effet, la présence de PD-L1 sur les cellules épithéliales intestinales permet le développement de LT régulateurs induits qui contrôlent l'activité auto-immune des LT effecteurs. En empêchant la liaison de PD-1 à PD-L1 à l'aide d'un anticorps dans

une coculture entre des cellules épithéliales intestinales de patients MICI et des LT de donneurs sains, la production d'IFNγ, et donc l'inflammation, augmente (Nakazawa et al., 2004).

PD-1 et ses ligands sont donc essentiels à la mise en place, puis à la préservation de la tolérance centrale et périphérique, et l'altération de leurs fonctions inhibitrices déclenche le développement de maladies auto-immunes.

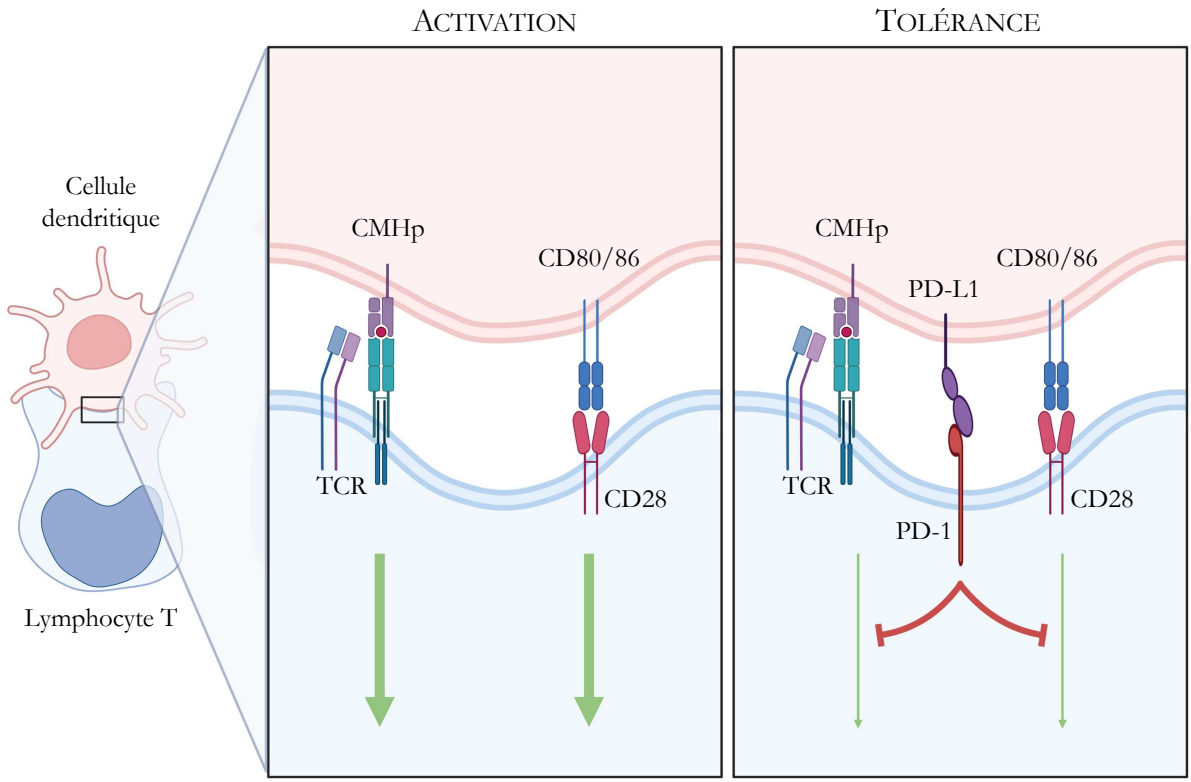


Figure 20 : Induction de la tolérance par PD-1

## 4.2 Potentiel thérapeutique dans les infections et le cancer

Dans un contexte différent de ceux de l'homéostasie et de l'auto-immunité, les effets de la voie PD-1 sont opposés. En effet, la voie peut être exploitée par des pathogènes chroniques et des cellules tumorales pour favoriser l'échappement immunitaire. Dans ces situations, le blocage des interactions entre PD-1 et ses ligands peut améliorer les fonctions des LT et réduire la charge virale ou tumorale.

**L'EPUISEMENT DES LYMPHOCYTES T**. Lorsque les LT sont exposés à des antigènes de manière chronique et répétée, ils adoptent un phénotype que l'on nomme « épuisé », *exhausted*, qui les empêche d'effectuer leurs fonctions efficacement. Ce phénomène a d'abord été décrit dans des LT $CD8^+$ de souris infectées par le virus chronique de la chorioméningite lymphocytaire (Zajac et al., 1998), puis chez l'Homme, chez des patients infectés par le virus de l'immunodéficience humaine (Kostense et al., 2001), les virus de l'hépatite B et C (Gruener et al., 2001 ; Reignat et al., 2002), mais également chez des patients atteints de cancers (Lee et al., 1999). Une caractéristique principale de l'épuisement des LT est la surexpression de multiples récepteurs inhibiteurs comme PD-1, CTLA-4, Lag-3, Tim-3, TIGIT et d'autres (Wherry, 2011). La découverte que le blocage de la voie PD-1 pouvait partiellement inverser l'épuisement et conduire à une réduction de la charge virale (Barber et al., 2006) ou tumorale (Hirano et al., 2005)a constitué une avancée significative sur le plan thérapeutique. Ces données ont montré que les LT épuisés ne sont pas irréversiblement dysfonctionnels, mais qu'ils peuvent retrouver leurs fonctions effectrices par le blocage de la voie PD-1, ce qui a ouvert le champ à de nombreuses thérapies visant à bloquer l'interaction entre PD-1 et ses ligands.

**LES IMPLICATIONS THERAPEUTIQUES.** Des anticorps monoclonaux ciblant les protéines inhibitrices comme CTLA-4 et PD-1 ont ouvert une voie à une nouvelle génération d'approches thérapeutiques du cancer. Ces stratégies d'inhibition des points de contrôle, ou *immune checkpoint blockade*, ont pour objectif d'atténuer les mécanismes régulateurs qui bloquent l'efficacité des LT infiltrants les tumeurs (TIL) (Callahan and Wolchok, 2013 ; Sharma et al., 2011). Ces anticorps bloquant l'interaction entre PD-1 et PD-L1 ont fait preuve d'un succès remarquable dans de nombreux essais cliniques (Brahmer et al., 2012 ; Topalian et al., 2012). Néanmoins, la plupart des patients ne présentent pas une rémission stable à la suite du traitement ciblant PD-1. Ainsi, mieux comprendre le fonctionnement de l'inhibition des LT par PD-1 est fondamental afin d'améliorer ces traitements. De nombreuses études sont en cours pour définir des biomarqueurs permettant

de prédire quels patients bénéficieront d'un traitement ciblant PD-1. La présence de LT $CD8^+$ dans (Tumeh et al., 2014) et de hauts niveaux d'expression de PD-L1 dans la tumeur (Herbst et al., 2014) ont été corrélés à de meilleurs taux de réponse. Dans de nombreux cas, l'expression de PD-L1 dans les tumeurs corrèle avec l'infiltration de LT $CD8^+$ (Taube et al., 2012), suggérant la présence d'une réponse inflammatoire en cours. Cependant, l'expression de PD-L1 ne corrèle pas toujours avec des résultats thérapeutiques : certaines tumeurs $PD\text{-}L1^+$ répondent faiblement au blocage de la voie PD-1 (Garon et al., 2015), alors que d'autres tumeurs $PD\text{-}L1^-$ présentent de bonnes réponses (Robert et al., 2015). Un autre biomarqueur proposé pour prédire les réponses aux traitement bloquant la voie PD-1, est l'analyse de la clonalité des TCR dans la tumeur. En effet, il a été montré qu'une clonalité des TCR augmentée corrèle avec de meilleures réponses aux inhibiteurs de PD-1 (Roh et al., 2017), suggérant qu'une population de LT plus clonale permette une meilleure immunité antitumorale. Plus récemment, un nouveau biomarqueur a été identifié : le ratio entre les LT $CD8^+PD\text{-}1^+$ par rapport aux LT régulateurs $PD\text{-}1^+$ dans le microenvironnement tumoral (Kumagai et al., 2020). Le blocage de PD-1 induit une récupération des fonctions des LT dysfonctionnels, donc des fonctions antitumorales des LT $CD8^+$ et immunosuppressives des LT régulateurs. Ainsi, la présence d'un ratio LT $CD8^+$/LT régulateurs élevé prédit une réponse efficace au blocage de PD-1.

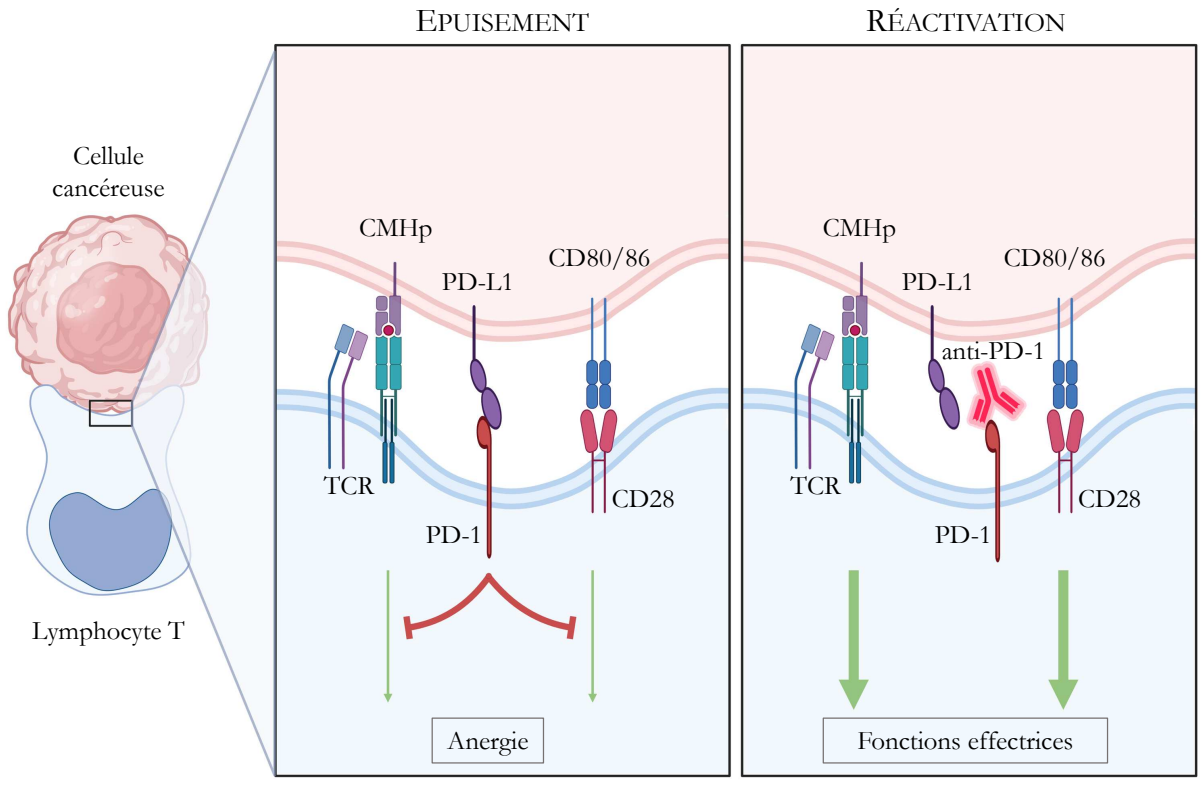


Figure 21 : Principe de l'immunothérapie anti-PD-1/PD-L1

## 4.3 Structure et régulation de l'expression de PD-1

**STRUCTURE DE PD-1 ET SES LIGANDS.** PD-1 et ses ligands sont des membres de la famille des récepteurs B7/CD28/CTLA-4, qui sont des glycoprotéines transmembranaires de type I partageant une structure composée d'un domaine extracellulaire d'immunoglobuline (Ig) de type variable (IgV), d'une région transmembranaire et d'une queue cytoplasmique qui sert de site d'ancrage pour les protéines de signalisation ou d'échafaudage (Zhang et al., 2004). La queue cytoplasmique de PD-1 possède deux motifs structurels contenant des tyrosines, un *immunoreceptor tyrosine-based inhibitory motif* (ITIM) et un *immunoreceptor tyrosine-based switch motif* (ITSM) (Shinohara et al., 1994). À l'aide de mutations dans ces régions, il a été montré que la fonction inhibitrice de PD-1 dépend de la phosphotyrosine ITSM, qui recrute de préférence la phosphatase-2 contenant le domaine de la région d'homologie 2 de Src (SHP-2), ce qui entraîne une déphosphorylation et une inhibition des voies de signalisation en aval (Chemnitz et al., 2004 ; Yokosuka et al., 2012). Les deux ligands de PD-1 ont un domaine IgV et un domaine IgC extracellulaire, similaire aux autres membres de la famille B7. PD-L1 et PD-L2 ont un court domaine cytoplasmique conservé entre différentes espèces (Dong et al., 1999 ; Latchman et al., 2001). PD-L1 et PD-L2 diffèrent par leur affinité pour PD-1, PD-L2 a une affinité 3 fois plus élevée pour PD-1 comparé à PD-L1. CD80 est un autre partenaire de liaison pour PD-L1, mais ne peut pas se lier à PD-L2 (Butte et al., 2007).

Contrairement à d'autres membres de la famille B7 comme CD28, CTLA-4 et ICOS, PD-1 ne possède pas le résidu cystéine permettant de former un dimère. PD-1, PD-L1 et PD-L2 existent et interagissent sous la forme de monomères (Zak et al., 2015). Il a été montré que le complexe PD-1/PD-L1 forme une interface présentant une grande similitude structurelle avec l'interface entre le TCR et le CMHp (Lin et al., 2008). Comme l'interaction TCR/CMHp, la liaison PD-1/PD-L1 exclut également la phosphatase CD45 en raison de sa taille (Carbone et al., 2017).

La voie canonique PD-1/PD-L1 implique la liaison de PD-1 et PD-L1 en *trans*, quand ces protéines sont exprimées à la surface de LT et de CPA (ou de cellules cancéreuses), respectivement. Il a été montré que l'interaction PD-1/PD-L1 peut également avoir lieu en *cis* sur certaines cellules cancéreuses et des CPA infiltrant des tumeurs, lorsque ces cellules expriment à la fois PD-1 et PD-L1 (Zhao et al., 2018). Cette interaction en *cis* bloque les signaux inhibiteurs de la voie PD-1/PD-L1 canonique en diminuant la disponibilité de ligands PD-L1 sur la CPA.

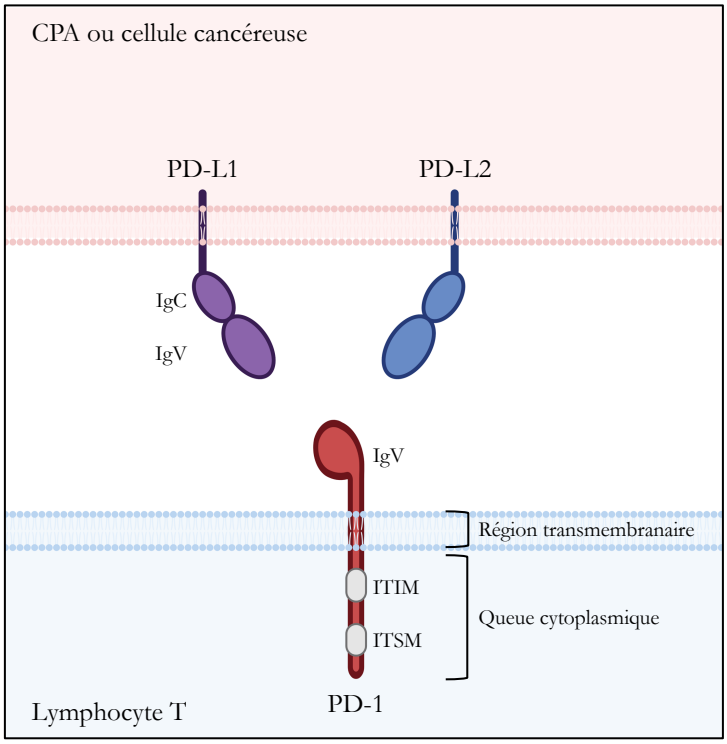


Figure 22 : Structure de PD-1 et ses ligands

**EXPRESSION DE PD-1 ET SES LIGANDS.** Le récepteur PD-1 est exprimé pendant le développement thymique et induit dans différentes cellules hématopoïétiques en périphérie par la signalisation de récepteurs d'antigène et par des cytokines. PD-1 est exprimé par les thymocytes immatures double négatifs ($CD4^-CD8^-$) pendant le réarrangement du TCRβ (Nishimura et al., 1996) et de manière inductible sur les LT périphériques $CD4^+$ et $CD8^+$, les *natural killer* (NK), les *natural killer T* (NKT), les lymphocytes B, les monocytes, et certaines DC après activation (Keir et al., 2008). L'expression de PD-1 par les DC a d'ailleurs été corrélée à un déficit des réponses antibactériennes (Yao et al., 2009) et antitumorales (Lim et al., 2016), et la délétion de PD-1 spécifiquement dans les cellules myéloïdes induit une immunité antitumorale (Strauss et al., 2020), ce qui met en avant que les LT ne sont pas les seules cellules immunitaires ciblées par la voie PD-1/PD-L1.

PD-1 est induit par la signalisation du TCR ou du récepteur des lymphocytes B (BCR) (Agata et al., 1996) et reste fortement exprimé dans un contexte de stimulation d'antigène persistante, comme dans le cas d'infections chroniques ou de cancer. L'expression de PD-1 est également induite par des cytokines comme l'IL-2, l'IL-7, l'IL-15, l'IL-21 (Kinter et al., 2008)mais également l'IFNα (Terawaki et al., 2011). L'expression de surface de PD-1 est régulée post-traductionnellement par la protéine Fut8, une fucosyltransférase des oligosaccharides de PD-1, et l'inhibition de la fucosylation augmente les réponses antitumorales (Okada et al., 2017). L'expression de PD-1 est également régulée par l'E3 ligase FBXO38, qui polyubiquitine PD-1 et induit sa dégradation par le protéasome (Meng et al., 2018).

L'expression de PD-L1 et PD-L2 est régulée par le milieu inflammatoire. Les cytokines sont de puissants activateurs de l'expression de PD-L1 et PD-L2. Les interférons de type 1 et de type 2 et le TNFα induisent l'expression de PD-L1 sur les LT, les LB, les cellules endothéliales et les cellules épithéliales. Les cytokines IL-2, IL-7, IL-15 augmentent également PD-L1 sur les LT (Kinter et al., 2008). Différentes interleukines sont également capables de stimuler l'expression de PD-L1 sur les LB et les monocytes. Comme PD-1, l'expression de PD-L1 est régulée de manière post-traductionnelle par glycosylation et ubiquitination (Li et al., 2016). La glycosylation de PD-L1 est essentielle pour l'interaction PD-1/PD-L1. Des anticorps ciblant la version glycosylée de PD-L1 bloquent l'interaction avec PD-1 et induisent l'internalisation et la dégradation de PD-L1, induisant la rémission de souris porteuses de tumeurs triple-négatives du sein (Li et al., 2018).

## 4.4 Signalisation de la voie PD-1

**INTERACTION ENTRE PD-1 ET SHP-2.** La queue cytoplasmique de PD-1 contient un motif ITSM qui permet le recrutement de la phosphatase SHP-2, qui a été décrite comme étant responsable de la déphosphorylation et de l'inhibition des voies de signalisation en aval (Chemnitz et al., 2004). A l'aide d'anticorps ciblant la tyrosine phosphorylée de l'ITSM (Y248), il a été montré que PD-1 est phosphorylé en réponse à une stimulation simultanée du TCR et de PD-1 (Bardhan et al., 2019). La phosphorylation de la tyrosine 248 de l'ITSM de PD-1 dans des LT humains est corrélée à une altération de leurs fonctions effectrices. Cette phosphorylation a notamment été détectée dans des LT de ganglions drainant des tumeurs, et chez des patients atteints de glioblastomes (Bardhan et al., 2019). SHP-2 a été décrit comme étant le médiateur clé des fonctions inhibitrices des PD-1. Cette protéine possède deux domaines SH2, un domaine phosphatase PTP (*protein tyrosine phosphatase)* et une queue hydrophobique avec deux sites de phosphorylation de la tyrosine. A l'état basal, les domaines SH2 bloquent la région phosphatase et contiennent SHP-2 en conformation auto-inhibitrice fermée. L'interaction du domaine SH2 en N-terminal avec une phosphotyrosine perturbe son interaction avec le domaine phosphatase et active l'enzyme. La liaison des deux domaines SH2 est nécessaire à l'activation complète de SHP-2 (Neel et al., 2003). Ainsi, les phosphotyrosines des motifs ITIM et ITSM de PD-1 se lient aux deux domaines SH2 de SHP-2, relâchant ainsi le domaine phosphatase pour induire son activité enzymatique (Marasco et al., 2020). Un deuxième mode d'activation de SHP-2 par PD-1 a été proposé. Après la phosphorylation de PD-1, les deux domaines SH2 de SHP-2 peuvent se lier chacun à une molécule PD-1, formant alors un dimère PD-1/PD-1 (Patsoukis et al., 2020). Dans ce contexte, seul le motif ITSM à forte liaison est nécessaire, ce qui explique comment un seul site d'ancrage de la queue cytoplasmique de PD-1 peut activer SHP-2 et induire des fonctions inhibitrices.

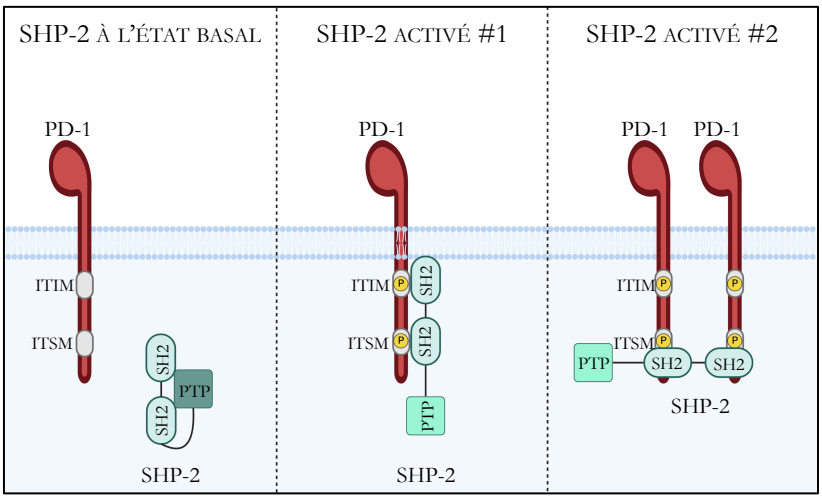


Figure 23 : Interaction entre PD-1 et SHP-2

**LES VOIES DE SIGNALISATION CIBLEES PAR PD-1.** De nombreuses études ont cherché à déterminer les effets de PD-1 sur les voies de signalisation activées par le TCR et les récepteurs costimulateurs, pour comprendre comment la liaison de PD-1 inhibe l'expansion, les fonctions effectrices et la production de cytokines des LT. Cette question fait aujourd'hui encore l'objet d'un débat puisque certaines études ont montré que PD-1 cible principalement le TCR et les voies de signalisation en aval du TCR (Chemnitz et al., 2004 ; Li et al., 2021 ; Mizuno et al., 2019 ; Sheppard et al., 2004 ; Yokosuka et al., 2012), alors que d'autres ont mis en évidence au contraire que la cible principale de PD-1 est le corécepteur CD28 (Hui et al., 2017 ; Kamphorst et al., 2017 ; Krueger and Rudd, 2017). Certaines équipes ont par ailleurs proposé que PD-1 cible le TCR et CD28 de la même manière (Celis-Gutierrez et al., 2019). Malgré le débat au sujet de la cible principale de PD-1, l'accord commun désigne SHP-2 comme le seul partenaire direct identifié de PD-1, et le tient responsable de la médiation des signaux inhibiteurs de PD-1. C'est pourquoi il était inattendu que les souris présentant une délétion de SHP-2 spécifique des LT puissent bénéficier d'un blocage de PD-1 dans le contexte du cancer. Cela suggère l'existence potentielle d'autres signalisation de PD-1, ou d'autres implications indépendantes de la signalisation, pouvant assurer la médiation de la fonction inhibitrice de PD-1 en l'absence de SHP-2 (Rota et al., 2018). Il a d'abord été proposé que la phosphatase SHP-1 pourrait se lier à PD-1 en absence de SHP-2 et compenser les effets inhibiteurs (Celis-Gutierrez et al., 2019). Cette suggestion a été infirmée par la mise en évidence que des LT double déficients pour SHP-1 et SHP-2 étaient toujours capables d'induire une inhibition de la prolifération et de la production des cytokines, même si les effets étaient diminués par rapport aux LT *wild-type* (Xu et al., 2020).

La phosphatase SHP-2 n'est pas seulement impliquée dans la signalisation dépendante de PD-1, elle est aussi essentielle à la formation du signalosome du TCR (Presotto et al., 2017). Comme l'expression de PD-1 est induite après activation et que la protéine est localisée dans les *microclusters* de TCR lors de son interaction avec PD-L1 (Yokosuka et al., 2012), on peut penser que les molécules de PD-1 sont regroupées et stabilisées par leur interaction avec PD-L1 autour des molécules de TCR, et qu'elles servent de "commutateurs" entre les formations de signalosomes positifs et les formations de signalosomes négatifs. Certaines protéines identifiées comme partenaires moléculaires du signalosome de PD-1 font également partie de celui du TCR, comme Grb2, Lck et ZAP-70 (Celis-Gutierrez et al., 2019).

## 4.5 Les fonctions effectrices inhibées par PD-1

L'engagement de PD-1 par ses ligands lors d'une stimulation antigénique induit, comme nous l'avons vu précédemment, le recrutement de SHP-2 qui déphosphoryle des protéines clé des voies du TCR et de costimulation par CD28. Cela provoque l'inhibition de différentes fonctions effectrices des LT :

- **La prolifération** est très sensible à l'inhibition par PD-1. Normalement, la reconnaissance d'un antigène par le TCR induit une prolifération importante des LT. En présence de PD-L1 et de faibles quantités de PD-1, la prolifération est diminuée de 40%. Lorsque PD-1 est présent sur les LT en plus grandes quantités, la prolifération est presque totalement bloquée (Wei et al., 2013). PD-1 empêche la prolifération des LT en bloquant la progression du cycle cellulaire dans la phase G1 (Patsoukis et al., 2012).

- **La cytotoxicité** des CTL est inhibée par PD-1 lors de l'interaction avec ses ligands. En effet, l'expression de granzyme B et de la perforine est diminuée (Wu et al., 2014), et la mesure directe du nombre de cellules cibles éliminées en présence de l'interaction PD-1/PD-L1 a révélé une nette diminution par rapport aux LT $CD8^+$ $PD\text{-}1^-$ (Wei et al., 2013). Bloquer l'interaction entre PD-1/PD-L1 à l'aide d'anticorps monoclonaux permet de restaurer l'activité cytotoxique des CTL et de réduire la taille de tumeurs *in vivo* (Hirano et al., 2005).

- **La sécrétion de cytokines** est diminuée par PD-1 lors de l'activation des LT. Plusieurs cytokines essentielles à l'inflammation, la prolifération, l'activation et la survie des LT sont ciblées comme l'IL-2, l'IL-10, le TNFα, l'IFNɣ (Freeman et al., 2000 ; Rosskopf et al., 2018 ; Wei et al., 2013).

- **La glycolyse** est également ciblée par PD-1, ce qui empêche le switch métabolique de l'OXPHOS vers la glycolyse lors de l'activation des LT. PD-1 favorise plutôt la lipolyse et l'oxydation des acides gras (Patsoukis et al., 2015). Ainsi, en augmentant l'oxydation des acides gras qui est le programme métabolique nécessaire à la persistante des LT mémoires quiescents, PD-1 favorise le développement de LT mémoires (Kalia et al., 2021).

## 4.6 PD-1 dans la formation de la synapse immunologique

La majeure partie des études publiées au sujet de PD-1 se sont impliquées à caractériser les fonctions inhibitrices de la protéine pour développer des thérapies dans différents contextes pathologiques. Il est largement accepté que PD-1 inhibe l'activation des LT et les fonctions effectrices qui en résultent. Seulement, une activation efficace réside en la formation d'une synapse immunologique et le remodelage du cytosquelette d'actine associé, et peu d'articles caractérisant les effets de PD-1 sur la formation de la SI ont été publiés jusqu'à présent.

**LA STABILITE DES CONTACTS.** Quelques études contradictoires ont été publiées, caractérisant la stabilité des contacts formés entre des LT et des CPA. D'une part, il a été montré dans un modèle murin *in vivo* de LT spécifiques d'antigènes tolérogènes, que les interactions PD-1/PD-L1 inhibent le signal d'arrêt des LT sur les CPA (Fife et al., 2009). Un autre groupe a ensuite montré que les TIL purifiés à partir de souris porteuses de tumeurs, forment des conjugués instables avec les cellules tumorales *ex vivo* (Ambler et al., 2020). Enfin, une troisième publication a suggéré que les LT exprimant PD-1 sont incapables de former des SI matures et stables avec des CPA exprimant PD-L1/L2 (Tocheva et al., 2020). A l'inverse, il a été montré dans un modèle murin d'infection virale chronique, que les LT $CD4^+$ et $CD8^+$ spécifiques du virus sont moins mobiles et forment des SI plus stables que les LT issus d'une infection virale aiguë (Zinselmeyer et al., 2013). Dans contexte, l'inhibition de la motilité des LT et l'augmentation de la stabilité des SI sont dépendantes de la liaison de PD-1 à PD-L1, et le blocage thérapeutique de l'interaction rétablit la motilité et la stabilité des SI des LT seulement 30 minutes après le traitement.

**LE CYTOSQUELETTE D'ACTINE.** Des données publiées récemment suggèrent que PD-1 serait impliqué dans l'inhibition du cytosquelette d'actine à la SI. Un groupe a montré que PD-1 inhibe l'étalement de LT $CD8^+$ de souris en présence de CMHp et de PD-L1, qui est lié au remodelage du cytosquelette d'actine (Li et al., 2021). Aussi, par une analyse de phosphoprotéomique, il a été identifié que la voie PD-1 cible les phosphotyrosines qui régulent le remodelage du cytosquelette et la formation de la SI (Tocheva et al., 2020). Enfin, il a été proposé que la zone hypodense d'actine au centre de la SI n'apparaît pas dans les TIL, mais ce défaut n'est pas restauré par le blocage de la voie PD-1/PD-L1 (Ambler et al., 2020), donc il pourrait être provoqué par d'autres facteurs propres aux TIL plutôt qu'à PD-1. Bien que PD-1 soit très étudié depuis plusieurs années, les mécanismes inhibiteurs des LT ne sont à ce jour toujours pas entièrement décryptés.

# CHAPITRE 5

## Objectifs de la thèse

Dans cette cinquième partie de l'introduction je présenterai les objectifs, questions et hypothèses qui ont guidé mon projet de thèse.

## Objectifs de la thèse

PD-1 offre un potentiel thérapeutique unique qui, sous condition d'une meilleure compréhension fondamentale de son mode de fonctionnement, pourrait bénéficier d'une efficacité largement accrue chez nombre de patients. Néanmoins, il reste des déficits de compréhension à ce sujet, notamment le rôle que joue PD-1 dans la formation de la synapse immunologique, ainsi que l'implication des motifs de signalisation de la protéine dans ce dernier. Il a récemment été suggéré que PD-1 altère les voies de remodelage du cytosquelette qui sont essentielles à la formation d'une synapse immunologique, mais également finement liées au métabolisme cellulaire. Enfin, il est connu que PD-1 altère le métabolisme des lymphocytes T en favorisant l'oxydation des acides gras au détriment de la glycolyse. Au vu des liens précédemment établis entre le métabolisme et le cytosquelette d'actine, le ciblage du remodelage par PD-1 pourrait représenter un nouvel acteur central de ses fonctions inhibitrices. Ainsi, mon projet de thèse a été guidé par trois questions fondamentales :

1. Quels sont les effets de PD-1 sur les différents réseaux de cytosquelette d'actine à la synapse immunologique ?
2. Quelles sont les implications de ces altérations sur les fonctions effectrices des lymphocytes T, en particulier sur la cytotoxicité des lymphocytes T $CD8^+$ ?
3. Est-ce que ces altérations sont dépendantes des motifs de signalisation de PD-1 ?

Dans un premier temps, j'ai développé les outils nécessaires à l'étude des effets de PD-1 sur la synapse immunologique. Pour ce faire, j'ai mis au point deux systèmes de formation de synapse : le premier, simpliste, permet d'activer les lymphocytes T exprimant PD-1 à l'aide de surfaces de verre recouvertes d'anticorps stimulants le TCR et la voie de costimulation CD28 et de PD-L1, pour activer simultanément les voies activatrices et la voie PD-1/PD-L1. Un deuxième système, utilisant des cellules présentatrices d'antigène artificielles pour activer les LT, m'a ensuite permis d'étudier l'impact de PD-1 à la synapse sur un modèle plus physiologique de conjugués entre deux cellules. À partir de lymphocytes T primaires humains $CD8^+$ exprimant PD-1 à la suite de leur activation, ou de Jurkat exprimant PD-1, j'ai pu identifier les défauts d'actine associés à l'engagement de PD-1 à l'aide de différentes techniques de microscopies à fluorescence et à haute résolution. A l'aide d'approches de biologie moléculaire j'ai ensuite caractérisé la voie de signalisation ciblée par PD-1 responsable de ce défaut du remodelage de cytosquelette d'actine.

Dans un second temps, j'ai cherché à élucider le lien existant entre les défauts observés sur le cytosquelette d'actine à la synapse immunologique, et les fonctions effectrices des lymphocytes T. Plus précisément, les réseaux d'actine à la synapse ont été décrits comme étant intimement liés à l'efficacité de la cytotoxicité des lymphocytes T $CD8^+$. Cette fonction est également essentielle d'un point de vue thérapeutique, puisque le rationnel des anticorps bloquant PD-1/PD-L1 est de revigorer les lymphocytes T $CD8^+$ pour restaurer leur capacité antitumorale. Ainsi, j'ai comparé les capacités des LT $CD8^+$ exprimant PD-1 à sécréter les granules cytolytiques et analysé la polarisation des granules et du centrosome dans des cellules formant des synapses en présence ou en absence de PD-L1.

Enfin, j'ai étudié l'implication des motifs de signalisation de PD-1 permettant le recrutement de SHP-2 dans les défauts observés sur l'actine à la synapse. En comparant les effets de la protéine PD-1 mutée sur les tyrosines essentielles de ces motifs par rapport à la protéine sauvage sur le remodelage d'actine à la synapse, j'ai pu mettre en évidence des résultats qui seront présentés dans le premier article de la partie résultats.

Le lien entre l'altération du cytosquelette d'actine par PD-1 et le métabolisme a fait l'objet d'une collaboration avec l'équipe de Chiara Stringari à l'École Polytechnique. En raison de difficultés techniques et d'un manque de consistance des résultats, nous avons finalement soumis un article, présenté dans la deuxième section des résultats du manuscrit, comparant le métabolisme et l'actine des lymphocytes T au repos par rapport aux lymphocytes T activés. Les données préliminaires sur les liens des effets de PD-1 entre l'actine et le métabolisme seront présentés et discutés dans la partie discussion et perspectives de ce manuscrit.

Ce manuscrit de thèse se conclut par la présentation en annexe des travaux auxquels j'ai pris part, en complément de mon projet principal, durant la période de ma thèse. Les deux premières annexes sont issues de travaux effectués au sein du laboratoire de Claire Hivroz à l'Institut Curie, portant sur le lien entre les forces établies à la synapse immunologique et le cytosquelette d'actine. La troisième annexe est le fruit d'une collaboration avec l'équipe de Michel Sadelain au Memorial Sloan Kettering Cancer Center, portant sur le développement d'un nouveau système de CAR-T cells. Grâce aux méthodes développées pour mon projet principal, j'ai pu comparer la formation et l'efficacité des synapses entre des CAR-T d'ancienne et de nouvelle génération avec des cellules cibles.

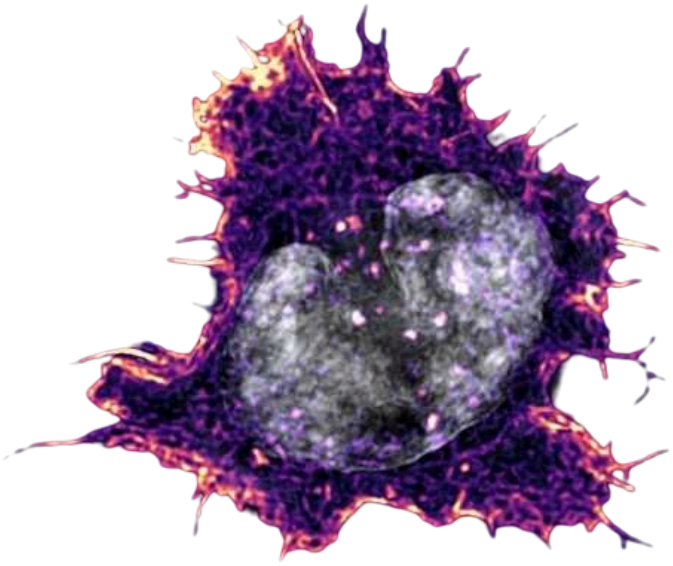

# RESULTATS

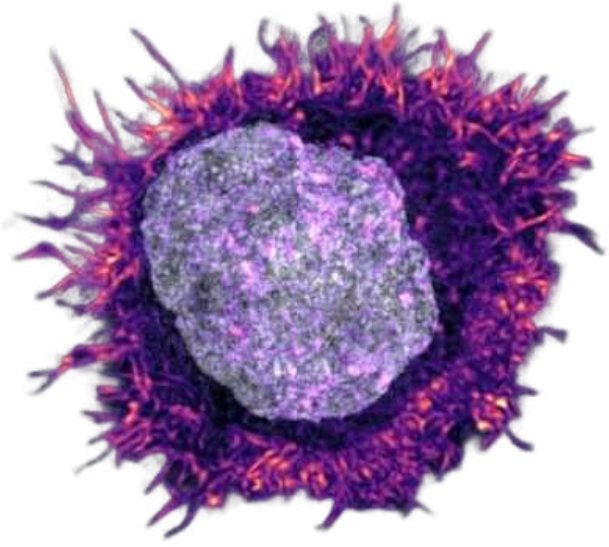

## Article 1 : PD-1 inhibits T cell actin remodeling at the immune synapse independently of its signaling motifs

1er auteur

Article en révision, Science Signaling


**Résumé**

La liaison du récepteur PD-1 (Programmed cell death protein 1) à ses ligands, PD-L1 et PD-L2, régule négativement les réponses immunitaires. Cette caractéristique inhibitrice de l'activation des lymphocytes T a identifié PD-1 comme une cible d'immunothérapie pour traiter certains cancers. Malgré de nombreuses études visant à déceler les mécanismes d'inhibition des lymphocytes T par PD-1, ils restent partiellement élucidés.

Sachant que le remodelage dynamique de l'actine est essentiel pour les fonctions des cellules T, nous avons caractérisé les effets de la liaison de PD-1 à PD-L1 sur le remodelage de l'actine à la synapse immunitaire. Pour ce faire, nous avons analysé par microscopie la formation de synapses immunitaires entre des cellules T cytotoxiques $CD8^+$ humaines ou Jurkat PD-$1^+$ et des cellules présentatrices d'antigènes artificielles, pouvant « présenter » des anticorps activateurs et exprimant ou non PD-L1.

Nous montrons, dans les deux modèles de cellules T, que la liaison de PD-1 à PD-L1 inhibe l'étalement induit par la stimulation de CD3/CD28. Cette inhibition est caractérisée par une absence du réseau de lamellipode distal dense en F-actine et de la région centrale hypodense en F-actine à la synapse. L'inhibition du remodelage de l'actine induite par PD-1 empêche également la déformation caractéristique des cellules T et diminue la libération des granules cytotoxiques. Nous montrons que ces effets sur le remodelage de l'actine ne dépendent pas des deux motifs de signalisation considérés jusqu'à présent comme responsables des effets co-inhibiteurs de PD-1.

Notre étude met en évidence un nouveau mécanisme de suppression de l'activité des lymphocytes T médiée par PD-1, qui repose sur la régulation négative de la dynamique du cytosquelette d'actine, de manière indépendante de la signalisation.

**Contribution à l'article**

Cet article est le fruit de mon projet de thèse principal. J'y ai donc pris part de son élaboration, à son exécution expérimentale, l'analyse des résultats, jusqu'à l'écriture de l'article.

Concernant le travail expérimental, j'ai généré et cultivé l'ensemble des modèles cellulaires : lymphocytes T primaires, lignée de LT Jurkat, cellules présentatrices artificielles, transductions lentivirales, transfections.

Concernant les figures de l'article, j'ai mis au point les protocoles, généré et analysé toutes les données présentées dans l'article. Certaines expériences (Fig3B-C ; Fig4E ; Fig5D-E) ont été reproduites par des collègues pour renforcer les statistiques de notre étude.

Plus précisément, j'ai mis au point les protocoles suivants :

- La culture et la génération de lymphoblastes primaires humain $CD8^+$ exprimant PD-1
- L'activation et l'inhibition des lymphocytes T par les cellules présentatrices artificielles
- L'étalement des lymphocytes T sur des surfaces recouvertes d'anti-CD3/CD28 en présence de PD-L1
- L'activation et la lyse des lymphocytes T sur plaque pour analyser l'expression protéique de pHS1 par western blot
- Le test de cytotoxicité analysé par cytométrie en flux

Quant à l'écriture du manuscrit, j'ai monté l'ensemble des figures, rédigé la partie résultats et contribué à la rédaction du reste de l'article.

# PD-1 inhibits T cell actin remodeling at the immune synapse independently of its signaling motifs

**Authors:** Noémie Paillon[1, 2], Violette Mouro[1], Stéphanie Dogniaux[1], Mathieu Maurin[1], Hermine Ferran[1, 2], Juan-José Saez Pons[1], Laurence Bataille[1], Andrés Ernesto Zucchetti[1], Claire Hivroz[1*]

**Affiliations:**
[1]Institut Curie, PSL Research University, INSERM, U932 "Integrative analysis of T cell activation" team; Paris, France.
[2]Université Paris Cité; Paris, France.
[*]Corresponding author, claire.hivroz@curie.fr

**Abstract**: Programmed cell Death-1 receptor (PD-1) engagement by its ligands, PD-L1, and PD-L2, negatively regulates T cell-mediated immune responses. Despite the compelling studies on the inhibitory effects of PD-1 on T cell activation and on the clinical effects of PD-1 targeted immunotherapy, the mechanisms involved in PD-1 inhibition are only partially unraveled. Knowing that dynamic remodeling of actin is crucial for T cell functions, we characterized the effects of PD-1 binding to PD-L1 on actin remodeling at the immune synapse. To do so, we analyzed by microscopy the formation of immune synapses between PD-1$^+$ Jurkat or human primary CD8$^+$ cytotoxic T cells and antigen-presenting cells (APCs) that can "present" activating antibodies and express or not PD-L1. We show, in both T cell models, that PD-1 binding to PD-L1 inhibits the spreading induced by CD3/CD28 stimulation. This inhibition is characterized by an absence of the F-actin-dense distal lamellipodial network and the F-actin hypodense central region at the synapse. PD-1-induced actin remodeling inhibition also prevents the characteristic change in T cell shape and decreases cytotoxic granule release. Strikingly, we show that these effects on actin remodeling do not depend on the two signaling motifs, i.e., the immunoreceptor tyrosine-based inhibitory motif (ITIM) and immunoreceptor tyrosine-based switch motif (ITSM) so far considered to be responsible for the PD-1 co-inhibitory effects. Our study highlights a new mechanism for PD-1-mediated suppression of T cell activity, which relies on the signaling-independent regulation of actin cytoskeleton dynamics.

**One Sentence Summary:** Paillon et al. show herein that PD-1, a T cell checkpoint receptor and target of cancer immunotherapy, alters the T cell actin cytoskeleton remodeling at the immune synapse. In contrast to all the PD-1 inhibitory effects reported so far, this cytoskeleton alteration does not require the signaling motifs present in the intracellular domain of PD-1. This study reveals a new mechanism by which PD-1 inhibits T cell activation.

**Keywords:** PD-1; immune synapse; T lymphocytes; actin

**Main Text:**

**INTRODUCTION**

Programmed cell death protein 1 (PD-1) was discovered 30 years ago (*1*). It was soon revealed that PD-1 engagement protects against tissue damage and autoimmune diseases by inducing and maintaining T-cell tolerance and inhibiting self-reactive T cells, but also by causing cell exhaustion during chronic antigen stimulation (*2*). This critical role has brought great opportunities to exploit the inhibitory functions of PD-1 and its ligands PD-L1 and PD-L2 in clinical applications such as cancers and autoimmune diseases (*3*, *4*). Despite its demonstrated importance in the treatment of human cancer, the mechanisms of PD-1–mediated inhibition of T cell functions remain partially understood. Early work demonstrated that binding of PD-1 to PD-L1 causes the phosphorylation of two tyrosines from the PD-1 cytoplasmic domain present in an immunoreceptor tyrosine-based inhibitory motif (ITIM) and immunoreceptor tyrosine-based switch motif (ITSM) (*5*, *6*). It was then shown that phosphorylated PD-1 preferentially recruits the cytosolic tyrosine phosphatase SHP-2 (*7–9*) that induces the dephosphorylation of TCR proximal signaling molecules (*7*, *10*). This interpretation was challenged by a study showing that the main target of PD-1-induced dephosphosphorylation was CD28 rather than TCR-associated molecules (*11*). The role of SHP-2 itself in the PD-1 inhibitory effect on T cell activation was also challenged by results showing that T cell-specific deletion of SHP-2 in mice did not improve antitumor immunity and did not alter antitumor responses of these mice to PD-1 antibody treatment (*12*, *13*). These controversies indicate the importance to continue characterizing the inhibitory effects of PD-1 in T cells.

Initial TCR binding to cognate peptide-MHC (pMHCs) induces a massive reorganization of the T cell cortical actin cytoskeleton, forming a specialized cell–cell interface termed the immune synapse (*14*, *15*). This synapse assembly is characterized by discrete actin networks: the most prominent actin network at the immune synapse is the dense actin network that defines the distal part of the immune synapse (*16*, *17*). This network is mainly composed of branched actin filaments which look like the lamellipodial region of a migrating cell and has thus been called lamellipodium. It forms within minutes after initial TCR stimulation resulting in T cell spreading on the antigen-presenting cells (APC) surface. It is followed by an actin retrograde flow, which forms a filamentous-actin (F-actin) hypodense central region leading to the formation of the so-called bull's eye immune synapse (*18*, *19*). This actin cytoskeleton sustains the coordination of key cellular activities. This is exemplified by primary immunodeficiencies caused by mutations in genes encoding actin regulatory proteins that show strong defects in T lymphocyte functions (*20*). Indeed, actin remodeling at the immune synapse regulates many functions of T lymphocytes. Among others, it promotes T cell spreading on interacting APC (*21–23*), and thus cell-cell contact, it provides a scaffold for the assembly of signaling complexes (*14*, *24*) regulates the formation of the cytotoxic immune synapse and the efficient killing of target cells (*21*, *25*). Part of these effects may be due to the role that F-actin dynamics play by actively exerting force at the molecular levels on receptors and signaling molecules and at the cellular levels on T lymphocytes and APC (*17*, *26*). Indeed, these forces can, among others, modify the binding kinetics of receptor-ligands couples (*27*) and transmit signals after the conversion of mechanical forces to biochemical signals by changes in conformation, clusterization of molecules, or opening of ion channels (*28*). At the cellular level, forces exerted by the actin cytoskeleton control the dynamic topology of the immune synapse, and thus of the cells engaged in the contact (*29*), they participate in changing membrane curvature (*30*) and potentiate target cell killing (*31*, *32*).

Knowing the importance of actin remodeling in many T cell functions, we assessed whether some of the PD-1-dependent inhibitory effects may be related to the regulation of actin remodeling at the immune synapse. To do so, we analyzed the immune synapse formation between PD-1

transduced Jurkat T cells or human primary PD-1$^+$ CD8$^+$ cytotoxic T cells and engineered APCs, that express or not PD-L1, coated with activating antibodies. Our data show that PD-1 binding to PD-L1 inhibits the CD3/CD28-induced spreading of both PD-1$^+$ Jurkat and primary CD8$^+$ cytotoxic T cells. More specifically, it prevents the formation of the F-actin-dense distal lamellipodial network and of the F-actin hypodense central region and of the change in morphology of the T cell at the immune synapse. This inhibition of actin remodeling is, at least in part, responsible for the inhibition by PD-1 of cytotoxic granule release. Unexpectedly, we show that PD-1-dependent inhibition of actin remodeling does not depend on the ITSM and ITIM motifs of PD-1.

Our results highlight a totally new mechanism by which PD-1 inhibits immune synapse formation and functions in T lymphocytes independently of its signaling ability.

## RESULTS

### PD-1 alters T cell spreading

We aimed at understanding the impact and consequences of PD-1/PD-L1 interaction on the formation of the immune synapse. As a model, we used either primary activated CD8$^+$ T cells expressing PD-1, or the Jurkat T cell line stably transduced with human PD-1 (Fig S1). Upon stimulation of the T-cell receptors (TCR) and co-receptors, T cells spread over the antigen-presenting cells (APCs) surface (*33*). *In vitro*, this mechanism can be mimicked by coating surfaces with anti-CD3 and anti-CD28 antibodies, to activate T cells through the TCR complex and the co-stimulatory CD28 pathway. Using this system, we compared the cell spreading of T cells on glass surfaces coated with anti-CD3/CD28 antibodies together with a recombinant PD-L1-Fc chimera protein or an IgG1-Fc as a control, to test the impact of PD-1/PD-L1 on T cell spreading. We followed T cell spreading area and F-actin remodeling by labeling the T cells with fluorescent phalloidin (Fig 1A). We observed an altered spreading upon PD-1 engagement in both PD-1$^+$ CD8$^+$ T cells and PD-1$^+$ Jurkat. The actin-rich lamellipodium formation at the periphery of the synapse (*34*) was inhibited, resulting in a significant decrease in the spreading area (Fig 1B-C) and of the F-actin intensity (Fig 1D-E) at the synapse. In wild-type Jurkat T cells that do not express PD-1, the presence of PD-L1 on the surface did not induce any reduction in the spreading area, lamellipodium formation, or F-actin intensity (Fig S1C-D). Moreover, primary PD-1$^+$ CD8$^+$ T cells treated with the PD-1-blocking antibody Nivolumab neither showed a defect in spreading nor in F-actin intensity (Fig S1E), demonstrating that these effects are indeed induced by PD-1 binding to PD-L1. Together, these results show that PD-1 binding to PD-L1 alters T cell spreading and F-actin remodeling at the synapse induced by TCR and CD28 stimulation.

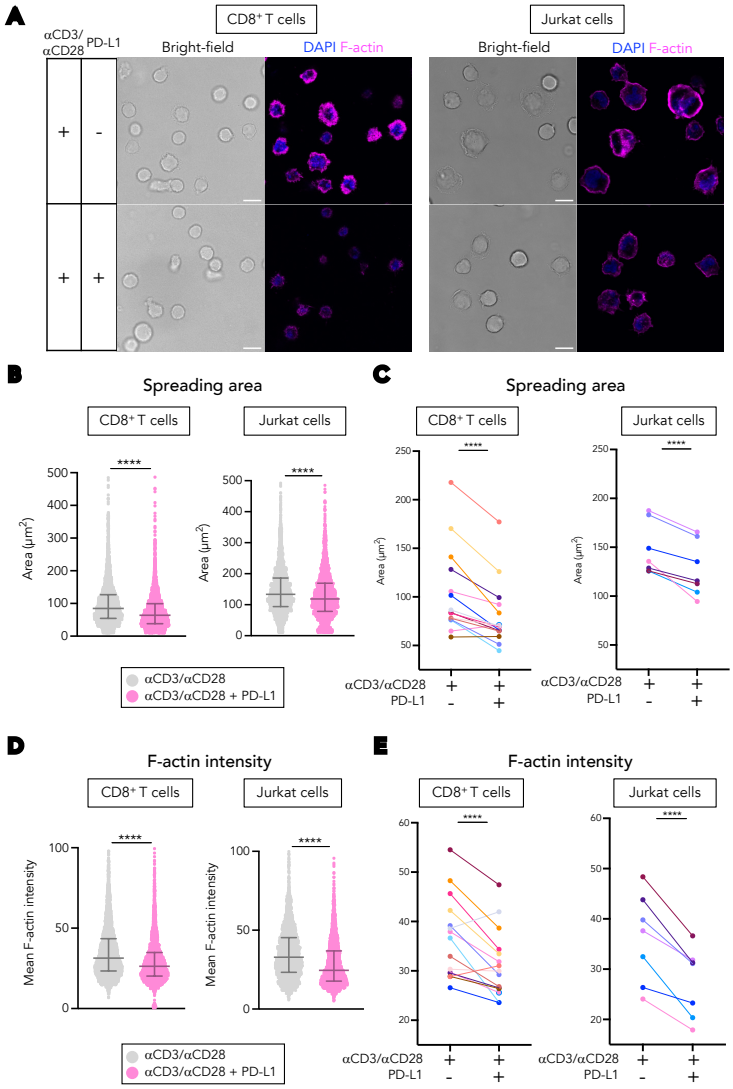


**Figure 1**. **PD-1 alters T cell spreading.** (**A**) Representative images of the effect of PD-1 on T cell spreading. Images were acquired by confocal microscopy; one Z plane of the contact zone between cells and slide is shown. Scale bar: 10µm. (**A-E**) PD-1$^+$ CD8$^+$ T cells or PD-1$^+$ Jurkat T cells were incubated for 10min on glass surfaces coated with poly-L-lysine, anti-CD3/CD28 antibodies together with PD-L1-Fc or IgG1-Fc as a control. Cells were then fixed, permeabilized and stained with DAPI (blue) and phalloidin (magenta). (**B-C**) Spreading area and (**D-E**) F-actin intensity of PD-1$^+$ CD8$^+$ T cells and PD-1$^+$ Jurkat cells after 10min spreading measured by confocal microscopy. (**B, D**) Data are presented as median with interquartile range. Mann-Whitney T-test ****P≤ 0.0001. (**C, E**) PD-1$^+$ CD8$^+$ T cells: each color represents one healthy donor, PD-1$^+$ Jurkat T cells: each color represents one experiment. PD-1$^+$ CD8$^+$ T cells N = 10 independent experiment, 15 healthy donors. PD-1$^+$ Jurkat cells N = 7 independent experiments. 2-way ANOVA, ****P≤ 0.0001.

**PD-1 inhibits actin remodeling at the immune synapse**

To test whether PD-1-induced actin defect was also observed upon conjugate formation with an APC, we developed a model of engineered APCs (Fig S2A). We used the erythroleukemia, MHC-lacking cell line K562 (*35*) and transduced it with the high-affinity IgG receptor, CD64 (FcγRI) (*36*). These engineered APCs can capture the Fc fraction of anti-CD3 and anti-CD28 antibodies via CD64 (*37*) (Fig S2B) and "present" them to any T cell to stimulate the TCR- and CD28 pathways. To compare the formation of the immune synapse in the presence or absence of PD-1 engagement, we transduced the CD64 expressing APCs with a plasmid encoding PD-L1-GFP or GFP as a control (called hereafter APC-PD-L1 or APC, Fig S2C). These APCs were able to activate T cells upon anti-CD3/CD28 presentation, as exemplified by CD25 upregulation by T cells co-cultured with $APC^{+aCD3/CD28}$ (Fig S2D). The expression of PD-L1 by the APCs inhibited CD25 upregulation of PD-$1^+$ Jurkat T cells but not of wild-type Jurkat T cells (Fig S2D). After 30min co-culture with APCs or APC-PD-L1 presenting or not anti-CD3/CD28 antibodies, we analyzed the different immune synapses formed by Jurkat T cells overexpressing PD-1-YFP and LifeAct-mCherry to follow the F-actin (*38*). As expected, T cells interacting with $APC^{+aCD3/CD28}$ formed an actin-rich lamellipodium at the periphery of the contact zone and an actin-hypodense region at the center of the contact (*39*, *40*). These cells adopted a phagocytic-like convex shape (Fig 2A) as described (*41*). In the absence of activating antibodies, T cells remained round, and F-actin localized homogeneously at the cortex of the cell (Fig 2A-C). In the absence of PD-L1 on the APC, PD-1 was homogeneously present at the cell surface (Fig 2A, D-E). The mere expression of PD-L1 at the APC surface induced the recruitment of PD-1 in the contact zone as previously described (*7*) and did not require TCR-triggering (Fig 2A, 2D-E). T cells forming a synapse with APC-PD-L1 neither adopted a convex morphology nor formed the actin-rich lamellipodium and actin-hypodense region at the immune synapse (Fig 2A, B-C). In the absence of activation, PD-1/PD-L1 interaction inhibited the slight F-actin enrichment at the contact zone (Fig 2A, B-C), suggesting that PD-1 does not only inhibit TCR-dependent actin remodeling. We then measured the solidity, i.e., the convexity of the shape adopted by PD-$1^+$ $CD8^+$ T cells forming conjugates with APCs or APC-PD-L1. We observed that PD-1 engagement increased PD-$1^+$ $CD8^+$ T cell solidity, showing that the characteristic T cell deformation at the immune synapse was lost as in PD-$1^+$ Jurkat T cells (Fig 2F-G). PD-$1^+$ $CD8^+$ T cell solidity was also affected by the presence of PD-L1 on the APC in the absence of activating antibodies. However, the alteration of the actin remodeling at the immune synapse upon PD-1 engagement did not hinder conjugate formation between T cells and APCs (Fig S2E-F). Live imaging of PD-$1^+$ Jurkat T cells interacting with PD-$L1^-$ (movie 1) or PD-$L1^+$ (movie 2) APCs coated with anti-CD3/CD28 antibodies recapitulated these defects. In the absence of PD-L1 on the APC, PD-1 was not enriched at the immune synapse and the T cell progressively showed enrichment of F-actin at the periphery of the contact and a characteristic deformation. In the presence of PD-L1 on the APC, PD-1 was strongly enriched in the contact zone, the F-actin was not remodeled, and the T cell stayed round. However, at early times points after contact, before PD-1 was entirely recruited, F-actin enriched in the contact zone in both cases (see minute 08:15 movie 1 and minute 01:30 movie 2) suggesting that PD-1 engagement does not alter early contact formation.

Altogether, these results suggest that PD-1/PD-L1 interaction prevents correct actin remodeling at the immune synapse, leading to the absence of the formation of the actin-rich lamellipodium of the characteristic deformation of T cell at the immune synapse.

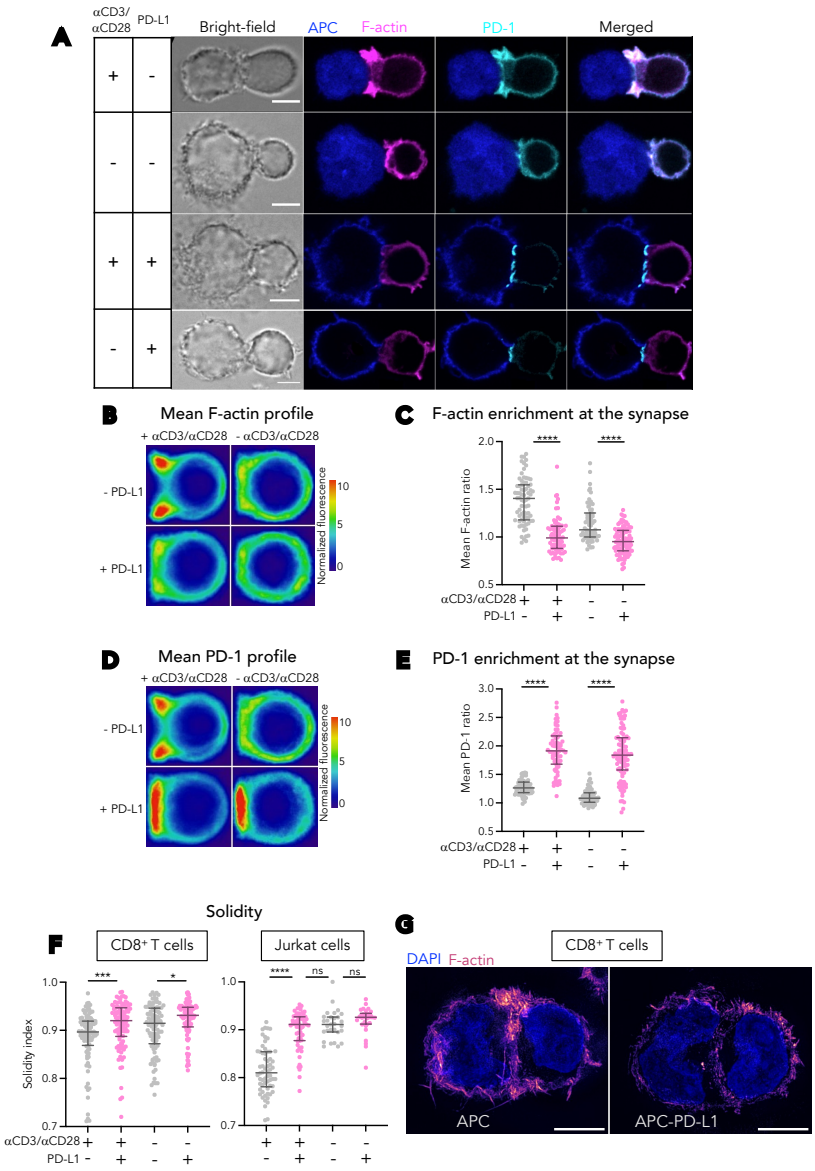


**Figure 2. PD-1 inhibits actin remodeling at the immune synapse.** (**A**) Representative images of immune synapse formation in the presence and absence of PD-1 engagement. Images were acquired by confocal microscopy; one sagittal Z plane of the immune synapse is shown. Scale bar: 5µm. (**A-E**) Jurkat T cells expressing PD-1-YFP (cyan) and LifeAct-mCherry (magenta) were co-cultured for 30min with APCs or APC-PD-L1, either coated with anti-CD3/CD28 antibodies or not. Conjugates were then fixed, permeabilized, and stained with anti-GFP, anti-mCherry, and anti-PD-L1. APCs were stained with Celltracker CMAC blue and APC-PD-L1 were identified by PD-L1 labeling. (**B, D**) Mean profiles of F-actin and PD-1 distribution in PD-1-YFP$^{+}$ Jurkat cells upon conjugate formation with APCs or APC-PD-L1. Cells were normalized to the same size and fluorescent

intensity and the average projection of all cells was done to see signal distribution, using a linear LUT to show signal accumulation. (**C, E**) Quantification of the enrichment of F-actin and PD-1 at the cortex in the contact zone compared to the cortex at the back of the cells. N = 3 independent experiments with >60 conjugates per condition. Data are presented as median with interquartile range. Mann-Whitney T-test ****P≤ 0.0001, ***P≤ 0.001. (**F**) Quantification of the solidity calculated as the area of the F-actin mask divided by the convex area in PD-$1^+$ $CD8^+$ T cells and PD-$1^+$ Jurkat T cells forming 30 min conjugates with APCs or APC-PD-L1, coated or not with anti-CD3/CD28 antibodies. PD-$1^+$ CD8: N = 2 independent experiments, 4 healthy donors, >60 conjugates/condition. PD-$1^+$ Jurkat T cell: N = 3 independent experiments, >60 conjugates/condition. Data are presented as median with interquartile range. Mann-Whitney T-test ***P≤ 0.001, *P ≤ 0.05. (**G**) Representative image of the solidity of primary PD-$1^+$ $CD8^+$ T cells forming an immune synapse with APCs or APC-PD-L1 for 30min. Images were acquired by 3D-SIM, images are a projection of 20 sagittal Z planes. Scale bar: 5µm.

**PD-1 inhibits the Arp2/3 complex activity**

Immune synapse formation is regulated by different actin meshwork in T cells. At the periphery of the contact, an actin-rich lamellipodium forms, whereas the center of the contact is hypodense in F-actin (*42*). Upon immune synapse formation, the Arp2/3 complex localizes to the periphery of the contact zone and nucleates the actin-rich lamellipodium (*17*). To better characterize the alteration in actin remodeling induced by PD-1, we used high-resolution 3D Structured Illuminated Microscopy (3D SIM) to image the spreading of PD-$1^+$ $CD8^+$ T cells. We observed a loss of the characteristic branched actin lamellipodium upon PD-1 engagement (Fig 3A). One of the molecules playing a key role in actin remodeling at the immune synapse is HS1, the leukocyte-specific homolog of cortactin. When phosphorylated, HS1 activates Arp2/3-induced actin polymerization and stabilizes branched actin structures (*22*, *43*). We assessed if PD-1/PD-L1 interaction altered Arp2/3 complex activity by following the phosphorylation of HS1. PD-$1^+$ $CD8^+$ T cells were activated in plastic wells coated with anti-CD3/CD28 antibodies with PD-L1-Fc or IgG1-Fc as a control and then lysed in the wells. T cell activation induced the phosphorylation of HS1 (pHS1, Fig 3B). As expected, inhibiting the Arp2/3 complex with CK666 treatment decreased the phosphorylation of HS1 induced by anti-CD3/CD28 antibodies. Similarly, PD-1 interaction with PD-L1 reduced the amount of pHS1 in PD-$1^+$ $CD8^+$ T cells activated 10min with anti-CD3/CD28 antibodies from most healthy donors. This is shown in Figure 3B which presents the normalized pHS1 measured by western blot, which decreased in 6 out of 8 donors. Another representation of the data is shown in Figure 3C which represents the fold change in pHS1 between T cells from the same 8 donors activated in the absence or presence of PD-L1. Six donors had a fold change <1 and two slightly above 1. We then confirmed in conjugates that the phosphorylation of the actin-regulatory protein HS1 was also affected by the engagement of PD-1. In PD-$1^+$ Jurkat T cells, enrichment of pHS1 at the immune synapse was inhibited when Arp2/3 was blocked by CK666 treatment. PD-1 binding to PD-L1 also inhibited pHS1 recruitment at the immune synapse upon activation (Fig 3D-E). Since WASp promotes actin polymerization through the Arp2/3 complex (*20*, *44*) and is recruited to the immune synapse upon TCR stimulation (*45*), we imaged the recruitment of WASp in primary PD-$1^+$ $CD8^+$ T cells. Following PD-1 engagement, WASp distributed symmetrically over the whole periphery of the cell instead of being enriched in the lamellipodium at the synapse (Fig S3). Altogether, these results suggest that PD-1 engagement inhibits the nucleation of branched actin regulated by the Arp2/3 complex.

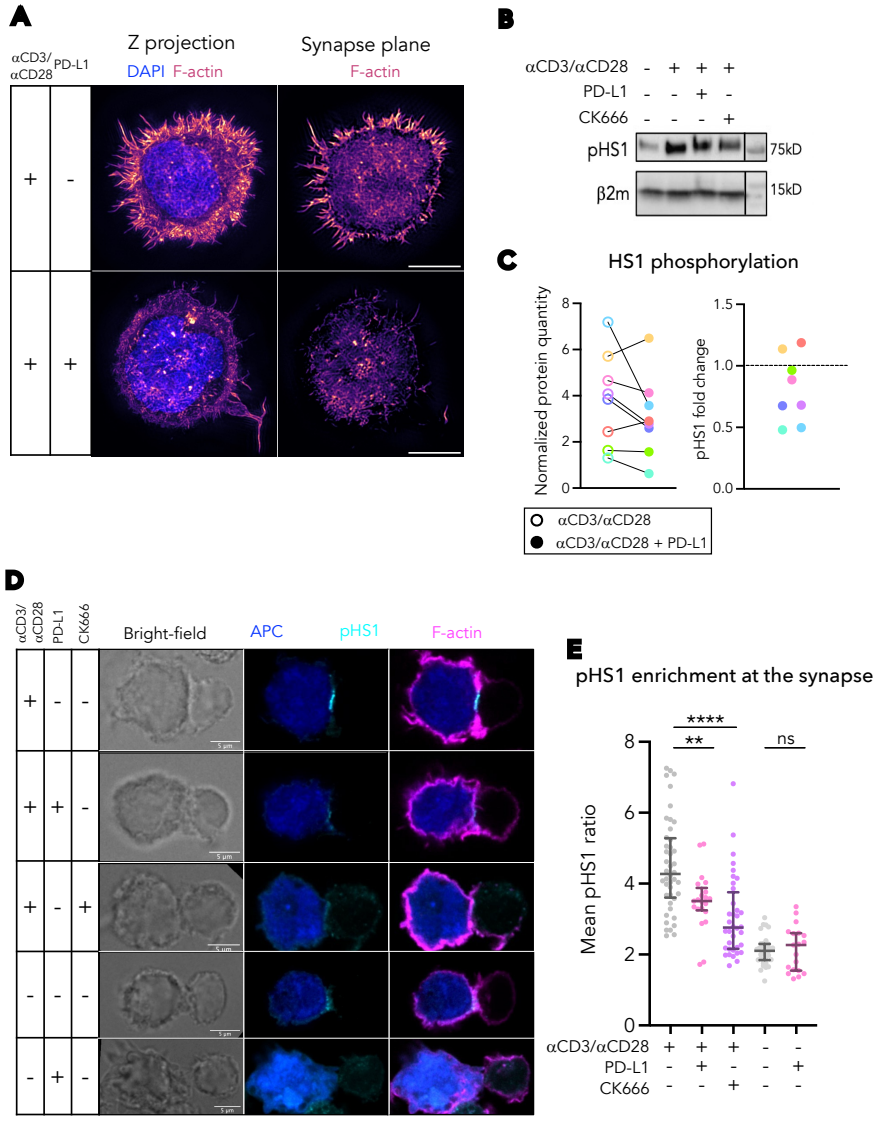


**Figure 3. PD-1 inhibits Arp2/3 complex activity.** (**A**) Representative images of the effect of PD-1 on the F-actin meshwork of spreading PD-1$^+$ CD8$^+$ T cells. Cells were incubated for 10min on a glass surface coated with poly-L-lysine, anti-CD3/CD28 antibodies and PD-L1-Fc or IgG1-Fc as a control. Cells were then fixed, permeabilized and stained with DAPI (blue) and phalloidin (magenta). Images were acquired by 3D-SIM microscopy. Left panel: Z projection of the cells, right panel: one Z plane of the contact zone between cell and slide is shown. Scale bar: 5µm. (**B-C**) PD-1$^+$ CD8$^+$ T cells were activated for 10min on a plate coated with anti-CD3/CD28 antibodies and PD-L1-Fc or IgG1-Fc as a control. After activation, cells were lysed in the plate and protein content was migrated on a gel. Beta-2-microglobulin was used as a loading control. (**B**) Representative western blot assay. (**C**) Left graph: Quantification of HS1 phosphorylation normalized by beta-2-microglobulin quantity. Right

graph: Fold change value for each donor. N = 4 independent experiments, 8 healthy donors, each color represents one donor. (**D**) Representative images of the effect of PD-1 on HS1 phosphorylation in conjugates. Images were acquired by confocal microscopy; one sagittal Z plane of the immune synapse is shown. Scale bar: 5µm. (**D-E**) PD-1$^+$ Jurkat T cells were co-cultured with APCs or APC-PD-L1, coated with anti-CD3/CD28 antibodies or not for 30min. To assess HS1 phosphorylation upon Arp2/3 inhibition cells were treated with 100µM CK666 for 1h. Conjugates were then fixed, permeabilized, and stained for anti-pHS1 (cyan) and phalloidin (magenta). APCs and APC-PD-L1 were stained with Celltracker CMFDA (blue) and APC-PD-L1 were identified by PD-L1 labeling. (**E**) Enrichment of HS1 phosphorylation at the cortex in the contact zone compared to the cortex at the back of the cells. N = 1 experiment with >20 conjugates per condition. Mann-Whitney T-test ****P≤ 0.0001; **P ≤ 0.01. Data are presented as median with interquartile range.

**PD-1-induced inhibition of actin remodeling accounts for cytotoxicity defects**

The killing capacity of CD8$^+$ cytotoxic T cells was shown to be affected by PD-1 engagement (*46*, *47*). We first confirmed that it was indeed the case in our model (Fig S4A). Actin-related mechanisms regulate granule secretion by cytotoxic T cells (*48*). Indeed, centralized actin reduction at the immune synapse precedes degranulation and initiates granule secretion at the immune synapse (*49*), whereas cortical actin recovery at the immune synapse leads to the termination of lytic granule secretion (*50*). Since we show herein that PD-1 inhibits the formation of the actin-ring lamellipodium at the immune synapse, we assessed the effect of PD-1 engagement on the degranulation of PD-1$^+$ CD8$^+$ T cells. To do so, we followed the cell surface expression of CD107a (LAMP-1) and CD107b (LAMP-2, data not shown) in human PD-1$^+$ CD8$^+$ T cells upon activation in the absence or presence of PD-L1. The degranulation was slightly but significantly decreased by PD-1 engagement in all donors (Fig 4A-B). This degranulation defect could be due to either 1- a granule polarization defect, or 2- a physical barrier created by the actin at the contact zone, preventing granule fusion and exposure of LAMP-1 and LAMP-2 at the plasma membrane. To test the first hypothesis, we measured the cytolytic granule and centrosome polarity in PD-1$^+$ CD8$^+$ T cells forming conjugates with APCs or APC-PD-L1 (Fig 4C). We observed no defect in the polarization of cytolytic granules and centrosome upon PD-1 engagement (Fig 4C-E, Fig S4B). These organelles were efficiently polarized to the synapse upon TCR engagement, whether PD-L1 was present on the APC or not. To test the second hypothesis, that PD-1-induced loss of actin depletion at the contact zone would lead to a physical barrier blocking granule release, we treated the PD-1$^+$ CD8$^+$ T cells in presence of PD-L1 with very low doses of latrunculin B (0.01µM), an inhibitor of actin polymerization, to release the physical barrier created by the actin meshwork at the contact zone (*51*). By doing so, we were able to rescue the degranulation defect caused by PD-1 engagement (Fig 4F-G). However, treating the cells with the same concentration of latrunculin B did not restore the killing capacity (Fig S4A). Altogether, these results suggest that PD-1-induced inhibition of cytotoxic granule release is related to the inhibition of actin remodeling at the immune synapse. This inhibition leads to the presence of a dense actin meshwork at the contact zone, acting as a physical barrier blocking cytolytic granule release.

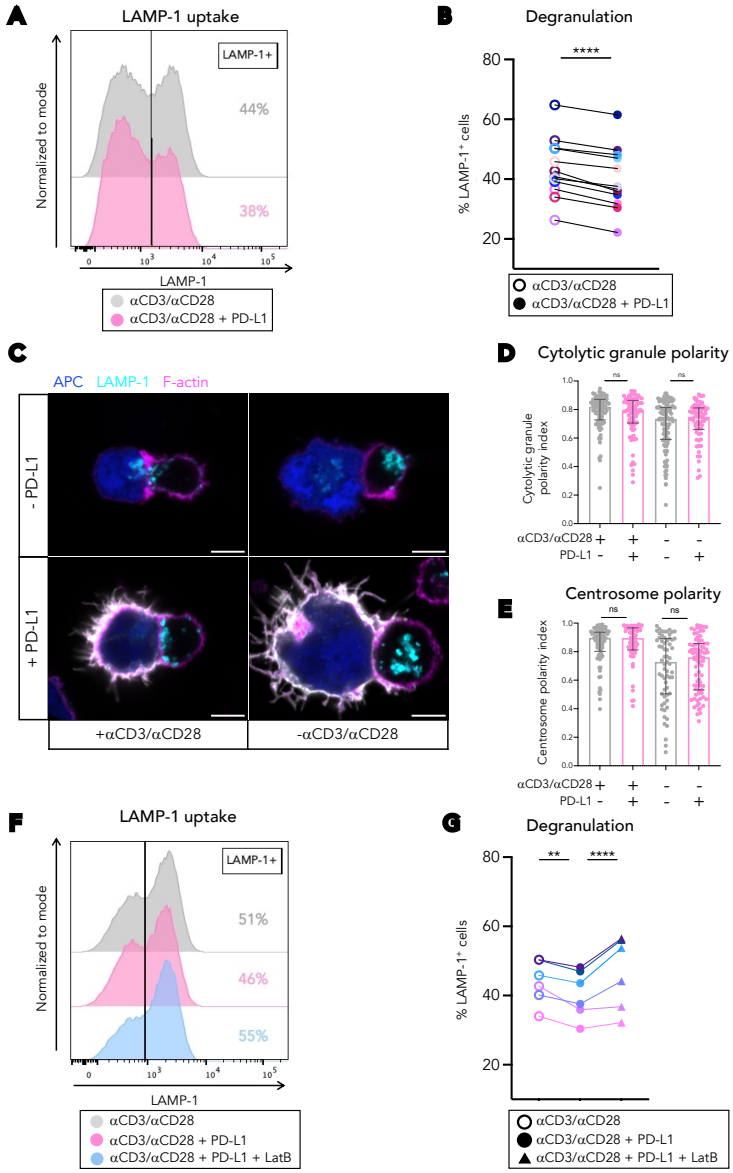


**Figure 4. PD-1-induced inhibition of actin remodeling accounts for cytotoxicity defects.** (**A**) Representative flow cytometry plot and (**B**) quantification of anti-LAMP1-FITC uptake after 4 hours of activation of PD-1$^{+}$ CD8$^{+}$ T cells on plates coated with anti-CD3/CD28 antibodies with PD-L1-Fc or IgG1-Fc as a control. N = 6 independent experiments, 12 healthy donors, each color represents one donor. 2-way ANOVA, ****P≤ 0.0001. (**C**) Representative images of cytolytic granule polarization in PD-1$^{+}$ CD8$^{+}$ T cells forming immune synapses. (**C-E**) PD-1$^{+}$ CD8$^{+}$ T cells forming conjugates for 30min with APCs or APC-PD-L1 stained with Celltracker CMAC (blue) coated with anti-CD3/CD28 or not. Conjugates were then fixed, permeabilized, and stained for anti-LAMP1 (cyan) and phalloidin (magenta). APCs and APC-PD-L1 were stained with

Celltracker CMAC (blue) and APC-PD-L1 were identified by PD-L1 labeling. Images were acquired by confocal microscopy; one sagittal Z plane of the immune synapse is shown. Scale bar: 5µm. (**D**) Quantification of cytolytic granule polarity and (**E**) centrosome polarity to the immune synapse for each condition. (**D**) N = 2 independent experiments, 4 healthy donors. (**E**) N = 2 independent experiments, 3 healthy donors. Data are presented as median with interquartile range. Mann-Whitney T-test. (**F**) Representative flow cytometry plot and (**G**) quantification of anti-LAMP1-FITC uptake after 4 hours activation of PD-$1^+$ $CD8^+$ T cells on plates coated with anti-CD3/CD28 antibodies with PD-L1-Fc or IgG1-Fc as a control and treated or not with Latrunculin B (0.01µM). N = 3 independent experiments, 6 healthy donors. 2-way ANOVA, **P ≤ 0.01; ****P≤ 0.0001.

**Inhibition of actin remodeling by PD-1 engagement is signaling-independent**

We next wanted to assess the mechanisms involved in the inhibition of actin remodeling by PD-1. During our investigation of the effect of PD-1 engagement on immune synapse formation, we noticed that upon encounter with two APCs presenting activating antibodies, T cells could form two characteristic immune synapses showing recruitment and opening of the actin and change in the T cell plasma membrane curvature in the synaptic zone (Fig 5A, movie 3). Interestingly, when a PD-$1^+$ Jurkat T cell interacted with two APCs, one expressing PD-L1 and one that did not, the formation of the synapse was affected by the APC-PD-L1: PD-1 was strongly recruited, the T cell did not deform, and F-actin was not cleared from the contact zone. In contrast, the same T cell was able to form an immune synapse: actin-rich lamellipodium cleared F-actin in the central zone and formation of a convex contact with the PD-L1 negative APC (Fig5A, movie 4). This suggested that PD-1 had a very local effect on the formation of the immune synapse but did not completely block the capacity of T cells to form an immune synapse with another APC. Thus, we assessed if the observed inhibition of actin remodeling required PD-1 signaling. PD-1 contains two tyrosine motifs in its cytoplasmic domain one in an ITIM (VDY$^{223}$GEL) and one in an ITSM (TEY$^{248}$ATI). Mutations of the ITIM/ITSM tyrosines have been shown to abolish some inhibitory effects of PD-1 on T cell activation by recruitment of the phosphatase SHP-2 (*6*, *7*, *52*). We generated a mutant version of PD-1 by replacing the tyrosines Y223 and Y248 with phenylalanines. We first confirmed that some of the inhibitory effects of PD-1 on T cell activation were dampened by the mutations: IL-2 secretion, CD25 upregulation, and PLCγ phosphorylation were less inhibited when the Jurkat T cells expressed PD-1 Y223/248F than when they expressed wild-type PD-1 (Fig S5A-C). PD-1 wild-type and Y223/248F were expressed at similar levels (MFI for mutant was always slightly less than for the wild type, FigS5D) in Jurkat T cells and were both recruited at the immune synapse upon PD-L1 presence on the APC (FigS5D-F). We then assessed the effect of the mutant version of PD-1 on T cell spreading. The spreading area, as well as the F-actin intensity at the synapse, were inhibited to the same extent in Jurkat T cells expressing PD-1 wild-type as PD-1 Y223/248F (Fig 5B-C). We then assessed the effect of these mutations on the formation of immune synapses with an APC. Engagement of the mutated PD-1 Y223/248F inhibited the formation of the peripheral F-actin-rich lamellipodium, accompanied by enrichment of peripheral F-actin, and of the central F-actin hypodense region at the immune synapse (Fig 5D-F). Moreover, this signaling deficient PD-1 mutant also inhibited the characteristic T cell deformation on the APC (Fig 5D, E, G). Even though the enrichment of F-actin at the synapse with APC-PD-L1 was slightly increased in T cells expressing PD-1 Y223/248F compared to PD-1 wild-type, it remained significantly lower than in T cells forming a synapse with a PD-L1 negative APC. Altogether, these results show that neither inhibition of F-actin remodeling nor changes in T cell morphology at the immune synapse depend on the PD-1 signaling motifs.

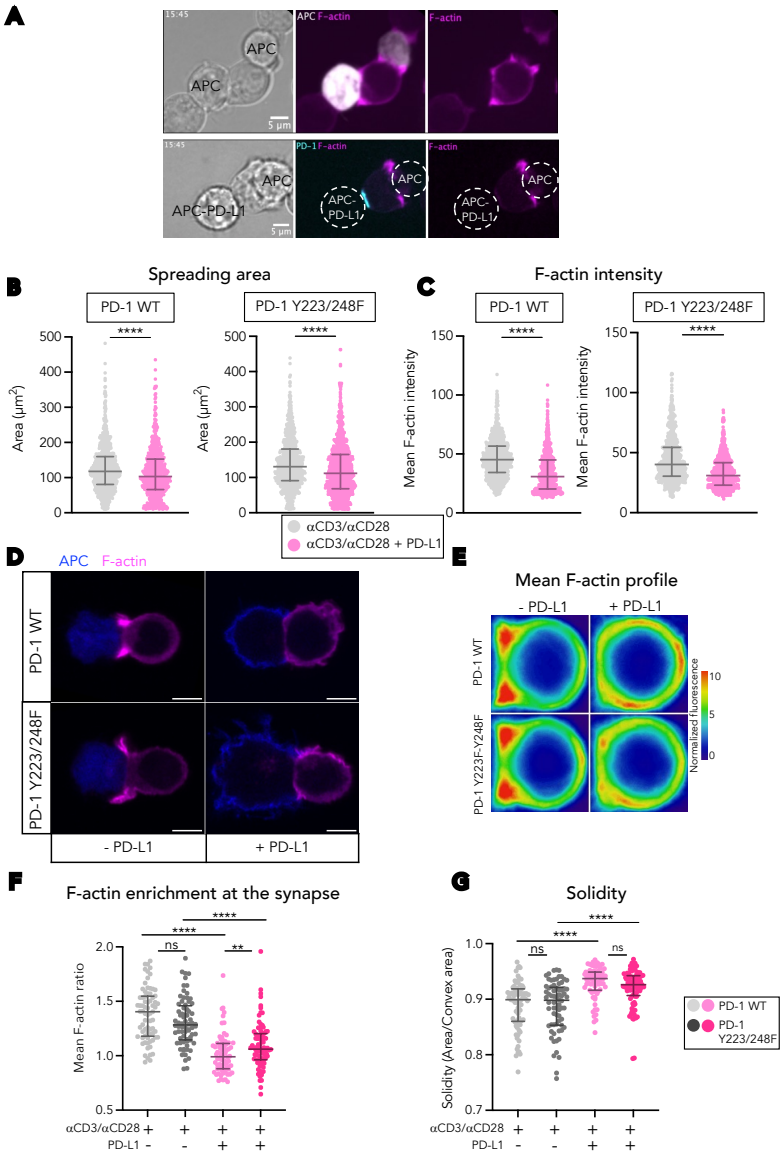


**Figure 5. Inhibition of actin remodeling by PD-1 engagement is signaling-independent.** (**A**) Representative images of the local effect of PD-1 on immune synapse formation. Left panel: PD-1$^{+}$ Jurkat T cells expressing LifeAct-mCherry (magenta) were co-cultured for 30min with APCs stained with Celltracker CMAC (cyan), coated with anti-CD3/CD28 antibodies. Right panel: PD-1-YFP$^{+}$ (cyan) LifeAct-mCherry$^{+}$ (magenta) Jurkat T cells (magenta) were co-cultured for 30min with APCs and APC-PD-L1, coated with anti-CD3/CD28. Images were acquired by spinning disk microscopy, every 45sec for 30min; one sagittal Z plane of the immune synapse at 15:45min is shown. Scale bar: 10µm. (**B**) Spreading area and (**C**) F-actin intensity of Jurkat T cells expressing PD-1 wild-type (WT) or PD-1 Y223/248F after 10min spreading on glass surfaces coated with

poly-L-lysine and anti-CD3/CD28 antibodies with PD-L1-Fc or IgG1-Fc as a control. Cells were then fixed, permeabilized, and stained with DAPI (blue) and phalloidin, spreading area was measured by confocal microscopy. N = 2 independent experiments with >600 cells per condition. Data are presented as median with interquartile range. Mann-Whitney T-test ****P≤ 0.0001. (**D**) Representative images of the effect of PD-1 mutation on immune synapse formation. Images were acquired by confocal microscopy; one sagittal Z plane of the immune synapse is shown. Scale bar: 5µm. (**D-G**) Jurkat T cells expressing PD-1-YFP or PD-1-Y223/248F-YFP and LifeAct-mCherry were co-cultured for 30min with APCs or APC-PD-L1 coated with anti-CD3/CD28 antibodies. Conjugates were then fixed, permeabilized, and stained with anti-mCherry (magenta). APCs were stained with Celltracker CMAC (blue) and APC-PD-L1 were identified by PD-L1 labeling (blue). (**E**) Mean profile of F-actin distribution in Jurkat cells expressing PD-1 WT or PD-1 Y223/248F upon activation with APCs expressing or not PD-L1, coated with anti-CD3/CD28 antibodies. Cells were normalized to the same size and fluorescent intensity and the average projection of all cells was done to see signal distribution, using a linear LUT to show signal accumulation. (**F**) Quantification of the enrichment of F-actin at the cortex in the contact zone compared to the cortex at the back of the cells. (**G**) Quantification of the solidity calculated as the area of the F-actin mask divided by the convex area in Jurkat T cells expressing PD-1 WT or PD-1 Y223/248F after forming 30min conjugates with APCs or APC-PD-L1 coated with anti-CD3/CD28 antibodies. (**D-G**) N = 3 independent experiments with >70 conjugates per condition. Data is presented as median with interquartile range. Mann-Whitney T-test ****P≤ 0.0001, **P ≤ 0.01

**DISCUSSION**

Our findings show that PD-1 binding to PD-L1 significantly affects T cell actin remodeling at the immune synapse. This inhibition results in an altered spreading of T cells upon activation by anti-CD3/CD28 antibodies, as already described on $CD8^+$ T cells from TCR transgenic mice plated on pMHC +/- PD-L1 (*53*). It also results in dampened formation of ring-like lamellipodia in T cells interacting with APCs. This is accompanied by an inhibition of the characteristic changes in T cell shape, i.e. formation of a convex interaction zone with an increased contact surface with the APC and the formation of a central zone hypodense in filamentous actin. Our results also suggest that the absence of actin clearance at the center of the immune synapse results in a defect in cytotoxic granules secretion by cytotoxic T cells (Fig 4A-B). Moreover, we show for the first time that PD-1 inhibitory effects on actin remodeling are independent of its ITSM and ITIM motifs.

Although PD-1 has been discovered more than 30 years ago (*1*) and has been the subject of intense scrutiny, the mechanisms involved in its co-inhibitory function are only partially characterized and sometimes controversial. For example, the effects of the binding of PD-1 to PD-L1 on the formation of T cell/APC conjugates have been described in the literature but are inconsistent. In an *in vivo* mouse model of tolerized antigen-specific T cells, the continuous interactions between PD-1 and PD-L1 were shown to inhibit the stop signal of T cells on APCs (*54*). In contrast, in a mouse model of persistent viral infection, virus-specific $CD4^+$ and $CD8^+$ T cells were “paralyzed” (less motile) and formed more stable immune synapses as compared to T cells from acute viral infection (*55*). In this case, inhibition of T cell motility and increase in immune synapse stability were strictly dependent on PD-1 binding to PD-L1. Indeed, the therapeutic blockade of PD-1/PD-L1 restored T cell motility after 30 minutes of treatment. Moreover, $PD\text{-}1^+$ T cells formed more stable immune synapses with planar activating lipid bilayers containing PD-L1 than control activating lipid bilayers (*55*). In yet another model, tumor-infiltrating T lymphocytes (TILs), purified from tumor-bearing mice, were shown, *ex vivo,* to form unstable conjugates with tumor cells (*56*). Of note, in this study, acute *ex vivo* blockade of PD-1/PD-L1 interaction did not restore

the stability of TIL/tumor conjugates, suggesting that this instability was constitutional of the TILs and not directly related to PD-1 engagement (*56*). Finally, in a study using Jurkat T cells expressing PD-1 and Raji B cells expressing PD-L1 and PD-L2 as APCs, the authors concluded that "PD-1 expressing Jurkat T cells were unable to form stable mature synapses with Raji B cells" (*57*). Yet, the conclusions were drawn from static microscopy images showing that PD-1 engagement inhibited the recruitment of F-actin at the immune synapse (*57*). In the present study, we observed similar defects in actin remodeling (Fig 2), but the number of conjugates between T cells ($PD\text{-}1^+$ Jurkat or primary $PD\text{-}1^+CD8^+$ T cells) and $PD\text{-}L1^+$ APC, as measured by flow cytometry, was not decreased (Fig S2F). Moreover, although we did not strictly assess the motility of T cells upon PD-1 engagement, these cells were still able to form an immune synapse with PD-L1 negative APCs (movie 4), showing that they were not paralyzed. Also, they did not present a cell shape compatible with greater motility on the APC, suggesting that in our model PD-1 engagement neither inhibits the stop signal, nor the formation of conjugates. Our results also show that PD-1 engagement does not inhibit all the events related to synapse formation. Indeed, the polarization of the centrosome towards the APC was neither inhibited in Jurkat T cells nor in $CD8^+$ primary T cells. This is somewhat at odds with the expected effects of PD-1 engagement on early signaling. Indeed, the tyrosine kinase activity of ZAP-70 was shown to control the polarization of the T cell centrosome at the immune synapse (*58–60*) and PD-1 was shown to, at least partially, inhibit tyrosine phosphorylation of ZAP-70 (*10*). Yet, in other models, ZAP-70 phosphorylation was unaffected (*8*, *11*). Our results also show that PD-1 engagement does not inhibit the polarization of cytotoxic granules toward the target cell. This agrees with the fact that granule secretion is controlled by centrosome polarization at the immune synapse (*61*), which, as described earlier, is not affected by PD-1 engagement. This is, to our knowledge, the first report on the effect of PD-1 engagement on cytotoxic granule polarization in T cells. Although the cytotoxic granules are normally polarized to the immune synapse upon PD-1 engagement, we noticed that their release was altered (Fig 2B). Early interaction between T lymphocyte and APC is mediated by actin-rich protrusions that form an interdigitated contact site with the APC and lead to a rapid accumulation of F-actin across the contact site (*32*, *49*, *60*, *62*, *63*). In our model, this early F-actin recruitment is not inhibited by PD-1 engagement (movies 2-4). Normally, this initial actin accumulation at the interface is followed by its clearance from the center and the formation of a ring-like lamellipodium at the periphery of the immune synapse (*21*, *49*). We show herein that PD-1 binding to PD-L1 inhibits the formation of this lamellipodium structure and the formation of the F-actin hypodense central region (Fig 2). Since the loss of cortical actin is required for granule delivery, while its recovery drives secretion termination (*50*), the inhibition of degranulation by PD-1 is thus probably related to the absence of actin clearance at the immune synapse. Our results showing that inhibition of actin polymerization by a low concentration of Latrunculin B restores granule secretion (Fig 4F-G) are compatible with this interpretation. This inhibition of actin clearance may also alter the secretion of some cytokines as previously shown (*51*). Formation of the peripheral lamellipodium requires the assembly of branched actin, which depends on the Arp2/3 complex (*16*, *17*) and allows the spreading of T cells. In our study, using high-resolution microscopy, we show that when PD-1 is engaged the peripheral branched actin network is not formed at the synapse. This is accompanied by the absence of recruitment of WASp and pHS1, two proteins that are involved in branching nucleation (*17*). This actin remodeling generates mechanical forces (*29*, *64*) that promote T cell activation (*17*, *26*, *31*, *65*). Cytotoxic T lymphocytes (CTLs) use these mechanical forces to strain the surface of the target cells, which increases killing efficacy by potentiating the pore-forming activity of perforin (*31*). The cytoskeletal regulator WASp and the Arp2/3 actin nucleation complex are involved in synaptic force exertion and efficient killing (*32*,

*66*, *67*). The cytoskeletal forces also shape the local membrane curvature of the cytolytic immune synapse, modulating the synapse topography and promoting the perforation of the target membrane by perforin (*30*). Inhibition by PD-1 of actin remodeling and the characteristic change of T cell topography at the cytolytic synapse, reported herein, may witness the dampening of mechanical forces exerted by the T cell on the APC. This probably contributes to the inhibition of cytotoxicity and might explain why although a low concentration of Latrunculin B restores granule secretion it does not restore cytotoxicity.

In most reviews (*68–70*), PD-1 inhibitory effects are associated with its ability to recruit the SH2-containing tyrosine phosphatase SHP-2. Engagement of PD-1 with either of its two ligands, PD-L1 (PD-1 ligand 1; B7-H1; CD274) or PD-L2 (B7-DC; CD273) during antigen stimulation results in the phosphorylation of two tyrosine residues in the cytoplasmic region of PD-1, the recruitment of SHP-2 to the membrane-distal phosphotyrosine followed by dephosphorylation of various signaling molecules by SHP-2 (*7*, *8*, *11*, *71*). Yet, our findings show that some of the inhibitory effects do not require these two tyrosine residues. Indeed, PD-L1-induced inhibitions of: - spreading, - formation of the actin ring, and - T cell deformation at the immune synapse are comparable in Jurkat T cells expressing a wild-type PD-1 or a mutant of PD-1 on these two tyrosines. This may account for the fact that some inhibitory effects are conserved in T cells in which PD-1 cannot associate with SHP-2 or SHP-1 (*71*) and with our data showing that although the inhibition of IL-2 and CD25 expression is decreased in Jurkat T cells expressing the tyrosine double mutant, it is not completely lost (Fig S5A-B).

So, what could be the mechanisms involved in these signaling-independent inhibitory effects of PD-1? The intense recruitment of PD-1 in the contact zone (Fig 2D-E) may "isolate" the membrane patch enriched in PD-1 from the membrane undulations that generate forces (*72*). Thus, locally, little forces would be applied to the bonds formed by receptors/ligands pairs, which are in the vicinity of PD-1 such as TCR-pMHC (*7*, *73*) and CD2-CD58 (*74*). Since mechanical forces can influence signaling (*26*, *75–77*), the mere clustering of PD-1 may participate in the inhibitory effects induced by its engagement. This inhibitory effect would rely on the small molecular size of the PD-1-PD-L1 pair, its affinity, its molecular "flexibility" and its density. It would not depend on the signaling activity of PD-1. This remains to be demonstrated.

In conclusion, we propose herein a new mechanism that does not depend on signaling, by which PD-1 affects T cell activation and functions through inhibition of actin remodeling. This mechanism is probably particularly important for acute inhibition of T cell functions such as granule release, force exertion at the immune synapse, and perhaps cell migration. Given the central role of PD-1 in regulating many functions in several cell populations of the immune system, our findings may provide an avenue for better understanding the role of this new mechanism in the regulation of the immune response by PD-1.

## MATERIALS AND METHODS

All reagents and antibodies cited above are listed in Table S1.

### Cells

Peripheral blood mononuclear cells (PBMCs) from healthy donors were isolated using a ficoll density gradient. Buffy coats from healthy donors were obtained from Établissement Français du Sang in accordance with INSERM ethical guidelines. $CD8^+$ T cells were purified using the $CD8^+$ T cell isolation Kit, human. Primary T cells were activated in six-well plates pre-coated with

2.5µg/mL anti-CD3e overnight, in presence of 2.5µg/mL soluble anti-CD28 for 6 days before use to induce PD-1 expression and cultured at 37°C with 5% $CO_2$ in RPMI 1640 Glutamax supplemented with 10% fetal calf serum, 10 000 U/mL penicillin-streptomycin, 1M Hepes, 50mM 2-Mercaptoethanol, 20 U/mL recombinant IL-2 and 20 ng/mL IFN-alpha.
All cell lines stemming from Jurkat T cells (94% homology with Jurkat clone E6.1 validated by the SSTR method on the DSMZ website) were cultured at 37°C with 5% $CO_2$ in RPMI 1640 Glutamax supplemented with 10% fetal calf serum and were passed every 2-3 days at approximatively 0.5 x $10^6$ cells/mL.
All cell lines stemming K562 CCL-243 ATCC were cultured at 37°C 5% $CO_2$ in RPMI 1640 Glutamax supplemented with 10% fetal calf serum and were passed every 2–3 days at ~$0.8 \times 10^6$ cells/ml.

**Lentivirus production, cell transduction and cell transfection**

Replication-defective lentiviral particles were obtained by transfecting HEK-293T cells with Gag, Pol, rev, encoding plasmid (psPAX2), envelop encoding plasmid (pMD2.G), and PEI Max. After 48h, lentiviruses were recovered in the supernatant and concentrated by ultracentrifugation. Jurkat and K562 cells were transduced with the constructs listed in Table S2, and the positive fraction was sorted by flow cytometry (SH800 Cell Sorter, Sony Biotechnology) or selected by puromycin selection to establish stable cell lines. K562 were transfected by Neon™ Transfection System (Invitrogen) with plasmids expressing PD-L1 or empty plasmids following provider protocol.

**Drugs and inhibitors**

Latrunculin B was used at 0.01µM and added to the wells at the same time as cells for activation. CK666 was used at 100µM and incubated for 1 hour at 37°C before T cell activation in the presence of the inhibitor.

**Flow cytometry**

**Staining**

Cells were washed in PBS, 0.5% BSA, 1mM EDTA and incubated with anti-CD3 FITC, anti-CD28 PE, anti-CD64 PE, anti-PD-1 PE, anti-PD-L1 BV421 for 30min at 4°C. After washing the cells twice with the same buffer, protein expression was analyzed by flow cytometry. All following cytometry data were acquired using the MACSQuant VYB. The data were analyzed with FlowJo Software version 10.8.2 (Becton, Dickinson & Company).

**Degranulation assay**

Degranulation assays were performed as previously described (*78*). Briefly, 96-well plates were coated with 2µg/mL anti-CD3 and 5µg/mL IgG1 or 5µg/mL PD-L1 in PBS overnight at 4°C. PD-$1^+$ $CD8^+$ T cells activated for 6 days were resuspended at $3.10^6$ cells/mL in RPMI, 10% FCS, and 1% HEPES. Cells were incubated in the plates at 37°C 5% $CO_2$ for 4h in the presence of anti-CD107a-FITC (LAMP-1) and anti-CD107b-PE (LAMP-2). Latrunculin B 0.01µM was added at the same time in the wells. After incubation, cells were washed in PBS and fixed with fixation buffer for 20min at 4°C. After washing the cells with PBS, 0.5% BSA, 1mM EDTA, CD107a/b uptake was analyzed by flow cytometry.

**Cytotoxicity assay**

K562-CD64 (APCs) and K562-CD64-PDL1 (APC-PD-L1) were first stained with CellTrace Violet for 20min at 37°C in PBS, then washed once with complete medium and coated with 10µg/mL anti-CD3 and 10µg/mL anti-CD28 antibodies for 20min at 37°C in warm medium. After washing the APCs and APC-PD-L1 to remove unbound antibodies, cells were resuspended in complete medium and mixed at $CD8^+$-to-target ratios indicated. After 4 hours of co-culture at 37°C 5% $CO_2$, cells were washed in PBS and stained with Live/Dead eFluor 780 for 20min at 4°C. After washing cells with PBS, cells were fixed with fixation buffer for 20min at 4°C. After washing the cells with PBS, 0.5% BSA, and 1 mM EDTA, killing rates were analyzed by flow cytometry. Killing rates were calculated by flow cytometry as follows:

$$100 - \%\ of\ live\ APCs\ normalized\ to\ control\ wells\ viability$$

**Conjugate formation**

$PD\text{-}1^+$ Jurkat T cells were first stained with CellTrace Violet for 20min at 37°C 5%$CO_2$ in PBS, then washed once with complete medium. APCs and APC-PD-L1 were coated with 10µg/mL anti-CD3 and 10µg/mL anti-CD28 for 20min at 37°C 5%$CO_2$. Cells were resuspended at $1.10^6$ cells/mL, mixed at a 1:1 ratio pelleted with a short spin before incubation for conjugate formation at 37°C 5% $CO_2$ for 20min to assess conjugate formation rates or overnight to measure CD25 upregulation and IL-2 secretion. To follow CD25 upregulation, the cells were stained with anti-CD25 PE-Cy7 in PBS, 0.5% BSA, 1mM EDTA for 30min at 4°C and then washed before acquisition. ELISA measurement of -2 secretion was done following the protocol of the provider (see Table S1) and absorbance was read at 450nm with a CLARIOstar (BMG Labtech). To determine the percentage of conjugates formed in each condition, unspecific conjugates were removed by 15x pipetting, after which cells were fixed with fixation buffer for 20min at 4°C. After washing the cells with PBS, 0.5% BSA, and 1 mM EDTA, conjugate formation was analyzed by flow cytometry.

**T cell activation and phospho-blot analysis**

96-well plates were coated with 1µg/mL anti-CD3, 10µg/mL anti-CD28 and 5µg/mL IgG1 or 5µg/mL PD-L1 in PBS overnight at 4°C. $PD\text{-}1^+$ $CD8^+$ T cells or $PD\text{-}1^+$ Jurkat T cells were washed in RPMI and resuspended at $6.10^6$ cells/mL in RPMI. Cells were incubated in the pre-coated plates at 37°C 5% $CO_2$ for 10min and lysed directly in the plates with RIPA 10X supplemented with phosphatase inhibitor cocktail and protease inhibitor cocktail for 15min at 4°C and then treated with benzonase. Lysates were centrifuged for 15min at maximum speed at 4°C and Laemmli with NuPAGE sample reducing agent were added to the supernatants followed by heating the samples for 5min at 95°C. Supernatants were loaded on 4-15% protein gels and transferred to PVDF membranes. Membranes were blocked at room temperature for 45min with TBS1X, Tween 0.05%, and 5% BSA, and incubated overnight at 4°C with primary antibodies anti-phospho-HS1 and anti-beta-2-microglobulin. After three washes in TBS1X, Tween 0.05%, membranes were incubated for 45min at room temperature with the secondary antibody peroxidase goat anti-rabbit IgG1. Proteins were revealed with Clarity Western ECL Substrate and chemiluminescence was detected with a Bio-Rad ChemiDoc MP imaging system. Western blots were quantified with the Image Lab software (Bio-Rad).

**Spreading assay for immunofluorescence**

12mm ø coverslips were cleaned with 70% ethanol, then washed with $H_2O$ and coated with 0.02% poly-L-lysine for 20min at room temperature. After washing in PBS, the coverslips were coated with 0.1µg/mL anti-CD3, 10µg/mL anti-CD28, and 5µg/mL IgG1 or 5µg/mL PD-L1 overnight at 4°C. Coverslips were washed once in PBS before adding the cells. PD-$1^+$ $CD8^+$ T cells or PD-$1^+$ Jurkat T cells were resuspended at $1.10^6$ cells/mL in warm complete medium and 100 000 cells/coverslip were incubated for 10min at 37°C 5% $CO_2$. Coverslips were then washed once with PBS and fixed with 4% paraformaldehyde for 10min at room temperature. After washing once with PBS, excess paraformaldehyde was quenched with PBS, 10mM glycine for 10min at room temperature. Cells were permeabilized with PBS, 0.2% BSA, and 0.05% saponin for 30min at room temperature. For the staining, cells were incubated in the same buffer with DAPI and phalloidin coupled to Alexa Fluor 647 or 568 for 30min at room temperature protected from light. After washing twice with PBS, BSA, saponin, and twice in PBS, coverslips were soaked in $H_2O$ and mounted with 5µL Fluoromount G on slides and dried protected from light at room temperature overnight before microscope acquisition.

**Conjugate formation for immunofluorescence**

12mm ø coverslips were cleaned with 70% ethanol, then washed with $H_2O$ and coated with 0.02% poly-L-lysine for 20min at room temperature and then washed with PBS. APCs and APC-PD-L1 were first stained with Celltracker CMAC or Celltracker CMFDA for 20min at 37°C in PBS then washed once with complete medium and coated with 10µg/mL anti-CD3 and 10µg/mL anti-CD28 for 20min at 37°C in warm medium. After washing the APCs and APC-PD-L1 to remove unbound antibodies, cells were resuspended at $2.10^6$ cells/mL in complete medium and mixed with PD-$1^+$ $CD8^+$ or PD-$1^+$ Jurkat T cells at a 1:1 ratio. 200 000 mixed cells were incubated for 30min at 37°C 5% $CO_2$ on the coverslips. Coverslips were then washed once with PBS and fixed with 4% paraformaldehyde for 10min at room temperature. After washing once with PBS, excess paraformaldehyde was quenched with PBS, 10mM glycine for 10min at room temperature. Cells were permeabilized with PBS, 0.2% BSA, and 0.05% saponin for 30min at room temperature. For the primary antibodies staining, cells were incubated in the same buffer with anti-mCherry, anti-GFP, anti-acetylated tubulin, anti-PD-L1 BV421, anti-phospho-HS1, anti-LAMP-1, anti-WASP for 1h at room temperature. After washing the coverslips three times with the PBS, BSA, and saponin buffer, the secondary antibodies were added in the same buffer and incubated at room temperature protected from light for 30min. After washing twice with PBS, BSA, saponin, and twice in PBS, coverslips were soaked in $H_2O$ and mounted with 5µL Fluoromount G on slides and dried protected from light at room temperature overnight before microscope acquisition.

**Conjugate formation for live imaging**

15mm ø glass-bottom cell culture dishes were coated with 0.02% poly-L-lysine for 20min at room temperature and then washed with PBS. APCs and APC-PD-L1 were stained with Celltracker CMAC for 20min at 37°C in PBS then washed once with complete medium and coated with 10µg/mL anti-CD3 and 10µg/mL anti-CD28 for 20min at 37°C in warm medium. APCs and Jurkat T cells expressing PD-1-YFP and LifeAct-mCherry were resuspended in RPMI without phenol red. APCs were deposited on the dishes 10min at 37°C before acquisition. T cells were added in

the chamber of the spinning disk microscope, at 37°C 5% $CO_2$. Images were acquired every 45sec on 4 regions of interest for 30min.

**Microscopy and image analysis**

**Microscopes**

Confocal images were acquired on an inverted Leica DmI8 microscope equipped with an SP8 confocal using a 63x (1.4 NA), oil immersion objective. Z-stacks of images were acquired. 3D-SIM images were acquired on a Delta Vision OMX v4 microscope equipped with an Olympus 100x (1.42 NA), Plan Apo N, oil immersion objective. Image reconstruction was performed under Linux using the SoftWoRx image software. Live imaging was performed using an inverted Eclipse Ti-E (Nikon) spinning disk CSU-X1 (Yokogawa) confocal microscope integrated in Metamorph software and equipped with a 60x (1.4 NA) oil immersion objective.

**Image analysis and statistical analysis**

All image analyses were performed on Fiji-ImageJ software (*79*) using custom codes available upon request. All graphs and statistical analyses were made with GraphPad PRISM version 9.5.0 for Mac (GraphPad Software, San Diego, CA, https://www.graphpad.com).

**Analysis of spreading area and F-actin intensity**

To analyze cell spreading on surfaces, only the Z-stack plane corresponding to the contact between cells and the surface was considered and a projection of the DAPI was used to individualize each cell. Briefly, a binary mask of cell areas was obtained after a threshold on the F-actin channel, and cells were separated using the segmented image obtained with the find maxima function applied on the DAPI. After segmentation, for each cell, spreading area and F-actin intensity at the immune synapse were measured.
Macros used: Macro_Spreading1.ijm; Macro_Spreading2.ijm; Macro_Spreading3.ijm

**Synapse extraction and conjugate reorientation**

First, single-cell conjugates were cropped and saved manually. Then, for each conjugate, the sagittal Z plane and the orientation of the synapse were manually determined. The selected plane was reoriented so that the T cell and the APC were always positioned the same (T cell on the right, APC on the left) and the conjugated T cell was cropped. Both oriented conjugates and cropped T cells were saved.
Macros used: Macro_SynapseExtraction.ijm

**Analysis of F-actin, PD-1, pHS1 enrichment at the synapse**

For all extracted conjugated T cells, a binary mask was created on the F-actin channel to define the cell cortex. For the cortical synaptic region, only the cortex in the first 20% of the image was considered. Then the mean intensity of F-actin, PD-1, or pHS1 was measured in the cortical synaptic region and in the rest of the cortex. The enrichment was computed as the ratio between the mean intensity at the synaptic cortex compared to the mean intensity of the non-synaptic cortex.
Macros used: Macro_EnrichmentSynapse.ijm

**Analysis of mean cell F-actin and PD-1 distribution**
To map the mean cell distribution of F-actin or PD-1 in a set of images, for all the extracted conjugated T cell images of one condition, first, all intensities and image sizes were measured, and images were normalized to the same size and total intensity. Then, an average projection of all the normalized cells was done to obtain an average pattern of signal distribution. To compare conditions between them, obtained maps were normalized to the same size and intensity and the same LUT and display were applied for all.
Macros used: Macro_MeanCell1.ijm, Macro_MeanCell2.ijm; Macro_MeanCell3.ijm

**Analysis of cytolytic granule and centrosome polarity**
To measure the cytolytic granule and centrosome polarity to the immune synapse, the oriented conjugates were used to define the contact line between both cells corresponding to the synapse. Briefly, taking the phalloidin staining, a binary mask of both cells was determined. Then, a mask of the APC cell was done using either the Celltracker staining (for APCs) or the PD-L1 staining (for APC-PD-L1). T cells masks were thus determined as total cells – APC and the immune synapse was determined as the contact line between APC and T cells mask. For polarity measurement, first, a mask was done on the cytolytic granules using LAMP-1 staining or on the acetylated tubulin staining using the brightest part to get the centrosome.
A distance map corresponding to the distance to the synapse was generated and the distance of the cytolytic granules or centrosome was measured and normalized to the maximum distance measured on the T cell.
Macros used: Macro_Polarity1.ijm; Macro_Polarity2.ijm

**Analysis of T cell solidity**
To measure the deformation of the cells at the immune synapse, for extracted conjugated T cell image, either cortical masks obtained from the analysis of protein enrichment at the synapse or T cell masks generated from the analysis of polarity were used. Then the solidity of this object was measured (area of the cell/convex hull area).
Macros used: Macro_Synapse_extraction.ijm; Macro_Polarity1.ijm

**References and Notes**


1. Y. Ishida, Y. Agata, K. Shibahara, T. Honjo, Induced expression of PD-1, a novel member of the immunoglobulin gene superfamily, upon programmed cell death. *EMBO J.* **11**, 3887–3895 (1992).
2. M. E. Keir, M. J. Butte, G. J. Freeman, A. H. Sharpe, PD-1 and Its Ligands in Tolerance and Immunity (2008), doi:10.1146/annurev.immunol.26.021607.090331.
3. K. N. Berger, J. J. Pu, PD-1 pathway and its clinical application: A 20 year journey after discovery of the complete human PD-1 gene. *Gene*. **638**, 20–25 (2018).
4. T. Okazaki, S. Chikuma, Y. Iwai, S. Fagarasan, T. Honjo, A rheostat for immune responses: The unique properties of PD-1 and their advantages for clinical application. *Nat Immunol*. **14**, 1212–1218 (2013).
5. T. Shinohara, M. Taniwaki, Y. Ishida, M. Kawaichi, T. Honjo, Structure and Chromosomal Localization of the Human PD-1 Gene (PDCD1). *Genomics*. **23**, 704–706 (1994).
6. T. Okazaki, A. Maeda, H. Nishimura, T. Kurosaki, T. Honjo, PD-1 immunoreceptor inhibits B cell receptor-mediated signaling by recruiting src homology 2-domain-containing tyrosine phosphatase 2 to phosphotyrosine. *Proceedings of the National Academy of Sciences*. **98**, 13866–13871 (2001).
7. T. Yokosuka, M. Takamatsu, W. Kobayashi-Imanishi, A. Hashimoto-Tane, M. Azuma, T. Saito, Programmed cell death 1 forms negative costimulatory microclusters that directly inhibit T cell receptor signaling by recruiting phosphatase SHP2. *Journal of Experimental Medicine*. **209**, 1201–1217 (2012).

8. J. Celis-Gutierrez, P. Blattmann, Y. Zhai, N. Jarmuzynski, K. Ruminski, C. Grégoire, Y. Ounoughene, F. Fiore, R. Aebersold, R. Roncagalli, M. Gstaiger, B. Malissen, Quantitative Interactomics in Primary T Cells Provides a Rationale for Concomitant PD-1 and BTLA Coinhibitor Blockade in Cancer Immunotherapy. *Cell Rep*. **27**, 3315-3330.e7 (2019).
9. X. Xu, B. Hou, A. Fulzele, T. Masubuchi, Y. Zhao, Z. Wu, Y. Hu, Y. Jiang, Y. Ma, PD-1 and BTLA regulate T cell signaling differentially and only partially through SHP1 and SHP2. *Journal of Cell Biology*. **219** (2020).
10. K. A. Sheppard, L. J. Fitz, J. M. Lee, C. Benander, J. A. George, J. Wooters, Y. Qiu, J. M. Jussif, L. L. Carter, C. R. Wood, D. Chaudhary, PD-1 inhibits T-cell receptor induced phosphorylation of the ZAP70/CD3ζ signalosome and downstream signaling to PKCθ. *FEBS Lett*. **574**, 37–41 (2004).
11. E. Hui, J. Cheung, J. Zhu, X. Su, M. J. Taylor, H. A. Wallweber, D. K. Sasmal, J. Huang, J. M. Kim, I. Mellman, R. D. Vale, T cell costimulatory receptor CD28 is a primary target for PD-1-mediated inhibition. *Science (1979)*. **355**, 1428–1433 (2017).
12. G. Rota, C. Niogret, A. T. Dang, C. R. Barros, N. P. Fonta, F. Alfei, L. Morgado, D. Zehn, W. Birchmeier, E. Vivier, G. Guarda, Shp-2 Is Dispensable for Establishing T Cell Exhaustion and for PD-1 Signaling In Vivo. *Cell Rep*. **23**, 39–49 (2018).
13. T. Zhang, W. Guo, Y. Yang, W. Liu, L. Guo, Y. Gu, Y. Shu, L. Wang, X. Wu, Z. Hua, Y. Ke, Y. Sun, Y. Shen, Q. Xu, Loss of SHP-2 activity in CD4+ T cells promotes melanoma progression and metastasis. *Scientific Reports 2013 3:1*. **3**, 1–10 (2013).
14. C. Wülfing, M. M. Davis, A receptor/cytoskeletal movement triggered by costimulation during T cell activation. *Science (1979)*. **282**, 2266–2269 (1998).
15. A. Grakoui, S. K. Bromley, C. Sumen, M. M. Davis, A. S. Shaw, P. M. Allen, M. L. Dustin, The immunological synapse: A molecular machine controlling T cell activation. *Science (1979)*. **285**, 221–227 (1999).
16. J. A. Hammer, J. C. Wang, M. Saeed, A. T. Pedrosa, Origin, Organization, Dynamics, and Function of Actin and Actomyosin Networks at the T Cell Immunological Synapse. *Annu Rev Immunol*. **37**, 201–224 (2019).
17. D. Blumenthal, J. K. Burkhardt, Multiple actin networks coordinate mechanotransduction at the immunological synapse. *Journal of Cell Biology*, 1–12 (2020).
18. C. R. F. Monks, B. A. Freiberg, H. Kupfer, N. Sciaky, A. Kupfer, Three-dimensional segregation of supramolecular activation clusters in T cells. *Nature 1998 395:6697*. **395**, 82–86 (1998).
19. M. L. Dustin, J. A. Cooper, The immunological synapse and the actin cytoskeleton: molecular hardware for T cell signaling. *Nature Immunology 2000 1:1*. **1**, 23–29 (2000).
20. L. Dupré, K. Boztug, L. Pfajfer, Actin Dynamics at the T Cell Synapse as Revealed by Immune-Related Actinopathies. **9** (2021), doi:10.3389/fcell.2021.665519.
21. A. le Floc'h, Y. Tanaka, N. S. Bantilan, G. Voisinne, G. Altan-Bonnet, Y. Fukui, M. Huse, Annular PIP3 accumulation controls actin architecture and modulates cytotoxicity at the immunological synapse. *Journal of Experimental Medicine*. **210**, 2721–2737 (2013).
22. T. S. Gomez, S. D. McCarney, E. Carrizosa, C. M. Labno, E. O. Comiskey, J. C. Nolz, P. Zhu, B. D. Freedman, M. R. Clark, D. J. Rawlings, D. D. Billadeau, J. K. Burkhardt, HS1 Functions as an Essential Actin-Regulatory Adaptor Protein at the Immune Synapse. *Immunity*. **24**, 741–752 (2006).
23. J. C. Nolz, T. S. Gomez, P. Zhu, S. Li, R. B. Medeiros, Y. Shimizu, J. K. Burkhardt, B. D. Freedman, D. D. Billadeau, The WAVE2 Complex Regulates Actin Cytoskeletal Reorganization and CRAC-Mediated Calcium Entry during T Cell Activation. *Current Biology* (2006), doi:10.1016/j.cub.2005.11.036.
24. Y. Kaizuka, A. D. Douglass, R. Varma, M. L. Dustin, R. D. Vale, Mechanisms for segregating T cell receptor and adhesion molecules during immunological synapse formation in Jurkat T cells. *Proc Natl Acad Sci U S A*. **104**, 20296–20301 (2007).
25. C. Gawden-Bone, G. M. Griffiths, Phospholipids: Pulling back the actin curtain for granule delivery to the immune synapse. *Front Immunol*. **10** (2019), doi:10.3389/fimmu.2019.00700.
26. C. Hivroz, M. Saitakis, Biophysical aspects of T lymphocyte activation at the immune synapse. *Front Immunol*. **7**, 1–12 (2016).
27. B. Liu, W. Chen, B. D. Evavold, C. Zhu, Accumulation of Dynamic Catch Bonds between TCR and Agonist Peptide-MHC Triggers T Cell Signaling. *Cell*. **157**, 357–368 (2014).
28. C. S. C. Liu, D. Raychaudhuri, B. Paul, Y. Chakrabarty, A. R. Ghosh, O. Rahaman, A. Talukdar, D. Ganguly, Cutting Edge: Piezo1 Mechanosensors Optimize Human T Cell Activation. *The Journal of Immunology*. **200**, 1255–1260 (2018).

29. A. Sawicka, A. Babataheri, S. Dogniaux, A. I. Barakat, D. Gonzalez-Rodriguez, C. Hivroz, J. Husson, Micropipette force probe to quantify single-cell force generation: application to T-cell activation. *Mol Biol Cell*. **28**, 3229–3239 (2017).
30. M. A. Govendir, D. Kempe, S. Sianati, J. Cremasco, J. K. Mazalo, F. Colakoglu, M. Golo, K. Poole, M. Biro, T cell cytoskeletal forces shape synapse topography for targeted lysis via membrane curvature bias of perforin. *Dev Cell*. **57**, 2237-2247.e8 (2022).
31. R. Basu, B. M. Whitlock, J. Husson, A. le Floc'h, W. Jin, A. Oyler-Yaniv, F. Dotiwala, G. Giannone, C. Hivroz, N. Biais, J. Lieberman, L. C. Kam, M. Huse, Cytotoxic T Cells Use Mechanical Force to Potentiate Target Cell Killing. *Cell*. **165**, 100–110 (2016).
32. F. Tamzalit, M. S. Wang, W. Jin, M. Tello-Lafoz, V. Boyko, J. M. Heddleston, C. T. Black, L. C. Kam, M. Huse, Interfacial actin protrusions mechanically enhance killing by cytotoxic T cells. *Sci Immunol*. **4** (2019), doi:10.1126/sciimmunol.aav5445.
33. M. L. Dustin, The Immunological Synapse. *Cancer Immunol Res*. **2**, 1023–1033 (2014).
34. S. C. Bunnell, V. Kapoor, R. P. Trible, W. Zhang, L. E. Samelson, Dynamic Actin Polymerization Drives T Cell Receptor–Induced Spreading: A Role for the Signal Transduction Adaptor LAT. *Immunity*. **14**, 315–329 (2001).
35. T. E. Roberts, U. Shipton, M. Moore, Role of MHC class-i antigens and the CD3 complex in the lysis of autologous human tumours by T-cell clones. *Int J Cancer*. **39**, 436–441 (1987).
36. P. Bruhns, B. Iannascoli, P. England, D. A. Mancardi, N. Fernandez, S. Jorieux, M. Daëron, Specificity and affinity of human Fcγ receptors and their polymorphic variants for human IgG subclasses. *Blood*. **113**, 3716–3725 (2009).
37. A. E. Zucchetti, N. Paillon, O. Markova, S. Dogniaux, C. Hivroz, J. Husson, Influence of external forces on actin-dependent T cell protrusions during immune synapse formation. *Biol Cell* (2021), doi:10.1111/boc.202000133.
38. J. Riedl, A. H. Crevenna, K. Kessenbrock, J. H. Yu, D. Neukirchen, M. Bista, F. Bradke, D. Jenne, T. A. Holak, Z. Werb, M. Sixt, R. Wedlich-Soldner, Lifeact: a versatile marker to visualize F-actin. *Nat Methods*. **5**, 605 (2008).
39. A. T. Ritter, K. L. Angus, G. M. Griffiths, The role of the cytoskeleton at the immunological synapse. *Immunol Rev*. **256**, 107–117 (2013).
40. T. S. Gomez, K. Kumar, R. B. Medeiros, Y. Shimizu, P. J. Leibson, D. D. D. Billadeau, Formins Regulate the Actin-Related Protein 2/3 Complex-Independent Polarization of the Centrosome to the Immunological Synapse. *Immunity*. **26**, 177–190 (2007).
41. F. Niedergang, V. di Bartolo, A. Alcover, Comparative anatomy of phagocytic and immunological synapses. *Front Immunol*. **7**, 18 (2016).
42. S. Murugesan, J. Hong, J. Yi, D. Li, J. R. Beach, L. Shao, J. Meinhardt, G. Madison, X. Wu, E. Betzig, J. A. Hammer, Formin-generated actomyosin arcs propel t cell receptor microcluster movement at the immune synapse. *Journal of Cell Biology*. **215**, 383–399 (2016).
43. A. M. Weaver, A. v. Karginov, A. W. Kinley, S. A. Weed, Y. Li, J. T. Parsons, J. A. Cooper, Cortactin promotes and stabilizes Arp2/3-induced actin filament network formation. *Current Biology*. **11**, 370–374 (2001).
44. M. Symons, J. M. J. Derry, B. Karlak, S. Jiang, V. Lemahieu, F. McCormick, U. Francke, A. Abo, Wiskott–Aldrich Syndrome Protein, a Novel Effector for the GTPase CDC42Hs, Is Implicated in Actin Polymerization. *Cell*. **84**, 723–734 (1996).
45. Y. Sasahara, R. Rachid, M. J. Byrne, M. A. de la Fuente, R. T. Abraham, N. Ramesh, R. S. Geha, Mechanism of recruitment of WASP to the immunological synapse and of its activation following TCR ligation. *Mol Cell*. **10**, 1269–1281 (2002).
46. F. Wei, S. Zhong, Z. Ma, H. Kong, A. Medvec, R. Ahmed, G. J. Freeman, M. Krogsgaard, J. L. Riley, Strength of PD-1 signaling differentially affects T-cell effector functions. *Proc Natl Acad Sci U S A*. **110**, 2–11 (2013).
47. V. R. Juneja, K. A. McGuire, R. T. Manguso, M. W. LaFleur, N. Collins, W. Nicholas Haining, G. J. Freeman, A. H. Sharpe, PD-L1 on tumor cells is sufficient for immune evasion in immunogenic tumors and inhibits CD8 T cell cytotoxicity. *Journal of Experimental Medicine*. **214**, 895–904 (2017).
48. T. Douanne, G. M. Griffiths, Cytoskeletal control of the secretory immune synapse. *Curr Opin Cell Biol*. **71**, 87–94 (2021).
49. A. T. Ritter, Y. Asano, J. C. Stinchcombe, N. M. G. Dieckmann, B. C. Chen, C. Gawden-Bone, S. van Engelenburg, W. Legant, L. Gao, M. W. Davidson, E. Betzig, J. Lippincott-Schwartz, G. M. Griffiths, Actin

Depletion Initiates Events Leading to Granule Secretion at the Immunological Synapse. *Immunity*. **42**, 864–876 (2015).
50. A. T. Ritter, S. M. Kapnick, S. Murugesan, P. L. Schwartzberg, G. M. Griffiths, J. Lippincott-Schwartz, Cortical actin recovery at the immunological synapse leads to termination of lytic granule secretion in cytotoxic T lymphocytes. *Proc Natl Acad Sci U S A*. **114**, E6585–E6594 (2017).
51. K. Chemin, A. Bohineust, S. Dogniaux, M. Tourret, S. Guégan, F. Miro, C. Hivroz, Cytokine Secretion by CD4 + T Cells at the Immunological Synapse Requires Cdc42-Dependent Local Actin Remodeling but Not Microtubule Organizing Center Polarity. *The Journal of Immunology*. **189**, 2159–2168 (2012).
52. J. M. Chemnitz, R. v. Parry, K. E. Nichols, C. H. June, J. L. Riley, SHP-1 and SHP-2 Associate with Immunoreceptor Tyrosine-Based Switch Motif of Programmed Death 1 upon Primary Human T Cell Stimulation, but Only Receptor Ligation Prevents T Cell Activation. *The Journal of Immunology*. **173**, 945–954 (2004).
53. K. Li, Z. Yuan, J. Lyu, E. Ahn, S. J. Davis, R. Ahmed, C. Zhu, PD-1 suppresses TCR-CD8 cooperativity during T-cell antigen recognition. *Nat Commun*. **12**, 1–13 (2021).
54. B. T. Fife, K. E. Pauken, T. N. Eagar, T. Obu, J. Wu, Q. Tang, M. Azuma, M. F. Krummel, J. A. Bluestone, Interactions between PD-1 and PD-L1 promote tolerance by blocking the TCR-induced stop signal. *Nat Immunol*. **10**, 1185–1192 (2009).
55. B. H. Zinselmeyer, S. Heydari, C. Sacristán, D. Nayak, M. Cammer, J. Herz, X. Cheng, S. J. Davis, M. L. Dustin, D. B. McGavern, PD-1 promotes immune exhaustion by inducing antiviral T cell motility paralysis. *Journal of Experimental Medicine*. **210**, 757–774 (2013).
56. R. Ambler, G. Edmunds, G. Toti, D. Morgan, C. Wülfing, PD-1 suppresses the maintenance of cell couples between cytotoxic T cells and tumor target cells within the tumor. *Sci Signal*. **4518**, 443788 (2020).
57. A. S. Tocheva, M. Peled, M. Strazza, K. R. Adam, S. Lerrer, S. Nayak, I. Azoulay-Alfaguter, C. J. R. Foster, E. A. Philips, B. G. Neel, B. Ueberheide, A. Mor, Quantitative phosphoproteomic analysis reveals involvement of PD-1 in multiple T cell functions. *Journal of Biological Chemistry*. **295**, 18036–18050 (2020).
58. B. Lowin-Kropf, V. S. Shapiro, A. Weiss, Cytoskeletal polarization of T cells is regulated by an immunoreceptor tyrosine-based activation motif-dependent mechanism. *Journal of Cell Biology*. **140**, 861–871 (1998).
59. N. Blanchard, V. di Bartolo, C. Hivroz, In the Immune Synapse, ZAP-70 Controls T Cell Polarization and Recruitment of Signaling Proteins but Not Formation of the Synaptic Pattern. *Immunity*. **17**, 389–399 (2002).
60. M. R. Jenkins, J. C. Stinchcombe, B. B. Au-yeung, Y. Asano, A. T. Ritter, A. Weiss, G. M. Griffiths, Distinct structural and catalytic roles for Zap70 in formation of the immunological synapse in CTL, 1–21 (2014).
61. J. C. Stinchcombe, E. Majorovits, G. Bossi, S. Fuller, G. M. Griffiths, Centrosome polarization delivers secretory granules to the immunological synapse. *Nature*. **443**, 462–465 (2006).
62. H. Ueda, M. K. Morphew, J. R. McIntosh, M. M. Davis, CD4 + T-cell synapses involve multiple distinct stages. *Proc Natl Acad Sci U S A*. **108**, 17099–17104 (2011).
63. C. J. Sanderson, A. M. Glauert, The mechanism of T-cell mediated cytotoxicity. VI. T-cell projections and their role in target cell killing. *Immunology*. **36**, 119–29 (1979).
64. J. Husson, K. Chemin, A. Bohineust, C. Hivroz, N. Henry, Force Generation upon T Cell Receptor Engagement. *PLoS One*. **6**, e19680 (2011).
65. M. Huse, Mechanical forces in the immune system. *Nat Rev Immunol*. **17**, 679–690 (2017).
66. L. O. Randzavola, K. Strege, M. Juzans, Y. Asano, J. C. Stinchcombe, C. M. Gawden-Bone, M. N. Seaman, T. W. Kuijpers, G. M. Griffiths, Loss of ARPC1B impairs cytotoxic T lymphocyte maintenance and cytolytic activity. *J Clin Invest* (2019), doi:10.1172/JCI129388.
67. S. Kumari, M. Mak, Y. Poh, M. Tohme, N. Watson, M. Melo, E. Janssen, M. Dustin, R. Geha, D. J. Irvine, Cytoskeletal tension actively sustains the migratory T-cell synaptic contact. *EMBO J*, 1–18 (2020).
68. E. K. Moore, M. Strazza, A. Mor, Combination Approaches to Target PD-1 Signaling in Cancer. *Front Immunol*. **13**, 3771 (2022).
69. T. Saito, Molecular dynamics of co-signal molecules in T-cell activation. *Adv Exp Med Biol*. **1189**, 135–152 (2019).
70. N. Patsoukis, Q. Wang, L. Strauss, V. A. Boussiotis, Revisiting the PD-1 pathway. *Sci Adv*. **1** (2020).
71. X. Xu, B. Hou, A. Fulzele, T. Masubuchi, Y. Zhao, Z. Wu, Y. Hu, Y. Jiang, Y. Ma, H. Wang, E. J. Bennett, G. Fu, E. Hui, PD-1 and BTLA regulate T cell signaling differentially and only partially through SHP1 and SHP2. *Journal of Cell Biology*. **219** (2020), doi:10.1083/JCB.201905085.

72. A. Pierres, V. Monnet-Corti, A. M. Benoliel, P. Bongrand, Do membrane undulations help cells probe the world? *Trends Cell Biol*. **19**, 428–433 (2009).
73. C. B. Carbone, N. Kern, R. A. Fernandes, E. Hui, X. Su, K. C. Garcia, R. D. Vale, In vitro reconstitution of T cell receptor-mediated segregation of the CD45 phosphatase. *Proc Natl Acad Sci U S A*. **114**, E9338–E9345 (2017).
74. P. Demetriou, E. Abu-Shah, S. Valvo, S. McCuaig, V. Mayya, A. Kvalvaag, T. Starkey, K. Korobchevskaya, L. Y. W. Lee, M. Friedrich, E. Mann, M. A. Kutuzov, M. Morotti, N. Wietek, H. Rada, S. Yusuf, J. Afrose, A. Siokis, P. Allan, T. Ambrose, C. Arancibia, A. Bailey, E. Barnes, E. Bird-Lieberman, J. Bornschein, O. Brain, B. Braden, J. Collier, J. Cobbold, E. Culver, J. East, L. Howarth, P. Klenerman, S. Leedham, R. Palmer, M. Pavlides, F. Powrie, A. Rodrigues, J. Satsangi, A. Simmons, P. Sullivan, H. Uhlig, A. Walsh, M. Meyer-Hermann, A. A. Ahmed, D. Depoil, M. L. Dustin, A dynamic CD2-rich compartment at the outer edge of the immunological synapse boosts and integrates signals. *Nat Immunol*. **21**, 1232–1243 (2020).
75. S. T. Kim, K. Takeuchi, Z. Y. J. Sun, M. Touma, C. E. Castro, A. Fahmy, M. J. Lang, G. Wagner, E. L. Reinherz, The αβ T Cell Receptor Is an Anisotropic Mechanosensor. *Journal of Biological Chemistry*. **284**, 31028–31037 (2009).
76. M. S. Lee, C. R. Glassman, N. R. Deshpande, H. B. Badgandi, H. L. Parrish, C. Uttamapinant, P. S. Stawski, A. Y. Ting, M. S. Kuhns, A Mechanical Switch Couples T Cell Receptor Triggering to the Cytoplasmic Juxtamembrane Regions of CD3ζζ. *Immunity*. **43**, 227–239 (2015).
77. A. Babich, S. Li, R. S. O'Connor, M. C. Milone, B. D. Freedman, J. K. Burkhardt, F-actin polymerization and retrograde flow drive sustained PLCγ1 signaling during T cell activation. *Journal of Cell Biology*. **197**, 775–787 (2012).
78. F. E. Sepulveda, A. Burgess, X. Heiligenstein, N. Goudin, M. M. Ménager, M. Romao, M. Côte, N. Mahlaoui, A. Fischer, G. Raposo, G. Ménasché, G. de Saint Basile, LYST Controls the Biogenesis of the Endosomal Compartment Required for Secretory Lysosome Function. *Traffic*. **16**, 191–203 (2015).
79. J. Schindelin, I. Arganda-Carreras, E. Frise, V. Kaynig, M. Longair, T. Pietzsch, S. Preibisch, C. Rueden, S. Saalfeld, B. Schmid, J. Y. Tinevez, D. J. White, V. Hartenstein, K. Eliceiri, P. Tomancak, A. Cardona, Fiji: an open-source platform for biological-image analysis. *Nature Methods 2012 9:7*. **9**, 676–682 (2012).

**Acknowledgments:** We would like to thank Xavier Lahaye for providing us with peripheral blood mononuclear cells and the members of the "Integrative analysis of T cell activation" (Institut Curie) for support and discussions. We thank also Ana-Maria Lennon-Duménil and Julien Husson for their critical reading of our manuscript and Loïc Dupré for insightful discussions. We acknowledge the Nikon Imaging Center (Institut Curie), and the Cell and Tissue Imaging Platforsm-PICT-IBiSA (Institut Curie, France–Bioimaging of the Genetics and Developmental Biology Department (UMR3215/U934) of Institut Curie, especially Aurélien Dauphin for 3D-SIM image acquisition, as well as the Recombinant Antibody Platform (TAb-IP) of Institut Curie.

**Funding:** This work was supported by funds from Institut Curie, INSERM, ANR (ANR-10-IDEX-0001-02 PSL* and ANR-11-LABX-0043; RetroTact ANR-20CE15-0009-01), the Fondation pour la Recherche Médicale (FRM, FRM DEQ20140329513) and the Fondation ARC pour la recherche sur le cancer. Noémie Paillon received a Ph.D. fellowship from ITMO Cancer in partnership with INSERM and from Ecole Doctorale Frontières de l'Innovation en Recherche et Education – Programme Bettencourt. The Cell and Tissue Imaging Platforsm-PICT-IBiSA was supported by ANR-10-INBS-04 and the European Research Council [ERC EPIGENETIX N°250367].

**Author contributions:**
NP: Conceptualized, performed, and analyzed most of the experiments, wrote the original draft, and reviewed and edited the final draft of the manuscript.
VM: Performed experiments, analyzed part of the data, and reviewed the manuscript.

SD: Designed and produced plasmids and lentiviruses, performed directed mutagenesis, and established stable cell lines.
MM: Methodology, software, formal analysis.
HF: Performed experiments and reviewed the manuscript.
JJSP: Reviewed the manuscript.
LB: Developed flow cytometry expertise and provided intellectual contribution.
AEZ: Provided expertise and feedback and discussed the results.
CH: Conceptualized, supervised, and administrated the project, and wrote the first and final draft of the manuscript.

**Competing interests:** There are no competing interests to declare.

**Data and materials availability:** All data, code, and materials used in the analysis are available upon request.

**Supplementary Materials**

Movies 1 to 4.

Figures S1 to S5.

Tables S1 and S2.

## Supplementary materials

**Movie 1. Live immune synapse formation.** Representative movie of immune synapse formation. Jurkat T cells expressing PD-1-YFP (green) and LifeAct-mCherry (red) were co-cultured with APCs coated with anti-CD3/CD28 antibodies for 30min. Conjugates were imaged every 45sec. Images were acquired by spinning disk microscopy; one sagittal Z plane of the immune synapse is shown. Scale bar: 5µm. N = 2 experiments.

**Movie 2. PD-1/PD-L1 interaction inhibits actin dynamics upon immune synapse formation.** Representative movie of the effect of PD-1 on immune synapse formation. Jurkat T cells expressing PD-1-YFP (green) and LifeAct-mCherry (red) were co-cultured with APC-PD-L1 and coated with anti-CD3/CD28 for 30min. Conjugates were imaged every 45sec. Images were acquired by spinning disk microscopy; one sagittal Z plane of the immune synapse is shown. Scale bar: 5µm. N = 2 experiments.

**Movie 3. T cells can form multiple immune synapses.** Representative live imaging of the formation of two simultaneous immune synapses. PD-1$^{+}$ Jurkat T cells expressing LifeAct-mCherry (magenta) were co-cultured for 30min with APCs stained with Celltracker CMAC (cyan), coated with anti-CD3/CD28. Conjugates were imaged every 45sec. Images were acquired by spinning disk microscopy; one sagittal Z plane of the immune synapse is shown. Scale bar: 5µm.

**Movie 4. PD-1-induced actin remodeling inhibition is local.** Representative live imaging of the local effect of PD-1 on immune synapse formation. Jurkat T cells expressing PD-1-YFP (cyan) and LifeAct-mCherry (magenta) were co-cultured for 30min with APCs and APC-PD-L1, coated with anti-CD3/CD28 antibodies. Conjugates were imaged every 45sec. Images were acquired by spinning disk microscopy; one sagittal Z plane of the immune synapse is shown. Scale bar: 5µm.

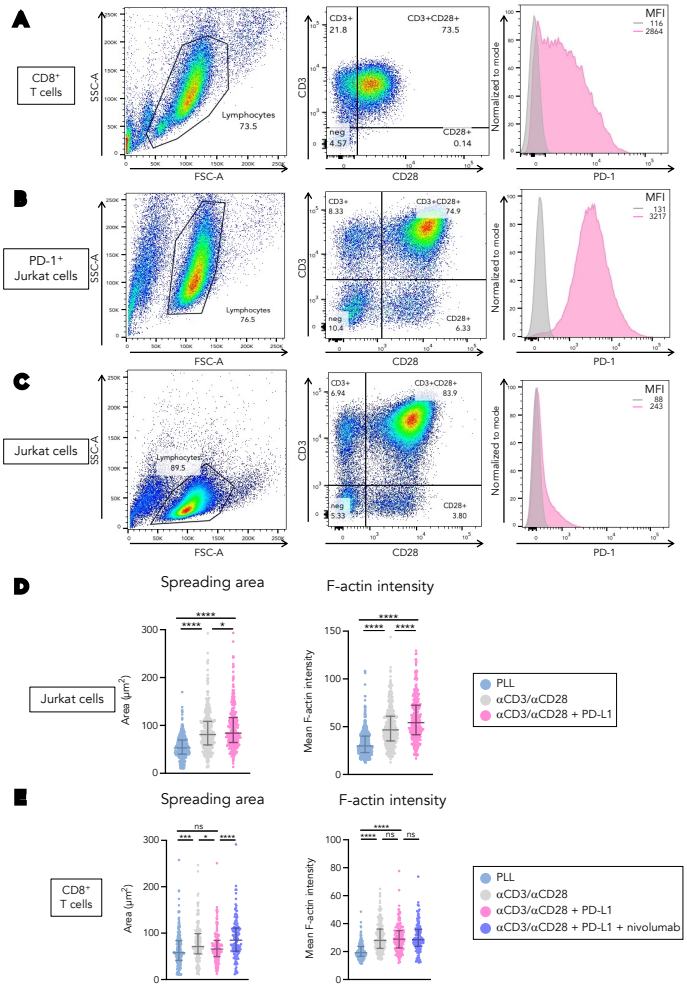


**Figure S1. PD-L1 alone does not inhibit T cell spreading.** (**A-C**) Representative FACS expression profile of CD3, CD28, and PD-1 in (**A**) PD-1$^{+}$ CD8$^{+}$ T cells, (**B**) PD-1$^{+}$Jurkat T cells, and (**C**) untransduced Jurkat T cells gated on lymphocytes using size (FSC) and granularity (SSC). (**D**) Spreading area and F-actin intensity of untransduced Jurkat cells after 10min spreading on glass surfaces coated with poly-L-lysine (PLL) alone or with anti-CD3/CD28 antibodies and PD-L1-Fc or IgG1-Fc as a control. After activation, cells were fixed, permeabilized, and stained with DAPI and phalloidin. Spreading area and F-actin intensity were measured by confocal microscopy. N = 1 experiment, >300 cells for each condition. N = 1 experiment with > 300 cells/condition (**E**) Spreading area and F-actin intensity of PD-1$^{+}$ CD8$^{+}$ T cells after 10min spreading on glass surfaces coated with poly-L-lysine alone or with anti-CD3/CD28 antibodies and PD-L1-Fc or IgG1-Fc as a control. Cells were incubated with the Nivolumab anti-PD-1 antibody or IgG4 as a control for 10min before activation. After activation, cells were fixed, permeabilized, and stained for DAPI and phalloidin. Spreading area and F-actin intensity were measured by confocal microscopy. Data are presented as median with interquartile range. N = 1 experiment with > 130 cells/condition. Mann-Whitney T-test ****P≤ 0.0001, ***P≤ 0.001, *P ≤ 0.05.

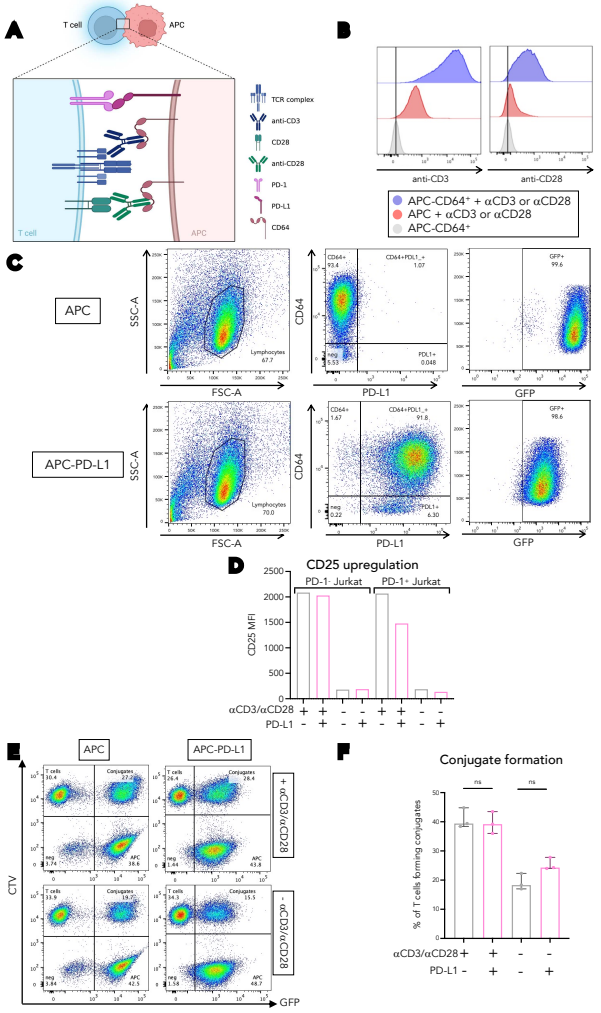


**Figure S2. Presentation of the engineered APC model.** (**A**) Schematic representation of the developed engineered APC model. The cell line K652 was stably transduced with the Fc-receptor CD64 (called APC thereafter) to capture anti-CD3/CD28 antibodies and present them to T cells for activation. The CD64$^{+}$ cell line was stably transduced with PD-L1 (called APC-PD-L1 thereafter) to co-engage TCR/CD28 and PD-1 simultaneously. (**B**) The ability of the APCs to bind anti-CD3 and anti-CD28 antibodies. Cells were coated with biotinylated anti-CD3 or anti-CD28 antibodies, and the coating was revealed with streptavidin coupled to Alexa Fluor 488 by FACS analysis. (**C**) FACS expression profile of CD64, PD-L1, and GFP in the APC-GFP and APC-PD-L1-GFP cells gated on APCs using size (FSC) and granularity (SSC). (**D**) CD25 upregulation of wild-type or PD-1$^{+}$ Jurkat cells after 12 hours of co-culture with APCs or APC-PD-L1, coated or not with anti-CD3/CD28 antibodies. N = 1 experiment performed with technical triplicates. (**E**) Representative conjugate formation assay. CTV-stained PD-1$^{+}$ Jurkat cells were co-cultured with APC-GFP or APC-PD-L1-GFP at a 1:1 ratio. After 20min conjugate formation, cells were fixed, and conjugate formation was measured by flow cytometry. (**F**) Conjugate formation among T cells for each condition. N = 3 independent experiments with technical replicates. Data are presented as median with interquartile range. Mann-Whitney T-test, ns: non significative.

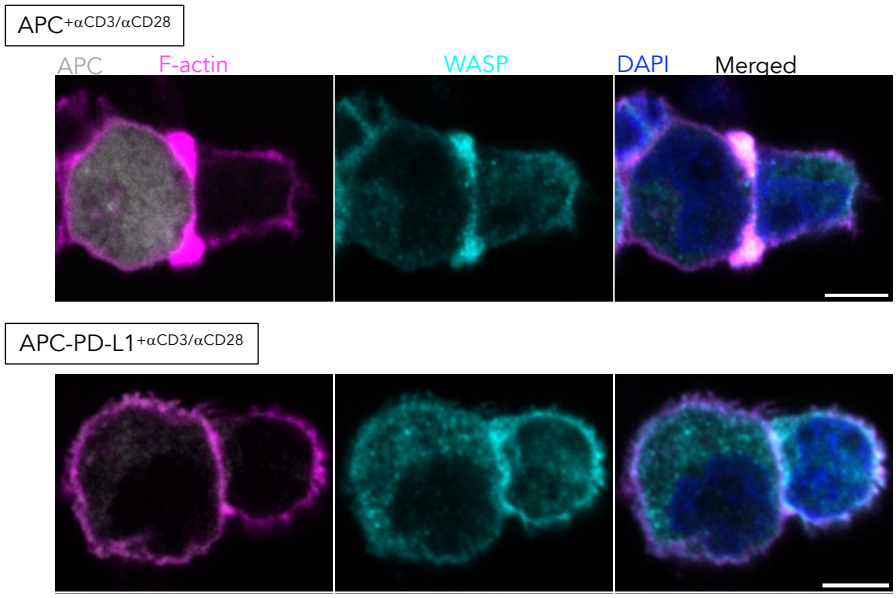


**Figure S3. PD-1 alters WASP distribution at the immune synapse.** Representative images of the effect of PD-1 on WASp distribution. PD-1$^+$ CD8$^+$ T cells were co-cultured for 30min with APC-GFP (grey) or APC-PD-L1-GFP (grey) coated with anti-CD3/CD28. Conjugates were then fixed, permeabilized, and stained with anti-WASp (cyan), phalloidin (magenta), and DAPI (blue). Images were acquired by confocal microscopy; one sagittal Z plane of the immune synapse is shown. Scale bar: 5µm.

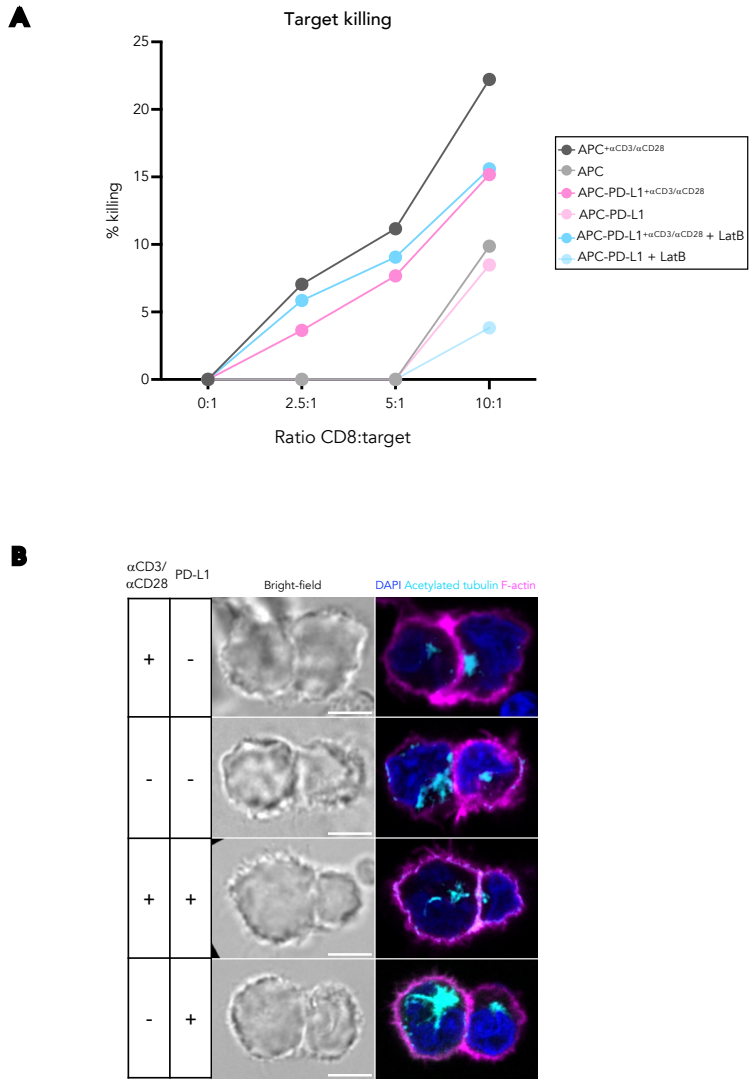


**Figure S4. PD-1 does not affect centrosome polarization to the immune synapse.** (**A**) Cytotoxic capacity of PD-1$^+$ CD8$^+$ T cells co-cultured for 4h with APCs or APC-PD-L1 coated with anti-CD3/CD28 antibodies or not and treated or not with Latrunculin B (0.01µM). APCs were stained with Celltrace Violet before co-culture and death was determined using a Live/Dead staining. Killing capacity is expressed as a percentage of dead APCs at the CD8-to-target ratios indicated. Representative assay from 2 independent experiments, 4 healthy donors. (**B**) Representative images of the effect of PD-1 on centrosome polarization. PD-1$^+$ CD8$^+$ T cells (on the right) were co-cultured for 30min with APC-GFP or APC-PD-L1-GFP (on the left) coated with anti-CD3/CD28 antibodies or not. Conjugates were then fixed, permeabilized, and stained for anti-acetylated tubulin to label the centrosome (cyan), phalloidin (magenta), and DAPI (blue). Images were acquired by confocal microscopy; one sagittal Z plane of the immune synapse is shown. Scale bar: 5µm.

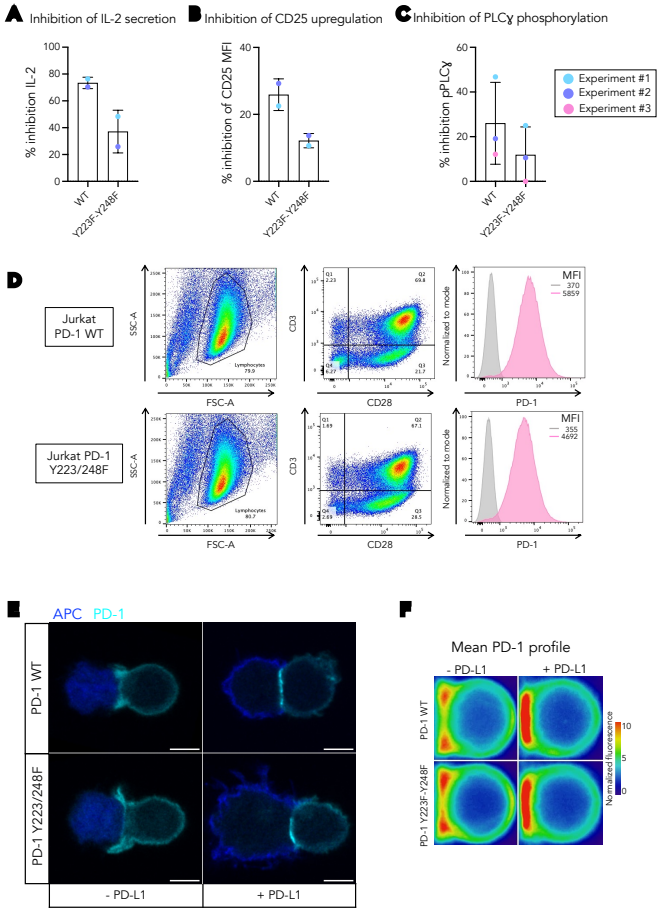


**Figure S5. PD-1 tyrosine mutations rescue part of T cell activation.** (**A**) Inhibition rate of IL-2 secretion measured by ELISA, (**B**) CD25 upregulation measured by flow cytometry, and (**C**) PLCγ phosphorylation measured by western blot. (**A-B**) PD-1$^+$ Jurkat cells expressing PD-1 wild-type (WT) or PD-1 Y223/248F were activated overnight with APCs or APC-PD-L1 coated or not with anti-CD3/CD28 antibodies. N = 2 independent experiments. (**C**) PD-1$^+$ Jurkat cells expressing PD-1 wild-type (WT) or PD-1 Y223/248F were activated for 10min on plates coated with anti-CD3/CD28 antibodies and PD-L1-Fc or IgG1-Fc as a control. N = 2 independent experiments. Data are presented as median with interquartile range. (**D**) FACS expression profile of CD3, CD28, and PD-1 in Jurkat cells expressing PD-1 WT or PD-1 Y223/248 gated on APCs using size (FSC) and granularity (SSC). (**E**) Representative images of the effect of PD-1 mutation on immune synapse formation. Jurkat T cells expressing PD-1-YFP or PD-1-Y223/248F-YFP (cyan) and LifeAct-mCherry were co-cultured for 30min with APC-GFP or APC-PD-L1-GFP, coated with anti-CD3/CD28 antibodies. Conjugates were then fixed, permeabilized, and stained with anti-GFP. Images were acquired by confocal microscopy; one sagittal Z plane of the immune synapse is shown. Scale bar: 5µm. N = 3 experiments with >60 conjugates per condition. Scale bar: 5µm (**F**) Mean profile of PD-1 distribution in Jurkat cells expressing PD-1 WT or PD-1 Y223/248F upon activation with an APC expressing or not PD-L1, coated with anti-CD3/CD28 antibodies. Cells were normalized to the same size and fluorescent intensity and the average projection of all cells was done to see signal distribution, using a linear LUT to show signal accumulation. N = 3 independent experiments with >60 conjugates per condition.

| Reagent type | Reagent name | Provider | Reference | Additional information |
|---|---|---|---|---|
| Antibody | Anti-GFP | CurieCoreTech | A-R-H#11 | IF (1/200) |
| Antibody | Anti-mCherry | CurieCoreTech | A-P-R#13 | IF (1/200) |
| Antibody | Anti-PD-L1 BV421 | BioLegend | 374507 | IF (1/50), FC (1/200) |
| Antibody | Anti-LAMP-1 | abcam | ab24170 | IF (1/500) |
| Antibody | Anti-acetylated tubulin | CurieCoreTech | A-R-H#39 | IF (1/50) |
| Antibody | Anti-WASP | abcam | ab59278 | IF (1/100) |
| Antibody | Anti-phospho-HS1 (Tyr397) | Cell Signaling Technology | 13708S | IF (1/50) |
| Antibody | Anti-CD3 FITC | BioLegend | 317306 | FC (1/200) |
| Antibody | Anti-CD28 PE | eBioscience | 12-0289-42 | FC (1/200) |
| Antibody | Anti-CD64 PE | BioLegend | 305007 | FC (1/200) |
| Antibody | Anti-PD-1 PE | BioLegend | 329906 | FC (1/200) |
| Antibody | Anti-LAMP-1 (CD107a) FITC | BioLegend | 328607 | FC (1/30) |
| Antibody | Anti-LAMP-2 (CD107b) PE | BioLegend | 354305 | FC (1/30) |
| Antibody | Anti-CD25 PE-Cy7 | eBioscience | 25-0259-42 | FC (1/400) |
| Antibody | Anti-phospho-HS1 (Tyr397) | Cell Signaling Technology | 8714S | WB (1/1000) |
| Antibody | Anti-β2-microglobulin | Cell Signaling Technology | 12851S | WB (1/1000) |
| Antibody | Anti-CD3 (OKT3) | BioLegend | 317325 | 0.1-10µg/mL |
| Antibody | Anti-CD28 (CD28.2) | BioLegend | 302933 | 2.5-10µg/mL |
| Antibody | HRP goat IgG anti-rabbit IgG (H+L) | Jackson ImmunoResearch | 111-035-144 | WB (1/10 000) |
| Antibody | Goat anti-Rabbit IgG (H+L), Alexa Fluor™ 488 | Invitrogen | A11034 | IF (1/200) |
| Antibody | Goat anti-Human IgG (H+L), Alexa Fluor™ Plus 488 | Invitrogen | A48276 | IF (1/200) |
| Antibody | Goat anti-Rabbit IgG (H+L), Alexa Fluor™ 568 | Invitrogen | A11011 | IF (1/200) |
| Antibody | OPDIVO (Nivolumab) | Bristol Myers Squibb | - | 100µg/mL |
| Antibody | Anti-Beta-Gal-hIgG4 | Invivogen | bgal-mab4 | 100µg/mL |
| Biochemical reagent | RIPA 10X | Cell Signaling Technology | 9806 | |
| Biochemical reagent | Halt™ Phosphatase Inhibitor Single-Use Cocktail | Thermo Scientific | 78426 | |
| Biochemical reagent | Complete, EDTA-free (Protease inhibitor cocktail tablets) | Roche | 11873580001 | |
| Biochemical reagent | Thermo Scientific™ Pierce™ Universal Nuclease for Cell Lysis | Thermo Scientific | 88702 | |
| Biochemical reagent | 4x Laemmli Sample Buffer | Bio-Rad | 1610747 | |
| Biochemical reagent | NuPAGE sample reducing agent 10X | Invitrogen | NP0009 | |
| Biochemical reagent | 4–15% Mini-PROTEAN™ TGX Stain-Free™ Protein Gels | Bio-Rad | 4568086 | |
| Cell culture reagent | RPMI Medium 1640 (1X) + Glutamax | Gibco | 61870-010 | |
| Cell culture reagent | RPMI Medium 1640 (1X) + L-Glutamine - Phenol Red | Gibco | 11835-030 | |
| Cell culture reagent | fetal calf serum | Eurobio | CVFSVF00-01 | |
| Cell culture reagent | Penicillin-streptomycin (10 000UI/ml) | Gibco | 15140-122 | 100 U/mL |
| Cell culture reagent | 96-well plates | TPP | 9296 | |
| Cell culture reagent | Hepes | Gibco | 15630-056 | 1M |
| Cell culture reagent | 2-Mercaptoethanol | Gibco | 31350-010 | 50mM |
| Cell culture reagent | BSA | Euromedex | 04-100-812 | 0.2-5% |
| Cell culture reagent | EDTA | Invitrogen | 15575-038 | 1mM |
| Cell culture reagent | PBS without CA&MG | Eurobio | CS1PBS01K BP | |
| Chermical compound; drug | PEI Max | Polysciences,Inc | 24765-1 | 0,63mM |
| Chemical compound; drug | Latrunculin B | Tocris | 3974 | 0.01µM |
| Chemical compound; drug | CK666 | Tocris | 3950 | 100µM |
| Chemical compound; drug | Fixation buffer | BD Biosciences | 554655 | |
| Chemical compound; drug | Phalloidin AF647 | Invitrogen | A22287 | 1/200 |
| Chemical compound; drug | Phalloidin AF568 | Invitrogen | A12380 | 1/200 |
| Chemical compound; drug | DAPI | Invitrogen | D1306 | 1/2000 |
| Chemical compound; drug | poly-L-lysine | Sigma-Aldrich | P8920 | 0.02% |
| Chemical compound; drug | Image-iT™ Fixative Solution (4% formadehyde) | Invitrogen | FB002 | 4% |
| Chemical compound; drug | Glycine | Sigma-Aldrich | G8898 | 10mM |
| Chemical compound; drug | Saponin | Sigma-Aldrich | S4521 | 0.05% |
| Chemical compound; drug | Fluoromount G | SouthernBiotech | 0100-01 | |
| Commercial kit | CellTrace Violet | Invitrogen | C34557 | 1/10 000 |
| Commercial kit | Live/Dead eFluor 780 | Invitrogen | 65-0865-14 | 1/1500 |
| Commercial kit | Clarity Western ECL Substrate | Bio-Rad | 1705061 | |
| Commercial kit | 100 µL Neon Transfection system | Invitrogen | MPK10096 | 1450 V, 10 ms, 3 pulses |
| Commercial kit | LS columns | Miltenyi | 130-042-401 | |
| Commercial kit | Celltracker CMAC | Invitrogen | C2110 | 1/1000 |
| Commercial kit | Celltracker CMFDA | Invitrogen | C2925 | 1/1000 |
| Commercial kit | OptEIA™ Human IL-2 ELISA Set | BD Biosciences | 555190 | |
| Commercial kit | CD8+ T Cell Isolation Kit, human | Miltenyi Biotech | 130-096-495 | |
| Cytokine | rh IL-2 | Immunotools | 11340025 | 20 U/mL |
| Cytokine | rh IFN-a2a | Immunotools | 11343506 | 20 ng/mL |
| Material | 12mm ø cover slips | Menzel Gläser - Thermo Scientific | CBAD00120RA120MNZ#0 | |
| Material | Superfrost plus slides | Menzel Gläser - Thermo Scientific | J1800AMNZ | |
| Material | 15mm ø glass bottom cell culture dish | NEST Scientific | 801002 | |
| Recombinant protein | IgG1-Fc | Biotechne | 110-HG | 5µg/mL |
| Recombinant protein | PD-L1-Fc | Biotechne | 156-B7 | 5µg/mL |
| Software | FlowJo Software version 10.8.2 | Becton, Dickinson & Company | | |
| Software | Image Lab software | Bio-Rad | | |
| Software | Fiji-ImageJ | (Schindelin et al., 2012) | | |
| Software | GraphPad PRISM | GraphPad Software | Version 9.5.0 | |
| Software | Metamorph | Molecular Devices | | |

**Table S1. Table of the used reagents and antibodies.**

| Name in the text | Plasmid | Original vector | Cloning primer 5'—>3' | Insert | Technique | Vector type | Transfection method | Cell line |
|---|---|---|---|---|---|---|---|---|
| PD-1 Jurkat | pDH1-PD1-EF1 | pDest DH1-EF1 puro | F-AAAAAGCAGGCTTCACCATGCAGATCCCACAGGCGCC | PD1-WT | Gateway ® Technology with Clonase ® II (Invitrogen #2535-029 and 12535-037) | Lentiviral | Transduction | Jurkat E6.1 |
| | | | R-AGAAAGCTGGGTGTCAGAGGGGCCAAGAGCAGTG | | | | | |
| PD-1 Y223/248F Jurkat | pDH1-PD1-EF1-223-248-Tyr-Mut | pDest DH1-EF1 puro | F-CTCTGTGGACTTCGGGGAGCTGG (mut Tyr 223) | PD1-Mut Tyr 223-248 | Q5 Site-Directed Mutagenesis Kit (NEB#E0552S) | Lentiviral | Transduction | Jurkat E6.1 |
| | | | R-AACACAGGCACGGCTGAG (mut Tyr 223) | | | | | |
| | | | F-GCAGACGGAGTTCGCCACCATTGTC (mut Tyr 248) | | | | | |
| | | | R-TCAGGGACACAGGGCACG (mut Tyr 248) | | | | | |
| PD-1-YFP Jurkat | pWXLD-PD1-YFP | V38 pDest WXLD | F-AAAAAGCAGGCTTCACCATGCAGATCCCACAGGCGCC | PD1-YFP | Gateway ® Technology with Clonase ® II (Invitrogen #2535-029 and 12535-037) | Lentiviral | Transduction | Jurkat E6.1 |
| | | | R-AGAAAGCTGGGTGTTACTTGTACAGCTCGTCCAT | | | | | |
| PD-1 Y223/248F-YFP Jurkat | pWXLD-PD1-223-248-Tyr-Mut-YFP | V38 pDest WXLD | F-CTCTGTGGACTTCGGGGAGCTGG (mut Tyr 223) | PD1-Mut Tyr 223-248 | Q5 Site-Directed Mutagenesis Kit (NEB#E0552S) | Lentiviral | Transduction | Jurkat E6.1 |
| | | | R-AACACAGGCACGGCTGAG (mut Tyr 223) | | | | | |
| | | | F-GCAGACGGAGTTCGCCACCATTGTC (mut Tyr 248) | | | | | |
| | | | R-TCAGGGACACAGGGCACG (mut Tyr 248) | | | | | |
| APC-PD-L1 | pUNO-PD-L1 | | # PUNO1-HCD274 (Invivogen) | PD-L1-WT | | Expression vector | Transfection - NeonTM Transfection System (Invitrogen) | K562 CCL-243 |
| APC-PD-L1-GFP | pTRIP-SFFV-PD-L1-GFP | pTRIP-SFFV-GFP | F-GCCGCGGCCGCGGGCTAGCGGCCACCATGAGGATATTTGCTGTCTTTATATTC | PD-L1-WT | BamHI with NEBuilder® HiFi DNA Assembly Master Mix (NEB#E2621S) | Lentiviral | Transduction | K562 CCL-243 |
| | | | R-CCATGGTGGCGACCGGTGGGGCCGTCTCCTCCAAATGTGTATC | | | | | |
| APC-GFP | pTRIP-SFFV-GFP | pTRIP-SFFV-GFP | (Manel Ref papier) | | | | | |
| APC | pUNO1-MCS | | puno1-mcs (Invivogen) | _ | | Expression vector | Transfection - NeonTM Transfection System (Invitrogen) | K562 CCL-243 |
| Jurkat-LifeAct-mCherry | pTRIP-SFFV-LifeAct-mCherry | pTRIP-SFFV-GFP | F-GCCGCGGCCGCGGGCTAGCGGCCACCATGGGCGTGGCC | | BamHI/XhoI - with NEBuilder® HiFi DNA Assembly Master Mix (NEB#E2621S) | Lentiviral | Transduction | Jurkat E6.1 |
| | | | R-GCTCCATGTTTTTCTAGGTCTCACTTGTACAGCTCGTCCATGCC | | | | | |

**Table S2. Table of the used vectors and antibodies.**

## Article 2 : Label-free single-cell live imaging reveals fast metabolic switch in T lymphocytes

Co-1er auteur

Article en révision, Molecular Biology of the Cell

**Résumé**

L'activation des lymphocytes T induit un basculement métabolique qui génere l'énergie nécessaire à la prolifération, la survie et l'alimentation de leurs fonctions. Il est donc essentiel d'étudier le métabolisme associé aux changements fonctionnels et structurels subcellulaires.

Nous avons utilisé une méthode de microscopie à fluorescence à deux photons (2P-FLIM) non invasive et sans marquage pour cartographier la dynamique spatiale et temporelle de la co-enzyme métabolique NADH au cours de l'activation des lymphocytes T. Les mesures par 2P-FLIM des ratios de NADH libre et lié aux protéines fournissent une lecture de l'état redox ($NAD^+$/ NADH) des cellules, et donc de leurs taux de phosphorylation oxydative et de glycolyse.

En utilisant cette méthode, nous avons suivi la dynamique de la fraction de NADH lié (fb NADH) dans des cellules uniques vivantes. En comparant la fb NADH entre des cellules T au repos et activées, nous montrons que l'activation des cellules T induit un basculement rapide de la phosphorylation oxydative vers la glycolyse. Ce changement ne nécessite que 10 minutes et reste stable pendant au moins une heure. L'analyse tridimensionnelle (3D) révèle que la distribution intracellulaire de la fb NADH est symétrique dans les cellules au repos, alors qu'elle augmente au niveau de la zone de contact dans les cellules activées. Enfin, nous montrons que la fb NADH est négativement corrélée avec l'étalement des cellules T activées, suggérant un lien entre le remodelage de l'actine et les changements métaboliques. Cette étude montre que la mesure par 2P-FLIM de la fb NADH est bien adaptée pour suivre un changement métabolique rapide en 3D, dans des lymphocytes T uniques avec une résolution subcellulaire.

**Contribution à l'article**

Cet article résulte d'une collaboration avec l'équipe de Chiara Stringari (Laboratory for Optics & Biosciences, École Polytechnique). Son équipe ayant développé une méthode de mesure du métabolisme dans des cellules vivantes uniques en temps réel par 2P-FLIM, nous y avons perçu une opportunité de mesurer à la fois le métabolisme des lymphocytes T lors de leur activation en temps réel, mais également d'y ajouter l'information du remodelage du cytosquelette.

Pour ce faire, j'ai transduit la lignée Jurkat avec un vecteur lentiviral codant pour le LifeAct-mCherry. En utilisant le protocole d'activation des lymphocytes T sur des lames que j'avais mis au point précédemment pour l'imagerie en temps réel, nous avons adapté, ensemble avec la post-doctorante Lien Ung dans leur laboratoire à Polytechnique, la mesure du métabolisme et du remodelage d'actine simultanément.

Concernant le travail expérimental, nous avons effectué toutes les expériences ensemble, dans leur laboratoire avec Lien.

Concernant l'analyse des figures de l'article, j'ai écrit le programme d'analyse d'images pour mesurer l'aire des cellules, et effectué toutes les analyses des aires et de corrélation entre les aires et le métabolisme.

Quant à l'écriture du manuscrit, nous avons monté les figures et écrit les légendes ensemble avec Lien, puis j'ai apporté des modifications et corrections au manuscrit.

J'ai donc pris part à ce projet de son élaboration, à son exécution expérimentale, l'analyse des résultats, jusqu'à l'écriture de l'article.

# Label-free single-cell live imaging reveals fast metabolic switch in T lymphocytes

Noémie Paillon[1, 2*], Thi Phuong Lien Ung[3, *], Stéphanie Dogniaux[1], Chiara Stringari[3, #] & Claire Hivroz[1, #]

[1]Institut Curie, PSL Research University, INSERM, U932 "Integrative analysis of T cell activation" team, Paris, France

[2]Université Paris Cité, Paris, France

[3] Laboratory for Optics and Biosciences, Ecole Polytechnique, CNRS, INSERM, IP Paris, 91128 Palaiseau Cedex, France

*: contributed equally to the work, in alphabetical order.
#: co-corresponding authors. chiara.stringari@polytechnique.edu, claire.hivroz@curie.fr

Funding information: This work was supported by funds from Institut Curie, INSERM, ANR (ANR-10-IDEX-0001-02 PSL* and ANR-11-LABX-0043; RetroTact ANR-20CE15-0009-01; ANR-10-INBS-04 France BioImaging and ANR-11-EQPX-0029 Morphoscope2), the Fondation pour la Recherche Médicale (FRM, FRM DEQ20140329513) and the Fondation ARC pour la recherche sur le cancer and Human Frontier Science Program (HFSP RGY0078/2017 ChroMet) Noémie Paillon received a PhD fellowship from ITMO Cancer in partnership with INSERM and from Ecole Doctorale Frontières de l'Innovation en Recherche et Education – Programme Bettencourt.

Acknowledgements: We would like to thank Xavier Lahaye for providing us with peripheral blood mononuclear cells and the members of the "Integrative analysis of T cell activation" (Institut Curie) for support and discussions. We thank all the members of the "advances microscopies" group at the Laboratory for Optics and Biosciences for helpful discussions and advice. We thank Pierre Mahou and Emmanuel Beaurepaire for scientific discussions and technical help.

Author contributions: NP performed the experiments, analyzed the data and contributed to the writing. TPLU performed the experiments and analyzed the data. SD developed the lentiviral vector encoding LifeAct-mCherry. CS designed and supervised research and contributed to the writing. CH conceptualized, supervised and administrated the project, and wrote the manuscript.

DATA AVAILABILITY STATEMENT
The data that support the finding of the study are openly available in the Zenodo repository:
https://doi.org/10.5281/zenodo.7474053
https://doi.org/10.5281/zenodo.7473905

ABSTRACT

T cell activation induces a metabolic switch generating energy required for proliferation, survival, and fueling their functions. Thus, it is essential to monitor metabolism associated to subcellular functional and structural changes. We used non-invasive label-free two-photon fluorescence lifetime microscopy (2P-FLIM) to map the spatial and temporal dynamics of the metabolic NADH co-enzyme during T lymphocyte activation. 2P-FLIM measurements of the protein-bound and free NADH ratios provides a readout of the redox state ($NAD^+$/ NADH) of the cells, and thus of their OXPHOS and glycolysis rates. Using this method, we followed the dynamics of fraction of bound NADH (fb NADH) in live single cells. Comparing fb NADH between resting and activated T cells, we show that T cell activation induces a rapid switch toward glycolysis. The switch takes only 10 minutes and remains stable for at least one hour. Three-dimensional (3D) analysis revealed that the intracellular distribution of fb NADH is symmetrically distributed in resting cells, whereas increases at the contact zone in activated cells. Finally, we show that fb NADH negatively correlates with spreading of activated T cells, suggesting a link between actin remodeling and metabolic changes. This study shows that 2P-FLIM measurement of fb NADH is well suited to follow a fast metabolic switch in 3D, in single T lymphocytes with subcellular resolution.

INTRODUCTION:

T lymphocyte activation through the T cell receptor (TCR) and co-receptors such as CD28 induces a rapid transcription of numerous new messenger RNA (mRNA) transcripts and proteins. Activated T lymphocytes also undergo massive growth, doubling to quadrupling their size in 1 to 2 days as well as several cycles of divisions[1]. These different steps are demanding in energy and thus require a rewiring of T lymphocyte metabolism[2]. Indeed, T lymphocytes change their metabolism during immune response. Briefly naïve T cells that are metabolically quiescent, mainly rely on oxidative phosphorylation (OXPHOS) for their energetic needs. Effector T cells, which are very metabolically active have higher rates of both glycolysis and OXPHOS, whereas memory T cells, which are quiescent but metabolically primed rely on fatty acid oxidation and OXPHOS[2]. The field of immunometabolism has gained importance by showing that different T lymphocyte populations have different metabolic signatures, but also by unveiling that the metabolism does not only energetically supports cellular functions but also shape them[3]. These better understanding of immunometabolism of T cells paved the way to harnessing metabolism for therapeutic interventions. For examples, finding the right conditions to generate CAR T cells that are "metabolically fit"[4] or overcoming metabolic competition in the tumors microenvironment to improve anti-tumoral T cell responses[5]. There is thus an increasing need to better understand immunometabolism in T lymphocytes.

Many tools have been developed to measure cell metabolism and have been used in T lymphocytes. Among them, we can cite 13 C-based stable isotope labeling (SIL) techniques that facilitate tracing the metabolic fate of nutrients in cells[6], the Seahorse Extracellular Flux Analyzer, which simultaneously measures, in real-time, the extracellular acidification rate (ECAR; an indicator of glycolysis) and the oxygen consumption rate (OCR; an indicator of oxidative phosphorylation (OXPHOS)) from relatively low numbers of cells. Both these methods allow the metabolic analysis of cells in bulk. We can also cite the two recent elegant assays: SCENITH and SPICE-Met that rely respectively on – characterizing the energetic metabolism profile of cells by monitoring changes in protein synthesis levels in response to metabolic inhibitors[7], or on – sensing the ATP:ADP ratio in cells expressing the genetically encoded fluorescent biosensor[8]. The SCENITH assay, based on flow cytometry, monitors the metabolic profile at a single cell resolution but not in real time and has been used successfully in T cells[9]. The SPICE-Met assay is based on one or two-photon microscopy, can be used in real-time imaging on single cells, has been used successfully in T cells[10] but requires the expression of a transgene.

Most of the studies aiming at analyzing metabolism in T lymphocytes have been performed in cell populations at steady state or several hours after exposure to activation signals. Rapid changes (in the order of 30 to 60 min) in OXPHOS and aerobic glycolysis have yet been reported upon activation of T lymphocytes [11,12].

To tackle both the heterogeneity of the metabolic profiles and of their temporal dynamic, we used Two-photon Fluorescence Lifetime Microscopy (2P-FLIM) of the coenzyme NADH, as it reports on metabolic processes in a label-free and non-invasive way[13–15]. NADH is the principal electron acceptor in glycolysis in oxidative phosphorylation and its ubiquity renders NADH one of the most useful and informative intrinsic biomarkers for metabolism in live cells and tissues[16,17]. Through the readout of protein-bound and free NADH, 2P-FLIM provides sensitive measurements of the redox states ($NAD^+$/ NADH) of cells as well as OXPHOS and glycolysis rates[14,15,18–22]. 2P-FLIM has the spatio–temporal resolution required to characterize NADH subcellular compartments[23] and to measure metabolic shifts induced upon T lymphocyte activation[24] as well as metabolic polarization and heterogeneity in macrophages and microglia *in vitro*[25–27] as well as *in vivo* [28–31].

In the present study, we used 2P-FLIM of NADH to follow the dynamic of $NAD^+$/ NADH redox ratio (through the fraction of bound NADH) in Jurkat T cells (a leukemic T cell line) and primary human $CD4^+$ T lymphocytes, during activation. We activated the cells on glass slides coated with anti-CD3 + anti-CD28 antibodies, which induce polarization and spreading of T cells and mimic the immune synapse formation[32]. Our results show that T cell activation induces a rapid decrease of fraction of bound NADH, reflecting a decrease in oxidative phosphorylation/glycolysis ratio in activated T lymphocytes. This can be followed, upon time, at a single cell level and in 3D. The three-dimensional metabolic maps show that the distribution of fraction of bound NADH in the cell is changing in different cellular compartments upon immune synapse formation. Moreover, because remodeling of the actin cytoskeleton is one of the early hallmarks of T cell activation we expressed LifeAct-mCherry, a 17-amino-acid peptide, which stained filamentous actin (F-actin) structures in Jurkat T cells and followed the bound/free NADH ratio simultaneously with the spreading. This analysis showed that the fb NADH diminished in spreading cells suggesting that there might be a link between actin remodeling in T cells and metabolic changes.

Together, our data show that upon activation mimicking immune synapse formation, T lymphocytes dynamically modify their metabolism in time and space.

**MATERIALS AND METHODS**

*Cells*

Jurkat T cells (94% homology with Jurkat clone E6.1 validated by the SSTR method on the DSMZ website) were cultured at 37°C with 5% $CO_2$ in RPMI 1640 Glutamax (Gibco; 61870-010) supplemented with 10% fetal calf serum (Eurobio; CVFSVF00-01) and were passed every 2-3 days at approximatively 0.5 x $10^6$ cells/mL.

Peripheral blood mononuclear cells (PBMCs) from healthy donors were isolated using a ficoll density gradient. Buffy coats from healthy donors were obtained from Établissement Français du Sang in accordance with INSERM ethical guidelines. $CD4^+$ T cells were purified using the total $CD4^+$ negative isolation kit (Miltenyi Biotech; 130-096-533). Primary $CD4^+$ T cells were activated in six-well plates coated with anti-CD3e (OKT3; 317326; BioLegend) in presence of soluble anti-CD28 (CD28.2; 302914; BioLegend) during 6 days prior to use and cultured in RPMI 1640 Glutamax (Fisher Scientific; 61870-010) supplemented with 10% fetal calf serum (Eurobio, CVFSVF00-01), 10 000 U/mL penicillin-streptomycin (Gibco; 15140-122), 1M Hepes (Gibco, 15630-056), 50mM 2-Mercaptoethanol (Gibco; 31350-010) and 20 U/mL recombinant IL-2 (Immunotools; 11340025).

*Lentivirus production and Jurkat cell transduction*

Replication-defective lentiviral particles were obtained by transfecting HEK-293T cells with Gag, Pol, rev, encoding plasmid (pPAX2), envelop encoding plasmid (pMD2.G) and the LifeAct-mCherry construct encoded in a pWXLD vector. After 48h, lentiviruses were recovered in the supernatant and concentrated. Jurkat cells were transduced and the positive fraction was sorted by flow cytometry (SH800 Cell Sorter, Sony Biotechnology) to establish a stable LifeAct-$mCherry^+$ Jurkat cell line.

*T cell activation*

Poly-d-lysine coated 35mm glass-bottom dishes (MatTek; P35GC-1.0-14-C) were coated with 0,1µg/mL anti-CD3 (OKT3; 317326; BioLegend) and 10µg/mL anti-CD28 (CD28.2; 302914; BioLegend) at 4°C overnight and washed with PBS before use. 300 000 cells were resuspended

in RPMI 1640 without phenol red (Fisher Scientific, 10363083) supplemented with 10% fetal calf serum and plated on coated dishes prior imaging.

*Two-photon excited fluorescence lifetime imaging (FLIM).*

Imaging was performed on a laser scanning microscope (TriMScope, Lavision Biotec, Germany). A simplified scheme of the multiphoton microscope is shown in Fig. 1A. The excitation is provided by a dual-output femtosecond laser (Insight DS++, Spectra-Physics, Santa Clara, CA, USA) one with a first beam tuneable from 680 nm to 1300 nm (120 fs pulses, 80 MHz) and a second one with a fixed wavelength beam at 1040 nm (200 fs pulses). A water Immersion objective (25X, NA=1.05, XLPLN-MP, Olympus, Japan) is used to focus the laser on the sample and collect fluorescence signal. Fluorescence signal is epi-detected by a hybrid photomultiplier tube (R10467U, Hamamatsu, Japan).

To perform fluorescence lifetime microscopy of NADH, 740nm wavelength excitation was used with a typical power of 12 mW. A blue band-pass filter was installed in front of the detector to collect NADH autofluorescence (Semrock FF01–460/80). The red fluorescence of LifeAct-mCherry is simultaneously collected with a red band pass filter (Semrock FF01– 607/70). Time-correlated single photon counting (TCSPC) electronics (Lavision Biotec, Germany) measures the arrival time of the fluorescence photons with respect to the laser pulse and reconstructs the fluorescence lifetime decay. The laser trigger is taken from the fixed wavelength beam using a photodiode (PDA10CF-EC, Thorlab). Lifetime calibration of the FLIM system was performed by measuring the lifetime of fluorescein at pH9 with a single exponential of 4.04 ns (Fig.1C). We typically collected 200-300 photons during an acquisition time in the order of one minute for a 256x256 pixels image at a pixel dwell time of 60.8 µs/pixel. The three-dimensional (3D) FLIM imaging was performed with a Z-step of 3 µm and the total acquisition time of a 3D FLIM is in the order of two minutes.

*T Lymphocytes imaging*

T lymphocytes were imaged on a glass-bottom dish, containing a non-fluorescent assay medium (Fisher Scientific, 10363083) placed inside an incubation chamber at 37 °C and 5% $CO_2$ (Okolab, Pozzuoli, Italy).

We performed label-free fluorescence lifetime microscopy of NADH in a total of 87 ROIs with 700 cells in 2 independent experiments for the stable cell line and in a total of 56 ROIs with 1000 cells in 1 independent experiment for the primary cells.

To measure the metabolic trajectory in cells we treated the cells with a solution of 50 µM of rotenone (R8875; Sigma-Aldrich, St. Louis, MO, USA) to block the respiratory chain via complex I and 2-deoxy-D-glucose (D8375-10MG; Sigma-Aldrich, St. Louis, MO, USA) of 10mM to inhibit glycolysis.

*Analysis of the Fluorescence Lifetime microscopy images*

Intensity data were analyzed and treated with Fiji-ImageJ (NIH, Bethesda, MD, USA). All FLIM data were processed and analyzed with a custom written software Matlab (Mathworks, Natick, MA, USA). FLIM data were transformed from time domain to frequency domain by using a FFT and plotted in the phasor plot as previously described[14,33]. As our FLIM data were acquired in the time domain (Fig. 1C) we transformed the multi-exponential fluorescence intensity decay in every pixel of the image into a point in the 2D phasor plot of coordinates *g* and *s* (Fig.1E) with the following equations:

$$g_{i,j}(\omega)=\frac{\int_0^\infty I_{i,j}(t)*cos(\omega t)dt}{\int_0^\infty I_{i,j}(t)dt} \quad (1)$$

$$s_{i,j}(\omega)=\frac{\int_0^\infty I_{i,j}(t)*sin(\omega t)dt}{\int_0^\infty I_{i,j}(t)dt} \quad (2)$$

where i and j indicate the order pixel of the image and ω is the frequency. ω is calculated through the laser repetition rate $\omega=2\pi f$ ($f$=80 MHz). We calibrated our FLIM system by using a solution of fluorescein at pH 9 that has a single lifetime of 4.04 ns and we measured the lifetime of free NADH in solution of 0.4ns. The fraction of bound NADH is graphically calculated as the distance between the experimental point $(g_{exp}, s_{exp})$ and the location of free NADH $(g_{fNADH}, s_{fNADH})$ (Fig. 1E) using the following equation:

$$fB\_NADH = \sqrt{\left(g_{exp} - g_{fNADH}\right)^2 + \left(s_{exp} - s_{fNADH}\right)^2} \quad (3)$$

We performed 3D-FLIM single cell analysis using the red channel LifeAct-mCherry for the stable cell line and on the NADH intensity channel for the primary T cells (Fig. S1A). We first performed a Z projection of all the Z planes of the 3D stack (Fig. S1A). Using the LifeAct-mCherry channel, binary masks were created to identify and segment each single cell (Fig. S1B) using Fiji-ImageJ (NIH, Bethesda, MD, USA). Based on a Matlab custom written code, we applied the masks of single cells to the 3D fb NADH maps (Fig. S1C) to create 3D metabolic

maps of single cells (Fig. S1D). We then calculated the average fb NADH for every Z plane of the cell and in the entire volume of the cell.

RESULTS

**Two-photon fluorescence lifetime imaging (FLIM) of the metabolic coenzyme NADH in T lymphocytes.**

In this study, we implemented label-free two-photon fluorescence lifetime microscopy (2P-FLIM)[14,15] in living T lymphocytes to create non-invasive metabolic maps of the metabolic coenzyme NADH at a submicron resolution and measured the spatial and temporal dynamics of redox metabolism during T lymphocyte activation.

The principle of 2P-FLIM NADH is described in Fig. 1. To obtain excitation of NADH and LifeAct-mCherry simultaneously, we excited the T lymphocytes in culture with an excitation wavelength of 760nm, while the emitted fluorescence was collected in the blue and red spectral ranges respectively (Fig. 1A, 1B and Material and Methods). Representative 2P NADH two-photon (2P) intensity images of live T lymphocytes and simultaneously acquired 2P LifeAct-mCherry intensity images are shown in Fig. 1C and Fig. 1D. We performed FLIM of NADH in T lymphocytes using a commercial time-correlated single photon counting (TCSPC) system and we established experimental conditions that allow non-invasive longitudinal metabolic imaging of the same cells without any photodamage (Fig. 1C and Materials and Methods). The fluorescence lifetime of NADH changes upon binding to enzymes within the electron transport chain. Indeed, the protein-bound NADH lifetime is significantly longer than the free NADH lifetime, due to self-quenching in the free state[13]. Thus, fluorescence lifetime imaging (FLIM) is used to provide sensitive measurements of the free and protein-bound NADH ratio to estimate the contribution of glycolysis versus OXPHOS in ATP production[15–17].

The NADH FLIM images were analyzed through phasor analysis[14,34](Fig. 1E). To quantify the subcellular metabolism, we calculated the fraction of bound NADH (fb NADH) in every pixel of the image (Fig. 1E and Material and Methods) with respect to free NADH, which is proportional to the redox ratio NAD+/NADH[19] (see Material and Methods). The fb NADH map (Fig. 1F) highlights the metabolic heterogeneity among cells and the subcellular NADH compartmentalization. This experimental setup was applied to establish the cellular metabolic trajectory of human T lymphocytes in resting and activating conditions.

**FLIM imaging of the metabolic coenzymes NADH in resting and activated Jurkat T cells upon time.**

The aim of the study was to measure the temporal dynamics of fluorescence lifetime of NADH in T cells after activation, to determine the glycolytic capacity of T cells in real time. To do so, we used a model that has been developed to mimic activation of T cells at the immune synapse. Jurkat T cells, transduced with a lentiviral vector encoding LifeAct-mCherry to follow F-actin remodeling, were dropped on glass surfaces coated with either poly-L-Lysine (PLL) alone, or with PLL and anti-CD3 + anti-CD28 activating antibodies (Fig.1G). This activation is known to induce early signaling and is accompanied by spreading of T cells on the surface. Measurements were performed on Jurkat cells in 3D (Fig. S1 and Material and Methods) at 10, 30 and 60 minutes after plating the cells on PLL or activating antibodies (Fig. 1G). In the control, non-activated Jurkat cells plated on PLL, the distribution of the NADH two-photon fluorescence intensity presented a dim central area, corresponding to nuclei and a brighter cortical area reflecting the presence of mitochondria in the cytosol (Fig. 2A, upper raw). In fact, mitochondria have significantly higher NADH/NAD+ ratio (1:5 to 1:10) with respect to the nucleus and cytoplasm (1:400 to 1:700)[18,19] and NADH is fluorescent while NAD+ is not. In the presence of anti-CD3+CD28 antibodies, the 2P fluorescence intensity of NADH revealed a more even distribution close to the activating slide, reflecting changes in the morphology of activated T cells with a possible accumulation of mitochondria at the contact zone (surrogate immune synapse).

The fb NADH maps were calculated in every Z plane of the cell (Fig. S1C) and the metabolic signature of the entire cell was evaluated by averaging the fb NADH in 3D (Material and Method). Whereas the fb NADH did not change over time in Jurkat cells plated on PLL (Fig. 2B, upper panel), there was a general decrease of the fb NADH (shifted toward the blue Fig.2B and phasor plots representation Fig. 2C) in cells plated on activating antibodies (Fig. 2B, lower panel). These results were confirmed in primary pre-activated human helper T cells (Fig. S3).

Altogether these data suggest that anti-CD3+CD28 activation of Jurkat T cells and primary human $CD4^+$ T cells induces a rapid shift (from 10 minutes) along the metabolic trajectory from OXPHOS to glycolysis. To confirm that the metabolism induced in the different conditions is reflected by the fb NADH in T cells, we treated the cells with rotenone, which is a drug inhibiting the complex I of the mitochondrial electron transport chain, thus blocking OXPHOS (Fig. S2A). As shown in Fig. S2B-D, rotenone treatment in resting Jurkat T cells significantly decreased the fb NADH, reflecting a shift from OXPHOS to glycolysis in the treated T cells.

Conversely, treatment of activated Jurkat T cells with 2-deoxy-d-glucose (2-DG), which interferes with d-glucose metabolism induced a strong increase in fb NADH (Fig. S2B, S2C, S2E) reflecting the inhibition of glycolysis. This was true both in Jurkat (Fig. S2) and primary human $CD4^+$ T cells (Fig. S3E).

Altogether, these data show that FLIM analysis of the fb NADH in T cells can reveal dynamic variation of T cell metabolism upon activation.

**Monitoring fraction of bound NADH in single Jurkat cells over time reveals a rapid switch toward glycolysis upon activation**

Analysis described in the previous paragraph showed a heterogeneity among Jurkat T cells in the NADH fluorescence lifetimes (Fig. 2) both at resting state and in activating conditions. We thus performed analysis both at the pixel level and single cell level by considering the metabolic signature of the entire cell in 3D and averaging the fb NADH inside the mask defined by the LifeAct-mCherry fluorescence (Fig. S1B). The fb NADH of single cells in each Z was determined (Fig. S1C) by averaging the fb NADH over the segmented region of interest of the single cells in each Z plane. The mean value of fb NADH for the entire cell in 3D was calculated by averaging the fb values over all the Z planes. As shown in Fig. 3A and 3B we could follow the NADH intensity and fb NADH in each single cell longitudinally. Examples of 3 cells in the same field of view in resting (1 to 3) and activating (4 to 6) conditions are represented (Fig. 3C), which show that there was no significant change of the fb NADH in cells plated on PLL whereas there was a progressive decrease of the fb NADH in single cells activated on anti-CD3+CD28 coated surfaces. Analysis of ~700 cells confirmed that the fb NADH was significantly decreased in activated Jurkat T cells as compared to resting cells at all time points (10, 30 and 60 minutes) (Fig. 3D). It also showed that the fb NADH was significantly decreasing over time in activated T cells. This result was also confirmed in human primary $CD4^+$ cells, which showed no significant changes of the fb NADH under resting conditions but a decrease under activating conditions at all time points (Fig. S3C).

Altogether, these results suggest that T cell activation induces a rapid switch along the metabolic trajectory from OXPHOS to glycolysis, in the order of minutes that remains stable at least an hour.

**Three-dimension (3D) analysis of the fraction bound NADH in Jurkat T cells**

As described previously (Fig. S1), the analysis of the fb NADH was performed both in time and space, i.e. at different Z planes of single T cells. We studied the 3D distribution of the intracellular fb NADH in resting and activated conditions at the 3 chosen time points. As shown in representative images (Fig. 4A) and analysis of the intracellular fb NADH distribution in 700 Jurkat T cells (Fig. 4B), the fb NADH distribution showed a characteristic distribution in both quiescent and activated T cells. In both cases, the two highest values of fb NADH were found at the bottom plane (the contact zone with the slide: 0µm) and top of the cells that mainly contain mitochondria, while the central zone, where the nucleus is predominant, presents the lowest values of fb NADH (Fig. 4B). Moreover, for most Z planes, the fb NADH in activated T cells was lower than the fb NADH in resting cells (Fig. 4B), confirming the results obtained by averaging the fb values of all Z planes (Fig. 3) and suggesting no specific cellular compartmentalization of the activity. The difference between fb NADH in resting and activated T cells was accentuated over time (Fig. 4B) in every location of the cell, showing that the shift toward a glycolytic activity that starts few minutes after CD3/CD28 activation is steady. The distribution of fb NADH in the activated cells (Fig. 4C) shows asymmetry between the cell side in contact with the slide (the surrogate immune synapse) and its opposite, with a fb NADH that is higher in the contact zone than in the top of the cells. This asymmetry suggests that there is relatively more OXPHOS at the synaptic side than in the rest of the cell, whereas in resting cells the distribution of fb NADH is symmetric (Fig. 4C). This might be due to the polarized distribution of mitochondria at the immune synapse[35–37].

Altogether, these data show that 2P-FLIM of NADH in T cells can reveal temporal and spatial dynamic changes in their metabolism at a single cell level and in subcellular compartments.

**Following T cell spreading at the immune synapse together with the fraction bound NADH:**

To better follow the shape of the T cells during activation and define the cell binary "mask" described in Fig. S1B, we transduced Jurkat T cells with LifeAct-mCherry that labels filamentous actin. Within minutes of contact with an activating surface, the actin networks are dynamically and drastically remodeled[7] forming a bright F-actin ring at the cell periphery (Fig. 5A).

We thus simultaneously measured in 3D the spreading of T lymphocytes on the control (PLL) or activating surface (anti-CD3+anti-CD28) and of the fb NADH. As shown in representative images in Fig. 5A and quantification in Fig. 5B, activation of Jurkat T cells induced a spreading

of T cells on the activating surface at 10 minutes. At later time points, cells retracted as previously described[38].To investigate the relationships that may exist between actin remodeling at the immune synapse and changes in T cell metabolism, we plotted fb NADH as a function of cell area for all the cells (control and activated conditions) at the 3 time points. As shown in Fig. 5C, our data show that there is a negative correlation between cell spreading and fb NADH, which suggests that cells that remodel their actin cytoskeleton the most actively are more glycolytic. This is more striking at 10 min, when cells are spreading the most. We reproduced these results in human primary $CD4^+$ T cells (Fig. S3D) measuring the area of the cells using the NADH intensity since the cells did not express LifeAct-mCherry.

Altogether, these results show that two-photon fluorescence lifetime imaging (FLIM) of NADH in T cells can reveal dynamic changes in their metabolism at a single cell level and can be combined with the analysis of other parameters, such as actin remodeling, that can be followed by fluorescence imaging.

## DISCUSSION

Metabolic responses in T cells are highly dynamic and heterogeneous both temporally and spatially, which make them difficult to analyze. Therefore, quantitative, high-resolution, label-free methods to noninvasively examine metabolic processes in cells are particularly needed to better characterize and elucidate the role of different metabolic pathways in normal and pathophysiological conditions. Two-photon excited fluorescence is well appropriated for sensitive, quantitative, label-free, high-resolution assessments of metabolic activity *in vitro* and *in vivo*[17,39,40]. Several endogenous molecules, including NADH are autofluorescent. The fluorescence lifetime of NADH varies whether it is free or bound, thus can be used as a metabolic indicator[18]. NADH in the mitochondria is known to be primarily protein bound, resulting in a fraction bound NADH that has a longer lifetime than the free NADH in the cytosol and nucleus [41,42]. Thus, changes in the lifetime of NADH has been attributed to alterations in the relative levels of oxidative phosphorylation and glycolysis [14,19,43]. In this study, we implemented Two-Photon excitation of NADH and FLIM to map the temporal and spatial metabolic patterns in isolated human T cells, i.e., the widely used Jurkat cell line [44] and human primary $CD4^+$ T cells to follow the metabolic changes upon activation. Using metabolic inhibitors (Fig. S2 and S3), we determined the specificity of the fb NADH measurement to defined metabolic pathways: rotenone which induces a shift from OXPHOS to glycolysis by blocking the respiratory chain increased fb NADH in quiescent cells. Besides, 2-deoxy-d-

glucose (2-DG), which interferes with glucose metabolism induced a decrease in fb NADH in activated T cells that revealed the shift toward more OXPHOS. Our results show that T lymphocyte activation by the TCR/CD3 and the CD28 molecules rapidly (in 10 minutes) induces a decrease in fb NADH, witnessing a metabolic shift toward more glycolysis. The measurement of fb NADH in live cells enables an early observation of the metabolic switch upon T cell activation while most of the studies analyze metabolic changes after 24h to 48h of activation. The metabolic shift toward glycolysis reported in these cells can thus be due to transcription of genes encoding enzymes controlling glycolysis. Indeed, we have shown that human T lymphocytes activated by anti-CD3 and anti-CD28 activating antibodies increase transcription of genes encoding: Phosphofructokinase, Glyceraldehyde-3-Phosphate Dehydrogenase, Phosphoglycerate Kinase 1, phosphoglucomutase, Enolase and Pyruvate kinase [45], which are all enzymes controlling glycolysis. In the present study, the rapidity of the metabolic shift toward glycolysis strongly suggests that the process is transcription independent. Our results, which show a negative correlation between cell spreading and fb NADH, suggest a causal effect between actin remodeling and glycolytic activity of T cells. Indeed, direct interactions between glycolytic enzymes and filamentous actin have been reported and actin remodeling shown to regulate these enzymatic activities (reviewed in [46]). Such a regulation is exemplified by a study reporting that insulin induces the release of enolase A from F-actin via a PI3K and Rac dependent actin remodeling. Free aldolase then leads to an increase in total aldolase activity, driving glycolytic flux in insulin activated cells[47]. Interestingly, TCR/CD3 and CD28 activation also induce Rac and PI3K activation in T lymphocytes [48–50]. It would thus be interesting to explore if the rapid cytoskeleton remodeling observed in activated T cells also controls the availability of glycolytic enzymes in these cells. Alternatively, there might be no causal effect: spreading of T cells and increase in F-actin would reflect T cell activation: the more activated the cell, the more glycolytic it is.

This method was already used to show that the autofluorescence decay of NADH is sensitive to T cell subtypes and activation state[12]. Heterogeneity of NADH lifetime was reported in T lymphocytes in a given donor and among donors, it was also different between $CD3^+CD4^+$ and $CD3^+CD8^+$ activated T cells [12]. Moreover, the fraction of free NADH was lower in quiescent T cells from the blood of healthy donors than in T cells activated for 24 to 72h with tetrameric antibodies (anti-CD2/CD3/CD28) [12] and the authors of the study reported that the lifetime of NADH was consistently the most important biomarker for differentiating quiescent and activated T cells [12]. Our results showing heterogeneity in the fb NADH both in Jurkat cells,

which are known to present clonal heterogeneity [51] and in primary activated $CD4^+$ T cells are in accordance with this published study. The decreased fb NADH we observed in activated T cells is also consistent with this published study although the timing was different. One important difference is that we only measured the lifetime of NADH focusing on the OXPHOS and glycolysis pathways, whereas in the cited study [12], the Walsh at al. measured multiple metabolic intrinsic biomarkers (lifetime of NADH, lifetime of flavin adenine dinucleotide (FAD) and optical redox ratio (defined as NADH/(NADH+FAD)) that provide complementary information about different metabolic pathways and phenotypes including fatty acid synthesis and glutaminolysis [52,53]. Moreover, we concentrated on the early metabolic changes. Using fluorescence imaging of both endogeneous NADH and FAD, the authors reported an initial (at 30 minutes) decrease of the optical redox ratio in T lymphocytes that then increases over time (from 2h to 24h) [12]. It is thus difficult to directly compare the results we report herein with the results of Walsh et al due to different T cell activation, imaging timing and biomarker measurements. Yet, it would be of high interest to characterize and compare the spatial dynamics of metabolism switch in T cells induced, at early time points, by different activators (coated, soluble crosslinked antibodies, tetramers), using multiparametric metabolic imaging with Two-photon Fluorescence Lifetime Microscopy (2P-FLIM) of the coenzymes NADH and FAD simultaneously [22]. Of note, the rapid decrease in fb NADH in activated T cells that reflects an increase in the glycolytic activity of these T lymphocytes was reported in another model. In this case, the authors used the Seahorse Extracellular Flux Analyzer, and demonstrated, in mouse T lymphocytes, a rapid (within minutes) increase of glycolysis upon activation with crosslinked anti-CD3 and anti-CD28 antibodies[11]. This rapid aerobic glycolysis was transcription independent and due to activation of pyruvate dehydrogenase kinase 1 (PDHK1).

One other interest of the method and work we present is that it allows a spatial visualization of the metabolism inside single cells. In our study, we show that there is a gradient of fb NADH in T lymphocytes. In non-activated T lymphocytes, the fb NADH is evenly distributed in the cytoplasm while the central zone, representing mostly the nucleus, displays the lowest values (Fig. 4B). This can be explained by the absence of mitochondria in the nuclei. One interesting aspect of our results is the difference in the distribution of fb NADH in the activated cells, which shows asymmetry between the cell side in contact with the slide and its opposite. The fb NADH is higher at the contact zone than at the top of the cells, whereas in resting cells the distribution of fb NADH is symmetric at the two poles of the cells. This probably reflects the polarization of T lymphocytes toward the activating side, also called immune synapse, which

induces rapid polarized transport of mitochondria at the immune synapse [35,54]. This asymmetrical distribution of fb NADH is more pronounced at early time points (10 and 30 minutes) than at later time point (1h). This might reflect the fact that mitochondria first accumulate in the immediate vicinity (<200nm) of the immune synapse and then follow a retrograde movement toward the distal end of the T cell [37]. It would be interesting to study if the polarity of T cells affects their metabolism. To do so, we could compare the lifetime of NADH induced by coated antibodies (as herein), which mimics the contact with an antigen presenting cell and induce polarization and morphological changes of the T cells, with data obtained in non-polarizing conditions (soluble antibodies).

T lymphocytes are poised to rapidly respond to diverse stimuli, in different nutrient contexts, and different physiological and pathological conditions. This ability to rapidly adapt to many situations must be accompanied by rapid changes in their cellular metabolism to fulfill their need of energy. It is thus important to develop and implement methods, which can document the metabolism changes in these immune populations. We expect that the use of Two-photon Fluorescence Lifetime Microscopy (2P-FLIM) of the coenzyme NADH will provide valuable information on diverse T cell populations from non-pathological and pathological samples and in response to diverse stimulations.

REFERENCES


1. Marchingo, J. M. & Cantrell, D. A. Protein synthesis, degradation, and energy metabolism in T cell immunity. *Cell Mol Immunol* **19**, 303 (2022).
2. Geltink, R. I. K., Kyle, R. L. & Pearce, E. L. Unraveling the Complex Interplay Between T Cell Metabolism and Function. *Annu Rev Immunol* **36**, 461 (2018).
3. Buck, M. D., Sowell, R. T., Kaech, S. M. & Pearce, E. L. Metabolic Instruction of Immunity. *Cell* **169**, 570–586 (2017).
4. Irving, M., de Silly, R. V., Scholten, K., Dilek, N. & Coukos, G. Engineering chimeric antigen receptor T-cells for racing in solid tumors: Don't forget the fuel. *Front Immunol* **8**, 267 (2017).
5. Corrado, M. & Pearce, E. L. Targeting memory T cell metabolism to improve immunity. *J Clin Invest* **132**, (2022).

6. Jang, C., Chen, L. & Rabinowitz, J. D. Metabolomics and Isotope Tracing. *Cell* **173**, 822–837 (2018).
7. Argüello, R. J. *et al.* SCENITH: A Flow Cytometry-Based Method to Functionally Profile Energy Metabolism with Single-Cell Resolution. *Cell Metab* **32**, 1063-1075.e7 (2020).
8. Tantama, M., Martínez-François, J. R., Mongeon, R. & Yellen, G. Imaging energy status in live cells with a fluorescent biosensor of the intracellular ATP-to-ADP ratio. *Nat Commun* **4**, 2550 (2013).
9. Lopes, N. *et al.* Distinct metabolic programs established in the thymus control effector functions of γδ T cell subsets in tumor microenvironments. *Nat Immunol* **22**, 179–192 (2021).
10. Russo, E. *et al.* SPICE-Met: profiling and imaging energy metabolism at the single-cell level using a fluorescent reporter mouse. *EMBO J* **41**, e111528 (2022).
11. Menk, A. v. *et al.* Early TCR Signaling Induces Rapid Aerobic Glycolysis Enabling Distinct Acute T Cell Effector Functions. *Cell Rep* **22**, 1509–1521 (2018).
12. Walsh, A. J. *et al.* Classification of T-cell activation via autofluorescence lifetime imaging. *Nature Biomedical Engineering 2020 5:1* **5**, 77–88 (2020).
13. Datta, R., Heaster, T. M., Sharick, J. T., Gillette, A. A. & Skala, M. C. Fluorescence lifetime imaging microscopy: fundamentals and advances in instrumentation, analysis, and applications. *J Biomed Opt* **25**, 1 (2020).
14. Stringari, C. *et al.* Phasor approach to fluorescence lifetime microscopy distinguishes different metabolic states of germ cells in a live tissue. *Proc Natl Acad Sci U S A* **108**, 13582–13587 (2011).
15. Skala, M. C. *et al.* In vivo multiphoton microscopy of NADH and FAD redox states, fluorescence lifetimes, and cellular morphology in precancerous epithelia. *Proc Natl Acad Sci U S A* **104**, 19494–19499 (2007).
16. Heikal, A. A. Intracellular coenzymes as natural biomarkers for metabolic activities and mitochondrial anomalies. *http://dx.doi.org.proxy.insermbiblio.inist.fr/10.2217/bmm.10.1* **4**, 241–263 (2010).
17. Zipfel, W. R. *et al.* Live tissue intrinsic emission microscopy using multiphoton-excited native fluorescence and second harmonic generation. *Proc Natl Acad Sci U S A* **100**, 7075–7080 (2003).
18. Lakowicz, J. R., Szmacinski, H., Nowaczyk, K. & Johnson, M. L. Fluorescence lifetime imaging of free and protein-bound NADH. *Proceedings of the National Academy of Sciences* **89**, 1271–1275 (1992).
19. Bird, D. K. *et al.* Metabolic Mapping of MCF10A Human Breast Cells via Multiphoton Fluorescence Lifetime Imaging of the Coenzyme NADH. *Cancer Res* **65**, 8766–8773 (2005).
20. Vishwasrao, H. D., Heikal, A. A., Kasischke, K. A. & Webb, W. W. Conformational Dependence of Intracellular NADH on Metabolic State Revealed by Associated Fluorescence Anisotropy,. *Journal of Biological Chemistry* **280**, 25119–25126 (2005).
21. Stringari, C., Nourse, J. L., Flanagan, L. A. & Gratton, E. Phasor Fluorescence Lifetime Microscopy of Free and Protein-Bound NADH Reveals Neural Stem Cell Differentiation Potential. *PLoS One* **7**, e48014 (2012).
22. Ung, T. P. L. *et al.* Simultaneous NAD(P)H and FAD fluorescence lifetime microscopy of long UVA–induced metabolic stress in reconstructed human skin. *Sci Rep* **11**, (2021).
23. Sánchez-Ramírez, E. *et al.* Coordinated metabolic transitions and gene expression by NAD+ during adipogenesis. *J Cell Biol* **221**, (2022).

24. Walsh, A. J. *et al.* Classification of T-cell activation via autofluorescence lifetime imaging. *Nat Biomed Eng* **5**, 77 (2021).
25. Alfonso-García, A. *et al.* Label-free identification of macrophage phenotype by fluorescence lifetime imaging microscopy. *https://doi.org/10.1117/1.JBO.21.4.046005* **21**, 046005 (2016).
26. Abdul, M. *et al.* Microglia activation visualization via fluorescence lifetime imaging microscopy of intrinsically fluorescent metabolic cofactors. *https://doi.org/10.1117/1.NPh.7.3.035003* **7**, 035003 (2020).
27. Smokelin, I. S., Mizzoni, C., Erndt-Marino, J., Kaplan, D. L. & Georgakoudi, I. Optical changes in THP-1 macrophage metabolism in response to pro- and anti-inflammatory stimuli reported by label-free two-photon imaging. *https://doi.org/10.1117/1.JBO.25.1.014512* **25**, 014512 (2020).
28. Bernier, L. P. *et al.* Microglial metabolic flexibility supports immune surveillance of the brain parenchyma. *Nature Communications 2020 11:1* **11**, 1–17 (2020).
29. Heaster, T. M., Humayun, M., Yu, J., Beebe, D. J. & Skala, M. C. Autofluorescence imaging of 3D tumor-macrophage microscale cultures resolves spatial and temporal dynamics of macrophage metabolism. *Cancer Res* **80**, 5408–5423 (2020).
30. Heaster, T. M., Heaton, A. R., Sondel, P. M. & Skala, M. C. Intravital Metabolic Autofluorescence Imaging Captures Macrophage Heterogeneity Across Normal and Cancerous Tissue. *Front Bioeng Biotechnol* **9**, 312 (2021).
31. Miskolci, V. *et al.* In vivo fluorescence lifetime imaging of macrophage intracellular metabolism during wound responses in zebrafish. *Elife* **11**, (2022).
32. Bunnell, S. C., Kapoor, V., Trible, R. P., Zhang, W. & Samelson, L. E. Dynamic Actin Polymerization Drives T Cell Receptor–Induced Spreading: A Role for the Signal Transduction Adaptor LAT. *Immunity* **14**, 315–329 (2001).
33. Ranjit, S., Malacrida, L., Jameson, D. M. & Gratton, E. Fit-free analysis of fluorescence lifetime imaging data using the phasor approach. *Nature Protocols 2018 13:9* **13**, 1979–2004 (2018).
34. Becker, W. Fluorescence lifetime imaging – techniques and applications. *J Microsc* **247**, 119–136 (2012).
35. Quintana, A. *et al.* T cell activation requires mitochondrial translocation to the immunological synapse. *Proc Natl Acad Sci U S A* **104**, 14418–14423 (2007).
36. Baixauli, F. *et al.* The mitochondrial fission factor dynamin-related protein 1 modulates T-cell receptor signalling at the immune synapse. *EMBO J* **30**, 1238–1250 (2011).
37. He, L. *et al.* Dynamic Mitochondrial Migratory Features Associated with Calcium Responses during T Cell Antigen Recognition. *The Journal of Immunology* **203**, 760–768 (2019).
38. Ueda, H., Morphew, M. K., McIntosh, J. R. & Davis, M. M. CD4 + T-cell synapses involve multiple distinct stages. *Proc Natl Acad Sci U S A* **108**, 17099–17104 (2011).
39. Huang, S., Heikal, A. A. & Webb, W. W. Two-Photon Fluorescence Spectroscopy and Microscopy of NAD(P)H and Flavoprotein. *Biophys J* **82**, 2811–2825 (2002).
40. Georgakoudi, I. & Quinn, K. P. Optical Imaging Using Endogenous Contrast to Assess Metabolic State. *https://doi-org.proxy.insermbiblio.inist.fr/10.1146/annurev-bioeng-071811-150108* **14**, 351–367 (2012).
41. Zheng, W., Li, D. & Qu, J. Y. Time-resolved spectroscopic imaging reveals the fundamentals of cellular NADH fluorescence. *Optics Letters, Vol. 33, Issue 20, pp. 2365-2367* **33**, 2365–2367 (2008).
42. Blinova, K. *et al.* Mitochondrial NADH fluorescence is enhanced by complex I binding. *Biochemistry* **47**, 9636–9645 (2008).

43. Quinn, K. P. *et al.* Quantitative metabolic imaging using endogenous fluorescence to detect stem cell differentiation. *Scientific Reports 2013 3:1* **3**, 1–10 (2013).
44. Abraham, R. T. & Weiss, A. Jurkat T cells and development of the T-cell receptor signalling paradigm. *Nature Reviews Immunology 2004 4:4* **4**, 301–308 (2004).
45. Saitakis, M. *et al.* Different TCR-induced T lymphocyte responses are potentiated by stiffness with variable sensitivityDifferent TCR-induced T lymphocyte responses are potentiated by stiffness with variable sensitivity. *Elife* **6**, 1–29 (2017).
46. DeWane, G., Salvi, A. M. & DeMali, K. A. Fueling the cytoskeleton-links between cell metabolism and actin remodeling. *J Cell Sci* **134**, (2021).
47. Hu, H. *et al.* Phosphoinositide 3-Kinase Regulates Glycolysis through Mobilization of Aldolase from the Actin Cytoskeleton. *Cell* **164**, 433–446 (2016).
48. Tuosto, L., Michel, F. & Acuto, O. p95vav associates with tyrosine-phosphorylated SLP-76 in antigen-stimulated T cells. *Journal of Experimental Medicine* **184**, 1161–1166 (1996).
49. Reif, K., Nobes, C. D., Thomas, G., Hall, A. & Cantrell, D. A. Phosphatidylinositol 3-kinase signals activate a selective subset of Rac/Rho-dependent effector pathways. *Current Biology* **6**, 1445–1455 (1996).
50. Genot, E., Cleverley, S., Henning, S. & Cantrell, D. Multiple p21ras effector pathways regulate nuclear factor of activated T cells. *EMBO J* **15**, 3923–3933 (1996).
51. Hanlon, K. *et al.* Single-cell cloning of human T-cell lines reveals clonal variation in cell death responses to chemotherapeutics. *Cancer Genet* **237**, 69–77 (2019).
52. Liu, Z. *et al.* Mapping metabolic changes by noninvasive, multiparametric, high-resolution imaging using endogenous contrast. *Sci Adv* **4**, (2018).
53. Walsh, A. J. *et al.* Optical Metabolic Imaging Identifies Glycolytic Levels, Subtypes, and Early-Treatment Response in Breast Cancer. *Cancer Res* **73**, 6164–6174 (2013).
54. Torralba, D., Martín-Cófreces, N. B. & Sanchez-Madrid, F. Mechanisms of polarized cell-cell communication of T lymphocytes. *Immunol Lett* **209**, 11–20 (2019).

FIGURES LEGENDS

**Fig. 1: Experimental setup of *two-photon excitation Fluorescence Lifetime Imaging (FLIM).*** **A.** Scheme of the experimental setup used for this work. **B.** Principles of two-photon simultaneous excitation of NADH and LifeAct-mCherry fluorophores at 760 nm. Emission fluorescence of NADH and LifeAct-mCherry collected with band-pass filters 460/80 and 607/70 respectively. **C.** Fluorescence lifetime image contains a fluorescence lifetime decay in every pixel. The NADH intensity image is determined by the sum of the FLIM stack. **D.** LifeAct-mCherry intensity image simultaneously acquired in the red channel. **E.** The multi-exponential fluorescence intensity decay in every pixel of the image is transformed in the phasor plot by Fourier transform. Calculation of the fraction of bound NADH (fb NADH) is performed by measuring the distance of every pixel from the location of free NADH. **F.** Fraction of bound NADH is proportional to the redox ratio NADH/NAD+ ratio. **G.** Schematic representation of T-cell activation.

**Fig. 2: Metabolic shift during T cell activation revealed by NADH FLIM. A.** Representative images of NADH intensity**, B.** maps of fraction of bound NADH and **C.** phasor plot scatters of T cells in control and activated condition at three time point (10 min, 30 min and 1 hour). Every single point in the phasor plot is color coded after the fraction of bound NADH.

**Fig. 3: Single cell analysis of NADH FLIM reveals metabolic shift over time during T cell activation. A.** Representative images of NADH intensity and **B.** maps of fraction of bound NADH of T cells in control and activated condition at three time points (10 min, 30 min and 1 hour). **C.** Fraction of bound NADH of three representative single cells in control and activated conditions over time (10 min, 30 min and 1 hour). **D.** Quantification of fraction of bound NADH over time of control and activated T cells (10 min, 30 min and 1 hour). Data are presented by median with interquartile range. T-test: ****P<0.0001

**Fig. 4: Three-dimensional metabolic pattern in T cells during activation revealed by NADH FLIM. A.** Representative images of NADH intensity and fraction of bound NADH of single T cell in control at 10 mins in different Z planes. **B-C.** Quantification of fraction of bound NADH in control and activated condition in every Z plane of the cell over time (10 min, 30 min and 1 hour). Data are presented by mean ±SEM. T-test: *P ≤ 0.05, **P ≤ 0.01, *** ≤ 0.001, **** ≤ 0.0001. **B.** Statistics are indicated for each Z plane between control and activated conditions. **C.** Statistics are indicated for each timepoint between Z = 3µm and Z = 12µm.

**Fig. 5: T cell surface spreading during activation. A.** Representative images of LifeAct-mCherry intensity of T cells in control and activated condition at three time points (10 min, 30 min and 1 hour). **B.** Quantification of T cell area over time (10 min, 30 min and 1 hour) of control and activated T cells. Data is presented by median with interquartile range. **C.** Correlation scatter plot between areas of LifeAct-mCherry and fraction of bound NADH of control and activated T cells over time (10 min, 30 min and 1 hour). T-test: *** P ≤ 0.001

**Fig. S1: Workflow of 3D FLIM for single cell analysis. A.** NADH FLIM and LifeAct-mCherry Z-stack image **B.** The z projection is used to create single cell masks. **C.** 3D of the fraction of bound NADH **D.** The single cell mask is applied to the 3D FLIM raw data of fraction of bound NADH (fb NADH) in order to extract the FLIM data of single cell for every Z plane.

**Fig. S2: Metabolic trajectory in Jurkat T cells. A.** Schematic representation of the metabolic pathways inside the cells: oxidative phosphorylation (OXPHOS) and glycolysis. Glucose breakdown through glycolysis and the TCA (tricarboxylic acid) cycle generates reduced NADH and $FADH_2$. Cells with a glycolytic phenotype generate ATP rapidly in the cytoplasm and are characterized by a high ratio of NADH/$NAD^+$ and a low fraction of bound NADH. Cells relying on oxidative phosphorylation convert glucose to pyruvate, which is then oxidized in the TCA cycle generating the majority of ATP in the mitochondria and are characterized by a low ratio of NADH/$NAD^+$ and a high fraction of bound NADH. **B.** Intensity images (top panel) and fraction of bound NADH maps (bottom panel) of Jurkat T cells in control condition and with rotenone as well as in activated condition and with 2-Deoxy-D-glucose (2DG). *Rotenone blocks the respiratory chain* and leads to a decrease fraction of bound NADH, while 2DG prevents glycolysis and leads to an increase of bound NADH. **C.** Representative phasor plot of Jurkat T cells in different conditions: control, control treated with rotenone, activated, activated treated with 2-Deoxy-D-glucose. **D.** Decrease of fraction of bound NADH after rotenone treatment in control. **E.** Increase of fraction of bound NADH in activated Jurkat T cells with 2-Deoxy-D-glucose. Data are presented by mean with SEM. T-test: *** P ≤ 0.001

**Fig. S3. Single cell analysis of NADH FLIM reveals metabolic shift over time during primary T cell activation. A.** Representative images of NADH intensity (top panel) and maps of fraction of bound NADH images (bottom panel) of primary T cells in control and activated condition at three time points (10 min, 30 min and 1 hour). **B.** Quantification of primary T cell area over time (10 min, 30 min and 1 hour) of control and activated T cell. Data are presented by median with interquartile range. **C.** Quantification of fraction of bound NADH over time of control and activated T cell (10 min, 30 min and 1 hour). Data are presented by median with interquartile range. **D.** Correlation scatter plot between areas of LifeAct-mCherry and fraction of bound NADH of control and activated T cells over time (10 min, 30 min and 1 hour). **E.** Decrease of fraction of bound NADH after rotenone treatment in control and increase of fraction of bound NADH in activated cells with 2-Deoxy-D-glucose. Data are presented by median with interquartile range. T-test: *P ≤ 0.05, **P ≤ 0.01, ****P≤ 0.0001. N = 1 healthy donor run in duplicates.

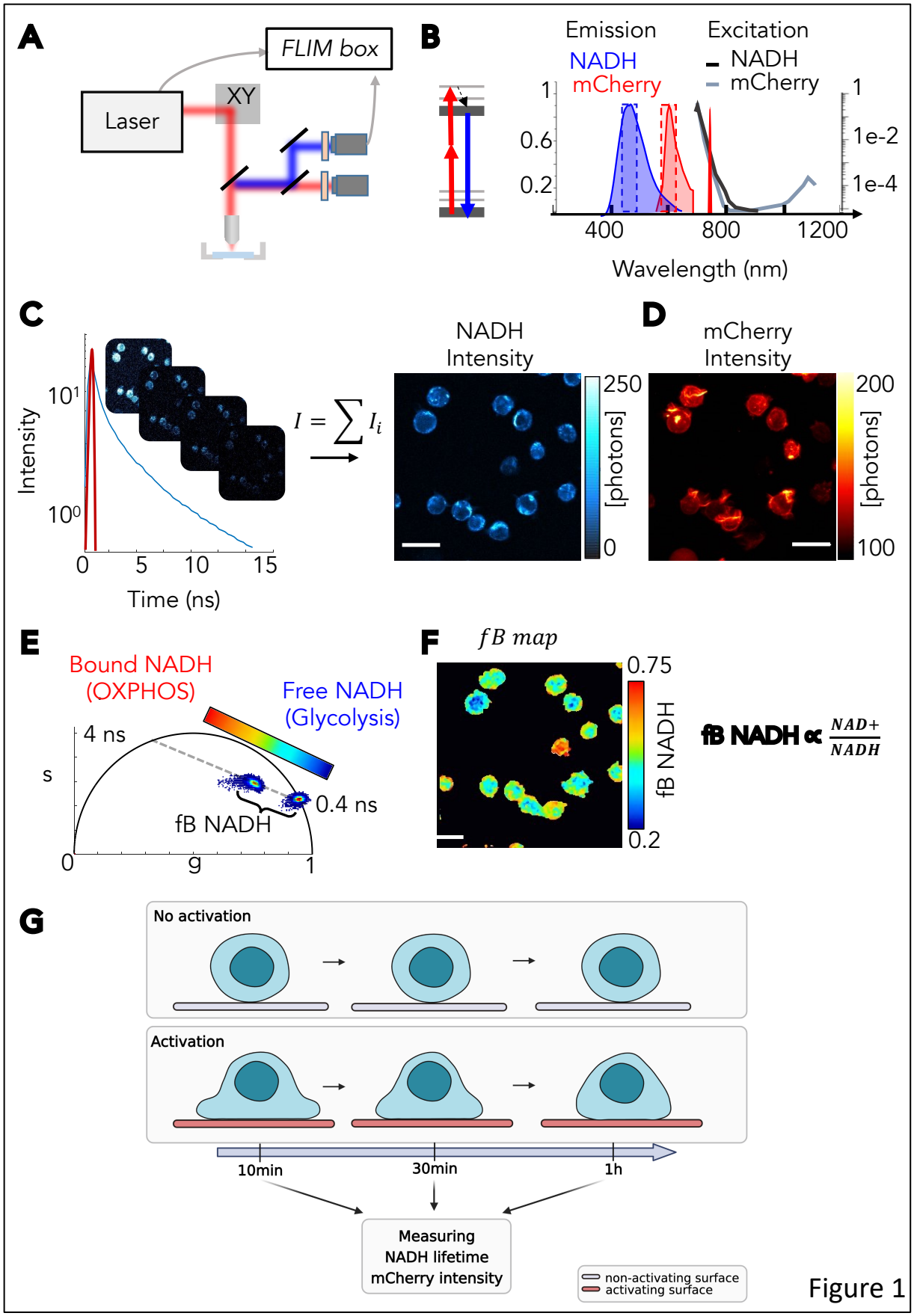
A
FLIM box
Laser
XY
B
Emission
Excitation
NADH
mCherry
NADH
mCherry
1
0.6
0.2
1
1e-2
1e-4
400
800
1200
Wavelength (nm)
C
Intensity
$10^1$
$10^0$
0
5
10
15
Time (ns)
$I = \sum I_i$
D
NADH
Intensity
250
[photons]
0
mCherry
Intensity
200
[photons]
100
E
Bound NADH
(OXPHOS)
Free NADH
(Glycolysis)
4 ns
s
0.4 ns
fB NADH
0
g
1
F
$fB\ map$
0.75
fB NADH
0.2
fB NADH ∝ NAD+/NADH
G
No activation
Activation
10min
30min
1h
Measuring
NADH lifetime
mCherry intensity
non-activating surface
activating surface

Figure 1

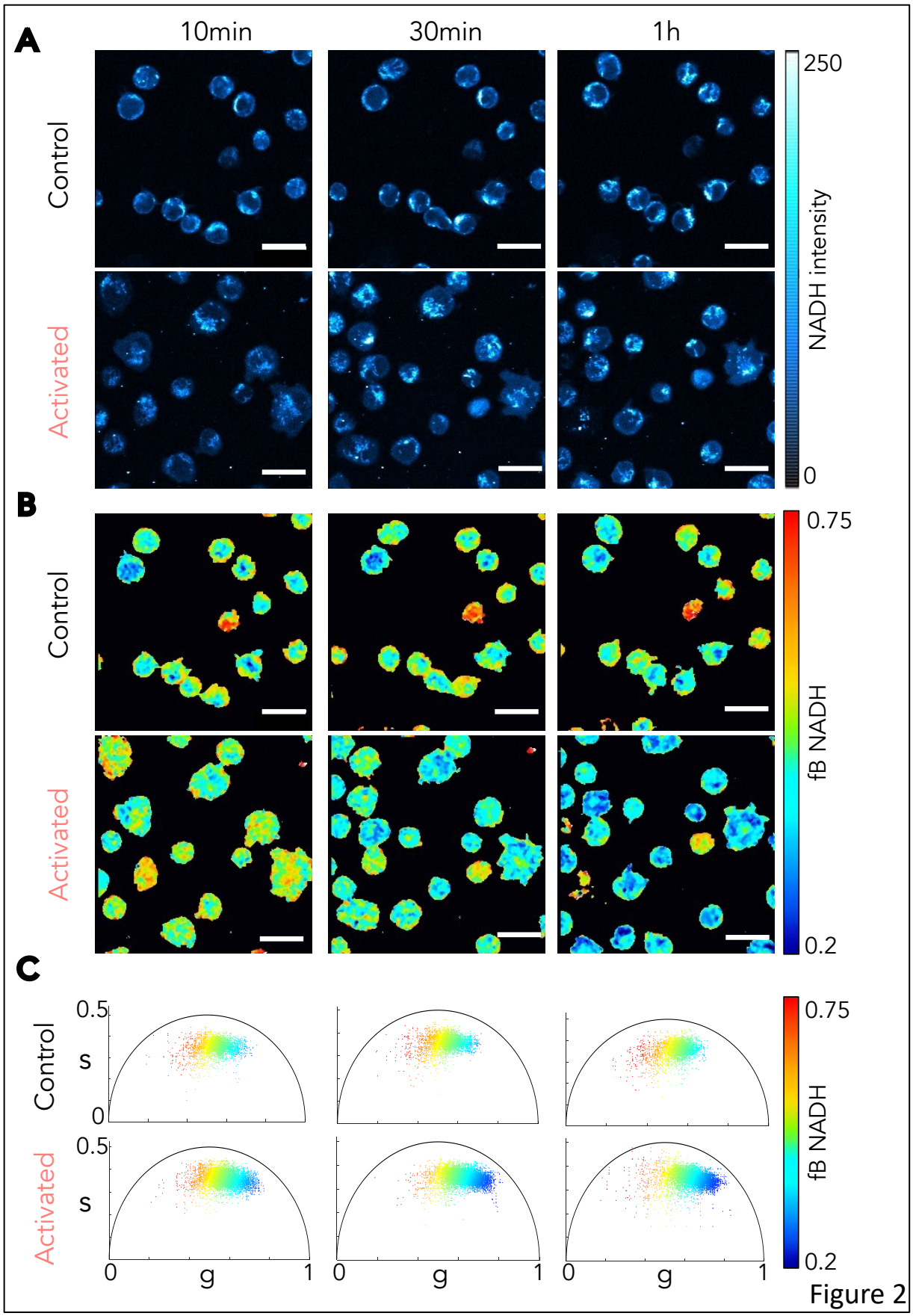
A
10min
30min
1h
Control
Activated
250
NADH intensity
0
B
Control
Activated
0.75
fB NADH
0.2
C
Control
Activated
0.5
s
0
0
g
1
0.75
fB NADH
0.2

Figure 2

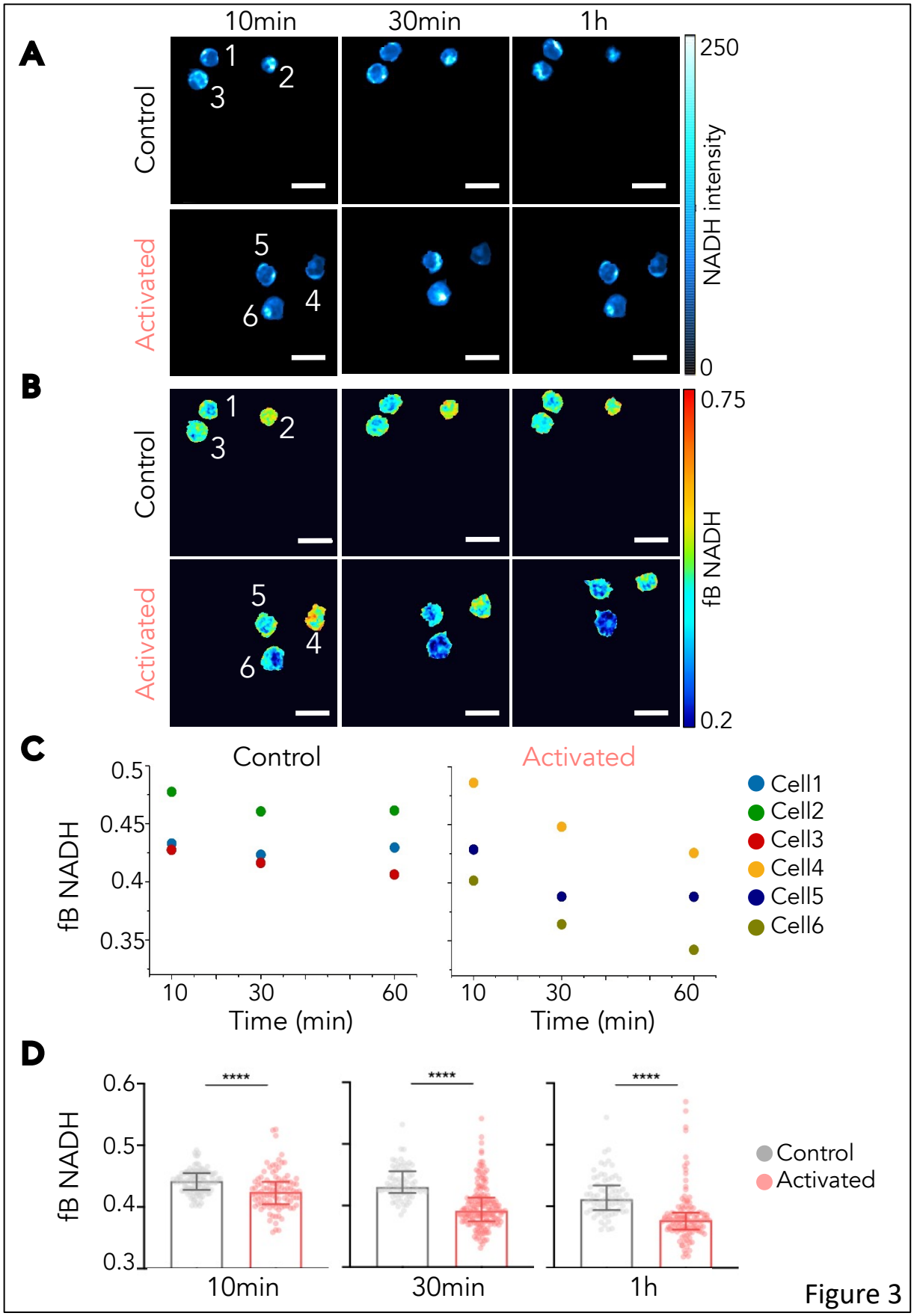
A
10min
30min
1h
Control
Activated
1
2
3
4
5
6
250
NADH intensity
0
B
0.75
fB NADH
0.2
C
Control
Activated
fB NADH
0.5
0.45
0.4
0.35
10
30
60
Time (min)
Cell1
Cell2
Cell3
Cell4
Cell5
Cell6
D
0.6
0.5
0.4
0.3
****
10min
30min
1h
Control
Activated

Figure 3

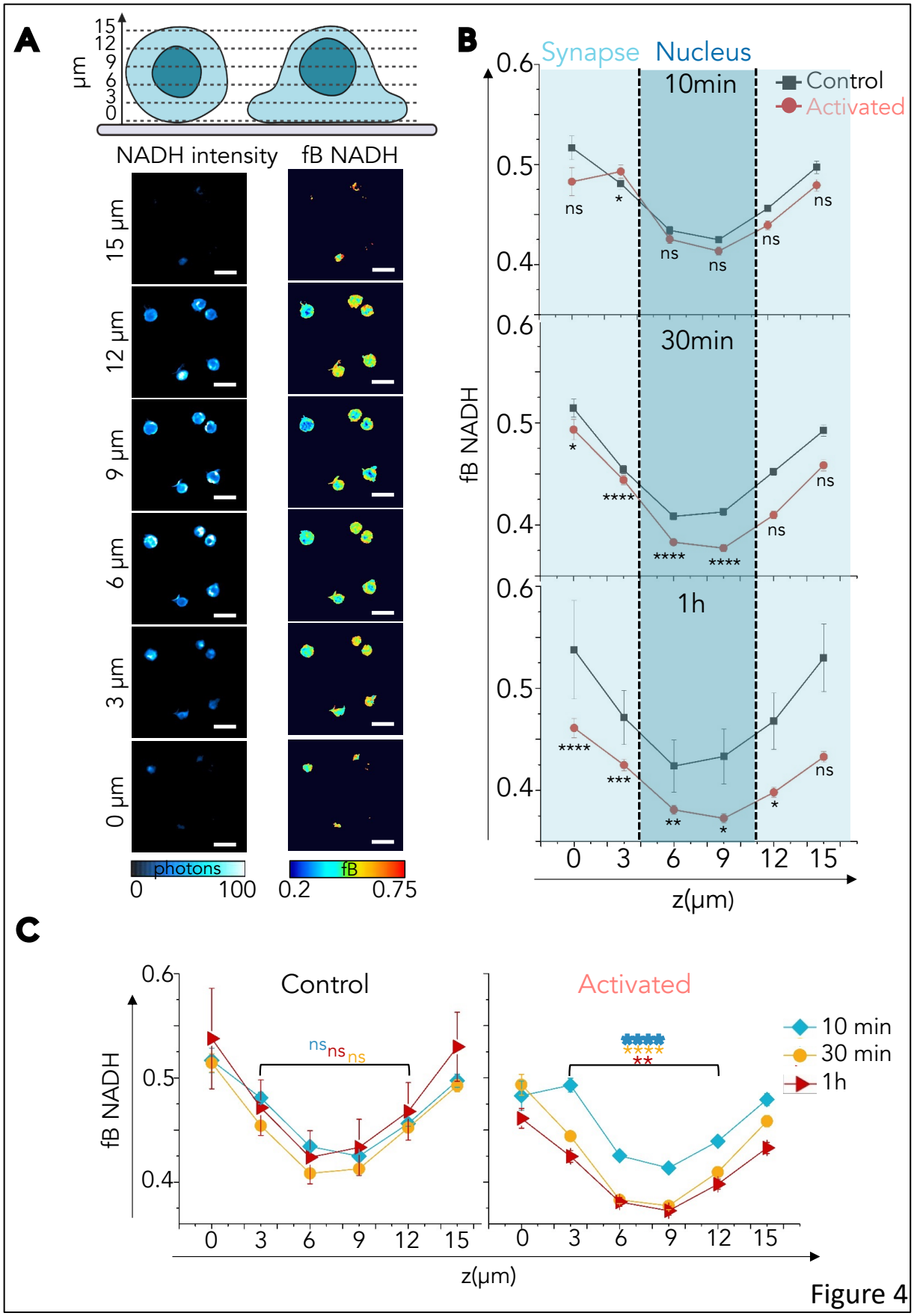
A
µm
15
12
9
6
3
0
NADH intensity
fB NADH
15 µm
12 µm
9 µm
6 µm
3 µm
0 µm
photons
0
100
fB
0.2
0.75
B
Synapse
Nucleus
10min
30min
1h
Control
Activated
fB NADH
0.6
0.5
0.4
ns
*
****
***
**
0
3
6
9
12
15
z(µm)
C
Control
Activated
fB NADH
10 min
30 min
1h
z(µm)

Figure 4

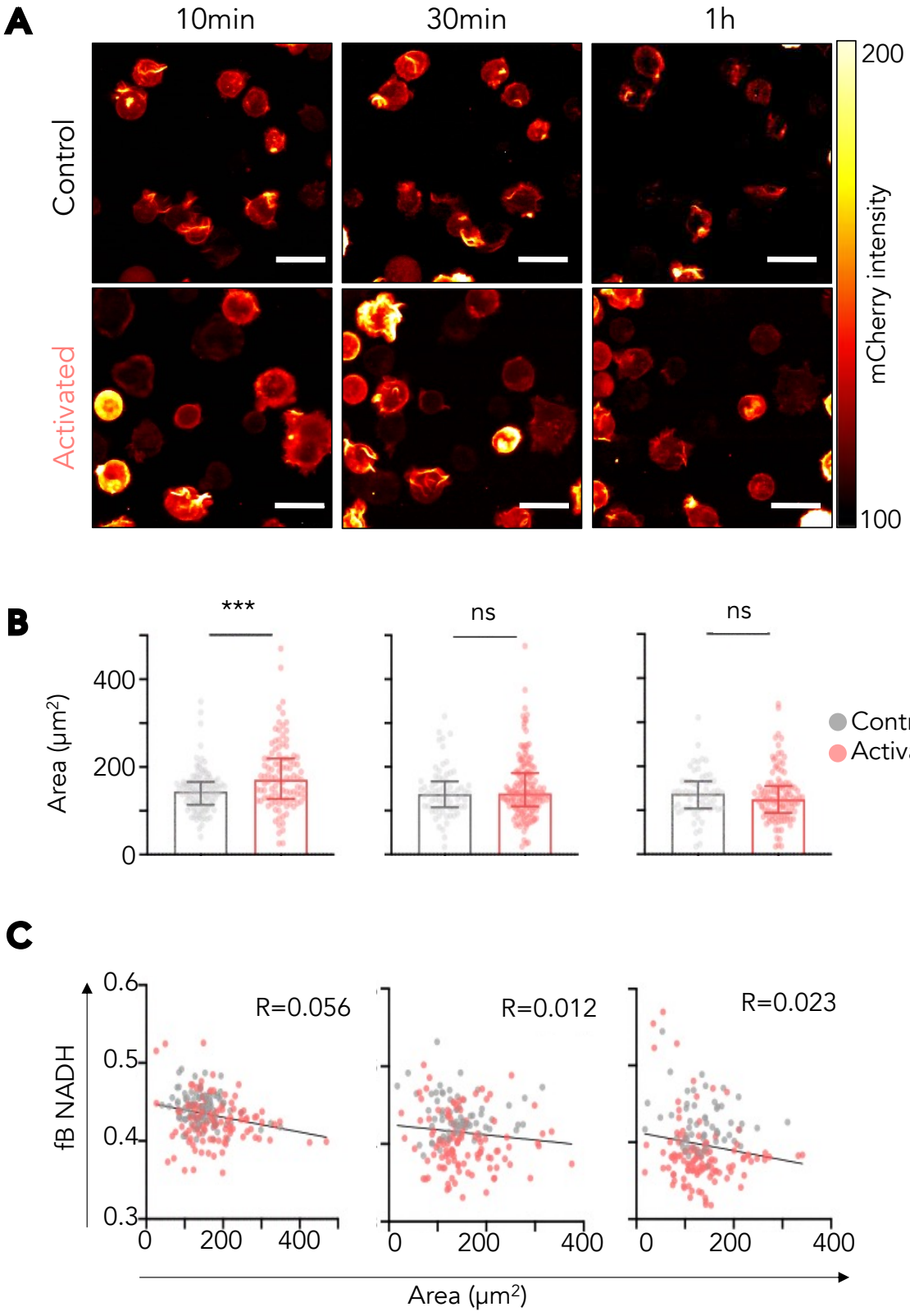
A
10min
30min
1h
Control
Activated
200
100
mCherry intensity
B
***
ns
ns
Area (μm²)
400
200
0
Control
Activated
C
fB NADH
0.6
0.5
0.4
0.3
R=0.056
R=0.012
R=0.023
0
200
400
Area (μm²)

Figure 5

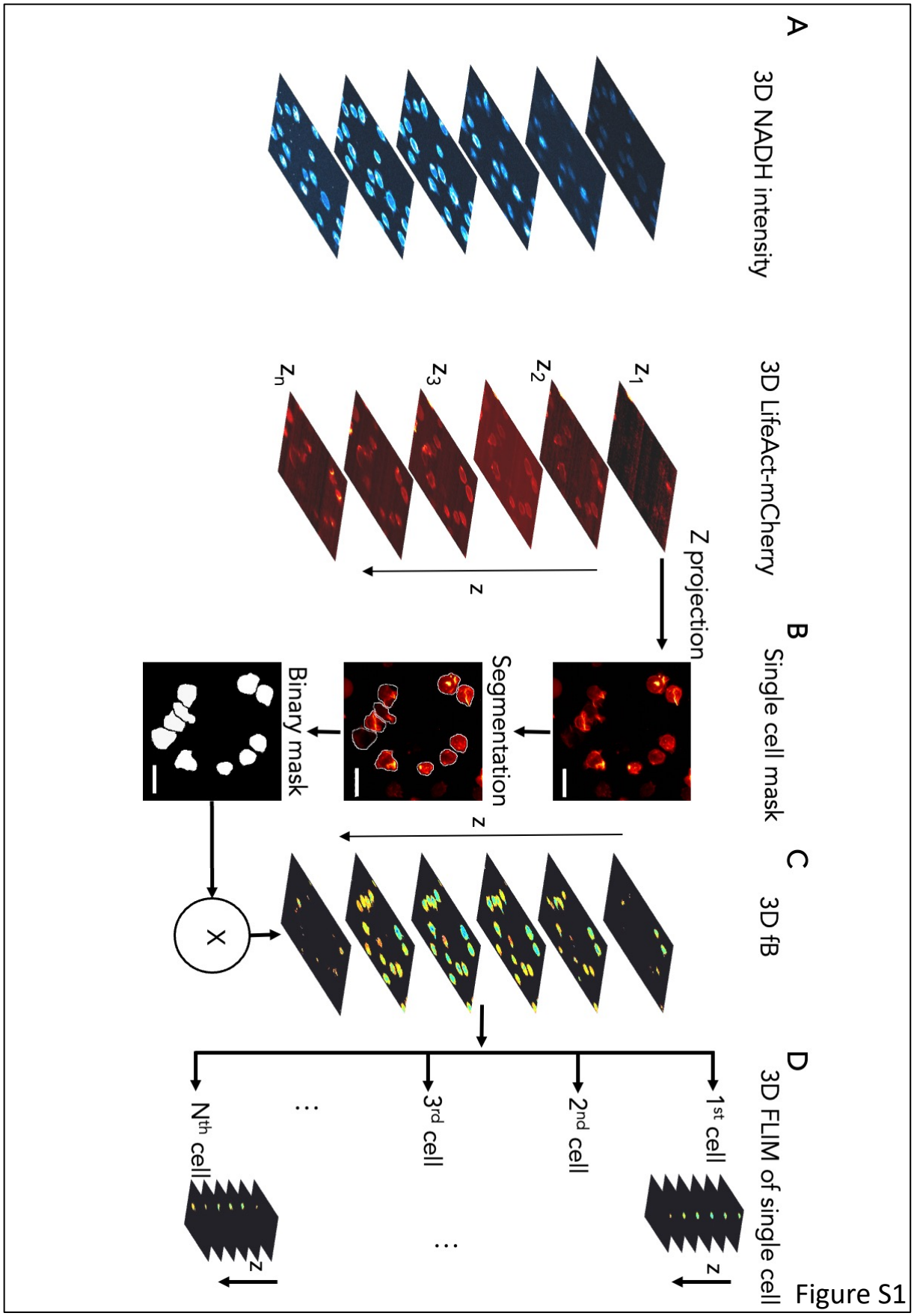
A
3D NADH intensity
B
3D LifeAct-mCherry
Single cell mask
C
3D fB
D
3D FLIM of single cell
Z projection
Segmentation
Binary mask
z
1st cell
2nd cell
3rd cell
Nth cell

Figure S1

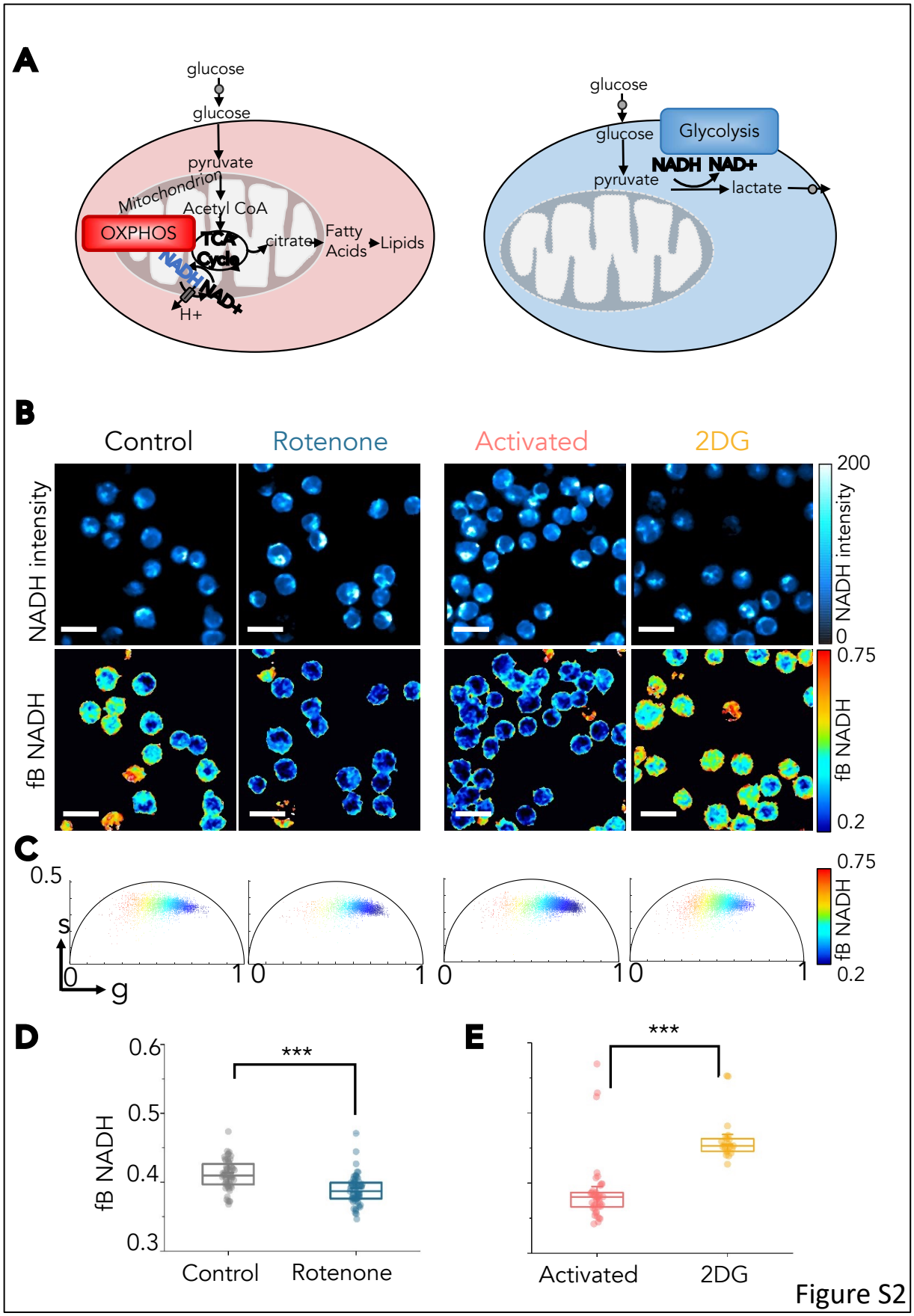
A
glucose
glucose
pyruvate
Mitochondrion
Acetyl CoA
OXPHOS
TCA Cycle
citrate
Fatty Acids
Lipids
NADH
NAD+
H+
glucose
glucose
Glycolysis
NADH NAD+
pyruvate
lactate
B
Control
Rotenone
Activated
2DG
NADH intensity
fB NADH
200
0
NADH intensity
0.75
0.2
fB NADH
C
0.5
s
0
g
1
0
1
0
1
0
1
0.75
fB NADH
0.2
D
0.6
0.5
0.4
0.3
fB NADH
***
Control
Rotenone
E
***
Activated
2DG

Figure S2

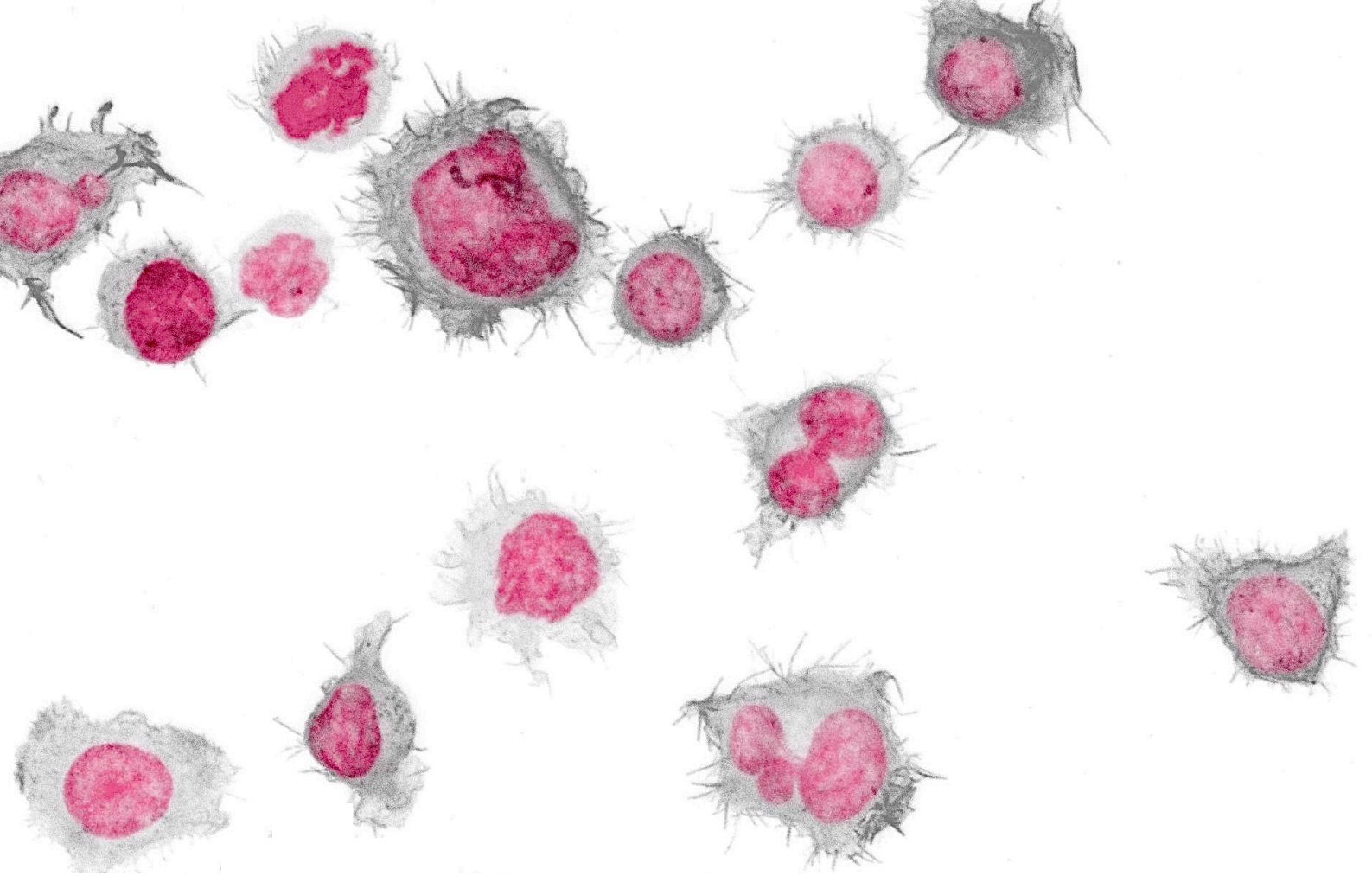

# DISCUSSION ET PERSPECTIVES

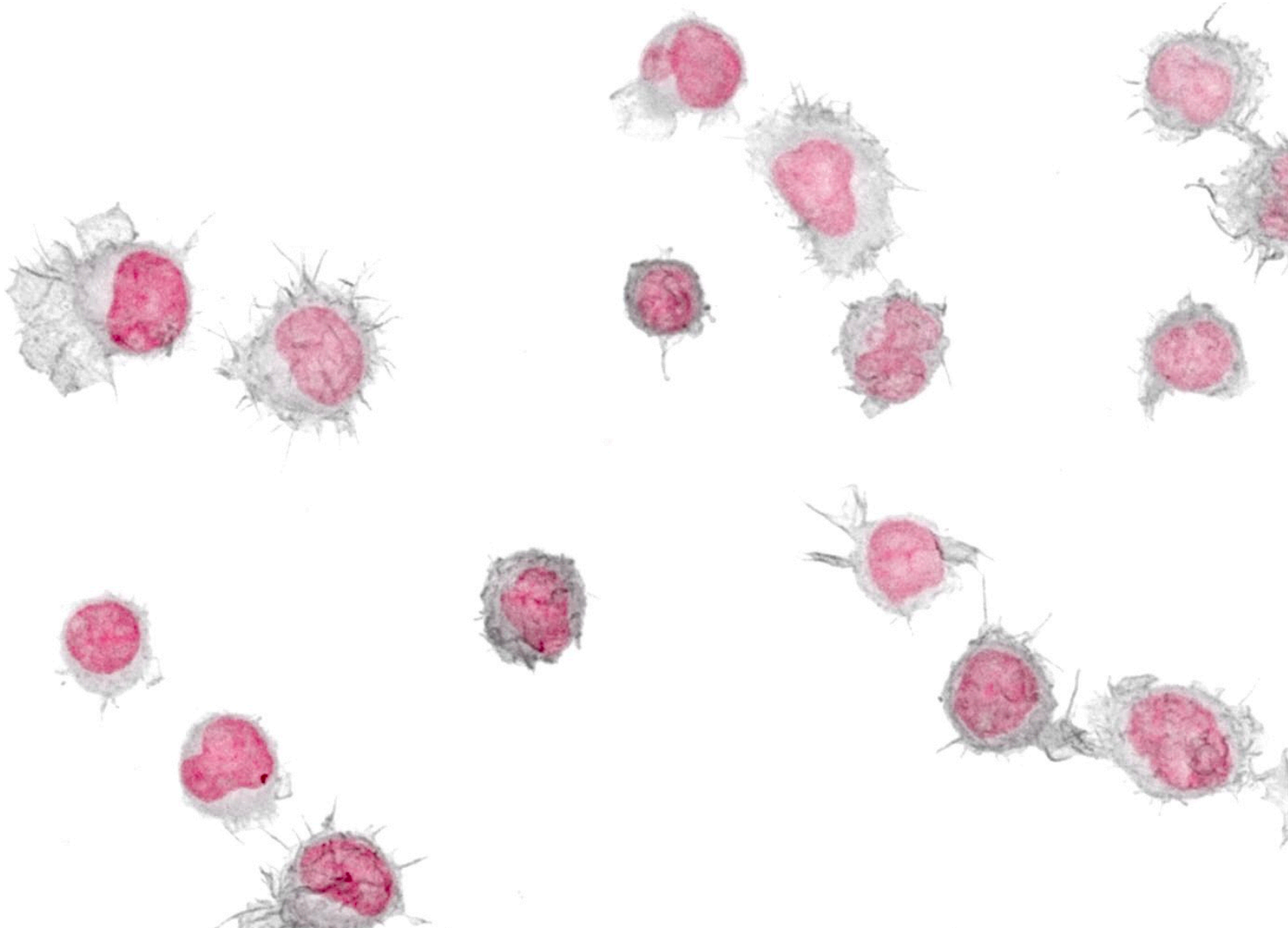

## 1. Inhibition du remodelage d'actine à la synapse immunologique par PD-1

Les effets inhibiteurs de PD-1 sur l'activation des LT ont été largement documentés, sans toutefois avoir apporté une caractérisation précise de l'impact de l'engagement de PD-1 sur la formation de la SI. Mon projet de thèse a permis de mettre en évidence que la liaison PD-1/PD-L1 induit une altération du remodelage du cytosquelette d'actine à la SI. En effet, la présence de PD-L1 sur les surfaces stimulatrices réduit l'étalement des LT exprimant PD-1 et l'enrichissement d'actine filamenteuse à la SI. Lors de la formation de conjugués entre un LT et une CPA, l'interaction PD-1/PD-L1 empêche la formation de l'anneau d'actine autour de la zone de contact, ainsi que la déformation des LT à la SI. Ce mécanisme semble être dépendant de l'activité du complexe Arp2/3, puisque PD-1 inhibe la phosphorylation de la protéine HS1 qui stabilise les réseaux d'actine branchée polymérisés par Arp2/3, et modifie la localisation de la protéine WASP qui active le complexe Arp2/3.

Nos résultats mettant en évidence l'inhibition de l'étalement des LT $CD8^+$ humains exprimant PD-1 sur des surfaces activatrices en présence de PD-L1 confirment les données publiées en 2021, qui avaient obtenus les mêmes résultats avec des LT $CD8^+$ murins en présence de CMHp et de PD-L1 (Li et al., 2021).

L'analyse phosphoprotéomique des cibles de PD-1 publiée en 2020 a identifié une diminution des phosphorylations des résidus tyrosine de protéines clé impliquées dans le remodelage du cytosquelette et la formation de la SI (Tocheva et al., 2020). Elle a notamment identifié une diminution de la phosphorylation de la protéine HS1, ce que nous avons confirmé dans notre modèle. En revanche, cette même étude a proposé que la formation de synapses matures entre des Jurkat exprimant PD-1 et des Raji exprimant PD-L1 et PD-L2 en présence de super antigène (SEE) serait inhibée, et que PD-1 empêcherait la formation de contacts avec des CPA. A l'inverse, nous avons montré que les LT PD-$1^+$ étaient capables de former autant de contacts avec des CPA exprimant PD-L1 qu'avec des CPA qui n'expriment pas le ligand. Notre conclusion, qui diffère de celle publiée, résulte peut-être de la manière dont les résultats ont été analysés. En effet, la quantification de Tocheva et al. a été effectuée à partir de l'observation des contacts entre les LT et les CPA par imagerie. Ils ont défini comme « SI matures », les conjugués présentant un recrutement d'actine à la SI et une déformation des LT. Les conjugués dans lesquels les LT ne présentaient pas ces caractéristiques ont été répertoriés comme des « SI transitoires ». Cependant, nous avons décrit les mêmes effets de PD-1 sur la qualité de formation de la SI, mais en mesurant

le nombre de conjugués formés après 20min par cytométrie en flux, nous avons mis en évidence qu'il ne varie pas lors de l'interaction PD-1/PD-L1. Cela suggère donc que PD-1 altère la qualité de la SI en empêchant le recrutement d'actine et la déformation des LT, mais qu'il n'empêche pas la formation de contacts avec des CPA comme il l'avait été suggéré.

Enfin, il a été proposé que la zone hypodense d'actine au centre de la SI n'apparaisse pas dans les TIL (Ambler et al., 2020). Selon cette étude, la stabilité des conjugués serait détériorée, mais les effets observés n'ont pas pu être restaurés par le blocage de la voie PD-1/PD-L1, ce qui suggère qu'ils seraient provoqués par des facteurs propres aux TIL, plutôt qu'à un effet intrinsèque de PD-1. Dans notre étude nous mettons également en évidence une absence de formation de la région hypodense d'actine lors de l'engagement de PD-1, mais n'observons pas les mêmes effets sur la formation des conjugués. L'avantage de notre modèle est que nos cellules sont des LT primaires de donneurs sains qui ont été activées et non pas des TIL. Cependant, nous les activons pendant 6 jours afin d'induire l'expression de PD-1, ce qui peut également provoquer une forme d'épuisement des LT. Ainsi, il serait intéressant de confirmer nos résultats en utilisant des anticorps empêchant l'interaction entre PD-1 et PD-L1 pour s'assurer qu'ils restaurent les défauts observés.

Pour caractériser plus précisément le mécanisme d'inhibition de l'actine par PD-1, il serait intéressant d'explorer les voies du remodelage d'actine altérées par l'interaction PD-1/PD-L1. Premièrement, nous pourrions étudier directement la localisation du complexe Arp2/3 lors de la formation d'une SI en présence ou en absence de PD-1. Il serait ensuite important de comprendre à quel niveau de la voie de signalisation PD-1 bloque le remodelage de l'actine branchée. En effet, nous avons observé que la localisation de WASP est altérée par l'engagement de PD-1, mais nous pourrions étudier l'activité de Cdc42 qui active WASP. Comme nos résultats suggèrent que PD-1 bloque la polymérisation d'actine branchée, il serait également intéressant de mesurer l'activité des formines et de voir si celle-ci est augmentée en contrepartie et provoque une augmentation de l'actine linéaire. Enfin, l'inhibition du remodelage d'actine pourrait également être induite par une augmentation de l'activité de protéines qui bloquent le remodelage d'actine, comme la gelsoline ou la cofiline. Il a d'ailleurs été proposé que l'activité de la cofiline est augmentée dans les TIL (Ambler et al., 2020), mais l'importance de PD-1 dans cet effet reste à être démontré. Enfin, il serait important de caractériser plus précisément la dynamique des évènements inhibiteurs : est-ce que l'actine est inhibée dès les premiers instants de la formation de la SI ? Ou est-ce que les premiers évènements de la formation de la SI, comme la formation d'une protrusion et l'interdigitation ont lieu, puis la suite des évènements est bloquée ? Nos résultats préliminaires obtenus par imagerie de cellules vivantes suggèrent que l'interaction PD-1/PD-L1 n'empêche pas la formation d'une

protrusion, mais qu'elle empêche l'aplatissement de la membrane à la SI. Il serait donc intéressant d'approfondir la caractérisation de la dynamique, afin de comprendre quel stade de formation de la SI est altéré par PD-1/PD-L1. Un autre aspect qu'il serait intéressant d'étudier plus en profondeur est l'effet de PD-1 sur le remodelage de l'actine indépendamment d'une stimulation du TCR. En effet, nous avons observé que l'interaction PD-1/PD-L1 diminue l'enrichissement de F-actine et la déformation des LT à la SI en l'absence de stimulation. Ce résultat suggère que PD-1 pourrait agir comme un rhéostat pour empêcher une activation non spécifique des LT.

Les systèmes que nous avons utilisés afin de mettre en évidence ces résultats possèdent également des limites. En effet, malgré l'avantage des surfaces de verres recouvertes d'anticorps et de PD-L1 représentant un modèle simplifié qui nous a permis de stimuler le TCR et la voie PD-1 simultanément et d'imager les LT au plan de la SI, l'inconvénient de ce modèle est que le verre est un substrat beaucoup plus rigide que la surface d'une cellule, ce qui réduit la physiologie du contact. Aussi, la présence des anticorps sur les lames rend les ligands du TCR immobiles et fixés sur une surface extrêmement rigide, ce qui n'est pas représentatif des contacts entre cellules dans lesquels les ligands peuvent se déplacer dans les membranes lipidiques. C'est pour ces raisons que nous avons mis au point le deuxième système, usant de CPA artificielles. Cependant, ce modèle n'est pas non plus parfaitement physiologique puisque les CPA présentent des anticorps anti-CD3/CD28 pour stimuler le TCR au lieu de présenter des peptides comme le feraient des CPA professionnelles. Aussi, nous avons fait le choix d'étudier les effets de PD-1 sur la formation de la SI en cas de stimulation des voies du TCR et de CD28, car une grande partie des effets inhibiteurs de PD-1 sont médiés par la voie CD28 (Hui et al., 2017). Pourtant, dans un contexte tumoral, de nombreuses cellules n'expriment pas les ligands de CD28. Il serait donc intéressant d'étudier les effets de PD-1 sur l'actine en absence de l'engagement de la voie de costimulation CD28. Enfin, nous avons effectué toutes nos expériences *in vitro*, et il serait important de confirmer que les effets de PD-1 sur le remodelage de l'actine puissent être observés également *in vivo* pour s'assurer d'une relevance physiologique de nos résultats, et une potentielle application thérapeutique.

## 2. Conséquences de l'inhibition de l'actine sur la cytotoxicité des lymphocytes T

Il est aujourd'hui largement accepté que PD-1 inhibe l'activité cytotoxique des CTL. Cela constitue le rationnel des thérapies visant à bloquer l'interaction PD-1/PD-L1 à l'aide d'anticorps monoclonaux pour retrouver l'activité antitumorale des CTL. Cependant, cette fonction inhibitrice de PD-1 a jusqu'ici été attribuée à sa capacité à recruter la phosphatase SHP-2 qui déphosphoryle des protéines clé des voies de signalisation du TCR et de CD28 (Kamphorst et al., 2017 ; Yokosuka et al., 2012). Nos résultats ont confirmé que PD-1 inhibe la cytotoxicité des CTL, mesurée par le nombre de cellules cibles éliminées, ainsi que la capacité des CTL à sécréter des granules cytolytiques lors d'une stimulation sur une surface recouverte d'anticorps en présence de PD-L1. Ce défaut de dégranulation n'est pas associé à une inhibition de la polarisation du centrosome et des granules cytolytiques à la SI. La sécrétion de granules cytolytiques peut être restaurée par l'ouverture pharmacologique du réseau d'actine à la SI, en traitant les LT avec de faibles doses de latrunculine. Cela suggère que l'inhibition du remodelage d'actine par PD-1 provoquerait la présence d'une barrière d'actine à la zone de contact qui empêcheraut la sécrétion des granules cytolytiques. Ces résultats proposent donc le remodelage d'actine comme un nouvel acteur impliqué dans l'inhibition de la cytotoxicité par PD-1. En revanche, l'ouverture pharmacologique du réseau d'actine n'a pas pu restaurer la cytotoxicité, ce qui signifie que d'autres facteurs que la barrière d'actine entrent en jeu pour expliquer le défaut de cytotoxicité induit par PD-1.

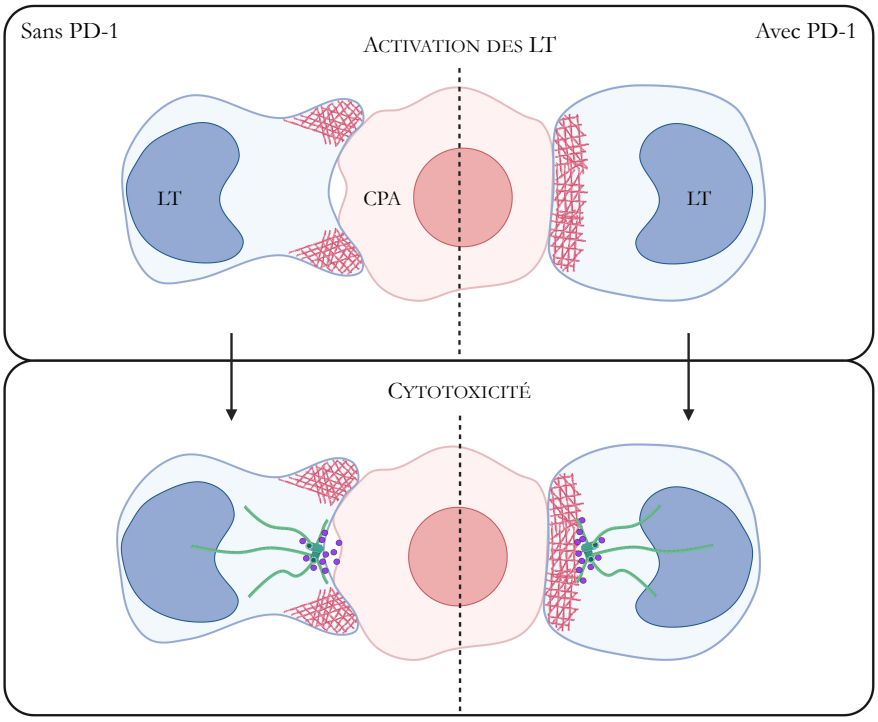


Figure 24 : Représentation graphique du modèle proposé

Un facteur qui pourrait expliquer pourquoi la lyse des cellules cibles n'est pas restaurée par l'ouverture pharmacologique de la barrière d'actine à la SI, serait l'inhibition des forces exercées à la SI par PD-1. En effet, il a été décrit que les forces exercées par les LT à la SI sont essentielles à la cytotoxicité des CTL, et dépendantes du remodelage d'actine (Basu et al., 2016). La protéine WASP permet la formation de structures protrusives au centre de la synapse qui forment des cratères dans les cellules cibles, où elles insèrent les granules cytolytiques (De Jesus et al., 2023). Comme PD-1 empêche la localisation de WASP à la SI, il serait intéressant de mesurer les forces exercées par les LT en présence et en absence de l'interaction PD-1/PD-L1. Les LT utilisent ces forces pour lyser les cellules cibles, donc leur inhibition expliquerait pourquoi l'ouverture de la barrière d'actine ne restaure que la sécrétion des granules cytolytiques mais pas la capacité cytotoxique des LT. Un autre résultat suggérant que PD-1 inhibe les forces exercées, est l'inhibition de la déformation des LT à la SI. En effet, il a été mis en évidence que la morphologie convexe des CTL à la SI est associée à l'exertion de forces (Govendir et al., 2022).

Afin d'apporter un premier élément de réponse à cette hypothèse, nous avons étudié la phosphorylation de la protéine CasL, qui témoigne d'une tension de membrane (Kumari et al., 2020). Pour le moment les résultats obtenus ne sont pas clairs, et suggèrent une inhibition de la tension de membrane par PD-1 dans le modèle Jurkat qui n'est pas reproductible dans tous les LT $CD8^+$ de donneurs sains qui ont été testés (PD-1 a inhibé la phosphorylation de CasL dans les LT de 3 donneurs sur 6 testés). Ainsi, il serait préférable d'opter pour une mesure des forces plus précise, en utilisant par exemple le système de mesure des forces de membranes à l'aide de micropipettes (Husson et al., 2011). Ce système utilise des billes recouvertes d'anticorps comme CPA, qui sont maintenues dans une micropipette. Une deuxième micropipette maintient le LT par aspiration et le met en contact avec la CPA. Les forces développées par le LT peuvent alors être mesurées grâce à la flexion de la micropipette qui le maintient. La tension exercée par les LT sur les membranes des CPA en présence ou en absence de l'interaction PD-1/PD-L1 pourrait également être mesurée à l'aide de microscopie mesurant les forces de traction, en utilisant des surfaces (Lekka et al., 2021) ou des microparticules déformables (De Jesus et al., 2023) recouvertes d'anticorps avec ou sans PD-L1.

Ces nouveaux résultats sur l'implication de l'inhibition du remodelage d'actine par PD-1 dans la cytotoxicité possèdent néanmoins quelques limites. En effet, nous n'avons pas pu déterminer l'importance de la signalisation par PD-1 dans les effets sur la cytotoxicité. Pour y répondre, nous avons généré une protéine PD-1 mutée sur les deux tyrosines essentielles au

recrutement de la phosphatase SHP-2, qui empêche théoriquement la signalisation inhibitrice par PD-1. Néanmoins, nous n'avons pas pu insérer cette protéine dans des LT primaires humains en raison de leur expression endogène de PD-1 lors de la stimulation, qui aurait nécessité de supprimer l'expression endogène de PD-1 et de la remplacer par la version mutante de la protéine par un *knock in*, qui est une technique compliquée à mettre au point. Pour cela, nous avons essayé d'utiliser une lignée cellulaire de LT $CD8^+$, les TALL-104 qui sont des lymphoblastes de leucémie lymphoblastique aiguë. Nous avions prévu de transduire cette lignée avec la version mutante de PD-1 et de comparer la cytotoxicité de ces LT par rapport aux cellules exprimant la version sauvage du gène. Néanmoins, nous avons rencontré des difficultés de culture cellulaire et avons donc choisi de continuer le projet avec des LT primaires. Ces difficultés techniques nous ont donc empêché, pour le moment, d'évaluer l'activité inhibitrice de la protéine mutante sur la dégranulation, et donc de déterminer si la signalisation de PD-1 est essentielle à ce mécanisme. Cette question pourrait être adressée à l'aide d'un inhibiteur des phosphatases SHP1/2 (il a été montré que SHP1 opère en absence de SHP-2), qui permettrait de bloquer la voie de signalisation par PD-1 pharmacologiquement dans des LT primaires, et d'établir son importance dans l'inhibition de la cytotoxicité. Néanmoins, la phosphatase SHP-2 est ubiquitaire et ne régule pas seulement la voie de signalisation induite par PD-1, donc son inhibition pourrait avoir des effets indirects sur d'autres voies de signalisation des LT. Un autre moyen d'adresser cette question serait de supprimer l'expression endogène de PD-1 dans les LT $CD8^+$ primaires par CRISPR, puis de les transduire avec le mutant de PD-1. L'inconvénient de cette méthode est que la transduction par lentivirus induirait une surexpression de la protéine plutôt qu'une expression au même niveau que la protéine endogène.

## 3. Indépendance des motifs de signalisation de PD-1 pour l'inhibition du remodelage d'actine

Les effets inhibiteurs de PD-1 sont généralement attribués à sa capacité à recruter la phosphatase SHP-2, qui déphosphoryle les protéines clé des voies du TCR et de CD28. PD-1 recrute SHP-2 grâce à la phosphorylation des tyrosines de ses motifs ITIM et ITSM. Leur mutation a été associée à une diminution des effets inhibiteurs de PD-1 sur l'activation des LT (Chemnitz et al., 2004 ; Okazaki et al., 2001 ; Yokosuka et al., 2012). En absence de SHP-2, la phosphatase SHP-1 peut se lier à PD-1 et compenser les effets inhibiteurs (Celis-Gutierrez et al., 2019). Cependant, les LT double déficients pour SHP-1/2 sont capables, dans une moindre mesure, d'inhiber la prolifération et la production de cytokines (Xu et al., 2020), et il reste donc à déterminer quel mécanisme est responsable de cette inhibition indépendante de SHP-1/2.

Pour déterminer si l'altération du remodelage de l'actine est dépendante du recrutement de SHP-2 par PD-1, nous avons généré un mutant de la protéine, en remplaçant les tyrosines des motifs ITIM et ITSM essentielles à son recrutement (Y223 et Y248) par des phénylalanines. Nous avons d'abord confirmé que la protéine mutée possède une capacité inhibitrice réduite par rapport à la protéine sauvage, en mettant en évidence une moindre inhibition de la sécrétion d'IL-2, de l'expression de CD25 et de la phosphorylation de PLCγ lors de l'activation des LT. Ensuite, nous avons comparé les effets inhibiteurs des versions mutante et sauvage de PD-1 sur le remodelage de l'actine et observé que la protéine mutante est capable de réduire l'étalement des LT et l'enrichissement de F-actine à la SI lors de leur stimulation sur une lame. Lors de la formation d'une SI avec une CPA, la perte de la capacité à former l'anneau d'actine et à se déformer à la SI est également conservée chez les LT exprimant la protéine PD-1 mutée. Ainsi, ce résultat est la première mise en évidence d'une fonction de PD-1 indépendante du recrutement de SHP-2 à ses motifs de signalisation.

L'altération du remodelage d'actine pourrait expliquer l'inhibition résiduelle observée lors de la mutation des motifs de signalisation de PD-1 (Chemnitz et al., 2004 ; Yokosuka et al., 2012), ou de la perte d'expression de SHP-1/2 (Xu et al., 2020). En effet, une explication possible serait que le blocage du cytosquelette d'actine par PD-1 empêcherait la génération de forces à la SI, qui sont essentielles à une déformation et une activation efficace des LT (Basu et al., 2016 ; De Jesus et al., 2023 ; Govendir et al., 2022). Afin de démontrer que l'inhibition résiduelle de l'activation des LT en absence des motifs de signalisation de PD-1 est bien dépendante de ses effets sur l'actine, il est

essentiel de comprendre le mécanisme de cette inhibition. Une hypothèse est que la taille de l'interaction PD-1/PD-L1, similaire au couple TCR/CMHp (Lin et al., 2008), permettrait d'exclure la phosphatase CD45 de la zone de contact (Carbone et al., 2017). L'interaction très rapprochée entre PD-1 et son ligand pourrait exclure CD45 de manière trop précoce, et ainsi empêcher la déphosphorylation activatrice de Lck lors de la formation d'une SI (Furlan et al., 2014). L'interaction rapprochée de PD-1/PD-L1 pourrait également provoquer un encombrement stérique, empêchant la formation de MC de TCR à la SI. Cela pourrait être testé en mesurant la concentration de TCR/CD3 dans la zone de contact, en présence ou en absence de PD-1/PD-L1. En effet, la protéine sauvage colocalise avec les MC de TCR, alors qu'une protéine PD-1 allongée par l'ajout de domaines immunoglobuline CD22 dans la partie extracellulaire ne se trouve plus dans la même région que les TCR (Yokosuka et al., 2012). Ainsi, nous avons généré ce même mutant de PD-1 en l'allongeant avec des domaines immunoglobuline de CD22 pour étudier ses effets sur le remodelage de l'actine. En parallèle, nous avons également généré un mutant de PD-1 dépourvu de son domaine intracytoplasmique, en délétant cette région 2 acides aminés après le domaine transmembranaire pour nous assurer que la partie intracytoplasmique ne pouvait pas recruter d'autres protéines que la phosphatase SHP-2, et ainsi écarter toute implication d'une signalisation induite par PD-1 dans les effets sur l'actine.

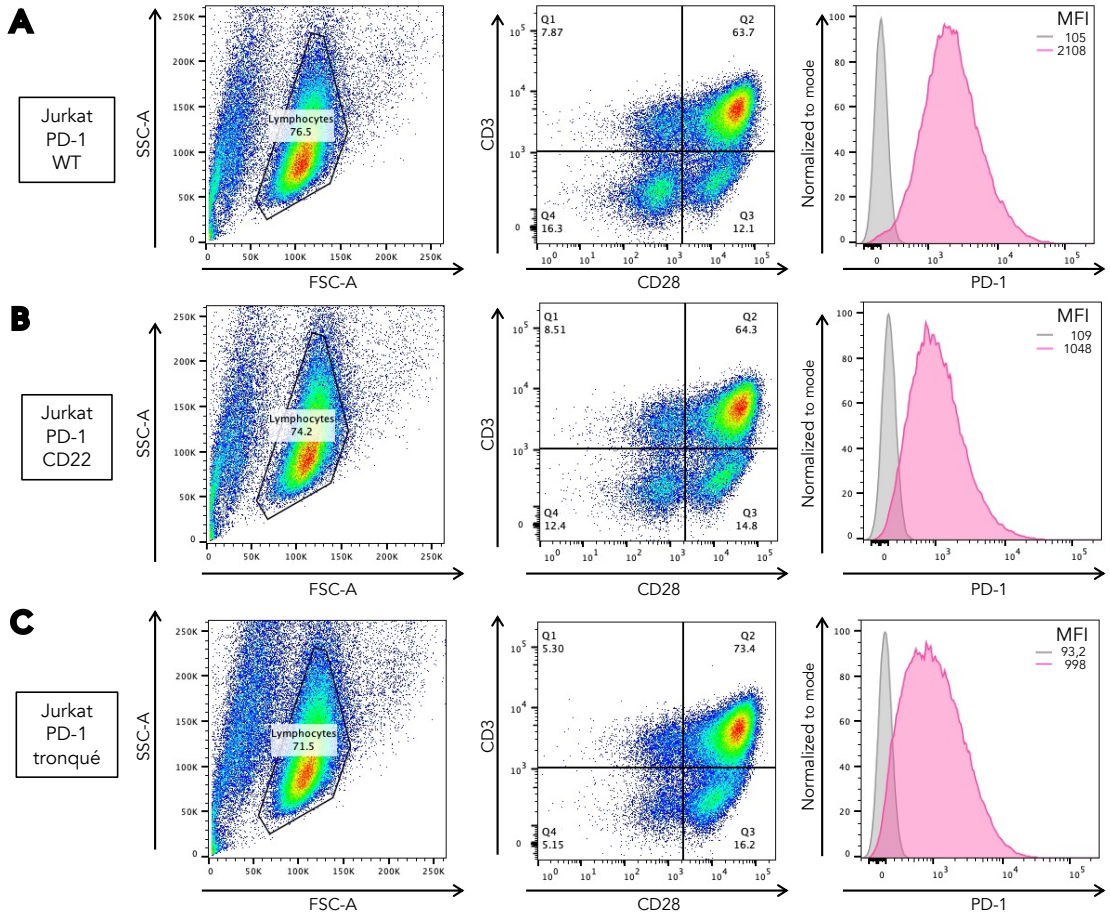


Figure 25 : Phénotype des LT exprimant les versions mutées de PD-1

Pour le moment, les protéines mutantes de PD-1 n'ont pas le même niveau d'expression membranaire que la protéine sauvage dans les Jurkat, ce qui rend difficile la comparaison des effets inhibiteurs de ces différentes versions de PD-1, puisqu'il a été montré que le niveau d'expression de PD-1 détermine ses effets inhibiteurs (Wei et al., 2013). Une solution serait donc de trier ces différentes populations pour obtenir des niveaux d'expression homogènes qui nous permettront de comparer les effets de PD-1 sur le remodelage de l'actine.

Un autre moyen de tester l'hypothèse de l'encombrement stérique induit par l'interaction PD-1/PD-L1, serait d'utiliser le système du récepteur artificiel FKBP et de son ligand FRB qui interagissent étroitement lors de l'ajout de rapamycine (Banaszynski et al., 2005). Ce système d'interaction artificielle dépourvue de toute signalisation permettrait de mimer l'interaction étroite entre PD-1 et PD-L1 et de déterminer si celle-ci provoque les défauts de remodelage du cytosquelette d'actine. Cependant, la rapamycine bloque la calcineurine et l'activité du complexe mTOR, et possède donc une activité immunosuppressive. Il faudrait donc plutôt envisager l'utilisation d'un analogue synthétique non-immunosuppressif de la rapamycine comme l'AP21967 (Bayle et al., 2006).

Les résultats présentés jusqu'ici n'ayant été mis en évidence que dans la lignée Jurkat surexprimant la protéine PD-1 sauvage ou mutée, il semble essentiel de confirmer ces résultats dans des cellules primaires. Comme précédemment pour comprendre le rôle des motifs de signalisation de PD-1 dans l'inhibition de la cytotoxicité, il serait important de confirmer ces résultats dans des LT primaires en utilisant un inhibiteur des phosphatases SHP1/2 ou en réalisant un *knock-in* pour remplacer l'expression de PD-1 endogène par celle de la version mutante de la protéine.

En définitif, nos résultats sont une première mise en évidence d'une inhibition par PD-1 de LT fonction des LT indépendamment de ses motifs de signalisation. Cependant, ils ne vont pas à l'encontre des effets inhibiteurs de PD-1 dépendants de SHP-2 précédemment mis en évidence. En effet, l'inhibition par PD-1 pourrait avoir lieu selon deux phases consécutives : la première, prenant effet dès les premiers instants du contact avec une CPA, serait indépendante de ses motifs de signalisation et affecterait le remodelage de l'actine, puis la seconde, une fois le recrutement de SHP-2 ayant eu lieu, permettrait de renforcer les effets induits en première phase en réduisant les signaux activateurs transmis par les voies de signalisation du TCR et de CD28 pour, ensemble, permettre une inhibition de l'activation des LT.

## 4. Mesure en direct du métabolisme dans des LT vivants

L'activation des LT induit une reprogrammation métabolique de l'OXPHOS à la glycolyse pour répondre à leurs besoins énergétiques à la prolifération, la survie et les fonctions effectrices. A l'aide d'une méthode de microscopie à deux photons mesurant la durée de vie de fluorescence dans des cellules vivantes développée en collaboration avec l'équipe de Chiara Stringari à l'École Polytechnique, nous avons pu mesurer le métabolisme des LT lors de l'activation, de manière non invasive. En effet, la mesure du ratio de NADH lié à des protéines et de NADH libre offre une lecture de l'état redox ($NAD^+$/NADH) des cellules, et indirectement de leurs taux d'OXPHOS et de glycolyse (Datta et al., 2020 ; Stringari et al., 2011). En suivant la fraction de NADH lié (fb NADH), nous avons mis en évidence que la reprogrammation métabolique lors de l'activation est très rapide, puisqu'elle intervient dès 10min d'activation. Cette méthode permet également de mesurer le métabolisme de cellules vivantes en 3D, et ainsi d'identifier quelles régions subcellulaires sont associées à chaque programme métabolique. Enfin, à l'aide d'un marqueur fluorescent de l'actine dans les LT (LifeAct-mCherry), nous avons pu identifier une corrélation entre l'étalement des LT et l'augmentation de la glycolyse.

Comme l'activation des LT est un mécanisme très rapide et dynamique, il est essentiel de mesurer la reprogrammation métabolique de manière précoce dans des cellules vivantes. Une étude a mis en évidence que la reprogrammation de l'OXPHOS vers la glycolyse s'effectue en deux étapes : la première, intervenant dans les minutes suivant la stimulation du TCR, est indépendante de transcription, traduction, CD28 et Akt. Elle est induite par l'activation de la kinase pyruvate déshydrogénase 1 (PDHK1). La deuxième, plus tardive, implique CD28 et Akt pour augmenter l'absorption de glucose et les enzymes glycolytiques (Menk et al., 2018). Notre étude a donc permis de confirmer qu'il existe une première étape de la reprogrammation métabolique précoce, et d'identifier un potentiel rôle de l'actine dans ce mécanisme.

Il a été décrit que PD-1 inhibe la glycolyse lors de l'activation des LT (Patsoukis et al., 2015). Comme nous avons identifié une altération du remodelage du cytosquelette d'actine induite par PD-1, et que plusieurs enzymes glycolytiques sont liées à l'actine (DeWane et al., 2021), il serait intéressant d'étudier un possible lien entre l'inhibition de l'actine et du métabolisme par PD-1. En empêchant le remodelage de l'actine, PD-1 pourrait séquestrer des enzymes glycolytiques nécessitant un remodelage pour leur activation, empêchant ainsi l'augmentation précoce de la

glycolyse lors de l'activation des LT. Pour tester cette hypothèse, nous avons mesuré la fraction de NADH lié 10min, 30min et 1h après l'activation de Jurkat PD-1$^+$ sur des surfaces recouvertes d'anti-CD3, anti-CD28, en présence ou en absence de PD-L1.

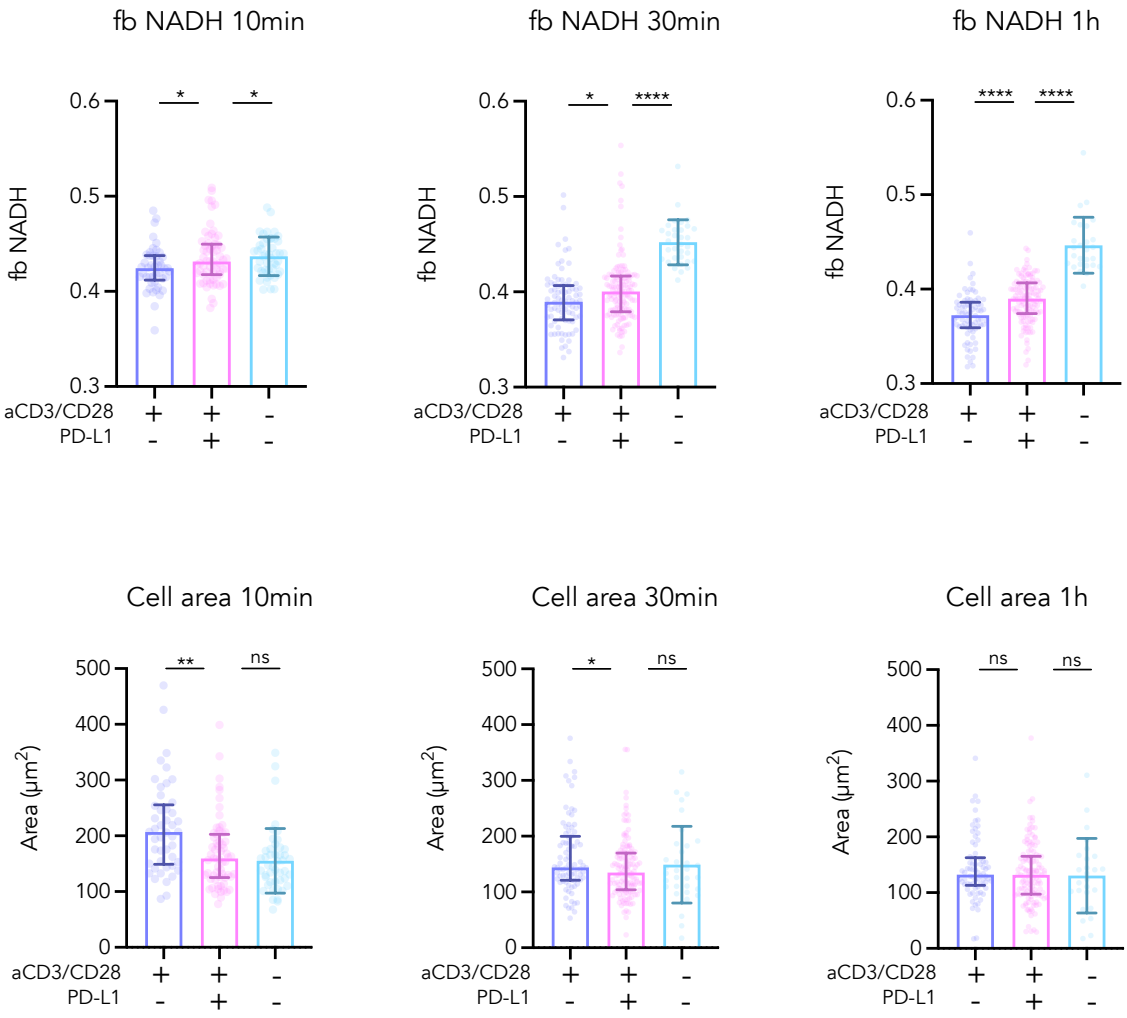


Figure 26 : Mesure simultanée du métabolisme et de l'étalement des LT lors d'une activation en présence de PD-1/PD-L1

Nous avons ainsi observé une diminution progressive de la fraction de NADH lié lors de l'activation des LT, représentative d'une augmentation de la glycolyse dès 10min d'activation. Cette diminution a été significativement réduite par la présence de PD-L1 sur la surface à tous les temps mesurés, signant une moindre reprogrammation vers la glycolyse dans la condition où PD-1 est engagé. La mesure de l'étalement des cellules a révélé une nette diminution en présence de PD-L1 à 10min, comme nous l'avions précédemment mis en évidence. Une rétraction des cellules a été observée à partir de 30min, qui a évolué à 1h, réduisant ainsi l'écart de l'aire des cellules étalées sur

des surface activatrices en présence ou en absence de PD-L1. Ces résultats suggèrent donc que PD-1 inhibe la reprogrammation de l'OXPHOS à la glycolyse de manière très précoce suivant l'activation (dès 10min). La corrélation entre l'étalement des cellules et l'inhibition de la glycolyse semble en revanche moins évidente, puisque la différence de taille diminue avec le temps, alors que la différence de NADH lié augmente entre 10min et 1h.

Afin de confirmer ces résultats, nous avons reproduit l'expérience en utilisant des LT $CD4^+$ primaires humains. Malheureusement, nous n'avons pas observé d'inhibition de la glycolyse induite par PD-1 chez ce donneur, et il faudrait donc reproduire l'expérience avec des cellules d'autres donneurs pour confirmer ou infirmer nos résultats obtenus sur le modèle de Jurkat PD-$1^+$. Il serait intéressant d'étudier l'activité et la localisation d'enzymes glycolytiques comme l'aldolase ou la PFK lors d'une stimulation en présence de PD-1, afin d'identifier un potentiel lien entre les effets de PD-1 sur l'actine et sur le métabolisme. Aussi, nous pourrions envisager de précipiter l'actine de LT activés en présence ou en absence de PD-1/PD-L1, et d'analyser en protéomique la composition des filaments d'actine dans les deux conditions. Cela pourrait nous permettre d'identifier des enzymes glycolytiques dérégulées par l'engagement de PD-1.

Les limites de ces résultats sont donc avant tout liées à l'absence de confirmation dans des LT primaires humains. Un autre inconvénient lié à la méthode utilisée pour obtenir ces résultats, est l'absence de mesure du métabolisme avant 10min. En effet, l'activation des LT est très rapide et commence dès les premières secondes suivant la stimulation du TCR. Ainsi, il serait intéressant de mesurer le métabolisme dès les premières secondes de stimulation, mais le système utilisé dans cette étude ne permet pas la mesure du métabolisme avant 10min, temps nécessaire à l'étalement des cellules sur les lames, puis à identifier les régions d'intérêt, et enfin à définir les réglages d'acquisition du microscope. Aussi, ce système de microscopie à deux photons mesurant la durée de vie de fluorescence n'est présent que dans des laboratoires d'optique, et semble très difficilement utilisable pour des biologistes. Il serait donc intéressant d'essayer de confirmer ces résultats à l'aide d'une autre méthode, comme l'utilisation d'un rapporteur fluorescent des ratios d'ATP : ADP, qui peut être mesuré directement par cytométrie ou par imagerie (Russo et al., 2022).

# REFERENCES


Agata, Y., Kawasaki, A., Nishimura, H., Ishida, Y., Tsubata, T., Yagita, H., Honjo, T., 1996. Expression of the PD-1 antigen on the surface of stimulated mouse T and B lymphocytes. Int Immunol 8, 765–772. https://doi.org/10.1093/intimm/8.5.765

Amatore, F., Gorvel, L., Olive, D., 2018. Inducible Co-Stimulator (ICOS) as a potential therapeutic target for anti-cancer therapy. Expert Opinion on Therapeutic Targets 22, 1–9. https://doi.org/10.1080/14728222.2018.1444753

Ambler, R., Edmunds, G., Toti, G., Morgan, D., Wülfing, C., 2020. PD-1 suppresses the maintenance of cell couples between cytotoxic T cells and tumor target cells within the tumor. Sci Signal 4518, 443788. https://doi.org/10.1101/443788

Andres, P.G., Howland, K.C., Dresnek, D., Edmondson, S., Abbas, A.K., Krummel, M.F., 2004. CD28 Signals in the Immature Immunological Synapse. The Journal of Immunology 172, 5880–5886. https://doi.org/10.4049/jimmunol.172.10.5880

Babich, A., Li, S., O'Connor, R.S., Milone, M.C., Freedman, B.D., Burkhardt, J.K., 2012. F-actin polymerization and retrograde flow drive sustained PLCγ1 signaling during T cell activation. Journal of Cell Biology 197, 775–787. https://doi.org/10.1083/jcb.201201018

Bachmann, M., McKall-Faienza, K., Schmits, R., Bouchard, D., Beach, J., Speiser, D.E., Mak, T.W., Ohashi, P.S., 1997. Distinct Roles for LFA-1 and CD28 during Activation of Naive T Cells: Adhesion versus Costimulation. Immunity 7, 549–557. https://doi.org/10.1016/s1074-7613(00)80376-3

Banaszynski, L.A., Liu, C.W., Wandless, T.J., 2005. Characterization of the FKBP,Rapamycin,FRB Ternary Complex. J Am Chem Soc 127, 4715–4721. https://doi.org/10.1021/ja043277y

Barber, D.L., Wherry, E.J., Masopust, D., Zhu, B., Allison, J.P., Sharpe, A.H., Freeman, G.J., Ahmed, R., 2006. Restoring function in exhausted CD8 T cells during chronic viral infection. Nature 439, 682–687. https://doi.org/10.1038/nature04444

Barber, E.K., Dasgupta, J.D., Schlossman, S.F., Trevillyan, J.M., Rudd, C.E., 1989. The CD4 and CD8 antigens are coupled to a protein-tyrosine kinase (p56lck) that phosphorylates the CD3 complex. Proceedings of the National Academy of Sciences 86, 3277–3281. https://doi.org/10.1073/pnas.86.9.3277

Bardhan, K., Aksoylar, H.I., Bourgeois, T. Le, Strauss, L., Weaver, J.D., Delcuze, B., Charest, A., Patsoukis, N., Boussiotis, V.A., 2019. Phosphorylation of PD-1-Y248 is a marker of PD-1-mediated inhibitory function in human T cells. Sci Rep 9, 1–9. https://doi.org/10.1038/s41598-019-53463-0

Basu, R., Whitlock, B.M., Husson, J., Le Floc'h, A., Jin, W., Oyler-Yaniv, A., Dotiwala, F., Giannone, G., Hivroz, C., Biais, N., Lieberman, J., Kam, L.C., Huse, M., 2016. Cytotoxic T Cells Use Mechanical Force to Potentiate Target Cell Killing. Cell 165, 100–110. https://doi.org/10.1016/j.cell.2016.01.021

Bayle, J.H., Grimley, J.S., Stankunas, K., Gestwicki, J.E., Wandless, T.J., Crabtree, G.R., 2006. Rapamycin Analogs with Differential Binding Specificity Permit Orthogonal Control of Protein Activity. Chem Biol 13, 99–107. https://doi.org/10.1016/J.CHEMBIOL.2005.10.017

Benvenuti, F., Lagaudrière-Gesbert, C., Grandjean, I., Jancic, C., Hivroz, C., Trautmann, A., Lantz, O., Amigorena, S., 2004. Dendritic Cell Maturation Controls Adhesion, Synapse Formation, and the Duration of the Interactions with Naive T Lymphocytes. The Journal of Immunology 172, 292–301. https://doi.org/10.4049/jimmunol.172.1.292

Bernstein, B.W., Bamburg, J.R., 2003. Actin-ATP Hydrolysis Is a Major Energy Drain for Neurons. Journal of Neuroscience 23, 1–6. https://doi.org/10.1523/jneurosci.23-01-00002.2003

Bertrand, F., Müller, S., Roh, K.H., Laurent, C., Dupré, L., Valitutti, S., 2013. An initial and rapid step of lytic granule secretion precedes microtubule organizing center polarization at the cytotoxic T lymphocyte/target cell synapse. Proc Natl Acad Sci U S A 110, 6073–6078. https://doi.org/10.1073/pnas.1218640110

Blumenthal, D., Burkhardt, J.K., 2020. Multiple actin networks coordinate mechanotransduction at the immunological synapse. Journal of Cell Biology 1–12. https://doi.org/10.1083/jcb.201911058

Brahmer, J.R., Tykodi, S.S., Chow, L.Q.M., Hwu, W.-J., Topalian, S.L., Hwu, P., Drake, C.G., Camacho, L.H., Kauh, J., Odunsi, K., Pitot, H.C., Hamid, O., Bhatia, S., Martins, R., Eaton, K., Chen, S., Salay, T.M., Alaparthy, S., Grosso, J.F., Korman, A.J., Parker, S.M., Agrawal, S., Goldberg, S.M., Pardoll, D.M., Gupta, A., Wigginton, J.M., 2012. Safety and Activity of Anti–PD-L1 Antibody in Patients with Advanced Cancer. New England Journal of Medicine 366, 2455–2465. https://doi.org/10.1056/NEJMoa1200694

Bromley, S.K., Iaboni, A., Davis, S.J., Whitty, A., Green, J.M., Shaw, A.S., Weiss, A., Dustin, M.L., 2001. The immunological synapse and CD28-CD80 interactions. Nature Immunology 2001 2:12 2, 1159–1166. https://doi.org/10.1038/ni737

Brossard, C., Feuillet, V., Schmitt, A., Randriamampita, C., Romao, M., Raposo, G., Trautmann, A., 2005. Multifocal structure of the T cell - Dendritic cell synapse. Eur J Immunol 35, 1741–1753. https://doi.org/10.1002/eji.200425857

Brown, A.C.N., Oddos, S., Dobbie, I.M., Alakoskela, J.M., Parton, R.M., Eissmann, P., Neil, M.A.A., Dunsby, C., French, P.M.W., Davis, I., Davis, D.M., 2011. Remodelling of Cortical Actin Where Lytic Granules Dock at Natural Killer Cell Immune Synapses Revealed by Super-Resolution Microscopy. PLoS Biol 9, e1001152. https://doi.org/10.1371/JOURNAL.PBIO.1001152

Brown, M.J., Hallam, J.A., Colucci-Guyon, E., Shaw, S., 2001. Rigidity of Circulating Lymphocytes Is Primarily Conferred by Vimentin Intermediate Filaments. The Journal of Immunology 166, 6640–6646. https://doi.org/10.4049/jimmunol.166.11.6640

Bunnell, S.C., Hong, D.I., Kardon, J.R., Yamazaki, T., McGlade, C.J., Barr, V.A., Samelson, L.E., 2002. T cell receptor ligation induces the formation of dynamically regulated signaling assemblies. Journal of Cell Biology 158, 1263–1275. https://doi.org/10.1083/jcb.200203043

Bunnell, S.C., Kapoor, V., Trible, R.P., Zhang, W., Samelson, L.E., 2001. Dynamic Actin Polymerization Drives T Cell Receptor–Induced Spreading: A Role for the Signal Transduction Adaptor LAT. Immunity 14, 315–329. https://doi.org/10.1016/S1074-7613(01)00112-1

Burkhardt, J.K., McIlvain, J.M., Sheetz, M.P., Argon, Y., 1993. Lytic granules from cytotoxic T cells exhibit kinesin-dependent motility on microtubules in vitro. J Cell Sci 104, 151–162. https://doi.org/10.1242/jcs.104.1.151

Burr, J.S., Savage, N.D.L., Messah, G.E., Kimzey, S.L., Shaw, A.S., Arch, R.H., Green, J.M., 2001. Cutting Edge: Distinct Motifs Within CD28 Regulate T Cell Proliferation and Induction of Bcl-XL. The Journal of Immunology 166, 5331–5335. https://doi.org/10.4049/jimmunol.166.9.5331

Butte, M.J., Keir, M.E., Phamduy, T.B., Sharpe, A.H., Freeman, G.J., 2007. Programmed Death-1 Ligand 1 Interacts Specifically with the B7-1 Costimulatory Molecule to Inhibit T Cell Responses. Immunity 27, 111–122. https://doi.org/10.1016/j.immuni.2007.05.016

Cai, E., Marchuk, K., Beemiller, P., Beppler, C., Rubashkin, M.G., Weaver, V.M., Gérard, A., Liu, T.L., Chen, B.C., Betzig, E., Bartumeus, F., Krummel, M.F., 2017. Visualizing dynamic microvillar search and stabilization during ligand detection by T cells. Science (1979) 356. https://doi.org/10.1126/science.aal3118

Call, M.E., Pyrdol, J., Wiedmann, M., Wucherpfennig, K.W., 2002. The Organizing Principle in the Formation of the T Cell Receptor-CD3 Complex. Cell 111, 967–979. https://doi.org/10.1016/S0092-8674(02)01194-7

Callahan, M.K., Wolchok, J.D., 2013. At the Bedside: CTLA-4- and PD-1-blocking antibodies in cancer immunotherapy. J Leukoc Biol 94, 41–53. https://doi.org/10.1189/JLB.1212631

Calvez, R., Lafouresse, F., de Meester, J., Galy, A., Valitutti, S., Dupré, L., 2011. The Wiskott-Aldrich syndrome protein permits assembly of a focused immunological synapse enabling sustained T-cell receptor signaling. Haematologica 96, 1415–1423. https://doi.org/10.3324/HAEMATOL.2011.040204

Carbone, C.B., Kern, N., Fernandes, R.A., Hui, E., Su, X., Garcia, K.C., Vale, R.D., 2017. In vitro reconstitution of T cell receptor-mediated segregation of the CD45 phosphatase. Proc Natl Acad Sci U S A 114, E9338–E9345. https://doi.org/10.1073/pnas.1710358114

Carisey, A.F., Mace, E.M., Saeed, M.B., Davis, D.M., Orange, J.S., 2018. Nanoscale Dynamism of Actin Enables Secretory Function in Cytolytic Cells. Current Biology 28, 489-502.e9. https://doi.org/10.1016/j.cub.2017.12.044

Cassioli, C., Baldari, C.T., 2022. Lymphocyte Polarization During Immune Synapse Assembly: Centrosomal Actin Joins the Game. Front Immunol 13. https://doi.org/10.3389/FIMMU.2022.830835

Celis-Gutierrez, J., Blattmann, P., Zhai, Y., Jarmuzynski, N., Ruminski, K., Grégoire, C., Ounoughene, Y., Fiore, F., Aebersold, R., Roncagalli, R., Gstaiger, M., Malissen, B., 2019. Quantitative Interactomics in Primary T Cells Provides a Rationale for Concomitant PD-1 and BTLA Coinhibitor Blockade in Cancer Immunotherapy. Cell Rep 27, 3315-3330.e7. https://doi.org/10.1016/j.celrep.2019.05.041

Cham, C.M., Driessens, G., O'Keefe, J.P., Gajewski, T.F., 2008. Glucose deprivation inhibits multiple key gene expression events and effector functions in CD8+ T cells. Eur J Immunol 38, 2438–2450. https://doi.org/10.1002/EJI.200838289

Cham, C.M., Gajewski, T.F., 2005. Glucose Availability Regulates IFN-γ Production and p70S6 Kinase Activation in CD8+ Effector T Cells. The Journal of Immunology 174, 4670–4677. https://doi.org/10.4049/JIMMUNOL.174.8.4670

Chan, D.C., 2020. Mitochondrial Dynamics and Its Involvement in Disease. https://doi.org/10.1146/annurev-pathmechdis-012419-032711 15, 235–259. https://doi.org/10.1146/ANNUREV-PATHMECHDIS-012419-032711

Chang, C.H., Curtis, J.D., Maggi, L.B., Faubert, B., Villarino, A. V., O'Sullivan, D., Huang, S.C.C., Van Der Windt, G.J.W., Blagih, J., Qiu, J., Weber, J.D., Pearce, E.J., Jones, R.G., Pearce, E.L., 2013. Posttranscriptional control of T cell effector function by aerobic glycolysis. Cell 153, 1239. https://doi.org/10.1016/j.cell.2013.05.016

Chang, J.T., Palanivel, V.R., Kinjyo, I., Schambach, F., Intlekofer, A.M., Banerjee, A., Longworth, S.A., Vinup, K.E., Mrass, P., Oliaro, J., Killeen, N., Orange, J.S., Russell, S.M., Weninger, W.,

Reiner, S.L., 2007. Asymmetric T lymphocyte division in the initiation of adaptive immune responses. Science (1979) 315, 1687–1691. https://doi.org/10.1126/science.1139393

Chemnitz, J.M., Parry, R. V., Nichols, K.E., June, C.H., Riley, J.L., 2004. SHP-1 and SHP-2 Associate with Immunoreceptor Tyrosine-Based Switch Motif of Programmed Death 1 upon Primary Human T Cell Stimulation, but Only Receptor Ligation Prevents T Cell Activation. The Journal of Immunology 173, 945–954. https://doi.org/10.4049/jimmunol.173.2.945

Chi, H., 2012. Regulation and function of mTOR signalling in T cell fate decisions. Nature Reviews Immunology 2012 12:5 12, 325–338. https://doi.org/10.1038/nri3198

Cogliati, S., Frezza, C., Soriano, M.E., Varanita, T., Quintana-Cabrera, R., Corrado, M., Cipolat, S., Costa, V., Casarin, A., Gomes, L.C., Perales-Clemente, E., Salviati, L., Fernandez-Silva, P., Enriquez, J.A., Scorrano, L., 2013. Mitochondrial Cristae Shape Determines Respiratory Chain Supercomplexes Assembly and Respiratory Efficiency. Cell 155, 160–171. https://doi.org/10.1016/J.CELL.2013.08.032

Combs, J., Kim, S.J., Tan, S., Ligon, L.A., Holzbaur, E.L.F., Kuhn, J., Poenie, M., 2006. Recruitment of dynein to the Jurkat immunological synapse. Proc Natl Acad Sci U S A 103, 14883–14888. https://doi.org/10.1073/pnas.0600914103

Comrie, W.A., Babich, A., Burkhardt, J.K., 2015. F-actin flow drives affinity maturation and spatial organization of LFA-1 at the immunological synapse. Journal of Cell Biology 208, 475–491. https://doi.org/10.1083/JCB.201406121

Comrie, W.A., Burkhardt, J.K., 2016. Action and traction: Cytoskeletal control of receptor triggering at the immunological synapse. Front Immunol 7, 68. https://doi.org/10.3389/FIMMU.2016.00068/BIBTEX

Daniel, J.L., Molish, I.R., Robkin, L., Holmsen, H., 1986. Nucleotide exchange between cytosolic ATP and F-actin-bound ADP may be a major energy-utilizing process in unstimulated platelets. Eur J Biochem 156, 677–683. https://doi.org/10.1111/J.1432-1033.1986.TB09631.X

Das, D.K., Feng, Y., Mallis, R.J., Li, X., Keskin, D.B., Hussey, R.E., Brady, S.K., Wang, J.H., Wagner, G., Reinherz, E.L., Lang, M.J., 2015. Force-dependent transition in the T-cell receptor β-subunit allosterically regulates peptide discrimination and pMHC bond lifetime. Proc Natl Acad Sci U S A 112, 1517–1522. https://doi.org/10.1073/PNAS.1424829112

Datta, R., Heaster, T.M., Sharick, J.T., Gillette, A.A., Skala, M.C., 2020. Fluorescence lifetime imaging microscopy: fundamentals and advances in instrumentation, analysis, and applications. J Biomed Opt 25, 1. https://doi.org/10.1117/1.JBO.25.7.071203

Davis, S.J., van der Merwe, P.A., 2006. The kinetic-segregation model: TCR triggering and beyond. Nature Immunology 2006 7:8 7, 803–809. https://doi.org/10.1038/NI1369

De Jesus, M., Settle, A.H., Vorselen, D., Gaetjens, T.K., Galiano, M., Wong, Y.Y., Fu, T.-M., Santosa, E., Winer, B.Y., Tamzalit, F., Wang, M.S., Bao, Z., Sun, J.C., Shah, P., Theriot, J.A., Abel, S.M., Huse, M., Gerstner, L. V, 2023. Topographical analysis of immune cell interactions reveals a biomechanical signature for immune cytolysis. bioRxiv 2023.04.16.537078. https://doi.org/10.1101/2023.04.16.537078

De Meester, J., Calvez, R., Valitutti, S., Dupré, L., 2010. The Wiskott-Aldrich syndrome protein regulates CTL cytotoxicity and is required for efficient killing of B cell lymphoma targets. J Leukoc Biol 88, 1031–1040. https://doi.org/10.1189/jlb.0410197

Demetriou, P., Abu-Shah, E., Valvo, S., McCuaig, S., Mayya, V., Kvalvaag, A., Starkey, T., Korobchevskaya, K., Lee, L.Y.W., Friedrich, M., Mann, E., Kutuzov, M.A., Morotti, M., Wietek, N., Rada, H., Yusuf, S., Afrose, J., Siokis, A., Allan, P., Ambrose, T., Arancibia, C., Bailey, A., Barnes, E., Bird-Lieberman, E., Bornschein, J., Brain, O., Braden, B., Collier, J., Cobbold, J., Culver, E., East, J., Howarth, L., Klenerman, P., Leedham, S., Palmer, R., Pavlides, M., Powrie, F., Rodrigues, A., Satsangi, J., Simmons, A., Sullivan, P., Uhlig, H., Walsh, A., Meyer-Hermann, M., Ahmed, A.A., Depoil, D., Dustin, M.L., 2020. A dynamic CD2-rich compartment at the outer edge of the immunological synapse boosts and integrates signals. Nature Immunology 2020 21:10 21, 1232–1243. https://doi.org/10.1038/S41590-020-0770-X

Dennehy, K.M., Elias, F., Na, S.-Y., Fischer, K.-D., Hünig, T., Lühder, F., 2007. Mitogenic CD28 Signals Require the Exchange Factor Vav1 to Enhance TCR Signaling at the SLP-76-Vav-Itk Signalosome. The Journal of Immunology 178, 1363–1371. https://doi.org/10.4049/JIMMUNOL.178.3.1363

DeWane, G., Salvi, A.M., DeMali, K.A., 2021. Fueling the cytoskeleton-links between cell metabolism and actin remodeling. J Cell Sci 134. https://doi.org/10.1242/JCS.248385/237339

Ditlev, J.A., Vega, A.R., Köster, D.V., Su, X., Tani, T., Lakoduk, A.M., Vale, R.D., Mayor, S., Jaqaman, K., Rosen, M.K., 2019. A composition-dependent molecular clutch between T cell signaling condensates and actin. Elife 8. https://doi.org/10.7554/ELIFE.42695

Dominguez, R., Holmes, K.C., 2011. Actin Structure and Function. https://doi-org.proxy.insermbiblio.inist.fr/10.1146/annurev-biophys-042910-155359 40, 169–186. https://doi.org/10.1146/ANNUREV-BIOPHYS-042910-155359

Dong, H., Zhu, G., Tamada, K., Chen, L., 1999. B7-H1, a third member of the B7 family, co-stimulates T-cell proliferation and interleukin-10 secretion. Nature Medicine 1999 5:12 5, 1365–1369. https://doi.org/10.1038/70932

Douanne, T., Griffiths, G.M., 2021. Cytoskeletal control of the secretory immune synapse. Curr Opin Cell Biol 71, 87–94. https://doi.org/10.1016/j.ceb.2021.02.008

Douglass, A.D., Vale, R.D., 2005. Single-Molecule Microscopy Reveals Plasma Membrane Microdomains Created by Protein-Protein Networks that Exclude or Trap Signaling Molecules in T Cells. Cell 121, 937–950. https://doi.org/10.1016/J.CELL.2005.04.009

Dupré, L., Aiuti, A., Trifari, S., Martino, S., Saracco, P., Bordignon, C., Roncarolo, M.G., 2002. Wiskott-Aldrich Syndrome Protein Regulates Lipid Raft Dynamics during Immunological Synapse Formation. Immunity 17, 157–166. https://doi.org/10.1016/S1074-7613(02)00360-6

Dustin, M.L., 2014. The immunological synapse. Cancer Immunol Res 2, 1023. https://doi.org/10.1158/2326-6066.CIR-14-0161

Dustin, M.L., 2008. T-cell activation through immunological synapses and kinapses. Immunol Rev. https://doi.org/10.1111/j.1600-065X.2008.00589.x

Dustin, M.L., Bromley, S.K., Kan, Z., Peterson, D.A., Unanue, E.R., 1997. Antigen receptor engagement delivers a stop signal to migrating T lymphocytes. Proc Natl Acad Sci U S A 94, 3909–3913. https://doi.org/10.1073/PNAS.94.8.3909/

Dustin, M.L., Kimmel, M.S., 2007. Cell adhesion molecules and actin cytoskeleton at immune synapses and kinapses. Curr Opin Cell Biol 19, 529–533. https://doi.org/10.1016/j.ceb.2007.08.003

Dustin, M.L., Sanders, M.E., Shaw, S., Springer, T.A., 1987. Purified lymphocyte function-associated antigen 3 binds to CD2 and mediates T lymphocyte adhesion. Journal of Experimental Medicine 165, 677–692. https://doi.org/10.1084/JEM.165.3.677

Eddy, R.J., Weidmann, M.D., Sharma, V.P., Condeelis, J.S., 2017. Tumor Cell Invadopodia: Invasive Protrusions that Orchestrate Metastasis. Trends Cell Biol 27, 595–607. https://doi.org/10.1016/J.TCB.2017.03.003

Espinoza-Sanchez, S., Metskas, L.A., Chou, S.Z., Rhoades, E., Pollard, T.D., 2018. Conformational changes in Arp2/3 complex induced by ATP, WASp-VCA, and actin filaments. Proceedings of the National Academy of Sciences 115, E8642–E8651. https://doi.org/10.1073/PNAS.1717594115

Fäßler, F., Dimchev, G., Hodirnau, V.V., Wan, W., Schur, F.K.M., 2020. Cryo-electron tomography structure of Arp2/3 complex in cells reveals new insights into the branch

junction. Nature Communications 2020 11:1 11, 1–10. https://doi.org/10.1038/S41467-020-20286-X

Fife, B.T., Guleria, I., Bupp, M.G., Eagar, T.N., Tang, Q., Bour-Jordan, H., Yagita, H., Azuma, M., Sayegh, M.H., Bluestone, J.A., 2006. Insulin-induced remission in new-onset NOD mice is maintained by the PD-1–PD-L1 pathway. Journal of Experimental Medicine 203, 2737–2747. https://doi.org/10.1084/JEM.20061577

Fife, B.T., Pauken, K.E., Eagar, T.N., Obu, T., Wu, J., Tang, Q., Azuma, M., Krummel, M.F., Bluestone, J.A., 2009. Interactions between PD-1 and PD-L1 promote tolerance by blocking the TCR-induced stop signal. Nat Immunol 10, 1185–1192. https://doi.org/10.1038/ni.1790

Finetti, F., Patrussi, L., Masi, G., Onnis, A., Galgano, D., Lucherini, O.M., Pazour, G.J., Baldari, C.T., 2014. Specific recycling receptors are targeted to the immune synapse by the intraflagellar transport system. J Cell Sci 127, 1924–1937. https://doi.org/10.1242/JCS.139337/263830/

Forlemu, N.Y., Njabon, E.N., Carlson, K.L., Schmidt, E.S., Waingeh, V.F., Thomasson, K.A., 2011. Ionic strength dependence of F-actin and glycolytic enzyme associations: A Brownian dynamics simulations approach. Proteins: Structure, Function, and Bioinformatics 79, 2813–2827. https://doi.org/10.1002/PROT.23107

Frauwirth, K.A., Riley, J.L., Harris, M.H., Parry, R. V., Rathmell, J.C., Plas, D.R., Elstrom, R.L., June, C.H., Thompson, C.B., 2002. The CD28 signaling pathway regulates glucose metabolism. Immunity 16, 769–777. https://doi.org/10.1016/S1074-7613(02)00323-0

Freeman, G.J., Long, A.J., Iwai, Y., Bourque, K., Chernova, T., Nishimura, H., Fitz, L.J., Malenkovich, N., Okazaki, T., Byrne, M.C., Horton, H.F., Fouser, L., Carter, L., Ling, V., Bowman, M.R., Carreno, B.M., Collins, M., Wood, C.R., Honjo, T., 2000. Engagement of the Pd-1 Immunoinhibitory Receptor by a Novel B7 Family Member Leads to Negative Regulation of Lymphocyte Activation. Journal of Experimental Medicine 192, 1027–1034. https://doi.org/10.1084/JEM.192.7.1027

Friedman, R.S., Beemiller, P., Sorensen, C.M., Jacobelli, J., Krummel, M.F., 2010. Real-time analysis of T cell receptors in naive cells in vitro and in vivo reveals flexibility in synapse and signaling dynamics. Journal of Experimental Medicine 207, 2733–2749. https://doi.org/10.1084/jem.20091201

Furlan, G., Minowa, T., Hanagata, N., Kataoka-Hamai, C., Kaizuka, Y., 2014. Phosphatase CD45 both positively and negatively regulates T cell receptor phosphorylation in reconstituted membrane protein clusters. Journal of Biological Chemistry 289, 28514–28525. https://doi.org/10.1074/jbc.M114.574319

Gall, J.G., 1966. Microtubule Fine Structure. Journal of Cell Biology 31, 639–643. https://doi.org/10.1083/JCB.31.3.639

Garboczi, D.N., Ghosh, P., Utz, U., Fan, Q.R., Biddison, W.E., Wiley, D.C., 1996. Structure of the complex between human T-cell receptor, viral peptide and HLA-A2. Nature 1996 384:6605 384, 134–141. https://doi.org/10.1038/384134a0

Garon, E.B., Rizvi, N.A., Hui, R., Leighl, N., Balmanoukian, A.S., Eder, J.P., Patnaik, A., Aggarwal, C., Gubens, M., Horn, L., Carcereny, E., Ahn, M.-J., Felip, E., Lee, J.-S., Hellmann, M.D., Hamid, O., Goldman, J.W., Soria, J.-C., Dolled-Filhart, M., Rutledge, R.Z., Zhang, J., Lunceford, J.K., Rangwala, R., Lubiniecki, G.M., Roach, C., Emancipator, K., Gandhi, L., 2015. Pembrolizumab for the Treatment of Non–Small-Cell Lung Cancer. New England Journal of Medicine 372, 2018–2028. https://doi.org/10.1056/NEJMOA1501824/

Geiger, B., Rosen, D., Berke, G., 1982. Spatial relationships of microtubule-organizing centers and the contact area of cytotoxic T lymphocytes and target cells. Journal of Cell Biology 95, 137–143. https://doi.org/10.1083/JCB.95.1.137

Geltink, R.I.K., Kyle, R.L., Pearce, E.L., 2018. Unraveling the Complex Interplay Between T Cell Metabolism and Function. https://doi-org.proxy.insermbiblio.inist.fr/10.1146/annurev-immunol-042617-053019 36, 461–488. https://doi.org/10.1146/ANNUREV-IMMUNOL-042617-053019

Gérard, A., Patino-Lopez, G., Beemiller, P., Nambiar, R., Ben-Aissa, K., Liu, Y., Totah, F.J., Tyska, M.J., Shaw, S., Krummel, M.F., 2014. Detection of Rare Antigen Presenting Cells through T cell-intrinsic meandering motility, mediated by Myo1g. Cell 158, 492. https://doi.org/10.1016/J.CELL.2014.05.044

Gerriets, V.A., Kishton, R.J., Nichols, A.G., MacIntyre, A.N., Inoue, M., Ilkayeva, O., Winter, P.S., Liu, X., Priyadharshini, B., Slawinska, M.E., Haeberli, L., Huck, C., Turka, L.A., Wood, K.C., Hale, L.P., Smith, P.A., Schneider, M.A., MacIver, N.J., Locasale, J.W., Newgard, C.B., Shinohara, M.L., Rathmell, J.C., 2015. Metabolic programming and PDHK1 control CD4+ T cell subsets and inflammation. J Clin Invest 125, 194–207. https://doi.org/10.1172/JCI76012

Gerriets, V.A., Rathmell, J.C., 2012. Metabolic pathways in T cell fate and function. Trends Immunol 33, 168–173. https://doi.org/10.1016/J.IT.2012.01.010

Gigoux, M., Shang, J., Pak, Y., Xu, M., Choe, J., Mak, T.W., Suh, W.K., 2009. Inducible costimulator promotes helper T-cell differentiation through phosphoinositide 3-kinase. Proc Natl Acad Sci U S A 106, 20371–20376. https://doi.org/10.1073/PNAS.0911573106

Gomez, T.S., Kumar, K., Medeiros, R.B., Shimizu, Y., Leibson, P.J., Billadeau, D.D.D., 2007. Formins Regulate the Actin-Related Protein 2/3 Complex-Independent Polarization of the Centrosome to the Immunological Synapse. Immunity 26, 177–190. https://doi.org/10.1016/j.immuni.2007.01.008

Gomez, T.S., McCarney, S.D., Carrizosa, E., Labno, C.M., Comiskey, E.O., Nolz, J.C., Zhu, P., Freedman, B.D., Clark, M.R., Rawlings, D.J., Billadeau, D.D., Burkhardt, J.K., 2006. HS1 Functions as an Essential Actin-Regulatory Adaptor Protein at the Immune Synapse. Immunity 24, 741–752. https://doi.org/10.1016/j.immuni.2006.03.022

Govendir, M.A., Kempe, D., Sianati, S., Cremasco, J., Mazalo, J.K., Colakoglu, F., Golo, M., Poole, K., Biro, M., 2022. T cell cytoskeletal forces shape synapse topography for targeted lysis via membrane curvature bias of perforin. Dev Cell 57, 2237-2247.e8. https://doi.org/10.1016/J.DEVCEL.2022.08.012

Grakoui, A., Bromley, S.K., Sumen, C., Davis, M.M., Shaw, A.S., Allen, P.M., Dustin, M.L., 1999. The immunological synapse: A molecular machine controlling T cell activation. Science (1979) 285, 221–227. https://doi.org/10.1126/science.285.5425.221

Green, J.M., Karpitskiy, V., Kimzey, S.L., Shaw, A.S., 2000. Coordinate Regulation of T Cell Activation by CD2 and CD28. The Journal of Immunology 164, 3591–3595. https://doi.org/10.4049/JIMMUNOL.164.7.3591

Gros, O.J., Damstra, H.G.J., Kapitein, L.C., Akhmanova, A., Berger, F., 2021. Dynein self-organizes while translocating the centrosome in T-cells. Mol Biol Cell 32, 855–868. https://doi.org/10.1091/MBC.E20-10-0668

Gruener, N.H., Lechner, F., Jung, M.-C., Diepolder, H., Gerlach, T., Lauer, G., Walker, B., Sullivan, J., Phillips, R., Pape, G.R., Klenerman, P., 2001. Sustained Dysfunction of Antiviral CD8 + T Lymphocytes after Infection with Hepatitis C Virus . J Virol 75, 5550–5558. https://doi.org/10.1128/JVI.75.12.5550-5558.2001

Guy, C.S., Vignali, K.M., Temirov, J., Bettini, M.L., Overacre, A.E., Smeltzer, M., Zhang, H., Huppa, J.B., Tsai, Y.H., Lobry, C., Xie, J., Dempsey, P.J., Crawford, H.C., Aifantis, I., Davis, M.M., Vignali, D.A.A., 2013. Distinct TCR signaling pathways drive proliferation and cytokine production in T cells. Nature Immunology 2013 14:3 14, 262–270. https://doi.org/10.1038/ni.2538

Hardie, D.G., 2007. AMP-activated/SNF1 protein kinases: conserved guardians of cellular energy. Nature Reviews Molecular Cell Biology 2007 8:10 8, 774–785. https://doi.org/10.1038/nrm2249

He, S., Kato, K., Jiang, J., Wahl, D.R., Mineishi, S., Fisher, E.M., Murasko, D.M., Glick, G.D., Zhang, Y., 2011. Characterization of the Metabolic Phenotype of Rapamycin-Treated CD8+ T Cells with Augmented Ability to Generate Long-Lasting Memory Cells. PLoS One 6, e20107. https://doi.org/10.1371/JOURNAL.PONE.0020107

Herbst, R.S., Soria, J.C., Kowanetz, M., Fine, G.D., Hamid, O., Gordon, M.S., Sosman, J.A., McDermott, D.F., Powderly, J.D., Gettinger, S.N., Kohrt, H.E.K., Horn, L., Lawrence, D.P., Rost, S., Leabman, M., Xiao, Y., Mokatrin, A., Koeppen, H., Hegde, P.S., Mellman, I., Chen, D.S., Hodi, F.S., 2014. Predictive correlates of response to the anti-PD-L1 antibody MPDL3280A in cancer patients. Nature 2014 515:7528 515, 563–567. https://doi.org/10.1038/nature14011

Hetrick, B., Han, M.S., Helgeson, L.A., Nolen, B.J., 2013. Small Molecules CK-666 and CK-869 Inhibit Actin-Related Protein 2/3 Complex by Blocking an Activating Conformational Change. Chem Biol 20, 701–712. https://doi.org/10.1016/J.CHEMBIOL.2013.03.019

Hirano, F., Kaneko, K., Tamura, H., Dong, H., Wang, S., Ichikawa, M., Rietz, C., Flies, D.B., Lau, J.S., Zhu, G., Tamada, K., Chen, L., 2005. Blockade of B7-H1 and PD-1 by monoclonal antibodies potentiates cancer therapeutic immunity. Cancer Res 65, 1089–1096.

Hong, J., Murugesan, S., Betzig, E., Hammer, J.A., 2017. Contractile actomyosin arcs promote the activation of primary mouse T cells in a ligand-dependent manner. PLoS One 12, e0183174. https://doi.org/10.1371/JOURNAL.PONE.0183174

Hooikaas, P.J., Damstra, H.G.J., Gros, O.J., van Riel, W.E., Martin, M., Smits, Y.T.H., Loosdregt, J. van, Kapitein, L.C., Berger, F., Akhmanova, A., 2020. Kinesin-4 kif21b limits microtubule growth to allow rapid centrosome polarization in t cells. Elife 9, 1–75. https://doi.org/10.7554/ELIFE.62876

Houten, S.M., Violante, S., Ventura, F. V., Wanders, R.J.A., 2016. The Biochemistry and Physiology of Mitochondrial Fatty Acid β-Oxidation and Its Genetic Disorders. Annual Review of Physiology 78, 23–44. https://doi.org/10.1146/ANNUREV-PHYSIOL-021115-105045

Howard, J., 1997. Molecular motors: structural adaptations to cellular functions. Nature 1997 389:6651 389, 561–567. https://doi.org/10.1038/39247

Hu, H., Juvekar, A., Lyssiotis, C.A., Lien, E.C., Albeck, J.G., Oh, D., Varma, G., Hung, Y.P., Ullas, S., Lauring, J., Seth, P., Lundquist, M.R., Tolan, D.R., Grant, A.K., Needleman, D.J., Asara, J.M., Cantley, L.C., Wulf, G.M., 2016. Phosphoinositide 3-Kinase Regulates Glycolysis through Mobilization of Aldolase from the Actin Cytoskeleton. Cell 164, 433–446. https://doi.org/10.1016/J.CELL.2015.12.042

Hu, K.H., Butte, M.J., 2016. T cell activation requires force generation. Journal of Cell Biology 213, 535–542. https://doi.org/10.1083/jcb.201511053

Hui, E., Cheung, J., Zhu, J., Su, X., Taylor, M.J., Wallweber, H.A., Sasmal, D.K., Huang, J., Kim, J.M., Mellman, I., Vale, R.D., 2017. T cell costimulatory receptor CD28 is a primary target for PD-1-mediated inhibition. Science (1979) 355, 1428–1433. https://doi.org/10.1126/science.aaf1292

Huse, M., 2011. Lymphocyte polarity, the immunological synapse and the scope of biological analogy. Bioarchitecture 1, 180–185. https://doi.org/10.4161/bioa.1.4.17594

Huse, M., Lillemeier, B.F., Kuhns, M.S., Chen, D.S., Davis, M.M., 2006. T cells use two directionally distinct pathways for cytokine secretion. Nature Immunology 2006 7:3 7, 247–255. https://doi.org/10.1038/ni1304

Husson, J., Chemin, K., Bohineust, A., Hivroz, C., Henry, N., 2011. Force Generation upon T Cell Receptor Engagement. PLoS One 6, e19680. https://doi.org/10.1371/JOURNAL.PONE.0019680

Imbert, V., Peyron, J.F., Farahi Far, D., Mari, B., Auberger, P., Rossi, B., 1994. Induction of tyrosine phosphorylation and T-cell activation by vanadate peroxide, an inhibitor of protein tyrosine phosphatases. Biochemical Journal 297, 163–173. https://doi.org/10.1042/BJ2970163

Ishida, Y., Agata, Y., Shibahara, K., Honjo, T., 1992. Induced expression of PD-1, a novel member of the immunoglobulin gene superfamily, upon programmed cell death. EMBO J 11, 3887–3895. https://doi.org/10.1002/j.1460-2075.1992.tb05481.x

Iwashima, M., Irving, B.A., van Oers, N.S.C., Chan, A.C., Weiss, A., 1994. Sequential Interactions of the TCR with Two Distinct Cytoplasmic Tyrosine Kinases. Science (1979) 193, 4279–4282. https://doi.org/10.1126/SCIENCE.7509083

Jacobs, S.R., Herman, C.E., MacIver, N.J., Wofford, J.A., Wieman, H.L., Hammen, J.J., Rathmell, J.C., 2008. Glucose Uptake Is Limiting in T Cell Activation and Requires CD28-Mediated Akt-Dependent and Independent Pathways. The Journal of Immunology 180, 4476–4486. https://doi.org/10.4049/JIMMUNOL.180.7.4476

Jenkins, E., Körbel, M., O'Brien-Ball, C., McColl, J., Chen, K.Y., Kotowski, M., Humphrey, J., Lippert, A.H., Brouwer, H., Santos, A.M., Lee, S.F., Davis, S.J., Klenerman, D., 2023. Antigen discrimination by T cells relies on size-constrained microvillar contact. Nature Communications 2023 14:1 14, 1–21. https://doi.org/10.1038/s41467-023-36855-9

Jenkins, M.K., Schwartz, R.H., 1987. Antigen presentation by chemically modified splenocytes induces antigen-specific T cell unresponsiveness in vitro and in vivo. Journal of Experimental Medicine 165, 302–319. https://doi.org/10.1084/JEM.165.2.302

Jenkins, M.R., Stinchcombe, J.C., Au-yeung, B.B., Asano, Y., Ritter, A.T., Weiss, A., Griffiths, G.M., 2014. Distinct structural and catalytic roles for Zap70 in formation of the immunological synapse in CTL 1–21. https://doi.org/10.7554/eLife.01310

Jung, Y., Riven, I., Feigelson, S.W., Kartvelishvily, E., Tohya, K., Miyasaka, M., Alon, R., Haran, G., 2016. Three-dimensional localization of T-cell receptors in relation to microvilli using a combination of superresolution microscopies. Proc Natl Acad Sci U S A 113, E5916–E5924. https://doi.org/10.1073/PNAS.1605399113/

Kaizuka, Y., Douglass, A.D., Vardhana, S., Dustin, M.L., Vale, R.D., 2009. The coreceptor CD2 uses plasma membrane microdomains to transduce signals in T cells. Journal of Cell Biology 185, 521–534. https://doi.org/10.1083/jcb.200809136

Kalia, V., Yuzefpolskiy, Y., Vegaraju, A., Xiao, H., Baumann, F., Jatav, S., Church, C., Prlic, M., Jha, A., Nghiem, P., Riddell, S., Sarkar, S., 2021. Metabolic regulation by PD-1 signaling promotes long-lived quiescent CD8 T cell memory in mice. Sci Transl Med 13. https://doi.org/10.1126/SCITRANSLMED.ABA6006/

Kamphorst, A.O., Wieland, A., Nasti, T., Yang, S., Zhang, R., Barber, D.L., Konieczny, B.T., Daugherty, C.Z., Koenig, L., Yu, K., Sica, G.L., Sharpe, A.H., Freeman, G.J., Blazar, B.R., Turka, L.A., Owonikoko, T.K., Pillai, R.N., Ramalingam, S.S., Araki, K., Ahmed, R., 2017. Rescue of exhausted CD8 T cells by PD-1-targeted therapies is CD28-dependent. Science (1979) 355, 1423–1427. https://doi.org/10.1126/science.aaf0683

Kanchanawong, P., Shtengel, G., Pasapera, A.M., Ramko, E.B., Davidson, M.W., Hess, H.F., Waterman, C.M., 2010. Nanoscale architecture of integrin-based cell adhesions. Nature 2010 468:7323 468, 580–584. https://doi.org/10.1038/nature09621

Kanellos, G., Frame, M.C., 2016. Cellular functions of the ADF/cofilin family at a glance. J Cell Sci 129, 3211–3218. https://doi.org/10.1242/JCS.187849/260148

Keir, M.E., Butte, M.J., Freeman, G.J., Sharpe, A.H., 2008. PD-1 and Its Ligands in Tolerance and Immunity. https://doi.org/10.1146/annurev.immunol.26.021607.090331

Kelly, B., O'Neill, L.A.J., 2015. Metabolic reprogramming in macrophages and dendritic cells in innate immunity. Cell Research 2015 25:7 25, 771–784. https://doi.org/10.1038/cr.2015.68

Kim, H.R., Mun, Y.V., Lee, K.S., Park, Y.J., Park, J.S., Park, J.H., Jeon, B.N., Kim, C.H., Jun, Y., Hyun, Y.M., Kim, M., Lee, S.M., Park, C.S., Im, S.H., Jun, C.D., 2018. T cell microvilli

constitute immunological synaptosomes that carry messages to antigen-presenting cells. Nature Communications 2018 9:1 9, 1–19. https://doi.org/10.1038/s41467-018-06090-8

Kinter, A.L., Godbout, E.J., McNally, J.P., Sereti, I., Roby, G.A., O'Shea, M.A., Fauci, A.S., 2008. The Common γ-Chain Cytokines IL-2, IL-7, IL-15, and IL-21 Induce the Expression of Programmed Death-1 and Its Ligands. The Journal of Immunology 181, 6738–6746. https://doi.org/10.4049/JIMMUNOL.181.10.6738

Kishore, M., Cheung, K.C.P., Fu, H., Bonacina, F., Wang, G., Coe, D., Ward, E.J., Colamatteo, A., Jangani, M., Baragetti, A., Matarese, G., Smith, D.M., Haas, R., Mauro, C., Wraith, D.C., Okkenhaug, K., Catapano, A.L., De Rosa, V., Norata, G.D., Marelli-Berg, F.M., 2017. Regulatory T Cell Migration Is Dependent on Glucokinase-Mediated Glycolysis. Immunity 47, 875-889.e10. https://doi.org/10.1016/J.IMMUNI.2017.10.017

Kong, K.F., Yokosuka, T., Canonigo-Balancio, A.J., Isakov, N., Saito, T., Altman, A., 2011. A motif in the V3 domain of the kinase PKC-θ determines its localization in the immunological synapse and functions in T cells via association with CD28. Nature Immunology 2011 12:11 12, 1105–1112. https://doi.org/10.1038/ni.2120

Kostense, S., Ogg, G.S., Manting, E.H., Gillespie, G., Joling, J., Vandenberghe, K., Veenhof, E.Z., Van Baarle, D., Jurriaans, S., Mich`, M., Klein, M.R., Miedema, F., 2001. High viral burden in the presence of major HIV-specific CD8 + T cell expansions: evidence for impaired CTL effector function. European Journal of Immunology 31, 677–686. https://doi.org/10.1002/1521-4141

Krueger, J., Rudd, C.E., 2017. Two Strings in One Bow: PD-1 Negatively Regulates via Co-receptor CD28 on T Cells. Immunity 46, 529–531. https://doi.org/10.1016/j.immuni.2017.04.003

Kuchnir Fygenson, D., Flyvbjerg, H., Sneppen, K., Libchaber, A., Leibler, S., 1995. Spontaneous nucleation of microtubules. Phys Rev E 51, 5058. https://doi.org/10.1103/PhysRevE.51.5058

Kuhn, J.R., Poenie, M., 2002. Dynamic polarization of the microtubule cytoskeleton during CTL-mediated killing. Immunity 16, 111–121. https://doi.org/10.1016/S1074-7613(02)00262-5

Kumagai, S., Togashi, Y., Kamada, T., Sugiyama, E., Nishinakamura, H., Takeuchi, Y., Vitaly, K., Itahashi, K., Maeda, Y., Matsui, S., Shibahara, T., Yamashita, Y., Irie, T., Tsuge, A., Fukuoka, S., Kawazoe, A., Udagawa, H., Kirita, K., Aokage, K., Ishii, G., Kuwata, T., Nakama, K., Kawazu, M., Ueno, T., Yamazaki, N., Goto, K., Tsuboi, M., Mano, H., Doi, T., Shitara, K., Nishikawa, H., 2020. The PD-1 expression balance between effector and regulatory T cells predicts the clinical efficacy of PD-1 blockade therapies. Nat Immunol. https://doi.org/10.1038/s41590-020-0769-3

Kumari, S., Depoil, D., Martinelli, R., Judokusumo, E., Carmona, G., Gertler, F.B., Kam, L.C., Carman, C. V., Burkhardt, J.K., Irvine, D.J., Dustin, M.L., 2015. Actin foci facilitate activation of the phospholipase C-γ in primary T lymphocytes via the WASP pathway. Elife 2015, 1–31. https://doi.org/10.7554/eLife.04953

Kumari, S., Mak, M., Poh, Y., Tohme, M., Watson, N., Melo, M., Janssen, E., Dustin, M., Geha, R., Irvine, D.J., 2020. Cytoskeletal tension actively sustains the migratory T-cell synaptic contact. EMBO J 1–18. https://doi.org/10.15252/embj.2019102783

Kumari, S., Vardhana, S., Cammer, M., Curado, S., Santos, L., Sheetz, M.P., Dustin, M.L., 2012. T lymphocyte myosin IIA is required for maturation of the immunological synapse. Front Immunol 3, 230. https://doi.org/10.3389/FIMMU.2012.00230

Kupfer, A., Dennert, G., 1984. Reorientation of the microtubule-organizing center and the Golgi apparatus in cloned cytotoxic lymphocytes triggered by binding to lysable target cells. The Journal of Immunology 133, 2762–2766. https://doi.org/10.4049/JIMMUNOL.133.5.2762

Kurowska, M., Goudin, N., Nehme, N.T., Court, M., Garin, J., Fischer, A., de Saint Basile, G., Ménasché, G., 2012. Terminal transport of lytic granules to the immune synapse is mediated by the kinesin-1/Slp3/Rab27a complex. Blood 119, 3879–3889. https://doi.org/10.1182/BLOOD-2011-09-382556

Lagarrigue, F., Kim, C., Ginsberg, M.H., 2016. The Rap1-RIAM-talin axis of integrin activation and blood cell function. Blood 128, 479–487. https://doi.org/10.1182/BLOOD-2015-12-638700

Latchman, Y., Wood, C.R., Chernova, T., Chaudhary, D., Borde, M., Chernova, I., Iwai, Y., Long, A.J., Brown, J.A., Nunes, R., Greenfield, E.A., Bourque, K., Boussiotis, V.A., Carter, L.L., Carreno, B.M., Malenkovich, N., Nishimura, H., Okazaki, T., Honjo, T., Sharpe, A.H., Freeman, G.J., 2001. PD-L2 is a second ligand for PD-1 and inhibits T cell activation. Nature Immunology 2001 2:3 2, 261–268. https://doi.org/10.1038/85330

Lau, C.-I., Barbarulo, A., Solanki, A., Saldaña, J.I., Crompton, T., Lau, C.-I., Barbarulo, A., Solanki, A., Saldaña, J.I., Crompton, T., 2017. The kinesin motor protein Kif7 is required for T-cell development and normal MHC expression on thymic epithelial cells (TEC) in the thymus. Oncotarget 8, 24163–24176. https://doi.org/10.18632/ONCOTARGET.15241

Le Floc'h, A., Huse, M., 2015. Molecular mechanisms and functional implications of polarized actin remodeling at the T cell immunological synapse. Cellular and Molecular Life Sciences 72, 537–556. https://doi.org/10.1007/S00018-014-1760-7

Lebensohn, A.M., Kirschner, M.W., 2009. Activation of the WAVE Complex by Coincident Signals Controls Actin Assembly. Mol Cell 36, 512–524. https://doi.org/10.1016/J.MOLCEL.2009.10.024

Lee, M.S., Glassman, C.R., Deshpande, N.R., Badgandi, H.B., Parrish, H.L., Uttamapinant, C., Stawski, P.S., Ting, A.Y., Kuhns, M.S., 2015. A Mechanical Switch Couples T Cell Receptor Triggering to the Cytoplasmic Juxtamembrane Regions of CD3ζζ. Immunity 43, 227–239. https://doi.org/10.1016/J.IMMUNI.2015.06.018

Lee, P.P., Yee, C., Savage, P.A., Fong, L., Brockstedt, D., Weber, J.S., Johnson, D., Swetter, S., Thompson, J., Greenberg, P.D., Roederer, M., Davis, M.M., 1999. Characterization of circulating T cells specific for tumor-associated antigens in melanoma patients. Nature Medicine 1999 5:6 5, 677–685. https://doi.org/10.1038/9525

Lekka, M., Gnanachandran, K., Kubiak, A., Zieliński, T., Zemła, J., 2021. Traction force microscopy – Measuring the forces exerted by cells. Micron 150. https://doi.org/10.1016/J.MICRON.2021.103138

Li, C.W., Lim, S.O., Chung, E.M., Kim, Y.S., Park, A.H., Yao, J., Cha, J.H., Xia, W., Chan, L.C., Kim, T., Chang, S.S., Lee, H.H., Chou, C.K., Liu, Y.L., Yeh, H.C., Perillo, E.P., Dunn, A.K., Kuo, C.W., Khoo, K.H., Hsu, J.L., Wu, Y., Hsu, J.M., Yamaguchi, H., Huang, T.H., Sahin, A.A., Hortobagyi, G.N., Yoo, S.S., Hung, M.C., 2018. Eradication of Triple-Negative Breast Cancer Cells by Targeting Glycosylated PD-L1. Cancer Cell 33, 187-201.e10. https://doi.org/10.1016/J.CCELL.2018.01.009

Li, C.W., Lim, S.O., Xia, W., Lee, H.H., Chan, L.C., Kuo, C.W., Khoo, K.H., Chang, S.S., Cha, J.H., Kim, T., Hsu, J.L., Wu, Y., Hsu, J.M., Yamaguchi, H., Ding, Q., Wang, Y., Yao, J., Lee, C.C., Wu, H.J., Sahin, A.A., Allison, J.P., Yu, D., Hortobagyi, G.N., Hung, M.C., 2016. Glycosylation and stabilization of programmed death ligand-1 suppresses T-cell activity. Nature Communications 2016 7:1 7, 1–11. https://doi.org/10.1038/ncomms12632

Li, K., Yuan, Z., Lyu, J., Ahn, E., Davis, S.J., Ahmed, R., Zhu, C., 2021. PD-1 suppresses TCR-CD8 cooperativity during T-cell antigen recognition. Nat Commun 12, 1–13. https://doi.org/10.1038/s41467-021-22965-9

Li, Y.-C., Chen, B.-M., Wu, P.-C., Cheng, T.-L., Kao, L.-S., Tao, M.-H., Lieber, A., Roffler, S.R., 2010. Cutting Edge: Mechanical Forces Acting on T Cells Immobilized via the TCR Complex Can Trigger TCR Signaling. The Journal of Immunology 184, 5959–5963. https://doi.org/10.4049/JIMMUNOL.0900775

Liang, S.C., Latchman, Y.E., Buhlmann, J.E., Tomczak, M.F., Horwitz, B.H., Freeman, G.J., Sharpe, A.H., 2003. Regulation of PD-1, PD-L1, and PD-L2 expression during normal and

autoimmune responses. Eur J Immunol 33, 2706–2716. https://doi.org/10.1002/EJI.200324228

Lim, T.S., Chew, V., Sieow, J.L., Goh, S., Yeong, J.P.S., Soon, A.L., Ricciardi-Castagnoli, P., 2016. PD-1 expression on dendritic cells suppresses CD8+ T cell function and antitumor immunity. Oncoimmunology 5. https://doi.org/10.1080/2162402X.2015.1085146

Lin, D.Y.W., Tanaka, Y., Iwasaki, M., Gittis, A.G., Su, H.P., Mikami, B., Okazaki, T., Honjo, T., Minato, N., Garboczi, D.N., 2008. The PD-1/PD-L1 complex resembles the antigen-binding Fv domains of antibodies and T cell receptors. Proc Natl Acad Sci U S A 105, 3011–3016. https://doi.org/10.1073/pnas.0712278105

Linsley, P.S., Ledbetter, J.A., 2003. The Role of the CD28 Receptor During T Cell Responses to Antigen. Annual Review of Immunology 11, 191–212. https://doi.org/10.1146/ANNUREV.IY.11.040193.001203

Liu, B., Chen, W., Evavold, B.D., Zhu, C., 2014. Accumulation of Dynamic Catch Bonds between TCR and Agonist Peptide-MHC Triggers T Cell Signaling. Cell 157, 357–368. https://doi.org/10.1016/J.CELL.2014.02.053

Liu, X., Kapoor, T.M., Chen, J.K., Huse, M., 2013. Diacylglycerol promotes centrosome polarization in T cells via reciprocal localization of dynein and myosin II. PNAS 110, 11976–11981. https://doi.org/10.1073/pnas.1306180110

Locard-Paulet, M., Voisinne, G., Froment, C., Menoita, M.G., Ounoughene, Y., Girard, L., Gregoire, C., Mori, D., Martinez, M., Luche, H., Garin, J., Malissen, M., Burlet-Schiltz, O., Malissen, B., Peredo, A.G. de, Roncagalli, R., 2020. LymphoAtlas: a dynamic and integrated phosphoproteomic resource of TCR signaling in primary T cells reveals ITSN2 as a regulator of effector functions. Mol Syst Biol 16, e9524. https://doi.org/10.15252/MSB.20209524

Lomakin, A.J., Lee, K.C., Han, S.J., Bui, D.A., Davidson, M., Mogilner, A., Danuser, G., 2015. Competition for actin between two distinct F-actin networks defines a bistable switch for cell polarization. Nature Cell Biology 2015 17:11 17, 1435–1445. https://doi.org/10.1038/ncb3246

Lötscher, J., Martí i Líndez, A.A., Kirchhammer, N., Cribioli, E., Giordano Attianese, G.M.P., Trefny, M.P., Lenz, M., Rothschild, S.I., Strati, P., Künzli, M., Lotter, C., Schenk, S.H., Dehio, P., Löliger, J., Litzler, L., Schreiner, D., Koch, V., Page, N., Lee, D., Grählert, J., Kuzmin, D., Burgener, A.V., Merkler, D., Pless, M., Balmer, M.L., Reith, W., Huwyler, J., Irving, M., King, C.G., Zippelius, A., Hess, C., 2022. Magnesium sensing via LFA-1 regulates CD8+ T cell effector function. Cell 185, 585-602.e29. https://doi.org/10.1016/j.cell.2021.12.039

Luther, M.A., Lee, J.C., 1986. The role of phosphorylation in the interaction of rabbit muscle phosphofructokinase with F-actin. Journal of Biological Chemistry 261, 1753–1759. https://doi.org/10.1016/s0021-9258(17)36003-9

Macintyre, A.N., Gerriets, V.A., Nichols, A.G., Michalek, R.D., Rudolph, M.C., Deoliveira, D., Anderson, S.M., Abel, E.D., Chen, B.J., Hale, L.P., Rathmell, J.C., 2014. The Glucose Transporter Glut1 Is Selectively Essential for CD4 T Cell Activation and Effector Function. Cell Metab 20, 61–72. https://doi.org/10.1016/J.CMET.2014.05.004

MacIver, N.J., Blagih, J., Saucillo, D.C., Tonelli, L., Griss, T., Rathmell, J.C., Jones, R.G., 2011. The Liver Kinase B1 Is a Central Regulator of T Cell Development, Activation, and Metabolism. The Journal of Immunology 187, 4187–4198. https://doi.org/10.4049/JIMMUNOL.1100367

Marasco, M., Berteotti, A., Weyershaeuser, J., Thorausch, N., Sikorska, J., Krausze, J., Brandt, H.J., Kirkpatrick, J., Rios, P., Schamel, W.W., Köhn, M., Carlomagno, T., 2020. Molecular mechanism of SHP2 activation by PD-1 stimulation. Sci Adv 6. https://doi.org/10.1126/SCIADV.AAY4458

Martin, P.J., Ledbetter, J.A., Morishita, Y., June, C.H., Beatty, P.G., Hansen, J.A., 1986. A 44 kilodalton cell surface homodimer regulates interleukin 2 production by activated human T lymphocytes. The Journal of Immunology 136, 3282–3287. https://doi.org/10.4049/JIMMUNOL.136.9.3282

Martín-Cófreces, N.B., Robles-Valero, J., Cabrero, J.R., Mittelbrunn, M., Gordón-Alonso, M., Sung, C.H., Alarcón, B., Vázquez, J., Sánchez-Madrid, F., 2008. MTOC translocation modulates IS formation and controls sustained T cell signaling. Journal of Cell Biology 182, 951–962. https://doi.org/10.1083/JCB.200801014

Mckeithan, T.W., 1995. Kinetic proofreading in T-cell receptor signal transduction. Proceedings of the National Academy of Sciences 92, 5042–5046. https://doi.org/10.1073/PNAS.92.11.5042

Mempel, T.R., Henrickson, S.E., von Andrian, U.H., 2004. T-cell priming by dendritic cells in lymph nodes occurs in three distinct phases. Nature 427, 154–159. https://doi.org/10.1038/NATURE02238

Meng, X., Liu, Xiwei, Guo, X., Jiang, S., Chen, T., Hu, Z., Liu, H., Bai, Y., Xue, M., Hu, R., Sun, S. cong, Liu, Xiaolong, Zhou, P., Huang, X., Wei, L., Yang, W., Xu, C., 2018. FBXO38 mediates PD-1 ubiquitination and regulates anti-tumour immunity of T cells. Nature 2018 564:7734 564, 130–135. https://doi.org/10.1038/s41586-018-0756-0

Menk, A. V., Scharping, N.E., Moreci, R.S., Zeng, X., Guy, C., Salvatore, S., Bae, H., Xie, J., Young, H.A., Wendell, S.G., Delgoffe, G.M., 2018. Early TCR Signaling Induces Rapid Aerobic Glycolysis Enabling Distinct Acute T Cell Effector Functions. Cell Rep 22, 1509–1521. https://doi.org/10.1016/j.celrep.2018.01.040

Michalek, R.D., Gerriets, V.A., Jacobs, S.R., Macintyre, A.N., MacIver, N.J., Mason, E.F., Sullivan, S.A., Nichols, A.G., Rathmell, J.C., 2011. Cutting Edge: Distinct Glycolytic and Lipid Oxidative Metabolic Programs Are Essential for Effector and Regulatory CD4+ T Cell Subsets. The Journal of Immunology 186, 3299–3303. https://doi.org/10.4049/JIMMUNOL.1003613

Mizuno, R., Sugiura, D., Shimizu, K., Maruhashi, T., Watada, M., Okazaki, I. mi, Okazaki, T., 2019. PD-1 primarily targets TCR signal in the inhibition of functional T cell activation. Front Immunol 10, 630. https://doi.org/10.3389/FIMMU.2019.00630

Monks, C.R.F., Freiberg, B.A., Kupfer, H., Sciaky, N., Kupfer, A., 1998. Three-dimensional segregation of supramolecular activation clusters in T cells. Nature 1998 395:6697 395, 82–86. https://doi.org/10.1038/25764

Moritz, M., Braunfeld, M.B., Guénebaut, V., Heuser, J., Agard, D.A., 2000. Structure of the γ-tubulin ring complex: a template for microtubule nucleation. Nature Cell Biology 2000 2:6 2, 365–370. https://doi.org/10.1038/35014058

Mullins, R.D., Heuser, J.A., Pollard, T.D., 1998. The interaction of Arp2/3 complex with actin: Nucleation, high affinity pointed end capping, and formation of branching networks of filaments. Proc Natl Acad Sci U S A 95, 6181–6186. https://doi.org/10.1073/PNAS.95.11.6181

Murugesan, S., Hong, J., Yi, J., Li, D., Beach, J.R., Shao, L., Meinhardt, J., Madison, G., Wu, X., Betzig, E., Hammer, J.A., 2016. Formin-generated actomyosin arcs propel t cell receptor microcluster movement at the immune synapse. Journal of Cell Biology 215, 383–399. https://doi.org/10.1083/jcb.201603080

Na, S., Collin, O., Chowdhury, F., Tay, B., Ouyang, M., Wang, Y., Wang, N., 2008. Rapid signal transduction in living cells is a unique feature of mechanotransduction. Proc Natl Acad Sci U S A 105, 6626–6631. https://doi.org/10.1073/PNAS.0711704105

Nakazawa, A., Dotan, I., Brimnes, J., Allez, M., Shao, L., Tsushima, F., Azuma, M., Mayer, L., 2004. The Expression and Function of Costimulatory Molecules B7h and B7-H1 on Colonic Epithelial Cells. https://doi.org/10.1053/j.gastro.2004.02.004

Nasi, M., Troiano, L., Lugli, E., Pinti, M., Ferraresi, R., Monterastelli, E., Mussi, C., Salvioli, G., Franceschi, C., Cossarizza, A., 2006. Thymic output and functionality of the IL-7/IL-7

receptor system in centenarians: implications for the neolymphogenesis at the limit of human life. Aging Cell 5, 167–175. https://doi.org/10.1111/J.1474-9726.2006.00204.X

Neel, B.G., Gu, H., Pao, L., 2003. The 'Shp'ing news: SH2 domain-containing tyrosine phosphatases in cell signaling. Trends Biochem Sci 28, 284–293. https://doi.org/10.1016/S0968-0004(03)00091-4

Nguyen, K., Sylvain, N.R., Bunnell, S.C., 2008. T Cell Costimulation via the Integrin VLA-4 Inhibits the Actin-Dependent Centralization of Signaling Microclusters Containing the Adaptor SLP-76. Immunity 28, 810–821. https://doi.org/10.1016/J.IMMUNI.2008.04.019

Nieminen, M., Henttinen, T., Merinen, M., Marttila-Ichihara, F., Eriksson, J.E., Jalkanen, S., 2006. Vimentin function in lymphocyte adhesion and transcellular migration. Nature Cell Biology 2006 8:2 8, 156–162. https://doi.org/10.1038/NCB1355

Nishimura, H., Agata, Y., Kawasaki, A., Sato, M., Imamura, S., Minato, N., Yagita, H., Nakano, T., Honjo, T., 1996. Developmentally regulated expression of the PD-1 protein on the surface of double-negative (CD4–CD8–) thymocytes. Int Immunol 8, 773–780. https://doi.org/10.1093/INTIMM/8.5.773

Nishimura, H., Honjo, T., Minato, N., 2000. Facilitation of β Selection and Modification of Positive Selection in the Thymus of Pd-1–Deficient Mice. Journal of Experimental Medicine 191, 891–898. https://doi.org/10.1084/JEM.191.5.891

Nishimura, H., Nose, M., Hiai, H., Minato, N., Honjo, T., 1999. Development of lupus-like autoimmune diseases by disruption of the PD-1 gene encoding an ITIM motif-carrying immunoreceptor. Immunity 11, 141–151. https://doi.org/10.1016/S1074-7613(00)80089-8

Norcross, M.A., 1984. A synaptic basis for T-lymphocyte activation. Ann Inst Pasteur Immunol (1985) 135, 113–134. https://doi.org/10.1016/S0769-2625(84)81105-8

Obeidy, P., Ju, L.A., Oehlers, S.H., Zulkhernain, N.S., Lee, Q., Galeano Niño, J.L., Kwan, R.Y.Q., Tikoo, S., Cavanagh, L.L., Mrass, P., Cook, A.J.L., Jackson, S.P., Biro, M., Roediger, B., Sixt, M., Weninger, W., 2020. Partial loss of actin nucleator actin-related protein 2/3 activity triggers blebbing in primary T lymphocytes. Immunol Cell Biol 98, 93–113. https://doi.org/10.1111/imcb.12304

Okada, M., Chikuma, S., Kondo, T., Hibino, S., Machiyama, H., Yokosuka, T., Nakano, M., Yoshimura, A., 2017. Blockage of Core Fucosylation Reduces Cell-Surface Expression of PD-1 and Promotes Anti-tumor Immune Responses of T Cells. Cell Rep 20, 1017–1028. https://doi.org/10.1016/J.CELREP.2017.07.027

Okazaki, T., Maeda, A., Nishimura, H., Kurosaki, T., Honjo, T., 2001. PD-1 immunoreceptor inhibits B cell receptor-mediated signaling by recruiting src homology 2-domain-containing

tyrosine phosphatase 2 to phosphotyrosine. Proceedings of the National Academy of Sciences 98, 13866–13871. https://doi.org/10.1073/PNAS.231486598

Ouporov, I. V., Knull, H.R., Thomasson, K.A., 1999. Brownian Dynamics Simulations of Interactions between Aldolase and G- or F-Actin. Biophys J 76, 17–27. https://doi.org/10.1016/S0006-3495(99)77174-2

Padrick, S.B., Doolittle, L.K., Brautigam, C.A., King, D.S., Rosen, M.K., 2011. Arp2/3 complex is bound and activated by two WASP proteins. Proc Natl Acad Sci U S A 108, E472–E479. https://doi.org/10.1073/PNAS.1100236108

Patsoukis, N., Bardhan, K., Chatterjee, P., Sari, D., Liu, B., Bell, L.N., Karoly, E.D., Freeman, G.J., Petkova, V., Seth, P., Li, L., Boussiotis, V.A., 2015. PD-1 alters T-cell metabolic reprogramming by inhibiting glycolysis and promoting lipolysis and fatty acid oxidation. Nat Commun 6. https://doi.org/10.1038/ncomms7692

Patsoukis, N., Duke-Cohan, J.S., Chaudhri, A., Aksoylar, H.I., Wang, Q., Council, A., Berg, A., Freeman, G.J., Boussiotis, V.A., 2020. Interaction of SHP-2 SH2 domains with PD-1 ITSM induces PD-1 dimerization and SHP-2 activation. Commun Biol 3, 1–13. https://doi.org/10.1038/s42003-020-0845-0

Patsoukis, N., Sari, D., Boussiotis, V.A., 2012. PD-1 inhibits T cell proliferation by upregulating p27 and p15 and suppressing Cdc25A. Cell Cycle 11, 4305–4309. https://doi.org/10.4161/cc.22135

Pernas, L., Scorrano, L., 2016. Mito-Morphosis: Mitochondrial Fusion, Fission, and Cristae Remodeling as Key Mediators of Cellular Function. https://doi.org/10.1146/annurev-physiol-021115-105011 78, 505–531. https://doi.org/10.1146/ANNUREV-PHYSIOL-021115-105011

Pollard, T.D., 2016. Actin and Actin-Binding Proteins. Cold Spring Harb Perspect Biol 8. https://doi.org/10.1101/CSHPERSPECT.A018226

Presotto, D., Erdes, E., Duong, M.N., Allard, M., Regamey, P.O., Quadroni, M., Doucey, M.A., Rufer, N., Hebeisen, M., 2017. Fine-Tuning of Optimal TCR Signaling in Tumor-Redirected CD8 T Cells by Distinct TCR Affinity-Mediated Mechanisms. Front Immunol 8, 1564. https://doi.org/10.3389/FIMMU.2017.01564

Probst, H.C., McCoy, K., Okazaki, T., Honjo, T., van den Broek, M., 2005. Resting dendritic cells induce peripheral CD8+ T cell tolerance through PD-1 and CTLA-4. Nature Immunology 2005 6:3 6, 280–286. https://doi.org/10.1038/NI1165

Quann, E.J., Merino, E., Furuta, T., Huse, M., 2009. Localized diacylglycerol drives the polarization of the microtubule-organizing center in T cells. Nature Immunology 2009 10:6 10, 627–635. https://doi.org/10.1038/NI.1734

Quintana, A., Schwindling, C., Wenning, A.S., Becherer, U., Rettig, J., Schwarz, E.C., Hoth, M., 2007. T cell activation requires mitochondrial translocation to the immunological synapse. Proc Natl Acad Sci U S A 104, 14418–14423. https://doi.org/10.1073/PNAS.0703126104

Raab, M., Pfister, S., Rudd, C.E., 2001. CD28 signaling via VAV/SLP-76 adaptors: Regulation of cytokine transcription independent of TCR ligation. Immunity 15, 921–933. https://doi.org/10.1016/S1074-7613(01)00248-5

Randzavola, L.O., Strege, K., Juzans, M., Asano, Y., Stinchcombe, J.C., Gawden-Bone, C.M., Seaman, M.N., Kuijpers, T.W., Griffiths, G.M., 2019. Loss of ARPC1B impairs cytotoxic T lymphocyte maintenance and cytolytic activity. J Clin Invest. https://doi.org/10.1172/JCI129388

Rathmell, J.C., Heiden, M.G.V., Harris, M.H., Frauwirth, K.A., Thompson, C.B., 2000. In the Absence of Extrinsic Signals, Nutrient Utilization by Lymphocytes Is Insufficient to Maintain Either Cell Size or Viability. Mol Cell 6, 683–692. https://doi.org/10.1016/S1097-2765(00)00066-6

Reignat, S., Webster, G.J.M., Brown, D., Ogg, G.S., King, A., Seneviratne, S.L., Dusheiko, G., Williams, R., Maini, M.K., Bertoletti, A., 2002. Escaping High Viral Load Exhaustion CD8 Cells with Altered Tetramer Binding in Chronic Hepatitis B Virus Infection. Journal of Experimental Medicine 195, 1089–1101. https://doi.org/10.1084/JEM.20011723

Reth, M., 1989. Antigen receptor tail clue. Nature 1989 338:6214 338, 383–384. https://doi.org/10.1038/338383b0

Rich, P.R., 2003. The molecular machinery of Keilin's respiratory chain. Biochem Soc Trans 31, 1095–1105. https://doi.org/10.1042/BST0311095

Ritter, A.T., Asano, Y., Stinchcombe, J.C., Dieckmann, N.M.G., Chen, B.C., Gawden-Bone, C., van Engelenburg, S., Legant, W., Gao, L., Davidson, M.W., Betzig, E., Lippincott-Schwartz, J., Griffiths, G.M., 2015. Actin Depletion Initiates Events Leading to Granule Secretion at the Immunological Synapse. Immunity 42, 864–876. https://doi.org/10.1016/j.immuni.2015.04.013

Ritter, A.T., Kapnick, S.M., Murugesan, S., Schwartzberg, P.L., Griffiths, G.M., Lippincott-Schwartz, J., 2017. Cortical actin recovery at the immunological synapse leads to termination of lytic granule secretion in cytotoxic T lymphocytes. Proc Natl Acad Sci U S A 114, E6585–E6594. https://doi.org/10.1073/pnas.1710751114

Rizvi, S.A., Neidt, E.M., Cui, J., Feiger, Z., Skau, C.T., Gardel, M.L., Kozmin, S.A., Kovar, D.R., 2009. Identification and Characterization of a Small Molecule Inhibitor of Formin-Mediated Actin Assembly. Chem Biol 16, 1158–1168. https://doi.org/10.1016/J.CHEMBIOL.2009.10.006

Robert, C., Long, G. V., Brady, B., Dutriaux, C., Maio, M., Mortier, L., Hassel, J.C., Rutkowski, P., McNeil, C., Kalinka-Warzocha, E., Savage, K.J., Hernberg, M.M., Lebbé, C., Charles, J., Mihalcioiu, C., Chiarion-Sileni, V., Mauch, C., Cognetti, F., Arance, A., Schmidt, H., Schadendorf, D., Gogas, H., Lundgren-Eriksson, L., Horak, C., Sharkey, B., Waxman, I.M., Atkinson, V., Ascierto, P.A., 2015. Nivolumab in Previously Untreated Melanoma without BRAF Mutation. New England Journal of Medicine 372, 320–330. https://doi.org/10.1056/NEJMOA1412082

Roberts, S.J., Somero, G.N., 1989. Properties of the interaction between phosphofructokinase and actin. Arch Biochem Biophys 269, 284–294. https://doi.org/10.1016/0003-9861(89)90110-0

Roberts, S.J., Somero, G.N., 1987. Binding of Phosphofructokinase to Filamentous Actin1. Biochemistry 26, 3437–3442.

Roh, W., Chen, P.L., Reuben, A., Spencer, C.N., Prieto, P.A., Miller, J.P., Gopalakrishnan, V., Wang, F., Cooper, Z.A., Reddy, S.M., Gumbs, C., Little, L., Chang, Q., Chen, W.S., Wani, K., De Macedo, M.P., Chen, E., Austin-Breneman, J.L., Jiang, H., Roszik, J., Tetzlaff, M.T., Davies, M.A., Gershenwald, J.E., Tawbi, H., Lazar, A.J., Hwu, P., Hwu, W.J., Diab, A., Glitza, I.C., Patel, S.P., Woodman, S.E., Amaria, R.N., Prieto, V.G., Hu, J., Sharma, P., Allison, J.P., Chin, L., Zhang, J., Wargo, J.A., Futreal, P.A., 2017. Integrated molecular analysis of tumor biopsies on sequential CTLA-4 and PD-1 blockade reveals markers of response and resistance. Sci Transl Med 9. https://doi.org/10.1126/SCITRANSLMED.AAH3560

Roncagalli, R., Cucchetti, M., Jarmuzynski, N., Grégoire, C., Bergot, E., Audebert, S., Baudelet, E., Menoita, M.G., Joachim, A., Durand, S., Suchanek, M., Fiore, F., Zhang, L., Liang, Y., Camoin, L., Malissen, M., Malissen, B., 2016. The scaffolding function of the RLTPR protein explains its essential role for CD28 co-stimulation in mouse and human T cells. J Exp Med 213, 2437. https://doi.org/10.1084/JEM.20160579

Rosskopf, S., Jahn-Schmid, B., Schmetterer, K.G., Zlabinger, G.J., Steinberger, P., 2018. PD-1 has a unique capacity to inhibit allergen-specific human CD4+ T cell responses. Sci Rep 8. https://doi.org/10.1038/S41598-018-31757-Z

Rota, G., Niogret, C., Dang, A.T., Barros, C.R., Fonta, N.P., Alfei, F., Morgado, L., Zehn, D., Birchmeier, W., Vivier, E., Guarda, G., 2018. Shp-2 Is Dispensable for Establishing T Cell

Exhaustion and for PD-1 Signaling In Vivo. Cell Rep 23, 39–49. https://doi.org/10.1016/j.celrep.2018.03.026

Roybal, K.T., Buck, T.E., Ruan, X., Cho, B.H., Clark, D.J., Ambler, R., Tunbridge, H.M., Zhang, J., Verkade, P., Wülfing, C., Murphy, R.F., 2016. Computational spatiotemporal analysis identifies WAVE2 and cofilin as joint regulators of costimulation-mediated T cell actin dynamics. Sci Signal 9. https://doi.org/10.1126/SCISIGNAL.AAD4149

Russo, E., Lemaître, F., Eatrice Corre, B., Chikina, A.S., Langa-Vives, F., Bousso, P., 2022. SPICE-Met: profiling and imaging energy metabolism at the single-cell level using a fluorescent reporter mouse. EMBO J 41, e111528. https://doi.org/10.15252/EMBJ.2022111528

Salazar-Fontana, L.I., Barr, V., Samelson, L.E., Bierer, B.E., 2003. CD28 Engagement Promotes Actin Polymerization Through the Activation of the Small Rho GTPase Cdc42 in Human T Cells. The Journal of Immunology 171, 2225–2232. https://doi.org/10.4049/JIMMUNOL.171.5.2225

Samelson, L.E., Patel, M.D., Weissman, A.M., Harford, J.B., Klausner, R.D., 1986. Antigen activation of murine T cells induces tyrosine phosphorylation of a polypeptide associated with the T cell antigen receptor. Cell 46, 1083–1090. https://doi.org/10.1016/0092-8674(86)90708-7

Sanchez, E., Liu, X., Huse, M., 2019. Actin clearance promotes polarized dynein accumulation at the immunological synapse. PLoS One 14. https://doi.org/10.1371/JOURNAL.PONE.0210377

Sanderson, C.J., Glauert, A.M., 1979. The mechanism of T-cell mediated cytotoxicity. VI. T-cell projections and their role in target cell killing. Immunology 36, 119–29.

Sawicka, A., Babataheri, A., Dogniaux, S., Barakat, A.I., Gonzalez-Rodriguez, D., Hivroz, C., Husson, J., 2017. Micropipette force probe to quantify single-cell force generation: application to T-cell activation. Mol Biol Cell 28, 3229–3239. https://doi.org/10.1091/MBC.E17-06-0385

Schindler, R., Weichselsdorfer, E., Wagner, O., Bereiter-Hahn, J., 2011. Aldolase-localization in cultured cells: Cell-type and substrate-specific regulation of cytoskeletal associations. Biochemistry and Cell Biology 79, 719–728. https://doi.org/10.1139/O01-137

Schmitz, H.D., Bereiter-Hahn, J., 2002. Glyceraldehyde-3-phosphate dehydrogenase associates with actin filaments in serum deprived NIH 3T3 cells only. Cell Biol Int 26, 155–164. https://doi.org/10.1006/CBIR.2001.0819

Schneider, H., Rudd, C.E., 2008. CD28 and Grb-2, relative to Gads or Grap, preferentially co-operate with Vav1 in the activation of NFAT/AP-1 transcription. Biochem Biophys Res Commun 369, 616–621. https://doi.org/10.1016/J.BBRC.2008.02.068

Sedwick, C.E., Morgan, M.M., Jusino, L., Cannon, J.L., Miller, J., Burkhardt, J.K., 1999. TCR, LFA-1, and CD28 Play Unique and Complementary Roles in Signaling T Cell Cytoskeletal Reorganization. The Journal of Immunology 162, 1367–1375. https://doi.org/10.4049/JIMMUNOL.162.3.1367

Selvaraj, P., Plunkett, M.L., Dustin, M., Sanders, M.E., Shaw, S., Springer, T.A., 1987. The T lymphocyte glycoprotein CD2 binds the cell surface ligand LFA-3. Nature 1987 326:6111 326, 400–403. https://doi.org/10.1038/326400A0

Sena, L.A., Li, S., Jairaman, A., Prakriya, M., Ezponda, T., Hildeman, D.A., Wang, C.-R., Schumacker, P.T., Licht, J.D., Perlman, H., Bryce, P.J., Chandel, N.S., 2013. Article Mitochondria Are Required for Antigen-Specific T Cell Activation through Reactive Oxygen Species Signaling. https://doi.org/10.1016/j.immuni.2012.10.020

Shah, K., Al-Haidari, A., Sun, J., Kazi, J.U., 2021. T cell receptor (TCR) signaling in health and disease. Signal Transduction and Targeted Therapy 2021 6:1 6, 1–26. https://doi.org/10.1038/s41392-021-00823-w

Sharma, P., Wagner, K., Wolchok, J.D., Allison, J.P., 2011. Novel cancer immunotherapy agents with survival benefit: recent successes and next steps. Nature Reviews Cancer 2011 11:11 11, 805–812. https://doi.org/10.1038/nrc3153

Shaw, A.S., Dustin, M.L., 1997. Making the T Cell Receptor Go the Distance: A Topological View of T Cell Activation. Immunity 6, 361–369. https://doi.org/10.1016/S1074-7613(00)80279-4

Sheppard, K.A., Fitz, L.J., Lee, J.M., Benander, C., George, J.A., Wooters, J., Qiu, Y., Jussif, J.M., Carter, L.L., Wood, C.R., Chaudhary, D., 2004. PD-1 inhibits T-cell receptor induced phosphorylation of the ZAP70/CD3ζ signalosome and downstream signaling to PKCθ. FEBS Lett 574, 37–41. https://doi.org/10.1016/j.febslet.2004.07.083

Shi, L.Z., Wang, R., Huang, G., Vogel, P., Neale, G., Green, D.R., Chi, H., 2011. HIF1α–dependent glycolytic pathway orchestrates a metabolic checkpoint for the differentiation of TH17 and Treg cells. Journal of Experimental Medicine 208, 1367–1376. https://doi.org/10.1084/JEM.20110278

Shinohara, T., Taniwaki, M., Ishida, Y., Kawaichi, M., Honjo, T., 1994. Structure and Chromosomal Localization of the Human PD-1 Gene (PDCD1). Genomics 23, 704–706. https://doi.org/10.1006/GENO.1994.1562

Sims, T.N., Soos, T.J., Xenias, H.S., Dubin-Thaler, B., Hofman, J.M., Waite, J.C., Cameron, T.O., Thomas, V.K., Varma, R., Wiggins, C.H., Sheetz, M.P., Littman, D.R., Dustin, M.L., 2007. Opposing Effects of PKCθ and WASp on Symmetry Breaking and Relocation of the Immunological Synapse. Cell 129, 773–785. https://doi.org/10.1016/J.CELL.2007.03.037

Siokis, A., Robert, P.A., Demetriou, P., Dustin, M.L., Meyer-Hermann, M., 2018. F-Actin-Driven CD28-CD80 Localization in the Immune Synapse. Cell Rep 24, 1151–1162. https://doi.org/10.1016/J.CELREP.2018.06.114

Soerens, A.G., Künzli, M., Quarnstrom, C.F., Scott, M.C., Swanson, L., Locquiao, J., Ghoneim, H.E., Zehn, D., Youngblood, B., Vezys, V., Masopust, D., 2023. Functional T cells are capable of supernumerary cell division and longevity. Nature 2023 614:7949 614, 762–766. https://doi.org/10.1038/s41586-022-05626-9

Spinelli, J.B., Haigis, M.C., 2018. The multifaceted contributions of mitochondria to cellular metabolism. Nature Cell Biology 2018 20:7 20, 745–754. https://doi.org/10.1038/s41556-018-0124-1

Spitaler, M., Emslie, E., Wood, C.D., Cantrell, D., 2006. Diacylglycerol and Protein Kinase D Localization during T Lymphocyte Activation. Immunity 24, 535–546. https://doi.org/10.1016/J.IMMUNI.2006.02.013

Springer, T.A., 1990. Adhesion receptors of the immune system.

Springer, T.A., Dustin, M.L., 2012. Integrin inside-out signaling and the immunological synapse. Curr Opin Cell Biol 24, 107–115. https://doi.org/10.1016/J.CEB.2011.10.004

Stinchcombe, J.C., Majorovits, E., Bossi, G., Fuller, S., Griffiths, G.M., 2006. Centrosome polarization delivers secretory granules to the immunological synapse. Nature 443, 462–465. https://doi.org/10.1038/nature05071

Strauss, L., Mahmoud, M.A.A., Weaver, J.D., Tijaro-Ovalle, N.M., Christofides, A., Wang, Q., Pal, R., Yuan, M., Asara, J., Patsoukis, N., Boussiotis, V.A., 2020. Targeted deletion of PD-1 in myeloid cells induces antitumor immunity. Sci Immunol 5, 1–15. https://doi.org/10.1126/sciimmunol.aay1863

Stringari, C., Cinquin, A., Cinquin, O., Digman, M.A., Donovan, P.J., Gratton, E., 2011. Phasor approach to fluorescence lifetime microscopy distinguishes different metabolic states of germ cells in a live tissue. Proc Natl Acad Sci U S A 108, 13582–13587. https://doi.org/10.1073/PNAS.1108161108/SUPPL_FILE/PNAS.201108161SI.PDF

Swamy, M., Beck-Garcia, K., Beck-Garcia, E., Hartl, F.A., Morath, A., Yousefi, O.S., Dopfer, E.P., Molnár, E., Schulze, A.K., Blanco, R., Borroto, A., Martín-Blanco, N., Alarcon, B., Höfer, T., Minguet, S., Schamel, W.W.A., 2016. A Cholesterol-Based Allostery Model of T Cell Receptor

Phosphorylation. Immunity 44, 1091–1101. https://doi.org/10.1016/J.IMMUNI.2016.04.011

Symons, M., Derry, J.M.J., Karlak, B., Jiang, S., Lemahieu, V., McCormick, F., Francke, U., Abo, A., 1996. Wiskott–Aldrich Syndrome Protein, a Novel Effector for the GTPase CDC42Hs, Is Implicated in Actin Polymerization. Cell 84, 723–734. https://doi.org/10.1016/S0092-8674(00)81050-8

Tamás, P., Hawley, S.A., Clarke, R.G., Mustard, K.J., Green, K., Hardie, D.G., Cantrell, D.A., 2006. Regulation of the energy sensor AMP-activated protein kinase by antigen receptor and Ca2+ in T lymphocytes. Journal of Experimental Medicine 203, 1665–1670. https://doi.org/10.1084/JEM.20052469

Tamzalit, F., Tran, D., Jin, W., Boyko, V., Bazzi, H., Kepecs, A., Kam, L.C., Anderson, K. v., Huse, M., 2020. Centrioles control the capacity, but not the specificity, of cytotoxic T cell killing. Proceedings of the National Academy of Sciences 201913220. https://doi.org/10.1073/pnas.1913220117

Tamzalit, F., Wang, M.S., Jin, W., Tello-Lafoz, M., Boyko, V., Heddleston, J.M., Black, C.T., Kam, L.C., Huse, M., 2019. Interfacial actin protrusions mechanically enhance killing by cytotoxic T cells. Sci Immunol 4. https://doi.org/10.1126/sciimmunol.aav5445

Taube, J.M., Anders, R.A., Young, G.D., Xu, H., Sharma, R., McMiller, T.L., Chen, S., Klein, A.P., Pardoll, D.M., Topalian, S.L., Chen, L., 2012. Colocalization of inflammatory response with B7-H1 expression in human melanocytic lesions supports an adaptive resistance mechanism of immune escape. Sci Transl Med 4. https://doi.org/10.1126/SCITRANSLMED.3003689

Tavano, R., Contento, R.L., Baranda, S.J., Soligo, M., Tuosto, L., Manes, S., Viola, A., 2006. CD28 interaction with filamin-A controls lipid raft accumulation at the T-cell immunological synapse. Nature Cell Biology 2006 8:11 8, 1270–1276. https://doi.org/10.1038/ncb1492

Terawaki, S., Chikuma, S., Shibayama, S., Hayashi, T., Yoshida, T., Okazaki, T., Honjo, T., 2011. IFN-α Directly Promotes Programmed Cell Death-1 Transcription and Limits the Duration of T Cell-Mediated Immunity. The Journal of Immunology 186, 2772–2779. https://doi.org/10.4049/JIMMUNOL.1003208

Thompson, S.B., Sandor, A.M., Lui, V., Chung, J.W., Waldman, M.M., Long, R.A., Estin, M.L., Matsuda, J.L., Friedman, R.S., Jacobelli, J., 2020. Formin-like 1 mediates effector t cell trafficking to inflammatory sites to enable t cell-mediated autoimmunity. Elife 9, 1–27. https://doi.org/10.7554/ELIFE.58046

Thumkeo, D., Katsura, Y., Nishimura, Y., Kanchanawong, P., Tohyama, K., Ishizaki, T., Kitajima, S., Takahashi, C., Hirata, T., Watanabe, N., Krummel, M.F., Narumiya, S., 2020. MDia1/3-

dependent actin polymerization spatiotemporally controls LAT phosphorylation by Zap70 at the immune synapse. Sci Adv 6. https://doi.org/10.1126/sciadv.aay2432

Tocheva, A.S., Peled, M., Strazza, M., Adam, K.R., Lerrer, S., Nayak, S., Azoulay-Alfaguter, I., Foster, C.J.R., Philips, E.A., Neel, B.G., Ueberheide, B., Mor, A., 2020. Quantitative phosphoproteomic analysis reveals involvement of PD-1 in multiple T cell functions. Journal of Biological Chemistry 295, 18036–18050. https://doi.org/10.1074/jbc.RA120.014745

Topalian, S.L., Hodi, F.S., Brahmer, J.R., Gettinger, S.N., Smith, D.C., McDermott, D.F., Powderly, J.D., Carvajal, R.D., Sosman, J.A., Atkins, M.B., Leming, P.D., Spigel, D.R., Antonia, S.J., Horn, L., Drake, C.G., Pardoll, D.M., Chen, L., Sharfman, W.H., Anders, R.A., Taube, J.M., McMiller, T.L., Xu, H., Korman, A.J., Jure-Kunkel, M., Agrawal, S., McDonald, D., Kollia, G.D., Gupta, A., Wigginton, J.M., Sznol, M., 2012. Safety, Activity, and Immune Correlates of Anti–PD-1 Antibody in Cancer. New England Journal of Medicine 366, 2443–2454. https://doi.org/10.1056/NEJMOA1200690

Tseng, S.-Y., Waite, J.C., Liu, M., Vardhana, S., Dustin, M.L., 2008. T Cell-Dendritic Cell Immunological Synapses Contain TCR-dependent CD28-CD80 Clusters That Recruit Protein Kinase Cθ. The Journal of Immunology 181, 4852–4863. https://doi.org/10.4049/JIMMUNOL.181.7.4852

Tumeh, P.C., Harview, C.L., Yearley, J.H., Shintaku, I.P., Taylor, E.J.M., Robert, L., Chmielowski, B., Spasic, M., Henry, G., Ciobanu, V., West, A.N., Carmona, M., Kivork, C., Seja, E., Cherry, G., Gutierrez, A.J., Grogan, T.R., Mateus, C., Tomasic, G., Glaspy, J.A., Emerson, R.O., Robins, H., Pierce, R.H., Elashoff, D.A., Robert, C., Ribas, A., 2014. PD-1 blockade induces responses by inhibiting adaptive immune resistance. Nature 515, 568–571. https://doi.org/10.1038/nature13954

Valitutti, S., 2012. The serial engagement model 17 years after: Fromtcr triggering to immunotherapy. Front Immunol 3, 272. https://doi.org/10.3389/FIMMU.2012.00272

Valitutti, S., Miller, S., Cella, M., Padovan, E., Lanzavecchia, A., 1995. Serial triggering of many T-cell receptors by a few peptide-MHC complexes. Nature 375, 148–151. https://doi.org/10.1038/375148A0

Van Der Merwe, P.A., Davis, S.J., Shaw, A.S., Dustin, M.L., 2000. Cytoskeletal polarization and redistribution of cell-surface molecules during T cell antigen recognition. Semin Immunol 12, 5–21. https://doi.org/10.1006/SMIM.2000.0203

Varma, R., Campi, G., Yokosuka, T., Saito, T., Dustin, M.L., 2006. T Cell Receptor-Proximal Signals Are Sustained in Peripheral Microclusters and Terminated in the Central

Supramolecular Activation Cluster. Immunity 25, 117–127. https://doi.org/10.1016/J.IMMUNI.2006.04.010

von Andrian, U.H., Hasslen, S.R., Nelson, R.D., Erlandsen, S.L., Butcher, E.C., 1995. A central role for microvillous receptor presentation in leukocyte adhesion under flow. Cell 82, 989–999. https://doi.org/10.1016/0092-8674(95)90278-3

Wang, M.S., Hu, Y., Sanchez, E.E., Xie, X., Roy, N.H., de Jesus, M., Winer, B.Y., Zale, E.A., Jin, W., Sachar, C., Lee, J.H., Hong, Y., Kim, M., Kam, L.C., Salaita, K., Huse, M., 2022. Mechanically active integrins target lytic secretion at the immune synapse to facilitate cellular cytotoxicity. Nat Commun 13, 3222. https://doi.org/10.1038/s41467-022-30809-3

Warburg, O., 1956. On the origin of cancer cells. Science (1979) 123, 309–314. https://doi.org/10.1126/SCIENCE.123.3191.309

Warburg, O., Gawehn, K., Geissler, A.W., 1958. Metabolism of leukocytes. Z Naturforsch B 13B, 515–6.

Wei, F., Zhong, S., Ma, Z., Kong, H., Medvec, A., Ahmed, R., Freeman, G.J., Krogsgaard, M., Riley, J.L., 2013. Strength of PD-1 signaling differentially affects T-cell effector functions. Proc Natl Acad Sci U S A 110, 2–11. https://doi.org/10.1073/pnas.1305394110

Wherry, E.J., 2011. T cell exhaustion. Nature Immunology 2011 12:6 12, 492–499. https://doi.org/10.1038/ni.2035

Wherry, E.J., Ahmed, R., 2004. Memory CD8 T-Cell Differentiation during Viral Infection. J Virol 78, 5535–5545. https://doi.org/10.1128/JVI.78.11.5535-5545.2004

Wiedemann, A., Depoil, D., Faroudi, M., Valitutti, S., 2006. Cytotoxic T lymphocytes kill multiple targets simultaneously via spatiotemporal uncoupling of lytic and stimulatory synapses. Proc Natl Acad Sci U S A 103, 10985–10990. https://doi.org/10.1073/PNAS.0600651103

Williams, M.A., Bevan, M.J., 2007. Effector and Memory CTL Differentiation. Annual Review of Immunology 25, 171–192. https://doi.org/10.1146/annurev.immunol.25.022106.141548

Wu, X., Zhang, H., Xing, Q., Cui, J., Li, J., Li, Y., Tan, Y., Wang, S., 2014. PD-1+ CD8+ T cells are exhausted in tumours and functional in draining lymph nodes of colorectal cancer patients. British Journal of Cancer 2014 111:7 111, 1391–1399. https://doi.org/10.1038/bjc.2014.416

Xu, H., Li, X., Liu, D., Li, J., Zhang, X., Chen, X., Hou, S., Peng, L., Xu, C., Liu, W., Zhang, L., Qi, H., 2013. Follicular T-helper cell recruitment governed by bystander B cells and ICOS-driven motility. Nature 2013 496:7446 496, 523–527. https://doi.org/10.1038/nature12058

Xu, X., Hou, B., Fulzele, A., Masubuchi, T., Zhao, Y., Wu, Z., Hu, Y., Jiang, Y., Ma, Y., Wang, H., Bennett, E.J., Fu, G., Hui, E., 2020. PD-1 and BTLA regulate T cell signaling differentially

and only partially through SHP1 and SHP2. Journal of Cell Biology 219. https://doi.org/10.1083/JCB.201905085

Yang, C., Svitkina, T., 2011. Filopodia initiation. Cell Adh Migr 5, 402–408. https://doi.org/10.4161/CAM.5.5.16971

Yao, S., Wang, S., Zhu, Y., Luo, L., Zhu, G., Flies, S., Xu, H., Ruff, W., Broadwater, M., Choi, I.H., Tamada, K., Chen, L., 2009. PD-1 on dendritic cells impedes innate immunity against bacterial infection. Blood 113, 5811–5818. https://doi.org/10.1182/BLOOD-2009-02-203141

Yi, J., Wu, X.S., Crites, T., Hammer, J.A., 2012. Actin retrograde flow and actomyosin II arc contraction drive receptor cluster dynamics at the immunological synapse in Jurkat T cells. Mol Biol Cell 23, 834–852. https://doi.org/10.1091/MBC.E11-08-0731

Yokosuka, T., Takamatsu, M., Kobayashi-Imanishi, W., Hashimoto-Tane, A., Azuma, M., Saito, T., 2012. Programmed cell death 1 forms negative costimulatory microclusters that directly inhibit T cell receptor signaling by recruiting phosphatase SHP2. Journal of Experimental Medicine 209, 1201–1217. https://doi.org/10.1084/jem.20112741

Zajac, A.J., Blattman, J.N., Murali-Krishna, K., Sourdive, D.J.D., Suresh, M., Altman, J.D., Ahmed, R., 1998. Viral Immune Evasion Due to Persistence of Activated T Cells Without Effector Function. Journal of Experimental Medicine 188, 2205–2213. https://doi.org/10.1084/JEM.188.12.2205

Zak, K.M., Kitel, R., Przetocka, S., Golik, P., Guzik, K., Musielak, B., Dömling, A., Dubin, G., Holak, T.A., 2015. Structure of the Complex of Human Programmed Death 1, PD-1, and Its Ligand PD-L1. Structure 23, 2341–2348. https://doi.org/10.1016/J.STR.2015.09.010

Zhang, X., Schwartz, J.C.D., Guo, X., Bhatia, S., Cao, E., Chen, L., Zhang, Z.Y., Edidin, M.A., Nathenson, S.G., Almo, S.C., 2004. Structural and Functional Analysis of the Costimulatory Receptor Programmed Death-1. Immunity 20, 337–347. https://doi.org/10.1016/S1074-7613(04)00051-2

Zhang, Y., Shen, H., Liu, H., Feng, H., Liu, Y., Zhu, X., Liu, X., 2017. Arp2/3 complex controls T cell homeostasis by maintaining surface TCR levels via regulating TCR+ endosome trafficking. Scientific Reports 2017 7:1 7, 1–13. https://doi.org/10.1038/S41598-017-08357-4

Zhao, Y., Harrison, D.L., Song, Y., Ji, J., Huang, J., Hui, E., 2018. Antigen-Presenting Cell-Intrinsic PD-1 Neutralizes PD-L1 in cis to Attenuate PD-1 Signaling in T Cells. Cell Rep 24, 379-390.e6. https://doi.org/10.1016/j.celrep.2018.06.054

Zinselmeyer, B.H., Heydari, S., Sacristán, C., Nayak, D., Cammer, M., Herz, J., Cheng, X., Davis, S.J., Dustin, M.L., McGavern, D.B., 2013. PD-1 promotes immune exhaustion by inducing

antiviral T cell motility paralysis. Journal of Experimental Medicine 210, 757–774. https://doi.org/10.1084/jem.20121416

Zucchetti, A.E., Paillon, N., Markova, O., Dogniaux, S., Hivroz, C., Husson, J., 2021. Influence of external forces on actin-dependent T cell protrusions during immune synapse formation. Biol Cell. https://doi.org/10.1111/boc.202000133

# ANNEXES

Les pages suivantes regroupent en annexe les articles auxquels j'ai collaboré durant ma thèse.

Annexe 1 : CTLA4 prohibits T cells from cross-dressing

Annexe 2 : HLA-independent T cell receptors for targeting tumors with low antigen density

Annexe 3 : Influence of external forces on actin-dependent T cell protrusions during immune synapse formation

Annexe 4 : Mechanobiology of antigen-induced T cell arrest

# Annexe 1 : CTLA4 prohibits T cells from cross-dressing

***Journal of Experimental Medicine*, Avril 2023**


**Résumé**

Cet aperçu (*insight*) est paru dans le *Journal of Experimental Medicine* à propos de l'article publié par Xiaozheng Xu et ses collaborateurs intitulé « CTLA4 depletes T cell endogenous and trogocytosed B7 ligands via *cis*-endocytosis ». Dans ce court aperçu, nous rapportons que les auteurs ont mis en évidence que la protéine inhibitrice CTLA4 internalise en *cis* les molécules stimulantes B7 précédemment "grignotées" par les cellules T sur les CPA, et empêche ainsi les interactions T-T stimulantes. Ils ont cherché à déterminer plus précisément si CTLA4 interfère avec CD28 pour réguler la trogocytose et les communications T-T qui s'ensuivent. Ils ont montré que les LT capturent des fragments de membrane plasmique de la CPA contenant les molécules CD80, CD86 et CMH. Cette capture est plus sensible à l'inhibition par les anticorps anti-CD28 que par les anticorps anti-CTLA4. Ces résultats suggèrent que l'acquisition rapide des molécules costimulantes CD80/86 par les cellules T est principalement médiée par la liaison de CD28 plutôt que par celle de CTLA4 lors du contact initial avec les CPA. Une fois les molécules stimulantes de la CPA capturées à l'aide de CD28, CTLA les internalise et les dégrade dans le LT. Les auteurs ont donc pu démontrer une collaboration entre les protéines CD28 et CTLA4 pour capturer et dégrader les molécules de costimulation B7.


**Contribution à l'article**

J'ai participé à la conception de cet aperçu en discutant des résultats présentés dans l'article par les auteurs, puis j'ai commenté, corrigé et modifié le texte. J'ai également effectué la représentation graphique de l'aperçu, illustrant et résumant les résultats principaux de l'article.

JEM Journal of Experimental Medicine

INSIGHTS

# CTLA4 prohibits T cells from cross-dressing

Noémie Paillon[1,2,3] and Claire Hivroz[1,2]

**In this issue of *JEM*, Xiaozheng Xu et al. (2023. *J. Exp. Med.* https://doi.org/10.1084/jem.20221391) report that the inhibitory protein CTLA4 internalizes in cis the B7 stimulatory molecules previously "gnawed" by T cells from antigen-presenting cells (APCs) and in doing so prevents stimulatory T–T interactions.**

CTLA4 is an essential negative regulator induced upon T cell activation that controls immune homeostasis. Whereas a lack of CTLA4 expression induces autoimmunity, its high expression is associated with immunosuppression. Thus, CTLA4 is a major target for immunotherapy, and its blockade by monoclonal antibodies has been used with success to treat cancer patients and overcome tumor-induced immune tolerance (Baumeister et al., 2016). CTLA4 inhibits T cell responses by competing with the CD28 co-stimulatory molecule for their shared ligands of the B7 family, CD80 and CD86. In addition to this direct competition, CTLA4 has also been shown to deplete B7 ligands from the surface of APCs through trans-endocytosis (Baumeister et al., 2016; Qureshi et al., 2011). So far, the proposed mechanism was cell extrinsic, with CTLA4 depleting costimulatory ligands from APCs via trans-endocytosis. Once endocytosed, CTLA4 and its ligands are routed to lysosomes where they are degraded. This is related to the high affinity of CTLA4 for its ligands and the rapid endocytic and recycling behavior of CTLA4 (Qureshi et al., 2012). CD28 has also been shown to induce the depletion of B7 ligands from the APC membranes (Hwang et al., 2000). Although they remained partially resolved, the mechanisms used by CTLA4 and CD28 to deplete B7 ligands seem different. CD28 induces trogocytosis of chunks of plasma membranes containing B7 ligands as well as other molecules such as MHC molecules that are shuttled and exposed to the T cell surface, whereas CTLA4 endocytoses the ligands, which are then degraded (Zenke et al., 2022). Trogocytosis is an active process allowing the transfer of plasma membrane proteins from one cell to another in a cell–cell contact-dependent manner. This applies to immune cells, which form cell–cell interactions called immune synapses where membrane-associated proteins are transferred between cells (Joly and Hudrisier, 2003). This transfer of molecules from the APC to the T cells leads to the cross-dressing of T cells that become proficient to present peptides and co-stimulatory molecules to other T cells.

In their study, Xiaozheng Xu and coworkers addressed the questions of the precise role of CD28 and CTLA4 in T cell cross-dressing and of how CTLA4 regulates T–T communications (Xu et al, 2023). They used CTLA4-expressing Jurkat leukemic T cells or human primary regulatory T cells (Tregs), which naturally express high amounts of CTLA4. The APCs were CD80$^-$/CD86$^-$ Raji B cells expressing fluorescently tagged CD80 or CD86, and the transfer of "material" from the APC to T cells was revealed by confocal and correlative light electron microscopy, as well as by flow cytometry.

Using these models, they showed that T cells capture plasma membrane fragments of the APC containing CD80, CD86, and MHC molecules. This capture was more

Insights from Noémie Paillon and Claire Hivroz.

sensitive to inhibition by anti-CD28 than anti-CTLA4 blocking antibodies. These results suggested that the rapid acquisition of the CD80/86 co-stimulatory molecules by T cells was primarily mediated by CD28 rather than CTLA4 binding during initial contact with APCs. Then, they tested if the cross-dressed T cells could induce T–T activation. Indeed, T cells pre-conditioned with Raji B cells expressing CD80/CD86 were more potent at activating T cells than T cells preconditioned with CD80$^-$/CD86$^-$ Raji B cells. In this assay anti-CTLA4 blocking antibodies enhanced T–T stimulation, suggesting that CTLA4 may control the CD80/86 availability within a T cell population. Indeed, anti-CTLA4 antibodies could block the capture of B7 molecules both in trans, during a T–T interaction, or in cis, by depleting the B7 molecules present on the same cell surface. The authors designed an experiment to test the last hypothesis and showed that CTLA4 induced cis depletion of B7 ligands. They preconditioned Tregs with CD80-GFP$^+$ Raji APCs, purified the GFP$^+$

[1]Institut Curie, Paris Sciences et Lettres University, Inserm U932, Immunity and Cancer, Paris, France; [2]Team Integrative Analysis of T Cell Activation, Paris, France; [3]Université Paris Cité, Paris, France.

Claire Hivroz: claire.hivroz@curie.fr.

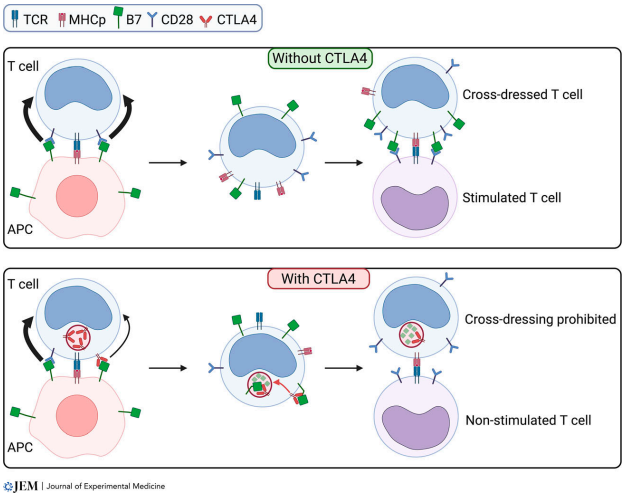


CTLA4-mediated cis-endocytosis of B7 ligands inhibits T–T stimulating interactions. Upper panel: CTLA4-negative T lymphocyte forming an immune synapse with an APC captures B7 and MHC-peptide (MHCp) molecules through CD28 (black bold arrow). This capture is stimulated by TCR triggering. The T cell is cross-dressed with B7 ligands and MHCp and can activate other T cells through T–T interactions. Lower panel: When the T lymphocyte expresses CTLA4, B7 ligands and MHCp are still captured by CD28 (black bold arrow) with a smaller contribution of CTLA4 to B7 capture (small black arrow). The B7 ligands are then cis-endocytosed by CTLA4 and degraded in lysosomal compartments. T–T interactions with these T cells presenting MHCp without CD28 ligands do not induce T cell stimulation. Figure created using Biorender.com.

Tregs, and cultured these cells in the presence of an excess of $CD28^{-/-}$ "filler" cells, to block T–T contacts and CTLA4 trans interactions. Cross-dressed Tregs were depleted of CD80-GFP in the presence of filler cells, but they were not depleted of HLA-DR. This depletion was blocked by anti-CTLA4 but not by anti-CD28 antibodies, revealing that CTLA4-driven depletion of CD80 occurs in cis. This depletion was promoted by TCR stimulation, which induces CTLA4 expression and was also efficient to deplete endogenous CD80 molecules. But what was the fate of the molecules captured in cis by CTLA4? Using confocal and electronic microscopy, the authors revealed a progressive accumulation of CTLA4 at sites of acquired APC-derived fragments and a concomitant accumulation of CD80-GFP within $CTLA4^+$ vesicles. Of note, the authors also showed that the endolysosomal trafficking domain of CTLA4 was necessary for the cis depletion of CD80. See summary in figure.

Altogether, Xu et al. (2023) reveal a new mechanism by which CTLA4-mediated cis-endocytosis depletes CD80/CD86 previously acquired in trans by CD28-mediated trogocytosis.

In this study, no difference was made between CTLA4 targeting of CD80 or CD86. Yet, a recent study has shown that this process results in separate fates for CTLA4 itself. For CD80, CTLA4 remains ligand-bound and traffics via late endosomes and lysosomes. In contrast, once endocytosed, CTLA4 detaches from CD86 and recycles back to the cell surface to allow further trans-endocytosis (Kennedy et al., 2022). Although Xu et al. (2023) looked carefully at the presence of CD80 and CD86 in the endocytic compartments labeled by CTLA4, these compartments were not characterized in terms of intracellular identity. It would be interesting to study if the separate fates reported for the CTLA4-mediated CD80 and CD86 trans-endocytosis also happen for cis-endocytosis of CD80 and CD86. Indeed, recycling of CTLA4 would allow several cycles of depletion and more efficiently support the inhibitory signaling required to maintain tolerance. Moreover, a physical interaction between CD80 and PD-L1 has recently been shown (Sugiura et al., 2019).This interaction takes place predominantly in cis between CD80 and PD-L1 on the same cell (Sugiura et al., 2019), blocking PD-L1 binding to PD-1 but still permitting CD80 interaction with CD28 and CTLA4. It was recently shown that CTLA4-mediated trans-endocytosis of CD80 results in a recovery of PD-L1 availability that is now free to interact with PD-1 and inhibits T cell activation (Kennedy et al., 2023; Tekguc et al., 2021). This CTLA4-mediated regulation of PD-L1 availability might also happen on CD80 cross-dressed $PD\text{-}L1^+$ T cells, switching from stimulatory antigen-presenting T cells into inhibitory T cells.

Another question of interest is whether the CTLA4-mediated cis-endocytosis of CD80/86 only targets molecules that are normally inserted in the plasma membrane or if it can also target CD80/CD86 inserted in a fragment of trogocytosed membrane decorating T cells. If not, the process would first require the fusion of the membranes and then the cis-endocytosis. It would be interesting to study if such fusion events can happen.

This study addresses an important question; it is indeed increasingly appreciated that during activation, T cells acquire APC-derived surface molecules via trogocytosis. One of the important consequences of this is that T cells redisplay APC-derived ligands on their surface and can thereby act as APCs to stimulate other T cells. Such T–T interactions have been implicated in the collective regulation of T cell proliferation and differentiation during immune responses. An antigen-capturing quorum-sensing mechanism has been proposed for $CD4^+$ T cells, whereby as the number of cross-dressed $CD4^+$ T cells increases, they outnumber the APCs, increasing the probability of T–T interactions (Helft et al., 2008). These interactions have been shown to lead to different outcomes such as inhibition of the expansion of antigen-experienced T cells (Helft et al., 2008), differentiation of Th17 (Boccasavia et al., 2021), fratricide killing of $CD8^+$ T cells (Huang et al., 1999), more vigorous restimulation of T helpers, or stronger suppressive activity of Tregs (Zhou et al., 2011). T–T interactions also promote synapse-based cytokine delivery between activating T cells (Sabatos et al., 2008). These trogocytosis-mediated events have also been shown to regulate chimeric

antigen receptors T cell response (Hamieh et al., 2019).

Distinct from the trans-endocytosis model, the T cell-intrinsic model reported by Xu et al. (2023) represents a new mechanism by which CTLA4 limits the amount and time that costimulatory molecules are displayed on the T cell surface. It probably mainly concerns Tregs cells that express high levels of CTLA4 but might also apply to effector T cells that express some CTLA4. Changing the ratio between co-stimulatory and co-inhibitory molecules exposed at the surface of T cells might alter the collective regulation within T cell populations.

What remains is to find a good in vivo model that will allow testing the role of cis-endocytosis of co-stimulatory molecules on T cell responses.

**Acknowledgments**

We want to thank Laurence Bataille for critical reading and discussion.

## References

Baumeister, S.H., et al. 2016. *Annu. Rev. Immunol.* https://doi.org/10.1146/annurev-immunol-032414-112049

Boccasavia, V.L., et al. 2021. *Cell Rep.* https://doi.org/10.1016/j.celrep.2021.108861

Hamieh, M., et al. 2019. *Nature.* https://doi.org/10.1038/s41586-019-1054-1

Helft, J., et al. 2008. *Blood.* https://doi.org/10.1182/blood-2007-09-114389

Huang, J.F., et al. 1999. *Science.* https://doi.org/10.1126/science.286.5441.952

Hwang, I., et al. 2000. *J. Exp. Med.* https://doi.org/10.1084/jem.191.7.1137

Joly, E., and D. Hudrisier. 2003. *Nat. Immunol.* https://doi.org/10.1038/ni0903-815

Kennedy, A., et al. 2023. *EMBO J.* https://doi.org/10.15252/embj.2022111556

Kennedy, A., et al. 2022. *Nature immunol.* https://doi.org/10.1038/s41590-022-01289-w

Qureshi, O.S., et al. 2012. *J. Biol. Chem.* https://doi.org/10.1074/jbc.M111.304329

Qureshi, O.S., et al. 2011. *Science.* https://doi.org/10.1126/science.1202947

Sabatos, C.A., et al. 2008. *Immunity.* https://doi.org/10.1016/j.immuni.2008.05.017

Sugiura, D., et al. 2019. *Science.* https://doi.org/10.1126/science.aav7062

Tekguc, M., et al. . 2021. *Proc. Natl. Acad. Sci. USA.* https://doi.org/10.1073/pnas.2023739118

Xu, X., et al. 2023. *J. Exp. Med.* https://doi.org/10.1084/jem.20221391

Zenke, S., et al. 2022. *Nat. Commun.* https://doi.org/10.1038/s41467-022-34156-1

Zhou, G., et al. 2011. *J. Immunol.* https://doi.org/10.4049/jimmunol.1002917

## Annexe 2 : HLA-independent T cell receptors for targeting tumors with low antigen density

***Nature Medicine*, Février 2022**

**Résumé**

Les récepteurs d'antigènes chimériques (CAR) sont des récepteurs d'antigènes qui déclenchent des réponses immunitaires puissantes. Un échappement tumoral associé à une faible expression de l'antigène cible apparaît comme une limitation potentielle de leur efficacité. Nous éditons ici le locus TRAC dans les cellules T du sang périphérique humain afin d'engager des cibles de surface cellulaire par le biais de leur complexe TCR-CD3 reconfiguré pour utiliser les mêmes chaînes lourdes et légères d'immunoglobulines qu'un CAR apparié. Nous démontrons que ces récepteurs de cellules T indépendants du système HLA (récepteurs HIT) offrent invariablement une sensibilité accrue aux antigènes et assurent la reconnaissance des tumeurs au-delà de ce que les CAR basés sur CD28, la conception la plus sensible à ce jour, peuvent fournir. Nous démontrons que la persistance fonctionnelle des cellules T HIT peut être augmentée par la coexpression constitutive de CD80 et de 4-1BBL. Enfin, nous validons la sensibilité accrue à l'antigène offerte par les récepteurs HIT dans des modèles murins de xénogreffe de leucémie à cellules B et de leucémie myéloïde aiguë, ciblant respectivement CD19 et CD70. Globalement, les récepteurs HIT sont parfaitement adaptés pour cibler des antigènes de surface cellulaire de faible abondance.

**Contribution à l'article**

J'ai participé à cette publication dans le cadre d'une collaboration avec l'équipe de Michel Sadelain (Sloan Kettering Cancer Center, New York City, Etats-Unis).

Concernant le travail expérimental, j'ai pris soin de cultiver les cellules CAR et HIT, ainsi que les cellules NALM6 présentant différentes quantités de CD19 à leur surface, envoyées par l'équipe de M. Sadelain. Concernant les données présentées dans les figures, j'ai généré, analysé et monté les figures suivantes :

- Figure 3 et figure S8 :
    - Formation de conjugués entre des NALM exprimant CD19 à leur surface en grande quantité (NALM6/WT) ou peu de CD19 (NALM6/7) et des lymphocytes T CAR ou HIT (Fig3C-D ; FigS8A)
    - Acquisition des images par microscopie confocale (Fig3C-D, FigS8A)
    - Analyse de l'enrichissement d'actine et des récepteurs CAR/HIT à la synapse immunologique (Fig3C)
    - Analyse de la polarité des lysosomes à la synapse immunologique (Fig3D, FigS8A)

nature medicine

ARTICLES

https://doi.org/10.1038/s41591-021-01621-1

Check for updates

# HLA-independent T cell receptors for targeting tumors with low antigen density

Jorge Mansilla-Soto[1,2,11] ✉, Justin Eyquem[1,2,7,11], Sascha Haubner[1,2], Mohamad Hamieh[1,2], Judith Feucht[1,2,8], Noémie Paillon[3], Andrés Ernesto Zucchetti[3], Zhuoning Li[4], Maria Sjöstrand[1,2], Pieter L. Lindenbergh[1,2], Michelle Saetersmoen[1,2,9], Anton Dobrin[1,2], Mathieu Maurin[3], Archana Iyer[1,2], Andreina Garcia Angus[1,2], Matthew M. Miele[4], Zeguo Zhao[1,2], Theodoros Giavridis[1,2,10], Sjoukje J. C. van der Stegen[1,2], Fella Tamzalit[2], Isabelle Rivière[1,5,6], Morgan Huse[2], Ronald C. Hendrickson[4,6], Claire Hivroz[3] and Michel Sadelain[1,2] ✉

**Chimeric antigen receptors (CARs) are receptors for antigen that direct potent immune responses. Tumor escape associated with low target antigen expression is emerging as one potential limitation of their efficacy. Here we edit the *TRAC* locus in human peripheral blood T cells to engage cell-surface targets through their T cell receptor–CD3 complex reconfigured to utilize the same immunoglobulin heavy and light chains as a matched CAR. We demonstrate that these HLA-independent T cell receptors (HIT receptors) consistently afford high antigen sensitivity and mediate tumor recognition beyond what CD28-based CARs, the most sensitive design to date, can provide. We demonstrate that the functional persistence of HIT T cells can be augmented by constitutive coexpression of CD80 and 4-1BBL. Finally, we validate the increased antigen sensitivity afforded by HIT receptors in xenograft mouse models of B cell leukemia and acute myeloid leukemia, targeting CD19 and CD70, respectively. Overall, HIT receptors are well suited for targeting cell surface antigens of low abundance.**

CARs are synthetic receptors that redirect the specificity and augment the therapeutic potency of T lymphocytes[1]. CARs engage antigen independently of human leukocyte antigen (HLA)[2,3] but only enable sustained T cell proliferation if they are endowed with both activating and costimulatory functions[4,5]. CD19-specific CARs that include either CD28 or 4-1BB costimulatory signaling domains have demonstrated remarkable efficacy in patients with relapsed and refractory acute lymphoblastic leukemia (ALL) or nonHodgkin lymphoma[6–8]. CARs targeting CD22 or BCMA have also elicited major responses in patients with refractory ALL and multiple myeloma (MM), respectively[9–11]. While remission rates have been noticeably elevated in numerous clinical trials, relapses are common[10–16]. One of the several underlying relapse mechanisms is antigen escape[9,10,17–20], which refers to a relapsing tumor that is either negative for the targeted antigen or expresses the latter at a low level. Whereas CAR T cells cannot directly engage tumors with complete antigen loss, the failure to eliminate antigen-low tumors raises questions about the sensitivity of CARs and the minimum antigen density that is required for effective tumor eradication.

Recent studies have determined that all CARs are not equal in terms of their antigen sensitivity. Comparing CARs specific for different antigens, we and others have observed that CD28-based CARs are more sensitive than those incorporating 4-1BB signaling domains in cytotoxicity assays[21–23]. In in vivo models of antigen escape, a CD28-based CAR was more adept to control the relapse of CD19-low ALL than the corresponding 4-1BB CAR[21]. These archetypal CARs contain three activation motifs. The incorporation of three additional immune-based tyrosine activation motifs (ITAMs) into BBz CARs increases the latter's antigen sensitivity, albeit still not matching that of a 28z CAR, while the disruption of ITAMs in 28z CARs diminishes the latter's antigen sensitivity[22]. Under CAR stress test conditions, wherein low T cell doses are purposefully administered to stringently challenge CAR T cells in vivo[21,24–26], CAR T cells generally fail to control leukemia presenting with less than a few thousand CD19 molecules per cell[21], consistent with clinical studies reporting tumor relapses with reduced target antigen expression[10,11,16,27].

Cognizant of the high sensitivity of the T cell receptor (TCR) for HLA–peptide complexes[28,29], we used *TRAC* locus editing[24] to establish in human primary T cells a new antigen receptor structure incorporating into the TCR–CD3 complex the same heavy and light chains as those assembled into a scFv within a corresponding CAR. These receptors, termed HLA-independent TCRs or HIT receptors, are more sensitive than CD28-based CARs and open new prospects for the targeting of low-density antigens.

## Results

**Basic functions of a CD19-specific HIT receptor.** To confer CD19 specificity to the TCR–CD3 complex, we targeted the *TRAC* locus[24]

[1]Center for Cell Engineering, Memorial Sloan Kettering Cancer Center, New York, NY, USA. [2]Immunology Program, Sloan Kettering Institute, New York, NY, USA. [3]Institute Curie, Université PSL, U932 INSERM, Integrative Analysis of T cell Activation Team, Paris, France. [4]Microchemistry and Proteomics Core Laboratory, Sloan Kettering Institute, New York, NY, USA. [5]Cell Therapy and Cell Engineering Facility, Memorial Sloan Kettering Cancer Center, New York, NY, USA. [6]Molecular Pharmacology Program, Memorial Sloan Kettering Cancer Center, New York, NY, USA. [7]Present address: Department of Medicine, Division of Hemato-Oncology, University of California San Francisco, San Francisco, CA, USA. [8]Present address: Cluster of Excellence iFIT, University Children's Hospital Tübingen, Tübingen, Germany. [9]Present address: Department of Cancer Immunology, Institute for Cancer Research, Oslo University Hospital, Oslo, Norway. [10]Present address: Mnemo Therapeutics, New York, NY, USA. [11]These authors contributed equally: Jorge Mansilla-Soto, Justin Eyquem. ✉e-mail: mansillj@mskcc.org; m-sadelain@ski.mskcc.org

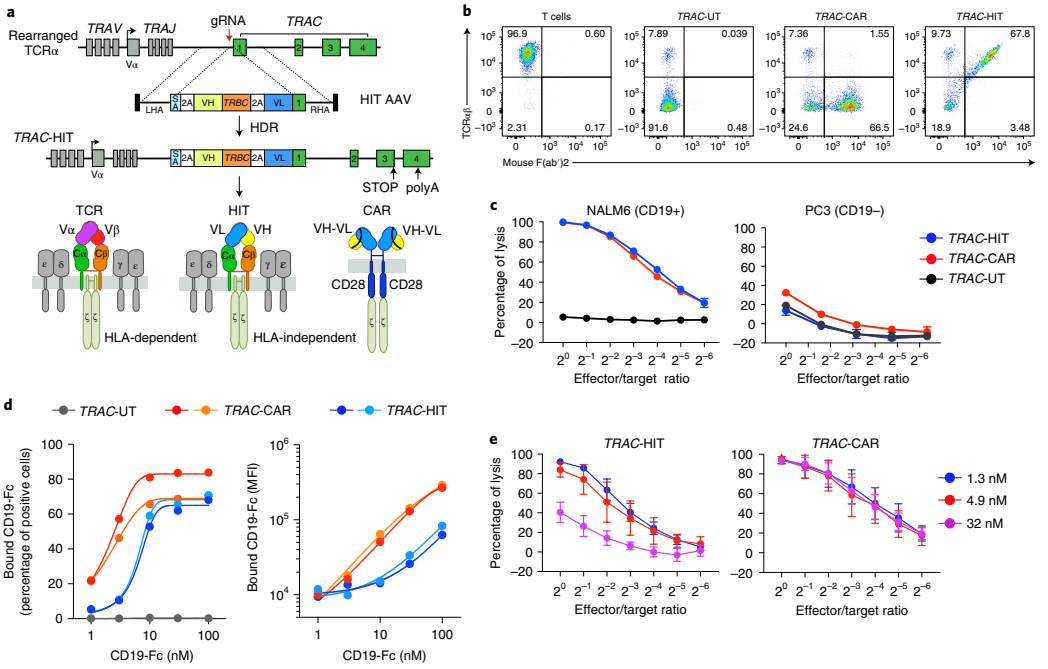


**Fig. 1 | *TRAC* locus editing to create an HLA-independent TCR (HIT receptor) directs TCR–CD3 complex-mediated antigen recognition. a**, Schematic diagram of the targeting strategy to generate a HIT receptor in situ at the *TRAC* locus. The targeting construct (HIT-AAV) contains a splice acceptor, followed by P2A cleaving peptide and the CD19-specifc HIT gene elements (a $V_H$-Cβ gene followed by P2A and the $V_L$ gene), which are joined to the *TRAC* exon1; all flanked by sequences homologous to the *TRAC* locus (left and right homology arm: LHA and RHA). Once integrated, the $V_H$-Cβ and $V_L$-Cα expression is driven by the endogenous TCRα promoter and polyA elements, while TCRα expression is disrupted. $V_H$-Cβ and $V_L$-Cα chains will associate to form the HIT heterodimer. The TCR–CD3 complex is depicted to highlight the similarities and contrast between HIT and TCR. The 19-28z CAR, utilizing the same $V_H$ and $V_L$ elements in the format of a scFv, is also depicted. TRAV: TCR alpha variable region. TRAJ: TCR alpha joining region. SA: Splice acceptor. P2A: *Porcine teschovirus* 2A sequence. **b**, Representative TCRαβ/F(ab')2 flow plot 4 days after transfection of T cells with *TRAC*-targeting CRISPR/Cas9 and HIT or CAR AAV6 transduction. **c**, Cytotoxic activity using an 18-h bioluminescence assay. FFL and CD19-expressing NALM6 (left), or FFL-expressing PC3 (CD19 negative, right) as target cells ($n = 2$ biological independent samples); additional specificity studies are shown in Extended Data Fig. 2. **d**, Binding capacity of HIT and CAR T cells measured by titrating CD19-Fc fusion. *TRAC*-HIT and *TRAC*-CAR T cells from two different donors were incubated with a recombinant human CD19-Fc fusion, which was then detected using an anti-hFc-PE antibody. Left panel: percentage positive cells detected; right panel: mean fluorescent intensity of the bound CD19-Fc. **e**, Representative cytotoxic activity using an 18 h bioluminescence assay, using FFL-expressing NALM6 as target cells ($n = 4$ independent experiments on four healthy donors). CD19-specific *TRAC*-HIT and *TRAC*-CAR T cells were generated using three different binding domains specific to a CD19 epitope but of distinct affinities (1.3, 4.9 and 32 nM). All data are mean ± s.e.m.

in human peripheral blood T cells to reconstruct the antigen-binding domain of the heterodimeric TCR to match that of a CD19 CAR[14]. To generate the HIT receptor (Fig. 1a), the CAR heavy chain sequence was fused to that of the TCR Cβ domain ($V_HCβ$), and the CAR light chain sequence to the genomic Cα sequence ($V_LCα$), thus generating chimeric $V_HCβ$ and $V_LCα$ chains linked by a P2A element (Fig. 1a) under the transcriptional control of endogenous TCR promoter and polyA elements. This genetic modification results in a substituted TCR specificity, replacing the HLA-restricted Vα–Vβ pair with HLA-independent CD19-specific $V_L$–$V_H$ binding domains. The disruption of the endogenous *TRAC* locus ablated cell-surface CD3 expression, which remained undetected when knocking-in the 19-28z CAR[24], but was restored to the cell surface in cells engineered to express $V_HCβ$ and $V_LCα$ (Fig. 1b and Extended Data Fig. 1a). T cells expressing either 19-28z (*TRAC*-CAR) or the $V_HCβ/V_LCα$ heterodimer (*TRAC*-HIT) stained positively with the same polyclonal antibody used to detect the SJ25C1 scFv[30] in the 19-28z CAR[14] (Fig. 1b and Extended Data Fig. 1a,b). *TRAC*-edited T cell populations specifically lysed CD19+ target cells, confirming the formation of an active CD19 HIT receptor, and did not lyse CD19$^-$ target cells (Fig. 1c and Extended Data Fig. 2). Both *TRAC*-HIT and *TRAC*-CAR bound soluble CD19 protein with HIT T cells exhibiting lower overall binding capacity per cell compared to CAR T cells (Fig. 1d). Both CAR and HIT receptors elicited similar cytokine responses upon exposure to NIH/3T3 cells overexpressing CD19 (Extended Data Fig. 3a). Following repeated exposure to antigen, both receptors similarly internalized (Extended Data Fig. 3b) and maintained a similar CD4/CD8 T cell ratio in engineered peripheral blood T cells (Extended Data Fig. 3c).

Recognition of CD19 was not limited to the heavy and light chains of SJ25C1, and was likewise obtained with the variable chains of FMC63, another CD19-specific scFv[13,31] (Extended Data Fig. 1c), further supporting the structural compatibility of antibody and TCR Ig-like domains[32–34]. The HIT structure we report here differs

from other recently reported HLA-independent, CD3-associated receptors[35–38], all of which retain their endogenous clonotypic TCR and thus generate dual-specific T cells. These other receptors either have scFvs fused to CD3 components[35] or interact with the endogenous TCR–CD3 complex[36], or are composed of IgV-TCRC chimeras comprising γδ[37] or mouse αβTCR[38] constant regions to avoid mispairing with endogenous TCR chains. Importantly, the HIT receptor design endows the T cell with a single specificity.

As the SJ25C1 and FMC63 CD19-specific scFvs have a similar, high affinity, we investigated an additional set of three CD19-specific scFvs, all specific for the same epitope but differing in their affinity (1.3, 4.9 and 32 nM, respectively). The paired *TRAC*-HIT and *TRAC*-CAR T cells similarly bound to soluble CD19 (Extended Data Fig. 4), but while the three 28z CARs directed comparable cytolysis of NALM6, the HIT receptors showed diminishing cytolysis with decreasing affinity (Fig. 1e). This observation suggested that HIT receptors, which do not benefit from CD4 or CD8 coreceptors like typical TCRs, may operate differently from TCRs, which prompted us to evaluate whether HIT T cells could respond to low antigen levels.

**HIT receptors provide greater antigen sensitivity than CARs.** To assess the antigen sensitivity of HIT receptors, we established a panel of NALM6 variants stably expressing a range of CD19 levels (Extended Data Fig. 4a–d). A striking difference between *TRAC*-HIT and *TRAC*-CAR T cells promptly emerged, showing that HIT T cells could lyse clones that 19-28z CAR T cells could not (Fig. 2). Both receptors were similarly effective against NALM6 and NALM6 variants expressing within tenfold less CD19 than wild-type (WT) NALM6 (Fig. 2a,b and Extended Data Fig. 4f,g). As CD19 levels further decreased, *TRAC*-CAR T cells no longer killed their target, in contrast to *TRAC*-HIT T cells (Fig. 2a,b and Extended Data Fig. 5f,g). We next quantified CD19 levels in a subset of NALM6 variants, identifying clones with 20–2,000 CD19 molecules, well below the count of 27,000 measured in parental NALM6 (Fig. 2c,d and Extended Data Fig. 5e). *TRAC*-CAR T cells could effectively lyse NALM6 variants down to ~200 molecules per cell but not less, while *TRAC*-HIT T cells still effectively lysed clones with ~20 molecules per cell (Fig. 2e). The same results were obtained with the $V_H$ and $V_L$ chains from either SJ25C1 (refs. [14]) or FMC63 (ref. [13,31]; Extended Data Fig. 5f). Notably, we compared HIT receptor sensitivity to the more sensitive 28z CARs (Majzner et al.[22], Priceman et al.[23] and Extended Data Fig. 5g).

This observation was extended with another HIT receptor specific for CD22, constructed with variable chains taken from a CD22-specific CAR[9,21]. Both the CD19 and CD22 HIT receptors lysed MM1S (Extended Data Fig. 6), a BCMA-positive myeloma cell line displaying very low-level expression of those two antigens (confirmed by fluorescence-activated cell sorting (FACS) analysis and quantitative mass spectrometry) (Extended Data Fig. 6a,b), but not the CD19 or CD22-specific CARs. In contrast, both BCMA-specific CAR[10,21] and HIT receptors lysed MM1S (Extended Data Fig. 6c and Extended Data Fig. 2). Altogether, these results confirm that HIT receptors endow T cells with greater antigen sensitivity than canonical CARs.

This conclusion is further supported by the cytokine response of *TRAC*-HIT T cells elicited by low antigen density target cells. Expression of interferon-γ (IFN-γ), interleukin-2 (IL-2) and tumor necrosis factor α (TNF-α) was three- to tenfold higher in both CD4 and CD8 T cells upon exposure to NALM6 cells expressing ~20 CD19 molecules per cell, compared to *TRAC*-CAR T cells (Fig. 2f). Above 200 CD19 molecules per cell, *TRAC*-CAR and *TRAC*-HIT T cells showed similar cytokine profiles (Fig. 2f).

We hypothesized that this increased sensitivity of HIT receptors is due to their greater signaling response and measured the phosphorylation of CD3ζ and ZAP70 and downstream ERK1/2 (ref. [39]). HIT-engineered T cells indeed showed greater CD3ζ, ZAP70 and ERK1/2 phosphorylation upon exposure to the low antigen density NALM6/12-4 compared to *TRAC*-CAR T cells (Fig. 2g and Extended Data Fig. 7). This difference was even greater with antigen levels below 200 molecules per cell (NALM6/7), where CAR T cells showed hardly any detectable pERK1/2 upon exposure to the CD19+ cells in contrast to HIT T cells (Fig. 2g and Extended Data Fig. 7). At higher antigen densities (NALM6/WT and NALM6/12-4), *TRAC*-HIT and *TRAC*-CAR T cells showed comparable levels of pERK1/2 and a similar percentage of pERK1/2 positive cells (Fig. 2h and Extended Data Fig. 7). In aggregate, these studies point to a threshold of about 200 CD19 molecules per cell for effective 19-28z CAR-mediated T cell activation in vitro while only ~20 molecules suffice for *TRAC*-HIT T cells.

**HIT T cells display faster degranulation and cytotoxicity.** To gain further insight into the mechanism for the HIT receptor's greater antigen sensitivity, we performed quantitative phosphoproteomic analyses of *TRAC*-HIT T cells when activated with low antigen targets (NALM6/7), comparing their profile to *TRAC*-CAR T cells (Fig. 3a). *TRAC*-HIT T cells showed a higher number of phospho-peptides after a 10-min incubation with NALM6/7 (Fig. 3a), thus providing further support for their greater sensitivity to low antigen levels. Phospho-peptides with a $P<0.05$ ($-\log_{10}>1.3$) detected in two independent experiments with different T cell donors were further analyzed (Fig. 3b). Applying a cutoff $\log_2$ ratio of 0.7, *TRAC*-HIT T cells showed enrichment of a set of phospho-peptides involved in T cell activation and actin remodeling (Fig. 3b). These included signaling molecules such as CD3 epsilon, LAT, GRAP2, AHNAK and SLAMF1 (refs. [40–42]) and proteins involved in actin remodeling (ARPC1B)[43].

These findings prompted us to analyze actin remodeling as well as lysosome localization in *TRAC*-HIT and *TRAC*-CAR T cells when exposed to high and low antigen levels. We specifically quantified the F-actin enrichment and LAMP-1 lysosomes at the immunological synapse (IS) in over 60 NALM6–T cell conjugates (two different T cell donors). We observed no significant difference in F-actin enrichment between HIT and CAR T cells (Fig. 3c and Extended Data Fig. 8a) but found that CAR and HIT localization at the IS are dependent on the antigen level on the target cell (Fig. 3c and Extended Data Fig. 8a). HIT T cells showed a more uniform distribution of LAMP-1 lysosomes at the IS than CAR T cells (variance $P=0.0006$) when incubated with low antigen NALM6/7 (Fig. 3d), but not with high-antigen NALM6 (Extended Data Fig. 8a). We thus hypothesized that HIT T cells would be more proficient at degranulation than CAR T cells when exposed to low antigen levels. We assessed degranulation by measuring CD107a in T cells incubated for 1 h and 4 h with different NALM6 targets. *TRAC*-HIT T cells degranulated faster and significantly more frequently than *TRAC*-CAR T cells when incubated with NALM6 cells expressing ~20 molecules of CD19 (NALM6/7; Fig. 3e and Extended Data Fig. 8b,c). This difference vanished with antigen levels above 200 CD19 molecules (NALM6/12-4 and NALM6/WT; Fig. 3e and Extended Data Fig. 8b,c).

Based on the above observations on phospho-proteomics, lysosome mobilization and degranulation, we predicted that *TRAC*-HIT T cells will be more rapid than *TRAC*-CAR T cells at killing targets with low antigen levels. We therefore measured the time required for target lysis kinetics by HIT and CAR T cells in single-cell conditions (1:1 T cell:target cell in single wells)[21]. *TRAC*-CAR and *TRAC*-HIT T cells displayed similar kinetics when incubated with NALM6 WT and NALM/12-4 targets, but TRAC-HIT T cells were faster when exposed to NALM6/7 (Fig. 3f). Altogether, we conclude that HIT receptors impart increased antigen sensitivity to T cells by, at least in part, enabling greater mobilization and release of lytic granules than CARs in the context of low antigen density.

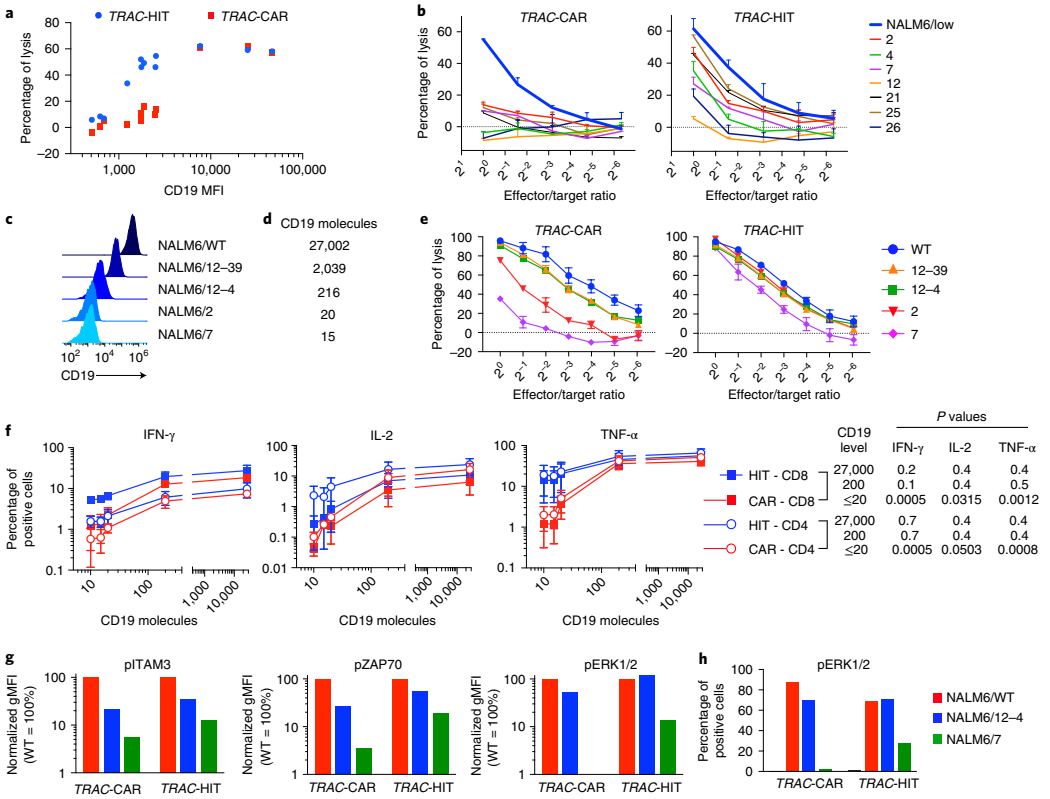


**Fig. 2 | *TRAC*-HIT T cells exhibit increased sensitivity for tumor cells expressing low antigen levels relative to *TRAC*-CAR T cells. a**, Cytotoxic activity using a 4-h bioluminescence assay at a 1:1 ratio of *TRAC*-HIT/*TRAC*-CAR T cells (effectors) and FFL + NALM6 cells expressing different CD19 surface levels (targets). Average killing and mean fluorescent intensity from $n = 2$ independent experiments on two donors. **b**, Representative cytotoxic activity using an 18 h bioluminescence assay, using FFL-expressing NALM6 clones as target cells (clone numbers as in Extended Data Fig. 5b); NALM6/low was used as a positive control; $n = 2$ biological independent samples. **c**, CD19 flow histograms for WT and NALM6 clones expressing decreasing levels of CD19. **d**, Quantification of surface CD19 levels using FACS and PE-calibration beads. NALM6 cells were stained PE-antiCD19 antibody. CD19 gMFIs for NALM6/WT, NALM6/12-39 and NALM6/12-4 were used to determine the number of CD19 molecules per cell using the standard curve obtained with the calibration beads. CD19 gMFIs for NALM6/2, NALM6/7 and NALM6/12 were used to establish a ratio with NALM6/12-4 because their values were outside the linear range of the standard curve. **e**, Cytotoxic activity using an 18-h bioluminescence assay at different effector:target ratios for *TRAC*-HIT/*TRAC*-CAR T cells and FFL + NALM6 cells expressing different CD19 surface levels (panel **c**); $n = 2$ biological independent samples. **f**, Percentage of *TRAC*-HIT or *TRAC*-CAR T cells (both CD4 and CD8 cells) with positive expression of IFN-γ, IL-2 or TNF-α after intracellular staining after coculture with NALM6 clones expressing the indicated levels of CD19. Right, Mann–Whitney *P* values when using NALM6 WT (27,000), NALM6 12-4 (200) and NALM6 12, 7 and 2 (≤20) target cells. $n = 3$ independent experiments on three different T cell donors. **g**,**h**, Levels of phospho-ITAM3, phospho-ZAP70 or phospho-ERK1/2 in *TRAC*-HIT or *TRAC*-CAR T cells when incubated with NALM6 WT, 12-4 or 7 targets at a 1:2 ratio. **g**, Levels are presented as a percentage of the signal detected in T cells incubated with NALM6 WT target. **h**, Percentage of *TRAC*-HIT or *TRAC*-CAR T cells containing phospho-ERK1/2. **g**,**h**, The data presented are representative of two independent experiments using two different T cell healthy donors. Except for **g** and **h** all data are mean ± s.e.m.

**HIT T cells outperform CAR T cells against low antigen tumors.** We investigated the capacity of *TRAC*-HIT T cells to control tumors expressing different antigen levels in vivo. In a 'stress test' setting, wherein we deliberately infuse subcurative T cell doses to quantify and compare T cell potency[21,24,26], we first compared *TRAC*-HIT T cells to first and second-generation[5] *TRAC*-CAR T cells in controlling NALM6, a commonly investigated pre-B acute lymphoblastic leukemia[21,24,26]. As the 28z CAR is more sensitive than BBz, BBzz and 28-1XX CARs[21–23], we focused on 28z CARs for comparison in our in vivo studies. Over the first 3 weeks, *TRAC*-HIT T cells vastly outperformed first-generation CAR T cells (19z1) and strikingly rivaled the second-generation CAR T cells, despite lacking engineered costimulation like the 1928z CAR (Fig. 4a). The gap between *TRAC*-19z1 and CD19 *TRAC*-HIT, which both are activating receptors lacking embedded costimulatory domains, illustrates the greater efficacy of the CD3 complex relative to that of a ζ chain fusion receptor. When targeting a low abundance NALM6 variant (12-4), we observed superior tumor elimination by *TRAC*-HIT T cells, most notably in the first week ($P = 0.002$, Fig. 4b).

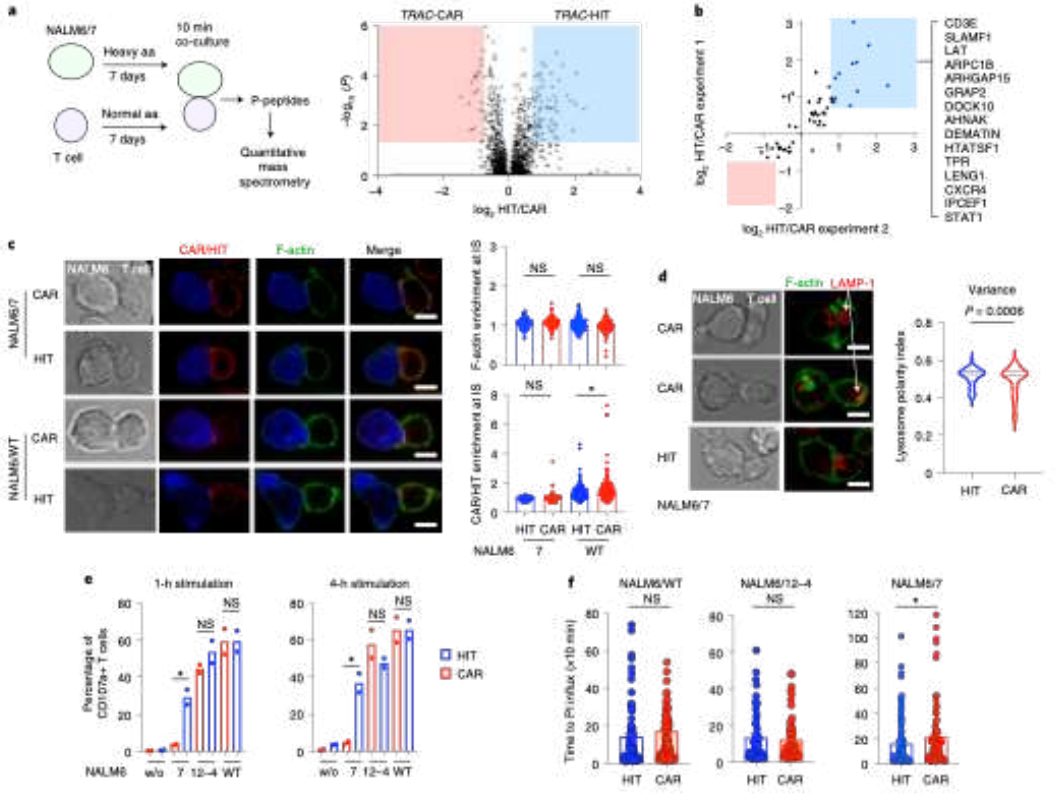


**Fig. 3 | *TRAC*-HIT T cells exhibit increased degranulation and rapid killing activity upon exposure to low antigen levels. a**, Summary of the quantitative phosphoproteomic analysis. Heavy amino acid-labeled NALM6/7 cells were incubated with either *TRAC*-HIT or *TRAC*-CAR T cells for 10 min. Purified phospho-peptides were analyzed by mass spectrometry. Volcano plot shows total and enriched phospho-peptides in *TRAC*-HIT (blue square) and *TRAC*-CAR (red square) T cells. **b**, Phospho-peptides (two independent experiments; two different healthy T cell donors) with a $P < 0.05$ ($-\log_{10} > 1.3$) are plotted as $\log_2$ HIT/CAR (experiment 1 versus experiment 2); *P* values were calculated by paired *t*-test analysis (integrated in Proteome Discoverer software). Phospho-peptides enriched in *TRAC*-HIT (blue square) T cells are shown at the right. **c**, Representative confocal and bright field images of conjugates of CAR or HIT T cells interacting for 30 min with NALM6/7 or NALM6/WT cells (blue) labeled with goat antimouse (red) and phalloidin (green). Quantification of actin (upper panel) and CAR/HIT (lower panel) mean fluorescence intensity at the immune synapse region, divided by the mean intensity measured in the total T cell cortex. Each dot represents one cell; horizontal lines are median. Scale bars, 5 µm. Data from two independent experiments; $n = 60$. $^{**}P < 0.01$; NS, not significant (Mann–Whitney U-test). **d**, Confocal and bright field images of CAR or HIT T cell conjugates interacting for 30 min with NALM6/7 cells labeled for LAMP-1 (red) and actin (green). Quantification of lysosome polarity (distance to the immune synapse compared to average lysosomal distance to the total T cell cortex). This distance was normalized with the maximum distance found in the T cell and expressed as a polarity index between 1 (lysosomes at the synapse) and 0 (lysosomes at the opposite of the synapse). Data from two independent experiments; $n = 59$. *P* values obtained by unpaired *t*-test analysis. Scale bars, 5 µm. White arrows indicate LAMP-1 signal. **e**, Degranulation measured by CD107a staining upon incubating HIT/CAR T cells for 1 h and 4 h with NALM6 cells of different CD19 levels. *P* values obtained by unpaired *t*-test analysis; $n = 2$ biological independent samples, and data are representative of two independent experiments. Asterisk (*) represents a *P* value of <0.05. **f**, Single-cell time-lapse imaging cytotoxicity assay. Time from conjugate formation to propidium iodide (PI) influx in target cells; left: NALM6/WT (HIT, $n = 93$; CAR, $n = 78$), middle NALM6/12-4 (HIT, $n = 53$; CAR, $n = 57$), right NALM6/7 (HIT, $n = 104$; CAR, $n = 94$). For each target cell: two independent experiments with two T cell donors. *P* values obtained by unpaired *t*-test analysis; asterisk (*) means $P < 0.05$. All data are mean ± s.e.m.

In considering the advantage afforded to the CAR by the incorporation of a costimulatory domain (Fig. 4a) and the latter's absence in the HIT receptor, we tested the hypothesis that providing costimulatory support to *TRAC*-HIT T cells would enable the latter to outperform the 1928z CAR by extending their persistence. To this end, we coexpressed ligands for CD28 and 4-1BB in the T cells, which we previously showed enhances the persistence of first[44] and second-generation[26] CARs. Consistent with earlier findings[26,44,45], coexpression of these two ligands (annotated 80/BBL) increased the therapeutic potency of *TRAC*-HIT T cells, whereas coexpression of either ligand alone did not (Extended Data Fig. 9a). In two models, targeting either CD19 or BCMA, *TRAC*-HIT+80/BBL T cells yielded greater survival than 28z CAR T cells (Fig. 4c,d and Extended Data Fig. 10a,b).

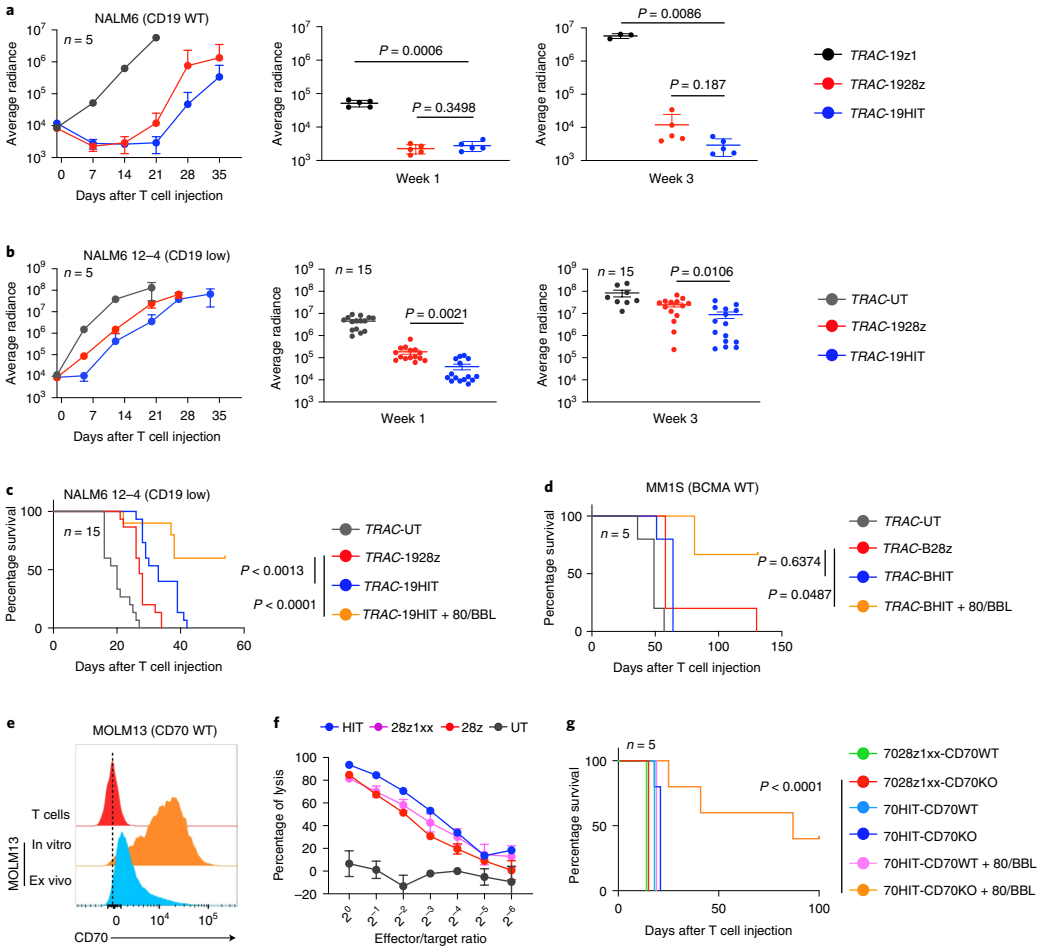


**Fig. 4 | *TRAC*-HIT T cells outperform *TRAC*-CAR T cells in controlling low antigen tumor cells in vivo. a**, Tumor burden (average radiance) of NALM6 WT-bearing mice treated with $5\times10^5$ *TRAC*-HIT or *TRAC*-CAR T cells ($n=5$), analyzed through a 35-day period, at week 1 or week 3. Quantification is the average photon count of ventral and dorsal acquisitions per animal at all given timepoints. A two-tailed unpaired *t*-test was used to compare each group pair. **b**, Tumor burden (average radiance) of NALM6/12-4-bearing mice treated with $4\times10^5$ *TRAC*-HIT or *TRAC*-CAR T cells ($n=15$), analyzed through a 35-day period, at week 1 or week 3. A two-tailed unpaired *t*-test was used to compare each group pair. **c**, Kaplan–Meier analysis of survival of NALM6/12-4-bearing mice treated with $4\times10^5$ *TRAC*-HIT or *TRAC*-CAR T cells ($n=15$). **d**, Kaplan–Meier analysis of survival of MM1S-bearing mice treated with $2\times10^5$ *TRAC*-HIT or *TRAC*-CAR T cells ($n=5$). **e**, CD70 flow histograms for MOLM13 cells in vitro and ex vivo (from mouse bone marrow samples), and nonactivated T cells (negative control). **f**, Cytotoxic activity using an 18-h bioluminescence assay at different effector:target ratios for *TRAC*-70HIT/*RV*-CAR T cells (7028z and 7028z1xx) and FFL+MOLM13 cells; $n=3$. Additional specificity studies are shown in Extended Data Fig. 2. **g**, Kaplan–Meier analysis of survival of MOLM13-bearing mice treated with $4\times10^5$ *TRAC*-HIT or *TRAC*-CAR T cells ($n=5$). **c**, **d** and **g**, *P* values were determined by a log-rank Mantel–Cox test (survival). All data are mean ± s.e.m. The tumor burden of individual animals is shown in Supplementary Figs. 1–3.

In the NALM6/12-4 leukemia model, *TRAC*-19HIT + 80/BBL outperformed *TRAC*-CAR T cells ($P=0.0001$, Fig. 4c). Furthermore, in the MM1S myeloma model, where BCMA is more abundant (~11,000 molecules per cell) than CD19 in NALM6/12-4 (~200), *TRAC*-BHIT + 80/BBL T cells likewise outperformed *TRAC*-BCAR T cells ($P=0.048$, Fig. 4d). Thus, T cells expressing the HIT receptor alone provided sensitive tumor recognition but did not significantly prolong mouse survival until they were supported by 80/BBL-based costimulation (Fig. 4d and Extended Data Fig. 10c). Bone marrow analyses on days 10 and 17 showed that the improved early tumor control obtained in *TRAC*-HIT compared to *TRAC*-CAR-treated animals was not the result of increased T cell numbers. CD4 and CD8 *TRAC*-HIT T cells were present in similar numbers to *TRAC*-CAR T cells on day 10 and were less abundant by day 17 (Extended Data Fig. 9b,c). *TRAC*-HIT + 80/BBL T cells on the other hand exceeded *TRAC*-HIT and *TRAC*-CAR T cells at both timepoints. Altogether,

these in vivo studies establish that T cells reprogrammed with a HIT receptor display greater in vivo antigen sensitivity than a CAR, and that prolonged tumor control by HIT T cells can be achieved by providing supportive cell-intrinsic costimulation.

We provide an additional example targeting another clinically relevant target of low abundance, CD70 in acute myeloid leukemia (AML)[46,47]. We utilized the AML cell line MOLM13 which is derived from FLT3-ITD relapsed AML and expresses ~370 CD70 molecules per cell based on ex vivo bone marrow analysis (Fig. 4e). 70HIT and 70CAR T cells effectively lysed CD70+MOLM13 in vitro (Fig. 4f) but not CD70$^-$ target cells (Extended Data Fig. 2). However, neither CAR nor HIT T cells were effective in vivo (Fig. 4g and Extended Data Fig. 10e). CD70 expression is induced in activated T cells and high CD70 levels are detectable in a sizable fraction of CAR-transduced T cells (Brugnoni et al.[48] and Extended Data Fig. 10d), which may result in HIT/CAR-mediated fratricide T cell killing and/or HIT/CAR malfunction when targeting CD70. We therefore ablated CD70 expression in the infused T cells (Extended Data Fig. 10d) and found that antiAML efficacy was indeed improved. In this instance again, 70HIT + 80/BBL T cells vastly outperformed the CAR T cells ($P < 0.0001$, Fig. 4g and Extended Data Fig. 10e).

## Discussion

A general comparison of CARs and TCRs is rendered difficult by the multiplicity of CAR structures and the distinct nature of their respective ligands (various cell surface molecules versus HLA–peptide complexes). Nonetheless, the HIT design reported here allows us to examine a TCR-like structure and a CAR that engage the same target using the same heavy and light immunoglobulin chains. CARs and HIT receptors both direct effective killing of target cells that express thousands of target molecules. However, as the target antigen numbers diminish to the hundreds, the HIT receptor exceeds the antigen sensitivity afforded by CARs, including the more sensitive CD28-based CARs. This difference allows, as we show here, for HIT-engineered T cells to reject tumors that CAR T cells struggle to control. Based on in vitro cytolysis experiments, HIT receptors are at least tenfold more sensitive to antigen than CARs. This heightened sensitivity is consistent with that attributed to the physiological TCR–CD3 complex. In vitro studies suggest that TCRs only require one to three ligands to be engaged for cytolysis[28,29], but the number of required TCR ligands for effective in vivo tumor elimination is less well defined (one study calculated that 30–60 ligands per cell would be required to support T cell expansion[49,50]). Future studies are needed to better quantify threshold antigen levels required for effective CAR, HIT and TCR-based therapies.

We found that *TRAC*-HIT T cells can lyse target cells with low antigen density and that their degranulation and lytic kinetics are faster than those of CAR T cells when antigen is limiting. Our phosphoproteomic and morphological studies support a mechanism whereby HIT engagement is more effective in remodeling actin or recruiting lysosomes. This may entail the activation of ARPC1B, which is necessary for the establishment of lamellipodia as well as the actin reorganization required for cell migration and immune synapse formation[43]. Our analyses also point to signaling differences that underpin differential antigen sensitivity, such as the activation of LAT, which our study and another suggest is poorly recruited by CARs[51]. The HIT versus CAR system we describe here is poised to provide many more future insights into comparing their functions. More quantitative and sensitive techniques are still needed to accurately quantify receptor expression, measure receptor affinities, early signaling events and the dynamic structure of the immune synapse, as are structural studies to determine how CAR and HIT receptors engage their cognate target.

Heavy and light chains have previously been used in the context of T cell receptors through different means[35–38]. However, their antigen sensitivity or their ability to exert tumor control has not been evaluated against low antigen density tumors[35–37] other than for the STAR receptor[38]. In all these instances[35–38], T cells were dual-specific as they retained their endogenous TCR and expressed the VL–VH fusion proteins from randomly integrated lentiviral vectors. Dual specificity may impact antigen sensitivity, as the VL and VH fusion proteins compete with endogenous αβTCR chains or assembly with CD3 complex components. Among these receptors, the STAR receptor[38] is the only one reported to have increased sensitivity compared to 28z and BBz CARs, in line with our observations, although the minimal number of target molecules needed to trigger T cell activation has not been addressed. The HIT receptor design minimizes competition with the endogenous TCR through the disruption of the TCRα, provides homogenous HIT receptor expression from the *TRAC* locus and abrogates T cell alloreactivity.

As we show here, HIT receptors enable effective targeting of low density antigens but they require additional support to enhance their therapeutic efficacy. Unlike second-generation CARs[4,5], HIT receptors are not endowed with costimulatory components, but costimulatory support can be engineered separately into the T cell, as previously established with other antigen receptors[26,44,52,53] and extended in this study. Given the similarity of HIT receptors and TCRs, our findings provide a strong rationale for similarly endowing TCR-engineered and natural T cells with generic costimulatory support, for example via constitutive CD80 and 4-1BBL coexpression, to increase their persistence and potency.

The different activation and therapeutic thresholds of TCRs, HITs and CARs open new possibilities for cancer immunotherapy. CARs are effective against high density antigens and may have reduced potential to damage normal tissues that express subthreshold levels of the targeted antigen. This therapeutic window, however, raises the risk of escape of low-expressor tumor cells. HIT receptors, on the other hand, are better suited for targets expressed in the lower ranges, as exemplified here in our in vivo models targeting CD19 and CD70. HIT receptors will be especially valuable against tumor-specific targets of low abundance, for which the risk of reactivity against normal tissues expressing the antigen is averted by default, or when paired with another receptor in an 'and' gate. *TRAC*-HIT T cells should thus expand the realm of tumors that can be targeted by engineered T cells.

## Online content

Any methods, additional references, *Nature Research* reporting summaries, source data, extended data, supplementary information, acknowledgements, peer review information; details of author contributions and competing interests; and statements of data and code availability are available at https://doi.org/10.1038/s41591-021-01621-1.

Received: 30 July 2020; Accepted: 8 November 2021;
Published online: 13 January 2022

## References

1. Sadelain, M., Riviere, I. & Riddell, S. Therapeutic T cell engineering. *Nature* **545**, 423–431 (2017).
2. Eshhar, Z. et al. The T-body approach: potential for cancer immunotherapy. *Springer Semin. Immunopathol.* **18**, 199–209 (1996).
3. Sadelain, M., Riviere, I. & Brentjens, R. Targeting tumours with genetically enhanced T lymphocytes. *Nat. Rev. Cancer* **3**, 35–45 (2003).
4. Maher, J., Brentjens, R. J., Gunset, G., Riviere, I. & Sadelain, M. Human T-lymphocyte cytotoxicity and proliferation directed by a single chimeric TCRzeta /CD28 receptor. *Nat. Biotechnol.* **20**, 70–75 (2002).
5. van der Stegen, S. J., Hamieh, M. & Sadelain, M. The pharmacology of second-generation chimeric antigen receptors. *Nat. Rev. Drug Discov.* **14**, 499–509 (2015).
6. June, C. H. & Sadelain, M. Chimeric antigen receptor therapy. *N. Engl. J. Med.* **379**, 64–73 (2018).
7. Brudno, J. N. & Kochenderfer, J. N. Chimeric antigen receptor T-cell therapies for lymphoma. *Nat. Rev. Clin. Oncol.* **15**, 31–46 (2018).

8. Turtle, C. J. et al. CD19 CAR-T cells of defined CD4+:CD8+ composition in adult B cell ALL patients. *J. Clin. Invest.* **126**, 2123–2138 (2016).
9. Fry, T. J. et al. CD22-targeted CAR T cells induce remission in B-ALL that is naive or resistant to CD19-targeted CAR immunotherapy. *Nat. Med.* **24**, 20–28 (2018).
10. Brudno, J. N. et al. T cells genetically modified to express an anti-B-cell maturation antigen chimeric antigen receptor cause remissions of poor-prognosis relapsed multiple myeloma. *J. Clin. Oncol.: Off. J. Am. Soc. Clin. Oncol.* **36**, 2267–2280 (2018).
11. Cohen, A. D. et al. B cell maturation antigen-specific CAR T cells are clinically active in multiple myeloma. *J. Clin. Invest.* **129**, 2210–2221 (2019).
12. Maude, S. L. et al. Tisagenlecleucel in children and young adults with B-cell lymphoblastic leukemia. *N. Engl. J. Med.* **378**, 439–448 (2018).
13. Neelapu, S. S. et al. Axicabtagene ciloleucel CAR T-cell therapy in refractory large B-cell lymphoma. *N. Engl. J. Med.* **377**, 2531–2544 (2017).
14. Park, J. H. et al. Long-term follow-up of CD19 CAR therapy in acute lymphoblastic leukemia. *N. Engl. J. Med.* **378**, 449–459 (2018).
15. Schuster, S. J. et al. Tisagenlecleucel in adult relapsed or refractory diffuse large B-cell lymphoma. *N. Engl. J. Med.* **380**, 45–56 (2019).
16. Shah, N. N. et al. CD4/CD8 T-cell selection affects chimeric antigen receptor (CAR) T-cell potency and toxicity: updated results from a phase I anti-CD22 CAR T-cell trial. *J. Clin. Oncol.: Off. J. Am. Soc. Clin. Oncol.* **38**, 1938–1950 (2020).
17. Majzner, R. G. & Mackall, C. L. Tumor antigen escape from CAR T-cell therapy. *Cancer Discov.* **8**, 1219–1226 (2018).
18. Libert, D. et al. Serial evaluation of CD19 surface expression in pediatric B-cell malignancies following CD19-targeted therapy. *Leukemia* **34**, 3064–3069 (2020).
19. Shah, N. N. & Fry, T. J. Mechanisms of resistance to CAR T cell therapy. *Nat. Rev. Clin. Oncol.* **16**, 372–385 (2019).
20. Xu, X. et al. Mechanisms of relapse after CD19 CAR T-cell therapy for acute lymphoblastic leukemia and its prevention and treatment strategies. *Front. Immunol.* **10**, 1–15 (2019).
21. Hamieh, M. et al. CAR T cell trogocytosis and cooperative killing regulate tumour antigen escape. *Nature* **568**, 112–116 (2019).
22. Majzner, R. G. et al. Tuning the antigen density requirement for CAR T-cell activity. *Cancer Discov.* **10**, 702–723 (2020).
23. Priceman, S. J. et al. Co-stimulatory signaling determines tumor antigen sensitivity and persistence of CAR T cells targeting PSCA+ metastatic prostate cancer. *Oncoimmunology* **7**, 1–13 (2018).
24. Eyquem, J. et al. Targeting a CAR to the TRAC locus with CRISPR/Cas9 enhances tumour rejection. *Nature* **543**, 113–117 (2017).
25. Feucht, J. et al. Calibration of CAR activation potential directs alternative T cell fates and therapeutic potency. *Nat. Med.* **25**, 82–88 (2019).
26. Zhao, Z. et al. Structural design of engineered costimulation determines tumor rejection kinetics and persistence of CAR T cells. *Cancer cell* **28**, 415–428 (2015).
27. Lee, D. W. et al. T cells expressing CD19 chimeric antigen receptors for acute lymphoblastic leukaemia in children and young adults: a phase 1 dose-escalation trial. *Lancet* **385**, 517–528 (2015).
28. Purbhoo, M. A., Irvine, D. J., Huppa, J. B. & Davis, M. M. T cell killing does not require the formation of a stable mature immunological synapse. *Nat. Immunol.* **5**, 524–530 (2004).
29. Sykulev, Y., Joo, M., Vturina, I., Tsomides, T. J. & Eisen, H. N. Evidence that a single peptide-MHC complex on a target cell can elicit a cytolytic T cell response. *Immunity* **4**, 565–571 (1996).
30. Brentjens, R. J. et al. Eradication of systemic B-cell tumors by genetically targeted human T lymphocytes co-stimulated by CD80 and interleukin-15. *Nat. Med.* **9**, 279–286 (2003).
31. Maude, S. L. et al. Chimeric antigen receptor T cells for sustained remissions in leukemia. *N. Engl. J. Med.* **371**, 1507–1517 (2014).
32. Gross, G., Waks, T. & Eshhar, Z. Expression of immunoglobulin T-cell receptor chimeric molecules as functional receptors with antibody-type specificity. *Proc. Natl Acad. Sci. USA* **86**, 10024–10028 (1989).
33. Kuwana, Y. et al. Expression of chimeric receptor composed of immunoglobulin-derived V regions and T-cell receptor-derived C regions. *Biochem. Biophys. Res. Commun.* **149**, 960–968 (1987).
34. Sher, B. T., Nairn, R., Coligan, J. E. & Hood, L. E. DNA sequence of the mouse H-2Dd transplantation antigen gene. *Proc. Natl Acad. Sci USA* **82**, 1175–1179 (1985).
35. Baeuerle, P. A. et al. Synthetic TRuC receptors engaging the complete T cell receptor for potent anti-tumor response. *Nat. Commun.* **10**, 1–12 (2019).
36. Helsen, C. W. et al. The chimeric TAC receptor co-opts the T cell receptor yielding robust anti-tumor activity without toxicity. *Nat. Commun.* **9**, 1–13 (2018).
37. Xu, Y. et al. A novel antibody-TCR (AbTCR) platform combines Fab-based antigen recognition with gamma/delta-TCR signaling to facilitate T-cell cytotoxicity with low cytokine release. *Cell Disco.* **4**, 1–13 (2018).
38. Liu, Y. et al. Chimeric STAR receptors using TCR machinery mediate robust responses against solid tumors. *Sci. Transl. Med.* **13**, 1–16 (2021).
39. MacKay, M. et al. The therapeutic landscape for cells engineered with chimeric antigen receptors. *Nat. Biotechnol.* **38**, 233–244 (2020).
40. Gaud, G., Lesourne, R. & Love, P. E. Regulatory mechanisms in T cell receptor signalling. *Nat. Rev. Immunol.* **18**, 485–497 (2018).
41. Matza, D. et al. A scaffold protein, AHNAK1, is required for calcium signaling during T cell activation. *Immunity* **28**, 64–74 (2008).
42. Schwartzberg, P. L., Mueller, K. L., Qi, H. & Cannons, J. L. SLAM receptors and SAP influence lymphocyte interactions, development and function. *Nat. Rev. Immunol.* **9**, 39–46 (2009).
43. Randzavola, L. O. et al. Loss of ARPC1B impairs cytotoxic T lymphocyte maintenance and cytolytic activity. *J. Clin. Invest.* **129**, 5600–5614 (2019).
44. Stephan, M. T. et al. T cell-encoded CD80 and 4-1BBL induce auto- and transcostimulation, resulting in potent tumor rejection. *Nat. Med.* **13**, 1440–1449 (2007).
45. Nguyen, P. et al. Route of 41BB/41BBL costimulation determines effector function of B7-H3-CAR.CD28ζ T cells. *Mol. Ther. Oncolytics* **18**, 202–214 (2020).
46. Perna, F. et al. Integrating proteomics and transcriptomics for systematic combinatorial chimeric antigen receptor therapy of AML. *Cancer Cell* **32**, 506–519 (2017).
47. Riether, C. et al. Targeting CD70 with cusatuzumab eliminates acute myeloid leukemia stem cells in patients treated with hypomethylating agents. *Nat. Med.* **26**, 1459–1467 (2020).
48. Brugnoni, D. et al. CD70 expression on T-cell subpopulations: study of normal individuals and patients with chronic immune activation. *Immunol. Lett.* **55**, 99–104 (1997).
49. Kimachi, K., Croft, M. & Grey, H. M. The minimal number of antigen-major histocompatibility complex class II complexes required for activation of naive and primed T cells. *Eur. J. Immunol.* **27**, 3310–3317 (1997).
50. Henrickson, S. E. et al. T cell sensing of antigen dose governs interactive behavior with dendritic cells and sets a threshold for T cell activation. *Nat. Immunol.* **9**, 282–291 (2008).
51. Dong, R. et al. Rewired signaling network in T cells expressing the chimeric antigen receptor (CAR). *EMBO J.* **39**, 1–14 (2020).
52. Liu, X. et al. A chimeric switch-receptor targeting PD1 augments the efficacy of second-generation CAR T cells in advanced solid tumors. *Cancer Res.* **76**, 1578–1590 (2016).
53. Oda, S. K. et al. A CD200R-CD28 fusion protein appropriates an inhibitory signal to enhance T-cell function and therapy of murine leukemia. *Blood* **130**, 2410–2419 (2017).

## Methods

All animal research complies with the ethical regulations from the MSKCC Institutional Animal Care and Use Committee.

**Data reporting.** The experiments were not randomized, and the investigators were not blinded to allocation during experiments and outcome assessment, except where noted. Guide RNA: the sequence targeted by *TRAC* gRNA is located upstream of the transmembrane domain of the TCRα[6]. *TRAC* gRNA target sequence: 5′-CAGGGTTCTGGATATCTGT. *CD70* gRNA target sequence: 5′-GGGCTTGGTGATCTGCCTCG. *TRAC* and *CD70* gRNAs were ordered from Synthego with 2′-*O*-methyl 3′-phosphorothioate modifications in the first and last three nucleotides[54]. Guide RNA was resuspended with TE buffer at 40 µM.

**Cas9 protein and RNP formation.** Cas9 protein (40 µM) was obtained from QB3-Berkeley Macrolab core facility. *TRAC* ribonucleoprotein (RNP) was prepared by mixing Cas9 protein and *TRAC* gRNA at 1:1 molar ratio and incubated at 37 °C for 15 min, and immediately used for T cell targeting experiments.

**AAV.** We designed and cloned the pAAV-*TRAC*-19HIT by replacing the 1928z-polyA sequence of our previously described pAAV-*TRAC*-1928z plasmid[6]. To express a HIT receptor at the *TRAC* locus, the $V_H$-Cβ-P2A-$V_L$ sequence is cloned in between the P2A and the *TRAC* exon1 elements (chimeric $V_H$-Cβ and $V_L$-Cα (exon1) sequences are provided in Supplementary Information), thus resulting in $V_H$-Cβ and $V_L$-Cα expression under the control of TCRα promoter. CD19-specific HITs are generated using $V_H$ and $V_L$ elements derived from the SJ25C1 or FMC63 CAR genes previously described[23] or from three human scFvs of different affinities that recognize the same epitope (a kind gift of Ken Mohler from Juno Therapeutics). HIT $V_H$ and $V_L$ sequences used to produce CD22 and BCMA-specific HITs are derived from previously described CAR genes[23]. *TRAC*-1928z and *TRAC*-19BBz as in June and Sadelain[6]; *TRAC*-1928z1, *TRAC*-2228z and *TRAC*-BCMA28z were cloned by replacing 1928z in the *TRAC* AAV construct with the 19z1 (ref. [23]), 2228z[23] and BCMA28z[23] sequences. Recombinant AAV6 viruses (with AAV2 ITRs) were produced by Vigene, with titers expressed as GC ml$^{-1}$.

**Lentiviral vector construction, production and transduction.** PGK100-CD19 lenti plasmid was generated by cloning the PGK100 promoter[6] and CD19 (ref. [23]) sequences into a SIN lentiviral plasmid (pLM backbone)[55]. Vesicular stomatitis virus glycoprotein G pseudotyped lentiviral supernatants derived from transfected 293 T cells were used to transduce NALM6/12 cells (see below) to generate stable NALM6 cells expressing CD19 at very low levels. Transduction was performed in 6-well plates containing 4 µg ml$^{-1}$ polybrene. Cells with less than 5% transduction efficiency were used to clone the new CD19-expressing NALM6 clones by limited dilution in round-bottom 96-well plates.

**Gammaretroviral vector construction, production and transduction.** Plasmids encoding the SFGγ retroviral vector[56] were used to clone the bicistronic construct to express human CD80 (ref. [23]) and 41BBL[25] genes. CD80 and 41BBL SFGγ retroviral vectors have previously been described[25]. Vesicular stomatitis virus glycoprotein G pseudotyped retroviral supernatants derived from transduced gpg29 fibroblasts (H29) were used to construct stable retroviral-producing cell lines[53]. T cells were transduced with retroviral supernatants by centrifugation on RetroNectin-coated plates (Takara), as described previously[6]. CD80 and 41BBL expression was detected by FACS using mouse antihuman CD80-PE and 41BBL-PE antibodies (BD Biosciences).

**Cell lines.** FFL-expressing NALM6 cells and CD19-expressing NIH/3T3 cells were cultured as described (Eyquem et al.[24]). NALM6/medium and NALM6/low cell lines (~10,000 and ~1,500 molecules per cell, respectively) were previously described[23]. CRISPR–Cas9-edited NALM6 cells were generated as described[53], and cloned using the limited dilution technique. NALM6 clones with very low CD19 levels were selected for this study. NALM6/12-4 and NALM6/12-39 are derivatives of clone NALM6/12, which was transduced with the PGK100-CD19 lentivector as described above. All NALM6 cell lines were maintained in RPMI 1040 medium supplemented with 10% fetal bovine serum (FBS; HyClone), 10 mM HEPES (Invitrogen), 2 mM L-glutamine (Invitrogen), 1× NEAA (Invitrogen), 1 mM sodium pyruvate (Invitrogen), 50 µM β-mercaptoethanol, 10 U ml$^{-1}$ penicillin, 10 µg ml$^{-1}$ streptomycin (Gibco) and 2.5 µg ml$^{-1}$ plasmocyn (InvivoGen). Cells were split every 2–3 days and plated at $0.5\times10^6$ cells ml$^{-1}$. MM cell line MM1S expressing FFLuc-mCherry (a kind gift of D. Maria Themeli) was cultured in RPMI 1040 medium supplemented with 10% FBS (HyClone FetalClone I), 2 mM L-glutamine (Invitrogen), 1 mM sodium pyruvate (Invitrogen), 10 mM HEPES (Invitrogen), 10 U ml$^{-1}$ penicillin, 10 µg ml$^{-1}$ streptomycin (Gibco) and 2.5 µg ml$^{-1}$ plasmocyn (InvivoGen). Cells were split every 2–3 days and plated at $1\times10^6$ cells ml$^{-1}$. Acute myeloid leukemia cell line MOLM13 (a kind gift of Dr. Marion Subklewe) were transduced with FFLuc-GFP retroviral vector and further sorted (gated on GFP + fraction). FFLuc-GFP-MOLM13 cells were cultured in RPMI 1040 medium supplemented with 10% FBS (HyClone FetalClone I), 2 mM L-glutamine (Invitrogen), 10 U ml$^{-1}$ penicillin and 10 µg ml$^{-1}$ streptomycin (Gibco). Cells were split every 2–3 days and plated at $0.5\times10^6$ to $2\times10^6$ cells ml$^{-1}$.

**CD19, BCMA and CD70 quantification.** NALM6 cells ($0.2\times10^6$), MM1S cells ($0.1\times10^6$) and in vitro and ex vivo MOLM13 cells ($1\times10^6$) were stained with 5 µl phycoerythrin (PE)-antiCD19 antibody (clone SJ25C1, BD Biosciences), 10 µl PE-antiBCMA antibody (clone 19F2, Biolegend) and 4 µl PE-antiCD70 antibody (clone 113-16, Biolegend), respectively, in 100 µl MACS buffer for 30 min at 4 °C, washed and analyzed by FACS. Phycoerythrin Fluorescence Quantitation Kit (BD Biosciences) was used according to the manufacturer's protocol to determine the number of CD19, BCMA and CD70 molecules per cell. To quantify CD19 in NALM6/2, NALM6/7, NALM6/12, CD19 geometric mean fluorescent intensities (gMFIs) were used to calculate a ratio with NALM6/12-4 CD19 gMFI. Based on the number of CD19 molecules determined for NALM6/12-4, the ratios were used to calculate the number of CD19 molecules per cell in the aforementioned cell lines.

**Quantitative mass spectrometry.** NALM6 and MM1S cell pellets (~4 million cells) were lysed in 8 M urea, 200 mM EPPS (4-(2-hydroxyethyl)-1-piperazinepropanesulfonic acid), pH 8.5 with protease (complete mini ethylenediamine tetraacetic acid free, Roche) and phosphatase inhibitors (cocktail 2 and 3, Sigma). Samples were then sonicated (Diagenode Bioruptor) for three cycles (1 min on/1 min off). The Pierce bicinchoninic acid (BCA) assay was then used to determine the protein concentrations. Aliquots of 100 µg were taken for each sample (based on BCA assay) and reduced with 5 mM TCEP (tris(2-carboxyethyl)phosphine hydrochloride), alkylated with 10 mM iodoacetamide and quenched with 10 mM dithiothreitol. Samples were diluted to about 100 µl with lysis buffer and precipitated by chloroform-methanol[57]. Pellets were resuspended in 50 µl 200 mM EPPS buffer, digested with Lys-C protease at a 1:50 protease-to-protein ratio for 5 h at 37 °C, then overnight with trypsin (1:50) at 37 °C.

Anhydrous acetonitrile was added at a final volume of 30%. TMTPro (16-plex) reagents were added to peptides at a 2.8:1 (TMT reagent-to-peptide ratio) and incubated for 1 h at room temperature (RT). A label check was performed to determine mixing ratios, labeling efficiency and number of missed cleavages by pooling 1 µg from each sample, desalting, then analyzing by mass spectrometry. Samples were mixed 1:1 across all channels, dried to remove acetonitrile, then desalted using C18 solid-phase extraction Sep-Pak (Waters) and vacuum centrifuged to dryness.

Peptides were reconstituted in 1 ml of 2% ACN/25 mM ammonium bicarbonate (ABC) and fractionated into 48 fractions. Briefly, an Ultimate 3000 high-performance liquid chromatography (Dionex) coupled to an Ultimate 3000 Fraction Collector using a Waters XBridge BEH130 C18 column (3.5 µm, 4.6×250 mm) was operated at 1 ml min$^{-1}$. Buffer A consisted of 100% water, buffer B consisted of 100% acetonitrile and buffer C consisted of 25 mM ABC. The fractionation gradient operated as follows: 1% B to 5% B in 1 min, 5% B to 35% B in 61 min, 35% B to 60% B in 5 min, 60% B to 70% B in 3 min, 70% B to 1% B in 10 min, with 10% C the entire gradient to maintain pH. The 48 fractions were then concatenated to 12 fractions (that is fractions 1, 13, 25, 37 were pooled, followed by fractions 2, 14, 26, 38 and so on) so that every 12th fraction was used to pool. Pooled fractions were vacuum centrifuged then reconstituted in 1% ACN/0.1% FA for liquid chromatography triple quadropole mass spectrometry (LC–MS/MS).

Fractions were analyzed by LC–MS/MS using a nanoAQUITY UPLC (Waters) with a 50 cm (inner diameter 75 µm) EASY-Spray Column (PepMap RSLC, C18, 2 µm, 100 Å) heated to 60 °C coupled to a Orbitrap Fusion Lumos Tribrid Mass Spectrometer (Thermo Fisher Scientific). Peptides were separated at a flow rate of 300 nl min$^{-1}$ using a linear gradient of 1% to 35% acetonitrile (0.1% FA) in water (0.1% FA) over 4 h and analyzed by specific precursor selection (SPS)-MS3. MS1 scans were acquired over a range of $m/z$ 375–1,500, 120 K resolution, AGC target of $4\times10^5$ and maximum injection time (IT) of 50 ms. MS2 scans were acquired on MS1 scans of charge 2–7 using an isolation of 0.7 $m/z$, collision induced dissociation with activation of 35%, turbo scan and maximum IT of 50 ms. MS3 scans were acquired using SPS of ten isolation notches, $m/z$ range 100–1,000, 50 K resolution AGC target of $1\times10^5$, HCD activation of 65% and maximum IT of 150 ms. The dynamic exclusion was set at 38 s.

Raw data files were processed using Proteome /Discoverer (PD) v.2.4.0.305 (Thermo Scientific). For each of the TMT experiments, raw files from the all fractions were merged and searched with the SEQUEST HT search engine with a *Homo sapiens* UniProt protein database downloaded on 9 January 2019 (176,946 entries). Methionine oxidation was set as variable modification, while Cys carbamidomethylation, TMT16plex (K) and TMT16plex (N-term) were specified as fixed modifications. The precursor and fragment mass tolerances were 10 ppm and 0.6 Da, respectively. A maximum of two trypsin missed cleavages were permitted. Searches used a reversed sequence decoy strategy to control peptide false discovery rate (FDR) and 1% FDR was set as threshold for identification.

**T cell isolation, activation and culture.** Buffy coats from healthy volunteer donors were obtained from the New York Blood Center. Peripheral blood mononuclear cells were isolated by density gradient centrifugation and typically frozen in 90% FBS/10% dimethylsulfoxide. Frozen peripheral blood mononuclear cells were cultured for 1 h in T cell medium (see below; >85% viability) and then used for T cell isolation. T lymphocytes were purified using the Pan T cell isolation kit

(Miltenyi Biotech). T cells (>90% viability) were activated with Dynabeads (1:1 beads:cell) Human T-Activator CD3/CD28 (Thermo Fisher) in X-vivo 15 medium (Lonza) supplemented with 5% human serum (Gemini Bioproducts) with 5 ng ml$^{-1}$ human recombinant interleukin-7 (Peprotech) and 5 ng ml$^{-1}$ human recombinant interleukin-15 (Peprotech) at a density of $10^6$ cells ml$^{-1}$. The medium was changed every 2 days, and cells were replated at 1–1.5 × $10^6$ cells ml$^{-1}$.

**Gene editing and targeting.** Forty-eight hours after initiating T cell activation, the CD3/CD28 beads were magnetically removed, and the T cells were cultured for an extra day. T cells were transfected by electrotransfer of *TRAC* RNP using the Nucleofector II device (Lonza). Then 2 × $10^6$ or 10 × $10^6$ cells were resuspended with P3 buffer (Lonza) and mixed with 60 or 300 pmol *TRAC* RNP in a total volume of 20 or 100 µl, respectively. Following electroporation and considering 66.7% viability, cells were diluted into culture medium at 1 × $10^6$ cells ml$^{-1}$, and incubated at 37 °C, 5% carbon dioxide ($CO_2$). Recombinant AAV6 donor vector was added to the culture 30 min to 1 h after electroporation, at a multiplicity of infection of 3 × $10^5$ GC per cell. Subsequently, edited cells were cultured using standard conditions (37 °C and expanded in T cell growth medium, replenished as needed to maintain a density of 1–1.5 × $10^6$ cells ml$^{-1}$ every 2 days). For the generation of CD70-targeting CAR T cells, T cells were electroporated with *TRAC* and *CD70* RNPs, followed by AAV transduction (70 HIT T cells) or SFGγ-retroviral vectors (70 CAR T cells), immediately or 20–24 h after electroporation, respectively.

**Multiple antigen-stimulation assay.** NIH/3T3 expressing human CD19 were used as artificial antigen-presenting cells as described[6]. For repeated proximal stimulations, single-stimulation cells were transferred to a new well plated with CD19+ NIH/3T3 after 24 h (two stimulations) or every 12 h (four stimulations). For each condition, T cells were counted and analyzed by FACS for HIT and CAR every 12 h and CD4, CD8 and differentiation markers (CD45RA and CD62L) expression at the end of the experiment (48 h).

**Cytotoxicity assays.** The cytotoxicity of *TRAC*-HIT and *TRAC*-CAR T cells was determined by standard FFL-based assay[6]. FFL-expressing NALM6, PC3 or MM1S served as target cells. The effector (E) and tumor target (T) cells were cocultured in duplicates at the indicated E/T ratio using black-walled 96-well plates with 1 × $10^5$ target cells in a total volume of 100 µl per well in T cell medium. Four or 18 h later, 100 µl luciferase substrate (Bright-Glo, Promega) was directly added to each well. Emitted light was detected in a luminescence plate reader, and lysis was calculated using the formula 100 × (1 − (RLUsample)/(RLUtarget alone)).

**Single-cell cytotoxicity assay.** *TRAC*-HIT and *TRAC*-CAR T cells were stimulated once with CD19+ NIH/3T3 cells as described above, and expanded for 1 week in T cell medium. The day before the assay was started, HIT and CAR expression was quantified by FACS. Single-cell CTL assays were performed as described[23]. In brief, chamber slides containing a micro-well grid (50 × 50 × 50 µm$^3$ per well) were loaded with 1 × 10 CellTrace Violet-containing HIT$^+$/CAR$^+$ T cells, along with unlabeled NALM6 cells at a ratio of 1:1 in the presence of 1.5 µM propidium iodide (PI, Life Technologies). Images were acquired with an AxioObserver.Z1 microscope (Carl Zeiss) using ×10/0.45 or ×20/0.8 objectives. Fifteen positions (1 position equals 36 micro-wells) for each chamber were imaged every 10 min for 24 h. Acquired images were processed using a custom macro written on ImageJ software. Each individual well was scanned for the presence of T cells (CellTrace Violet). These wells were then analyzed to identify wells containing a one effector (E) T cell and one single target (T) cell, and interactions were recorded. In wells in which conjugate formation led to target death (lytic conjugates; PI-positive wells), the duration of interaction between E:T was recorded from the formation to the interruption of the conjugate. Contact events lasting for only 1 frame (10 min) were not included. All analyses were performed in a blinded fashion.

**Cytokine analyses.** To measure intracellular levels, 1 x $10^6$ *TRAC*-HIT or *TRAC*-CAR T cells were incubated with NALM6 targets at 1:1 ratio for 4 h in the presence of Brefeldin A. T cells were fixed and permeabilized using BD Cytofix/Cytoperm Plus kit as per the recommendation of the manufacturer (BD Biosciences), followed by staining with anticytokine antibodies (Brilliant Violet 785 antihuman TNF-α antibody (clone MAb11, catalog no. 502948, Biolegend); Brilliant Violet 421 antihuman IFN-γ antibody (clone B27, catalog no. 506538, Biolegend); PE antihuman IL-2 Antibody, (clone MQ1-17H12, catalog no. 500307, Biolegend); BUV395 mouse antihuman CD4 (clone SK3, catalog no. 563550, BD Biosciences); BV711 mouse antiHuman CD45 (clone HI30, catalog no. 564357, BD Biosciences); Fixable Viability Stain 510 (catalog no. 564406, BD Biosciences) is used to exclude dead cells). Cytokine levels were determined by FACS.

To measure secreted cytokine levels, 0.5 × $10^6$ *TRAC*-HIT or *TRAC*-CAR T cells were incubated with 0.3 × $10^6$ CD19+ NIH/3T3 cells per well in a 24-well plate at 37 °C for 24 h. Supernatants were collected and cytokines were quantified using BD Cytometric Bead Array kits (IL-2-558270; IFN-γ-560111; TNF-α-560112; BD Biosciences) and flow cytometry.

**Intracellular phosphoprotein analyses.** *TRAC*-HIT and *TRAC*-CAR T cells were stained with Fixable Viability Dye eFluor 506 (eBioscience 65-0866-14) and rested for 30 min in standard tissue culture conditions. *TRAC*-HIT or *TRAC*-CAR T cells were incubated with Nalm6 target cells for 15 min at a *TRAC*-HIT/CAR T cell-to-target ratio of 1:2. After antigen stimulation, the cells were fixed with Phosflow Fix Buffer I (BD Biosciences 557870). Fixed cells were stained for the HIT/CAR with AF647-GAM, followed by 2% mouse serum (15 min at 4 °C), and subsequently permeabilized with Phosflow Perm Buffer III (BD Biosciences 558050) following the manufacturer's procedure. Permeabilized samples were stained with antibodies detecting phosphorylated CD3ζ ITAM3 (pY142; BD Biosciences 558448), ZAP70 (pY319; BD Biosciences 557881) and ERK1/2 (pT202/pY204; BioLegend 369506).

**CD19 binding assays.** CAR/HIT T cells were incubated in 100 µl MACS buffer containing increasing concentrations of recombinant hCD19-hFc (R&D Systems, CF 9269-CD-050), at 4 °C for 60 min. After a wash with 2 ml of MACS buffer, cells were resuspended in 100 µl MACS buffer containing antihuman IgG-PE (1:100 dilution), and further incubated for 30 min at 4 °C for 30 min. Then, cells were washed as above, spun down, resuspended in 300 µl MACS buffer and analyzed by FACS.

**Cell stimulation and staining for CD107a expression.** To measure degranulation in response to target cell stimulation, effector cells were incubated with target cells at a 1:1 ratio. CD107a (APC) antibody was added to culture before stimulation. Unstimulated cells were incubated without target cells to detect spontaneous expression of CD107a. Cells were incubated at 37 °C in 5% $CO_2$ and analyzed at two different timepoints: 1 h and 4 h. The cells were washed twice with PBS and stained using conjugated antibody, CD45 (BV650) for 15 min at RT. Next, the cells were washed and fixed using Cytofix Fixation kit according to the manufacturer's protocol (BD Biosciences) and analyzed on the Aurora flow cytometer (Cytek).

**Flow cytometry.** CD19 and BCMA-specific HIT and CAR expression was measured with Alexa-Fluor-647-conjugated goat antimouse F(ab')2 antibody (AF647-GAM, Jackson ImmunoResearch, 115-606-003). CD22-specific HIT and CAR expression was measured with biotinylated protein L (Thermo Scientific) followed by BV510–streptavidin (BD Biosciences). TCRαβ was detected with mouse antihuman TCRαβ-FITC (Miltenyi Biotec). For T cell phenotyping the following antibodies were used: mouse antihuman BUV395-CD4 (563552), APC-cy7-CD8 (557834), BB-515 CD45RA clone HI100 (RUO, 564552), BV421-CD62L (563862), BV510-CD279 (PD1, 563076) from BD Biosciences; FITC-CD45RA (11-0458-42), PerCP-eFluor710-CD223 (LAG3, 46-2239-42) from eBiosciences and FITC mouse antihuman CD366 (TIM3, 345032) from BioLegend. The phenotype of primary cells and cell lines was determined using the following antihuman antibodies: CD19-PE (clone SJ25C1, BD), CD22-PE (clone S-HCL-1, BD), BCMA-BV421 (clone 19F2, BD), CD3-BUV737 (clone UCHT, BD), PD1-BV711 (clone EH121, BD), LAG3-BV650 (clone 11C3C65, Biolegend), TIM3-BV785 (clone F38-2E2, Biolegend), CD45-BV711 (clone HI30, BD Biosciences). Countbright beads (Invitrogen) were used to determine the absolute number of cells according to the manufacturer's protocol. 7-AAD or 4,6-diamidino-2-phenylindole was used to exclude dead cells. For fixed cells, eFluor506 fixable viability dye (eBioscience) was used. Fc Receptor Binding Inhibitor Antibody Human (eBioscience) and Fc block mouse (Miltenyi) were used to block Fc receptors. For degranulation studies, CD107a was measured in CD45+ cells by using antihuman CD45-BV650 (Biolegend, clone HI30) and antihuman CD107a-APC (Biolegend, clone H4A3) antibodies. Flow cytometric data were acquired on a 5-laser Aurora (Cytek Biosciences) or BD LSR-II, and analyzed in FlowJo v.10.1 (BD) or FCS Express 7 Flow (De Novo Software).

**Quantitative phosphoproteomic analysis.** The NALM6/7 cell line was cultured for at least one week in the presence of heavy amino acids as described[21]. For each replicate, 20 million NALM6/7 were incubated with 20 million CAR/HIT T cells for 10 min at 37 °C, and immediately washed with cold PBS, centrifuged and frozen in dry ice. Cell pellets were lysed with 300 µl buffer containing 8 M urea and 200 mM EPPS (pH at 8.5) with protease inhibitor (Roche) and phosphatase inhibitor cocktails 2 and 3 (Sigma). Benzonase (Millipore) was added to a concentration of 50 µ ml$^{-1}$ and incubated (RT, 15 min) followed by sonication (Covaris) for four cycles (30 s on/30 s off) at 4 °C. Samples were centrifuged at 4 °C, 14,000*g* for 10 min and supernatant extracted. The BCA protein concentration assay was used for determining protein concentration. Protein disulfide bonds were reduced with 5 mM tris (2-carboxyethyl) phosphine (RT, 15 min), then alkylated with 10 mM iodoacetamide (RT, 30 min, dark). The reaction was quenched with 10 mM dithiothreitol (RT, 15 min). Equivalent volumes of lysate aliquots were taken for each sample (100–200 ug in each sample) and diluted to approximately 100 µl with lysis buffer. Samples were subject to chloroform/methanol precipitation as previously described[1]. Pellets were reconstituted in 50 µl of 200 mM EPPS buffer and digested with Lys-C (1:50 enzyme-to-protein ratio) and incubated at 37 °C for 4 h. Trypsin was then added (1:50 enzyme-to-protein ratio) and digested for 37 °C overnight. Anhydrous acetonitrile was added to make a final volume of 30% ACN. Samples were TMT-labeled as described[1]. Briefly, samples were TMT-tagged by adding 10 µl (20 µg µl$^{-1}$) TMT or (28 µg µl$^{-1}$) TMTPro reagents for each respective sample and incubated for 1 h (RT). A ratio check was performed by taking a 1-µl aliquot from each sample and desalted by StageTip method[2] to

confirm labeling efficiency. TMT tags were then quenched with hydroxylamine to a final concentration of 0.3% for 15 min (RT). Samples were pooled in their entirety then vacuum centrifuged to dryness. Dried samples were reconstituted in 1 ml of 3% ACN/1% TFA, desalted using a 100 mg tC18 Sep-Pak (Waters) and lyophilized overnight. Phospho-peptides were enriched using the Thermo High-Select Fe-NTA Phosphopeptide Enrichment Kit (catalog no. A32992). The phosphopeptide elute was vacuum centrifuged to dryness and reconstituted in 100 µl of 1% ACN/25 mM ABC. A StageTip was constructed by placing two plugs with a narrow bore syringe of a C18 disk (3 M Empore Solid Phase Extraction Disk, no. 2315) into a 200-µl tip (VWR, catalog no. 89079-458). StageTips were conditioned with 100 µl of 100% ACN, 70% ACN/25 mM ABC, then 1% ACN/25 mM ABC. A phospho-enriched sample was loaded onto the StageTip and eluted into six fractions of 3%, 5%, 8%, 10%, 12% and 70% ACN/25 mM ABC with 100 µl each. Fractions were immediately dried down by vacuum centrifugation and reconstituted in 0.1% formic acid (FA) for LC–MS/MS. Phospho-enriched fractions were analyzed by LC–MS/MS using a NanoAcquity (Waters) with a 50 cm EASY-Spray Column (PepMap RSLC, C18, 2 µm, 100 Å, 75 µm internal diameter) heated to 60 °C coupled to a Orbitrap Eclipse Tribrid Mass Spectrometer (Thermo Fisher Scientific). Peptides were separated by direct injection at a flow rate of 300 nl $min^{-1}$ using a gradient of 5% to 30% acetonitrile (0.1% FA) in water (0.1% FA) over 3 h then to 50% ACN in 30 min and analyzed by SPS-MS3. MS1 scans were acquired over a range of *m/z* 375–1,500, 120 K resolution, AGC target (standard) and maximum injection time (IT) of 50 ms. MS2 scans were acquired on MS1 scans of charge 2–7 using an isolation of 0.5 *m/z*, collision induced dissociation with activation of 32%, turbo scan and max IT of 120 ms. MS3 scans were acquired using SPS of ten isolation notches, *m/z* range 110–1,000, 50 K resolution, AGC target (custom, 200%), HCD activation of 65% and max IT of 150 ms. The dynamic exclusion was set at 60 s. Raw data files were processed using PD v.2.4.1.15 (Thermo Scientific). For each of the TMT experiments, raw files from all fractions were merged and searched with the SEQUEST HT search engine with a *Homo sapiens* UniProt protein database downloaded on 9 January 2019 (176,945 entries). Cysteine carbamidomethylation was specified as fixed modifications, while methionine oxidation, acetylation of the protein N-terminus, TMT6plex/TMTpro (K) and TMT6plex/TMTpro (N-term), phosphorylation (STY), label13C(6) (K) and label13C(6)15N(4) (R) were set as variable modification. The precursor and fragment mass tolerances were 10 ppm and 0.6 Da, respectively. A maximum of two trypsin missed cleavages were permitted. Searches used a reversed sequence decoy strategy to control peptide FDR and 1% FDR was set as threshold for identification. Phosphosite localization was assigned by PD IMP-ptmRS node. Phospho-peptides without heavy labels measured in all replicates were $\log_2$-transformed and plotted. Another search using PD v.2.4.1.15 also performed to check common phospho-peptides between experiment 1 and experiment 2 with only searching for light labeled amino acids. By applying filter $\log_2$FC >0.75 and *P* value <0.05, two phospho-peptides (from LAT and ARPC1B) are newly identified and these peptides were manually checked in Thermo XCalibur using *m/z*, retention time and charge state to confirm PD results.

**Quantification of F-actin, LAMP-1 (lysosome) and CAR/HIT receptor at the IS.** Twelve millimeter ø coverslips (VWR; 631–0666) were washed with 70% ethanol and precoated with 0.02% of poly-L-lysine (Sigma-Aldrich; P8920) for 20 min at RT and were washed three times in water before being dried. NALM6 and CAR/HIT T cells were resuspended at a concentration of $2\times10^6$ cells $ml^{-1}$ in complete medium. 100,000 cells of each cell type were added in an Eppendorf and the final volume was resuspended to mix the cells before being added on the coverslips for 30 min at 37 °C 5% $CO_2$ for conjugate formation. Coverslips were washed once with cold PBS before fixation. Cells were fixed with 4% paraformaldehyde (Life Technologies; FB002) for 10 min at RT, washed once in PBS and excess of paraformaldehyde was quenched for 10 min with PBS 10 mM glycine (Thermo Fisher Scientific; G8898). Cells were permeabilized for 30 min at RT with PBS 0.2% bovine serum albumin (BSA; Euromedex; 04-100-812) 0.05% Saponin (Sigma-Aldrich; S4521). Primary antibodies were added in the same buffer for 1 h at RT: anti LAMP-1 (Abcam, ab24170), goat antimouse Alexa Fluor 647, Alexa Fluor 546 phalloidin (Thermo Fisher; A22283). Cells were washed three times in permeabilization buffer and then incubated at RT for 30 min in the same buffer with a goat antirabbit coupled to Alexa Fluor 405 (Life Technologies A31556). After washing once with PBS BSA saponin, and once with PBS, coverslips were soaked three times in PBS, three times in water and mounted with 4–6 µl of Fluoromount G (Southern Biotech; 0100-01) on slides (KNITTEL Starfrost) and dried overnight protected from light before microscope acquisition. Images were acquired with a Leica DmI8 inverted microscope equipped with a SP8 confocal unit using a ×63 (1.4 numerical aperture) objective. Z-stack images were acquired. Actin/GAM synaptic enrichment and lysosomes polarity were analyzed in Fiji and ImageJ softwares using scripts generated for semi-automated analysis.

In a first part, single images corresponding to the median plane of each conjugate were extracted from the Z-stacks. T cells were cropped and oriented in the same way regarding their synapse as described[58]. In a second part, after synapse extraction, for each crop, a mask of the T cell, the target cell and of the lysosomes were obtained after applying a threshold on the GAM, F-actin and LAMP-1 channels, respectively.

To obtain the contact zone corresponding to the synapse, the target cell was enlarged and the overlapping region with the T cell mask was selected and skeletonized. To define lysosomes polarity, a distance map showing the distance to the synapse line was computed and the average lysosomal distance was measured. This distance was normalized with the maximum distance found in the T cell. Thus, we obtained a polarity index between 1 (lysosomes at the synapse) and 0 (lysosomes at the opposite of the synapse). To measure actin/GAM enrichment at the synapse, a mask of the cortical region was defined and the mean actin intensity at the synaptic cortex was measured and compared to the mean actin intensity in the total cortex.

**Mouse systemic tumor model.** We used 8–12-week-old NOD/SCID/IL-2Rγ-null (NSG) male mice (Jackson Laboratory), under a protocol approved by the MSKCC Institutional Animal Care and Use Committee. For the ALL models, a total of $0.5\times10^6$ FFLuc-GFP NALM6/WT or NALM6/12-4 cells were administered by tail vein injection per mouse. Four days later, $0.5\times10^6$ or $0.4\times10^6$ *TRAC*-HIT or *TRAC*-CAR T cells were administered by tail vein injection per mouse, respectively. For the MM model, a total of $4\times10^6$ FFLuc-mCherry MM1S cells were administered by tail vein injection per mouse. Seven days later, $0.2\times10^6$ *TRAC*-HIT or *TRAC*-CAR T cells were administered by tail vein injection per mouse. For the AML model, a total of $1\times10^6$ FFLuc-GFP MOLM13 cells were administered by tail vein injection per mouse. Four days later, $0.4\times10^6$ *TRAC*-HIT or RV-CAR T cells were administered by tail vein injection per mouse. tumor burden was measured by bioluminescence imaging using the Xenogen IVIS Imaging System (Xenogen). Living Image software (Xenogen) was used to analyze acquired bioluminescence data. The survival end point of the mouse experiment varies depending on the tumor model (20–60 days for NALM6, 20–100 days for MOLM13 or 60–150 days for MM1S) and is determined when the animal shows clear clinical signs of distress. Maximum tumor burden is defined by hindlimb paralysis or other clinical signs of distress, at which point the animal must be euthanized. There were no instances at which this maximum was exceeded.

**Bone marrow analyses.** For the NALM6/12 mouse model, five mice per group were euthanized at day 10 or day 17, and bone marrow cells were isolated as described[6]. Cells were stained for CD45 (APC-Cy7), HIT or CAR (AF647), CD4 (BUV395), CD8 (PE-Cy7), PD1 (BV480), TIM3 (BV785), LAG3 (PercP-eFluor710), CD19 (BUV737) and GFP (tumor cells) and analyzed by FACS in the presence of counting beads (Countbright; Invitrogen).

**Statistics.** All experimental data are presented as mean ± s.e.m. No statistical methods were used to predetermine sample size. Appropriate statistical tests were used to analyze data, as described in the figure legends. Statistical analysis was performed on GraphPad Prism v.7 software and R. Single-cell CTL (micro-well) assay was evaluated using test of proportions. Cytotoxicity analysis in the CTL assay was performed using two-way analysis of variance or repeated measures analysis of variance followed by Tukey's multiple comparison test. The cytokine level between two groups were compared using Mann–Whitney *U*-test. Significance was set at $P<0.05$.

**Reporting summary.** Further information on research design is available in the Nature Research Reporting Summary linked to this article.

## Data availability

All requests for raw and analyzed preclinical data and materials will be promptly reviewed by the corresponding authors (M.S. and J.M.S.) to determine if they are subject to intellectual property or confidentiality obligations. Any data and materials that can be shared will be released via a material transfer agreement (requested to Michel Sadelain). Sequences for the TRAC-HIT receptors have been submitted under patent no. WO2019157454A1 (19HIT). The TRAC-HIT sequences can be found in the Supplementary Information file.

## Code availability

We have generated scripts for the automated analyses of the single-cell CTL assays as well as the actin, CAR, HIT and LAMP-1 signals in the confocal images. Request for these scripts will be promptly reviewed by the corresponding authors (M.S. and J.M.S.) to determine if they are subject to intellectual property or confidential obligations. Any script that can be shared will be released via a material transfer agreement (requested to Michel Sadelain).

## References

54. Hendel, A. et al. Chemically modified guide RNAs enhance CRISPR-Cas genome editing in human primary cells. *Nat. Biotechnol.* **33**, 985–989 (2015).
55. Papapetrou, E. P. et al. Genomic safe harbors permit high beta-globin transgene expression in thalassemia induced pluripotent stem cells. *Nat. Biotechnol.* **29**, 73–78 (2011).
56. Rivière, I., Brose, K. & Mulligan, R. C. Effects of retroviral vector design on expression of human adenosine deaminase in murine bone marrow transplant recipients engrafted with genetically modified cells. *Proc. Natl Acad. Sci. USA* **92**, 6733–6737 (1995).

57. Navarrete-Perea, J., Yu, Q., Gygi, S. P. & Paulo, J. A. Streamlined tandem mass tag (SL-TMT) protocol: an efficient strategy for quantitative (phospho) proteome profiling using tandem mass tag-synchronous precursor selection-MS3. *J. Proteome Res.* **17**, 2226–2236 (2018).
58. Zucchetti, A. E. et al. Tethering of vesicles to the Golgi by GMAP210 controls LAT delivery to the immune synapse. *Nat. Commun.* **10**, 1–17 (2019).

## Acknowledgements

We thank Gertrude Gunset for logistical and technical assistance. We also thank the SKI Cell Therapy and Cell Engineering (CTCEF), Molecular Cytology, Flow Cytometry, Integrated Genomics Operation, Microchemistry and Proteomics, Antitumor Assessment and Animal Core Facilities for their expert assistance. This work was supported by the Lake Road Foundation, the Lymphoma and Leukemia Society, the Pasteur-Weizmann/Servier award, the Leopold Griffuel award and the NCI Cancer Center Support Grant no. P30 CA008748. SKI cores were in part supported by the Tow Foundation, Cycle for Survival, the Marie-Josée and Henry R. Kravis Center for Molecular Oncology and NCI grant P30 CA08748. A.D., M.S. and T.G. were supported by fellowships from the Canadian Institutes of Health Research, the Fogarty Foundation and the Alexander S. Onassis Public Benefit Foundation, respectively.

## Author contributions

J.M.-S. and J.E. designed the study, performed experiments, analyzed and interpreted data and wrote the manuscript. S.H. designed and performed experiments, and analyzed data. M.H., J.F., N.P., A.E.Z., Z.L., M.S., P.L.L., M. Saetersmoen, A.D. and M.M. performed experiments and analyzed data. A.I. performed statistical analysis. A.G.A., M.M.M., Z.Z., T.G., S.J.C.v.d.S. and F.T. performed experiments. M. Huse designed experiments. I.R., R.C.H. and C.H. designed experiments and interpreted data. M.S. designed the study, analyzed and interpreted data, and wrote the manuscript.

## Competing interests

Memorial Sloan Kettering has submitted a patent application based in part on results presented in this manuscript (WO2019157454A1, J.M.-S., J.E. and M.S. are listed among the inventors). R.C.H. reports stock ownership in Merck. M.S. reports research funding from Juno Therapeutics, Fate Therapeutics, Takeda Pharmaceuticals and Atara Biotherapeutics, unrelated to the present research. M.S., I.R. and J.E. are scientific cofounders of Mnemo Therapeutics. M.S. serves on the scientific advisory board of St. Jude Children Research Hospital. All other authors declare no competing interests.

## Additional information

**Extended data** are available for this paper at https://doi.org/10.1038/s41591-021-01621-1.

**Supplementary information** The online version contains supplementary material available at https://doi.org/10.1038/s41591-021-01621-1.

**Correspondence and requests for materials** should be addressed to Jorge Mansilla-Soto or Michel Sadelain.

**Peer review information** *Nature Medicine* thanks Cliona Rooney and the other, anonymous, reviewer(s) for their contribution to the peer review of this work. Saheli Sadanand was the primary editor on this article and managed its editorial process and peer review in collaboration with the rest of the editorial team.

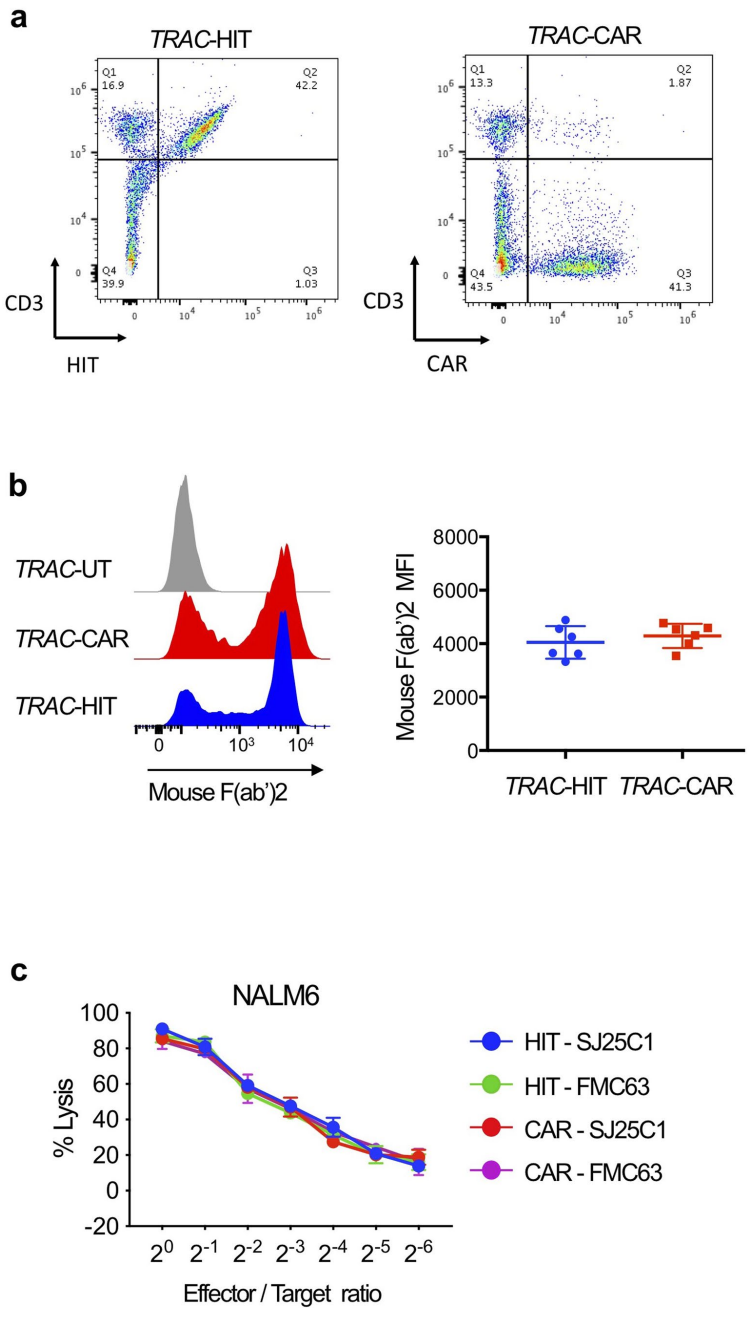


**Extended Data Fig. 1 | See next page for caption.**

**Extended Data Fig. 1 | HIT receptor expression driven by the TCRα promoter rescues CD3 expression and directs lysis of CD19 + target cells.** **a**. Representative flow cytometry analysis showing HIT, CAR, and CD3 expression. *TRAC*-HIT and *TRAC*-CAR T cells were generated as in Fig. 1b. CD3 surface expression is only observed in *TRAC*-HIT T cells due to the presence of Cα and Cβ in the HIT receptor. **b**. HIT/CAR mean fluorescence intensity (MFI) measured by FACS using AF647-GAM. (left) HIT/CAR histograms (representative experiment) and (right) HIT/CAR MFI; $n = 6$ independent experiments, 3 donors. **c**. Representative cytotoxic activity using an 18 h bioluminescence assay, using firefly luciferase (FFL)-expressing NALM6 as targets cells ($n = 2$ independent experiments on 3 healthy donors). CD19-specific *TRAC*-HIT and *TRAC*-CAR T cells were generated using two different CD19-specific binding domains, SJ25C1 and FMC63. All data are mean ± s.e.m.

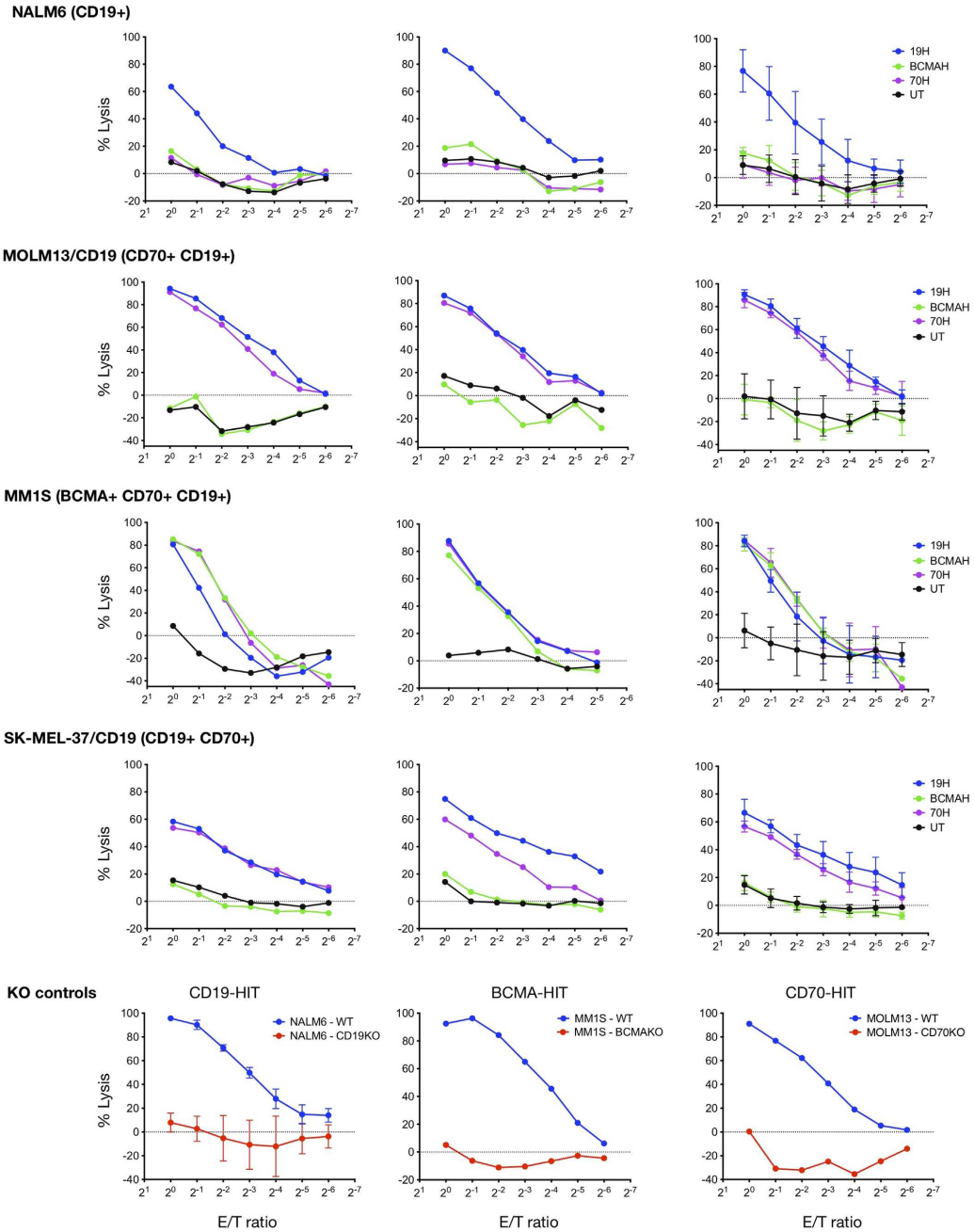


**Extended Data Fig. 2 | See next page for caption.**

**Extended Data Fig. 2 | HIT receptors provide antigen-specific T cell-mediated cytotoxicity.** Cytotoxic activity using an 18 h bioluminescence assay, using firefly luciferase (FFL)-expressing targets cells ($n = 2$ independent experiments on 2 healthy donors). CD19-, BCMA-, and CD70-specific *TRAC*-HIT T cells, and untransduced (UT) T cell controls were incubated with either NALM6 (CD19 + ), MOLM13/CD19 (CD70 + , CD19 + ), MM1S (BCMA + , CD70 + , CD19 + ), SK-MEL-37/CD19 (CD19 + , CD70 + ), and knock-out (KO) control cell lines. CD19, BCMA, and CD70 genes were CRISPR/Cas9-edited in NALM6, MM1S, and MOLM13 cell lines, respectively. Top 4 groups show data for donor 1 (left panel), donor 2 (middle panel), and both together (right panel). All data are mean ± s.e.m.

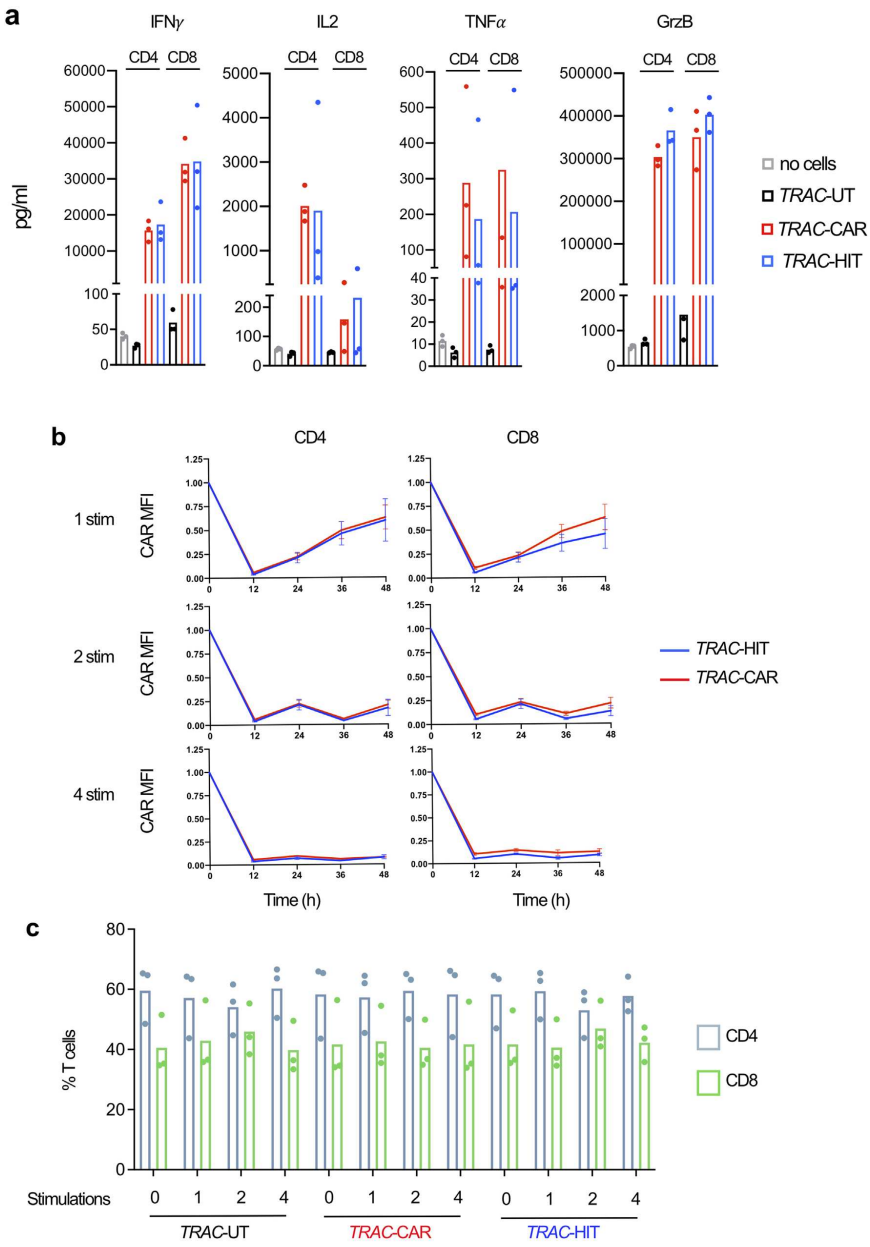


**Extended Data Fig. 3 | See next page for caption.**

**Extended Data Fig. 3 | HIT receptor elicits cytokine response upon antigen stimulation; cell surface HIT receptor expression is modulated by exposure to antigen. a**. *TRAC*-Untransduced (UT), *TRAC*-HIT (HIT) and *TRAC*-CAR (CAR) T cells were stimulated on CD19 + target for 24 h before supernatant were collected and analysed by flow cytometry to quantify IFNγ, IL-2, TNFα, and granzyme B (n = 3 independent experiments on 3 donors). **b**. *TRAC*-HIT and *TRAC*-CAR T cells stimulated on CD19 + target cells 1, 2 or 4 times over a 48 h period were analysed by flow cytometry using the GAM, CD4, and CD8 antibodies. Plots indicate relative HIT or CAR MFI (1 = MFI at 0 h) of CD4 and CD8 *TRAC*-HIT or *TRAC*-CAR T cells, respectively. (n = 3 independent experiments on 3 donors). **c**. Untransduced (UT), HIT and CAR T cells stimulated on CD19 + target cells either 0, 1, 2 or 4 times over a 48 h period were analysed by flow cytometry. Plots indicate the percentage of the CAR positive T cells measured by flow cytometry analysis of CD4 and CD8 (n = 3 independent experiments on 3 donors). All data are mean ± s.e.m.

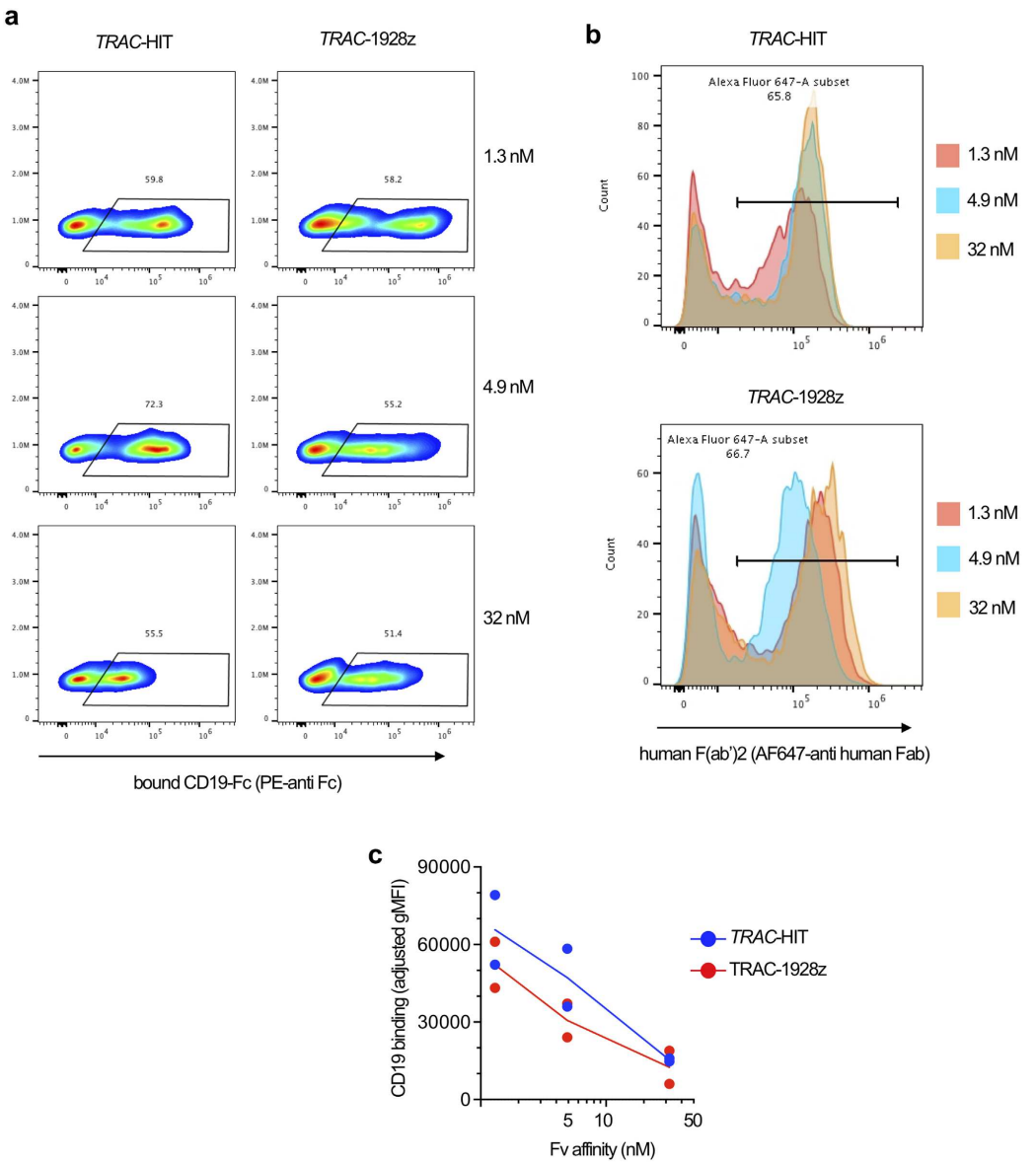


**Extended Data Fig. 4 | Antigen binding depends on HIT receptor affinity. a**. Representative flow cytometry analysis showing CD19 binding. *TRAC*-HIT and *TRAC*-CAR T cells were incubated with a recombinant human CD19-Fc fusion, which was then detected using an anti-hFc-PE antibody. **b**. HIT/CAR mean fluorescence intensity (MFI) measured by FACS using AF647-goat anti human (GAH) antibody (representative experiment). **c**. Plot of CD19 binding (adjusted gMFI) vs CD19 binder affinity (n = 2 independent experiments). Geometric MFI for CD19 biding (PE signal from **a**.) was adjusted to the gMFI of the HIT/CAR receptor (AF647 signal from **b**.) All data are mean ± s.e.m.

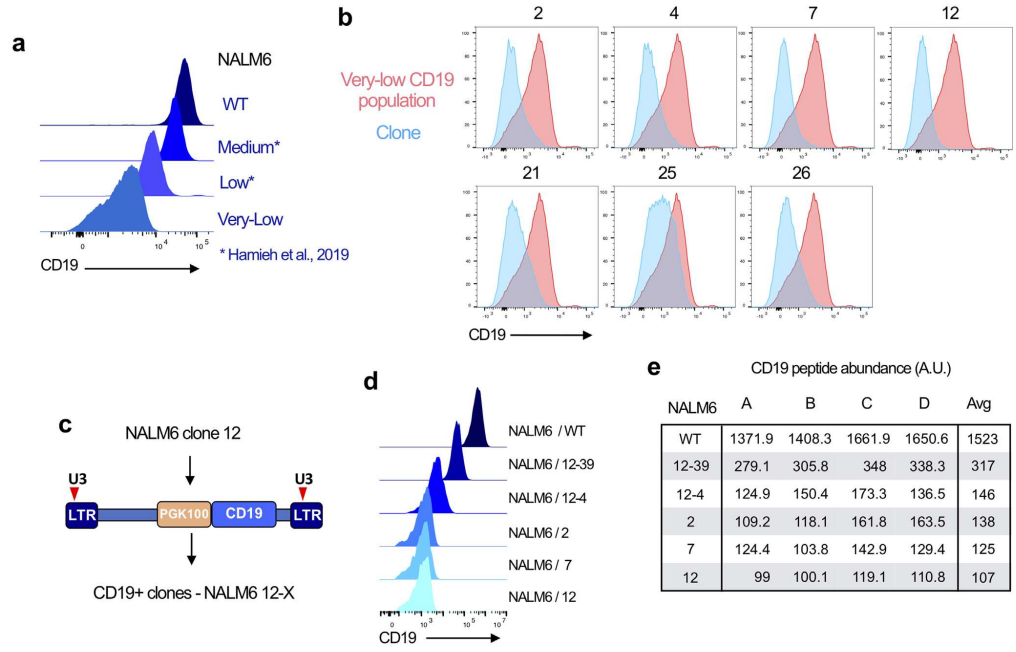


e

CD19 peptide abundance (A.U.)

| NALM6 | A | B | C | D | Avg |
|---|---|---|---|---|---|
| WT | 1371.9 | 1408.3 | 1661.9 | 1650.6 | 1523 |
| 12-39 | 279.1 | 305.8 | 348 | 338.3 | 317 |
| 12-4 | 124.9 | 150.4 | 173.3 | 136.5 | 146 |
| 2 | 109.2 | 118.1 | 161.8 | 163.5 | 138 |
| 7 | 124.4 | 103.8 | 142.9 | 129.4 | 125 |
| 12 | 99 | 100.1 | 119.1 | 110.8 | 107 |

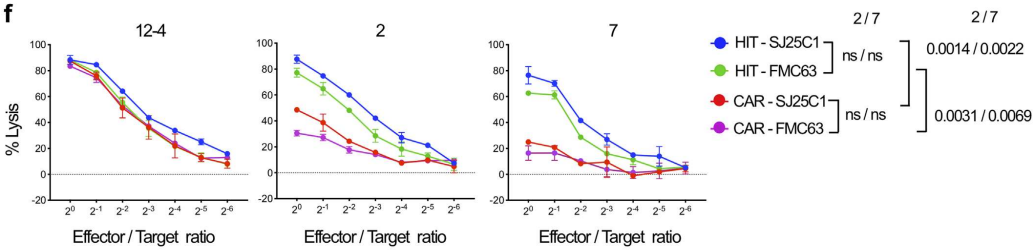


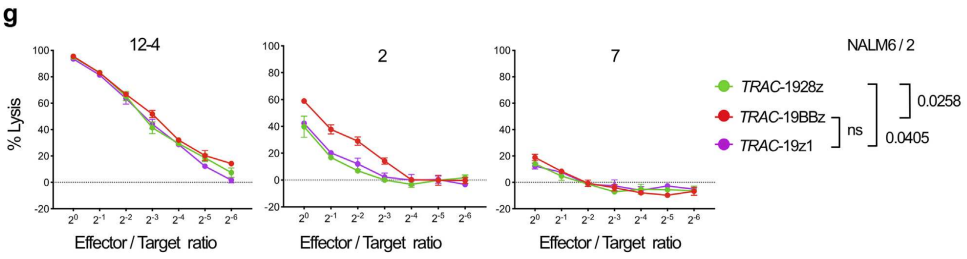


**Extended Data Fig. 5 | See next page for caption.**

**Extended Data Fig. 5 | HIT receptors provide greater antigen sensitivity than CARs. a**. Representative histogram of the CD19 expression in NALM6/WT, NALM6/Medium[21], NALM6/Low[21], and CRISPR-edited NALM6/Very Low (this study). **b**. NALM6/Very Low cells were used to generate single cell clones by limited dilution. CD19 expression was evaluated for each clone (blue histogram) along with the initial NALM6/Very Low cell population (red histogram); clone number indicated above the histogram plot. **c**. Schematics of the SIN lentiviral vector used to express low levels of CD19 in NALM6/12 cells. PGK100: short PGK promoter, which is a weak promoter[24]. **d**. Panel of NALM6 cells expressing different CD19 levels, which is represented as a histogram. NALM6/12-4 and NALM6/12-39 are derivatives of NALM6/12, which was transduced with the lentiviral vector described in **c**. **e**. Total CD19 protein quantification using mass spectrometry. Protein levels are expressed in terms of peptide abundance (A.U.), which can be compared across all samples analysed at the same time. A-D represent 4 independent analyses. AVG, average of A-D values. **f**. Representative cytotoxic activity using an 18 h bioluminescence assay, using FFL-expressing NALM6 as targets cells (clone numbers as in **b** and **d**); n = 2. CD19-specific *TRAC*-HIT and *TRAC*-CAR T cells were generated using two different CD19-specific binding domains, SJ25C1 and FMC63. Anova test was used to compare the CTL curves of all T cells for NALM6/2 and NALM6/7 cells. **g**. Representative cytotoxic activity using an 18 h bioluminescence assay, using FFL-expressing NALM6 as targets cells (same as in **f**); n = 2. CD19-specific *TRAC*-1928z, *TRAC*-19BBz, and *TRAC*-19z1 T cells were prepared as described in Materials and methods. Anova test was used to compare the CTL curves of all T cells for NALM6/2 cells. All data are mean ± s.e.m.

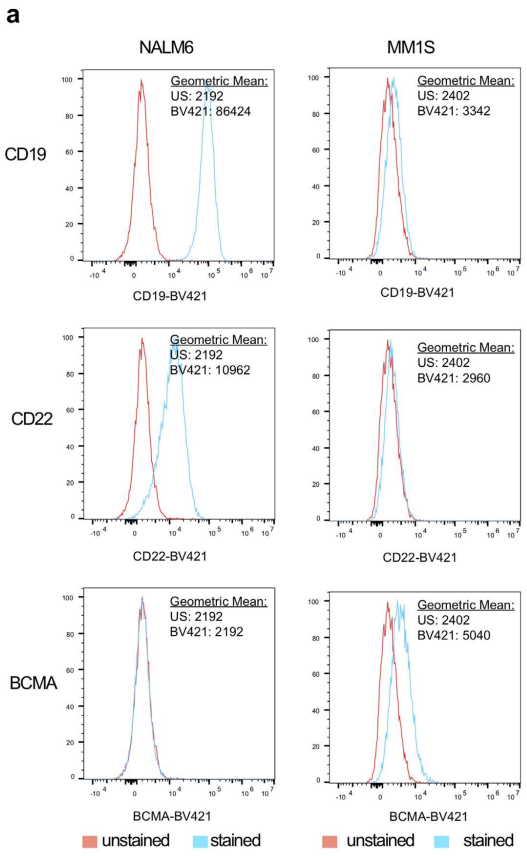


**b**

peptide abundance (A.U.)

| Protein | Cell line | A | B | C | D | Avg |
|---|---|---|---|---|---|---|
| CD19 | MM1S | 77.6 | 38.2 | 100.4 | 68.3 | 71 |
| CD19 | NALM6 | 1371.9 | 1408.3 | 1661.9 | 1650.6 | 1523 |
| CD22 | MM1S | 144.4 | 141.8 | 118.3 | 97.8 | 126 |
| CD22 | NALM6 | 512.5 | 490.9 | 681.3 | 631.7 | 579 |
| BCMA | MM1S | NA | NA | 508.7 | 604.4 | 557 |
| BCMA | NALM6 | NA | NA | 42.3 | 38.7 | 41 |

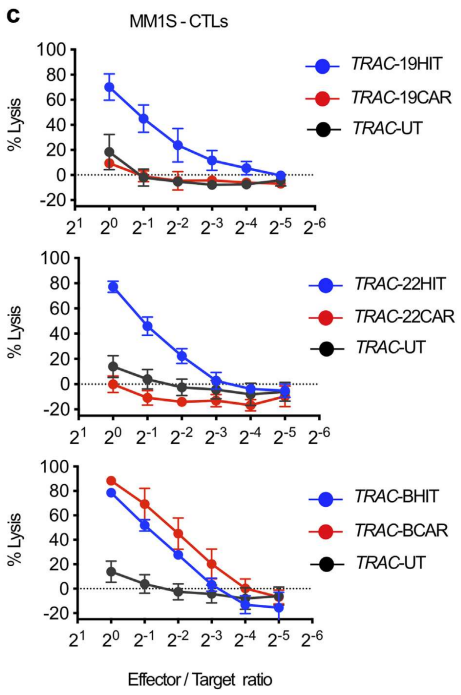


**Extended Data Fig. 6 | CD19, CD22, and BCMA HIT receptors elicit T cell-mediated lysis of multiple myeloma cells. a**. Representative flow cytometry analysis showing CD19, CD22, and BCMA expression in MM1S and NALM6/WT cells. **b**. Total CD19, CD22, and BCMA protein quantification using mass spectrometry. Protein levels are expressed in terms of peptide abundance (A.U.), which can be compared across all samples analysed at the same time. A-D represent 4 independent analyses. AVG, average of A-D values. **c**. Representative cytotoxic activity using an 18-h bioluminescence assay, using FFL-expressing MM1S as targets cells, which were incubated at the indicated E/T ratios with CD19-, CD22-, or BCMA-specific *TRAC*-HIT and *TRAC*-CAR T cells; n = 3. All data are mean ± s.e.m. Additional specificity studies are shown in Extended Data Fig. 2.

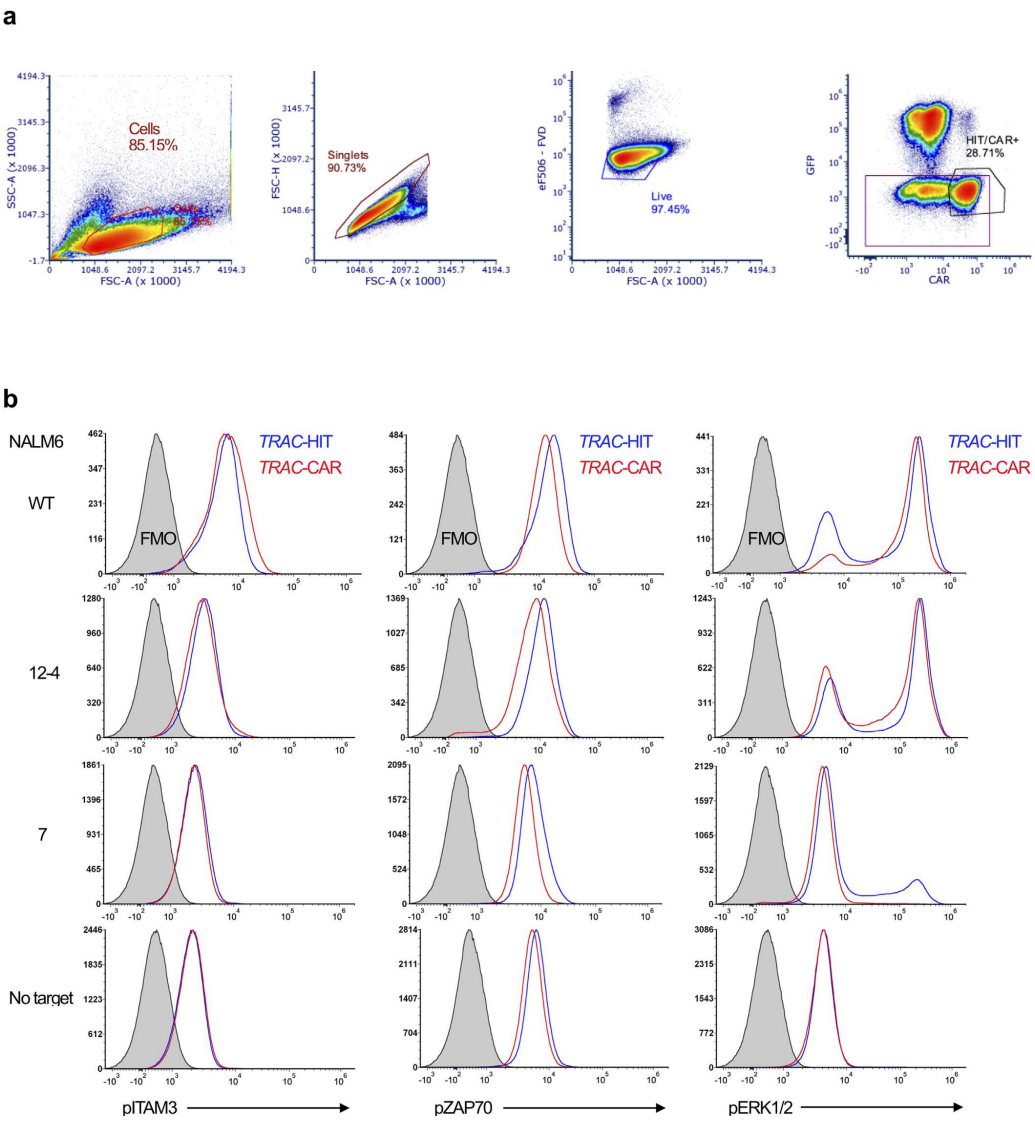


**Extended Data Fig. 7 | HIT T cells show increased signalling response to low antigen levels. a**. Gating strategy used to quantify ITAM3, ZAP70, and ERK1/2 phosphorylation in *TRAC*-HIT/CAR T cells (histograms shown in **b**.). **b**. Representative flow cytometry analysis showing histograms for intracellular phospho-ITAM3, phospho-ZAP70, and phospho-ERK1/2 in *TRAC*-HIT (left) and *TRAC*-CAR (right) T cells when incubated with NAML6/WT, NALM6/12-4, or NALM6/7 target cells at 1:2 ratio for 15 min, or with no target (No stim.). FMO: fluorescence minus one control. Geometric MFIs were obtained for each curve, and used to generate the plots presented in Fig. 2g. All data are mean ± s.e.m.

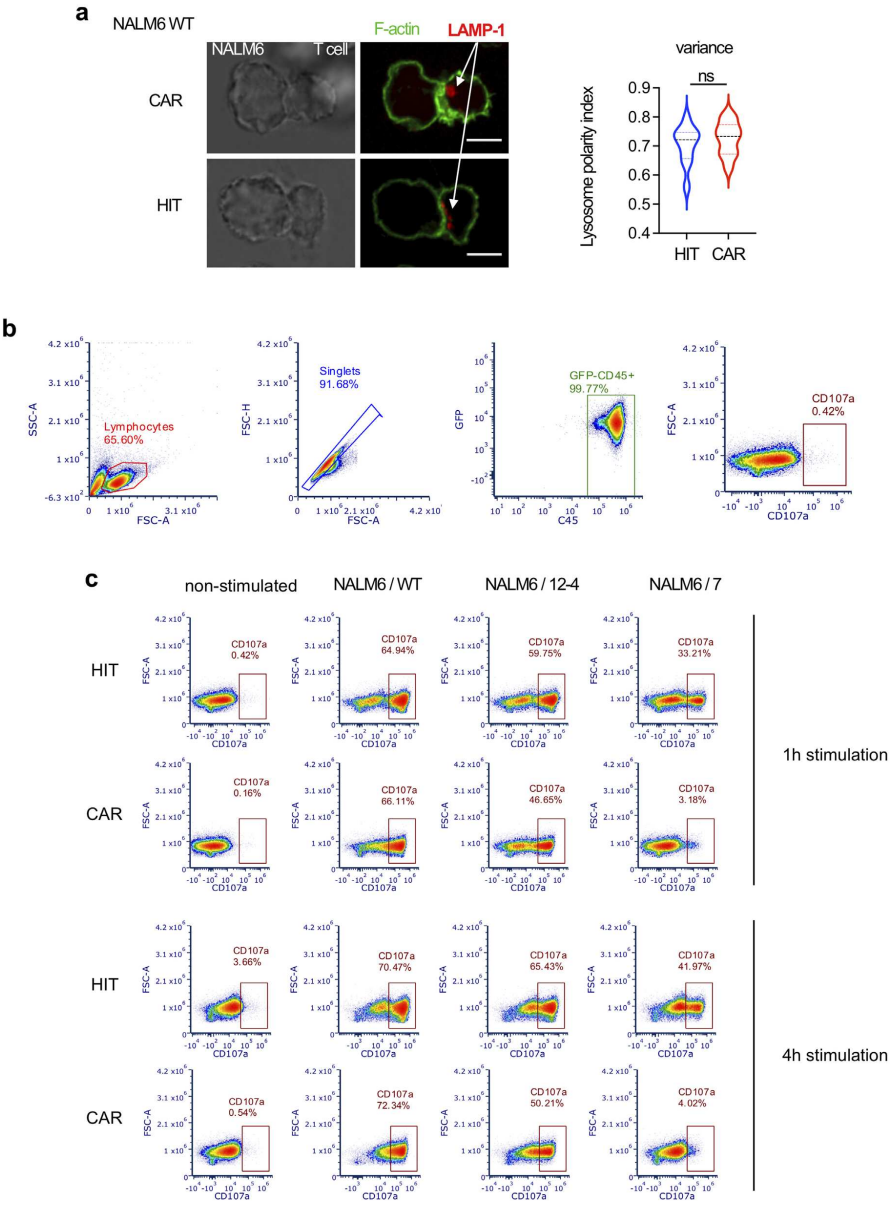


**Extended Data Fig. 8 | HIT T cells display increased degranulation upon stimulation. a**. Confocal and bright field images of conjugates of T cells expressing the CAR or HIT receptor and interacting for 30 min with NALM6/WT cells labeled for LAMP-1 (red channel) and Alexa Fluor 546 phalloidin (F-actin staining showed in green). Quantification of the lysosome polarity assessed as the distance to the immune synapse and compared with the average lysosomal distance to the total cortex of the T cell. This distance was normalized with the maximum distance found in the T cell and expressed as a polarity index between 1 (lysosomes at the synapse) and 0 (lysosomes at the opposite of the synapse. Data from two independent experiments; n = 59. Variance p-values were obtained by using unpaired t-test analysis. All data are mean ± s.e.m. Scale bar = 5 µm. White arrows indicate LAMP-1 signal. **b**. FACS plot gates used to quantify T cell degranulation (CD107a + cells). **b**. Representative (n = 2 independent experiments) analyses of CD107a levels in *TRAC*-HIT (top) and *TRAC*-CAR (bottom) T cells when incubated for 1 h (left) or 4 h (right) without or with NALM6 targets of different CD19 levels.

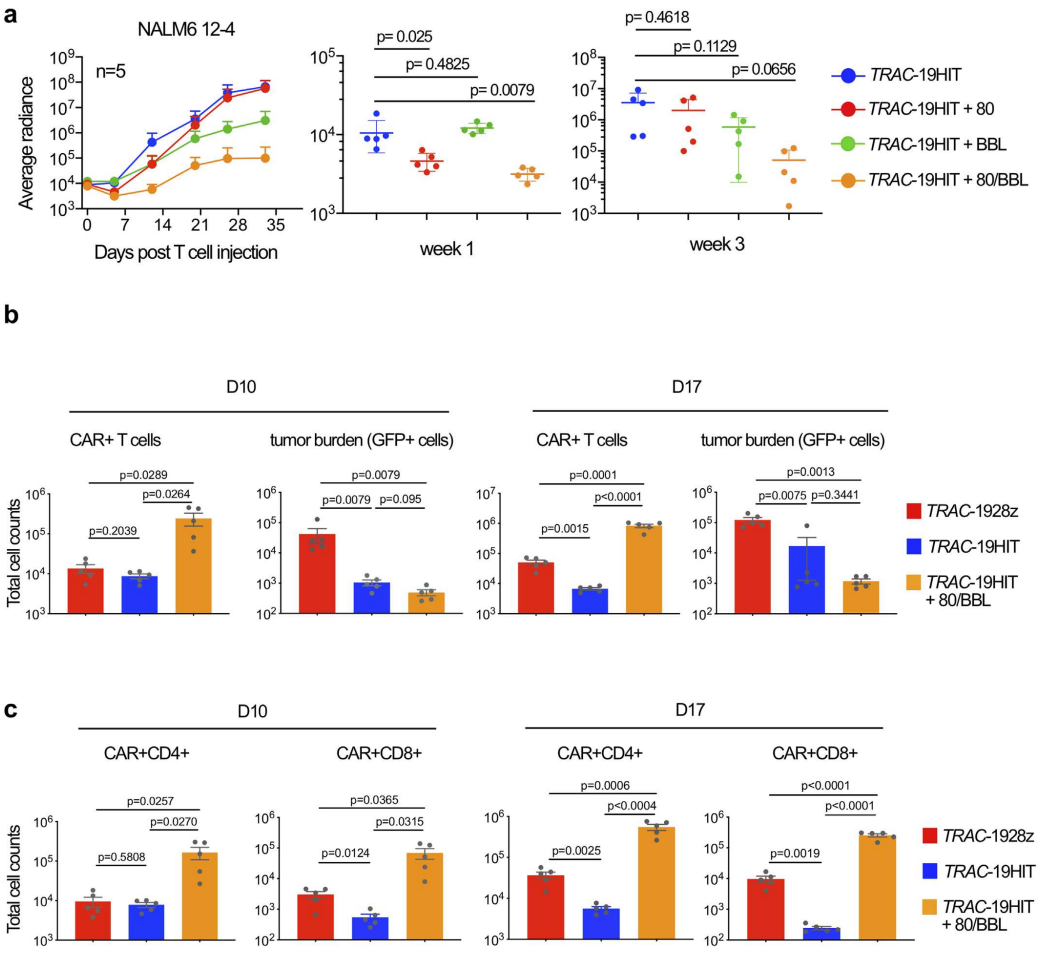


**Extended Data Fig. 9 | Control of low-antigen tumours by HIT T cells is enhanced by extending T cell persistence by co-expression of CD80 and 4-1BBL. a**. NALM6/12-4-bearing mice were treated with $4\times10^5$ *TRAC*-HIT T cells co-expressing the annotated costimulatory ligand. Tumour burden was quantified weekly over a 35-day period, at week 1 or week 3. Each line represents 5 mice. **b**. NALM6/12-4-bearing mice were treated with $4\times10^5$ CAR T cells ($n=5$ per group; dot = one mouse) and euthanized at days 10 and 17 after infusion; bone marrow *TRAC*-HIT or *TRAC*-CAR T cells and NALM6 cells were analysed and counted by FACS. **c**. Same as in **b**, except that bone marrow *TRAC*-HIT or *TRAC*-CAR CD4 and CD8 T cells counted by FACS. Two-tailed unpaired Student's *t*-tests were used for statistical analyses. All data are mean ± s.e.m. Tumor burden of individual animals are shown in Supplementary Fig. 2.

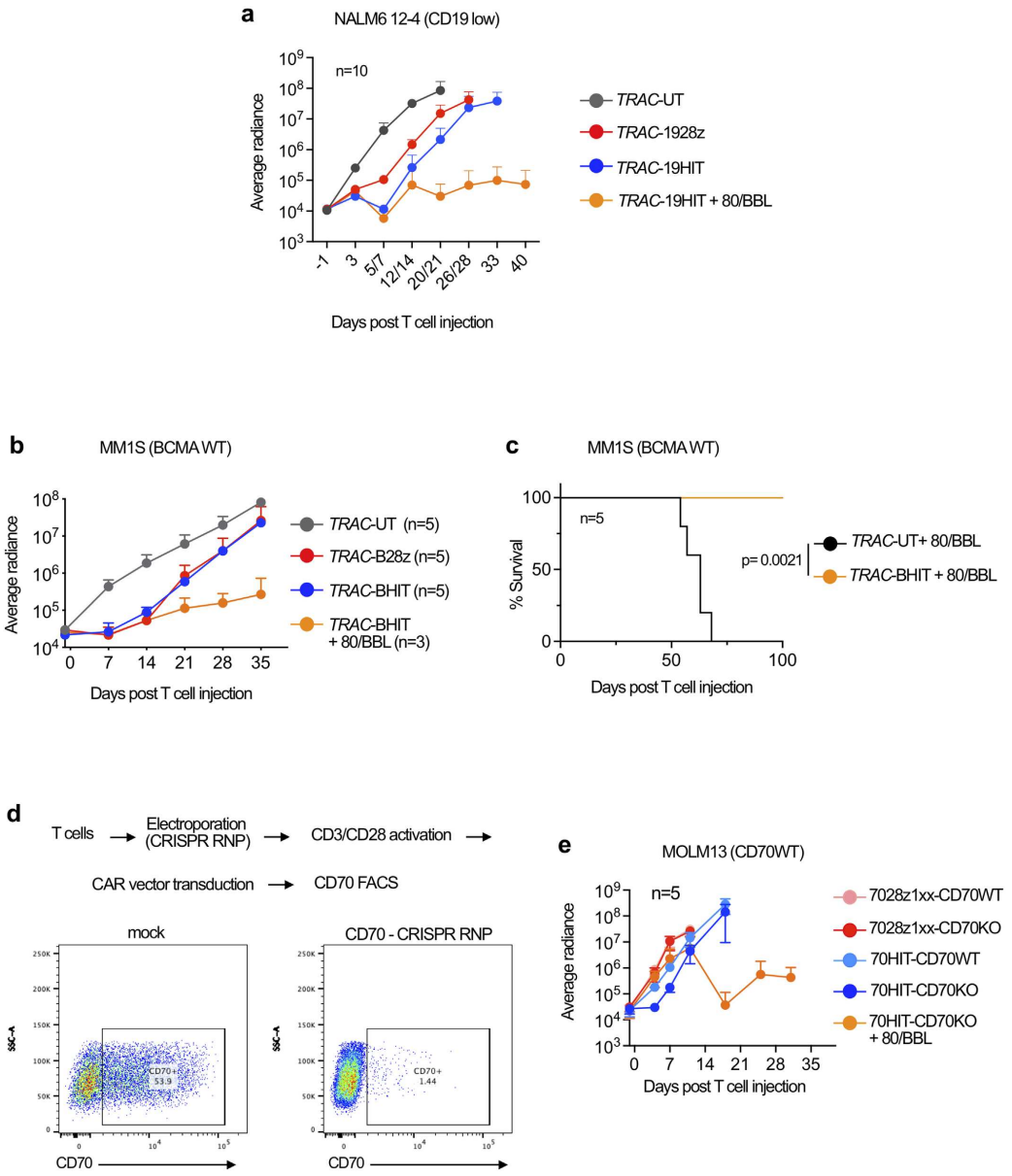


**Extended Data Fig. 10 | Co-expression of costimulatory ligands CD80 and 4-1BBL enhances the therapeutic potential of HIT cells. a**. Tumour burden (average radiance) of NALM6/12-4-bearing mice treated with $4\times10^5$ *TRAC*-HIT or *TRAC*-CAR T cells ($n=5$), analysed through a 35-day period. **b**. Tumour burden (average radiance) of MM1S-bearing mice treated with $2\times10^5$ *TRAC*-HIT or *TRAC*-CAR T cells ($n=5$), analysed through a 35-day period. **c**. Kaplan-Meier analysis of survival of MM1S-bearing mice treated with $4\times10^5$ BCMA-specific *TRAC*-HIT or *TRAC*-HIT + 80/BBL T cells ($n=5$). **d**. Representative FACS plots of surface CD70 expression in activated CAR-T cells 4 days after electroporation without (mock) or with CD70-specific CRISPR/Cas9 RNP. **e**. Tumour burden (average radiance) of MOLM13-bearing mice treated with $4\times10^5$ *TRAC*-HIT or *RV*-CAR T cells ($n=5$), analysed through a 35-day period. All data are mean ± s.e.m. Tumor burden of individual animals are shown in Supplementary Figs. 2,3.

# Annexe 3 : Influence of external forces on actin-dependent T cell protrusions during immune synapse formation

***Biology of the Cell*, Mai 2021**


**Résumé**

Lors de la reconnaissance antigénique, les cellules T produisent des protrusions riches en actine qui génèrent des forces impliquées dans l'activation des cellules T. Ces forces sont influencées par les propriétés mécaniques des cellules présentatrices d'antigènes (CPA). Cependant, le mécanisme selon lequel les forces externes générées par les CPA influencent la dynamique de la protrusion d'actine reste inconnu.

En utilisant une sonde de force à micropipette, nous avons appliqué des forces de compression ou de traction contrôlées sur des lymphocytes T primaires activés par une microbille couverte d'anticorps, et mesuré les effets de ces forces sur la protrusion générée par les lymphocytes T.

Nous avons constaté que l'application de forces de compression diminuait légèrement la longueur, le moment auquel la protrusion cesse de croître et se rétracte, et la vitesse de formation de la protrusion ; alors que les forces de traction augmentaient fortement ces paramètres. Dans les deux cas, les forces appliquées n'ont pas modifié le temps nécessaire aux cellules T pour commencer à faire croître la protrusion. En explorant les événements moléculaires contrôlant la dynamique de la protrusion, nous avons montré que l'inhibition du complexe Arp2/3 altère la dynamique de la protrusion en réduisant à la fois sa longueur maximale et sa vitesse de croissance et en augmentant le délai de début de croissance. Enfin, les cellules T ont développé des protrusions similaires dans des conditions plus physiologiques, c'est-à-dire lorsqu'elles sont activées par une CPA au lieu d'une microbille activatrice.

Nos résultats suggèrent que la formation de la protrusion génératrice de force par les cellules T est fixée par un temps constant intracellulaire et que sa dynamique est sensible aux forces externes. Ils montrent également que l'assemblage de l'actine médié par le complexe Arp2/3 est impliqué dans la formation et la dynamique de la protrusion.


**Contribution à l'article**

J'ai mis au point le système de cellule présentatrice d'antigène artificielle qui a été utilisé dans l'article, ainsi que le protocole d'activation des lymphocytes T par ces CPA. J'ai également relu et apporté des commentaires et modifications au texte.

Biol. Cell (2021) **0,** 1–14 DOI: 10.1111/boc.202000133

Research article

# Influence of external forces on actin-dependent T cell protrusions during immune synapse formation

**Andrés Ernesto Zucchetti*, Noémie Paillon*, Olga Markova†, Stéphanie Dogniaux*, Claire Hivroz* and Julien Husson†[1]**

*Integrative Analysis of T Cell Activation Team, Institut Curie, PSL Research University, Paris, Cedex 05, France †LadHyX, CNRS, Ecole Polytechnique, Institut Polytechnique de Paris, Palaiseau 91120, France

*Background Information.* We have previously observed that in response to antigenic activation, T cells produce actin-rich protrusions that generate forces involved in T cell activation. These forces are influenced by the mechanical properties of antigen-presenting cells (APCs). However, how external forces, which can be produced by APCs, influence the dynamic of the actin protrusion remains unknown. In this study, we quantitatively characterised the effects of external forces in the dynamic of the protrusion grown by activated T cells.

*Results.* Using a micropipette force probe, we applied controlled compressive or pulling forces on primary T lymphocytes activated by an antibody-covered microbead, and measured the effects of these forces on the protrusion generated by T lymphocytes. We found that the application of compressive forces slightly decreased the length, the time at which the protrusion stops growing and retracts and the velocity of the protrusion formation, whereas pulling forces strongly increased these parameters. In both cases, the applied forces did not alter the time required for the T cells to start growing the protrusion (delay). Exploring the molecular events controlling the dynamic of the protrusion, we showed that inhibition of the Arp2/3 complex impaired the dynamic of the protrusion by reducing both its maximum length and its growth speed and increasing the delay to start growing. Finally, T cells developed similar protrusions in more physiological conditions, that is, when activated by an APC instead of an activating microbead.

*Conclusions.* Our results suggest that the formation of the force-generating protrusion by T cells is set by an intracellular constant time and that its dynamic is sensitive to external forces. They also show that actin assembly mediated by actin-related protein Arp2/3 complex is involved in the formation and dynamic of the protrusion.

*Significance.* Actin-rich protrusions developed by T cells are sensory organelles that serve as actuators of immune surveillance. Our study shows that forces experienced by this organelle modify their dynamic suggesting that they might modify immune responses. Moreover, the quantitative aspects of our analysis should help to get insight into the molecular mechanisms involved in the formation of the protrusion.

Additional supporting information may be found online in the Supporting Information section at the end of the article.

## Introduction

T cell activation is key in establishing an adaptive immune response and it requires a direct contact between T cells and antigen-presenting cells (APC) where the T cell receptor recognises the antigenic peptide presented by the major histocompatibility complex. This contact region between both cells forms the immune synapse (IS) and controls several aspects of T cell functions (Dustin and Choudhuri, 2016). We have previously reported that during the IS formation by activation with an antibody-covered microbead mimicking an APC, the

[1]To whom correspondence should be addressed (email: julien.husson@polytechnique.edu)

**Key words:** Arp2/3, CD4+ T cells, cytoskeleton, helper T cells, T lymphocytes.

**Abbreviations:** AFM, atomic force microscope; APC, antigen presenting cell; ILP, invadosome-like protrusion; IS, immune synapse; MFP, micropipette force probe; MHC, major histocompatibility complex; TCR, T cell receptor

**Figure 1 | (A) Micropipette force probe (MFP)**
A stiff micropipette holds a T cell. A flexible micropipette of bending stiffness $k$ aspirates firmly an activating microbead. The deflexion $d$ of the micropipette (not to scale) is controlled to apply the desired force level during cell activation, $F_{act} = k \times d$. (**B**) Representative curve of the bead position (measuring cell length) versus time. The maximal protrusion length is $\Delta L_{max}$. The initial cell–bead contact is ensured by applying an initial compressive force $F_{comp}$, after which an average force $F_{act}$ is applied during the rest of the experiment (with an added small force modulation to perform other mechanical measurements, see text).

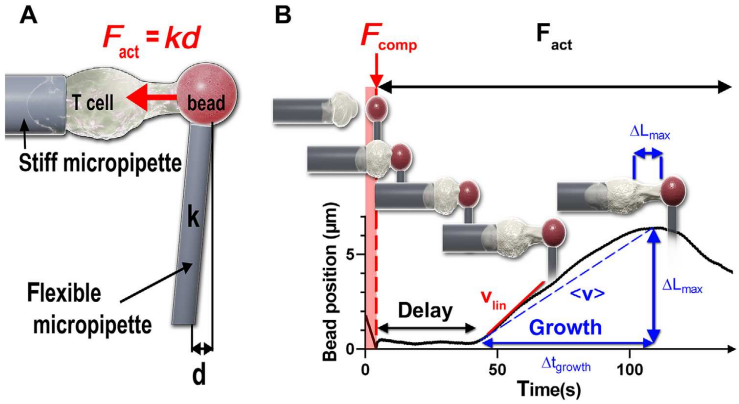


T cell produces an actin-rich protrusion. This protrusion generates forces and adapts its growth to the stiffness of the activating surface (Basu et al., 2016; Husson et al., 2011; Sawicka et al., 2017). Seemingly similar protrusions have been observed in T cells contacting another cell, an artificial activating surface, or during transmigration (Cai et al., 2017; Carman et al., 2007; Jung et al., 2016; Sage et al., 2012; Tamzalit et al., 2019; Ueda et al., 2011; Yan et al., 2019). Many questions remain regarding the characteristics of this protrusion. One of them is if and how these force-developing protrusions are modified by forces that are produced by APCs such as dendritic cells (Choraghe et al., 2020; Heuzé et al., 2013; Ricart et al., 2011) but also what is the molecular machinery controlling the dynamic of these protrusions. In this report, we further dissect the dynamics of T cell protrusion by exploring the effect of well-defined forces exerted by the cell environment. We also show that the dynamic of the protrusion depends on the ARP2/3 complex. Finally, we observe and characterise the formation of the actin-protrusion in T cells interacting with an APC model instead of a microbead.

## Results

### Description of the setting and Characterization of the activation-induced protrusion

We have previously automatised the micropipette force probe (MFP) to apply controlled forces to T lymphocytes (Sawicka et al., 2017; Zak et al., 2019). The MFP uses a flexible micropipette as a cantilever that aspirates an activating microbead. This bead is brought into contact with a leukocyte held by another micropipette. In the present study, we used human primary CD4+ T lymphocytes purified from donor blood and commercial microbeads coated with anti-CD3 + anti-CD28 mAbs known to induce a signalling cascade in T cells and the generation of a protrusion inducing pushing and pulling forces on the activating bead (Husson et al., 2011; Sawicka et al., 2017). The cell–bead contact is ensured by compressing the bead against the cell until a desired force level $F_{comp}$ is reached (Figure 1A and Supplementary Video 1). It takes few seconds to reach $F_{comp}$, after which the setup automatically shifts the position of the base of the flexible micropipette to exert a defined force $F_{act}$ on the cell during the rest of the experiments (lasting typically 200 s). $F_{act}$ can be a compressive ($F_{act} > 0$

by convention) or pulling force ($F_{act} < 0$). On top of the level of force $F_{act}$, the setup superimposes a small oscillatory force of amplitude 0.025–0.050 nN and frequency $f = 1$ Hz. This force modulation is used to extract the mechanical properties of the cell over time, which evolve during activation, that is, the lymphocyte becoming stiffer and more viscous during activation (Zak et al., 2019). Here, we do not focus on these mechanical changes, but having used the force modulation during our measurements, we checked that the force modulation did not influence the result when $F_{act}$ was comparable to the amplitude of the modulation (Supplementary Material 1). Furthermore, experiments were performed at room temperature to limit the thermal drift of the micropipettes. We have shown that at 37°C, T cells react faster than at room temperature, but in a qualitatively comparable manner (Zak et al., 2019). During T cell activation, we measured the cell length, which remained constant for some time after $F_{act}$ was applied. This period is herein called delay (Figure 1B). This delay ended when the cell started growing a protrusion that was detected by a change in bead position. The growth was first slow, then entered a relatively constant velocity $v_{lin}$, then slowed down and stopped before switching to a shrinkage phase. We measured $v_{lin}$, the duration of the growth $\Delta t_{growth}$ and the maximal length reached by the protrusion $\Delta L_{max}$, from which we deduced the average growth speed $\langle v \rangle = \Delta L_{max}/\Delta t_{growth}$ (Figure 1B). $v_{lin}$ was correlated with $\langle v \rangle$ ($v_{lin} \sim 1.4\ \langle v \rangle$; see Supplementary Material 2), but less variable than $\langle v \rangle$ among cells, so we refer to $v_{lin}$ in this report.

### Influence of force on protrusion's delay, length and speed

Because physiologically, T lymphocytes interact with APCs that might exert some forces on their side, we wondered if the protrusion would be influenced by an external force during activation. To answer this question, we applied the same initial compressive force $F_{comp}$ but varied $F_{act}$. The influence of $F_{act}$ on the maximum length $\Delta L_{max}$ was clear: the higher the compression ($F_{act} > 0$), the shorter the protrusion, and the larger the absolute value of the pulling force ($F_{act} < 0$), the longer the protrusion (Figure 2A). We further asked if the growing speed $v_{lin}$ was influenced. We observed that compressive forces ($F_{act} > 0$) did not affect $v_{lin}$. In contrast, $v_{lin}$ significantly increased under pulling force ($F_{act} < 0$) (Figure 2B). Neither compressive nor pulling forces altered the delay. The average delay for all the $F_{act}$ applied was 38 ± 20 s ($N = 151$ cells, $n = 9$ experiments; Figure 2C). Finally, $\Delta t_{growth}$ was not influenced by compressive forces but increased under pulling forces (Figure 2D).

**Figure 2 | Influence of the applied force during activation $F_{act}$ on several parameters (all cells were submitted to $F_{comp} = 0.36$ nN)**

(**A**) Maximal protrusion length $\Delta L_{max}$. (**B**) Growth speed $v_{lin}$. (**C**) Delay. (**D**) Growth duration $\Delta t_{growth}$. Data in **A**–**D** represent eight experiments, each dot is an average over 7–20 cells, except in **B** where the average is over 3–17 cells. Gray area represents SDs. Statistical tests: two-tailed *t*-test with Welch's correction (*$P < 0.05$; **$P < 0.01$; ***$P < 0.001$).

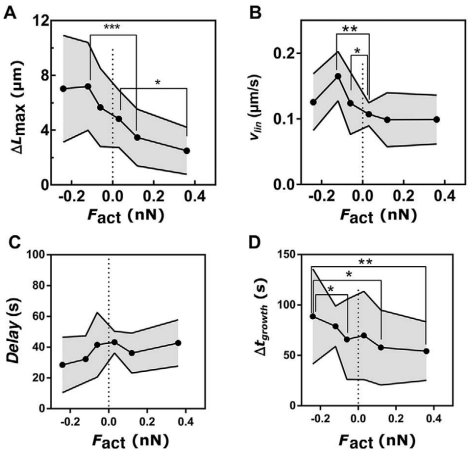


### Link between protrusion's diameter and maximal length

Qualitative observations on our data suggested that the diameter of the protrusion depended on its length (Figure 3A). We thus first quantified the diameter ($D_{prot}$) of the protrusion at the contact place with the bead at the moment where the protrusion reached its maximal length ($\Delta L_{max}$) for several values of $F_{act}$ (Figure 3B). We then plotted the maximal length of the protrusion versus its diameter, for all values of $F_{act}$, and data collapsed on a master curve (Figure 3C), showing that $\Delta L_{max}$ and $D_{prot}$ are intimately linked:

**Figure 3 ( | (A) Images of the micropipette force probe (images denoised, contrasted and the background was removed, bar: 5 µm)**

Cells were submitted to increasing level of force ($F_{act} = -0.24$ nN, $-0.05$ nN, $+0.12$ nN and $+0.36$ nN, top to bottom). (**B**) $D_{prot}$ as a function of $F_{act}$ (cells were all initially submitted to $F_{comp} = 0.36$ nN). Gray area represents SDs. Each dot represents an average over 7–20 cells across eight experiments. (**C**) Maximal protrusion length $\Delta L_{max}$ as a function of its tip diameter $D_{prot}$, for various applied forces $F_{act}$. Cells were all submitted to an initial compression $F_{comp} = 0.36$ nN. Errors bars are SDs. Each dot represents an average over 2–12 cells across eight experiments, except a dot representing a single cell for $F_{act} = 0.03$ nN. The dashed line is a fit assuming a maximal volume of actin of $\sim$7 µm$^3$ in the protrusion when reaching its maximal length. (**D**) Volume and surface area of T cells at initial time and when the protrusion was the longest. ****$P < 0.0001$ for a two-tailed $t$-test. (**E**) $D_{prot}$ for different values of $F_{comp}$ and $F_{act}$, and diameter $D_{Hertz}$ of the initial cell–bead contact diameter based on the Hertz model (see *Materials and Methods*).

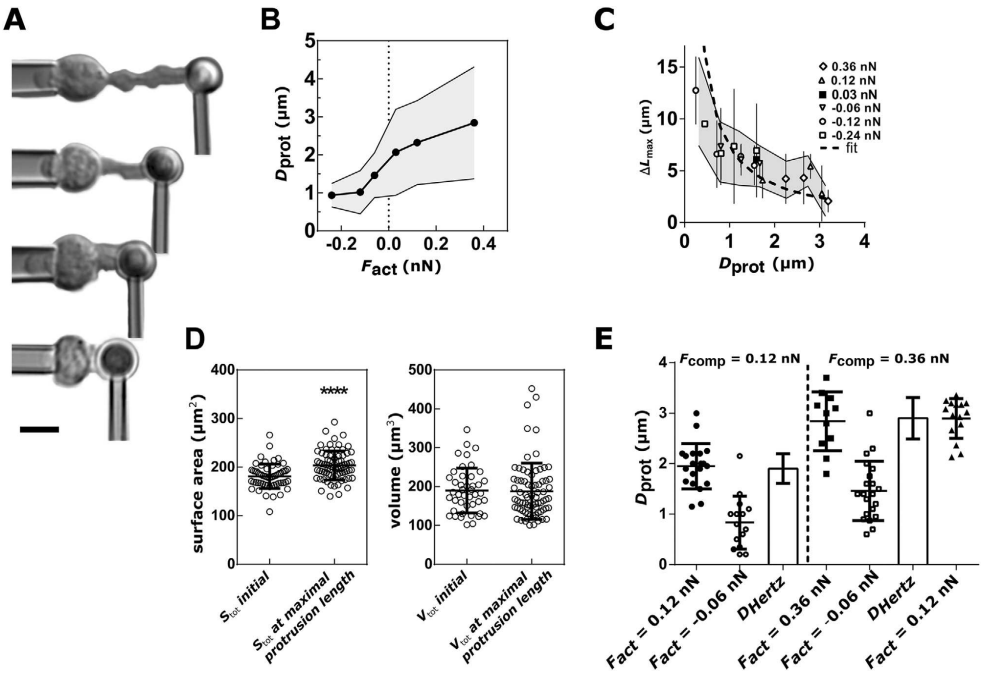


the longest protrusions were also the thinnest, whatever the level of applied force.

### Non-limiting role of membrane stores

We reasoned that this relationship between maximal length and diameter of the protrusion could reflect a physical constraint: the growth of the protrusion could be limited by a maximal amount of membrane stores, which would imply that longer protrusions would be thinner due to limited maximal area. To test this hypothesis, we quantified cell surface area (see *Materials and Methods*) at the beginning of the experiments and when the protrusion was the longest. The difference was significant (initial area of $181 \pm 25$ µm$^2$ versus largest area of $203 \pm 30$ µm$^2$, $n = 8$ experiments, $N = 76$ cells; Figure 3D) but small; cell surface area was only 12% larger than its initial value. We have shown previously that CD4 T cells have more than 20% of surface reservoirs in a resting state, and that they can mobilise

much larger membrane stores (up to 100% of surface area) during active processes such as transendothelial migration and spreading on an activating surface (Guillou et al., 2016a). Hence, there are large reservoirs available to the T cell beyond 12% area expansion, and limited surface area cannot explain the end of the protrusion's growth. We also considered volume as a physical constraint, but the maximum cell volume was the same as the initial one (maximal volume: $190 \pm 58$ μm$^3$; initial volume: $188 \pm 72$ μm$^3$, $N = 44$ and 76 cells, across $n = 8$ experiments; Figure 3D). Note that the volume of the protrusion starts from zero and increases linearly with time, but represents a small fraction of cell volume. Indeed, when modelled as a cylinder, the volume of the cylindrical protrusion equals its section multiplied by its length. By taking an approximate length of 5 μm and a diameter of about 2 μm, one gets a volume of the protrusion of roughly 16 μm$^3$, which is only 9% of the initial cell volume.

### Role of initial compressive force and contact area on protrusion's diameter and maximal length

The master curve in Figure 3C shows that whatever $F_{act}$, the maximal length $\Delta L_{max}$ is determined by $D_{prot}$, so understanding what sets $D_{prot}$, can provide an insight on what set the maximal protrusion length $\Delta L_{max}$. We considered the influence of the initial compressive force on $D_{prot}$, reasoning that this protrusion's diameter, measured just at the moment at which the protrusion stops growing (a moment we call the switch), could be determined by the initial cell–bead contact area. This initial contact area is determined by the level of the initial compression on the cell, $F_{comp}$: the larger $F_{comp}$, the larger the initial cell–bead contact. It is difficult to determine this initial contact area from the movies acquired during experiments, but it can be quantified using the Hertz model (Johnson, 1985; Rosenbluth et al., 2006) (see *Materials and Methods* and Supplementary Material 3) knowing the applied force and the stiffness of the cell. We ran experiments in the simplest case, where $F_{act}$ was set equal to $F_{comp}$, thus keeping the compression constant during the whole experiment. We expected the protrusion diameter to be equal to the initial contact diameter, and indeed measurement showed an excellent agreement between $D_{prot}$ and the diameter $D_{Hertz}$ predicted by the Hertz model (Figure 3E). We then asked if the diameter would change if the compression $F_{act}$ was not equal but lower than $F_{comp}$. The resulting protrusion diameter $D_{prot}$ was still in excellent agreement with $D_{Hertz}$ set by the initial compressive force. This showed that when the protrusion is kept under compression ($F_{act} > 0$), the protrusion diameter is determined at the stage of the initial cell–bead contact by the level of the initial compressive force $F_{comp}$. When the protrusion was submitted to a pulling force during its growth ($F_{act} < 0$), two cases could be possible. In a first case, the protrusion diameter could be again determined by the initial compressive force and then remain the same even under pulling force. In the second case, one could expect that the pulling force detaches some bonds at the cell–bead interface, making the protrusion's diameter thinner. To determine which case occurred, we measured the diameter of the protrusion when the initial compression was followed by a small traction force $F_{act} = -0.06$ nN. This led to the second case mentioned above: the protrusion diameter was smaller than the initial one predicted by the Hertz model (Figure 3E). This means that the traction forces modulate the protrusion diameter by making it thinner. We hypothesise that this thinning is due to pulling forces ripping off part of the contacts at the cell–bead interface during protrusion's growth. These results strongly suggest that compressive and traction forces exerted by the APCs on the T cells modulate the formation and the dynamic of the protrusion generated by T lymphocytes.

### Maximal amount of mobilisable actin in the protrusion

Even though we excluded conservation of cell's total volume as setting the maximal length of the protrusion, the clear trend appearing in the master curve in Figure 3C (the longer the protrusion, the thinner), suggested testing if there could be a limitation imposed by a maximal amount of actin available. We reasoned that if available actin in the cell was limiting, each protrusion could stop when all this actin would be stored in the walls of the protrusion. We estimate the volume of actin in the protrusion walls, $V_{max}$, by multiplying the lateral surface area of the cylindrical protrusion, $S_{lat} = \pi D_{prot} \Delta L_{max}$, with the average thickness of the wall, $e \approx 0.3$ $\mu$m. This leads to a prediction that, if the maximal amount of actin is the same in each protrusion when it reaches its maximal length, then $\Delta L_{max}$ should be proportional to

**Figure 4 | Inhibition of Arp2/3 by CK666 leads to shorter (A), delayed (B) and slower growing (C) T cell protrusions, but does not change growth duration (D)**

DMSO control, $n = 2$ experiments, $N = 16$ cells; CK666: $n = 3$ experiments, $N = 20$ cells. Statistical tests: two-tailed unpaired *t*-tests with Welch correction.

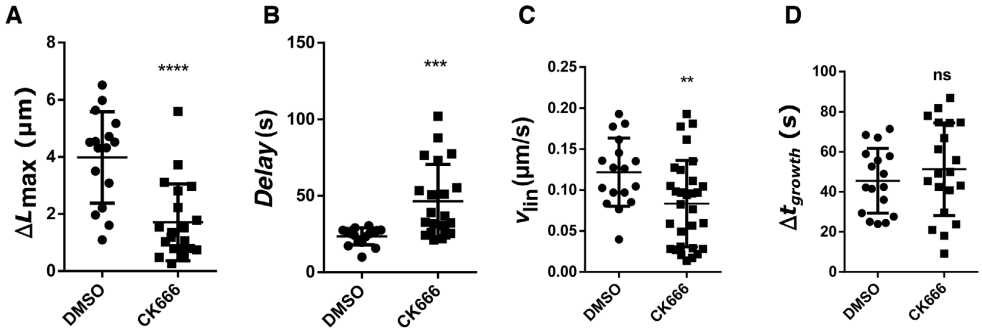


the inverse of $D_{\text{prot}}$, and proportional to the maximal actin volume, $V_{\text{max}}$: $\Delta L_{\text{max}} = \frac{V_{\text{max}}}{\pi D_{\text{prot}} \epsilon}$.

The remaining free parameter, the maximal actin volume $V_{\text{max}}$, could be adjusted by fitting the master curve in Figure 3C, leading to $V_{\text{max}} = 7\ \mu m^3$. The resulting fit is superimposed to the data in Figure 3C. In the discussion, we argue that this can represent a significant part of available actin and that data shown in Figure 3C are consistent with a limiting availability of free actin in the cell.

### Protrusion length, delay and speed are Arp2/3 dependent, growth duration is not

As shown herein and before, the protrusion is a very dynamic structure. We have previously shown that inhibition of actin polymerisation with Latrunculin A treatment abolishes the formation of protrusions by T lymphocytes (Husson et al., 2011). To get more insights into the molecular mechanism supporting the generation by T cells of these protrusions, we asked whether the Arp2/3 complex, which controls nucleation of actin polymerisation and branching of filaments, was involved. To do so, we treated cells with the Arp2/3 inhibitor CK666. As opposed to the above-mentioned treatment with Latrunculin A, Arp2/3 inhibition did not abolish the growth of the protrusion. Yet, the effect of CK666 was strong: protrusions reached a lower maximum length (Figure 4A), started growing later (Figure 4B), with a reduced speed (Figure 4C). In contrast, protrusions growth duration was not significantly altered (Figure 4D). It is worth mentioning that CK666 treatment did not significantly change cell initial stiffness (Supplementary Material 4), which might not be intuitive, but is consistent with measurements by others (Fritzsche et al., 2017).

### F-actin is enriched in the protrusion, including in a cell–cell system

We have shown before that the protrusion growth is actin dependent, and that qualitatively, the protrusion appears as an actin cylinder devoid of microtubules (Husson et al., 2011). To further understand how actin is reorganised during the protrusion formation, we focused on the F-actin distribution inside the protrusion. We performed confocal imaging of cells fixed at different timepoints (2, 5 and 10 min after introducing cells and beads on a coverslip, see *Materials and Methods*). F-actin was depleted in the centre of the protrusion (Figure 5A), recapitulating our observation that the protrusion is a hollow tube formed by F-actin. The protrusion walls were enriched in F-actin when compared with the rest of the cell cortex (Figure 5C). The enrichment was progressive, starting from the base of the protrusion (see example in Figure 5A), and the fluorescence intensity reaching a maximal level in the region of the wall in contact

**Figure 5 | F-actin organisation**

(**A**) Top: maximum intensity confocal stack projection (F-actin in red, nucleus in blue and brightfield in gray). Bottom: only the F-actin image from top is shown using false colours to visualise the enrichment in F-actin in the protrusion walls. A line is drawn on half of the cortical part of the activated cell, the corresponding intensity profile is shown in **B**. The arrow indicates the base of the protrusion. Scale bar is 5 µm. (**B**) Fluorescence intensity along the line drawn in **A**. The distance is counted starting from the bead towards the back of the cell. The arrow corresponds to the base of the protrusion. (**C**) Fluorescence intensity of F-actin in the cortex of primary T cells activated by a bead. For each cell, the average intensity in the protrusion was compared with the average intensity in the cortex located outside the protrusion. Each dot represents a single cell ($N = 83$ cells, $n = 2$ experiments, Wilcoxon matched-pairs signed rank test). (**D**) Two examples of protrusions between a primary T-lymphocyte and a K64 cell. F-actin is shown in red for both cells and the K64 cells are shown in blue. (**E**) Fluorescence intensity analysed as in **C**, the average intensity in the protrusion was compared with the average intensity in the cortex located outside the protrusion in T cells in contact with K-64 cells (each dot represents a T cell, $N = 50$ cells across $n = 2$ experiments, two-tailed $t$-test).

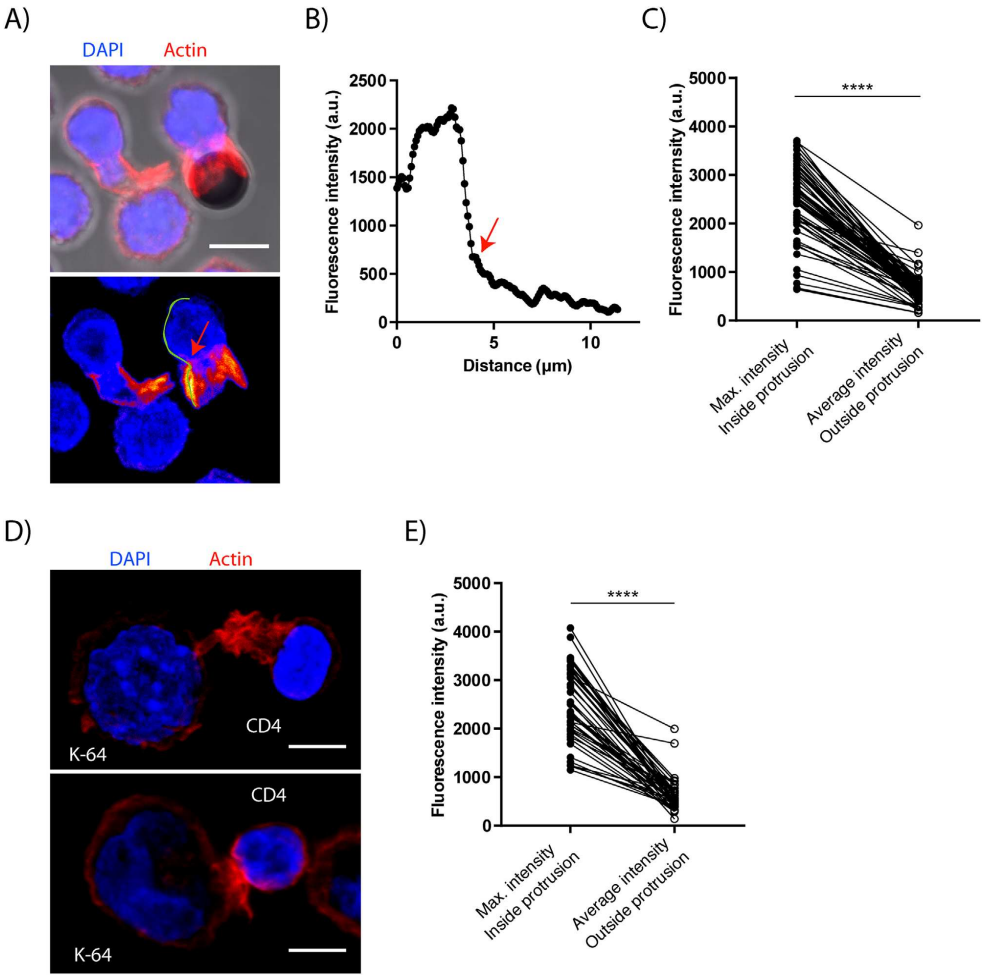

with the bead (Figure 5B), thus forming a thick actin ring reminiscent of what has been observed in 2D studies of the immunological synapse (Cannon and Burkhardt, 2002). Finally, we studied the formation of the actin protrusions in a more physiological model of conjugates formed between T lymphocytes and APC. As model APCs, we used K562 cells expressing the Fc receptor CD64 (named K64, see *Materials and Methods*) and loaded them with anti-CD3/CD28 activating antibodies like the coated beads used previously. APCs were attached to coverslips. Human CD4+ Jurkat T cells were then added, and conjugates were fixed after 5 min. The confocal images obtained were very similar to the ones obtained with beads coated with activating mAbs: they showed the formation of protrusion by T cells interacting with activating APC. Moreover, these protrusions showed similar features: a hollow tube enriched in F-actin as compared with the T cell cortex (Figures 5D–5E). These results confirm that when activated by APCs, T cells develop force-generating protrusions that look similar to the protrusions generated when T cells are activated by beads in the MFP setting.

## Discussion

Previous works have shown that during the IS formation, T cells produce an actin protrusion that generates forces and adapts its growth to the stiffness of the activating surface (Basu et al., 2016; Husson et al., 2011; Sawicka et al., 2017). The physiological role and the biophysical characteristics of this protrusion remain unknown. In this report, we have applied controlled forces to leukocytes using a MFP to study in detail the behaviour of protrusions emitted by T cells following TCR engagement. This method allows getting precise parameters such as the delay required to grow the protrusion, length and diameter of the protrusion, speed of growth and the time at which the protrusion stops growing and retracts (the switch time). Quantifying these parameters can provide valuable information on the molecular mechanisms behind the generation of this protrusion. Our results suggest that the formation of the protrusion is set by an intracellular constant time and that its dynamic is sensitive to external forces. The application of compressive forces slightly decreased the length, duration and velocity of the protrusion formation, whereas pulling forces strongly increase these parameters. We also show that actin assembly mediated by actin-related protein Arp2/3 complex is involved in the formation and dynamic of the protrusion. We addressed the relevance of our study in physiological conditions by showing with confocal microscopy that the protrusion is also emitted by T cells interacting with an artificial APC, suggesting that the protrusion formation is not an artefact due to the bead size or stiffness. Finally, we observed an enrichment of F-actin in the protrusion forming a thick actin ring at the contact with the activating surface, reminiscent of what has been observed in 2D studies of the immunological synapse (Cannon and Burkhardt, 2002).

Similarities exist between the protrusions that we observed and other protrusive structures: T cells were already shown to form protrusive structures that can "invade" the membrane of APC (Cai et al., 2017; Sage et al., 2012; Ueda et al., 2011). Such protrusions were first described in T lymphocytes during transcellular diapedesis through endothelial cells (Carman et al., 2007) and called invadosome-like protrusions (ILPs). More recently the group of M. Huse also described protrusive structures developed at the IS by cytotoxic T cells that present similarities with ILPs (Tamzalit et al., 2019), that is, they are enriched in LFA1 and require WASP and Arp2/3 for their formation (Carman et al., 2007). These protrusions are very similar to the protrusions analysed herein. All these protrusive structures also present similarities with podosomes (and differences, see below), which are dynamic F-actin rich cone-shaped structures (Labernadie et al., 2010), mostly described in myeloid cells. Indeed, podosomes like the protrusions described by others and us are WASP and Arp2/3 dependent for their formation (Kaverina, 2003; Linder et al., 2000). Moreover, podosomes also exert protrusive forces that depend on actin polymerisation and increase with the substrate stiffness (Labernadie et al., 2014). Thus, analyses like the one reported herein can provide valuable information on the molecular mechanisms behind the generation of these protrusions.

Concerning the potential role of these structures in T lymphocyte biology, the ILPs by tip toeing on the endothelial cells can help to find the least resistant path for diapedesis (Sage et al., 2012). Protrusive structures, by invading the APC, can also increase the surface of contact between both cells facilitating the binding between ligands and receptors (Ueda et al., 2011). In the case of cytotoxic T cells, protrusions

were shown to induce forces responsible for physical deformation and efficient killing of the targets (Basu et al., 2016). Finally, because the protrusions described herein are mechanosensitive, they can sense the stiffness of the APC they interact with (Husson et al., 2011; Sawicka et al., 2017). Since APC stiffness is one of the parameters modulated in inflammatory conditions (Bufi et al., 2015), these protrusive structures may also act as sensory organs to test this parameter and induce an adequate immune response (Saitakis et al., 2017).

The effect of the forces in the dynamic of the protrusion can be compared with the effect of forces on the dynamic of other biological structures. Yet, quantitative data combining both speed and force measurements are scarce in general, including for T cells. For instance, to our knowledge, there are no quantifications of the protrusive force generated by the lamellipodium at the leading edge of migrating T cells. Such lamellipodium, which presents similarities with the protrusions described in this study as it is enriched in branched actin, and its growth is Arp2/3 and WASP dependent, is seen in T cells that migrate at a speed of 0.2–0.5 μm/s (Aoun et al., 2020), quite faster than the ∼0.1 μm/s that we measured for T cell protrusions. In macrophage, Labernardie et al. (2014) observed periodic protrusions of podosomes of 20 nm with a typical period of 40 s, hence a typical growth speed of 0.5 nm/s, two orders of magnitude slower than T cell protrusions. However, these observations were done for macrophages adhering on a substrate. Even considering that, without a resisting substrate, podosome could grow up to ∼600 nm in height as observed previously by Labernadie et al. (2010) with a comparable timescale would lead to a growth typically ten times slower than T cell protrusions, suggesting that podosomes are not similar to T cell protrusions. Considering further quantitative data of both force and velocity in cell structures, Prass et al. (2006) have quantified the force generated by the lamellipodium of a fish keratocyte migrating against an atomic force microscope (AFM) cantilever. They measured a growth velocity under no force of ∼0.02 μm/s, which is much lower than the growing speed of about 0.11 μm/s that we measured for T cell protrusions. We can also compare the influence of force on growth speed. To perform this comparison, the surface over which the compressive force is applied has to be taken into account, to compare stresses (force per surface area) instead of forces. For a T cell protrusion, we assume that the surface of the actin cortex supporting the stress is the section of a cylinder of diameter $D_{\mathrm{prot}}$, thickness $e \sim 0.3$ μm (Chugh et al., 2017), and surface area $\pi D_{\mathrm{prot}} e$. The resulting stress is $\sigma = F_{\mathrm{act}}/(\pi D_{\mathrm{prot}} e)$, and numerically, for a compressive force $F_{\mathrm{act}} = 0.36$ nN, we get a compressive stress of ∼390 Pa. In the setup used by Prass et al. (2006), the cantilever contacts the lamellipodium over a surface of about 3 μm × 0.2 μm = 0.6 μm$^2$. Interestingly, the authors see barely any reduction of the growth speed at a force of up to about 0.6 nN, translating into a stress of about 1 kPa. This is consistent with our measurements, as we measured almost no reduction in speed up to an applied stress of 390 Pa. This means that T cells protrusion are much faster than a lamellipodium, but display the same insensitivity to compressive stresses as the lamellipodium of a keratocyte.

The dynamics of the T cell protrusions can also be compared with that of reconstituted actin gels, for which a wide range of growth velocity has been measured. When growing against an AFM cantilever, Bieling et al. (2016) measured a velocity of about 0.12 μm/s under no force, very close to our observations on protrusions. However, in a previous study with a similar setup but different molecular components, Parekh et al. (2005) measured a much lower speed in the range of 0.001–0.01 μm/s. The latter velocity range matches the one obtained by Baüer et al. (2017) in actin gels growing against magnetic colloids, whereas Marcy et al. (2004) found an intermediate value of ∼0.03 μm/s for actin comets growing against a microfiber. Next, to compare the influence of forces to the growing speed of actin comets (Marcy et al., 2004), we assume the latter to be actin-filled cylinders of diameter $D_{\mathrm{comet}} \approx 2$ μm, hence a section of surface area $\pi D^2{}_{\mathrm{comet}}/4$, leading to stress $\sigma = F/(\pi D^2{}_{\mathrm{comet}}/4)$ under a force $F$. Under a tensile stress of 130 Pa, Marcy et al. (2004) found an increase in the comet velocity of only 10% compared with the free growth, whereas we found an increase of about 50% in protrusions under the same tensile stress. Moreover, under a compressive stress of ∼390 Pa, as stated above, we see a weak effect of the force on the growing speed, whereas Marcy et al. (2004) saw a 30–40% decrease in growth velocity. In the case of gels grown against a cantilever, the decrease due to compressive force is much larger, gels are up to four folds slower

than free growth under a ∼390-Pa compressive stress (Bauër et al., 2017; Bieling et al., 2016). Thus, T cell protrusions are as fast as the faster growing gels, when compared with actin comets, protrusions are more sensitive to tensile stress and less sensitive to compressive stress. Gels grown against a cantilever are even more sensitive to compressive force. We conclude – maybe unsurprisingly – that the cell protrusions have different mechanical dynamics than reconstituted systems. Consistent with this, Bieling et al. (2016) showed that the presence of the Arp2/3 complex has a large influence on gel mechanical behaviour as opposed to random, isotropic crosslinked actin networks. In cells, where in addition to the Arp2/3 complex, many molecules, including filamin-A (Flanagan et al., 2001), $\alpha$-actinin, filamin (Esue et al., 2009), and other capping and branching factors (Pujol et al., 2012) are present to regulate the cortex assembly, we expect even more "exotic" behaviour of the cellular actin cortex. To further our understanding at the cell level, we plan to implement simultaneous force and fluorescence measurements to study how 3D actin flows are structured within the protrusion, possibly similar to flows during T cell migration and swimming (Aoun et al., 2020; Reversat et al., 2020). Furthermore, as *in vitro* studies have shown that actin dynamics depend on the level of external compressive forces (Bieling et al., 2016) and that actin waves can be triggered in cells under external forces (Kapustina et al., 2013), it might also be interesting in the future to study actin dynamics under different levels of compressive forces in T cells during their activation.

Our results also show that external forces differentially affect the duration of the protrusion growth (switch time). This switch seems to be set by an intracellular "clock" and its origin is yet not clear since we identified its existence in a previous study (Husson et al., 2011). Here, we observed that when a compressive force is applied, the duration of the growth and the delay barely depend on the amplitude of the compressive force. In our previous study using a different micropipette-based technique (a biomembrane force probe) (Husson et al., 2011), we measured a delay time of $45 \pm 7$ s remarkably close to the one measured in this study. We measured a growth duration that was $140 \pm 15$ s, versus 50–90 s in this study (Husson et al., 2011). Although the setup we used previously presented several differences, an important one is that the setup was not automated to apply a controlled force to the growing protrusion, and pulling forces applied to the growing protrusion were possibly relatively large. As we showed that the larger the amplitude of the pulling force, the longer the growth duration, this can explain why we found a longer growth duration in our previous study. When pulling force is exerted, the stronger the force, the longer the growth duration. Pulling forces are expected to help to unfold the surface membrane stores, hence allowing the protrusion to grow longer. We hypothesise that the switch time could depend on a limitation of these membrane stores unfolded by pulling forces. However, we excluded that the switch time was defined by limited membrane store by showing that the surface area expansion of the cell during activation is much lower than membrane reservoirs of CD4 T cells. We have previously quantified the membrane stores that these cells can mobilise during different active processes such as transendothelial migration or spreading on an activating surface (Guillou et al., 2016a).

Finally, we asked if the switch could be explained by the exhaustion of mobilisable stocks of actin to grow the protrusion. Inhibiting the Arp2/3 complex did not change the switch time, but increased the delay before growth. This showed that branched actin is necessary to build the protrusion, but that the switch does not depend on actin branching. This seems not easy to reconcile with a limiting amount of available actin setting the maximal length of the protrusion, except if the shorter protrusions observed in the presence of CK666 are much wider so that they contain as much actin as in untreated cells. Unfortunately, measuring the protrusion diameter of such a small protrusion is very difficult on the videos and we could not assess that. We estimated that the geometry of the protrusion when it reached its maximal length was consistent with a conserved maximal amount of actin contained in the protrusion of about 7 $\mu m^3$. This volume can be compared with the total amount of actin in the cell. We estimate a cortex thickness of 0.2 µm in a resting primary T cell with an average diameter of 6.7 µm (Guillou et al., 2016a). We obtain a volume of actin contained in the cortex of about 30 $\mu m^3$. Considering that the enrichment in actin in the protrusion relative to the cortex outside the protrusion leads to an increase in density of a factor of about three (as deduced from the increase in fluorescence

intensity that we measured; Figure 5), the protrusion could represent up to two thirds of the initial amount of actin present in the cortex of the resting cell. The fact that there seems to be a maximal amount of actin in the protrusion, and that it represents a significant percentage of the total amount of available actin suggests that the amount of available actin can be a factor that defines the switch. We will consider testing in the future the limited actin hypothesis, one possibility being to use recently developed photo-activable actin-associated inhibitors (Borowiak et al., 2020).

In conclusion, our study suggests that the switch and the delay are set by an intracellular constant time and that the maximal length of the protrusion is set by a constant growth speed. Our study provides key insights that help to better understand the mechanism involved in the formation of the actin protrusion emitted by the T cell, a process at the core of T cell activation.

## Materials and methods

### Micropipette force probe

The MFP is a micropipette-based assay using a flexible micropipette as a cantilever (Sawicka et al., 2017). The flexible micropipette aspirates a bead covered with antibodies at its tip. In this study, beads were Dynabeads® Human T-Activator CD3/CD28 for T Cell Expansion and Activation from Gibco, purchased from Thermo Fisher Scientific (ref. 11131D). Micropipettes were prepared as described elsewhere (Basu et al., 2016; Guillou et al., 2016b, 2016a; Sawicka et al., 2017) using borosilicate glass capillaries (Harvard Apparatus) with a micropipette puller (P-97; Sutter Instruments), cutting them with a microforge (MF-200; World Precision Instruments) and bending them at a 45° angle with another microforge (MF-900; Narishige). Micropipettes were held by micropipette holders (IM-H1; Narishige) placed at a 45° angle relative to the plane of the microscope stage, so that micropipette tips were in the focal plane of an inverted microscope under brightfield or DIC illumination (Ti2; Nikon Instruments) equipped with a 100× oil immersion, 1.3 NA objective (Nikon Instruments) and placed on an air suspension table (Newport). The flexible micropipette was linked to a micropositioner (Thorlabs) placed on top of a single-axis stage controlled with a closed loop piezo actuator (TPZ001; Thorlabs). The bending stiffness $k$ of the flexible micropipette (about 0.1–0.3 nN/µm) was measured against a standard microindenter calibrated with a commercial force probe (model 406A; Aurora Scientific). Experiments were performed in glass-bottom Petri dishes (Fluorodish; WPI). Once an activating microbead was aspirated by the flexible micropipette, a T cell was picked up at the bottom of the Petri dish, held by a stiff micropipette with an aspiration pressure of 30–60 Pa (imposed by lowering the water level in a reservoir connected to the micropipette), and brought in adequate position using a motorised micromanipulator (MP-285; Sutter Instruments). This aspiration pressure is necessary to hold the cell to prepare and during experiments. In a previous study, we showed that below and expansion of the cell membrane area of a resting T cell of about 20%, the mechanical properties of cell is not affected. Below this threshold, cell surface area expansion leads to an increase in cell effective stiffness that could potentially affect cell response (Guillou et al., 2016a), but we did not exceed this 20% threshold Images were acquired using a Flash 4.0 or ORCA-spark CMOS camera (Hamamatsu Photonics). The setup automatically detects the position of the bead at the tip of the force probe at a rate of about 400 and imposes the position of the base of the flexible micropipette by controlling the position of the piezo stage. The deflection of the force probe is the difference between the position of the bead and the position of the piezo stage. Thus, the force applied to the cell is the product of this deflection by the bending stiffness $k$. A retroaction implemented in Matlab (Mathworks) controlling both the camera via the Micromanager software (Edelstein et al., 2014) and the piezo stage moves the latter in reaction to the measurement of the bead position in order to keep a desired deflection of the cantilever, so that a defined force is applied to the cell at any given time. Experiments were performed at room temperature to avoid thermal drift.

### Cells

Mononuclear cells were isolated from peripheral blood of healthy donors on a ficoll density gradient. Buffy coats from healthy donors (both male and female donors) were obtained from Etablissement Français du Sang in accordance with INSERM ethical guidelines. Human total CD4+ isolation kit (Miltenyi Biotech; 130-096-533) was used for the purification of T cells. Arp2/3 inhibition (Figure 4) was performed with a 30-min preincubation with CK666 (25 µM), which was left in the extracellular medium during experiments. DMSO content in control was 0.1% v/v.

K562 CCL-243 ATCC transduced with lentiviral particles encoding for CD64 (named K64 cells) were cultured at 37°C 5% $CO_2$ in RPMI 1640 Glutamax (Gibco; 61870-010) supplemented with 10% foetal calf serum (FCS; Corning; 35-079-CV, lot no. 35079011) and were passed every 2–3 days at ~$0.5 \times 10^6$ cells/ml.

### Production of lentiviruses and infection of K562 cells

Non-replicative VSV-g pseudotyped lentiviral particles were produced by transfecting HEK-293T cells with Gag, Pol, rev, encoding plasmid (pPAX2), envelop encoding plasmid (pMD2.G) and the CD64 construct (provided by Philipe Bernaroch) encoded in a pWXLD vector. Lentivirus were recovered in supernatant after 2 days and concentrated. $5 \times 10^6$ K562 cells were infected for 24 h, and used 3–5 days post infection.

### Coverslips and dishes preparation for immunofluorescence assay

12 mm ø coverslips (VWR; 631–0666) for fixed cells were precoated with 0.02% of poly-L-lysine (Sigma–Aldrich; P8920) for 20 min at room temperature and were washed three times in water before being dried and kept for maximum of 2 days.

#### Preparation of CD4+ and CD3/CD28 beads conjugates

CD4+ T cells were resuspended at $2 \times 10^6$ in 1 ml of RPMI medium. An equal volume of magnetic beads ($2 \times 10^6$) coated with anti-CD3 and anti-CD28 (Gibco; 11132D) was added. The cells–beads mix was incubated on a coverslip for the appropriate time (2, 5 and 10 min) at 37°C. Coverslips were then washed once with cold PBS before fixation.

#### Preparation of primary CD4-T cells and K64 cells conjugates

K64 cells were washed, resuspended at a concentration of $1 \times 10^6$ cells/ml, then loaded with anti CD3 (OKT3 clone; eBioscience; 16-0037-85; 10 µg/ml final concentration) and anti-CD28 (LEAF Purified anti-human CD28 from CD28.2 clone; Biolegend; BLE302923 at 10 µg/ml final concentration) for 30 min at 37°C before being washed once and resuspended at a concentration of $1 \times 10^6$ cells/ml. 150,000 K64 cells were incubated on coverslips for 30 min, washed once with warmed PBS and 250,000 CD4 T cells resuspended in RPMI 10% FCS were added for 5 min. Coverslips were washed once with cold PBS before fixation.

#### Fixation

Cells were fixed with 4% paraformaldehyde (Life Technologies; FB002) for 15 min at room temperature, washed once in PBS and excess of paraformaldehyde was quenched for 10 min with PBS 10 mM glycine (Thermo Fisher Scientific; G8898). Coverslips were kept at 4°C in PBS until permeabilisation and staining.

#### Staining and mounting

Cells were permeabilised for 30 min at room temperature with PBS 0.2% bovine serum albumin (BSA; Euromedex; 04-100-812) 0.05% Saponin (Sigma–Aldrich; S4521). Cells were then incubated at room temperature for 30 min in the same buffer with Alexa Fluor 647 phalloidin (Invitrogen; A22287). After washing once with PBS BSA Saponin, and once with PBS, coverslips were soaked three times in PBS, three times in water, and mounted with 4–6 µl of Fluoromount G (SouthernBiotech; 0100–01) on slides (KNITTEL Starfrost) and dried overnight protected from light before microscope acquisition.

#### Confocal microscopy and image analysis

Images were acquired with a Leica DmI8 inverted microscope equipped with an SP8 confocal unit using either a 40× (1.35NA) or 63× (1.4NA) objective. Single plane images or Z-stack of images were acquired. Images were analysed on Fiji and ImageJ software using scripts generated for automated or semi-automated analysis.

#### Hertz model

The Hertz model (Johnson, 1985; Rosenbluth et al., 2006) applies to the deformation of an elastic medium when indented by a sphere. The model can be extended in the case of the indentation of an elastic sphere (representing the cell) by an infinitely stiff spherical indenter (representing the microbead), which leads to the following relationship between the compressive force $F$ applied by the indenter on the elastic sphere and indentation $\delta$ of the latter: $F = \frac{4}{3} \frac{E_{\text{Young}}}{1-\nu^2} \sqrt{R_{\text{eff}}} \delta^{\frac{3}{2}}$, where $E_{\text{Young}}$ is the effective Young's modulus of the cell, $R_{\text{eff}}$ is an effective radius given by $1/R_{\text{eff}} = 1/R_{\text{cell}} + 1/R_{\text{bead}}$, with $R_{\text{cell}}$ the cells radius and $R_{\text{bead}}$ the bead radius, $\nu$ is the Poisson ratio of the cell taken as 0.5 (i.e., the cell is considered incompressible (Moeendarbary et al., 2013; Wu et al., 2018).

We first used this model during the initial indentation of T cells by the activating microbead. During an experiment, the base of the flexible pipette holding the bead is translated at a constant velocity towards the cell. Upon contact, the bead starts applying an increasing compressible force to the cell, until it reaches the force level $F_{\text{comp.}}$ During this initial compressive phase, we measured both applied force and cell indentation. We fitted the experimental $F$–$\delta$ curve using the above $F$–$\delta$ relationship (Supplementary Material 3).

Furthermore, the Hertz model predicts that the radius $a$ of the cell–bead contact area is such that $a^2 = R_{\text{eff}}\ \delta$. By substituting a in the $F$-$\delta$ relationship above, we get: $F = \frac{4}{3} \frac{E_{\text{Young}}}{1-\nu^2} \frac{a^3}{R_{\text{eff}}}$; hence, $a$ can be calculated knowing cell properties and applied force by inverting the previous relationship, leading to: $a = \left(\frac{FR_{\text{eff}}}{\frac{4}{3}\frac{E_{\text{Young}}}{1-\nu^2}}\right)^{\frac{1}{3}}$.

#### Volume and surface area calculation

The surface and volume of the cells were calculated assuming an axisymmetrical geometry of the cell around the axis defined by the cell centre and bead centre (horizontal axis in Supplementary Video 1). The contour of cells was hand-traced using image j software (Schneider et al., 2012) using a segmented line, thus defining small cylinders of diameter equal to the local cell diameter and of small (submicron) thickness. Once sliced in elementary cylinders, the lateral area or volume of these cylinders is readily computed. The sum leads to the desired cell surface area and volume.

## Author contribution

A.E.Z. designed, performed and quantified the confocal microscopy experiments and contributed to writing the manuscript. N.P. set up the K64 cells as artificial APC. S.D. prepared shRNA lentivirus and purified plasmids encoding chimeric molecules. O.M. designed and realised the graphical abstract and contributed to writing the manuscript; C.H. provided key material, discussed the results and contributed to writing the manuscript. J.H. designed, performed and analysed all the MFP experiments, analysed the confocal images, conceived the study and wrote the manuscript.

## Funding

This work has benefited from the financial support of the LabeX LaSIPS (ANR-10-LABX-0040-LaSIPS) managed by the French National Research Agency under the 'Investissements d'avenir' program (ANR-11-IDEX-0003-02). This work was also supported by Ecole polytechnique, a CNRS PEPS funding, and

an endowment in cardiovascular cellular engineering from the AXA Research Fund. For her salary, N.P. benefits from the financial support of ITMO Cancer Aviesan (Alliance Nationale pour les Sciences de la Vie et de la Santé/National Alliance for Life Sciences & Health) within the framework of the Cancer Plan (ED 474/ITMO Cancer Aviesan partnership). The project 'Mechanical probing of tumor infiltrating lymphocytes' benefits from a funding by the Bettencourt Schueller Foundation.

## Acknowledgements

J.H. thank M.E. Serrentino and E. Husson for fruitful discussion and J. Heuvingh for insight on *in vitro* actin dynamics. J.H. thank the LadHyX members for technical support.

## Conflict of interest statement

The authors have declared no conflict of interest.

## References

Aoun, L., Farutin, A., Garcia-Seyda, N., Nègre, P., Rizvi, M.S., Tlili, S., Song, S., Luo, X., Biarnes-Pelicot, M., Galland, R., Sibarita, J.B., Michelot, A., Hivroz, C., Rafai, S., Valignat, M.P., Misbah, C. and Theodoly, O. (2020). Amoeboid swimming is propelled by molecular paddling in lymphocytes. Biophys. J. **119**, 1157–1177.

Basu, R., Whitlock, B.M.B.M., Husson, J., Le Floc'h, A., Jin, W., Oyler-Yaniv, A., Dotiwala, F., Giannone, G., Hivroz, C., Biais, N., Lieberman, J., Kam, L.C. and Huse, M. (2016). Cytotoxic T cells use mechanical force to potentiate target cell killing. Cell **165**, 100–110.

Bauër, P., Tavacoli, J., Pujol, T., Planade, J., Heuvingh, J. and Du Roure, O. (2017). A new method to measure mechanics and dynamic assembly of branched actin networks. Sci. Rep. **7**, 15688.

Bieling, P., Li, T. De, Weichsel, J., McGorty, R., Jreij, P., Huang, B., Fletcher, D.A. and Mullins, R.D. (2016). Force feedback controls motor activity and mechanical properties of self-assembling branched actin networks. Cell **164**, 115–127.

Borowiak, M., Küllmer, F., Gegenfurtner, F., Peil, S., Nasufovic, V., Zahler, S., Thorn-Seshold, O., Trauner, D. and Arndt, H.D. (2020). Optical manipulation of F-actin with photoswitchable small molecules. J. Am. Chem. Soc. **142**, 9240–9249.

Bufi, N., Saitakis, M., Dogniaux, S., Buschinger, O., Bohineust, A., Richert, A., Maurin, M., Hivroz, C. and Asnacios, A. (2015). Human primary immune cells exhibit distinct mechanical properties that are modified by inflammation. Biophys. J. **108**, 2181–2190.

Cai, E., Marchuk, K., Beemiller, P., Beppler, C., Rubashkin, M.G., Weaver, V.M., Gérard, A., Liu, T.L., Chen, B.C., Betzig, E., Bartumeus, F. and Krummel, M.F. (2017). Visualizing dynamic microvillar search and stabilization during ligand detection by T cells. Science (80-.). **356**.

Cannon, J.L. and Burkhardt, J.K. (2002). The regulation of actin remodeling during T-cell-APC conjugate formation. Immunol. Rev. **186**, 90–99.

Carman, C., Sage, P. and Sciuto, T. (2007). Transcellular diapedesis is initiated by invasive podosomes. Immunity **26**, 784–797.

Choraghe, R.P., Kołodziej, T., Buser, A., Rajfur, Z. and Neumann, A.K. (2020). RHOA-mediated mechanical force generation through Dectin-1. J. Cell Sci. **133**, jcs236166.

Chugh, P., Clark, A.G., Smith, M.B., Cassani, D.A.D., Dierkes, K., Ragab, A., Roux, P.P., Charras, G., Salbreux, G. and Paluch, E.K. (2017). Actin cortex architecture regulates cell surface tension. Nat. Cell Biol. **19**, 689–697.

Dustin, M.L. and Choudhuri, K. (2016). Signaling and polarized communication across the T cell immunological synapse. Annu. Rev. Cell Dev. Biol. **32**, 303–325.

Edelstein, A.D., Tsuchida, M. A., Amodaj, N., Pinkard, H., Vale, R.D. and Stuurman, N. (2014). Advanced methods of microscope control using μManager software. J. Biol. Methods **1**, 10.

Esue, O., Tseng, Y. and Wirtz, D. (2009). A-actinin and filamin cooperatively enhance the stiffness of actin filament networks. PLoS One **4**, 1–6.

Flanagan, L.A., Chou, J., Falet, H., Neujahr, R., Hartwig, J.H. and Stossel, T.P. (2001). Filamin A, the Arp2/3 complex, and the morphology and function of cortical actin filaments in human melanoma cells. J. Cell Biol. **155**, 511–518.

Fritzsche, M., Li, D., Colin-York, H., Chang, V.T., Moeendarbary, E., Felce, J.H., Sezgin, E., Charras, G., Betzig, E. and Eggeling, C. (2017). Self-organizing actin patterns shape membrane architecture but not cell mechanics. Nat. Commun. **8**, 17–19.

Guillou, L., Babataheri, A., Saitakis, M., Bohineust, A., Dogniaux, S., Hivroz, C., Barakat, A.I. and Husson, J. (2016a). T-lymphocyte passive deformation is controlled by unfolding of membrane surface reservoirs. Mol. Biol. Cell **27**, 3574–3582.

Guillou, L., Babataheri, A., Puech, P.-H., Barakat, A.I. and Husson, J. (2016b). Dynamic monitoring of cell mechanical properties using profile microindentation. Sci. Rep. **6**, 21529.

Heuzé, M.L., Vargas, P., Chabaud, M., Le Berre, M., Liu, Y.J., Collin, O., Solanes, P., Voituriez, R., Piel, M. and Lennon-Duménil, A.M. (2013). Migration of dendritic cells: Physical principles, molecular mechanisms, and functional implications. Immunol. Rev. **256**, 240–254.

Husson, J., Chemin, K., Bohineust, A., Hivroz, C. and Henry, N. (2011). Force generation upon T cell receptor engagement. PLoS One **6**, e19680.

Johnson, K.L. (1985). Contact mechanics. J. Am. Chem. Soc. **37**, 1–17.

Jung, Y., Riven, I., Feigelson, S.W., Kartvelishvily, E., Tohya, K., Miyasaka, M., Alon, R. and Haran, G. (2016). Three-dimensional localization of T-cell receptors in relation to microvilli using a combination of superresolution microscopies. Proc. Natl. Acad. Sci. USA **113**, E5916–E5924.

Kapustina, M., Elston, T.C. and Jacobson, K. (2013). Compression and dilation of the membrane-cortex layer generates rapid changes in cell shape. J. Cell Biol. **200**, 95–108.

Kaverina, I. (2003). Podosome formation in cultured A7r5 vascular smooth muscle cells requires Arp2/3-dependent de-novo actin polymerization at discrete microdomains. J. Cell Sci. **116**, 4915–4924.

Labernadie, A., Thibault, C., Vieu, C., Maridonneau-Parini, I. and Charriere, G.M. (2010). Dynamics of podosome stiffness revealed by atomic force microscopy. Proc. Natl. Acad. Sci. USA **107**, 21016–21021.

Labernadie, A., Bouissou, A., Delobelle, P., Balor, S., Voituriez, R., Proag, A., Fourquaux, I., Thibault, C., Vieu, C., Poincloux, R., Charrière, G.M. and Maridonneau-Parini, I. (2014). Protrusion force microscopy reveals oscillatory force generation and mechanosensing activity of human macrophage podosomes. Nat. Commun. **5**, 5343.

Linder, S., Higgs, H., Hüfner, K., Schwarz, K., Pannicke, U. and Aepfelbacher, M. (2000). The polarization defect of Wiskott-Aldrich syndrome macrophages is linked to dislocalization of the Arp2/3 complex. J. Immunol. **165**, 221–225.

Marcy, Y., Prost, J., Carlier, M.-F. and Sykes, C. (2004). Forces generated during actin-based propulsion: a direct measurement by micromanipulation. Proc. Natl. Acad. Sci. USA **101**, 5992–5997.

Moeendarbary, E., Valon, L., Fritzsche, M., Harris, A.R., Moulding, D.A., Thrasher, A.J., Stride, E., Mahadevan, L. and Charras, G.T. (2013). The cytoplasm of living cells behaves as a poroelastic material. Nat. Mater. **12**, 253–261.

Parekh, S.H., Chaudhuri, O., Theriot, J.A. and Fletcher, D.A. (2005). Loading history determines the velocity of actin-network growth. Nat. Cell Biol. **7**, 1119–1123.

Prass, M., Jacobson, K., Mogilner, A. and Radmacher, M. (2006). Direct measurement of the lamellipodial protrusive force in a migrating cell. J. Cell Biol. **174**, 767–772.

Pujol, T., Du Roure, O., Fermigier, M. and Heuvingh, J. (2012). Impact of branching on the elasticity of actin networks. Proc. Natl. Acad. Sci. USA **109**, 10364–10369.

Reversat, A., Gaertner, F., Merrin, J., Stopp, J., Tasciyan, S., Aguilera, J., de Vries, I., Hauschild, R., Hons, M., Piel, M., Callan-Jones, A., Voituriez, R. and Sixt, M. (2020). Cellular locomotion using environmental topography. Nature **582**, 582–585.

Ricart, B.G., Yang, M.T., Hunter, C.A., Chen, C.S. and Hammer, D.A. (2011). Measuring traction forces of motile dendritic cells on micropost arrays. Biophys. J. **101**, 2620–8.

Rosenbluth, M.J., Lam, W.A. and Fletcher, D.A. (2006). Force microscopy of nonadherent cells: a comparison of leukemia cell deformability. Biophys. J. **90**, 2994–3003.

Sage, P.T., Varghese, L.M., Martinelli, R., Sciuto, T.E., Kamei, M., Dvorak, A.M., Springer, T.A., Sharpe, A.H. and Carman, C. V. (2012). Antigen recognition is facilitated by invadosome-like protrusions formed by memory/effector T cells. J. Immunol. **188**, 3686–3699.

Saitakis, M., Dogniaux, S., Goudot, C., Bufi, N., Asnacios, S., Maurin, M., Randriamampita, C., Asnacios, A. and Hivroz, C. (2017). Different TCR-induced T lymphocyte responses are potentiated by stiffness with variable sensitivity. Elife **6**, 1–29.

Sawicka, A., Babataheri, A., Dogniaux, S., Barakat, A.I., Gonzalez-Rodriguez, D., Hivroz, C. and Husson, J. (2017). Micropipette force probe to quantify single-cell force generation: application to T cell activation. Mol. Biol. Cell **28**, mbc.E17-06-0385.

Schneider, C. A., Rasband, W.S. and Eliceiri, K.W. (2012). NIH Image to ImageJ: 25 years of image analysis. Nat. Methods **9**, 671–675.

Tamzalit, F., Wang, M.S., Jin, W., Tello-Lafoz, M., Boyko, V., Heddleston, J.M., Black, C.T., Kam, L.C. and Huse, M. (2019). Interfacial actin protrusions mechanically enhance killing by cytotoxic T cells. Sci. Immunol. **4**, eaav5445.

Ueda, H., Morphew, M.K., McIntosh, J.R. and Davis, M.M. (2011). CD4+ T-cell synapses involve multiple distinct stages. Proc. Natl. Acad. Sci. USA **108**, 17099–17104.

Wu, P.-H., Aroush, D.R.-B., Asnacios, A., Chen, W.-C., Dokukin, M.E., Doss, B.L., Durand-Smet, P., Ekpenyong, A., Guck, J., Guz, N. V., Janmey, P.A., Lee, J.S.H., Moore, N.M., Ott, A., Poh, Y.C., Ros, R., Sander, M., Sokolov, I., Staunton, J.R., Wang, N., Whyte, G. and Wirtz, D. (2018). A comparison of methods to assess cell mechanical properties. Nat. Methods **15**, 491–498.

Yan, S.L.S., Hwang, I.Y., Kamenyeva, O. and Kehrl, J.H. (2019). In vivo F-actin filament organization during lymphocyte transendothelial and interstitial migration revealed by intravital microscopy. IScience **16**, 283–297.

Zak, A., Violeta, S., Cortés, M., Sadoun, A., Babataheri, A., Dogniaux, S., Dupré-crochet, S., Hudik, E., He, H., Barakat, A.I., Carrasco, Y.R., Hamon, Y., Puech, P.H., Hivroz, C., Nüsse, O. and Husson, J. (2019). Single-cell immuno-mechanics: rapid viscoelastic changes are a hall- mark of early leukocyte activation. bioRxiv.

Received: 24 October 2020; Revised: 22 December 2020; Accepted: 23 December 2020; Accepted article online: 20 January 2021

# Annexe 4 : Mechanobiology of antigen-induced T cell arrest

***Biology of the Cell*, Juillet 2020**

**Résumé**

Pour établir une réponse immunitaire, les lymphocytes T doivent d'abord trouver des antigènes rares présents à la surface des cellules présentatrices d'antigènes (CPA). Ils y parviennent en migrant rapidement dans l'espace encombré des tissus et en échantillonnant constamment la surface des CPA. Lors de la reconnaissance de l'antigène, les lymphocytes T ralentissent et se polarisent vers la CPA, formant finalement un interface spécialisé connu sous le nom de synapse immunologique. Ces conjugués se forment à la suite de l'interaction entre des paires de récepteurs/ligands qui subissent une contrainte mécanique due à la réorganisation continue du cytosquelette cellulaire. Dans cette revue, nous discutons de l'implication des forces mécaniques pendant la reconnaissance des antigènes par les cellules T en migration. Nous explorerons cette question d'un point de vue conceptuel et technique, dans le but de fournir de nouvelles perspectives dans le domaine émergent de la mécanobiologie.

**Contribution à la revue**

J'ai participé à la conception de cette revue en partageant ma bibliographie ciblée sur le thème. J'ai également relu et apporté des commentaires et modifications au texte.

Biol. Cell (2020) **112,** 196–212 DOI: 10.1111/boc.201900093

Review

# Mechanobiology of antigen-induced T cell arrest

**Mélanie Chabaud*†‡, Noémie Paillon*, Katharina Gaus†‡ and Claire Hivroz***

*Institut Curie-PSL Research University, INSERM U932, Paris, France, †EMBL Australia Node in Single Molecule Science, School of Medical Sciences, University of New South Wales, Sydney, NSW, Australia, and ‡ARC Centre of Excellence in Advanced Molecular Imaging, University of New South Wales, Sydney, NSW, Australia

To mount an immune response, T cells must first find rare antigens present at the surface of antigen-presenting cells (APCs). They achieve this by migrating rapidly through the crowded space of tissues and constantly sampling the surface of APCs. Upon antigen recognition, T cells decelerate and polarise towards the APC, ultimately forming a specialised interface known as the immunological synapse. These conjugates form as the result of the interaction between pairs of receptors/ligands that are under mechanical stress due to the continuously reorganising cell cytoskeleton. In this review, we discuss the involvement of mechanical forces during antigen recognition by migrating T cells. We will explore this question from a conceptual and technical perspective, with the aim of providing new insights into the emerging field of mechanobiology.

## Introduction

T cells continuously circulate between blood, lymphoid tissues and lymph nodes in search for their cognate antigens presented at the surface of antigen-presenting cells (APCs) on major histocompatibility complex (MHC) molecules. Effective recognition of antigen by the T cell receptor (TCR) therefore occurs on motile T cells undergoing constant morphological change (Von Andrian and Mempel, 2003). Intravital imaging using two-photon microscopy has revealed the complexity of T cell migration patterns and the diverse nature of T cell–APC interactions leading to T cell activation (Bousso and Robey, 2003; Mempel et al., 2004; Miller et al., 2002; Stoll et al., 2002). A classical sequence of three phases has been observed during T cell priming *in vivo* (Mempel et al., 2004). During the first hours, T cells transiently contact antigen-bearing dendritic cells (DCs). In the second phase, they establish stable contacts with DCs leading to their activation. In the third phase, T cells that are now competent for clonal expansion as well as cytokine production, resume a dynamic behaviour (Mempel et al., 2004). Two-photon imaging highlighted that crawling naïve T cells are highly motile, migrating at around 10–15 µm/min (Hugues et al., 2004; Miller et al., 2002) among the dense network of fibroblastic reticular cells (FRC) (Bajénoff et al., 2006) in a manner described as a random walk (Miller et al., 2004a) with some features of a Levy walk (Fricke et al., 2016). Naive T cells in lymph nodes adopt a search strategy which is 'information-poor and exploration-based' to detect rare cognate antigen-bearing DCs, a strategy adapted to the complexity of their environment and relying on migrating fast while contacting as many APCs as possible (Krummel et al., 2016).

Migrating T cells typically display a polarised morphology with an actin-rich lamellipodium at the leading edge and a lamella adjacent to the lamellipodium. The lamellipodium is mostly composed of branched actin filaments that are nucleated by Arp2/3, whereas the lamella contains bundled actin with actomyosin activity. The cell

To whom correspondence should be addressed (email: claire.hivroz@curie.fr)

**Key words:** Cell migration, Plasma membrane, Synapse.

**Abbreviations:** AITCP, adhesion-induced T cell priming; APC, antigen presenting cell; BFP, biomembrane force probe; CRAC, Calcium release-activated channels; DC, dendritic cell; DNA, deoxyribonucleic acid; ER, endoplasmic reticulum; ERM, ezrin-radixin-moesin; F-actin, filamentous actin; FRET, fluorescence resonance energy transfer; GPI, glycosylphosphatidylinositol; ICAM-1, intercellular adhesion molecule 1; ITAM, immunoreceptor tyrosine-based activation motif; LFA-1, lymphocyte function-associated antigen 1; MHC, major histocompatibility complex; MS, mechanosensitive; MTOC, microtubule organizing centre; PLC, phospholipase C; pMHC, peptide-MHC; pN, piconewton; Rac-1, Rac family small GTPase 1; SACC, stretch-activated calcium channels; SMAC, supramolecular activation clusters; SOCE, store operated calcium entry; TCR, T cell receptor; TFM, traction force microscopy; TGT, tension gauge tethers; TRP, transient receptor potential; WASP, Wiskott-Aldrich syndrome protein; WT, wild type.

rear or uropod is a highly contractile area enriched in Myosin II but relatively depleted in F-actin (Dustin, 2008). Upon antigen engagement, T cells undergo considerable cytoskeletal remodelling and polarisation, which involves F-actin polymerisation and microtubule-organising centre (MTOC) reorientation towards the T cell–APC contact area as well as membrane reorganisation (Billadeau et al., 2007). Altogether, this remodelling facilitates the polarised recruitment and segregation of cellular components into a specialised junction known as the immunological synapse. This structure serves has a dynamic platform for T cell–APC communication and promotes and sustains T cell activation (Grakoui et al., 1999). The immunological synapse is a radially symmetrical structure comprising three distinct zones termed supramolecular activation clusters (SMACs) (Monks et al., 1998). A central area (cSMAC) contains microclusters of TCR/pMHC and associated signalling proteins such as CD28. A peripheral ring of adhesions molecules containing the adhesion protein LFA-1 (interacting with its ligand ICAM-1 on the APC surface) is referred to as the pSMAC. Finally, a distal region (dSMAC), where branched-actin network forms a ring, constitutes the outer boundary of the IS. This is the region where large molecules such as the tyrosine phosphatase CD45 accumulate. Filamentous actin (F-actin) within the dSMAC undergoes rapid retrograde flow, driven by both actin polymerisation and actomyosin II arc contraction, which drives centripetal transport of signalling clusters of TCR and integrins towards the centre of the immunological synapse (Murugesan et al., 2016; Varma et al., 2006). Given the molecular and architectural similarities between the SMACs found in the immunological synapse and the different zones of a migrating cell, Michael Dustin proposed that these two structures are related (Dustin, 2008). The establishment of the immunological synapse upon antigen recognition could derived from a "symmetrisation" of the actomyosin network. In this context, an asymmetric distribution would favour T cell migration, whereas a radially symmetric network would lead to T cell arrest. Breaking the symmetry of the stable immunological synapse generates a moving adhesive junction that has been defined by M. Dustin as a kinapse, which allows signal integration by T cells while moving over the surface of APCs (Dustin, 2007). A recent elegant study by Kumari et al. (2020) showed that cytoskeletal tension generated in the plane of the immunological synapse by antigen-triggered mechanism actively promotes T-cell synapse symmetry. The authors show that focal nucleation of actin via Wiskott–Aldrich syndrome protein (WASP) induces actin filaments in the central zone of the immunological synapse. Contraction of these filaments by Myosin II creates a tension that counterbalances the fluctuation of the lamellar fluctuations in the periphery of the T cell facilitating the stabilisation of a symmetric synapse. The degradation of WASP, by yet to describe mechanisms destabilises the actin filaments allowing the polarisation of the T cells that recover their migratory behaviour (Kumari et al., 2020). This focal nucleation of actin might correspond to actin protrusions described by Tamzalit et al. (2019) in $CD8^+$ cytotoxic T cells that extend from central and intermediate locations within the synapse. These protrusions, which depend on the cytoskeletal regulator WASP and the Arp2/3 actin nucleation complex, like the actin foci described by Kumari et al. (2020), were reported to exert forces and to facilitate efficient killing (Tamzalit et al., 2019).

The role played by mechanical forces in T cell functions emerged as a new research field in the last 10 years (Hivroz and Saitakis, 2016; Huse, 2017; Rossy et al., 2018). However, the biophysical aspects of the T cell stop signal that leads to the formation of a stable synapse still remains poorly understood. This may be due to the experimental approaches used so far that mainly employ round and/or non-migrating cells (reviewed here (Huse, 2017; Pageon et al., 2018)). Therefore, these experiments fail to recapitulate the transition from a migratory state to a static state. While reviewing the contribution of forces generated at the cell–cell interface onto T cell cytoskeleton and membrane remodelling, we here propose a 'tool box' of experimental set-ups that may help in characterising the biophysical aspects of the T cell stop signal.

## Antigen recognition by migrating T cells generate mechanical forces at the cell–cell interface

The dynamic interactions between T cells and APCs imply that engaged TCRs are subjected to significant mechanical stress, originated from the actin-based

protrusion and Myosin II-based contraction occurring at the immunological synapse. Optical tweezers experiments performed on T cells migrating towards chemoattractant revealed that protrusive forces at the leading edge can be as high as 1000 pN (Yang et al., 2015). This highlights that TCR/pMHC bonds are submitted to very important forces during cell migration. Importantly, the fact that T cells are activated by surface-anchored pMHC but not by soluble pMHC confirms that physical constraint is required for T cell activation (Ma et al., 2008a). The TCR was indeed reported to be a mechanosensor (Kim et al., 2009). Using optically trapped beads presented to single T cell, Kim et al. (2009) showed that the induction of $Ca^{2+}$ flux (a classical readout of early TCR signalling) only occurs after the application of a tangential force of 50 pN onto the attached bead. Another study, in which artificial APCs expressing engineered TCR ligands have been used, confirmed that mechanical forces applied on the TCR initiates Src signalling (Li et al., 2010). Importantly, the TCR undergoes conformational changes when external forces are applied onto it. This, in turn, regulates peptide discrimination and pMHC bond lifetime (Das et al., 2015). When forces of around 10 pN are applied onto the TCR, it enhances the lifetime of TCR–pMHC interaction in the case of agonists: a phenomenon known as 'catch-bound' described by the group of Cheng Zhu (Liu et al., 2014) and already reported for selectins (Marshall et al., 2003) and integrins (Kong et al., 2009). Conversely, for antagonists, application of forces shortens bond lifetimes, also called slip bonds. Hence, generating forces may offer a way to mechanically probe the strength of TCR–pMHC bonds. In that spirit, single-molecule force spectroscopy measurements indicate that the stability of the TCR–pMHC complex at different levels of mechanical strain provides a mechanism to enhance antigen discrimination (Hong et al., 2018). This has been proposed to help T cells to discriminate between strong agonists and low agonists/antagonists that would not overcome the forces exerted onto them (Hong et al., 2018). Since strong agonists presented by APCs are sparse and rare compared with the profusion of self-peptides, prolonging bond lifetimes could represent a strategy to establish an effective immune response.

Since the T cell–APC interface is extremely dynamic, a 'TCR deformation model' that takes into account the existence of mechanical stress applied onto the TCR has been proposed to explain how TCR triggering is initiated (Ma et al., 2008b). This model suggests that pulling forces generated by the cytoskeleton are transmitted to the TCR. Traction force microscopy (TFM) and BFP techniques showed that T cells generate contractile forces derived from the actomyosin network after TCR activation (Bashour et al., 2014; Hui et al., 2015; Husson et al., 2011; Sawicka et al., 2017). These forces have recently been measured at the level of TCR–pMHC single bond using DNA-based force sensors. T cells, by way of their cytoskeleton, can transmit forces of 12—19 pN to their TCR within seconds following pMHC binding (Liu et al., 2016). Using a 'lockable' version of this tension sensor, the same group showed that the TCR mechanically samples pMHCs with forces >4.7 pN (Ma et al., 2019). Using pMHC of different affinities, the authors further demonstrate that the mechanical sampling and scanning property of the TCR correlates with pMHC affinity (Ma et al., 2019). Hence, the mechanical regulation of TCR–pMHC bonds (slip-bonds versus catch-bonds) could impact the nature of T cell–APC contacts (motile versus static).

## Antigen recognition by migrating T cells leads to profound membrane remodelling and increase in tension

Crawling lymphocytes undergo massive morphology changes especially when squeezing across tissues and other cells. Despite the large deformations that a migrating T cell endures *in vivo*, plasma membrane integrity is preserved. These 'passive' deformations are supplied by the unfolding of surface membrane reservoirs (Guillou et al., 2016). Indeed, short microvilli cover the surface of circulating lymphocytes (Majstoravich et al., 2004) and are used as sensory organs to optimise the search for cognate pMHC (Cai et al., 2017). The excess external membrane contained in microvilli and membrane folds is rapidly available for T cells to increase their surface area while maintaining a constant cell volume. Using electron scanning microscopy, this membrane reservoir has been estimated to represent 40–50% of the apparent T cell membrane surface area in the form of microvilli for resting and activated T cells and in the form of membrane ruffles for Jurkat T cells (Guillou et al., 2016;

Majstoravich et al., 2004). Once T cells detect their cognate antigen, they slow down and start spreading onto the APCs ending by the establishment of firm contacts. T cells undergoing spreading on coverslips coated with activating antibodies increase substantially their apparent membrane surface area, by up to 150% of their initial surface area (Guillou et al., 2016). Therefore, the mobilisation of the external membrane reservoir is not sufficient for cell spreading and another reservoir is probably used to sustain large 'active' deformations. The proposed pool of membrane is internal organelles that would be released at the surface through exocytosis. This has been observed during the engulfment of particles through phagocytosis by macrophages (Bajno et al., 2000; Braun et al., 2004; Niedergang et al., 2003) and by neutrophils (Herant et al., 2005) but also when fibroblasts spread (Gauthier et al., 2011). Such release was reported to be mediated by the elevation of membrane tension that upon reaching a certain threshold – once all the external membrane pool is depleted and can no longer buffer plasma membrane tension (Raucher and Sheetz, 1999) – triggers exocytosis (Gauthier et al., 2011).

The elevation of membrane tension was also proposed to orchestrate the dynamic process of phagocytosis (Masters et al., 2013). Indeed, a critical increase in membrane tension was measured during phagocytosis and was shown to control the switch between two distinct phases (Masters et al., 2013). During phase 1, initial pseudopod extension is driven by Rac1-mediated actin polymerisation against the plasma membrane, ultimately leading to the flattening of all membrane folds. The second phase occurs once a peak in membrane tension is reached, directly altering Rac1 activity and triggering exocytosis. In phase 2, pseudopod extension relies on the release of internal vesicles containing GPI-anchored proteins that bring additional membrane at the cell surface (Masters et al., 2013). The inhibition of Rac1 activity by increased membrane tension was also reported in migrating neutrophils (Diz-Muñoz et al., 2016; Houk et al., 2012). The authors have proposed that membrane tension restricts protrusion formation to the leading edge by exerted long-range inhibition. On the other hand, the notion of long-range signalling relying on the propagation of membrane tension has been challenged by recent findings (Shi et al., 2018). In their study, Shi et al. (2018) performed membrane tether experiments on endothelial cells and found that tension fails to propagate across the cell due to flow resistance coming from cytoskeleton-bound transmembrane proteins. Interestingly, they further showed that local elevation in membrane tension can lead to local activation of mechanosensitive (MS) ion channels and further vesicle fusion. Thus, local variations in tension can trigger specific outcome in specific sub-cellular domains. Although the mechanisms by which membrane tension regulates cellular processes remain to be clarified, these studies provide a conceptual framework to highlight how cell mechanics and biochemical processes are interlinked. Antigen-scanning T cells also actively protrude onto APCs in a manner akin phagocytosis. The formation of the phagocytic cup and the formation of the immunological synapse indeed share similar features and mechanisms (Niedergang et al., 2016). It may therefore worth considering membrane tension as a potential organiser of T cell polarity during the dynamic process of antigen detection.

What are the other players involved in the regulation of membrane tension? Plasma membrane tension results from the minor contribution of the 'in-plane' tension in the lipid bilayer and from the major contribution of the attachment of the plasma membrane to the actin cortex (Sheetz, 2001; Sheetz and Dai, 1996). Membrane-to-cortex attachment is a critical mechanical parameter and modulates processes relying on cellular deformation such as protrusion formation in fibroblasts (Raucher and Sheetz, 2000) and migration of mesendoderm progenitors (Diz-Muñoz et al., 2010). Several proteins can link the plasma membrane to the underlying cytoskeleton such as Ezrin–Radixin–Moesin (ERM) (Fehon et al., 2010; Niggli and Rossy, 2008) and class-I Myosins (Nambiar et al., 2009).

Ezrin has been shown to regulate membrane tension in epithelial cells (Rouven Brückner et al., 2015) as well as in primary mouse T cells (Liu et al., 2012). Interestingly, Liu et al. (2012) have shown that expression of a phosphomimetic constitutively active mutant of Ezrin in mouse T cells increases their membrane tension and slows their homing in lymph node by decreasing their migration across the endothelium. This was accompanied by the absence of lamellipodial extension in response to chemokine stimulation (Liu et al., 2012). Ezrin has also been shown to accumulate at the periphery of T cell-APC contact

area upon TCR activation (Roumier et al., 2001). Interestingly, overexpression of a truncated form of Ezrin in T cells strongly perturbs the formation of the immunological synapse and affects TCR clustering with more numerous and spread TCR clusters indicative of a less mature synapse (Roumier et al., 2001). The authors proposed that Ezrin normally reinforces cell–cell interaction and microclusters coalescence at the immunological synapse needed for sustained T cell activation (Roumier et al., 2001). Overall, these studies shed light on the role played by proteins that mediate membrane-to-cytoskeleton attachment – such as ERMs – in the regulation of plasma membrane tension. They further suggest that the regulation of membrane tension is necessary for the establishment of a mature and functional synapse. On the other hand, ERM inactivation was shown to favour the formation of T cell–APC conjugates by reducing T cell rigidity, allowing a higher cellular deformability (Faure et al., 2004). As such, ERM proteins are rapidly and transiently dephosphorylated, therefore inactivated, upon TCR engagement to provide higher deformability (Faure et al., 2004). Hence, it appears that the ability of T cells to interact with APCs is tightly coordinated by variations in membrane tension orchestrated by membrane-to-cortex anchoring proteins.

Other candidates for regulating plasma membrane tension of lymphocytes and their migratory behaviour are class I myosins. They are also membrane-to-cytoskeleton anchored proteins that play a prominent role as force-sensitive motors and can modulate membrane tension *in vitro* and in several cell types such as epithelial cells and fibroblasts (Laakso et al., 2008; Nambiar et al., 2009). In addition, Class-I Myosins regulate cortical tension, cellular deformability (Dai et al., 1999) and cell migration of the amoeba *Dictyostelium discoideum* (Novak and Titus, 1997). Interestingly, a study has demonstrated the involvement of a class I myosin isoform – Myosin IG – in regulating membrane tension and motility of primary mouse T cells (Gérard et al., 2014). The authors observed that lymphoblasts migrating in microfabricated channels display transient phases of arrest that are preceded by Myosin IG recruitment at the leading edge. In parallel, membrane tether force measurements revealed that Myosin IG-deficient T cells have a lower membrane tension than WT T cells (Gérard et al., 2014). Does the recruitment of Myosin IG at the cell front during phases of arrest correlate with higher tension? To answer such question, it would require to measure locally membrane tension at the leading edge when the cell stops and to correlate this modification of the tension with the recruitment of Myosin 1G. This may be possible using an approach described in our tool box.

## Does membrane remodelling and increase in tension trigger $Ca^{2+}$ influx?

$Ca^{2+}$ mobilisation is known to be necessary and sufficient to deliver a 'stop signal' to migrating T cells (Donnadieu et al., 1994; Dustin et al., 1997; Miller et al., 2004b). Indeed, TCR triggering induces an increase in intracellular $Ca^{2+}$, activating signalling pathways responsible for cytoskeletal remodelling (Babich and Burkhardt, 2013), cell spreading (Bunnell et al., 2001) and the formation of a stable immunological synapse (Babich and Burkhardt, 2013; Delon et al., 1998; Negulescu et al., 1996). This role of $Ca^{2+}$ in the stabilisation of the immunological synapse has recently been questioned by the work of Kumari et al. (2020), which has demonstrated that although $Ca^{2+}$ increase is required for the initial stop of T cells, it is not involved in the maintenance of a stable synapse. $Ca^{2+}$ signalling in response to antigen recognition involves PLC$\gamma$ that generates inositol 1,4,5-triphosphate ($IP_3$) mediating $Ca^{2+}$ release from the endoplasmic reticulum (ER) via the opening of $IP_3$ receptors. This, in turn, activates $Ca^{2+}$ release-activated channels (CRAC) at the plasma membrane through the redistribution of STIM-1 to the ER–plasma membrane junctions where it interacts with Orai1, the pore-forming subunit of the CRAC channel, ultimately triggering extracellular $Ca^{2+}$ entry (Babich and Burkhardt, 2013; Lewis, 2001; Wu et al., 2006). This mechanism is known as the store-operated $Ca^{2+}$ entry (SOCE) (Luik and Lewis, 2007). Calcium influx through CRAC channels plays a crucial role in T cell activation, as revealed by the presence of immunodeficiencies in patients with mutations in the genes encoding STIM1 and Orai1 (Feske et al., 2006; Picard et al., 2009). Calcium influx through CRAC channels are thus essential for T cell functions (Vaeth et al., 2017) as it controls actin organisation and dynamics at the immunological synapse (Hartzell et al., 2016). In addition to its role in T cell arrest following TCR

activation, CRAC channels have also been shown to regulate basal T cell migration (i.e., in absence of extrinsic cell contacts or antigen recognition). Indeed, transient $Ca^{2+}$ entry through Orai1 channels correlates with spontaneous pauses both *in vitro* under confinement and *in vivo* (Dong et al., 2017). This highlights the prominent role of $Ca^{2+}$ in regulating T cell migratory behaviour.

Although the role of CRAC channels in T cell functions has clearly been demonstrated, other $Ca^{2+}$ channels may be involved. Indeed, there is direct evidence that mechanical forces exerted on the TCR induce a rise in intracellular $Ca^{2+}$ (Kim et al., 2009; Li et al., 2010). Yet, the contribution of MS ion channels and especially of stretch-activated calcium channels (SACCs) in $Ca^{2+}$ mobilisation and T cell activation has poorly been explored so far. We will herein review the current knowledge and research advancement as well as speculate on the potential role of these MS $Ca^{2+}$ channels in T cell mechanosensitivity.

SACCs belong to the transient receptor potential (TRP) ion channels superfamily and are sensitive to mechanical forces while being $Ca^{2+}$ permeable (Nilius et al., 2007). In cultured endothelial cells, MS channels are involved in substrate rigidity sensing and are used by cells to spontaneously generate rigidity-dependent localised $Ca^{2+}$ increase (Kobayashi and Sokabe, 2010). In this context, they have been suggested to constitute an intrinsic force measurement system that may regulate cell migration (Kobayashi and Sokabe, 2010). MS channels have also been reported to steer cell migration of fibroblasts (Wei et al., 2009). Indeed, mechanical forces such as shear stress applied at the leading edge of migrating fibroblasts provoke $Ca^{2+}$ flickers. These flickers are triggered by $Ca^{2+}$ influx through SACCs, here TRPM7, further amplified by $Ca^{2+}$ release from the ER. Flickers activity directly correlates with zones of traction force generation and are dependent on cytoskeletal and morphological integrity. Their amplitude and occurrence are associated with a decrease in directional persistence (Wei et al., 2009). Therefore, high $Ca^{2+}$ microdomains may activate several $Ca^{2+}$-dependent events critical to cell polarisation. These flickers take place in the lamella region of migrating fibroblasts which would correspond to the pSMAC of arrested T cells where actomyosin arcs generate traction forces on the TCR (Hong et al., 2017). Whether SACCs-dependent $Ca^{2+}$ flickers generated by local traction forces during T cell–APC interaction could lead to T cell deceleration remains to be addressed.

The implication of MS ion channels such as TRPC3 (Wenning et al., 2011) and TRPV1 (Bertin et al., 2014) in TCR-induced $Ca^{2+}$ influx and downstream TCR signalling have been reported. However, these studies did not investigate whether it involves mechanical stress. TRPV2, on the other hand, was shown by patch-clamp assay to generate stretch-activated current in T cells but neither its capacity to mediate $Ca^{2+}$ entry nor its role in T cell activation were assessed (Pottosin et al., 2015). A recently described potent MS channel called Piezo 1 (Coste et al., 2010) that can be activated by forces of around 10 pN (Wu et al., 2016) – which corresponds to the range of forces developed by T cells – has been reported to play a critical role in T cell activation (Liu et al., 2018). Piezo1-deficient primary human T cells proliferated less in response to APCs activation and exhibited impaired $Ca^{2+}$ influx upon TCR stimulation. Interestingly, chemical activation of Piezo1 obviates the need to immobilise anti-CD3 antibodies for optimal TCR triggering, suggesting that TCR mechanical stimulation may not be required when MS channels activity is already engaged. Liu et al. (2018) further showed that Piezo1-driven $Ca^{2+}$ influx leads to cortical actin rearrangement. The authors thus propose a model in which membrane stretch induced by the formation of the immunological synapse triggers Piezo1 activation, causing $Ca^{2+}$ entry, thereby leading to cytoskeletal remodelling to optimise T cell activation (Liu et al., 2018). Whether a similar mechanobiochemical regulation of TCR/pMHC engagement drives antigen-induced T cell arrest remains to be determined.

In this review, we would like to raise the question of whether T cell–APC conjugate formation, while a T cell is migrating, may induce local membrane stretches and $Ca^{2+}$ entry at the contact zone that would promote T cell arrest. A hypothetical mechanistic model of antigen-induced T cell arrest is depicted in Figure 1. An increase in membrane tension could potentially lead to local extracellular $Ca^{2+}$ entry through MS channels that would then be amplified and sustained by the classical SOCE pathway. T cells could probe the APC membrane giving rise to local, short-lived $Ca^{2+}$ at the contact zone as reported for Jurkat T cells upon touching anti-CD3 coated beads (Wolf et al., 2015). $Ca^{2+}$ entry may locally neu-

**Figure 1** | **See Legend on next page**

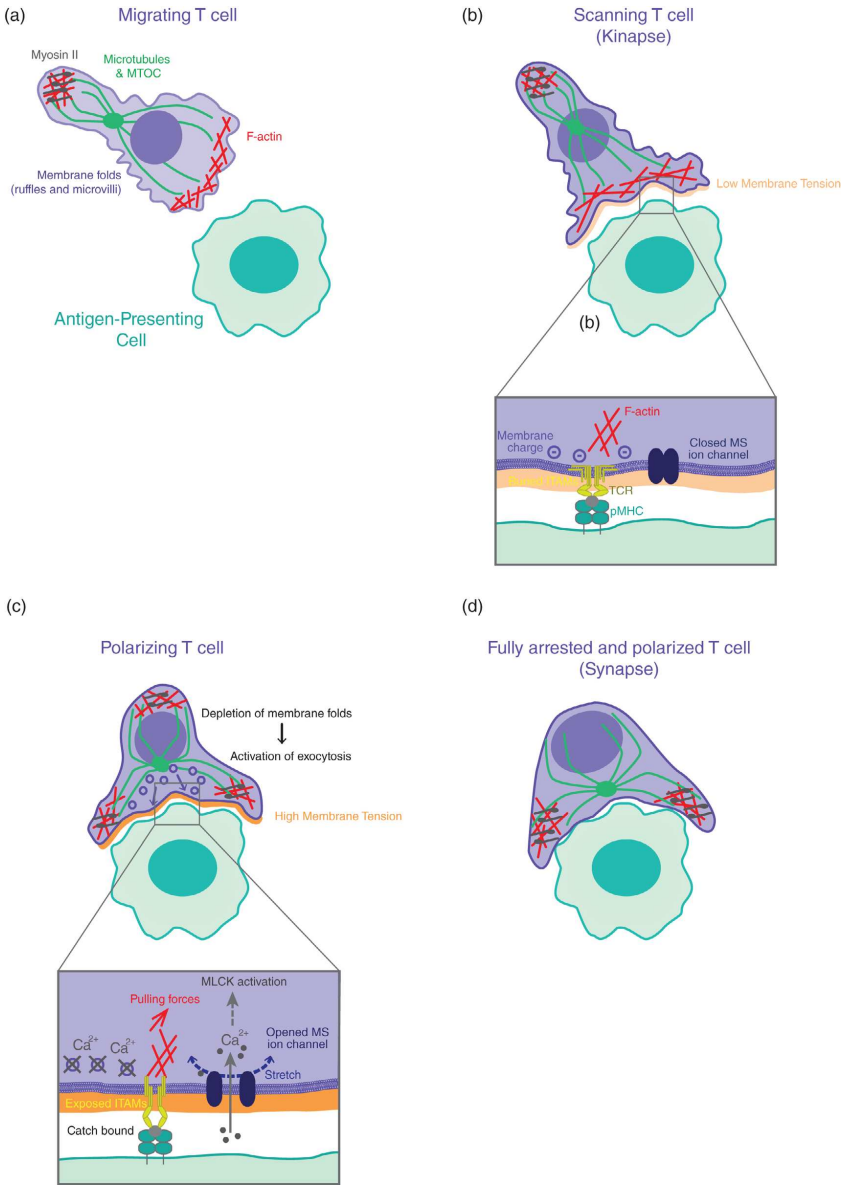

**Figure 1 | A proposed mechanistic model for antigen-induced T cell arrest**
(**A**) Migrating T cells display an actin-rich leading edge and a Myosin II-rich trailing edge, creating a back-to-front contractility gradient favouring T cell motility. The microtubule-organising centre (MTOC) is located at the cell rear behind the nucleus. T cells possess external membrane reservoir in the form of membrane folds (ruffles and microvilli). (**B**) T cells scan the surface of antigen-presenting cells (APCs) in search for their cognate antigen forming motile kinapse. Initially, T cells partially spread onto the APCs using the pool of membrane available in their membrane folds. At this stage, membrane tension is kept low as it is buffered by the unfolding of membrane ruffles and microvilli. Therefore, mechanosensitive (MS) ion channels are not activated and entry of extracellular $Ca^{2+}$ does not occur. As a result, the positively charged ITAMs motif of the TCR stay inaccessible, being buried in the lipid bilayer due to the presence of negatively charged phospholipids. (**C**) Spreading T cells then undergo complete depletion of their membrane folds. This leads to an increase in plasma membrane tension and induces the activation of exocytosis to sustain T cell spreading. Membrane stretches cause the opening of MS ion channels promoting the entry of extracellular $Ca^{2+}$. In turn, $Ca^{2+}$ ions neutralise the negatively charged phospholipids of the plasma membrane resulting in the release of the ITAMs. F-actin then applies pulling forces onto the TCR that sustain signalling through a catch bound mechanism. In parallel, $Ca^{2+}$ influx may locally activate the Myosin light chain kinase through its calmodulin domain. This recruitment at the cell–cell contact zone ultimately destabilises the contractility gradient and promotes T cell arrest. (**D**) Finally, T cells fully stop and can maintain long-lasting contacts with APC establishing an immunological synapse. F-actin is now concentrated at the outer cell edge forming the so-called actin ring, Myosin II is enriched in the immediate vicinity of the actin ring and the MTOC is polarised at the centre of the immunological synapse.

tralise the negative charge of plasma membrane phospholipids, freeing the cytoplasmic domains of the TCR–CD3 complex – normally buried in the lipid bilayer to prevent spontaneous ITAM phosphorylation – thus initiating TCR signalling (Ma et al., 2017a, 2017b; Shi et al., 2013). Of note, Hartzell et al. (2016) suggested the possibility that mobile CRAC channels complexes create local sites of high $Ca^{2+}$ concentration necessary for TCR ITAMs release from the plasma membrane allowing TCR signalling. Localised $Ca^{2+}$ microdomains could also mediate the recruitment of key cytoskeletal components that would destabilise the polarity of the T cell migratory machinery, thus resulting in T cell deceleration. Interestingly, $Ca^{2+}$ regulates Myosin II activity though the activation of Myosin light chain kinase (MLCK) by its $Ca^{2+}$-calmodulin domain (Vicente-Manzanares et al., 2009). Thereby, $Ca^{2+}$ entry through SACCs may locally activate MLCK and induce a re-polarisation of Myosin II from the uropod to the pre-synaptic junction responsible for T cell arrest. In other immune cell types such as immature DCs, Myosin II recruitment at the leading edge has been reported to be necessary for DCs to transiently stop in order for them to process internalised antigens (Chabaud et al., 2015). Whether T cell arrest relies on Myosin II redistribution from the cell rear to the contact zone is not clear yet. The role of Myosin II in the formation of the immunological synapse is controversial and has already been reviewed (Hammer and Burkhardt, 2013). As such, how Myosin II back-to-front gradient predominating during T cell migration is destabilised during antigen recognition and whether the extent of Myosin II recruitment at the T cell–APC contact site could mediate antigen-induced T cell remains an open question.

## Forces generated at the cell–cell interface are modulated by adhesion molecules

When motile T cells encounter their cognate antigen at the surface of APCs, TCR signalling triggers a change in the conformation of the main integrin present at the T cell surface, the lymphocyte function-associated antigen 1 (LFA-1). Resting T cells mostly display inactive, bent LFA-1 molecules with very low ligand binding capacity. LFA-1 then undergoes a conformational change upon TCR stimulation that recruits the actin-binding protein talin to the $\beta$-chain of LFA-1. This triggers the extension of the $\beta$-chain allowing the transition from a low to an intermediate affinity state – a mechanism known as the 'inside-out signalling'. This event enables LFA-1 anchoring to its ligand ICAM-1 present at the surface of APCs, promoting the open, high affinity LFA-1 conformation (Kinashi, 2005). ICAM-1 binding delivers specific intracellular signals called the 'outside-in signals' that lower the threshold of the antigen dose required to achieve full T cell activation (Perez et al., 2003). Interestingly, LFA-1 binding to ICAM-1, as

 

TCR binding to pMHC, also exhibit catch bound behaviour when forces are applied onto these bonds (Chen et al., 2010). Hence, motile T cells interacting with APCs must generate tensile forces onto the TCR/pMHC bonds but also onto the LFA-1/ICAM-1 bonds that will increase their binding strength and lifetime. In addition, LFA-1 being an integrin, it can undergo 'cyclic mechanical reinforcement' characterised by an increase in bond lifetime as a result of short, transient period of high forces applied (Kong et al., 2013) as those generated by the periodic actin waves at the leading edge of antigen scanning lymphocytes.

Burkhardt and colleagues (Comrie et al., 2015a) have documented how the dynamic F-actin network regulates LFA-1 conformational change, ligand binding and distribution at the immunological synapse. They showed that actin retrograde flow and Myosin II contraction are required to induce and maintain LFA-1 in its high affinity conformation. Actin flows organise the distribution of the different LFA-1 conformational intermediates radially with the extended LFA-1 (intermediate affinity) at the pSMAC and the open conformation (high affinity) concentrated in a more central ring. It has been previously observed that WASP-mediated actin polymerisation confines high-affinity LFA-1 to the mid-cell zone (Lafouresse et al., 2012). As an actin nucleator, WASP polymerises actin and contributes to the generation of actin retrograde flow, explaining its impact onto the spatial distribution of LFA-1. Comrie et al. (2015a,b) demonstrated convincingly that mechanical forces derived from actin flows and ligand binding itself (the 'induced fit' component) are functionally interconnected and are both required for full LFA-1 affinity maturation. Indeed, soluble ICAM-1 is not sufficient to promote LFA-1 conformational change in a context where TCR signalling and actin flows are intact. It is only when tension is generated by immobilised ligand that LFA-1 transitions to the open conformation. Under physiological conditions, ligand immobilisation is provided by the actin cytoskeleton of DCs, which constrains the mobility of ICAM-1 (Comrie et al., 2015b).

Comrie et al. (2015a) propose that F-actin drives a positive feedback loop in which TCR triggering induces robust actin flow that subsequently increases signalling through MS molecules such as LFA-1. Experiments performed with a FRET-based LFA-1 tension sensor has confirmed the significant tension across the $\beta$-subunit of LFA-1 upon ICAM-1 binding resulting in the stabilisation of active LFA-1 (Nordenfelt et al., 2016). During T cell migration, the actin retrograde flow applies tensile force that constrains the integrin into a tilted orientation (Nordenfelt et al., 2017). Stabilisation of high affinity LFA-1 by force application by the actin cytoskeleton thus provides a simple and elegant mechanism for coordinating cytoskeletal dynamics and ligand binding during T cell migration and further activation (Nordenfelt et al., 2016). After LFA-1 has been activated by the actin retrograde flow, it recruits focal adhesion proteins that act as a molecular clutch to slow down this retrograde flow (Case and Waterman, 2015; Jankowska et al., 2018). This results in a down-regulation of TCR signalling. Taken together, this demonstrates that LFA-1 is a mechanosensor, which potentiates TCR activation. Furthermore, these studies highlight how the modulation of the actin retrograde flow impacts T cell signalling.

Interestingly, LFA-1 has been reported to modulate the pattern of forces developed by T cells upon antigen recognition. Using a BFP approach to present beads covered with anti-CD3 to T cells, Husson et al. (2011) demonstrated that T cells exert pushing-pulling forces during antigen detection. In this study, T cells almost always undergo a pushing phase characterised by a massive protrusion extension (similar to a trunk) contacting the particle, followed by a pulling phase generating forces with a loading rate of around 2 pN/s which eventually leads to particle internalisation. In sharp contrast, when LFA-1 is co-engaged with the TCR complex, T cells rather form a cup-like protrusive structure and the pushing phase is significantly shorter. They further exert pulling forces of similar intensities to the one measured when engaging TCR alone, suggesting that TCR-signalling is the main contributor of pulling force generation. Thus, rather than producing forces, the presence of LFA-1 may optimise the contact with the target particle, thus preventing protrusion sliding onto the bead. Specifically, LFA-1 could provide an anchoring platform that would resist actin retrograde flow by promoting membrane-to-cytoskeleton tethering. Interestingly, mechanosensitivity to stiffness is biphasic during T cell spreading on activating substrates. When gels are coated with immobilised anti-CD3 only, T cells spread more on soft (20 kPa) than

on stiff (2440 kPa) gels. Conversely, when ICAM-1 is added, the spreading becomes monotonic, that is T cells spread similarly on soft and on stiff substrates. The authors propose that this ligand-specific response can be attributed to differences in force sensitivity and effective stiffness of the link formed between the ligand/receptor pairs and the actin cytoskeleton (Wahl et al., 2019). Therefore, the engagement of LFA-1 can couple the actin cytoskeleton to the plasma membrane to transmit efficiently the forces generated by TCR signalling to the underlying substrate. T cell spreading would thus be optimised as well as T cell arrest by extension. Of note, LFA-1/ICAM-1 interactions are indeed necessary for T cell arrest on DCs and for the formation of functional immunological synapse both *in vitro* (Abraham et al., 1999) and *in vivo* (Kandula and Abraham, 2004; Miller et al., 2004b; Scholer et al., 2008).

It is worth noting that more generally adhesion has been shown to pre-prime T cells so that the threshold for antigen detection is lowered. This phenomenon is called adhesion-induced T cell priming (AITCP) (Randriamampita et al., 2003). Although AITCP has been related to cAMP and ERK activation, the initial triggering of AITCP is still unclear. Besides, this phenomenon occurs in T cells adhering to diverse substrates (glass, fibronectin, ICAM-1, antibodies against MHC-I or $\beta 2$ integrins) (Conche et al., 2009; Randriamampita et al., 2003), suggesting the existence of a general mechanism rather than a specific receptor-induced signalling. Two non-exclusive hypotheses can be made: (1) a common signalosome may be recruited upon adhesion to these substrates (Conche et al., 2009); or (2) adhesion would induce pulling forces that mediate transient $Ca^{2+}$ influx through MS $Ca^{2+}$ channels. These $Ca^{2+}$ flickers could regulate T cell motility, as described for CRAC channels (Dong et al., 2017), that would optimise immune surveillance and favour T cell stop on APC when TCR is triggered by specific pMHC. Thus, engaging LFA-1 alone under tension – while T cells are crawling among the dense network of ICAM-1-covered DCs - could pre-prime T cells by inducing local rise in intracellular $Ca^{2+}$ derived from membrane stretches leading to the signalling event described in AITCP (Conche et al., 2009; Randriamampita et al., 2003). Yet, once established, it seems that the T cell synapse is sustained independently of integrin activation at least in naive $CD4^{+}$ T cells (Kumari et al., 2020).

## Is antigen-induced T cell arrest affected by the stiffness of APCs?

T cells are known to adapt their behaviour and immune responses to the mechanical properties of their environment and in particular to the stiffness of APCs (Hivroz and Saitakis, 2016; Saitakis et al., 2017). Whether the mechanical properties of APCs impact the stability of these contacts has not been addressed so far. Yet, during T cell activation, the loading rate of pulling forces generated by T cells increases with the stiffness of target particles (Husson et al., 2011; Sawicka et al., 2017). T cells also have the ability to quantitatively respond to substrate rigidity as shown by their increased capacity to adhere and to secrete cytokines on stiffer substrates (Judokusumo et al., 2012). In addition, substrate stiffness modulates T cell migration and morphological changes induced by TCR triggering (Saitakis et al., 2017). Of note, it has been reported that APCs exhibit distinct mechanical properties that can be modified by inflammation (Bufi et al., 2015). Thus, it might be interesting to assess the migratory behaviour of T cells when encountering different APCs and to determine whether a correlation exists between the rigidity of the APC and the capacity of a T cell to fully stop.

In cancer immunology, the nature of the interaction between T cells and cancer cells is particularly important. Cytotoxic T cells usually form stable contacts with tumour cells, which critically depends on extracellular $Ca^{2+}$ influx (Deguine et al., 2010). The formation of a stable synapse was also shown to enhance the efficiency of target cell lysis by cytotoxic T cells by confining the release of lytic granules at the synaptic interface (Beal et al., 2008). A recent study has focused on the nature of intercellular interactions within the tumour tissue based on morphometric aspects (Díaz et al., 2018). The authors performed 3D imaging of biopsy tissue blocks to determine the balance of synapse/kinapse present in two distinct histological regions of human glioma samples, neoplastic versus non-neoplastic. They found that bona-fide synapses are preferentially found in stromal areas whereas the frequency of kinapses was higher in malignant areas. Thus, the imbalance of synapse/kinapse state between the stroma and the malignant parenchyma is indicative of a defective antigen sensing function of T cells (Díaz et al., 2018). This impaired ability of T cells

to efficiently interact with cancer cells may be due to the presence of surrounding Tregs (Fecci et al., 2006) as reported in other conditions (Pace et al., 2012; Tadokoro et al., 2006; Tang et al., 2006); or to the expression by tumour cells of ligands engaging co-inhibitory receptors such as PD-1 and/or CTLA-4 (Brunner-Weinzierl and Rudd, 2018). Alternatively, defects in mechanosensing could be due to the mechanical properties of cancer cells. While the tumour tissue has been reported to be generally stiffer than normal tissue (Paszek et al., 2005), several studies have shown that individual malignant cells are more compliant than normal cells (Cross et al., 2007; Swaminathan et al., 2011; Xu et al., 2012). Whether cancer cell mechanical properties down-modulate immune recognition by affecting the T cell stop signal is not known so far. Interestingly, T cell cytotoxicity (i.e., pore forming activity of perforin) is potentiated by forces exerted at the immunological synapse that enable straining of the target cell surface (Basu et al., 2016). In this context, softer target cells are less prone to be killed because cell tension actually potentiates perforin activity. However, the stiffness of the APC does not control synapse stability, at least for naïve $CD4^+$ T cells (Kumari et al., 2020). The contribution of stiffness in the stability of synapses formed by activated/effector T cells remain to be analysed. Altogether, these studies highlight the contribution of the mechanical properties of target cells or APCs on the motility and functionality of lymphocytes.

## Conclusions

Studying the interplay between mechanical forces and chemical signalling during antigen recognition by migrating T cells is challenging. This is due, in part, to the experimental approaches commonly used in mechanobiology that are not adapted to moving cells. The recent development of DNA-based tension sensors and force probes coupled to existing microfabricated set-ups that are specifically designed to study immune cell migration, in conjunction with versatile micropatterning instrument could enable the development of new experimental procedures to explore the mechanical regulation of important dynamic processes such as antigen recognition by migrating T cells.

## Tool box: Experimental designs to understand the mechanobiology of antigen-induced T cell arrest

An important challenge to characterise the mechanobiology of antigen-induced T cell arrest is to be able to catch the dynamics of forces generated by T cells. In particular, we need experimental approaches to determine whether and how these forces drive the transition from a motile T cell to a static T cell. A set of experimental designs could allow such studies in the future. On one hand, the use of microfabricated channels has enabled to integrate the migratory behaviour of T cells with antigen recognition of different pMHC affinities to image cytoskeletal remodelling and the redistribution of signalling molecules (Moreau et al., 2015, 2017). On the other hand, micropatterning approaches are particularly well suited to control the area and the positioning of molecules coated onto various type of surfaces (Théry, 2010). In particular new photo-patterning tools such as PRIMO that allows 'printing' of several molecules sequentially afford flexibility in pattern design (Strale et al., 2016). This rapid and flexible photopatterning approach should allow to pattern different zones within the microfluidic channels. This is not achievable with standard UV patterning or with microcontact printing. We have tested this approach to create microchannels containing two zones coated with different molecules (Figure 2A). Using these patterned channels, we can follow a T cell transitioning from a migratory zone (zone printed with fibronectin) to an activating zone (zone printed with anti-CD3 antibodies) (Figure 2A). Playing with the coating of the migratory zone (non-adhesive versus different concentration of ICAM-1) should allow to address the role of AITCP in T cell arrest (Figure 2B). The next relevant approach would be to coat half of the microchannels with migratory molecules and the other half with pMHC coupled to DNA-based force probes developed by the group of Khalid Salaita (Liu et al., 2016) and to perform high spatiotemporal imaging of T cells in this setting (Figure 2C). This would help to estimate the level of forces generated when a migrating T cell encounters intermediate-affinity antigen giving rise to oscillatory T cells or when facing high-affinity antigen leading to a fully stopped T cell (Moreau et al., 2015). Thanks to live cell imaging, force quantification could be correlated to the level

**Figure 2 | See Legend on next page**

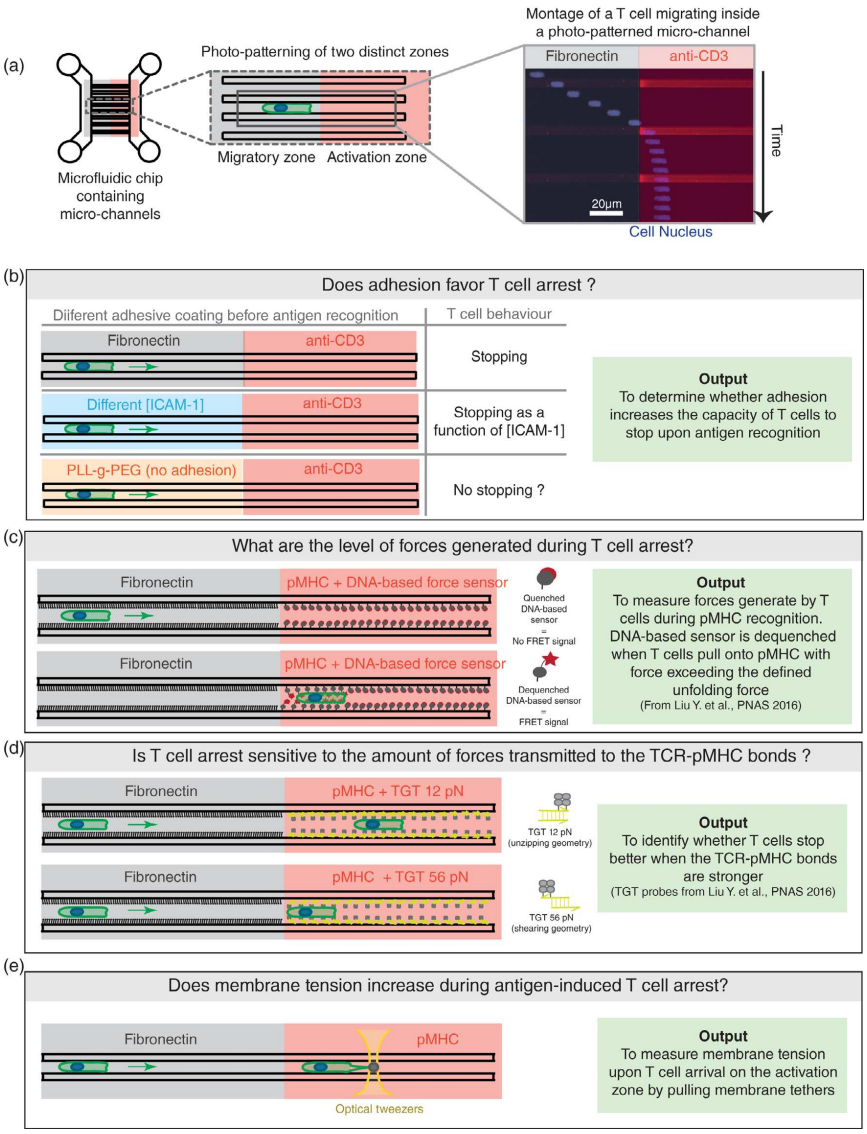

**Figure 2 | Experimental designs to understand the mechanobiology of antigen-induced T cell arrest**
(**A**) Schematic representation of microfabricated channels made of PDMS (polydimethylsiloxane) and sequentially patterned using the PRIMO technology (Strale et al., 2016) to create two distinct zones. T cells are then loaded into the microfluidic device and enter spontaneously inside micro-channels. Once inside a micro-channel, a T cell will encounter the migratory zone coated with fibronectin until reaching the activation zone coated with anti-CD3 antibodies. (Right) Sequential epifluorescence images (20×, one image every 30 s) of a Jurkat T cell stained with Hoechst (nucleus staining) migrating along the fibronectin-coated zone and stopping once encountering the anti-CD3-coated zone (OKT3 coating). Anti-CD3 zone was revealed using anti-mouse coupled to AlexaFluor546 and imaged every five frames to avoid photobleaching. (**B**) In order to assess the existence of a pre-priming of T cell arrest by adhesion as reported for T cell activation (Conche et al., 2009), we propose to coat the 'migratory zone' of the micro-channels with either strong adhesive ligands such as fibronectin or with different concentrations of ICAM-1, the ligand of the integrin LFA-1. As control, a non-adhesive zone can be obtained by a coating with PLL-g-PEG. (**C**) To estimate the level of forces generated when a migrating T cell encounters its antigen, we recommend to coat the 'activation zone' with pMHC covalently bound to DNA-based force sensors (developed by the group of Khalid Salaita (Liu et al.)). (**D**) In addition, to determine whether the level of self-generated forces transmitted to the TCR–pMHC bonds impacts the capacity of T cell to stop, we propose to use pMHC covalently bound to tension gauge tethers (TGT) (Liu et al., 2016). (**E**) Lastly, we propose to perform membrane tension measurement while a migrating T cell encounters its antigen by pulling membrane tethers with optical tweezers.

of intracellular $Ca^{2+}$ increase, a hallmark of T cell stopping upon antigen recognition (Lewis, 2001). In parallel, the use of tension gauge tethers (TGT) would help to discriminate the contribution of forces versus pMHC affinity in dictating T cell migratory behaviour (Figure 2D). The TGT offer a way to finely tuning the maximal forces that can be exerted onto them. Therefore, coating microchannels with pMHC coupled to TGT would give insight into the amount of forces required for T cell to stop. Further documentation of T cell polarisation – symmetrisation – as illustrated by actin cytoskeleton remodelling and MTOC polarisation could be added. In addition, by combining this two zones microfluidic chip with an optical tweezer set up, we should be able to follow the status of plasma membrane tension when a migrating T cell encounters its cognate pMHC (Figure 2E). It would require to pull a membrane tether while the cell is moving forward the activation zone. Taken together, the combination of microfabrication and dual coating with DNA-based force probes should be able to unravel the amount of forces necessary to induce the transition from a motile T cell to a fully arrested, synapse-forming T cell.

## Funding

Mélanie Chabaud was supported by a postdoctoral long-term fellowship from the Human Frontier Science Program (HFSP–LT000566/2016-L) and a UNSW Vice-Chancellor's postdoctoral research fellowship (The University of New South Wales, Australia). Noémie Paillon is supported by a PhD fellowship from ITMO Cancer in partnership with INSERM and from Ecole Doctorale Frontières de l'Innovation en Recherche et Education – Programme Bettencourt. Work was supported by funds from Institut Curie, INSERM, ANR (ANR-10-IDEX-0001-02 PSL* and ANR-11-LABX-0043).

## Conflict of interest statement

The authors have declared no conflict of interest.

## References

Abraham, C., Griffith, J., and Miller, J. (1999). The dependence for leukocyte function-associated antigen-1/ICAM-1 interactions in T cell activation cannot be overcome by expression of high density TCR ligand. J. Immunol. **162**, 4399 LP–4405.

Von Andrian, U.H., and Mempel, T.R. (2003). Homing and cellular traffic in lymph nodes. Nat. Rev. Immunol. **3**, 867–878.

Babich, A., and Burkhardt, J.K. (2013). Coordinate control of cytoskeletal remodeling and calcium mobilization during T-cell activation. Immunol. Rev. **256**, 80–94.

Bajénoff, M., Egen, J.G., Koo, L.Y., Laugier, J.P., Brau, F., Glaichenhaus, N., and Germain, R.N. (2006). Stromal cell networks regulate lymphocyte entry, migration, and territoriality in lymph nodes. Immunity **25**, 989–1001.

Bajno, L., Peng, X.-R., Schreiber, A.D., Moore, H.-P., Trimble, W.S., and Grinstein, S. (2000). Focal exocytosis of Vamp3-containing vesicles at sites of phagosome formation. J. Cell Biol. **149**, 697 LP–706.

Bashour, K.T., Gondarenko, A., Chen, H., Shen, K., Liu, X., Huse, M., Hone, J.C., and Kam, L.C. (2014). CD28 and CD3 have complementary roles in T-cell traction forces. Proc. Natl. Acad. Sci. U.S.A. **111**, 2241–2246.

Basu, R., Whitlock, B.M., Husson, J., Le Floc'h, A., Jin, W., Oyler-Yaniv, A., Dotiwala, F., Giannone, G., Hivroz, C., Biais, N., Lieberman, J., Kam, L,C., Huse, M. (2016). Cytotoxic T cells use mechanical force to potentiate target cell killing. Cell **165**, 100–110.
Beal, A.M., Anikeeva, N., Varma, R., Cameron, T.O., Norris, P.J., Dustin, M.L., and Sykulev, Y. (2008). Protein kinase C$\theta$ regulates stability of the peripheral adhesion ring junction and contributes to the sensitivity of target cell lysis by CTL. J. Immunol. **181**, 4815 LP–4824.
Bertin, S, de Jong, PR, Jefferies, WA, and Raz, E. (2014). Novel immune function for the TRPV1 channel in T lymphocytes. Channels (Austin) **8**(6): 479–480.
Billadeau, D.D., Nolz, J.C., and Gomez, T.S. (2007). Regulation of T-cell activation by the cytoskeleton. Nat. Rev. Immunol. **7**, 131–143.
Bousso, P., and Robey, E. (2003). Dynamics of CD8+ T cell priming by dendritic cells in intact lymph nodes. Nat. Immunol. **4**, 579–585.
Braun, V., Fraisier, V., Raposo, G., Hurbain, I., Sibarita, J.B., Chavrier, P., Galli, T., and Niedergang, F. (2004). TI-VAMP/VAMP7 is required for optimal phagocytosis of opsonised particles in macrophages. EMBO J. **23**, 4166–4176.
Brunner-Weinzierl, M.C., and Rudd, C.E. (2018). CTLA-4 and PD-1 control of T-cell motility and migration: implications for tumor immunotherapy. Front. Immunol. **9**, 2737.
Bufi, N., Saitakis, M., Dogniaux, S., Buschinger, O., Bohineust, A., Richert, A., Maurin, M., Hivroz, C., and Asnacios, A. (2015). Human primary immune cells exhibit distinct mechanical properties that are modified by inflammation. Biophys. J. **108**, 2181–2190.
Bunnell, S.C., Kapoor, V., Trible, R.P., Zhang, W., and Samelson, L.E. (2001). Dynamic actin polymerization drives T cell receptor-induced spreading: A role for the signal transduction adaptor LAT. Immunity **14**, 315–329.
Cai, E., Marchuk, K., Beemiller, P., Beppler, C., Rubashkin, M.G., Weaver, V.M., Gérard, A., Liu, T.-L., Chen, B.-C., Betzig, E., Bartumeus F., Krummel M.F. (2017). Visualizing dynamic microvillar search and stabilization during ligand detection by T cells. Science **356**, eaal3118.
Case, L.B., and Waterman, C.M. (2015). Integration of actin dynamics and cell adhesion by a three-dimensional, mechanosensitive molecular clutch. Nat. Cell Biol. **17**, 955–963.
Chabaud, M., Heuze, M.L., Bretou, M., Vargas, P., Maiuri, P., Solanes, P., Maurin, M., Terriac, E., Le Berre, M., Lankar, D., Piolot, T., Adelstein, R.S., Zhang, Y., Sixt, M., Jacobelli, J., Bénichou, O., Voituriez, R., Piel, M., Lennon-Duménil, A.M. (2015). Cell migration and antigen capture are antagonistic processes coupled by myosin II in dendritic cells. Nat. Commun. **6**, 7526.
Chen, W., Lou, J., and Zhu, C. (2010). Forcing switch from short- to intermediate- and long-lived states of the $\alpha$A domain generates LFA-1/ICAM-1 catch bonds. J. Biol. Chem. **285**, 35967–35978.
Comrie, W.A., Babich, A., and Burkhardt, J.K. (2015a). F-actin flow drives affinity maturation and spatial organization of LFA-1 at the immunological synapse. J. Cell Biol. **208**, 475 LP–491.
Comrie, W.A., Li, S., Boyle, S., and Burkhardt, J.K. (2015b). The dendritic cell cytoskeleton promotes T cell adhesion and activation by constraining ICAM-1 mobility. J. Cell Biol. **208**, 457 LP–473.
Conche, C., Boulla, G., Trautmann, A., and Randriamampita, C. (2009). T cell adhesion primes antigen receptor-induced calcium responses through a transient rise in adenosine 3′,5′-cyclic monophosphate. Immunity **30**, 33–43.
Coste, B., Mathur, J., Schmidt, M., Earley, T.J., Ranade, S., Petrus, M.J., Dubin, A.E., and Patapoutian, A. (2010). Piezo1 and Piezo2 are essential components of distinct mechanically activated cation channels. Science **330**, 55 LP–60.
Cross, S.E., Jin, Y.-S., Rao, J., and Gimzewski, J.K. (2007). Nanomechanical analysis of cells from cancer patients. Nat. Nanotechnol. **2**, 780–783.
Dai, J., Ting-Beall, H.P., Hochmuth, R.M., Sheetz, M.P., and Titus, M.A. (1999). Myosin I contributes to the generation of resting cortical tension. Biophys. J. **77**, 1168–1176.
Das, D.K., Feng, Y., Mallis, R.J., Li, X., Keskin, D.B., Hussey, R.E., Brady, S.K., Wang, J.-H., Wagner, G., Reinherz, E.L., Lang, M.J. (2015). Force-dependent transition in the T-cell receptor $\beta$-subunit allosterically regulates peptide discrimination and pMHC bond lifetime. Proc. Natl. Acad. Sci. U.S.A. **112**, 1517 LP–1522.
Deguine, J., Breart, B., Lemaître, F., Di Santo, J.P., and Bousso, P. (2010). Intravital imaging reveals distinct dynamics for natural killer and CD8+ T cells during tumor regression. Immunity **33**, 632–644.
Delon, J., Bercovici, N., Raposo, G., Liblau, R., and Trautmann, A. (1998). Antigen-dependent and -independent Ca2+ responses triggered in T cells by dendritic cells compared with B cells. J. Exp. Med. **188**, 1473–1484.
Díaz, L.R., Saavedra-López, E., Romarate, L., Mitxitorena, I., Casanova, P. V., Cribaro, G.P., Gallego, J.M., Pérez-Vallés, A., Forteza-Vila, J., Alfaro-Cervello, C., García-Verdugo, J.M., Barcia, C. Sr, Barcia, C. Jr (2018). Imbalance of immunological synapse-kinapse states reflects tumor escape to immunity in glioblastoma. JCI Insight **3**, 1–17.
Diz-Muñoz, A., Krieg, M., Bergert, M., Ibarlucea-Benitez, I., Muller, D.J., Paluch, E., and Heisenberg, C.P. (2010). Control of directed cell migration in vivo by membrane-to-cortex attachment. PLoS Biol. **8**, e1000544.
Diz-Muñoz, A., Thurley, K., Chintamen, S., Altschuler, S.J., Wu, L.F., Fletcher, D.A., and Weiner, O.D. (2016). Membrane tension acts through PLD2 and mTORC2 to limit actin network assembly during neutrophil migration. PLOS Biol. **14**, e1002474.
Dong, T.X., Othy, S., Greenberg, M.L., Jairaman, A., Akunwafo, C., Leverrier, S., Yu, Y., Parker, I., Dynes, J.L., and Cahalan, M.D. (2017). Intermittent Ca2+ signals mediated by orai1 regulate basal T cell motility. Elife **6**, 1–26.
Donnadieu, E., Bismuth, G., and Trautmann, A. (1994). Antigen recognition by helper T cells elicits a sequence of distinct changes of their shape and intracellular calcium. Curr. Biol. **4**, 584–595.
Dustin, M.L. (2007). Cell adhesion molecules and actin cytoskeleton at immune synapses and kinapses. Curr. Opin. Cell Biol. **19**, 529–533.
Dustin, M.L. (2008). T-cell activation through immunological synapses and kinapses. Immunol. Rev. **221**, 77–89.
Dustin, M.L., Bromley, S.K., Kan, Z., Peterson, D.A., and Unanue, E.R. (1997). Antigen receptor engagement delivers a stop signal to migrating T lymphocytes. Proc. Natl. Acad. Sci. U.S.A. **94**, 3909–3913.
Faure, S., Salazar-Fontana, L.I., Semichon, M., Tybulewicz, V.L.J., Bismuth, G., Trautmann, A., Germain, R.N., and Delon, J. (2004). ERM proteins regulate cytoskeleton relaxation promoting T cell-APC conjugation. Nat. Immunol. **5**, 272–279.
Fecci, P.E., Mitchell, D.A., Whitesides, J.F., Xie, W., Friedman, A.H., Archer, G.E., li, J.E.H., Bigner, D.D., Dranoff, G., and Sampson, J.H. (2006). Increased regulatory T-cell fraction amidst a diminished CD4 compartment explains cellular immune defects in patients with malignant glioma. Cancer Res. **66**, 3294-3023.
Fehon, R.G., McClatchey, A.I., and Bretscher, A. (2010). Organizing the cell cortex: the role of ERM proteins. Nat. Rev. Mol. Cell Biol. **11**, 276–287.
Feske, S., Gwack, Y., Prakriya, M., Srikanth, S., Puppel, S.H., Tanasa, B., Hogan, P.G., Lewis, R.S., Daly, M., and Rao, A. (2006). A mutation in Orai1 causes immune deficiency by abrogating CRAC channel function. Nature **441**, 179–185.
Fricke, G.M., Letendre, K.A., Moses, M.E., and Cannon, J.L. (2016). Persistence and adaptation in immunity: T cells balance the extent and thoroughness of search. PLoS Comput. Biol. **12**, 1–23.

 

Gauthier, N.C., Fardin, M.A., Roca-Cusachs, P., and Sheetz, M.P. (2011). Temporary increase in plasma membrane tension coordinates the activation of exocytosis and contraction during cell spreading. Proc. Natl. Acad. Sci. U.S.A. **108**, 14467 LP–14472.

Gérard, A., Patino-Lopez, G., Beemiller, P., Nambiar, R., Ben-Aissa, K., Liu, Y., Totah, F.J., Tyska, M.J., Shaw, S., and Krummel, M.F. (2014). Detection of rare antigen-presenting cells through T cell-intrinsic meandering motility, mediated by Myo1g. Cell **158**, 492–505.

Grakoui, A., Bromley, S.K., Sumen, C., Davis, M.M., Shaw, A.S., Allen, P.M., and Dustin, M.L. (1999). The immunological synapse: a molecular machine controlling T cell activation. Science **285**, 221–227.

Guillou, L., Babataheri, A., Saitakis, M., Bohineust, A., Dogniaux, S., Hivroz, C., Barakat, A.I., and Husson, J. (2016). T-lymphocyte passive deformation is controlled by unfolding of membrane surface reservoirs. Mol. Biol. Cell **27**, 3574–3582.

Hammer, J.A., and Burkhardt, J.K. (2013). Controversy and consensus regarding myosin II function at the immunological synapse. Curr. Opin. Immunol. **25**, 300–306.

Hartzell, C.A., Jankowska, K.I., Burkhardt, J.K., and Lewis, R.S. (2016). Calcium influx through CRAC channels controls actin organization and dynamics at the immune synapse. Elife **5**, 1–28.

Herant, M., Heinrich, V., and Dembo, M. (2005). Mechanics of neutrophil phagocytosis: behavior of the cortical tension. J. Cell Sci. **118**, 1789 LP–1797.

Hivroz, C., and Saitakis, M. (2016). Biophysical aspects of T lymphocyte activation at the immune synapse. Front. Immunol. **7**, 1–12.

Hong, J., Murugesan, S., Betzig, E., and Hammer, J.A. (2017). Contractile actomyosin arcs promote the activation of primary mouse T cells in a ligand-dependent manner. PLoS One **12**, e0183174.

Hong, J., Ge, C., Jothikumar, P., Yuan, Z., Liu, B., Bai, K., Li, K., Rittase, W., Shinzawa, M., Zhang, Y., Palin, A., Love, P., Yu, X., Salaita, K., Evavold, B.D., Singer, A., Zhu, C. (2018). A TCR mechanotransduction signaling loop induces negative selection in the thymus. Nat. Immunol. **19**, 1379–1390.

Houk, A.R., Jilkine, A., Mejean, C.O., Boltyanskiy, R., Dufresne, E.R., Angenent, S.B., Altschuler, S.J., Wu, L.F., and Weiner, O.D. (2012). Membrane tension maintains cell polarity by confining signals to the leading edge during neutrophil migration. Cell **148**, 175–188.

Hugues, S., Fetler, L., Bonifaz, L., Helft, J., Amblard, F., and Amigorena, S. (2004). Distinct T cell dynamics in lymph nodes during the induction of tolerance and immunity. Nat. Immunol. **5**, 1235–1242.

Hui, K.L., Balagopalan, L., Samelson, L.E., and Upadhyaya, A. (2015). Cytoskeletal forces during signaling activation in Jurkat T-cells. Mol. Biol. Cell **26**, 685–695.

Huse, M. (2017). Mechanical forces in the immune system. Nat. Rev. Immunol. **17**, 679–690.

Husson, J., Chemin, K., Bohineust, A., Hivroz, C., and Henry, N. (2011). Force generation upon T cell receptor engagement. PLoS One **6**, e19680.

Jankowska, K.I., Williamson, E.K., Roy, N.H., Blumenthal, D., Chandra, V., Baumgart, T., and Burkhardt, J.K. (2018). Integrins modulate T cell receptor signaling by constraining actin flow at the immunological synapse. Front. Immunol. **9**, 1–19.

Judokusumo, E., Tabdanov, E., Kumari, S., Dustin, M.L., and Kam, L.C. (2012). Mechanosensing in T lymphocyte activation. Biophys. J. **102**, L5-7.

Kandula, S., and Abraham, C. (2004). LFA-1 on CD4+ T cells is required for optimal antigen-dependent activation in vivo. J. Immunol. **173**, 4443 LP–4451.

Kim, S.T., Takeuchi, K., Sun, Z.Y.J., Touma, M., Castro, C.E., Fahmy, A., Lang, M.J., Wagner, G., and Reinherz, E.L. (2009). The $\alpha\beta$ T cell receptor is an anisotropic mechanosensor. J. Biol. Chem. **284**, 31028–31037.

Kinashi, T. (2005). Intracellular signalling controlling integrin activation in lymphocytes. Nat. Rev. Immunol. **5**:546–559.

Kobayashi, T., and Sokabe, M. (2010). Sensing substrate rigidity by mechanosensitive ion channels with stress fibers and focal adhesions. Curr. Opin. Cell Biol. **22**, 669–676.

Kong, F., García, A.J., Mould, A.P., Humphries, M.J., and Zhu, C. (2009). Demonstration of catch bonds between an integrin and its ligand. J. Cell Biol. **185**, 1275–1284.

Kong, F., Li, Z., Parks, W.M., Dumbauld, D.W., García, A.J., Mould, A.P., Humphries, M.J., and Zhu, C. (2013). Cyclic mechanical reinforcement of integrin-ligand interactions. Mol. Cell **49**, 1060–1068.

Krummel, M.F., Bartumeus, F., and Gérard, A. (2016). T cell migration, search strategies and mechanisms. Nat. Rev. Immunol. **16**, 193–201.

Kumari, S., Mak, M., Poh, Y., Tohme, M., Watson, N., Melo, M., Janssen, E., Dustin, M., Geha, R., and Irvine, D.J. (2020). Cytoskeletal tension actively sustains the migratory T-cell synaptic contact. EMBO J. **39**, 1–18.

Laakso, J.M., Lewis, J.H., Shuman, H., and Ostap, E.M. (2008). Myosin I can act as a molecular force sensor. Science **321**, 133 LP–136.

Lafouresse, F., Cotta-de-Almeida, V., Malet-Engra, G., Galy, A., Valitutti, S., and Dupré, L. (2012). Wiskott-Aldrich syndrome protein controls antigen-presenting cell-driven CD4 + T-cell motility by regulating adhesion to intercellular adhesion molecule-1. Immunology **137**, 183–196.

Lewis, R.S. (2001). Calcium signaling mechanims in T lymphocytes. Annu. Rev. Immunol. **19**, 497–521.

Li, Y.-C., Chen, B.-M., Wu, P.-C., Cheng, T.-L., Kao, L.-S., Tao, M.-H., Lieber, A., and Roffler, S.R. (2010). Cutting edge: mechanical forces acting on T cells immobilized via the TCR complex can trigger TCR signaling. J. Immunol. **184**, 5959 LP–5963.

Liu, B., Chen, W., Evavold, B.D., and Zhu, C. (2014). Accumulation of dynamic catch bonds between TCR and agonist peptide-MHC triggers T cell signaling. Cell **157**, 357–368.

Liu, C.S.C., Raychaudhuri, D., Paul, B., Chakrabarty, Y., Ghosh, A.R., Rahaman, O., Talukdar, A., and Ganguly, D. (2018). Cutting edge: Piezo1 mechanosensors optimize human T cell activation. J. Immunol. **200**, 1255–1260.

Liu, Y., Belkina, N. V., Park, C., Nambiar, R., Loughhead, S.M., Patino-Lopez, G., Ben-Aissa, K., Hao, J.J., Kruhlak, M.J., Qi, H., von Andrian, U.H., Kehrl, J.H., Tyska, M.J., Shaw, S. (2012). Constitutively active ezrin increases membrane tension, slows migration, and impedes endothelial transmigration of lymphocytes in vivo in mice. Blood **119**, 445–453.

Liu, Y., Blanchfield, L., Ma, V.P.-Y., Andargachew, R., Galior, K., Liu, Z., Evavold, B., and Salaita, K. (2016). DNA-based nanoparticle tension sensors reveal that T-cell receptors transmit defined pN forces to their antigens for enhanced fidelity. Proc. Natl. Acad. Sci. U.S.A. **113**, 5610 LP–5615.

Luik, R.M., and Lewis, R.S. (2007). New insights into the molecular mechanisms of store-operated Ca2+ signaling in T cells. Trends Mol. Med. **13**, 103–107.

Ma, R., Kellner, A. V., Ma, V.P.-Y., Su, H., Deal, B.R., Brockman, J.M., and Salaita, K. (2019). DNA probes that store mechanical information reveal transient piconewton forces applied by T cells. Proc. Natl. Acad. Sci. U.S.A. **116**, 16949–16954.

Ma, Y., Yamamoto, Y., Nicovich, P.R., Goyette, J., Rossy, J., Gooding, J.J., and Gaus, K. (2017a). A FRET sensor enables quantitative measurements of membrane charges in live cells. Nat. Biotechnol. **35**, 363–370.

Ma, Y., Poole, K., Goyette, J., and Gaus, K. (2017b). Introducing membrane charge and membrane potential to T cell signaling. Front. Immunol. **8**, 1–11.
Ma, Z., Sharp, K.A., Janmey, P.A., and Finkel, T.H. (2008a). Surface-anchored monomeric agonist pMHCs alone trigger TCR with high sensitivity. PLOS Biol. **6**, 0328–0342.
Ma, Z., Janmey, P.A., and Finkel, T.H. (2008b). The receptor deformation model of TCR triggering. FASEB J. **22**, 1002–1008.
Majstoravich, S., Zhang, J., Nicholson-Dykstra, S., Linder, S., Friedrich, W., Siminovitch, K.A., and Higgs, H.N. (2004). Lymphocyte microvilli are dynamic, actin-dependent structures that do not require Wiskott-Aldrich syndrome protein (WASp) for their morphology. Blood **104**, 1396–1403.
Marshall, B.T., Long, M., Piper, J.W., Yago, T., McEver, R.P., and Zhu, C. (2003). Direct observation of catch bonds involving cell-adhesion molecules. Nature **423**, 190–193.
Masters, T.A., Pontes, B., Viasnoff, V., Li, Y., and Gauthier, N.C. (2013). Plasma membrane tension orchestrates membrane trafficking, cytoskeletal remodeling, and biochemical signaling during phagocytosis. Proc. Natl. Acad. Sci. U.S.A. **110**, 11875–11880.
Mempel, T.R., Henrickson, S.E., and von Andrian, U.H. (2004). T-cell priming by dendritic cells in lymph nodes occurs in three distinct phases. Nature **427**, 154–159.
Miller, M.J., Wei, S.H., Parker, I., and Cahalan, M.D. (2002). Two-photon imaging of lymphocyte motility and antigen response in intact lymph node. Science **296**, 1869–1873.
Miller, M.J., Hejazi, A.S., Wei, S.H., Cahalan, M.D., and Parker, I. (2004a). T cell repertoire scanning is promoted by dynamic dendritic cell behavior and random T cell motility in the lymph node. Proc. Natl. Acad. Sci. U.S.A. **101**, 998–1003.
Miller, M.J., Safrina, O., Parker, I., and Cahalan, M.D. (2004b). Imaging the single cell dynamics of CD4+ T cell activation by dendritic cells in lymph nodes. J. Exp. Med. **200**, 847 LP–856.
Monks, C.R.F., Freiberg, B.A., Kupfer, H., Sciaky, N., and Kupfer, A. (1998). Three-dimensional segregation of supramolecular activation clusters in T cells. Nature **395**, 82–86.
Moreau, H.D., Lemaître, F., Garrod, K.R., Garcia, Z., Lennon-Duménil, A.-M., and Bousso, P. (2015). Signal strength regulates antigen-mediated T-cell deceleration by distinct mechanisms to promote local exploration or arrest. Proc. Natl. Acad. Sci. U.S.A. **112**, 12151–12156.
Moreau, H.D., Bousso, P., and Lennon-Duménil, A.-M. (2017). Microchannels for the study of T cell immunological synapses and kinapses. Methods Mol. Biol. **1584**, 347–354.
Murugesan, S., Hong, J., Yi, J., Li, D., Beach, J.R., Shao, L., Meinhardt, J., Madison, G., Wu, X., Betzig, E., Hammer, J.A. (2016). Formin-generated actomyosin arcs propel T cell receptor microcluster movement at the immune synapse. J. Cell Biol. **215**, 383-399.
Nambiar, R., McConnell, R.E., and Tyska, M.J. (2009). Control of cell membrane tension by myosin-I. Proc. Natl. Acad. Sci. U.S.A. **106**, 11972 LP–11977.
Negulescu, P.A., Krasieva, T.B., Khan, A., Kerschbaum, H.H., and Cahalan, M.D. (1996). Polarity of T cell shape, motility, and sensitivity to antigen. Immunity **4**, 421–430.
Niedergang, F., Colucci-Guyon, E., Dubois, T., Raposo, G., and Chavrier, P. (2003). ADP ribosylation factor 6 is activated and controls membrane delivery during phagocytosis in macrophages. J. Cell Biol. **161**, 1143 LP–1150.
Niedergang, F., Di Bartolo, V., and Alcover, A. (2016). Comparative anatomy of phagocytic and immunological synapses. Front. Immunol. **7**, 1–9.
Niggli, V., and Rossy, J. (2008). Ezrin/radixin/moesin: Versatile controllers of signaling molecules and of the cortical cytoskeleton. Int. J. Biochem. Cell Biol. **40**, 344–349.
Nilius, B., Owsianik, G., Voets, T., and Peters, J.A. (2007). Transient receptor potential cation channels in disease. Physiol Rev. **87**, 165–217.
Nordenfelt, P., Elliott, H.L., and Springer, T.A. (2016). Coordinated integrin activation by actin-dependent force during T-cell migration. Nat. Commun. **7**, 1–15.
Nordenfelt, P., Moore, T.I., Mehta, S.B., Kalappurakkal, J.M., Swaminathan, V., Koga, N., Lambert, T.J., Baker, D., Waters, J.C., Oldenbourg, R., Tani, T., Mayor, S., Waterman, C.M., Springer, T.A. (2017). Direction of actin flow dictates integrin LFA-1 orientation during leukocyte migration. Nat. Commun. **8**, 2047.
Novak, K.D., and Titus, M.A. (1997). Myosin I overexpression impairs cell migration. J. Cell Biol. **136**, 633 LP–647.
Pace, L., Tempez, A., Arnold-Schrauf, C., Lemaitre, F., Bousso, P., Fetler, L., Sparwasser, T., and Amigorena, S. (2012). Regulatory T cells increase the avidity of primary CD8+ T cell responses and promote memory. Science **338**, 532 LP–536.
Pageon, S. V., Govendir, M.A., Kempe, D., and Biro, M. (2018). Mechanoimmunology: Molecular-scale forces govern immune cell functions. Mol. Biol. Cell **29**, 1919–1926.
Paszek, M.J., Zahir, N., Johnson, K.R., Lakins, J.N., Rozenberg, G.I., Gefen, A., Reinhart-King, C.A., Margulies, S.S., Dembo, M., Boettiger, D., Hammer, D.A., Weaver, V.M. (2005). Tensional homeostasis and the malignant phenotype. Cancer Cell **8**, 241–254.
Perez, O.D., Mitchell, D., Jager, G.C., South, S., Murriel, C., McBride, J., Herzenberg, L.A., Kinoshita, S., and Nolan, G.P. (2003). Leukocyte functional antigen 1 lowers T cell activation thresholds and signaling through cytohesin-1 and Jun-activating binding protein 1. Nat. Immunol. **4**, 1083–1092.
Picard, C., McCarl, C.A., Papolos, A., Khalil, S., Lüthy, K., Hivroz, C., LeDeist, F., Rieux-Laucat, F., Rechavi, G., Rao, A., Fischer, A., Feske, S. (2009). STIM1 mutation associated with a syndrome of immunodeficiency and autoimmunity. N. Engl. J. Med. **360**, 1971–1980.
Pottosin, I., Delgado-Enciso, I., Bonales-Alatorre, E., Nieto-Pescador, M.G., Moreno-Galindo, E.G., and Dobrovinskaya, O. (2015). Mechanosensitive Ca2 +-permeable channels in human leukemic cells: Pharmacological and molecular evidence for TRPV2. Biochim. Biophys. Acta Biomembr. **1848**, 51–59.
Randriamampita, C., Boulla, G., Revy, P., Lemaitre, F., and Trautmann, A. (2003). T cell adhesion lowers the threshold for antigen detection. Eur. J. Immunol. **33**, 1215–1223.
Raucher, D., and Sheetz, M.P. (1999). Characteristics of a membrane reservoir buffering membrane tension. Biophys. J. **77**, 1992–2002.
Raucher, D., and Sheetz, M.P. (2000). Cell spreading and lamellipodial extension rate is regulated by membrane tension. J. Cell Biol. **148**, 127 LP–136.
Rossy, J., Laufer, J.M., and Legler, D.F. (2018). Role of mechanotransduction and tension in T cell function. Front. Immunol. **9**, 2638.
Roumier, A., Olivo-Marin, J.C., Arpin, M., Michel, F., Martin, M., Mangeat, P., Acuto, O., Dautry-Varsat, A., and Alcover, A. (2001). The membrane-microfilament linker ezrin is involved in the formation of the immunological synapse and in T cell activation. Immunity **15**, 715–728.
Rouven Brückner, B., Pietuch, A., Nehls, S., Rother, J., and Janshoff, A. (2015). Ezrin is a major regulator of membrane tension in epithelial cells. Sci. Rep. **5**, 1–16.
Saitakis, M., Dogniaux, S., Goudot, C., Bufi, N., Asnacios, S., Maurin, M., Randriamampita, C., Asnacios, A., and Hivroz, C. (2017). Different TCR-induced T lymphocyte responses are potentiated by stiffness with variable sensitivity. Elife **6**, e23190.
Sawicka, A., Babataheri, A., Dogniaux, S., Barakat, A.I., Gonzalez-Rodriguez, D., Hivroz, C., and Husson, J. (2017).

 

Micropipette force probe to quantify single-cell force generation: application to T-cell activation. Mol. Biol. Cell **28**, 3229–3239.
Scholer, A., Hugues, S., Boissonnas, A., Fetler, L., and Amigorena, S. (2008). Intercellular adhesion molecule-1-dependent stable interactions between T cells and dendritic cells determine CD8+ T cell memory. Immunity **28**, 258–270.
Sheetz, M.P. (2001). Cell control by membrane-cytoskeleton adhesion. Nat. Rev. Mol. Cell Biol. **2**, 392–396.
Sheetz, M.P., and Dai, J. (1996). Modulation of membrane dynamics and cell motility by membrane tension. Trends Cell Biol. **6**, 85–89.
Shi, X., Bi, Y., Yang, W., Guo, X., Jiang, Y., Wan, C., Li, L., Bai, Y., Guo, J., Wang, Y., Xu, C. (2013). Ca 2+ regulates T-cell receptor activation by modulating the charge property of lipids. Nature **493**, 111–115.
Shi, Z., Graber, Z.T., Baumgart, T., Stone, H.A., and Cohen, A.E. (2018). Cell membranes resist flow. Cell **175**, 1769–1779.e13.
Stoll, S., Delon, J., Brotz, T.M., and Germain, R.N. (2002). Dynamic imaging of T cell-dendritic cell interactions in lymph nodes. Science **296**, 1873–1876.
Strale, P.O., Azioune, A., Bugnicourt, G., Lecomte, Y., Chahid, M., and Studer, V. (2016). Multiprotein printing by light-induced molecular adsorption. Adv. Mater. **28**, 2024–2029.
Swaminathan, V., Mythreye, K., Tim O'Brien, E., Berchuck, A., Blobe, G.C., and Superfine, R. (2011). Mechanical Stiffness grades metastatic potential in patient tumor cells and in cancer cell lines. Cancer Res. **71**, 5075–5080.
Tadokoro, C.E., Shakhar, G., Shen, S., Ding, Y., Lino, A.C., Maraver, A., Lafaille, J.J., and Dustin, M.L. (2006). Regulatory T cells inhibit stable contacts between CD4+ T cells and dendritic cells in vivo. J. Exp. Med. **203**, 505 LP–511.
Tamzalit, F., Wang, M.S., Jin, W., Tello-Lafoz, M., Boyko, V., Heddleston, J.M., Black, C.T., Kam, L.C., and Huse, M. (2019). Interfacial actin protrusions mechanically enhance killing by cytotoxic T cells. Sci. Immunol. **4**, eaav5445.
Tang, Q., Adams, J.Y., Tooley, A.J., Bi, M., Fife, B.T., Serra, P., Santamaria, P., Locksley, R.M., Krummel, M.F., and Bluestone, J.A. (2006). Visualizing regulatory T cell control of autoimmune responses in nonobese diabetic mice. Nat. Immunol. **7**, 83–92.
Théry, M. (2010). Micropatterning as a tool to decipher cell morphogenesis and functions. J. Cell Sci. **123**, 4201–4213.
Vaeth, M., Yang, J., Yamashita, M., Zee, I., Eckstein, M., Knosp, C., Kaufmann, U., Jani, P.K., Lacruz, R.S., Flockerzi, V., Kacskovics, I., Prakriya, M., Feske, S. (2017). ORAI2 modulates store-operated calcium entry and T cell-mediated immunity. Nat. Commun. **8**, 14714.
Varma, R., Campi, G., Yokosuka, T., Saito, T., and Dustin, M.L. (2006). T cell receptor-proximal signals are sustained in peripheral microclusters and terminated in the central supramolecular activation cluster. Immunity **25**, 117–127.
Vicente-Manzanares, M., Ma, X., Adelstein, R.S., and Horwitz, A.R. (2009). Non-muscle myosin II takes centre stage in cell adhesion and migration. Nat. Rev. Mol. Cell Biol. **10**, 778–790.
Wahl, A., Dinet, C., Dillard, P., Nassereddine, A., Puech, P.H., Limozin, L., and Sengupta, K. (2019). Biphasic mechanosensitivity of T cell receptor-mediated spreading of lymphocytes. Proc. Natl. Acad. Sci. U.S.A. **116**, 5908–5913.
Wei, C., Wang, X., Chen, M., Ouyang, K., Song, L.S., and Cheng, H. (2009). Calcium flickers steer cell migration. Nature **457**, 901–905.
Wenning, A.S., Neblung, K., Strauß, B., Wolfs, M.J., Sappok, A., Hoth, M., and Schwarz, E.C. (2011). TRP expression pattern and the functional importance of TRPC3 in primary human T-cells. Biochim. Biophys. Acta Mol. Cell Res. **1813**, 412–423.
Wolf, I.M.A., Diercks, B.-P., Gattkowski, E., Czarniak, F., Kempski, J., Werner, R., Schetelig, D., Mittrücker, H.-W., Schumacher, V., von Osten, M., Lodygin, D., Flügel, A., Fliegert, R., Guse, A.H. (2015). Frontrunners of T cell activation: Initial, localized Ca2+ signals mediated by NAADP and the type 1 ryanodine receptor. Sci. Signal. **8**, ra102 LP–ra102.
Wu, J., Goyal, R., and Grandl, J. (2016). Localized force application reveals mechanically sensitive domains of Piezo1. Nat. Commun. **7**, 1–10.
Wu, M.M., Buchanan, J.A., Luik, R.M., and Lewis, R.S. (2006). Ca2+ store depletion causes STIM1 to accumulate in ER regions closely associated with the plasma membrane. J. Cell Biol. **174**, 803–813.
Xu, W., Mezencev, R., Kim, B., Wang, L., McDonald, J., and Sulchek, T. (2012). Cell stiffness is a biomarker of the metastatic potential of ovarian cancer cells. PLoS One **7**, e46609.
Yang, H., Gou, X., Wang, Y., Fahmy, T.M., Leung, A.Y.-H., Lu, J., and Sun, D. (2015). A dynamic model of chemoattractant-induced cell migration. Biophys. J. **108**, 1645–1651.

Received: 21 November 2019; Revised: 19 March 2020; Accepted: 29 March 2020; Accepted article online: 10 April 2020